

https://dspace.org/

Evidence of basin partitioning in the ue7 and upper Elsburg massives of the Turffontein subgroup, Witwatersrand basin (South Africa)

Obermeyer, Paul Grant

2022
https://hdl.handle.net/10539/34805

Downloaded from a DSpace repository. https://dspace.org/

EVIDENCE OF BASIN PARTITIONING IN THE UE7 AND UPPER ELSBURG MASSIVES OF THE TURFFONTEIN SUBGROUP, WITWATERSRAND BASIN (SOUTH AFRICA)

Paul Grant Obermeyer

A dissertation submitted to the Faculty of Science, University of the Witwatersrand;
in fulfilment of the requirements for the degree of
Master of Science.



UNIVERSITY OF THE
WITWATERSRAND,
JOHANNESBURG

School of Geosciences

University of the Witwatersrand

Johannesburg, South Africa

November 2020

DECLARATION

I declare that this Dissertation is my own, unaided work. It is being submitted for the Degree of Master of Science at the University of the Witwatersrand, Johannesburg. It has not been submitted before for any degree or examination at any other University.

_____

Paul Grant Obermeyer

_____day of _____20_____ in Johannesburg

DEDICATION

I would like to thank Sandra (my wife), Philip (my son) and my mother (Maureen) for their undying support and encouragement in completing this dissertation and for believing in me. I would also like thank VBKOM Consulting Engineers (Pty) Ltd for their support and the leave days allowed at short notice so I could submit my dissertation.

I would like to thank Mr Dirk Muntingh for his belief in my ability and for his mentorship and support over the years. I thank Prof. Roger Gibson and Dr Zubair Jinnah for their guidance, patience, and encouragement in completing this work.

I would also like to thank Gold Fields Limited and South Deep Gold Mine for allowing me to conduct and publish this study. I especially would like to thank Mr Tim Rowland (Gold Fields Vice-President Geosciences and Planning) for his support in this regard.

I dedicate this work to all geologists - past and present - who have had (and will have) the privilege to work on the South Deep orebody over the years, whose data collection has been (and will be) used to unravel the geological secrets of this amazing orebody.

ABSTRACT

The South Deep Gold Mine (SDGM), currently owned by Gold Fields, is located along the eastern edge of the West Rand Goldfield on the northern margin of the Witwatersrand Basin. It mines the Ventersdorp Contact Reef (VCR) as well as the "Upper Elsburg" conglomerates, comprising Elsburg Massives of the Modderfontein Member and the UE7, or Individual Reefs, of the underlying Waterpan Member of the Mondeor Formation (Turffontein Subgoup, Central Rand Group). The Upper Elsburgs are preserved as a rotating onlap stacked unconformity structure and sub-outcrop on a NNE trend against the overlying VCR. The Upper Elsburgs are unusual owing to their massive and thick conglomeratic beds with basal unconformities alternating with overlying quartzites, which contrasts with the traditionally mined thin, unconformity-bound, conglomerate reefs elsewhere in the Witwatersrand Basin. Limited regional palaeo-current data suggests SE to SSE sediment transport.

This study investigates whether stratigraphic and sedimentological evidence exists at SDGM that supports the existence of syn-depositional strike-slip tectonics associated with multiple E-W wrench faults transecting the ore resource. A total of 4502 drillholes representing some 18731 stacked reef intercepts were utilised to model corrected bed height, percentage conglomerate, and average and maximum clast size for each of the 16 modelled reef beds. The dataset covers an area of ~10 km² along a sub-outcrop strike length of ~6.5 km.

Based on mapped wrench faults, six fault blocks are identified across the study volume. Sedimentological-stratigraphic data were palinspastically reconstructed to remove post-VCR displacement. Colour-coded contour maps were generated from the palinspastically reconstructed data to graphically present each parameter for each bed for interpretation. Visual interpretation of possible data trends was conducted for comparison with the available regional data.

The overwhelming trend for all parameters across all blocks is NNW-SSE except in the northern-most block where trends for all parameters for some of the beds are NW-SE. During early deposition of the Elsburgs "C" Band of the UE7 Zone of the Mondeor Formation all blocks show a NNW-SSE trend, while during later UE7 Zone to early Elsburg Massives deposition, the northernmost block exhibits a predominant NW-SE trend which later reverted to NNW-SSE during …. deposition.

Bed height - the largest dataset - presented the best modelled parameter, while maximum clast size, though empirical, presented the poorest results owing to the limited data available.

Evidence for repetitive discontinuity in data for successive beds occurring across the wrench faults is interpreted as indicating syn-sedimentary strike-slip displacement on these structures. Each of the wrench faults presents a different syn-sedimentary history. The southern two wrench faults (90L Wrench and Fargo Wrench) appear to have been active throughout most of the deposition of the Upper Elsburgs, while the P1 Wrench started syn-sedimentary dislocation from early Elsburg Massives deposition onwards. The P2 Wrench appears to have been only sporadically active during deposition of the Elsburgs "C" Band times but became more consistently active throughout deposition of the Elsburg Massives.

The rotating onlap stratigraphic pattern at SDGM is interpreted as a single progressive unconformity or syn-tectonic cumulative wedge system attached to a tilted depositional surface linked to an uplifting structure, resulting

in laterally extensive aprons of alluvial sediment on the upper surface of the orogenic wedge during periods of non-deformation and possibly relate to a wedge-top depozone close to the orogenic front. Evidence for broadly E-W compressive tectonic stresses prevailing during Central Rand Group and VCR times is seen in the Tandeka Thrust located in the footwall of the West Rand Fault to the west of SDGM. The rotating onlap geometry of the Upper Elsburgs on SDGM, requires syn-sedimentary uplift in the hinterland (towards the west) and localised subsidence to the east to accommodate the active sedimentation within an overall compressive tectonic environment. The SDGM wrench fault system is interpreted as a network of right-lateral R' and X shears within the larger orogenic front fault system.

TABLE OF CONTENTS

CHAPTER 1: INTRODUCTION 1

1.1 Regional Context 1
1.1.1 Location of the Study Area 3
1.2 Aims and Hypothesis 3
1.2.1 Background to the Study 3
1.2.2 Hypothesis of the Study 7
1.2.3 Aims of the Study 7
1.2.4 Attribution of Work 8

CHAPTER 2: LITERATURE REVIEW 9

2.1 Regional Geology 9
2.1.1 Geological Setting of the Witwatersrand Basin 9
2.1.2 Stratigraphy of the Witwatersrand Basin 11
2.1.2.1 West Rand Group 13
2.1.2.2 Central Rand Group 13
2.2 Geology of the Study Area 14
2.2.1 Structure of South Deep Gold Mine 17
2.2.2 Detailed Stratigraphy of the UE7 and Upper Elsburg Massives on SDGM 19
2.2.3 Palaeo-current Data and Sedimentological Transport Directions on SDGM 23
2.3 Development of Geological Modelling at SDGM 24
2.3.1 Stratigraphic and Sedimentological Modelling Advancements at SDGM 24
2.3.2 Hybrid Geological Structure Plan and Model Generation (Pre-2007) 29
2.4 Depositional Environments and Strato-tectonic Models 34
2.4.1 Basin-edge Concept Model 34
2.4.2 Foreland Basin Model 35
2.4.3 Multiple Basin or Wilson Cycle Model 38
2.4.4 The Witwatersrand Basin – A Successor Basin 42
2.4.5 Witwatersrand Foreland Basin Partitioning 42
2.4.6 Wedge-top Depozone 47
2.4.7 Syn-sedimentary Tectonics, Post-tectonic Features and Timing 49
2.4.8 Further Enhancements 52
2.4.9 Growth Structures related to Blind Thrusting in Foreland Basins 53
2.4.10 Synopsis of Development of Strato-tectonic Models 55

CHAPTER 3: METHODOLOGY 57

3.1 Introduction, Background and Personal Involvement 57
3.1.1 Sedimentological Data Collection, Processing and Analysis 58
3.1.1.1 Bed Height 60
3.1.1.2 Percentage Conglomerate 65
3.1.1.3 Average and Maximum Clast Size 65
3.1.1.4 Palinspastic Reconstruction 65

CHAPTER 4: RESULTS 74

4.1 Dataset and Presentation 74
4.2 Stratigraphic Beds 76
4.2.1 ECBA 76
4.2.1.1 ECBA Bed Height 76
4.2.1.2 ECBA Percentage Conglomerate 76
4.2.1.3 ECBA Average and Maximum Clast Size 76
4.2.1.4 ECBA Detailed Plots 82
4.2.2 ECB 86

4.2.2.1 ECB Bed Height 86
4.2.2.2 ECB Percentage Conglomerate 86
4.2.2.3 ECB Average and Maximum Clast Size 86
4.2.2.4 ECB Detailed Plots 88
4.2.3 ECT 92
4.2.3.1 ECT Bed Height 92
4.2.3.2 ECT Percentage Conglomerate 92
4.2.3.3 ECT Average and Maximum Clast Size 92
4.2.3.4 ECT Detailed Plots 94
4.2.4 MAC 98
4.2.4.1 MAC Bed Height 98
4.2.4.2 MAC Percentage Conglomerate 98
4.2.4.3 MAC Average and Maximum Clast Size 98
4.2.4.4 MAC Detailed Plots 100
4.2.5 MBB 104
4.2.5.1 MBB Bed Height 104
4.2.5.2 MBB Percentage Conglomerate 104
4.2.5.3 MBB Average and Maximum Clast Size 104
4.2.5.4 MBB Detailed Plots 106
4.2.6 MBT 110
4.2.6.1 MBT Bed Height 110
4.2.6.2 MBT Percentage Conglomerate 110
4.2.6.3 MBT Average and Maximum Clast Size 110
4.2.6.4 MBT Detailed Plots 112
4.3 Consolidated Results Summaries 116

CHAPTER 5: DISCUSSION 118

5.1 Discussion Outline 118
5.2 Parameters, Data Reliability and Rules of Application 119
5.2.1 Bed height 119
5.2.2 Percentage Conglomerate 120
5.2.3 Average and Maximum Clast Size 120
5.3 Possible Sediment Transport Directions 121
5.4 SDGM General Interpretations and Observations 121
5.4.1 Bed Height Data Interpretation 123
5.4.2 Percentage Conglomerate Data Interpretation 125
5.4.3 Average and Maximum Clast Size 127
5.5 SDGM Structures 128
5.5.1 P1 Wrench 133
5.5.2 P2 Wrench 133
5.5.3 90L Wrench 133
5.5.4 Fargo Wrench 133
5.6 Applicability of Methodology to Other Areas 133
5.7 SDGM Regional Context and Interpretation 134
5.8 Conclusions and Recommendations 138

REFERENCES 140

APPENDIX 1 147

APPENDIX 2 159

a) ECBAQ 159
i) ECBAQ Bed Height 159
ii) ECBAQ Percentage Conglomerate 159
iii) ECBAQ Average and Maximum Clast Size 159
iv) ECBAQ Detailed Plots 165

b) ECB 169
i) ECB Bed Height 169
ii) ECB Percentage Conglomerate 170
iii) ECB Average and Maximum Clast Size 171
c) ECBQ 173
i) ECBQ Bed Height 173
ii) ECBQ Percentage Conglomerate 173
iii) ECBQ Average and Maximum Clast Size 173
iv) ECBQ Detailed Plots 179
d) ECMC 183
i) ECMC Bed Height 183
ii) ECMC Percentage Conglomerate 183
iii) ECMC Average and Maximum Clast Size 183
iv) ECMC Detailed Plots 189
e) ECMQ 193
i) ECMQ Bed Height 193
ii) ECMQ Percentage Conglomerate 193
iii) ECMQ Average and Maximum Clast Size 193
iv) ECMQ Detailed Plots 199
f) ECT 203
i) ECT Bed Height 203
ii) ECT Percentage Conglomerate 204
iii) ECT Average and Maximum Clast Size 205
g) ED 207
i) ED Bed Height 207
iv) ED Percentage Conglomerate 207
v) ED Average and Maximum Clast Size 207
vi) ED Detailed Plots 214
h) MAC 218
i) MAC Bed Height 218
ii) MAC Percentage Conglomerate 219
iii) MAC Average and Maximum Clast Size 220
i) MAD 222
i) MAD Bed Height 222
ii) MAD Percentage Conglomerate 222
iii) MAD Average and Maximum Clast Size 222
iv) MAD Detailed Plots 228
j) MIB 232
i) MIB Bed Height 232
ii) MIB Percentage Conglomerate 232
iii) MIB Average and Maximum Clast Size 232
iv) MIB Detailed Plots 238
k) MIT 242
l) MIT Bed Height 242
ii) MIT Percentage Conglomerate 242
iii) MIT Average and Maximum Clast Size 242
iv) MIT Detailed Plots 248
i) MIQ 252
i) MIQ Bed Height 252
ii) MIQ Percentage Conglomerate 252
iii) MIQ Average and Maximum Clast Size 252
iv) MIQ Detailed Plots 258
j) MBB 262
i) MBB Bed Height 262
ii) MBB Percentage Conglomerate 263
iii) MBB Average and Maximum Clast Size 264
k) MBT 266
i) MBT Bed Height 266

ii) MBT Percentage Conglomerate....267
iii) MBT Average and Maximum Clast Size....268
l) VCR....270
i) VCR Bed Height....270
ii) VCR Percentage Conglomerate....270
iii) VCR Average and Maximum Clast Size....270
iv) VCR Detailed Plots....276

List of Figures

Figure 1: Geological map of the Witwatersrand Basin, with younger cover sequences removed, depicting the location of the goldfields and the study area (modified after Tucker et al., 2016 after Frimmel et al., 2005). 1
Figure 2: The location of SDGM and its shafts in the West Rand Goldfield (adapted from Gold Fields, 2009 and Gold Fields, 2011). 3
Figure 3: The geology of the West Rand Goldfield after Tucker and Viljoen (1986) and McCarthy (2006), depicting the major faults and main reef sub-outcrops against the VCR. 4
Figure 4: Map of SDGM showing the major structural features and identified wrench fault blocks discussed in this study. Black dots indicate drillhole collar locations. 6
Figure 5: Surface and sub-surface distribution of the main Archaean stratigraphic units of the Kaapvaal Craton and the Witwatersrand Basin. Stars indicate drilled positions of Witwatersrand-equivalent rocks, while the red star indicates the approximate position of South Deep Gold Mine (modified after Frimmel and Hennigh, 2015; Frimmel, 2019). 9
Figure 6: Simplified geological map (with Ventersdorp and Karoo Supergroup stratigraphy removed) showing the geometric relationship between the Witwatersrand Basin and the Vredefort impact structure. The approximate position of SDGM indicated with the red star (modified after McCarthy, 2006; Tucker, 2016) 10
Figure 7: Stratigraphy of the Witwatersrand Supergroup and attempted correlation between the various goldfields with the West Rand goldfield stratigraphic column highlighted in the red stippled block. (modified after Frimmel, 2019; modified after McCarthy, 2006). 12
Figure 8: Stratigraphy of SDGM, as proposed by Obermeyer (2005) (modified after Tucker and Viljoen, 1986; Arthur, 1990 and SACS, 2006), related to the general stratigraphy of the Central Rand Group within the Witwatersrand Supergroup (SACS, 2006) (permission granted by Goldfields to reproduce). 15
Figure 9: Mine plan of SDGM showing the main geological and mining features including the main wrench structures (modified after Gold Fields, 2013). 17
Figure 10: The stratigraphy of the UE7 and Elsburg Massives at SDGM (permission granted by Goldfields to reproduce). 19
Figure 11: An approximate scaled stratigraphic column for SDGM with lithological expression and typical sedimentary descriptions for each bed (modified after Arthur, 1990). 22
Figure 12: Compiled palaeo-current data for various reefs mined in the West Rand and West Wits goldfields. Palaeo-current direction for the VCR in the South Deep area is indicated to be NW-to-SE to NNW-to-SSE. (modified after Robb et al. (1998) after Vermaakt and Chunnett, 1994). 23
Figure 13: A section of the South Deep Shareholders Plan (modified from Goldfields, 2013) depicting the major wrench structures and the VCR channel edges (trending NW-SE) identified by the stoped-out mine workings. 24
Figure 14: Oblique 3D view of the 2001 SDGM geological wireframe model (permission granted by Goldfields to reproduce). 25
Figure 15: The 2005 SDGM modelled unconformities with the SLC zone (modified after Muntingh et al., 2005). 26
Figure 16: The historical development of geological modelling at SDGM (permission granted by Goldfields to reproduce) 27
Figure 17: Schematic west to east section through the Upper Elsburgs at SDGM presenting their stratigraphic relationships and the stratigraphy as it is currently modelled (Obermeyer, 2005). The black vertical lines represent mining cross-cut positions relative to the stratigraphic make-up (permission granted by Goldfields to reproduce). 28
Figure 18: The advancements in modelled stratigraphic detail at SDGM over time (Obermeyer, 2005) (permission granted by Goldfields to reproduce). 29

Figure 19: Geological boundaries and modelling of working areas (2D) only for SDGM pre-2007 (modified after Obermeyer, 2004) (permission granted by Goldfields to reproduce). 30
Figure 20: A pictorial representation of the basin-edge concept model (modified after Brock and Pretorius, 1964). 35
Figure 21: Interpretation of the Witwatersrand Basin as a foreland basin on the Kaapvaal Craton related to orogenic collision along the Limpopo Mobile Belt. Witwatersrand basin highlighted in red shading. (modified after Burke et al., 1986). 37
Figure 22: Wilson Cycle model for the development of the Dominion, Witwatersrand and Ventersdorp basins (modified after Stanistreet and McCarthy, 1991; McCarthy, 2006)..... 39
Figure 23: The structural fault zones or lineaments affecting Witwatersrand sedimentation, defined by edges of basement fault blocks. The SDGM lies in the western part of Block 6 (modified after Stanistreet and McCarthy, 1991; McCarthy 1994). 40
Figure 24: Interpretation of tectonic setting of the Witwatersrand Basin and related basins of the Kaapvaal Craton adapted from Catuneanu (2001). 43
Figure 25: Flexural profile of a foreland system (modified after Catuneanu, 2001; modified from Beaumont et al., 1993; Crampton and Allen, 1995; DeCelles and Giles, 1996). 'V' is the progradation rate of the orogenic load and the associated foreland system. 44
Figure 26: Partitioning of the Witwatersrand and Pongola basins into foredeep, forebulge and backbulge flexural provinces (modified after Catuneanu 2001). 45
Figure 27: The Witwatersrand foredeep prior to Ventersdorp deformation; CRG = Central Rand Group, WRG = West Rand Group (modified after Catuneanu, 2001)..... 46
Figure 28: a) Schematic geometry of a traditional foreland basin model in section. b) The wedge-top depozone foreland basin model geometry as proposed by DeCelles and Giles (1996) (modified after DeCelles and Giles, 1996). 47
Figure 29: Schematic distribution of the sedimentary circulation in piggyback basins towards the foredeep (Suriano et al., 2015). 48
Figure 30: Schematic events chart for depositional and tectonic events for the Witwatersrand Basin region (modified after Dankert and Hein, 2010) with the relative position of the Turffontein Subgroup highlighted in red. 50
Figure 31: Interpreted seismic section through the Bank Fault on Western Ultra Deep Levels (modified after Gibson et al., 2000). 51
Figure 32: Interpreted seismic section across the listric West Rand Fault, showing the steeply dipping hanging wall (Kloof Block) and the blind Tandeka Thrust (modified after Manzi, 2013). 52
Figure 33: Simplified geometry of progressive unconformities. (a) Offlap-type progressive unconformity and (b) onlap-type progressive unconformity. “T” is the tectonic vertical uplift rate, and “S” is the deposition rate (modified from Riba, 1976; Ortner et al., 2016, Shi et al., 2019). 54
Figure 34: Interpreted line drawing sections of seismic sections from the Didi Shiraki piggy-back Basin, Georgia depicting typical extents of unconformities away from the zone of uplift and stratigraphic truncation of the onlapping strata (Alania et al., 2016)..... 55
Figure 35: Historical archived split surface drillhole core from drillhole MD38 (modified after Muntingh et al., 2005) (permission granted by Goldfields to reproduce). 59
Figure 36: a) Oblique view of a section of the 3D model of the Waterpan (UE7) and Modderfontein (Elsburg Massives) sedimentary wedge and the overlying VCR, dipping towards the south. B) A horizontal section view through the Waterpan/Modderfontein 3D model presenting the complicated strike relationships. C) An interpreted bedding strike from the horizontal wedge slice depicted in b), showing the variation in strike at sub-outcrop and the near E-W strike attained towards the east. 61
Figure 37: Variation in depth and reef strike for the ECB at SDGM. 62
Figure 38: A cumulative thickness plot of the Upper Elsburg reef package for the modelled portion of the SDGM within the study area 63

Figure 39: a) Standard trigonometric functions used to calculate vertical bed height (bv_1 or bv_1). B) Trigonometric functions used to convert vertical bed height to true bed height (b_t) at a dip of 17°..... 64
Figure 40: Fault blocks with original dataset before palinspastic reconstruction. Magnitude and direction of the palinspastic reconstruction vectors are represented by blue arrows. 66
Figure 41: Demonstration of palinspastic movement of the Modderfontein/Waterpan Sub-outcrop and drillhole data points for Block 4 relative to Block 3. 67
Figure 42: Rough contours for the ECB bed height in SDGM generated in Datamine Studio RM™ prior to palinspastic reconstruction. 68
Figure 43: Rough contours for the ECB bed height with the automatically generated wireframe. 69
Figure 44: A colour coded block model presenting bed height for the ECB. 70
Figure 45: a) A coloured contour plan of the ECB bed height using original uncorrected data. B) A coloured contour plan of the ECB bed height using palinspastically corrected drillhole data points... 71
Figure 46: a) Non-palinspastically reconstructed bed height data plot for the ECBA. B) Palinspastically reconstructed bed height dataset for the ECBA. 72
Figure 47: Model showing the main architectural elements of the multistage development of Witwatersrand palaeoplacers (modified after Tucker (1980) and Tucker et al. (2016)). 73
Figure 48: Palinspastic bed height reconstruction for ECBA. 77
Figure 49: Palinspastic percentage conglomerate reconstruction for ECBA. 78
Figure 50: Palinspastic average clast size reconstruction for ECBA. 79
Figure 51: Palinspastic maximum clast size construction for ECBA. 80
Figure 52: Palinspastic Reconstruction for the ECBA – All Parameters 81
Figure 53: Enlarged Block 2 palinspastic reconstruction for a) bed height for ECBA and b) for percentage conglomerate for ECBA. Yellow polygon in both a) and b) denotes zone of low bed height and high percentage conglomerate terminated on P2 Wrench. Black line indicates significant change in bed height. 83
Figure 54: Enlarged Block 3 palinspastic reconstruction for a) bed height for ECBA and b) for percentage conglomerate for ECBA. Pink polygon in a) and b) denotes area of low bed height and high percentage conglomerate. Black ellipses highlight highly variable alternating nodes for both bed height and percentage conglomerate along or adjacent to the 90L Wrench strike. 84
Figure 55: Enlarged Block 4 palinspastic reconstruction for a) bed height for ECBA and b) for percentage conglomerate for ECBA. Black dashed in line in a) and b) denotes possible offsets of a zone of higher bed height. 85
Figure 56: Palinspastic Reconstruction for the ECB – All Parameters 87
Figure 57: Enlarged Block 2 palinspastic reconstruction for a) bed height for ECB and b) for percentage conglomerate for ECB. Yellow polygon in a) and b) indicates zone of low bed height and variable percentage conglomerate. 89
Figure 58: Enlarged Block 3 palinspastic reconstruction for a) bed height for ECB and b) for percentage conglomerate for ECB. Yellow ellipses in b) indicate nodes of variable and alternating percentage conglomerate occurring up against or adjacent to geological structures. 90
Figure 59: Enlarged Block 4 palinspastic reconstruction for a) bed height for ECB and b) for percentage conglomerate for ECB. Yellow ellipses in a) and b) indicate nodes of variable and alternating percentage conglomerate occurring up against or adjacent to geological structures. 91
Figure 60: Palinspastic Reconstruction for the ECT – All Parameters 93
Figure 61: Enlarged Block 2 palinspastic reconstruction for a) bed height for ECT and b) for percentage conglomerate for ECT. Black dashed lines in a) and b) indicated a higher bed height zone offset across P1 Wrench and P2 Wrench. Purple polygon in b) indicates zone of lower bed height with higher percentage conglomerate. 95

Figure 62: Enlarged Block 3 palinspastic reconstruction for a) bed height for ECT and b) for percentage conglomerate for ECT. Yellow ellipse in a) and b) indicate trends along the strike of P2 Wrench and 90L Wrench of alternating nodes of high and low percentage conglomerate. 96
Figure 63: Enlarged Block 4 palinspastic reconstruction for a) bed height for ECT and b) for percentage conglomerate for ECT. Yellow ellipses a) in b) indicate a trend along the strike of 90L Wrench and Fargo Wrench of rapidly alternating nodes of high and low percentage conglomerate and higher and lower bed height. 97
Figure 64: Palinspastic Reconstruction for the MAC – All Parameters 99
Figure 65: Enlarged Block 2 palinspastic reconstruction for a) bed height for MAC and b) for percentage conglomerate for MAC. 101
Figure 66: Enlarged Block 3 palinspastic reconstruction for a) bed height for MAC and b) for percentage conglomerate for MAC. 102
Figure 67: Enlarged Block 4 palinspastic reconstruction for a) bed height for MAC and b) for percentage conglomerate for MAC. 103
Figure 68: Palinspastic Reconstruction for the MBB – All Parameters 105
Figure 69: Enlarged Block 2 palinspastic reconstruction for a) bed height for MBB and b) for percentage conglomerate for MBB. 107
Figure 70: Enlarged Block 3 palinspastic reconstruction for a) bed height for MBB and b) for percentage conglomerate for MBB. 108
Figure 71: Enlarged Block 4 palinspastic reconstruction for a) bed height for MBB and b) for percentage conglomerate for MBB. 109
Figure 72: Palinspastic Reconstruction for the MBT – All Parameters 111
Figure 73: Enlarged Block 2 palinspastic reconstruction for a) bed height for MBT and b) for percentage conglomerate for MBT. 113
Figure 74: Enlarged Block 3 palinspastic reconstruction for a) bed height for MBT and b) for percentage conglomerate for MBT. 114
Figure 75: Enlarged Block 4 palinspastic reconstruction for a) bed height for MBT and b) for percentage conglomerate for MBT. 115
Figure 76: A comparison of bed height between a typical UE7 conglomeratic bed and a quartzitic bed showing the slow southward increase in bed height for the conglomeratic bed versus the slow southward decrease in bed height for a quartzitic bed. 124
Figure 77: A comparison of bed height between a typical UE7 conglomeratic bed and a quartzitic bed showing the slow southward increase in bed height for the conglomeratic bed versus the slow southward decrease in bed height for a quartzitic bed. 125
Figure 78: A comparison of percentage conglomerate between a typical UE7 conglomeratic bed and a quartzitic bed showing the slow southward increase in percentage conglomerate for both the conglomeratic bed and quartzitic bed. 126
Figure 79: A comparison of percentage conglomerate between a typical Massives conglomeratic bed and a quartzitic bed showing the two areas with increased percentage conglomerate (highlighted in the yellow polygons) just north of the P1 Wrench Fault and in the vicinity of the 90L Wrench and Fargo Wrench Fault combination. 127
Figure 80: Strain ellipse representing stresses and fracture patterns concurrent with deposition of the Central Rand Group and VCR related to recorded and projected geological structures on SDGM. The yellow arrow indicates the mean sedimentary trends observable in in the results. (Strain ellipse modified after Jackson and Hudec; 2017). 137
Figure 81: Typical borehole layout as sourced from a borehole layout file (Obermeyer, 2004). Blue arrows indicate planned borehole azimuths from a planned borehole collar position. Each label represents a borehole number and a planned dip (permission granted by Goldfields to reproduce). . 147

Figure 82: Borehole collars for each borehole are checked relative to survey elevations on plan (Obermeyer, 2004) (permission granted by Goldfields to reproduce). 148
Figure 83: An example of a) a geological mapping plan and a corresponding b) underground mapping report showing some inconsistency in transfer of data (Obermeyer, 2004) (permission granted by Goldfields to reproduce). 149
Figure 84: a) Measured and plotted reef strikes with peg elevations. b) Structure base plan with transferred reef strike and survey peg elevation data (Obermeyer, 2004b). 150
Figure 85: The strike of the reef contours was calculated as a set of simple 3-point problems, while neighbouring fault block contours were correlated by applying mapped throws to the bounding faults (Obermeyer, 2004) (permission granted by Goldfields to reproduce). 151
Figure 86: Vertical projection distances for structures and contours were calculated using the difference in elevations between the borehole intersections on the new plan and the base plan (modified from Obermeyer, 2004) (permission granted by Goldfields to reproduce). 152
Figure 87: The vertical projection distances, calculated from the boreholes were transferred to the new plan, from the borehole plan as points. These points were triangulated and isolines, or vertical isopachs, were constructed (Obermeyer, 2004) (permission granted by Goldfields to reproduce). ... 153
Figure 88: The vertical isopachs gave vertical projection distances between the base plan and the next projected plan. The horizontal off-sets of the faults were calculated by means of trigonometry and the resultant trace line plotted (modified after Obermeyer, 2004) (permission granted by Goldfields to reproduce). 154
Figure 89: Projection and construction methodology of overlying or underlying beds to ensure accurate volumetrics (adapted from Obermeyer, 2004) (permission granted by Goldfields to reproduce). 155
Figure 90: Identification and interpretation of wrench faults at SDGM (modified after Obermeyer, 2004) (permission granted by Goldfields to reproduce). 156
Figure 91: Typical historical SDGM handwritten drillhole lithology log (Obermeyer, 2004) (permission granted by Goldfields to reproduce). 157
Figure 92: a) Modified Udden-Wentworth scale to better differentiate coarse sediment (modified from Blair and McPherson (1999). b) A reconstructed modified Udden-Wentworth scale as historically interpreted at SDGM for core logging. 158
Figure 93: Palinspastic bed height reconstruction for ECBAQ. 160
Figure 94: Palinspastic percentage conglomerate reconstruction for ECBAQ. 161
Figure 95: Palinspastic average clast size reconstruction for ECBAQ. 162
Figure 96: Palinspastic maximum clast size reconstruction for ECBAQ. 163
Figure 97: Palinspastic Reconstruction for the ECBAQ - All Parameters 164
Figure 98: Enlarged Block 2 palinspastic reconstruction for a) bed height for ECBAQ and b) for percentage conglomerate for ECBAQ. Black dashed line in as and b) indicates change in bed height. Yellow ellipse in a) and b) indicates a trend along the strike of 90L Wrench of rapidly alternating nodes of high and low percentage conglomerate. 166
Figure 99: Enlarged Block 3 palinspastic reconstruction for a) bed height for ECBAQ and b) for percentage conglomerate for ECBAQ. Red polygons in a) and b) indicate a zone of high bed height with low percentage conglomerate. 167
Figure 100: Enlarged Block 4 palinspastic reconstruction for a) bed height for ECBAQ and b) for percentage conglomerate for ECBAQ. Black dashed line in a) indicates possible offset of zone of higher bed height. 168
Figure 101: Palinspastic bed height reconstruction for ECB. 169
Figure 102: Palinspastic percentage conglomerate reconstruction for ECB. 170
Figure 103: Palinspastic average clast size reconstruction for ECB. 171
Figure 104: Palinspastic maximum clast size reconstruction for ECB. 172

Figure 105: Palinspastic bed height reconstruction for ECBQ. 174
Figure 106: Palinspastic percentage conglomerate reconstruction for ECBQ. 175
Figure 107: Palinspastic average clast size reconstruction for ECBQ. 176
Figure 108: Palinspastic maximum clast size reconstruction for ECBQ. 177
Figure 109: Palinspastic Reconstruction for the ECBQ - All Parameters 178
Figure 110: Enlarged Block 2 palinspastic reconstruction for a) bed height for ECBQ and b) for percentage conglomerate for ECBQ. Yellow polygon in a) and b) indicate a zone of lower bed height terminating on P2 Wrench Fault. 180
Figure 111: Enlarged Block 3 palinspastic reconstruction for a) bed height for ECBQ and b) for percentage conglomerate for ECBQ. Yellow line in a) and b) indicates a trend of lower bed height east of sub-outcrop with low percentage conglomerate. The yellow ellipse in b) indicates a trend along the strike of 90L Wrench of rapidly alternating nodes of high and low percentage conglomerate. 181
Figure 112: Enlarged Block 4 palinspastic reconstruction for a) bed height for ECBQ and b) for percentage conglomerate for ECBQ. Black line in a) indicates western limit to zone of higher bed height with no dislocation. Yellow ellipses in b) indicate a trend along the strike of 90L Wrench and Fargo Wrench of rapidly alternating nodes of high and low percentage conglomerate 182
Figure 113: Palinspastic bed height reconstruction for ECMC. 184
Figure 114: Palinspastic percentage conglomerate reconstruction for ECMC. 185
Figure 115: Palinspastic average clast size reconstruction for ECMC. 186
Figure 116: Palinspastic maximum clast size reconstruction for ECMC 187
Figure 117: Palinspastic Reconstruction for the ECMC - All Parameters 188
Figure 118: Enlarged Block 2 palinspastic reconstruction for a) bed height for ECMC and b) for percentage conglomerate for ECMC. Black dashed line in a) and b) indicates a change in bed height offset by P1 Wrench and P2 WrenchesWrench. The yellow polygon in a) and b) presents a zone of low bed height and high percentage conglomerate. 190
Figure 119: Enlarged Block 3 palinspastic reconstruction for a) bed height for ECMC and b) for percentage conglomerate for ECMC. Yellow ellipses in a) and b) indicate a trend along the strike of P2 Wrench and 90L WrenchesWrench of rapidly alternating nodes of high and low percentage conglomerate. 191
Figure 120: Enlarged Block 4 palinspastic reconstruction for a) bed height for ECMC and b) for percentage conglomerate for ECMC. Yellow polygon in a) and b) indicates zone of variable bed height and high percentage conglomerate. Yellow ellipse in b) indicates a trend along the strike of 90L Wrench of rapidly alternating nodes of high and low percentage conglomerate. 192
Figure 121: Palinspastic bed height reconstruction for ECMQ. 194
Figure 122: Palinspastic percentage conglomerate reconstruction for ECMQ. 195
Figure 123: Palinspastic average clast size reconstruction for ECMQ. 196
Figure 124: Palinspastic maximum clast size reconstruction for ECMQ. 197
Figure 125: Palinspastic Reconstruction for the ECMQ - All Parameters 198
Figure 126: Enlarged Block 2 palinspastic reconstruction for a) bed height for ECMQ and b) for percentage conglomerate for ECMQ. Black dashed line in a) and b) indicate a zone of slightly increased bed height corresponding to higher percentage conglomerate, offset by P2 Wrench. Yellow polygon indicates lower bed height zone with higher percentage conglomerate terminated against P1 Wrench. 200
Figure 127: Enlarged Block 3 palinspastic reconstruction for a) bed height for ECMQ and b) for percentage conglomerate for ECMQ. Yellow ellipses in a) indicate a trend along the strike of P2 Wrench and 90L Wrench of rapidly alternating nodes of high and low bed height. 201
Figure 128: Enlarged Block 4 palinspastic reconstruction for a) bed height for ECMQ and b) for percentage conglomerate for ECMQ. Black dashed line in a) and b) indicate a change in bed height offset by the 90L Wrench and Fargo WrenchesWrench. Yellow ellipse in a) indicates a trend along

the strike of 90L Wrench of rapidly alternating nodes of higher and lower percentage conglomerate. 202
Figure 129: Palinspastic bed height reconstruction for ECT. 203
Figure 130: Palinspastic percentage conglomerate reconstruction for ECT. 204
Figure 131: Palinspastic average clast size reconstruction for ECT. 205
Figure 132: Palinspastic maximum clast size reconstruction for ECT. 206
Figure 133: Palinspastic bed height reconstruction for ED. 209
Figure 134: Palinspastic percentage conglomerate reconstruction for ED. 210
Figure 135: Palinspastic average clast size reconstruction for ED. 211
Figure 136: Palinspastic maximum clast size reconstruction for ED 212
Figure 137: Palinspastic Reconstruction for the ED - All Parameters 213
Figure 138: Enlarged Block 2 palinspastic reconstruction for a) bed height for ED and b) for percentage conglomerate for ED. 215
Figure 139: Enlarged Block 3 palinspastic reconstruction for a) bed height for ED and b) for percentage conglomerate for ED. 216
Figure 140: Enlarged Block 4 palinspastic reconstruction for a) bed height for ED and b) for percentage conglomerate for ED. 217
Figure 141: Palinspastic bed height reconstruction for MAC. 218
Figure 142: Palinspastic percentage conglomerate reconstruction for MAC. 219
Figure 143: Palinspastic average clast size reconstruction for MAC. 220
Figure 144: Palinspastic maximum clast size reconstruction for MAC. 221
Figure 145: Palinspastic bed height reconstruction for MAD. 223
Figure 146: Palinspastic percentage conglomerate reconstruction for MAD. 224
Figure 147: Palinspastic average clast size reconstruction for MAD. 225
Figure 148: Palinspastic maximum clast size reconstruction for MAD. 226
Figure 149: Palinspastic Reconstruction for the MAD - All Parameters 227
Figure 150: Enlarged Block 2 palinspastic reconstruction for a) bed height for MAD and b) for percentage conglomerate for MAD. 229
Figure 151: Enlarged Block 3 palinspastic reconstruction for a) bed height for MAD and b) for percentage conglomerate for MAD. 230
Figure 152: Enlarged Block 4 palinspastic reconstruction for a) bed height for MAD and b) for percentage conglomerate for MAD. 231
Figure 153: Palinspastic bed height reconstruction for MIB. 233
Figure 154: Palinspastic percentage conglomerate reconstruction for MIB. 234
Figure 155: Palinspastic average clast size reconstruction for MIB. 235
Figure 156: Palinspastic maximum clast size reconstruction for MIB. 236
Figure 157: Palinspastic Reconstruction for the MIB - All Parameters 237
Figure 158: Enlarged Block 2 palinspastic reconstruction for a) bed height for MIB and b) for percentage conglomerate for MIB. 239
Figure 159: Enlarged Block 3 palinspastic reconstruction for a) bed height for MIB and b) for percentage conglomerate for MIB. 240
Figure 160: Enlarged Block 4 palinspastic reconstruction for a) bed height for MIB and b) for percentage conglomerate for MIB. 241
Figure 161: Palinspastic bed height reconstruction for MIT. 243
Figure 162: Palinspastic percentage conglomerate reconstruction for MIT. 244
Figure 163: Palinspastic average clast size reconstruction for MIT. 245
Figure 164: Palinspastic maximum clast size reconstruction for MIT 246
Figure 165: Palinspastic Reconstruction for the MIT - All Parameters 247

Figure 166: Enlarged Block 2 palinspastic reconstruction for a) bed height for MIT and b) for percentage conglomerate for MIT. 249
Figure 167: Enlarged Block 3 palinspastic reconstruction for a) bed height for MIT and b) for percentage conglomerate for MIT. 250
Figure 168: Enlarged Block 4 palinspastic reconstruction for a) bed height for MIT and b) for percentage conglomerate for MIT. 251
Figure 169: Palinspastic bed height reconstruction for MIQ. 253
Figure 170: Palinspastic percentage conglomerate reconstruction for MIQ. 254
Figure 171: Palinspastic average clast size Reconstruction for MIQ. 255
Figure 172: Palinspastic maximum clast size reconstruction for MIQ. 256
Figure 173: Palinspastic Reconstruction for the MIQ - All Parameters 257
Figure 174: Enlarged Block 2 palinspastic reconstruction for a) bed height for MIQ and b) for percentage conglomerate for MIQ. 259
Figure 175: Enlarged Block 3 palinspastic reconstruction for a) bed height for MIQ and b) for percentage conglomerate for MIQ. 260
Figure 176: Enlarged Block 4 palinspastic reconstruction for a) bed height for MIQ and b) for percentage conglomerate for MIQ. 261
Figure 177: Palinspastic bed height reconstruction for MBB. 262
Figure 178: Palinspastic percentage conglomerate reconstruction for MBB. 263
Figure 179: Palinspastic average clast size reconstruction for MBB. 264
Figure 180: Palinspastic maximum clast size reconstruction for MBB. 265
Figure 181: Palinspastic bed height reconstruction for MBT. 266
Figure 182: Palinspastic percentage conglomerate reconstruction for MBT. 267
Figure 183: Palinspastic average clast size reconstruction for MBT. 268
Figure 184: Palinspastic maximum clast size reconstruction for MBT. 269
Figure 185: Palinspastic bed height reconstruction for VCR. 271
Figure 186: Palinspastic percentage conglomerate reconstruction for VCR 272
Figure 187: Palinspastic average clast size reconstruction for VCR 273
Figure 188: Palinspastic maximum clast size reconstruction for VCR. 274
Figure 189: Palinspastic Reconstruction for the VCR - All Parameters 275
Figure 190: Enlarged Block 2 palinspastic reconstruction for a) bed height for VCR and b) for percentage conglomerate for VCR. 277
Figure 191: Enlarged Block 3 palinspastic reconstruction for a) bed height for VCR and b) for percentage conglomerate for VCR. 278
Figure 192: Enlarged Block 4 palinspastic reconstruction for a) bed height for VCR and b) for percentage conglomerate for VCR. 279

List of Tables

Table 1: Bed acronyms used at SDGM. 20
Table 2: Summary of data points per bed and parameters utilised in the data analysis. 74
Table 3: Summary table for bed height trends per structure block and bed. 116
Table 4: Summary table for percentage conglomerate trends per structure block and bed. 116
Table 5: Summary table for average clast size trends per structure block and bed. 117
Table 6: Summary table for maximum clast size trends per structure block and bed. 117
Table 7: Summary of findings relating to the structures observed in this study. 218

Table of Acronyms

Acronym	Full Name or Description
2D	Two dimensional
3D	Three dimensional
90L Wrench Fault	90 Level Wrench fault. A sinistral strike-slip fault which terminates the P2 Wrench Fault and is located within the South Deep Gold Mine workings
BIF	Banded iron formation
E9EC	Elsburg '9th' band conglomerate mined on the Randfontein Estates shafts and forms part of the informal "Middle Elsburg" reef package
EB	Elsburg Individual 'B' Band (a footwall quartzite with intercalated conglomerate beds (may be polymictic) directly in the footwall of the Elsburg Individual 'C' Band)
EC9	A name previously informally given (for modelling purposes) to the ECBA bed
ECB	Elsburg Individual 'C' Bottom Conglomerate
ECBA	Elsburg Individual 'C' Basal Conglomerate
ECBAQ	Elsburg Individual 'C' Basal Quartzite
ECBQ	Elsburg Individual 'C' Bottom Quartzite
ECMC	Elsburg Individual 'C' Middle Conglomerate
ECMQ	Elsburg Individual 'C' Middle Quartzite
ECT	Elsburg Individual 'C' Top Band
ED	Elsburg Individual 'D' Band Quartzite
FW	Underlying or "foot wall" to a discussed stratigraphic bed or unit
HW	Overlying or "hanging wall" to a discussed stratigraphic bed or unit
M	Magnetite-rich shale/iron formation (after Tucker et al., 2016)
MAC	Massives 'A' Band Conglomerate
MAD	Massives 'A' Band Degenerate Quartzite (includes the MAS)
MAS	Massives 'A' Band Sand (an Orthoquartzite at the top of the MAD)
Mb	Member (after Tucker et al., 2016)
MBB	Massives 'B' Band Bottom Conglomerate
MBT	Massives 'B' Band Top
MIB	Massives 'Intermediate' Band Bottom
MIQ	Massives 'Intermediate' Band Quartzite
MIT	Massives 'Intermediate' Band Top Conglomerate
ND	Not discernible
P1 Wrench	Panvlakte No. 1 Wrench fault. A dextral strike-slip fault which coalesces with the Panvlakte Fault Zone to the west of the South Deep Gold Mine workings
P2 Wrench	Panvlakte No. 2 Wrench fault. A dextral strike-slip fault which coalesces with the Panvlakte Fault Zone to the west of the South Deep Gold Mine workings
REY	rare earths and yttrium
SACS	Stratigraphic Terminology and Nomenclature
SDGM	South Deep Gold Mine
SLC	An informal term used on the mine to describe a zone of combined attenuated stacked beds ±10 m in height usually within 30 m to 40 m to the east of the Upper Elsburg Sub-outcrop where individual reefs are not discernible. This term was used up until 2007
SV1	Sub-vertical Shaft No. 1
SV2	Sub-vertical Shaft No. 2
SV2	Sub-vertical Shaft No. 3
UE1A/a Reef	Upper Elsburg 1 'A' Band, 'a' conglomerate (included within Middle Elsburg Reef Package)
UE5 Zone	Upper Elsburg 5 Zone which is a footwall stratigraphic unit on the West Rand
UE7 Zone	Upper Elsburg 7 Zone (encompasses the EA to ED Individuals quartzites and Reefs)
VCF	Venterspost Conglomerate Formation
VCR	Ventersdorp Contact Reef
WAGM	Western Areas Gold Mine

CHAPTER 1: INTRODUCTION

1.1 Regional Context

The Mesoarchaean Witwatersrand Basin represents the largest gold depository worldwide (McCarthy, 2006; Dankert and Hein, 2010; Frimmel, 2019). Exploration and mining activity have taken place here over more than a century, primarily in the known goldfields, leading to an understanding of its gross geometry (McCarthy, 2006). The Witwatersrand basin forms a roughly elliptical structural remnant on the Kaapvaal Craton. The major axis extends some 350 km (NE-SW), while the minor axis is approximately 200 km (NW-SE) in length (Figure 1) (Pretorius, 1979; Frimmel et al., 2005; Tucker et al., 2016).

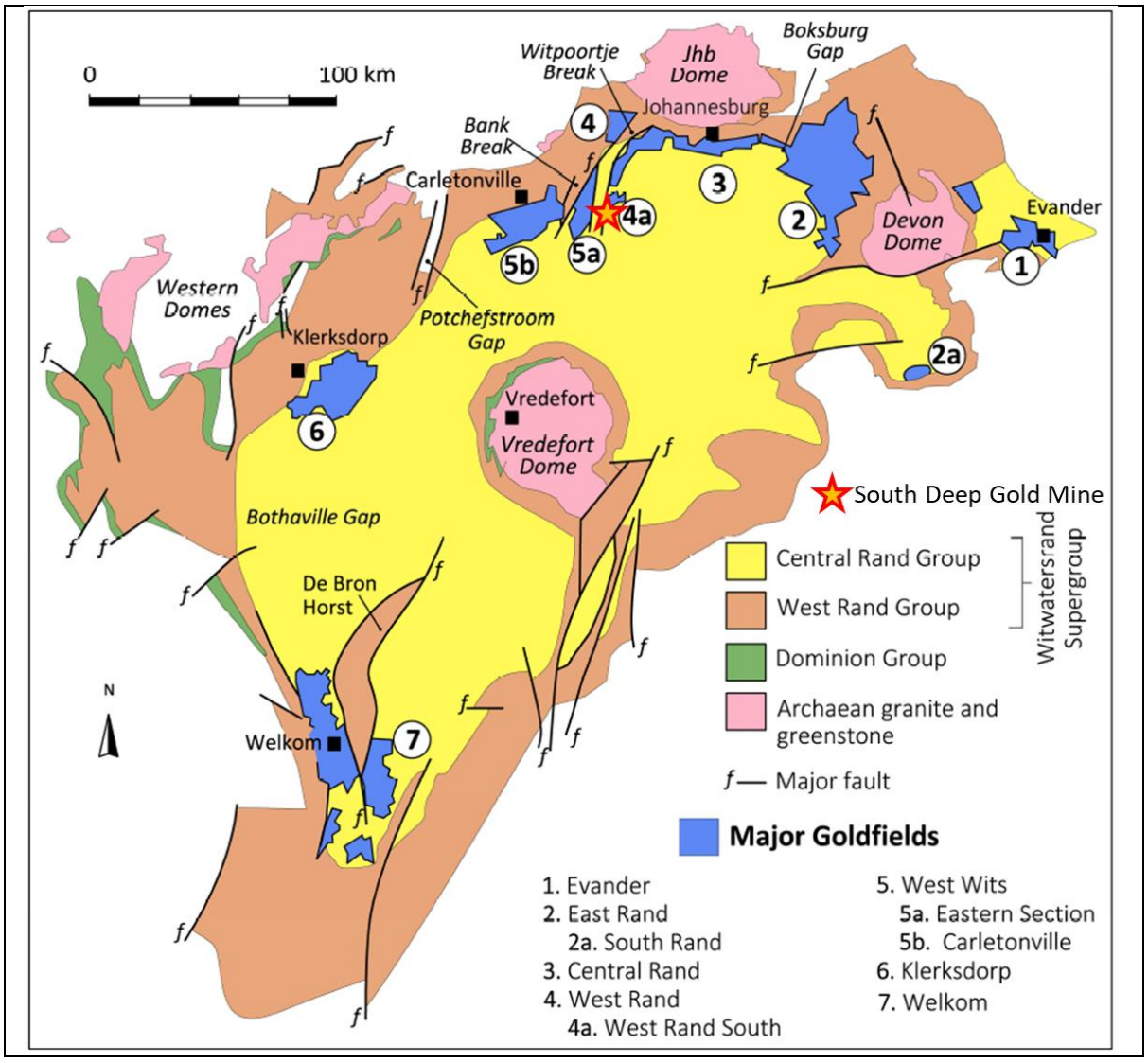


Figure 1: Geological map of the Witwatersrand Basin, with younger cover sequences removed, depicting the location of the goldfields and the study area (modified after Tucker et al., 2016 after Frimmel et al., 2005).

The Witwatersrand Basin is filled by sediments and minor volcanics of the Witwatersrand Supergroup, which comprises the lower West Rand Group and overlying Central Rand Group; the relation between the two groups is

unconformable (Tinker et al., 2002; Manzi et al., 2013; Frimmel, 2019), as confirmed by means of regional deep seismic surveys (Manzi et al., 2013; Frimmel, 2019). The full clastic wedge of the Witwatersrand Supergroup attains a maximum thickness exceeding 7000 m near the Klerksdorp Goldfield (Robb and Meyer, 1995; McCarthy, 2006 after SACS, 2006) and thins towards the southeast (Catuneanu, 2001; McCarthy, 2006).

The Dominion Group was unconformably deposited over the basement at 3074 ± 6 Ma (Armstrong et al., 1991). The Dominion Group consists primarily of metamorphosed volcanics with subsidiary clastic metasediments of greenschist to amphibolite metamorphic grade (Marsh, 2006).

The West Rand Group (which unconformably overlies a combination of the granite-greenstone basement of the Kaapvaal Craton and the Dominion Group) consists of approximately equal proportions of shale and quartzite, with subsidiary conglomerate towards the top of the group (Eriksson et al., 1981; Winter and Brink, 1991). The maximum West Rand Group age of 2914 ± 14 Ma (U–Pb detrital zircon age) was obtained from the basal Orange Grove Formation (Armstrong et al., 1991; Frimmel, 2019).

Gold occurs primarily within the conglomeratic horizons of the Central Rand Group, with minor mineralisation occurring sporadically in conglomerates of the West Rand Group (McCarthy, 2006). The base of the Central Rand Group (Johannesburg Subgroup) is younger than 2902 ± 13 Ma (U–Pb detrital zircon age) (Kositcin et al., 2003; Frimmel 2019) while the Krugersdorp Formation (near the top of the Johannesburg Subgroup) is younger than 2872 ± 6 Ma (U–Pb detrital zircon age) (Kositcin et al., 2003; Frimmel 2019). The upper Elsburg Formation is dated as younger than 2840 ± 3 Ma (U–Pb detrital zircon age) (Kositcin et al., 2003; Frimmel 2019). Lower age limits of the group are given by a U-Pb age on authigenic xenotime of 2780 ± 3 Ma (Kositcin et al. 2003; Frimmel, 2019) and by a U-Pb baddeleyite age from the overlying Klipriviersberg Group, lower Ventersdorp Supergroup,

The unique placer unit of the Venterspost Conglomerate Formation, colloquially called the Ventersdorp Contact Reef or "VCR", unconformably overlies the Central Rand Group. The VCR is overlain by the volcanics of the Ventersdorp Supergroup (ca. 2791-2779 ± 1 Ma based on U-Pb zircon and baddeleyite ages), (Gumsley et al. 2019), placing its' age at approximately between 2840 ± 3 Ma and 2791± 1 Ma, based on the Upper Elsburg age of Kositcin et al. (2003) and the oldest Ventersdorp Supergroup age of Gumsley et al. (2019).

Post-depositional greenschist metamorphism (partially attributed to burial), hydrothermal alteration (350 ± 50°C, at ca. 3 kbar) and tectonic processes have modified the rocks and their mineralisation (Wallmach and Meyer, 1990; Frimmel, 1994; Phillips and Law, 1994; Frimmel, 2019). Thrusting of the Southern Marginal Zone of the Limpopo Belt over the Kaapvaal Craton between 2690 Ma and 2670 Ma (Frimmel, 2019) is thought to have affected the northern portion of the Witwatersrand Basin. Emplacement of the 2054 Ma (Scoates J.S. and Friedman R.M., 2008; Frimmel, 2019) Bushveld Igneous Complex is also thought to have contributed to its alteration history. The 2023 Ma Vredefort impact resulted in basin-wide faulting and fracturing (Henkel and Reimold, 1998; Frimmel, 2019) which are purported to have had a significant influence and created a secondary permeability, possibly allowing fluids to circulate throughout the basin for a short time causing hydrothermal alteration (Frimmel et al., 1999).

1.1.1 Location of the Study Area

South Deep Gold Mine ("SDGM"), owned by Gold Fields Limited, is located in the West Rand Goldfield approximately 45 km southwest of Johannesburg (Figure 1). It lies along the eastern edge of the West Rand Goldfield and is bordered to the north by the Ezulwini Mine and to the west by the Kloof Mine (Figure 2).

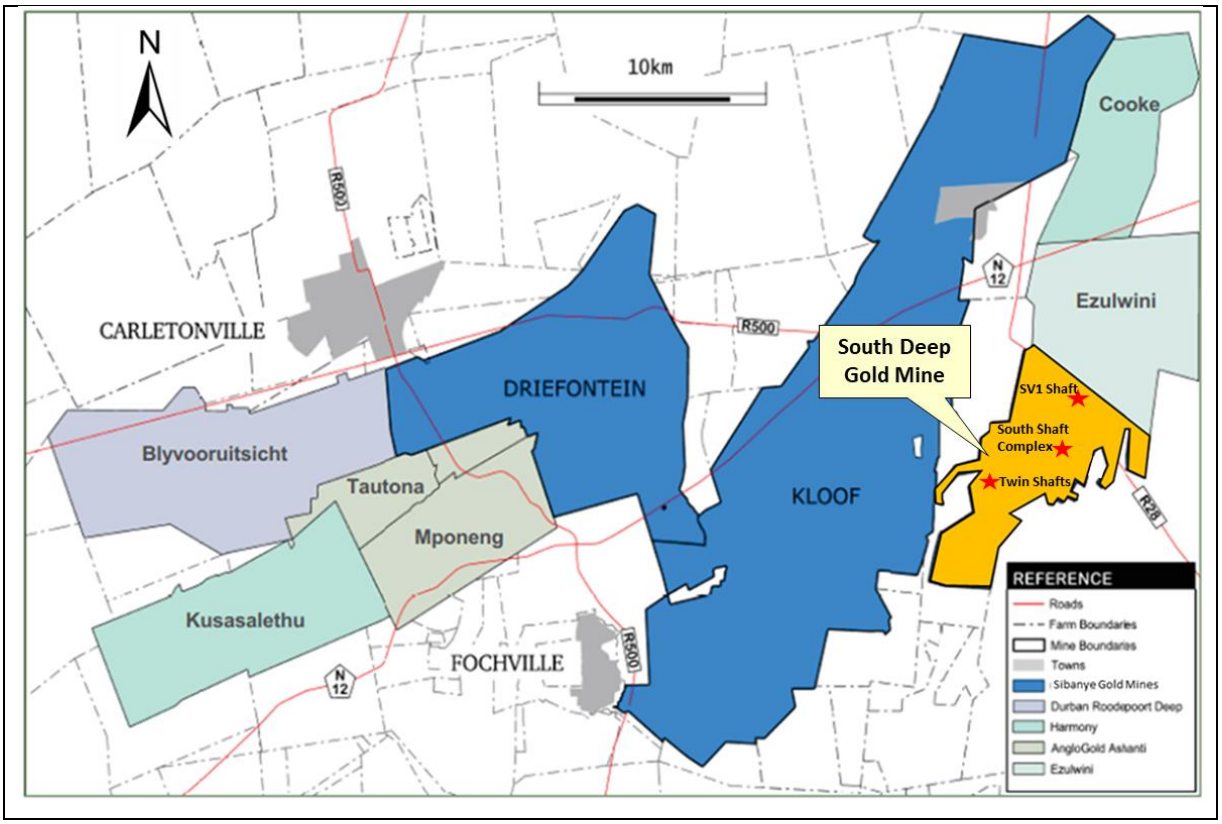


Figure 2: The location of SDGM and its shafts in the West Rand Goldfield (adapted from Gold Fields, 2009 and Gold Fields, 2011).

The R28 tarred road passes through the northern part of the property, between the towns of Westonaria and Vereeniging. The mine property extends for approximately 11 km N-S with a maximum E-W extent of approximately 8 km. The mine historically had two sets of surface-to-underground operational production mine shafts, but has subsequently closed the old Western Areas South Shaft Complex (with its three sub-vertical shafts SV1, SV2 and SV3) and now only operates the South Deep Twin Shaft Complex consisting of the South Deep Main and Vent shafts to access the newer and deeper working areas of the mine (Figure 2).

1.2 Aims and Hypothesis

1.2.1 Background to the Study

Little academic work has been generated on the Upper Elsburg reefs or on their syn- to post-depositional tectonic history. Tucker and Viljoen (1986) presented a regional view of the West Rand Goldfield and mentioned the Upper Elsburg Reef package on Western Areas Gold Mine, with little reference to their deposition or syn- to post-

depositional tectonic history. Osburn et al (2014) only discussed geological modelling of the Upper Elsburgs and stated the reefs presented a rotating onlap morphology. Manzi (2013) and Manzi et al. (2013) mention the Upper Elsburg Reef package while relating findings of the seismic studies undertaken on the West Rand, but did not allude to their morphology, due to their poor seismic resolution of the siliclastic wedge within the Central Rand Group. Tucker and Viljoen (1986) stated that one of the most notable features of the West Rand Goldfield (refer to Figure 3) is the system of faults defining the edges of the Witpoortjie-Panvlakte Horst bound to the east by the Panvlakte Fault and located directly west of SDGM (Figure 3).

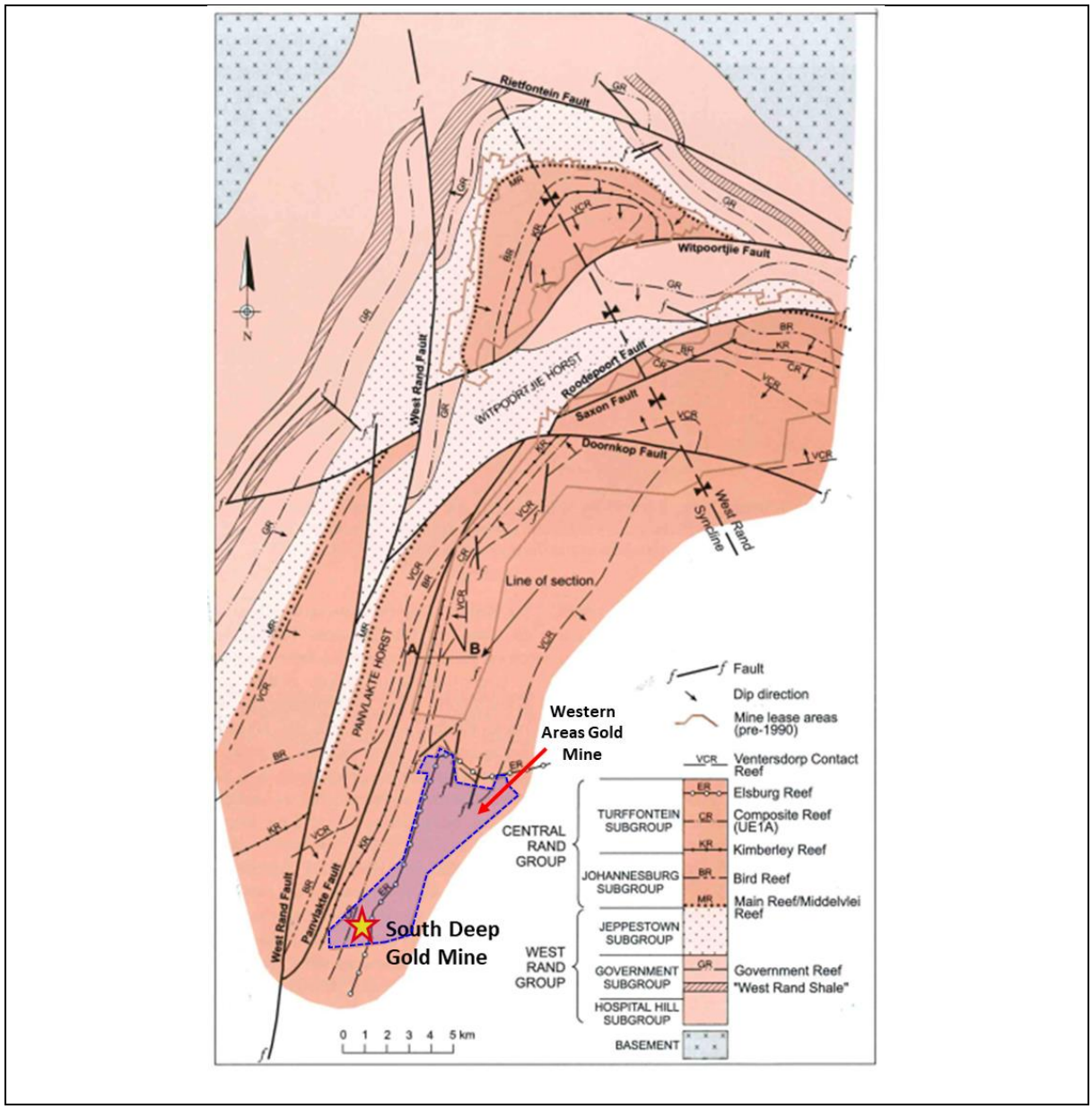


Figure 3: The geology of the West Rand Goldfield after Tucker and Viljoen (1986) and McCarthy (2006), depicting the major faults and main reef sub-outcrops against the VCR.

According to them, uplift on this structure resulted in a pebbly, braided alluvial plain along its length towards the east and initiated Elsburg sedimentation as evidenced in the Composite Reef in the form of a rotating onlap on the Cooke Shafts and Ezulwini Mine (Tucker and Viljoen, 1986; Burnett, 2008), thus inferring syn-sedimentary

tectonic activity on the Panvlakte Fault during Upper Elsburg times. Tucker and Viljoen (1986) indicated that E-W structures exist on the Cooke Mines and these displaced the NNW faults. The E-W structures are described as having generally small vertical throws and being locally intruded by some Ventersdorp aged dykes, with their last preserved movement probably being post-Transvaal in age (Tucker and Viljoen, 1986). Importantly, the E-W structures appear to have influenced original sediment deposition (Tucker and Viljoen, 1986). The authors also discussed the structural setting of WAGM and noted two primary fault orientations, namely approximately N-S normal faults and E-W striking strike-slip faults, which segment the orebody both vertically and horizontally such that it shows a right-lateral displacement of up to 2000 m (Tucker and Viljoen, 1986). The strike-slip faults were indicated to be predominantly pre-Transvaal in age as these structures do not displace the Black Reef, which unconformably overlies the Witwatersrand and Ventersdorp supergroups. The South Shaft section of WAGM today represents the northern section of SDGM.

In their analysis of seismic datasets in the West Rand Goldfield, Manzi et al. (2013) proposed that large-scale slip movements on the West Rand and Panvlakte faults were preceded by east-verging thrusting with associated folding along the Tandeka Thrust located in the footwall of the West Rand Fault. Owing to the paucity of strike-slip faults identified during a SDGM 2004 Seismic Survey, strike-slip tectonics was not considered. The Wrench Fault (Figure 4**Error! Reference source not found.**) which separates the current workings at SDGM from Future Mine was originally identified during a 1988 seismic survey (Arthur, 1990). Gibson (2005) interpreted this structure as dipping at approximately 75° towards the north. The right-lateral component of the Wrench Fault is difficult to discern from the seismic data due to the low contrasting lithologies (Gibson, 2005). The lateral displacement on this structure is currently estimated at ±950 m and is based on isopach data for the Upper Elsburg Reef package generated during the orebody modelling exercises conducted at SDGM between 2007 and 2010.

The mapped and modelled wrench structures as well as the Modderfontein/Waterpan (Upper Elsburg) sub-outcrop against the VCR form the structural basis for this study and are presented below in Figure 4. The structures have been mapped, actively correlated between cross-cut lines and overlying stoping horizons over the years and have been included in the orebody modelling since 2001.

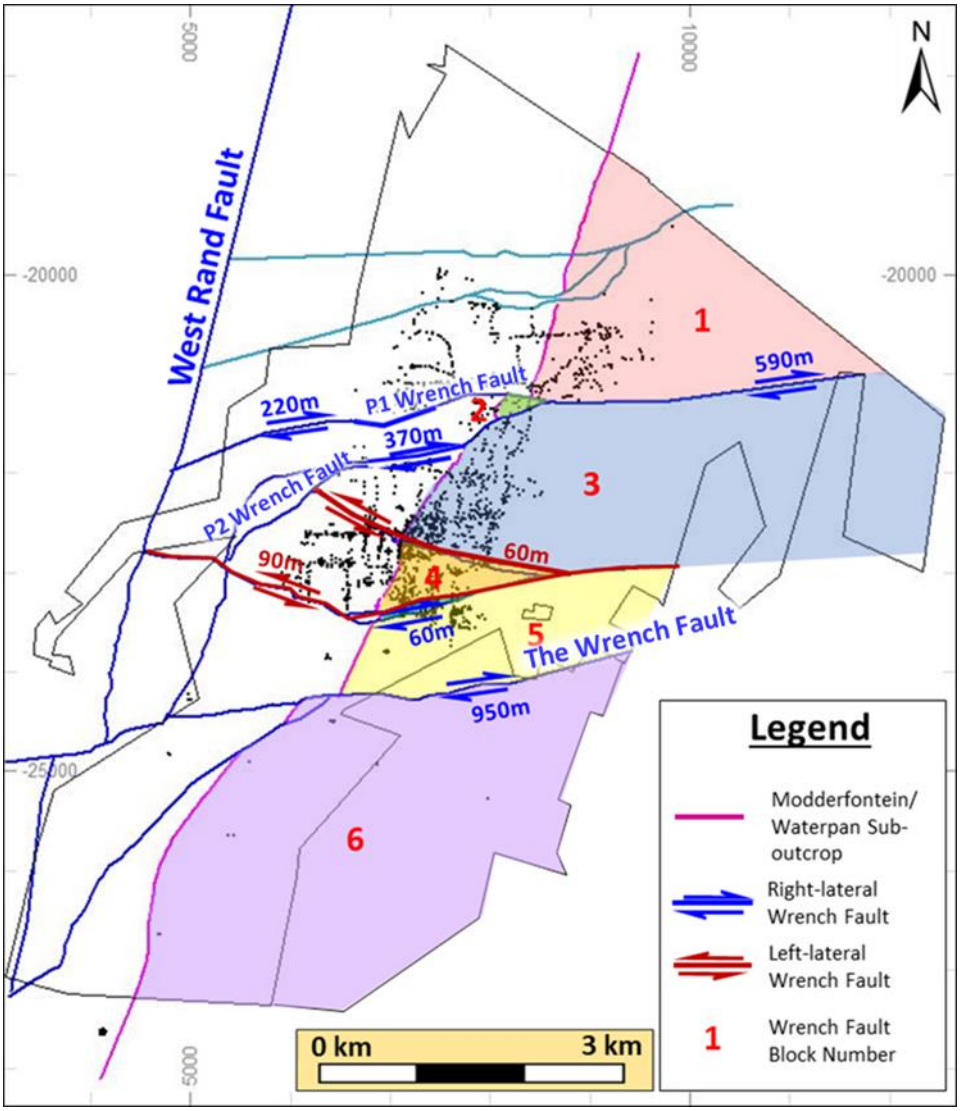


Figure 4: Map of SDGM showing the major structural features and identified wrench fault blocks discussed in this study. Black dots indicate drillhole collar locations.

The implications of the regional structural interpretations presented by Tucker and Viljoen (1986), Gibson (2005) and Manzi (2013) for mine-scale features have not fully been considered to date. Furthermore, very little pertaining to syn-sedimentary strike-slip or accommodation tectonics is discussed in published literature other than the E-W striking faults on the Cooke Shafts (Tucker and Viljoen, 1986) and the existence of strike-slip faulting on WAGM. All these studies (except Tucker and Viljoen (1986) for the Cooke Shafts) only note the apparent E-W strike of these structures and their post West Rand Fault age (Gibson, 2005). This contrasts with Stanistreet and McCarthy (1991) who did not consider individual goldfield structures but interpreted the regional tectonics of the Witwatersrand Basin as having a significant strike-slip component that played significant a role in sedimentation during Central Rand Group times.

No studies attempting to link the West Rand Goldfield to this model were ever undertaken with the exception of Tucker and Viljoen (1986). The stacked nature of the Upper Elsburg reef package lends itself to analysis of wrench tectonics, by virtue of its wedge geometry running almost normal to the wrench faults. Analysis of

sedimentological parameters in conjunction with the mapped wrench faults thus provides an opportunity to investigate the possible magnitude and potential period over which extended dislocation took place on individual wrench structures. This, in turn, would assist in the understanding of the regional wrench tectonics and possibly prove the previously implied or stated (Tucker and Viljoen, 1986; Stanistreet and McCarthy, 1991; Osburn et al. 2014) syn-sedimentary nature of these faults.

1.2.2 Hypothesis of the Study

The hypothesis of this study is that stratigraphic and sedimentological evidence exists at SDGM that supports the existence of syn-depositional strike-slip tectonics associated with the E-W wrench faults (right-lateral as well as left-lateral).

1.2.3 Aims of the Study

The aim of this study is to use stratigraphic and logged sedimentological evidence constructed from drillhole data to prove syn-depositional strike-slip tectonics related to the E-W wrench faults further to the south than previously indicated by Tucker and Viljoen (1986) at SDGM.

This study attempts to relate each of the 15 Upper Elsburg horizons and VCR on SDGM in terms of possible syn-sedimentary tectonic influence, with specific reference to the known and mapped E-W striking strike-slip faults that are found on the property as identified by Arthur (1990) and Obermeyer (2004). Palaeo-current data for the Upper Elsburg Reef package at SDGM is very sparse, to almost completely absent due to the massive nature of the conglomerates. The lack of palaeo-current data at SDGM has been highlighted in the past, but the challenges to obtain such data remain.

Research questions to be addressed by the proposed research constitute the following:

1) Can sedimentological characteristics of individual beds at SDGM be spatially related by means of palinspastic reconstruction to prove syn- to post-sedimentary lateral movement across E-W striking faults during and between deposition of the individual beds?
2) Are the beds at SDGM related or similar sedimentologically to the VCR as indicated by Osburn et al. (2014) thus possibly suggesting continuity of tectonism and sedimentary response between late Central Rand Group and Ventersdorp times?
3) What characteristics (in the absence of geostatistics and gold grade) are most useful in identifying syn-sedimentary movement across the E-W striking wrench structures?
4) Were all E-W striking wrench structures active during the sedimentation of the Upper Elsburg Reefs at all times?
5) Is there evidence for mine-scale wrench fault block compartmentalisation?

1.2.4 Attribution of Work

This project arises from the author's work on South Deep Gold Mine for 13 years as a geologist within a team of production geologists. Very little formal published literature was available to the geology team to assist in understanding and identifying the complex reefs and structures making up the South Deep Upper Elsburg orebody. In-house geological papers were based on very localised areas covering a few mining levels at a time and did not consider the larger context. Moving between production areas (shallower and older parts of the mine workings to deeper and younger workings) did not assist in that correlation between the different stratigraphic units was complicated by different stratigraphic nomenclature by different historical teams.

Through multiple on-mine studies and projects a unified stratigraphic framework for the mine was developed in order to increase the integrity of the geological modelling and the resultant Mineral Resource modelling for the mine and I wished to impart this knowledge on to future South Deep geologists in order to assist them, as well as to share my understanding of the Upper Elsburg Reef Package within an academic environment.

CHAPTER 2: LITERATURE REVIEW

2.1 Regional Geology

2.1.1 Geological Setting of the Witwatersrand Basin

The Kaapvaal Craton is host to the Witwatersrand Basin which is situated near its centre (Figure 5). The Witwatersrand goldfields (Figure 1) have been the source of approximately one-third of all the world's historically mined gold (53 kt) and also include one of the largest known uranium resources (>200 kt U_3O_8) (Frimmel, 2014; Frimmel 2019).

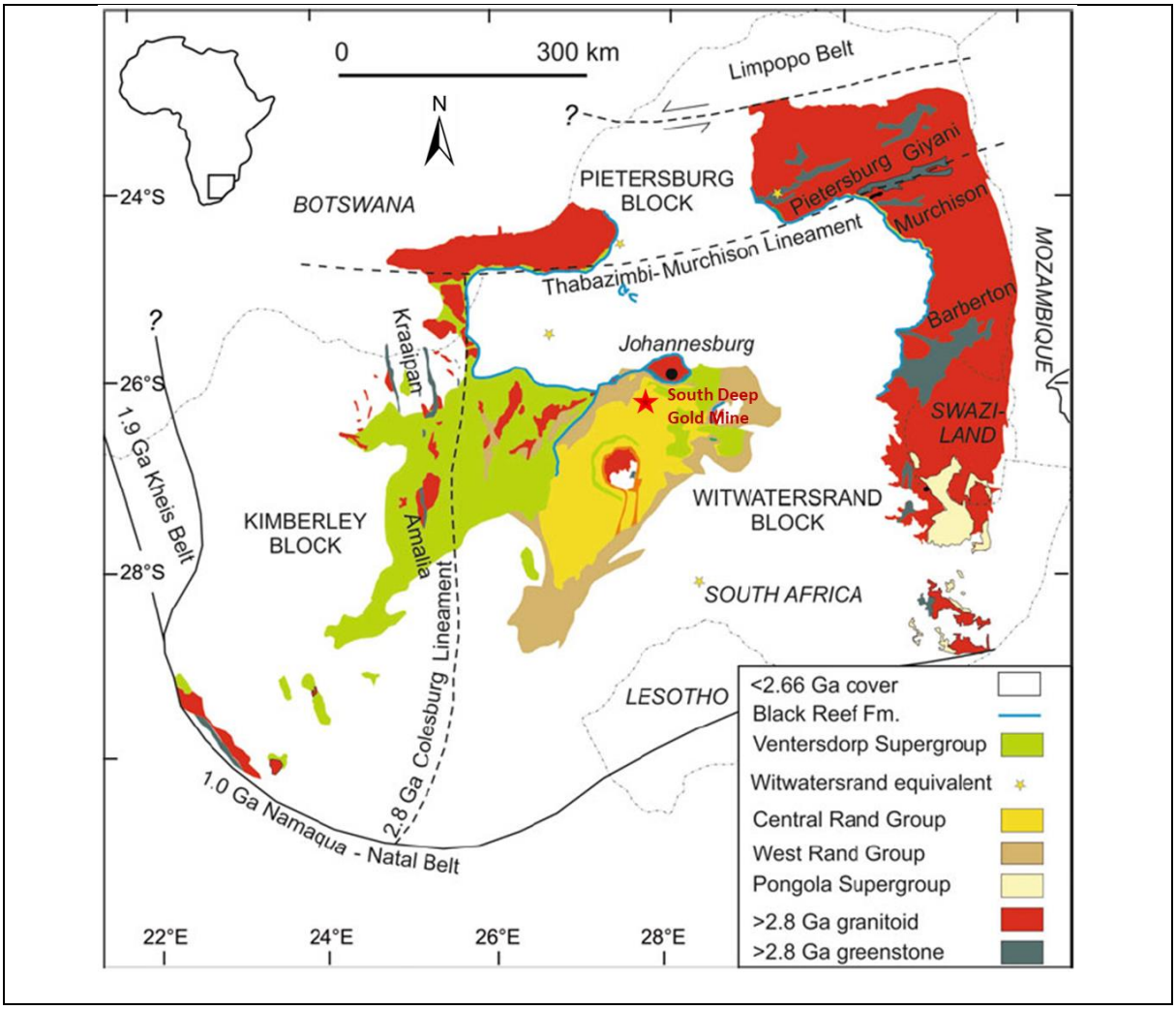


Figure 5: Surface and sub-surface distribution of the main Archaean stratigraphic units of the Kaapvaal Craton and the Witwatersrand Basin. Stars indicate drilled positions of Witwatersrand-equivalent rocks, while the red star indicates the approximate position of South Deep Gold Mine (modified after Frimmel and Hennigh, 2015; Frimmel, 2019).

The gold-bearing conglomerates occur almost exclusively in the dominantly arenaceous, upper, Central Rand Group, while the underlying West Rand Group mainly comprises iron rich shale and quartzites. The

Witwatersrand sediments are underlain by Dominion Group consisting of volcanics and minor clastic sediments, which overlie the older granite-greenstone basement.

The Ventersdorp Supergroup, the Transvaal Supergroup, and Karoo Supergroup unconformably overlie much of the Witwatersrand Basin. Geophysical surveys in the form of magnetics and gravity as well as localised diamond drilling have been used to test potential extensions to the Witwatersrand Basin (Tucker et al., 2016; Frimmel, 2019).

Correlatives of the Witwatersrand have been found beyond the recognised extent of basin in the Mozaan Group of the Pongola Supergroup, straddling the border between Swaziland and Kwazulu-Natal (Beukes and Cairncross, 1991). However, no substantial gold mineralisation has been found in this sedimentary sequence. A smaller correlative is the Uitkyk Formation, comprising quartzites and auriferous conglomerates in the Pietersburg Greenstone Belt (de Wit et al., 1993) with other occurrences to the north and southeast of the basin (McCarthy, 2006)

The Witwatersrand Basin also hosts to the eroded remnant of the world's largest known impact structure. This 2023 ± 2 Ma (Kamo et al., 1996), originally 250-300 km wide, feature comprises a 90-km-wide central uplift (the Vredefort Dome) and a surrounding rim syncline (Figure 6) that is largely responsible for the preservation of much of the basin (McCarthy, 2006; Tucker, 2016).

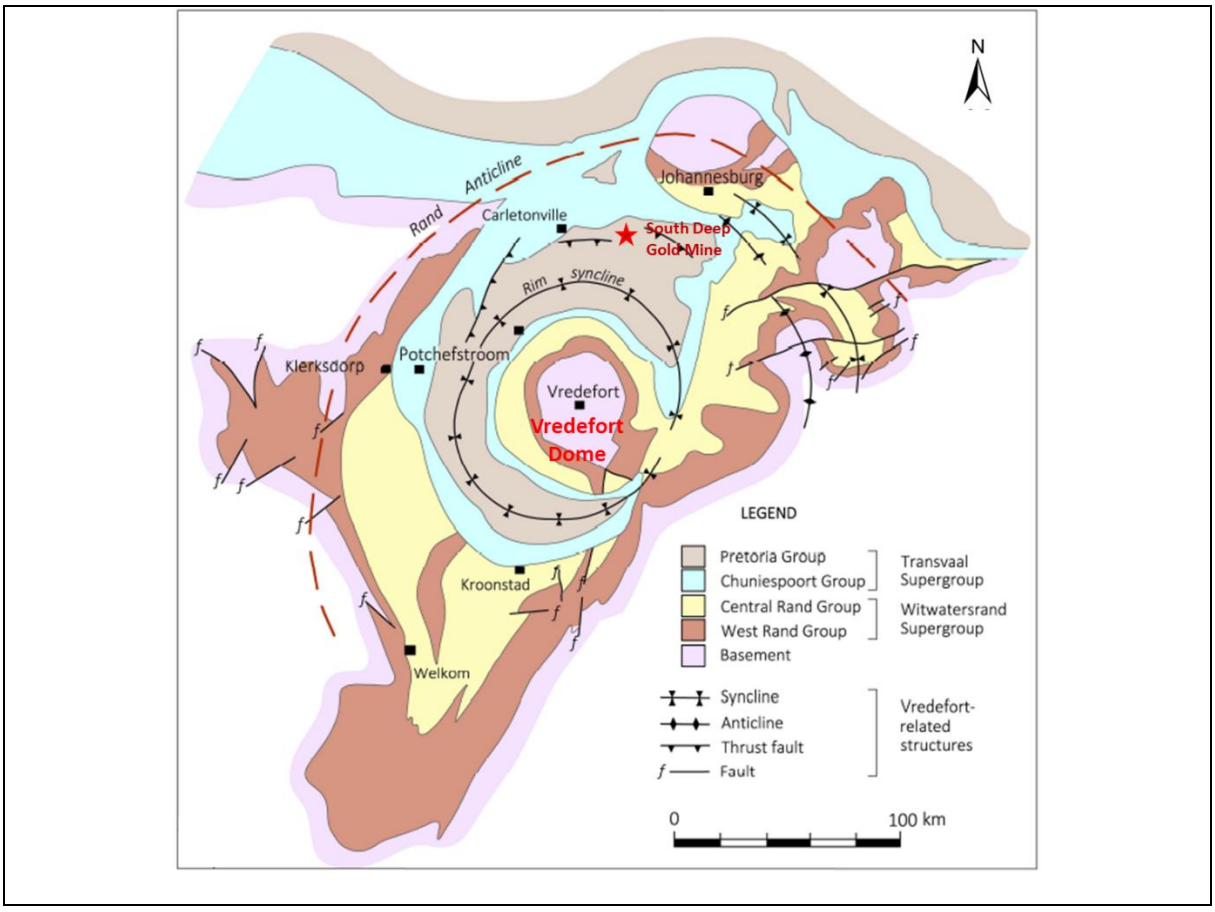


Figure 6: Simplified geological map (with Ventersdorp and Karoo Supergroup stratigraphy removed) showing the geometric relationship between the Witwatersrand Basin and the Vredefort impact structure. The approximate position of SDGM indicated with the red star (modified after McCarthy, 2006; Tucker, 2016)

Deformation linked to the impact is thought to have assisted the widespread percolation of fluids and partial remobilisation of mineralisation, leading to textural and geochemical features (Hayward, et al., 2005; Frimmel, 2019). The impact structure has been precluded as a source of the gold in that the metal contained in the Witwatersrand sediments predates the Vredefort event by 800-900 million years (Therriault et al., 1997; McCarthy, 2006; Frimmel, 2019).

2.1.2 Stratigraphy of the Witwatersrand Basin

The stratigraphy of the Witwatersrand Supergroup varies in thickness around the basin. The thickest preserved succession (>7000 m) occurs in the Klerksdorp Goldfield area whilst a total of only 900 m of the Central Rand Group is preserved in the Evander Goldfield in the eastern extremity of the basin (Pretorius, 1979; SACS, 2006) (Figure 7). The general, thinning of the preserved stratigraphy from the northwest towards the southeast has been an important consideration in basin-scale tectonic models (Pretorius, 1979; Catuneanu, 2001; see Section 2.6).

A simplified version of the regional expression of the Witwatersrand stratigraphy in various parts of the Basin (Tucker et al., 2016) is presented in Figure 7. The Witwatersrand Supergroup consists of the West Rand Group and the overlying Central Rand Group (McCarthy, 2006; SACS, 2006).

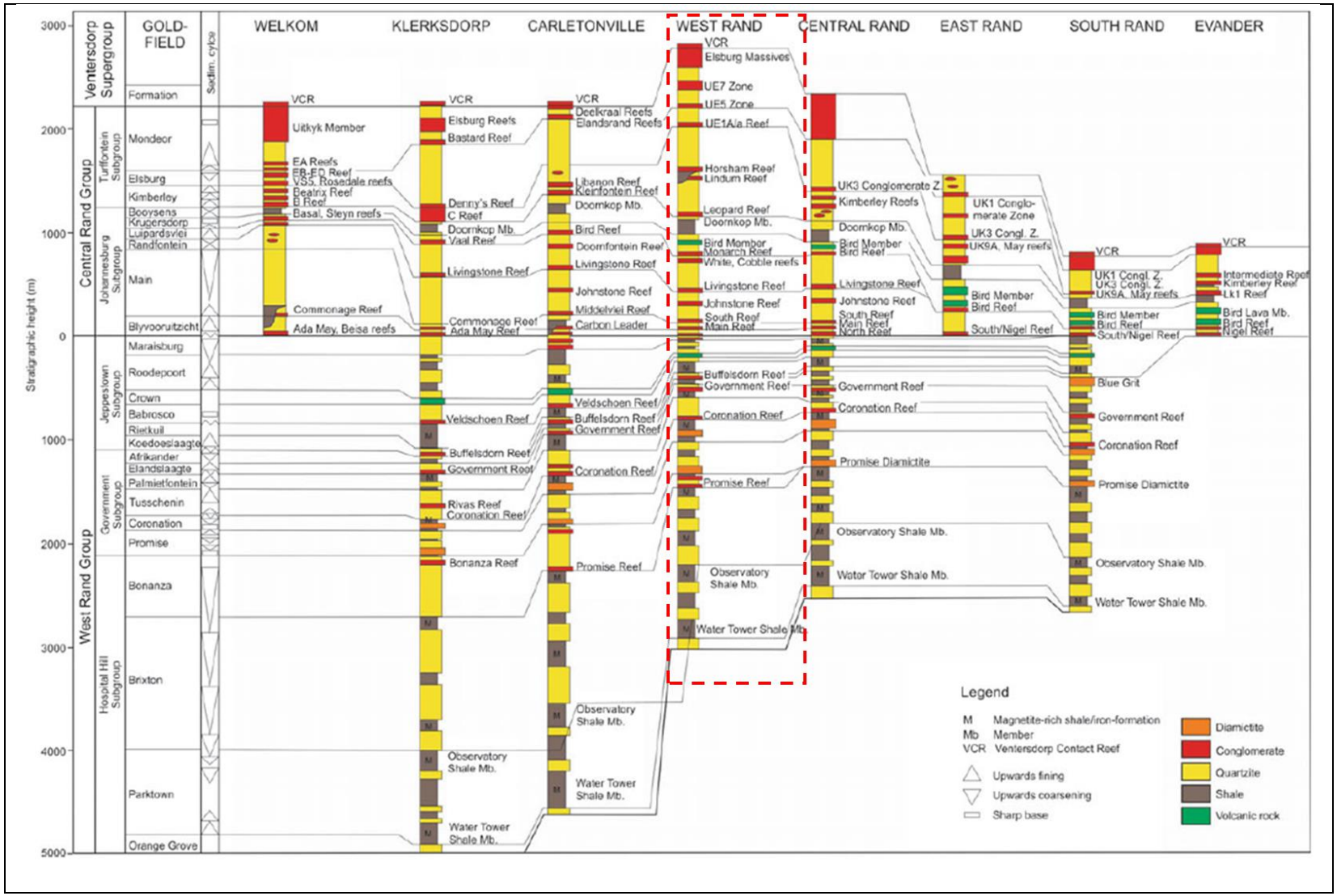


Figure 7: Stratigraphy of the Witwatersrand Supergroup and attempted correlation between the various goldfields with the West Rand goldfield stratigraphic column highlighted in the red stippled block. (modified after Frimmel, 2019; modified after McCarthy, 2006).

Generally, the strata of the Central Rand Group around the rim of the Witwatersrand Basin dip shallowly towards the centre of the preserved basin, with the exception of the flanks of the Vredefort Dome where a central core of up-domed granitic basement is rimmed by steeply dipping, generally overturned Witwatersrand, Ventersdorp and Transvaal supergroup strata (McCarthy, 2006; Dankert and Hein, 2010; Tucker et al., 2016). The shallow inward dips of strata in the goldfields are attributed to the outer limb of the rim syncline surrounding the dome. Central Rand Group strata along the northern margin of the basin have been subjected to folding as well as the development of low-angle thrust and normal faults developed tangentially to the impact structure. (Tucker et al., 2016). In the WelkomGoldfield along the southwestern margin of the basin the Central Rand Group strata are overturned as a result of eastward thrusting (McCarthy, 2006; Dankert and Hein, 2010).

2.1.2.1 **West Rand Group**

The West Rand Group was deposited unconformably over the Dominion Group and underlying Mesoarchaean basement gneisses, granites, and greenstones, and is characterised by approximately equal proportions of shale and quartzite (Pretorius, 1974; Tucker et al., 2016). The Hospital Hill Subgroup lies at the base and is unconformably overlain by the Government Subgroup that is, in turn, overlain by the Jeppestown Subgroup (Burke et al., 1986; McCarthy, 2006; Tucker et al., 2016). The shales are partly chemical in origin and are characterised by magnetite-bearing interlayers (Tankard et al., 1982; Tucker et al., 2016), are laterally persistent and are interpreted to represent distal shelf facies (Burke et al., 1986). As this project focusses on only the uppermost parts of the Central Rand Group and VCR stratigraphy, no further description is made of the West Rand Group.

2.1.2.2 **Central Rand Group**

The Central Rand Group disconformably overlies the West Rand Group and primarily consists of quartzites and subsidiary conglomerates (McCarthy, 2006; Tucker et al., 2016). It is divided into the lower Johannesburg Subgroup and the overlying Turffontein Subgroup (Burke et al., 1986; McCarthy, 2006; Tucker et al., 2016). The Central Rand Group primarily represents alluvial braid plain sedimentation with minor marine influence, and erosional local unconformities play a major role in placer formation (Catuneanu, 2001; McCarthy, 2006). It consists of generally progressively upward coarsening units with intermittent marine inundations as evidenced by the Booysens Formation shales (McCarthy, 2006) thus suggesting an upliftment and encroachment of the hinterland (Catuneanu, 2001). The Central Rand Group is unconformably to disconformably overlain by the Venterspost Formation or the VCR (McCarthy, 2006; Tucker et al., 2016).

2.1.2.2.1 West Rand Subgroup

The aggradational Johannesburg Subgroup consists primarily of fluvial braid plain quartzites interspersed with periodic erosional peneplanation episodes resulting in unconformable to disconformable surfaces as degradational braid plains or pediments (McCarthy, 2006; Tucker et al., 2016). Placers occurring as orthoquartzites with

conglomerate are commonly associated with these unconformities and disconformities (Minter, 1978; McCarthy, 2006; Tucker et al., 2016; Frimmel, 2019).

Several cycles of degradation occurred, each followed by either a transgression or by progradation of the braid plains (McCarthy, 2006; Tucker et al., 2016). The Blyvooruitzicht Formation, with its basal conglomerate (Ada May or Beisa reefs), occurs at the base of the Johannesburg Subgroup (Figure 7). The Main Formation, with the Main Reef/Carbon Leader at its base, unconformably overlies the Blyvooruitzicht Formation. The Main Formation was in turn followed, successively, by the Randfontein, Luipaardsvlei and Krugersdorp Formations. The Krugersdorp Formation is overlain by the shales of the Booysens Formation, which is interpreted as a significant basin-wide marine transgression (McCarthy, 2006; Tucker et al., 2016).

2.1.2.2.2 Turffontein Subgroup

The base of the Turffontein Subgroup is defined by the progradational braid plain deposits of the Kimberley Formation with periodic erosional degradation resulting in the placers of the Kimberley Reefs. Deep erosion channels filled with pyritic sands and shales formed during this period. The Kimberley Formation is overlain by the Elsburg Formation with its own important placer units or reefs such as the UE1A on the West Rand (Tucker and Viljoen, 1986; Tucker et al., 2016).

Overlying the Elsburg Formation is the Mondeor Formation, consisting of massive conglomerates or boulder beds (McCarthy, 2006; Tucker et al.; 2016, Frimmel, 2019) separated by quartzite units (Arthur, 1990; Muntingh et al., 2005). The sediments of the Mondeor Formation mature upwards and indicate a progressive marine regression (Tucker and Viljoen, 1986; Arthur, 1990; Tucker et al., 2016).

2.2 Geology of the Study Area

The regional dip of Central Rand Group strata in the area of SDGM is roughly towards the south-southeast with local variations and sub-outcrops against the overlying VCR which dips approximately southward. SDGM primarily mines conglomerates of the Mondeor Formation, which is located in the uppermost Central Rand Group stratigraphy (Figure 8**Error! Reference source not found.**).

Prospecting on what is now the SDGM commenced in 1950 (Tucker and Viljoen, 1986), with mining commencing under Western Areas Gold Mine ("WAGM") in 1961. Mining progressed up-dip (northward) from the original South Shaft towards the boundary with Ezulwini Mine (Figure 2) and stopped at the boundary approximately 1700 m below surface. Mining also extended southward and is currently located at approximately 2750 m below surface. The southern limit of future mining is projected to lie between 3300 m and 3400 m below surface (Gibson, 2005).

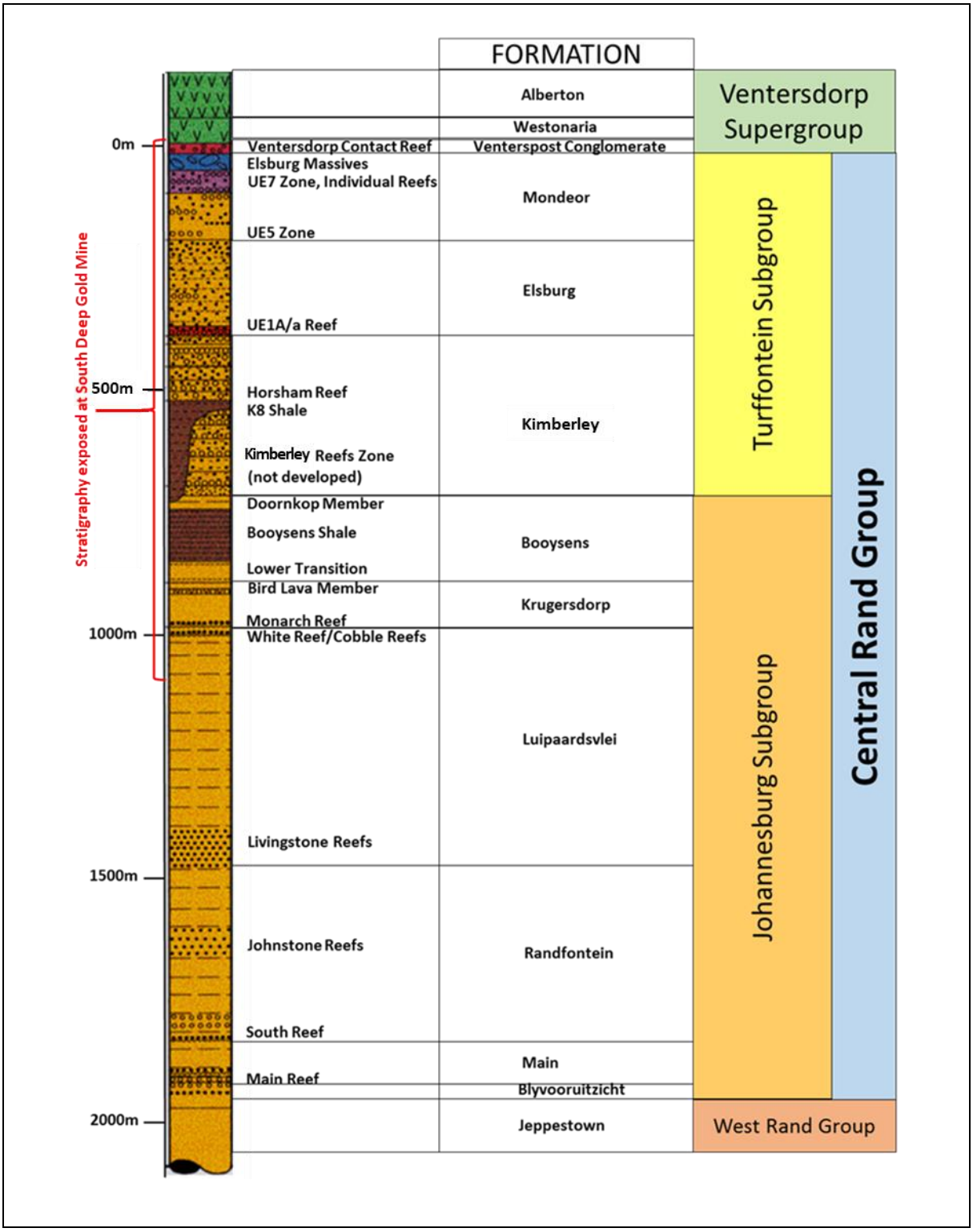


Figure 8: Stratigraphy of SDGM, as proposed by Obermeyer (2005) (modified after Tucker and Viljoen, 1986; Arthur, 1990 and SACS, 2006), related to the general stratigraphy of the Central Rand Group within the Witwatersrand Supergroup (SACS, 2006) (permission granted by Goldfields to reproduce).

SDGM mines the VCR as well as the informally named "Upper Elsburg" conglomerates, comprising the colloquially named Elsburg Massives of the Modderfontein Member (SACS, 2006) and the UE7, or Individual Reefs, of the underlying Waterpan Member (SACS, 2006; Figure 8). Both members lie stratigraphically within

the upper portion of the Mondeor Formation of the Turffontein Subgroup (Figure 8**Error! Reference source not found.**) (Tucker and Viljoen, 1986; adapted from Arthur, 1990 and SACS, 2006).

The mine extends approximately 11 km NNE-SSW along strike of the Upper Elsburg sub-outcrop against the VCR that nearly bisects the 4 km wide property (Figure 9**Error! Reference source not found.**). The main geological features (including the main recognised wrench structures) and areas of mining are depicted in Figure 9**Error! Reference source not found.**.

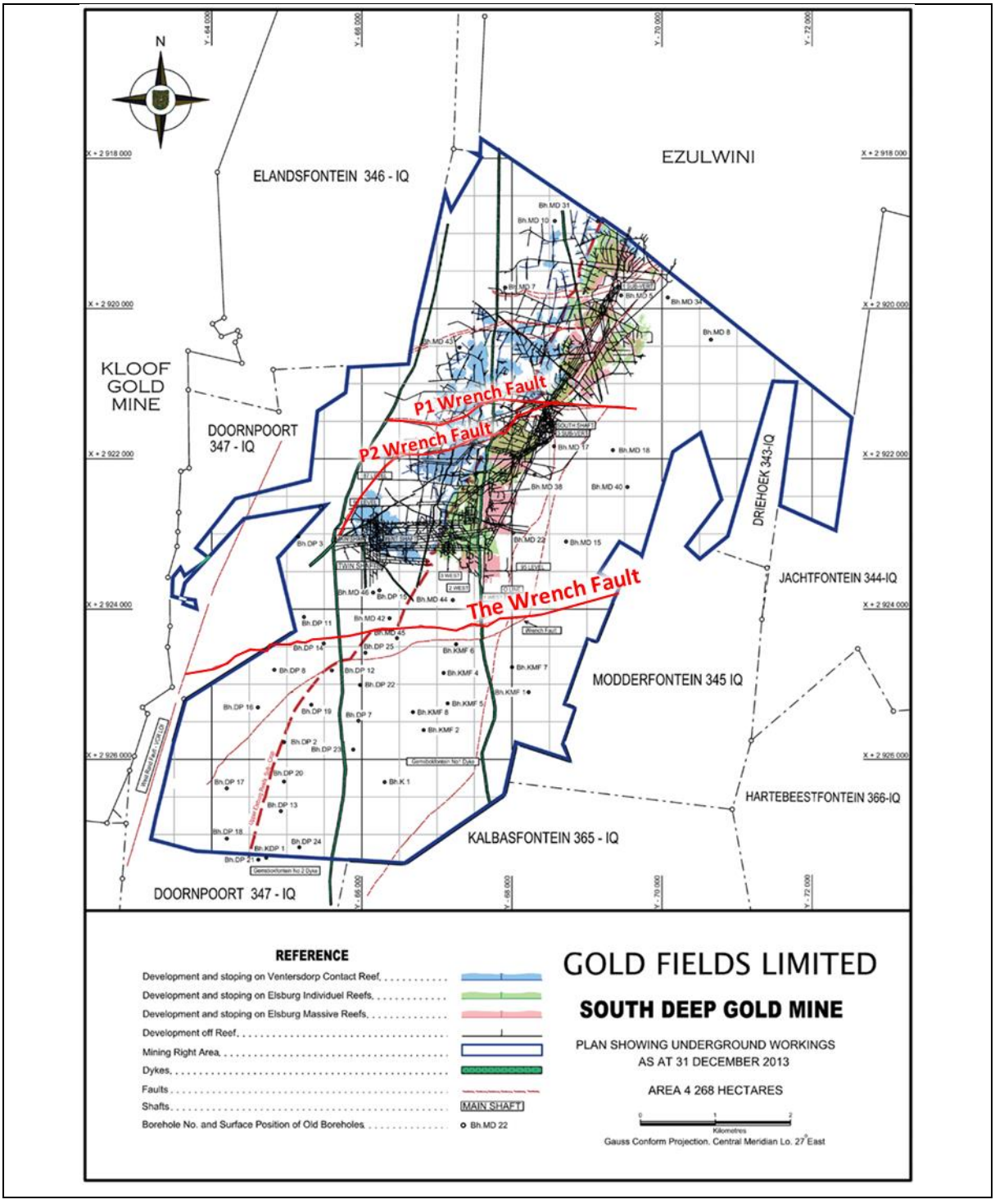


Figure 9: Mine plan of SDGM showing the main geological and mining features including the main wrench structures (modified after Gold Fields, 2013).

2.2.1 Structure of South Deep Gold Mine

The regional structural context of the West Rand Goldfield is presented in Figure 3. SDGM is located on the southern limb of the SSE-plunging West Rand Syncline (Tucker and Viljoen, 1986; McCarthy, 2006; Tucker et

al., 2016), to the east of the N-S striking Panvlakte-West Rand Fault horst block (Figure 3). The southern limb of the West Rand Syncline dips shallowly to the south (Tucker and Viljoen, 1986).

Tucker and Viljoen (1986) also recognised two main fault trends on WAGM located directly north of SDGM. The dominant fault system is a normal fault population trending roughly N-S in the north of the property and throwing predominantly down to the west (Figure 3). This fault system swings towards the southwest in the south towards SDGM. This SSW trend is readily recognised on SDGM and is generally sub-parallel to, or merges with the Panvlakte Fault Zone (Figure 4), which bounds the Panvlakte Horst to the west (Manzi et al., 2013).

Tucker and Viljoen (1986) and Tucker et al. (2016) discussed the structural setting of WAGM, where the Panvlakte Fault Zone generally displaces the stratigraphy down to the east. The South Shaft section of WAGM today represents the northern section of SDGM. The orientation of the reef within the fault blocks is not affected (Tucker and Viljoen, 1986). Two primary fault orientations were noted, namely N-S striking normal faults and E-W striking strike-slip faults, which segment the orebody both vertically and horizontally, with a right-lateral displacement of up to 2000 m with a variable vertical throw generally smaller in magnitude than the lateral displacement (Tucker and Viljoen, 1986). Generally, these faults exhibit a dextral strike-slip displacement with a down-to-the-north normal throw. In the north of the property some of the faults dip and throw down to the south (Tucker and Viljoen, 1986). The strike-slip faults were interpreted as predominantly pre-Transvaal in age as they do not displace the Black Reef, which unconformably overlies the Witwatersrand and Ventersdorp supergroups.

Tucker and Viljoen (1986) also discussed two categories of dykes. The older dykes are pre-Transvaal in age and trend E-W and NE-SW. Post-Transvaal dykes are generally of Pilanesberg age (1397±47 Ma by U-Pb method by Harmer and Armstrong, 2000) and trend N-S, attaining widths of ~30 m and indicating a significant post-sedimentation E-W extensional event. The older dykes are commonly displaced by the NNE striking faults, the wrench faults, and the younger Pilanesberg dykes. Very few - if any - faults are interpreted to displace the Pilanesberg dykes.

Subsequent to Arthur (1990), who did not discuss a tectonic interpretation, no additional literature has documented the geological structures on South Deep, with the exception of Obermeyer (2004). Obermeyer (2004) did not focus on the SDGM structural framework but presented a technical record of the processes to be followed to generate accurate structure plans for modelling purposes.

2.2.2 Detailed Stratigraphy of the UE7 and Upper Elsburg Massives on SDGM

The UE7 and Upper Elsburg Massives members at SDGM are made up of eight and seven beds, respectively (Figure 10**Error! Reference source not found.**). The beds are named using acronyms based on their stratigraphic location within their respective members, as well as on whether they constitute a conglomeratic reef or a middling quartzite. The full written names for each of the beds are seldom if ever used on the mine. The full names and how they are derived are included in this section as well as in the list of acronyms at the front of the thesis to assist the reader.

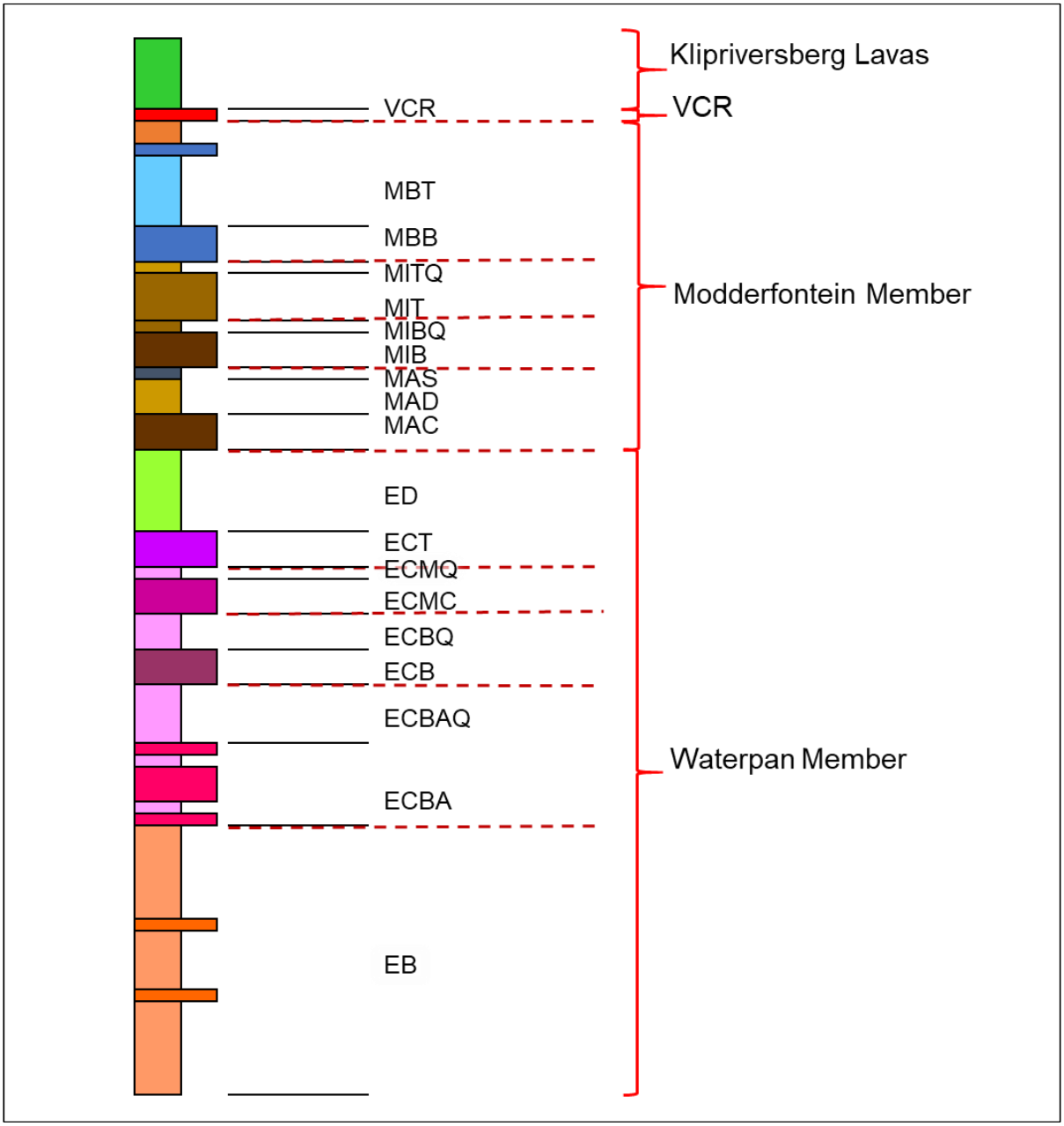


Figure 10: The stratigraphy of the UE7 and Elsburg Massives at SDGM (permission granted by Goldfields to reproduce).

A subset of the acronym table is added here in Table 1 for the reader's reference and should be reviewed in conjunction with Figure 10 and Figure 11.

Table 1: Bed acronyms used at SDGM

Bed Acronym	Full Name or Description
VCR	Ventersdorp Contact Reef
MBT	Massives 'B' Band Top
MBB	Massives 'B' Band Bottom Conglomerate
MIQ	Massives 'Intermediate' Band Quartzite
MIT	Massives 'Intermediate' Band Top Conglomerate
MIB	Massives 'Intermediate' Band Bottom
MAS	Massives 'A' Band Sand (an Orthoquartzite at the top of the MAD)
MAD	Massives 'A' Band Degenerate Quartzite (includes the MAS)
MAC	Massives 'A' Band Conglomerate
ED	Elsburg Individual 'D' Band Quartzite
ECT	Elsburg Individual 'C' Top Band
ECMQ	Elsburg Individual 'C' Middle Quartzite
ECMC	Elsburg Individual 'C' Middle Conglomerate
ECBQ	Elsburg Individual 'C' Bottom Quartzite
ECB	Elsburg Individual 'C' Bottom Conglomerate
ECBAQ	Elsburg Individual 'C' Basal Quartzite
ECBA	Elsburg Individual 'C' Basal Conglomerate
EB	Elsburg Individual 'B' Band (a footwall quartzite with intercalated conglomerate beds (may be polymictic) directly in the footwall of the Elsburg Individual 'C' Band)

The beds starting with "E" all belong to the UE7 and belonged to colloquially named stratigraphic "Elsburg Individuals, where each progressively coarser stratigraphic bed or "band" is represented by the second letter "B, C or D". The EC band has been further subdivided into a further "BA" for basal, "B" for bottom, "M" for mid and "T" for top. The suffix of "Q" or "C" represents the predominant lithology where distinction is required, where "Q" refers to quartzite and "C" refers to conglomerate (Arthur, 1990; Obermeyer, 2005).

The EC beds of the UE7 overlie the beds of the EB footwall unconformably and are primarily conglomeratic in nature. They are made up of numerous large-pebble conglomerate cycles that progressively become more argillaceous, i.e. less mature in character, upwards through the sequence (Arthur, 1990; Muntingh et al., 2005; Tucker et al., 2016).

The EC comprises 4 individual conglomerate zones named (from bottom to top) the ECBA (Elsburg Individual 'C' Basal Conglomerate), ECB (Elsburg Individual 'C' Bottom Conglomerate), ECMC (Elsburg Individual 'C' Middle Conglomerate) and the ECT (Elsburg Individual 'C' Top Band), all separated by interstitial argillaceous gritty to pebbly quartzites (Germs, 1989; Germs, 1990; Obermeyer, 2005). The interstitial argillaceous quartzites are named by using the name of the underlying reef zone with the suffix "Q". The conglomerate zones are commonly made up of at least two superimposed units, with the ECBA consisting of up to five conglomeratic pulses (Obermeyer, 2005). Page (1989) related this phenomenon in the ECT, with two superimposed conglomeratic cycles, as being an accommodation feature of a placer on a filled braidplain. As erosion rates in

the hinterland stabilise with little tectonic uplift, relaxation of the sedimentary system on the braidplain takes place, resulting in local subsidence and superposition of a new conglomeratic pulse.

The ED (ED Quartzite or Elsburg Individual 'D' Band Quartzite) conformably overlies the beds of the EC and is interpreted to be the final sandy phase of EC Sub-Unit sedimentation and consists of coarse to very coarse, khaki to khaki-green protoquartzite with intermittent laterally continuous pebble bands (Arthur, 1990; Muntingh, 2005; Obermeyer, 2005).

The ED is unconformably overlain by the conglomerates of the Elsburg Massives (Arthur, 1990). It is debatable whether the Modderfontein Member, colloquially known as the Elsburg Massives, belongs to the Mondeor Formation (SACS, 2006; McCarthy, 2006).

The Modderfontein Member consists of three reef zones, namely the MA, MI and MB units that together constitute the greatest volume of ore resources on SDGM. The “M” represents the upward progression from the “A” band, through the “I” or intermediate, followed by the “B” band. The third letter of every bed's name indicates whether it is the “B” bottom or “T” top bed within a band. In the case of the MA, the “C” refers to the primary lithologies, where “C” represents conglomerate, “D” represents “degenerate” (or quartzwacke) and “S” represents sand (Arthur, 1990; Obermeyer, 2005).

The lowermost of these units is the MA (Arthur, 1990), which consists of the MAC (Massives ‘A’ Band Conglomerate), which lies unconformably on top of the ED and EC units. The MAC consists of three major large-pebble conglomerate cycles and is typically pale grey in colour (Obermeyer, 2005). The MA package thickens towards the east, forming an immature zone at its top known as the MAD or Massives 'A' Band Degenerate Quartzite/Sand (MAD of Obermeyer, 2005). It is unconformably overlain by the orthoquartzitic, pale green MA Sand (MAS of Arthur, 1990; Obermeyer, 2005) or Massives 'A' Band Sand. The MA Conglomerate, overlain by the MA Degenerate Zone with its top MAS, together make up the MA Unit.

The MAS is overlain disconformably to conformably by the MIB (Massives ‘Intermediate’ Band Bottom), which varies from a coarse green, semi-siliceous quartzite with intermittent pebble lags in the north of SDGM, to a robust, medium pebble conglomerate within the current mining areas in the south. This bed is unconformably to disconformably overlain by the well-mineralised MIT (Massives 'Intermediate' Band Top Conglomerate) or MI “Top Band” that consists of typically two conglomerate cycles (Obermeyer, 2005).

The MI Top Band is conformably overlain by the green, siliceous, MI Quartzite or MIQ (Massives ‘Intermediate’ Band Quartzite) in the northern areas of the property. The MIQ changes to a robust, medium to large-pebble conglomerate in the southern areas of the property. The MIQ zone is unconformably to disconformably overlain by the well mineralised MB Bottom Band Conglomerate or MBB (Massives ‘B’ Band Bottom Conglomerate), which also consists of two or more distinct conglomerate cycles (Obermeyer, 2005). The MBB is conformably overlain by the MBT band (Massives ‘B’ Band Top), which typically consists of green quartzites interbedded with conglomerate bands in the northern parts of the mine. The MBT increase in percentage conglomerate in the southern parts of the current working. The MBT is unconformably to disconformably (towards the east) overlain by the VCR (Arthur, 1990).

The VCR is conformably overlain by the lavas of the Ventersdorp Supergroup.

The full Upper Elsburg and Elsburg Massives package attains a maximum thickness of approximately 130 m approximately 3 km east of the sub-outcrop. The Upper Elsburg Individuals and Elsburg Massives both approximate 50% each of the full stratigraphy. An approximate scale diagram depicting a typical full-scale exposure with general sedimentological descriptions and lithologies for the Elsburg Massives and UE7 is presented in Figure 11.

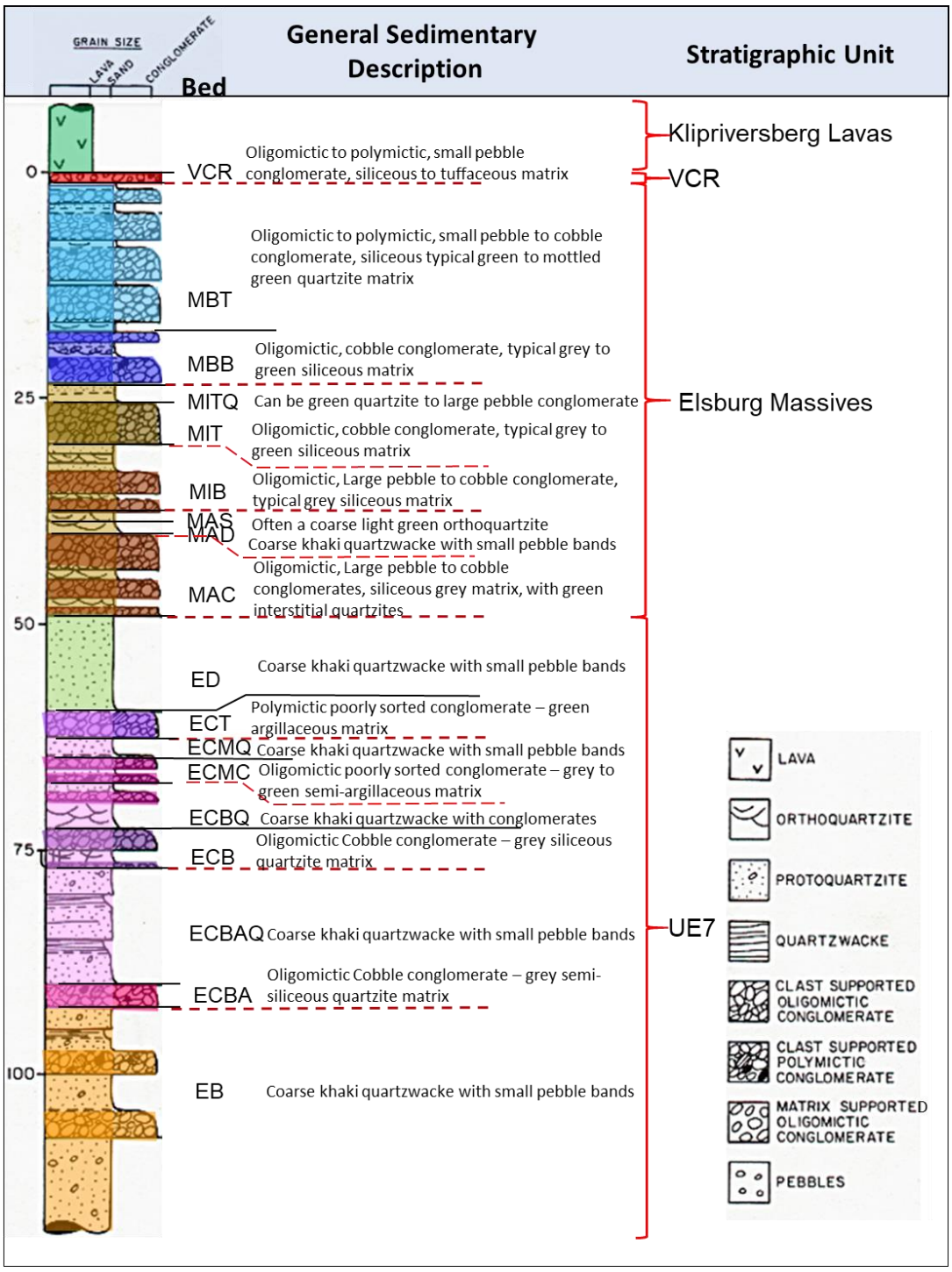


Figure 11: An approximate scaled stratigraphic column for SDGM with lithological expression and typical sedimentary descriptions for each bed (modified after Arthur, 1990).

2.2.3 Palaeo-current Data and Sedimentological Transport Directions on SDGM

Very little historical palaeo-current data from the various beds at South Deep have been collected. This is due to the massive nature of the reefs concerned, extensive mining with large excavations, and the associated safety concerns. However, historical published data and maps do provide a guide as to what palaeo-current directions should be expected. Vermaakt and Chunnett (1994) compiled palaeo-current data for the West Rand and the West Wits goldfields for the various primarily mined reefs in the areas, including the VCR, however, no data was presented on the Upper Elsburgs. In the SDGM area the palaeo-current direction for the VCR measured near the present Twin Shaft Complex is indicated to be towards the SE to SSE (Figure 12).

SDGM has subsequently used statistical and geostatistical parameters to assist in the Mineral Resource estimation processes (Osburn, et al., 2014). According to Osburn, et al. (2014) a strong correlation exists between sedimentological parameters and gold distribution within the Upper Elsburg and VCR sediments.

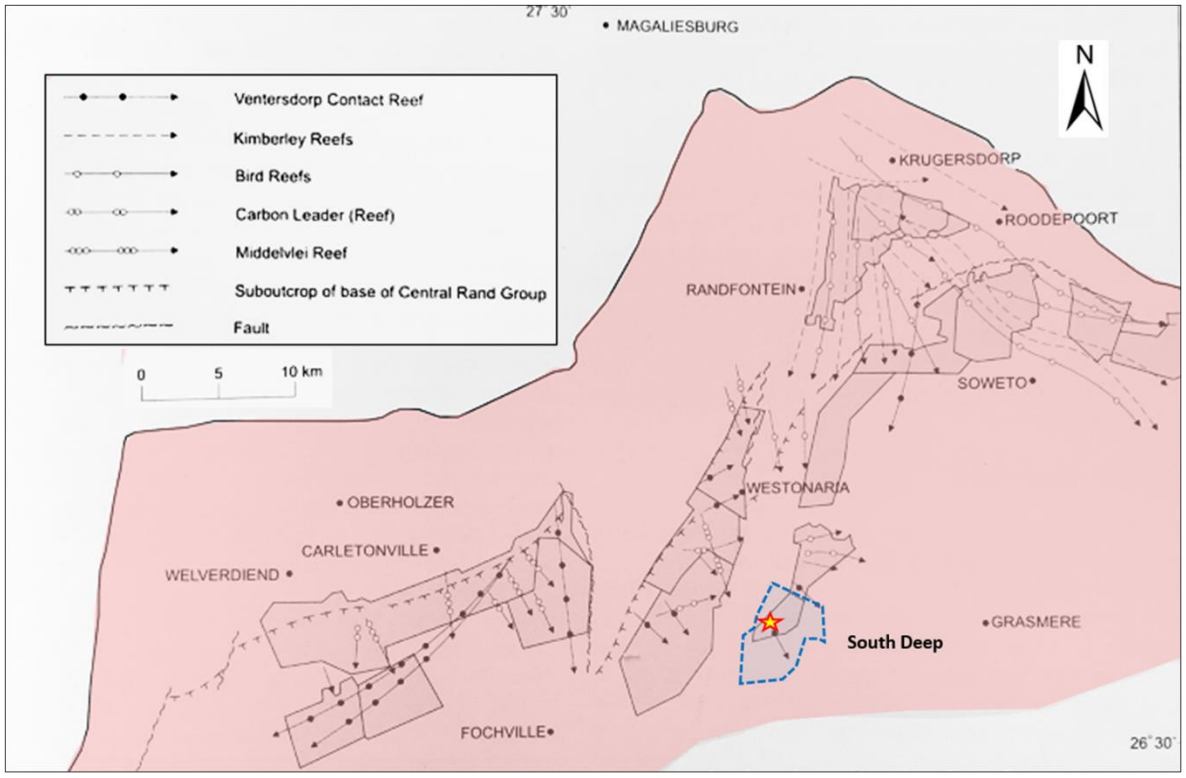


Figure 12: Compiled palaeo-current data for various reefs mined in the West Rand and West Wits goldfields. Palaeo-current direction for the VCR in the South Deep area is indicated to be NW-to-SE to NNW-to-SSE. (modified after Robb et al. (1998) after Vermaakt and Chunnett, 1994).

Due to the single reef character of the VCR, it is relatively easy to infer a preferable palaeo-current direction for whole channels by mapping out the edges of the stoped-out workings especially in the area around the Twin Shaft Complex, which render an approximate NW-to-SE trend as presented in Figure 13. However, the stacked nature of the Upper Elsburg reef package and the associated stacking of the workings makes it difficult to use the mine workings to identify payshoots or channel trends for the Upper Elsburg Reefs.

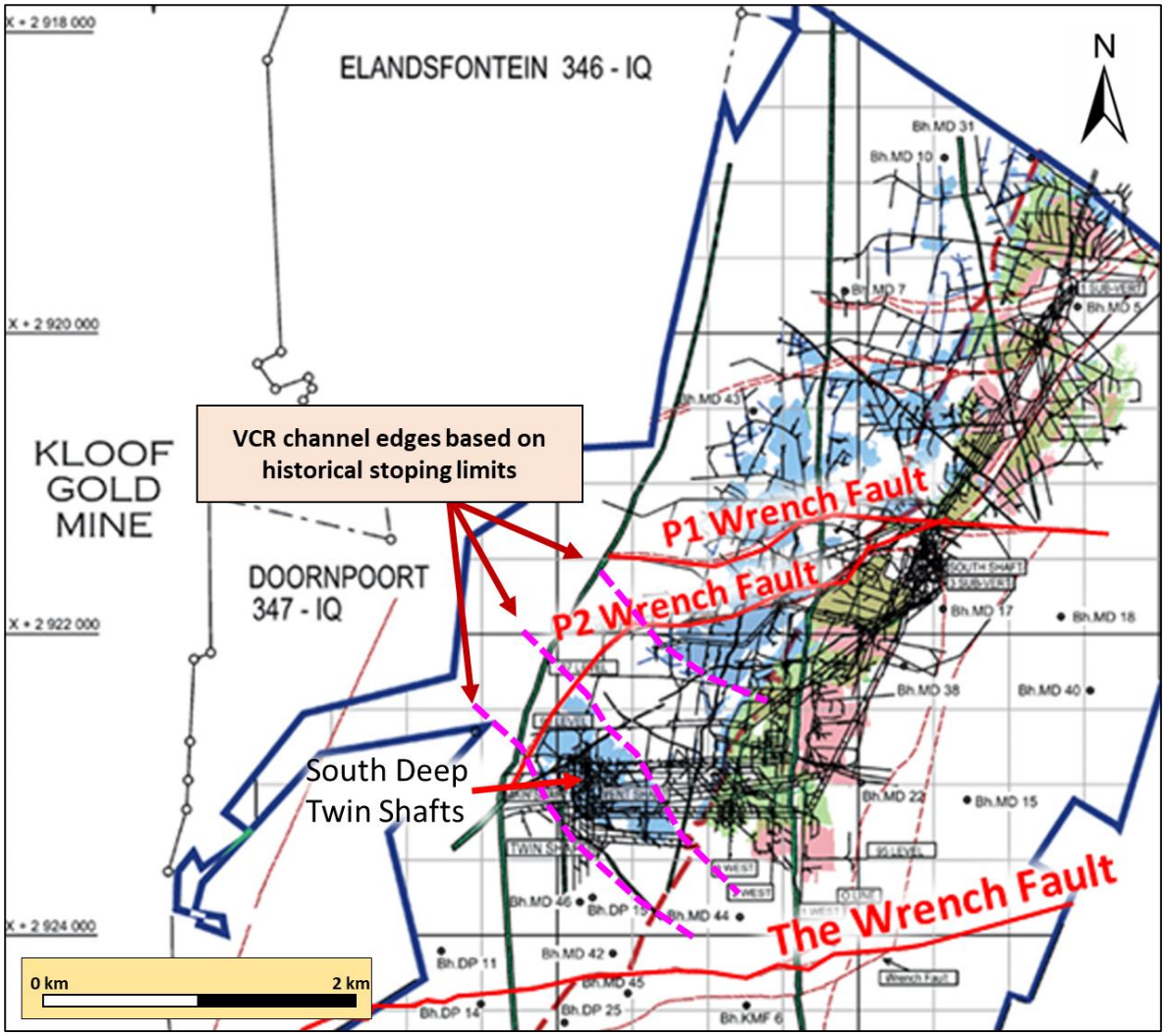


Figure 13: A section of the South Deep Shareholders Plan (modified from Goldfields, 2013) depicting the major wrench structures and the VCR channel edges (trending NW-SE) identified by the stoped-out mine workings.

2.3 Development of Geological Modelling at SDGM

2.3.1 Stratigraphic and Sedimentological Modelling Advancements at SDGM

Detailed sedimentological interpretations for the various beds in the UE7 and Elsburg Massive package requires an understanding of the local geological structure and modelling methodologies employed at SDGM. SDGM previously utilised a hybrid system (pre-2007) of hand-drawn 2D structure plans to generate 3D wireframe geological models in CAE Datamine Studio 3™. This hybrid system of modelling formed the foundation of the sedimentological database analysed in this study and is thus presented in detail. Progressions to full 3D digital modelling, with no interim structure plans after 2007 at SDGM are not discussed in detail. as indicated in Section **Error! Reference source not found.**

3D digital modelling generated from hand-drawn geological structure plans commenced in 2000. Only five stratigraphic zones were modelled, including a composite zone or "Shoreline Composite" ("SLC") where further stratigraphic definition was considered impractical, namely (Figure 14**Error! Reference source not found.**):

1) Ventersdorp Contact Reef (VCR)
2) Elsburg Massives (MBs)
3) UE7 ED Quartzite (ED)
4) UE7 ECs (EC)
5) Shoreline Composite Zone (SLC)

The "SLC" is an incorrect informal historical term used on the mine to describe a zone of combined attenuated stacked beds ±10 m in height usually within 30 m to 40 m to the east of the Upper Elsburg Sub-outcrop where individual reefs are not discernible and has no bearing on the origin of the sediments. The Upper Elsburg sediments are understood and accepted by mine geologists to be fluvial in origin.

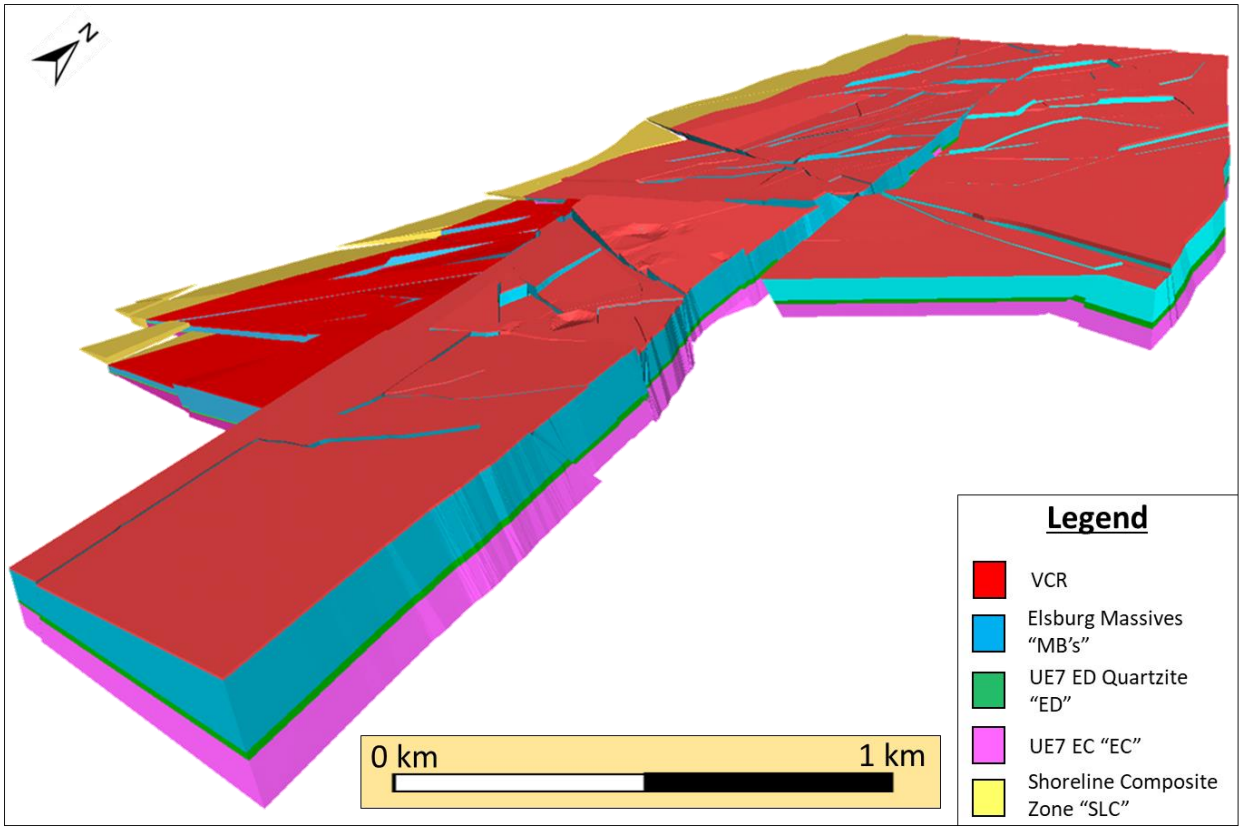


Figure 14: Oblique 3D view of the 2001 SDGM geological wireframe model (permission granted by Goldfields to reproduce).

The 2005 sedimentological study of Muntingh et al. (2005) divided the UE7 into four stratigraphic beds, namely the EC9, ECB, ECT and ED and the MBs of the Elsburg Massives into the MAs and MBs. The VCR and SLC were still included in the modelling. Sub-division of the UE7 and Elsburg Massives was supported by persistent,

correlatable, underlying stratigraphic unconformities that were traceable across the property. A total of eight stratigraphic sub-divisions were, thus, modelled subsequent to the study, namely:

1) VCR
2) MBs (Elsburg Massives "B" Band, consisting of the MIT, MBB and MBT)
3) MAs (Elsburg Massives "A" Band consisting of the MAC and the overlying MAD)
4) ED (UE7, ED Quartzite)
5) ECT (UE7 EC Top)
6) ECB (UE7 EC Bottom consisting of the ECB, ECB degenerate or ECBD and ECMQ)
7) EC9 and EC9Q (UE7 EC Basal or ECBA and ECBA Quartzite)
8) SLC (Shoreline Composite)

However, Muntingh et al. (2005) postulated the existence of 14 stratigraphic beds (Figure 15**Error! Reference source not found.**) and were the first to relate the importance of unconformities at SDGM to the occurrence of conglomerate beds and the location of possible mineralisation. This constituted the first property-wide sedimentological study for the UE7 and Elsburg Massives stratigraphies.

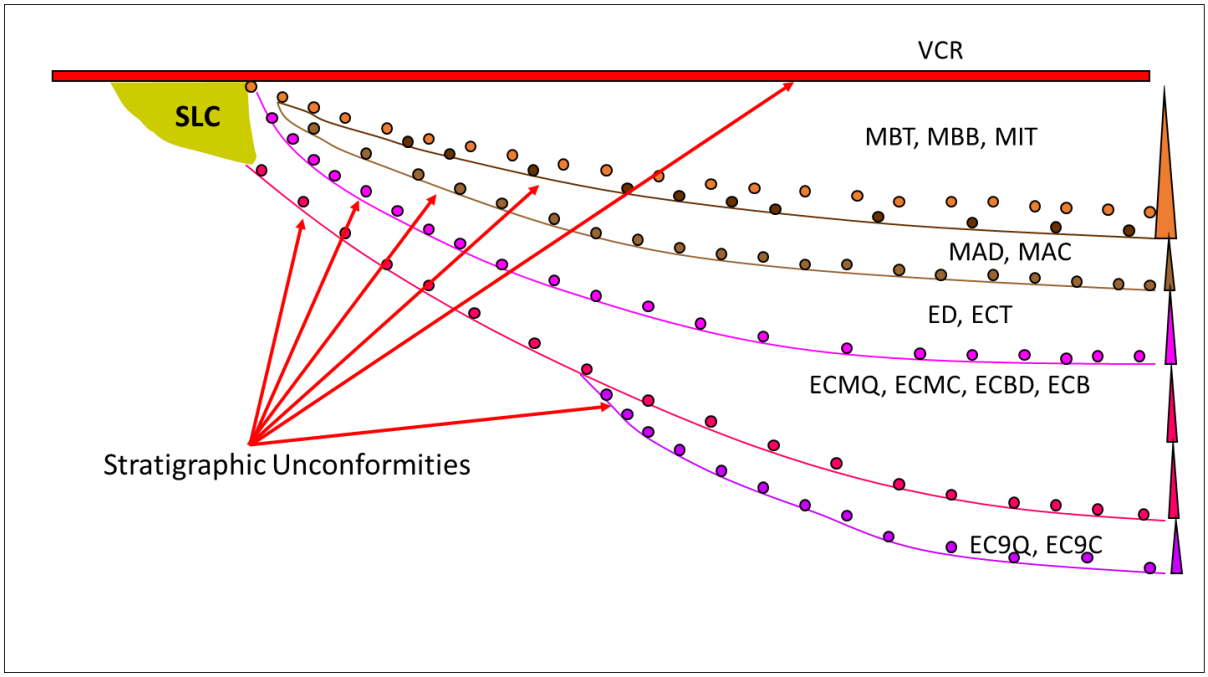


Figure 15: The 2005 SDGM modelled unconformities with the SLC zone (modified after Muntingh et al., 2005).

Recommendations stemming from Muntingh et al. (2005) included further stratigraphic sub-division of these Members for modelling purposes to enhance accuracy of future Mineral Resource estimates for the mine (Muntingh et al., 2005).

In 2007, 16 beds were identified, modelled and projected into the amalgamated SLC zone, resulting in its elimination in the modelling process. The SDGM structural model was further enhanced with the inclusion of the 2004 Seismic Survey data tied in with the existing mapped and interpreted geological structures. The advancements in SDGM geological modelling is presented in Figure 16**Error! Reference source not found.** and

the increase in modelled stratigraphic detail over time is presented in Figure 18**Error! Reference source not found.**.

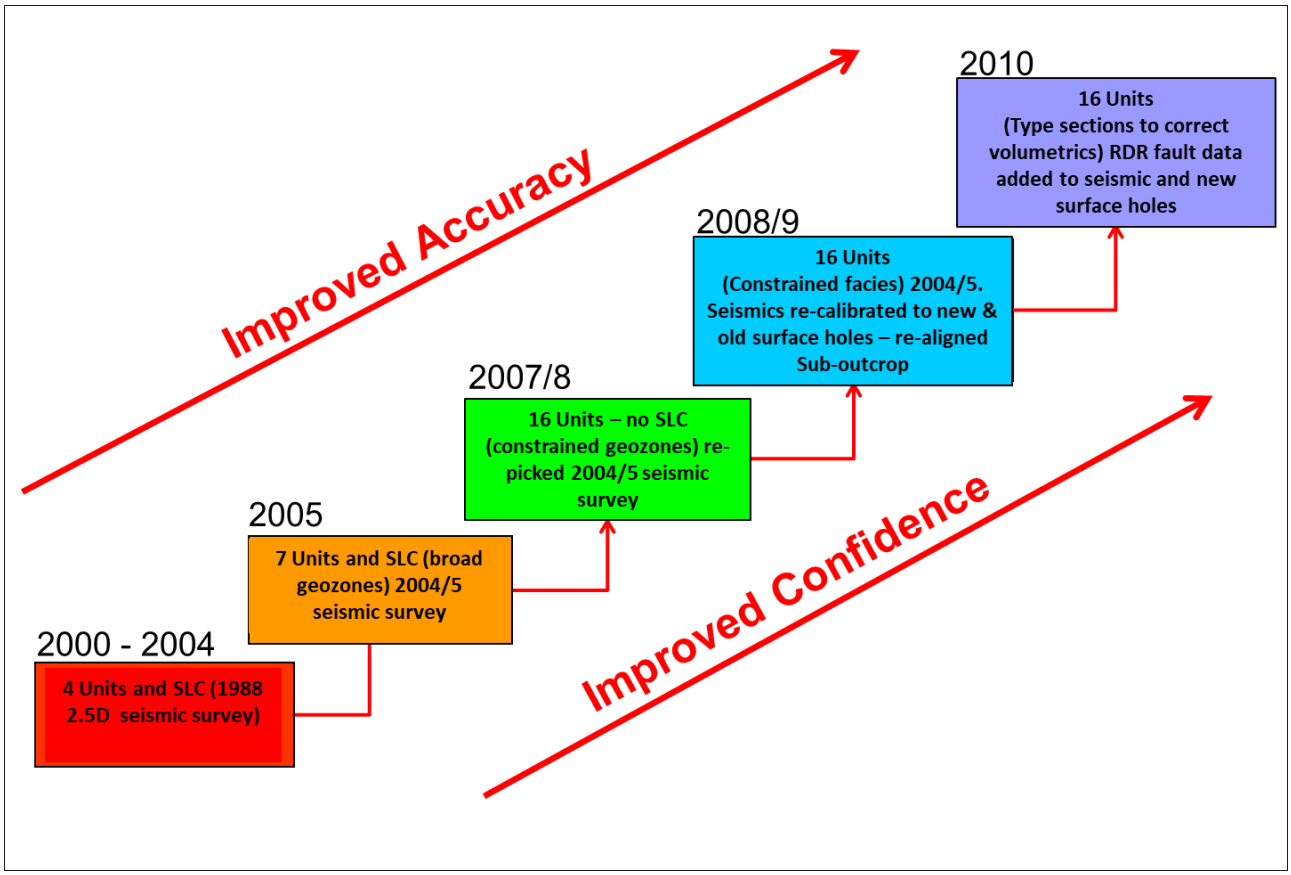


Figure 16: The historical development of geological modelling at SDGM (permission granted by Goldfields to reproduce)

The schematic W-E section presented in Figure 17**Error! Reference source not found.** presents the mine's interpreted relationships between the 16 main stratigraphic sub-divisions or beds comprising the Upper Elsburgs for reporting and modelling purposes (Obermeyer, 2005; Osburn et al., 2014). The stratigraphy represents a typical rotating onlap relationship (Germs and Reynolds, 1991) with numerous local unconformities and each subsequent reef cannibalising the underlying units.

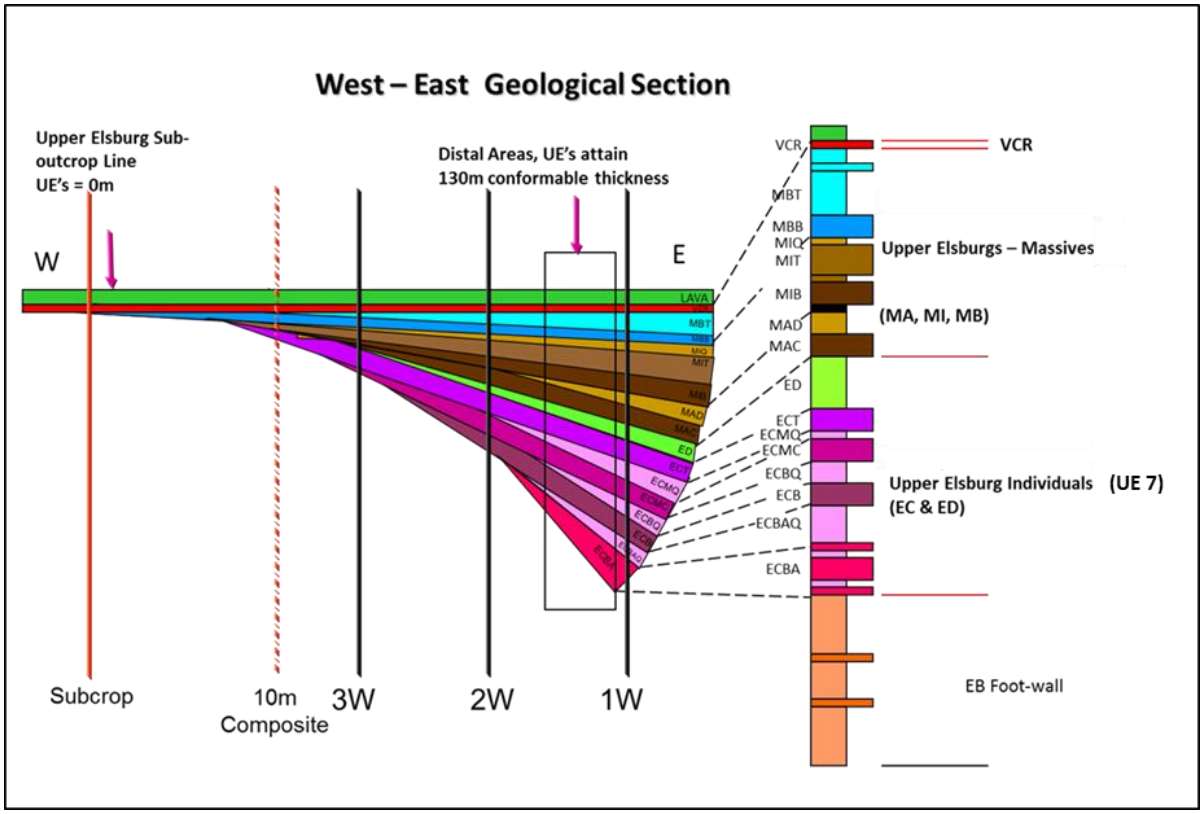


Figure 17: Schematic west to east section through the Upper Elsburgs at SDGM presenting their stratigraphic relationships and the stratigraphy as it is currently modelled (Obermeyer, 2005). The black vertical lines represent mining cross-cut positions relative to the stratigraphic make-up (permission granted by Goldfields to reproduce).

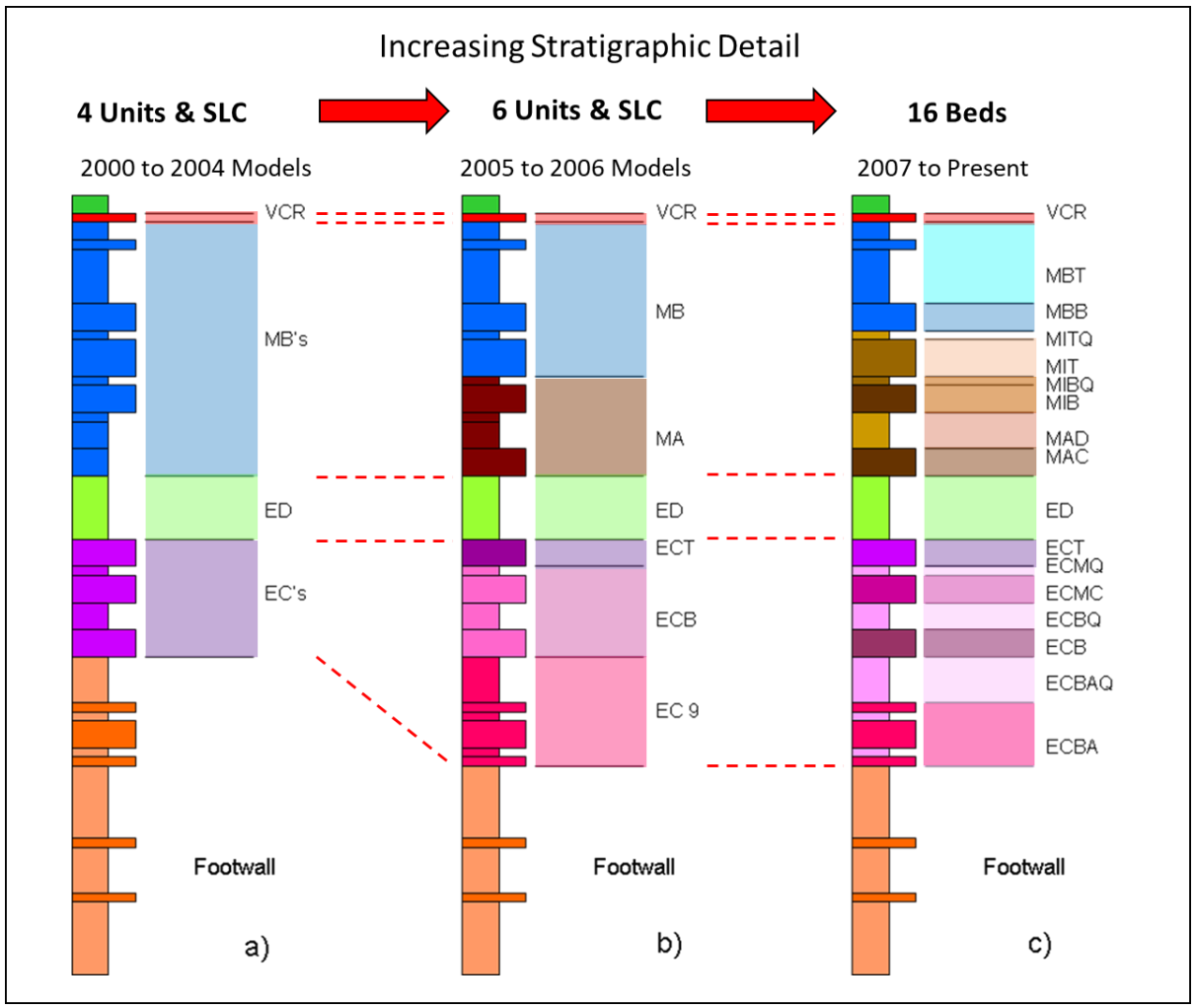


Figure 18: The advancements in modelled stratigraphic detail at SDGM over time (Obermeyer, 2005) (permission granted by Goldfields to reproduce).

Software upgrades and the speed of 3D model generation have improved in recent years, however, the 16-unit division that was first modelled in 2007 (Figure 17**Error! Reference source not found.**) and presented in detail in Figure 18**Error! Reference source not found.**, remain unchanged.

2.3.2 Hybrid Geological Structure Plan and Model Generation (Pre-2007)

Concerted attempts to generate cohesive and continuous structural models across the Upper Elsburgs were not attempted until 2001 (Obermeyer, 2004) and the existence of major lateral movement structures (wrench faults) in existing working areas was suspected, but not conclusively proven until 2001 (Obermeyer, 2004). Structure models only covered the working areas and did not consider structures outside of the workings.

The methodology for structure plan generation consisted of seven distinct phases (Obermeyer, 2004), namely:

i) Reference surface selection

ii) Borehole processing, verification, and plotting

iii) Geological mapping – plotting

iv) Base Plan construction – contours and geological structures

v) Vertical isopach construction

vi) Projection of geological structures and construction of contours for other horizons

vii) Identification of wrench structures.

i) Reference surface selection

Horizons within a geographical area, bound by continuous geological structure with the most exposure, or a large volume of available mapping data (Figure 83**Error! Reference source not found.**), were selected to construct a base plan from which all other structural bed surfaces were projected (Obermeyer, 2004).

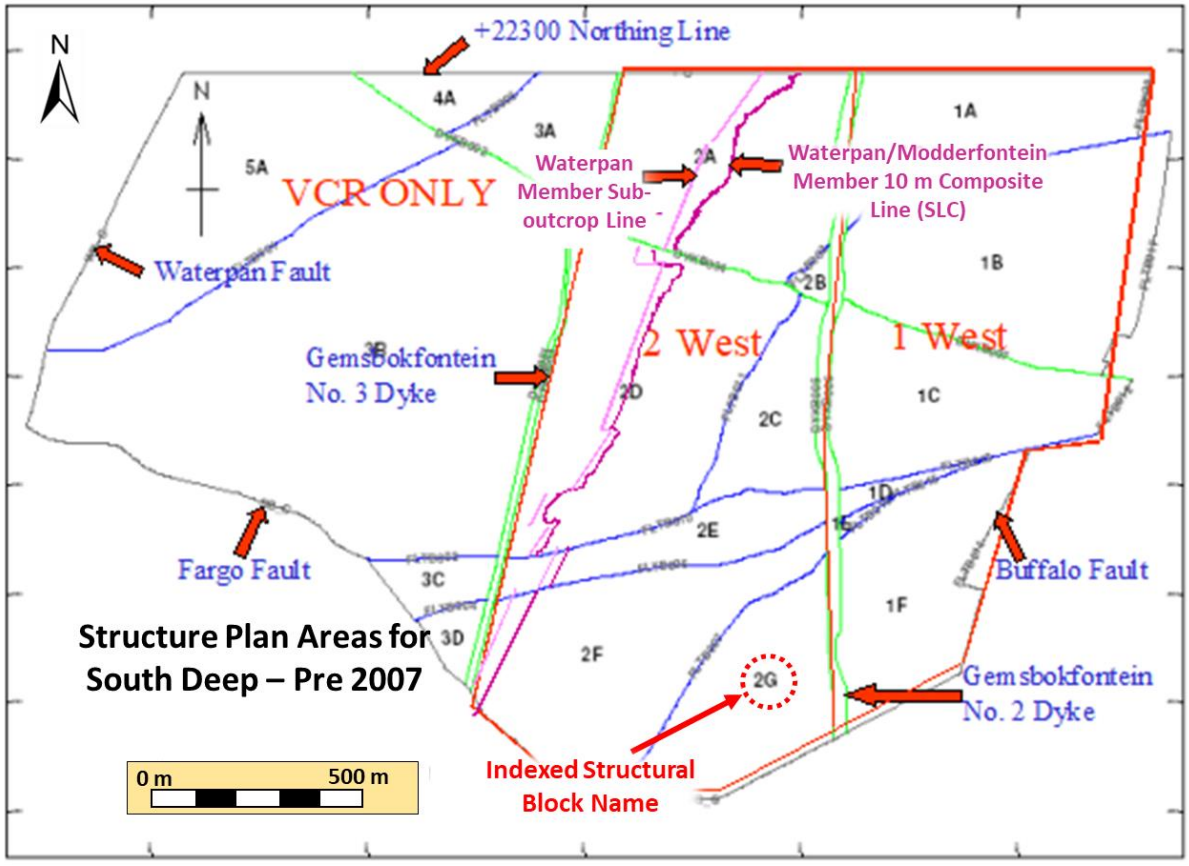


Figure 19: Geological boundaries and modelling of working areas (2D) only for SDGM pre-2007 (modified after Obermeyer, 2004) (permission granted by Goldfields to reproduce).

ii) Borehole processing, verification, and plotting

All the borehole files (hardcopy and digital logs) located within a specific structural block, bound by significant intrusions and/or potential wrench structures (Figure 19**Error! Reference source not found.**) and those located within a 100 m perimeter of the selected area were sourced by: a) borehole collar co-ordinates and b) borehole layout (Figure 81**Error! Reference source not found.**) (Obermeyer, 2004).

Layouts were sourced from the mine borehole layout files. Borehole collar positions were checked relative to existing mine development and mine stoping plans (Figure 82**Error! Reference source not found.**) (Obermeyer, 2004).

All borehole collars were verified to exist on the mine workings plans, and the layout collars correlated to the plotted drilling positions and elevations in order to prevent typographical or plotting errors being carried through to the modelling database. Incorrect collars (due to typographical errors and incorrect scaling) were rectified where possible, while those that could not be corrected were discarded. Calculated bed or reef contact elevations per bed were plotted onto a blank borehole reference plan for vertical holes (Figure 81**Error! Reference source not found.**). Inclined holes with their various bed intersection points were subsequently plotted separately on trace borehole trajectory lines, directly onto the working base plan and the subsequent projected surface plans (Obermeyer, 2004).

iii) Geological mapping – plotting

Hardcopy geological mapping files were reviewed together with the underground geological mapping plans to ensure that all mapping was plotted onto the original stope sheets. Outstanding mapping was plotted onto the original stope sheets for digitising as a permanent record and interpretation (Figure 83**Error! Reference source not found.**) (Obermeyer, 2004).

All mapping was traced onto a reference structure base plan. As stoping, in any specific area, often takes place on multiple stratigraphic horizons, mapping for all the overlying and underlying stopes and development was sourced and reviewed for completeness. These other stope sheets were taken and overlain on the base plan in order to check consistency in interpretation of geological structures between the various beds. Where structures existed on other horizons other than on the base horizon plan, these were projected to the base plan using trigonometry, where the difference in elevation between the horizons was calculated using mine survey pegs. This ensured an all-inclusive base plan of all mapped structures falling within a chosen area (Obermeyer, 2004).

iv) Base Plan construction – contours and geological structure

Following Step (iii), the base plan with the plotted underground mapping was laid over the borehole base plan and all relevant borehole reef intersection points with the projected reef elevations for later contour construction were transferred to the reference structure base plan. The inclined borehole "plan view" projected borehole traces with the relevant bed elevations and intersection positions, were calculated with trigonometry, or projected from sections (Figure 82**Error! Reference source not found.**), and plotted directly onto the base plan (Obermeyer, 2004).

Geological mapping data from the mine mapping files were then reviewed and target reef/bed contact elevations were calculated using mine survey pegs. Bed strikes and dips (obtained from routine underground

mapping) were also plotted onto the base plan. The mapped reef contact elevations were then checked for agreement with the surrounding borehole bed intersection points (Figure 84**Error! Reference source not found.**) (Obermeyer, 2004).

Where the difference between mapped bed elevations and borehole bed intersection point elevations exceeded 1.5 m, the relevant borehole log was reviewed, and calculations and plotting checked. Once plotting and verification of all bed elevation points was complete, mapping was tied up to form fault polygons (blocks). Contours at 5 m vertical elevation intervals were then constructed, using the "3-point problem" methodology, from the boreholes bed intersection points and underground mapped positions within the individual fault blocks (Figure 85**Error! Reference source not found.**). The strike of the constructed contours was reviewed relative to the mapped strike and dip measurements and a best fit obtained (Figure 85**Error! Reference source not found.**) (Obermeyer, 2004). Constructed fault throws, where contours were terminated against constructed faults, were compared to underground mapped and interpreted fault throws to validate the historical mapping. In instances where differences between constructed contour elevations and mapped elevations exceeded 1.5 m, boreholes, and other mapping in the area or in the over- or underlying stopes were reviewed for correction or possible re-interpretation. Where mapped fault throws were validated, reef strikes were adjusted such the fault throws honoured the mapped fault throw (Obermeyer, 2004).

Neighbouring fault block contours were tied up and correlated by applying mapped throws to the bounding faults as a guide and terminating bed contouring against these faults (Figure 85**Error! Reference source not found.**). This resulted in a continuous and complete structure model for the base plan horizon (Obermeyer, 2004).

Modelling resolution with the hand-drawn structure contours is limited to faults only exceeding 1 m in throw, thus not presenting the full spectrum of the existing fault population with respect to smaller faults. Incomplete mapping of historical workings resulted in some faults not being recorded on the plans. These faults were interpreted and inferred in areas where significant contour dislocations occurred. Their existence was corroborated during projection between the various horizons by ensuring dislocations were continuous throughout the projected stratigraphy.

v) Vertical isopach construction

Vertical isopachs were selected instead of true bed height or thickness due to the following:

1) The SDGM beds dip gently, and more importantly relatively consistently, to the south at an approximate 17°.
2) It is simpler to work on a true plan view, rather than compensating for the construction of a rotated view in the true plane of the reef, when generating 2D paper plans. A rotated plane construction would necessitate excessive rotation of all stoping development data, all borehole data and all the mapping data, by some 17°. This extensive rotation would significantly increase the probability of projection errors.

Vertical isopach calculations are demonstrated in section view in Figure 86**Error! Reference source not found.**.

Limitations with the hand-drawn vertical projection methodology include:

1) All plotting and projection of geological structures from the base plan are approximate and not precise.
2) Average applied bedding dips of 17° for borehole calculations relate approximate bed elevations and are not precise.

Mitigating factors to the approximate methodology employed include:

1) Projection between bed surfaces is relatively quick.
2) Relative accuracy is acceptable for the scale at which the 3D geological modelling and resultant mine planning are conducted.
3) The shallow dip of the beds at SDGM compared to the vertical projections employed relates to a maximum variance of 6° in trigonometric terms or as a maximum variance of <1% from the true bed elevation.

Following this, a blank plan for the horizon vertically closest to the base plan horizon (above or below), was laid over the original borehole plan and all pertinent borehole information regarding this horizon transferred onto the blank plan, including angled borehole reef intersections (Obermeyer, 2004).

To maintain accurate volumetrics within a fault block during contour construction, the vertical difference in bed height (vertical isopach point) between the original contour plan and the new beds' borehole intercepts was calculated and plotted. A 3-point problem methodology was utilised to generate vertical isopach lines by joining points of equal elevation difference, as demonstrated in Figure 87**Error! Reference source not found.** (Obermeyer, 2004).

vi) Projection of structures and construction of contours for the other horizons

Horizontal projection distances for structures were trigonometrically calculated using the mapped fault dips. The dip-corrected fault traces were then plotted on the projected plan (Figure 88**Error! Reference source not found.**) (Obermeyer, 2004).

The contours for the bed on the projected plane were then constructed by connecting points of equal elevation identified by cross-over points between vertical isopachs and the previous horizon's contour lines. Elevation difference points of 1 m between previous contours were generated to assist in defining projected bed elevations and to ensure correctly interpreted bed strike, as demonstrated in Figure 89**Error! Reference source not found.** (Obermeyer, 2004).

Cross-cut sections and sections through borehole clusters were reviewed to validate the projected bed elevations. All boreholes were checked for proximity to geological structures and for potential impact by these structures in the boreholes. Bed elevations defined by structurally impacted boreholes were corrected by adding or subtracting the mapped throw of the structure to the original indicated borehole zone thickness, to compensate for fault throws (Obermeyer, 2004).

vii) Identification of wrench structures

Geological structures correlating with consistent bends in the constructed vertical isopachs were identified and were inferred to be wrench structures. Isopachs were then cut off against the structure in order to indicate discontinuity of thickness and strike across the fault (Figure 90**Error! Reference source not found.**) (Obermeyer, 2004).

Where lateral movement on faults had been inferred on the first projection plan, consistency of the vertical displacement across a structure was reviewed for all modelled horizons. In all cases the interpreted wrench structures presented consistent horizontal isopach offsets but varying vertical throws for the various beds, thus supporting the interpretation of lateral displacement faults. In all cases these structures were found to cross the Upper Elsburg sub-outcrop against the VCR, where mapping and drilling confirmed lateral dislocation of the sub-outcrop line. The identified wrench structures varied in lateral displacement from 10 m to 950 m (Figure 4).

Both left-lateral and right-lateral displacement structures were identified: right-lateral (dextral) structures presented dislocations from 60 m to 950 m, whereas left-lateral (sinistral) structures depicted dislocations not exceeding 100 m (Figure 4**Error! Reference source not found.**). Right-lateral wrench faults were found to strike from E-W to ENE-WSW, while left-lateral wrench faults strike from WNW-ESE to ENE-WSW. Underground exposure of these structures where observable, show these structures to mostly dip at approximately 75° to the north and may be filled with mylonitic and/or dyke material.

2.4 Depositional Environments and Strato-tectonic Models

Numerous tectonic models have been proposed for the formation of the Witwatersrand Basin. The most prominent of these are discussed below. Interpretations have become more complicated and comprehensive as the understanding of tectonic systems have improved over time.

2.4.1 Basin-edge Concept Model

Depositional environments for the sediments in the Witwatersrand Supergroup have been speculated upon since the discovery of the Witwatersrand Goldfield. Pretorius (1979) classified these as terrestrial/continental, marginal or transitional marine, and marine. According to Pretorius (1979), various environments had their own proponents as regards the evolution of the Witwatersrand Basin. Recognised terrestrial environments ranged from fluvial, through lacustrine, paludal and desert, to glacial, while the marginal or transitional environments included deltaic, lagoonal and littoral conditions, whereas the marine class included neritic (between low tide to 200 m).

The first comprehensive attempt to relate the gold-bearing placers and their intercalated sedimentary packages across the basin to a basin-wide strato-tectonic model was by Brock and Pretorius (1964). Four major entry points of material into the basin located in structurally depressed portions of the basin rim between granite domes were proposed. The entry points were positioned near Benoni, Krugersdorp, Klerksdorp and Welkom and were interpreted as deltas associated with major peripheral faults on the north-western edge of the depository that

formed an active source of sediment. The faults were interpreted as normal dip-slip, implying an active extensional setting for Central Rand Group deposition. Brock and Pretorius (1964) called their model "The Basin Edge Concept" (Figure 20).

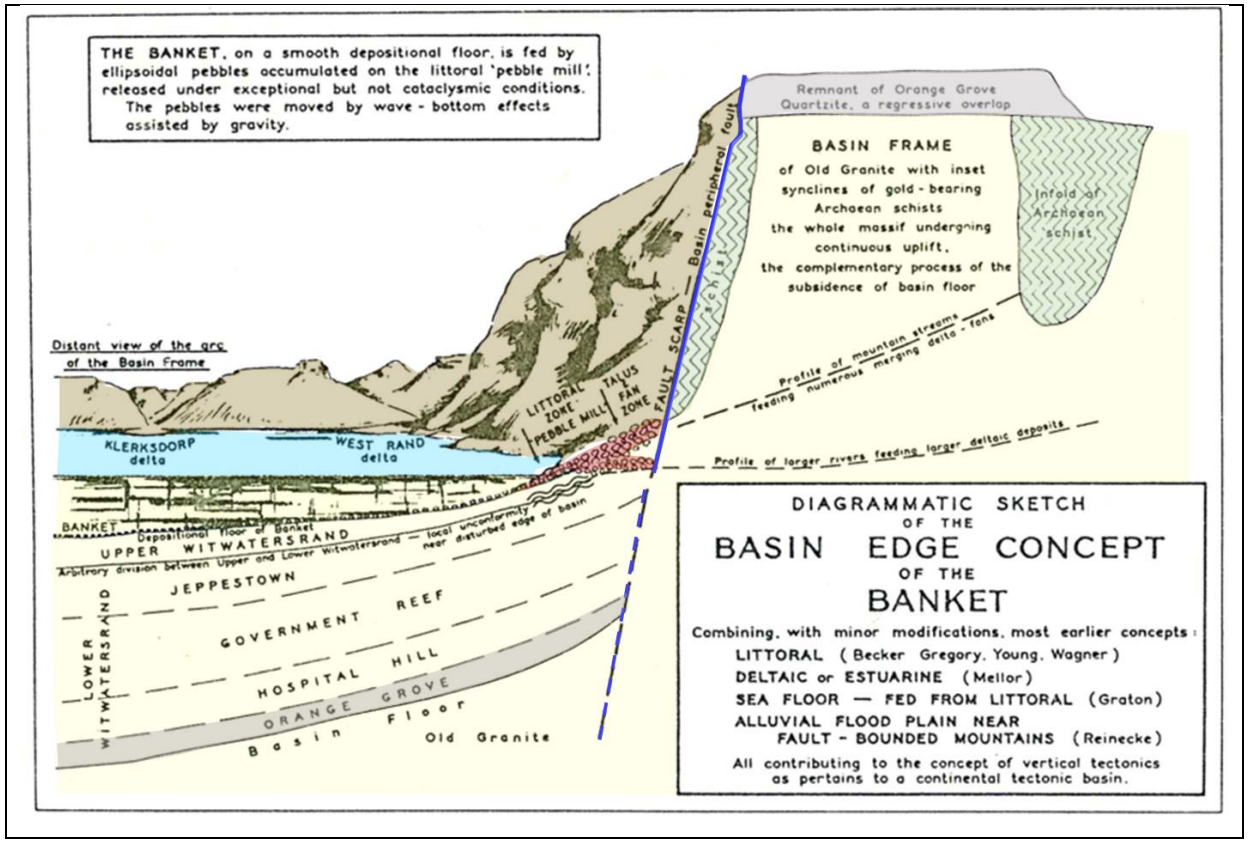


Figure 20: A pictorial representation of the basin-edge concept model (modified after Brock and Pretorius, 1964).

Bickle et al. (1982) proposed a rift-type, or crustal thinning model for the Witwatersrand Basin consisting of two stages of subsidence: the first related to rapid subsidence owing to thinning or crustal loading, followed by a protracted thermal stage where the lithosphere relaxed to equilibrium or isostatic thickness. Bickle et al. (1982) further postulated that in some early Precambrian basins, the cause of subsidence may have been crustal extension with developed fault grabens evolving into continental margins. Bickle et al. (1982) were recognised as being pioneers in terms of applying plate tectonics as a means of explaining the evolution of the Witwatersrand (Myers, et al. 1989).

2.4.2 Foreland Basin Model

Burke et al. (1986) were the first to propose a foreland basin tectonic environment for the formation of the Witwatersrand Basin. Foreland basins, which are elongated troughs adjacent to mountain belts, are characterised by the following (Burke et al., 1986):

1) Foreland basins are asymmetrical in cross section, presenting a thicker sedimentary package and steeper dips on the side adjacent to the mountains.

2) Foreland basins are bounded on the side nearest the mountains by thrust faults, while the opposite margin may present uplift with or without normal faulting throwing downwards toward the basin.
3) Sedimentary facies may include a lower "flysch" sequence and an upper "molasse" facies.
4) There is unlikely to be much magmatism in the basin.
5) The margin closest to the mountains may exhibit significant erosion or cannibalisation of sediments, with numerous unconformities occurring.
6) Deformation may be syn-sedimentary, younging and becoming weaker away from the mountain front.
7) A progressive migration of the depositional axis, normal faults and thrust faults occurs away from the mountains, especially in collisional-type foreland basins.
8) The basin may shrink with time in response to viscoelastic relaxation of the lithosphere.

Burke et al. (1986) remarked that the Witwatersrand Basin was remarkably similar in formation and characteristics to Phanerozoic basins as found cratonward of an Andean-type arc in the southern Andes of South America. The Limpopo Mobile Belt was interpreted as the remnants of to a collision-related plateau, similar to the active Tarim and Tsiadam Basins north of the Tibetan Plateau (Burke et al. 1986).

Burke et al. (1986) noted the West Rand Group thickens towards the northwest, where bedding has steep dips, while the Central Rand Group thickens towards the centre of the preserved portion of the basin. Both groups thin considerably towards the southeast, with shallower dips in the same direction. The authors argued that a change from "flysch" deposits to "molasse" type deposits is also reflected in the upward progression of the Witwatersrand stratigraphy. It was also demonstrated that the northwestern margin was bound by thrust fault systems and that the depositional axis of the Witwatersrand Basin progressively migrated some 10 km towards the southeast, away from the northwestern margin. The occurrence of unconformities and the associated cannibalism of the underlying units was noted along the active thrust fault-bound margins of the basin, which grade into disconformities towards the southeast. In addition, they noted that very little magmatic activity took place during the formation of the basin.

Burke et al. (1986) further depicted the Witwatersrand Basin, or trough, in relation to the Limpopo Mobile Belt, which was interpreted as having formed concurrently as a collision zone between the Kaapvaal Craton and the Zimbabwe Craton (Figure 21).

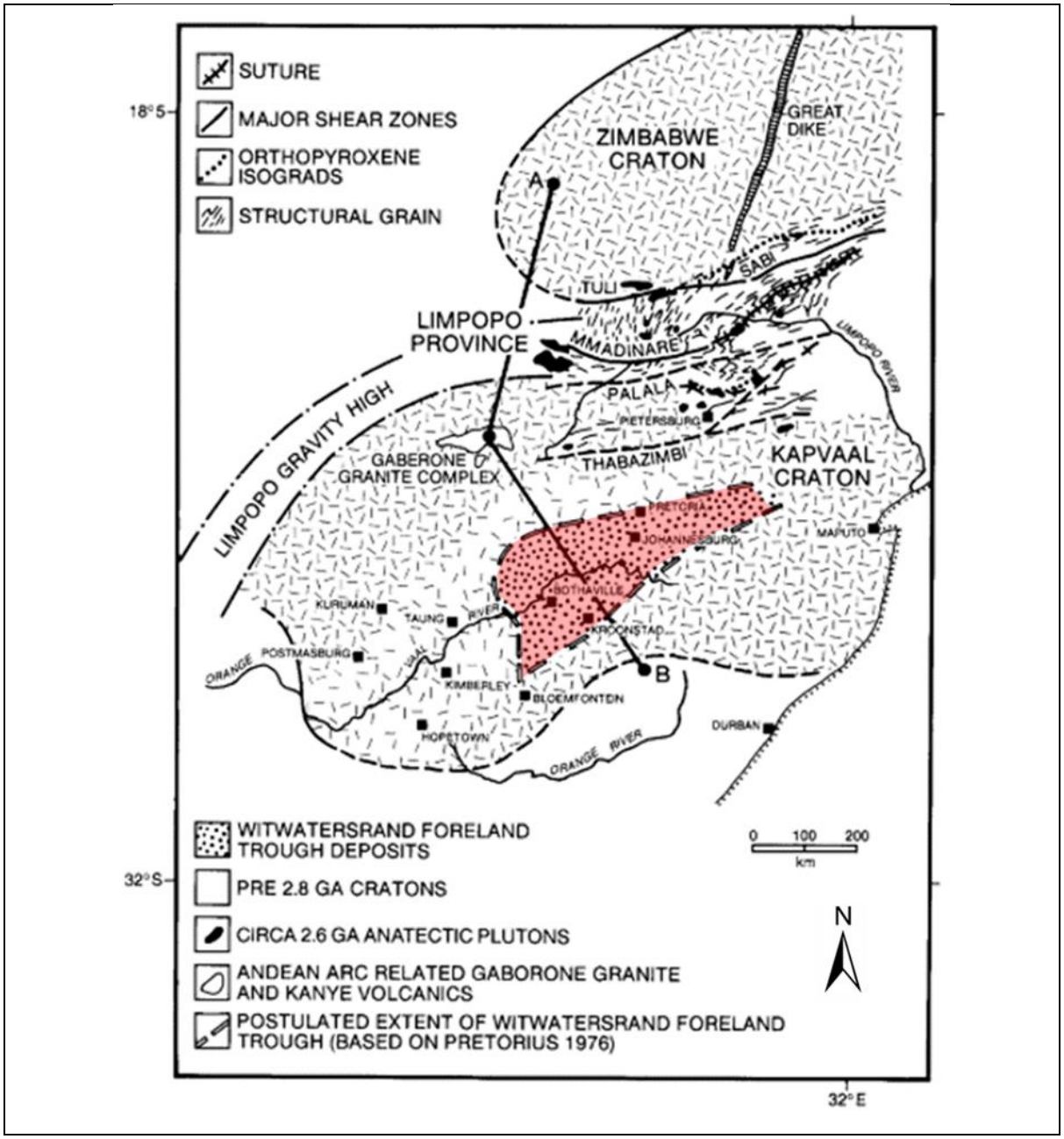


Figure 21: Interpretation of the Witwatersrand Basin as a foreland basin on the Kaapvaal Craton related to orogenic collision along the Limpopo Mobile Belt. Witwatersrand basin highlighted in red shading. (modified after Burke et al., 1986).

Winter (1987) independently also worked on a foreland basin model for the Witwatersrand Basin and came to similar conclusions to Burke et al. (1986), terming the process the “Witwatersrand Orogeny”.

2.4.3 Multiple Basin or Wilson Cycle Model

Stanistreet and McCarthy (1991) presented a multiple basin-style model during which the Limpopo Orogeny developed and attributed its stratigraphy to a full Wilson Cycle, as follows (Figure 22):

1) The Dominion Group was deposited in an extensional rift basin during a possible early extensional phase.
2) Thermal subsidence then occurred, leading to transgression and deposition of the Hospital Hill Subgroup.
3) A foreland basin associated with oceanic subduction beneath the northern margin of the Kaapvaal Craton resulted in thickening and shortening of the craton, during which time the upper West Rand Group and lowermost Central Rand Group were deposited.
4) A collisional tectonic escape stage occurred in which the upper part of the Central Rand Group was deposited. Central to this idea was the syn-sedimentary faulting in the form of major strike-slip structures that had a marked impact on local sedimentation, and which define the edges of basement fault blocks. as depicted in Figure 23.
5) The Klipriviersberg flood basalts (lower Ventersdorp Supergroup) were extruded into the Witwatersrand Basin through tectonic escape-related extension and oblique slip faulting.
6) Finally, the indentation of the Zimbabwe Craton into the Kaapvaal Craton occurred to form an impactogenal extensional rift basin in which the Platberg Group (upper Ventersdorp Supergroup) was deposited.

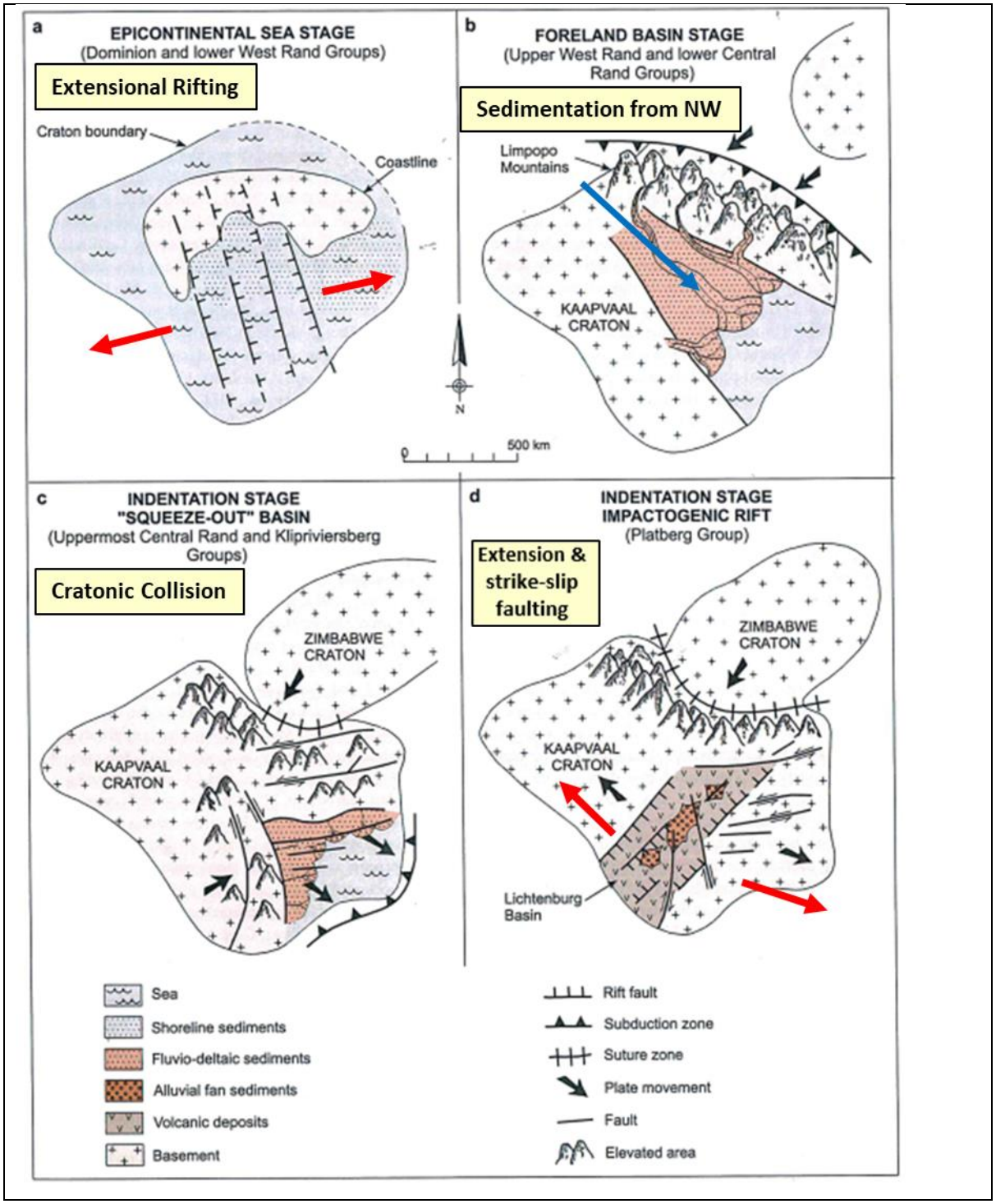


Figure 22: Wilson Cycle model for the development of the Dominion, Witwatersrand and Ventersdorp basins (modified after Stanistreet and McCarthy, 1991; McCarthy, 2006).

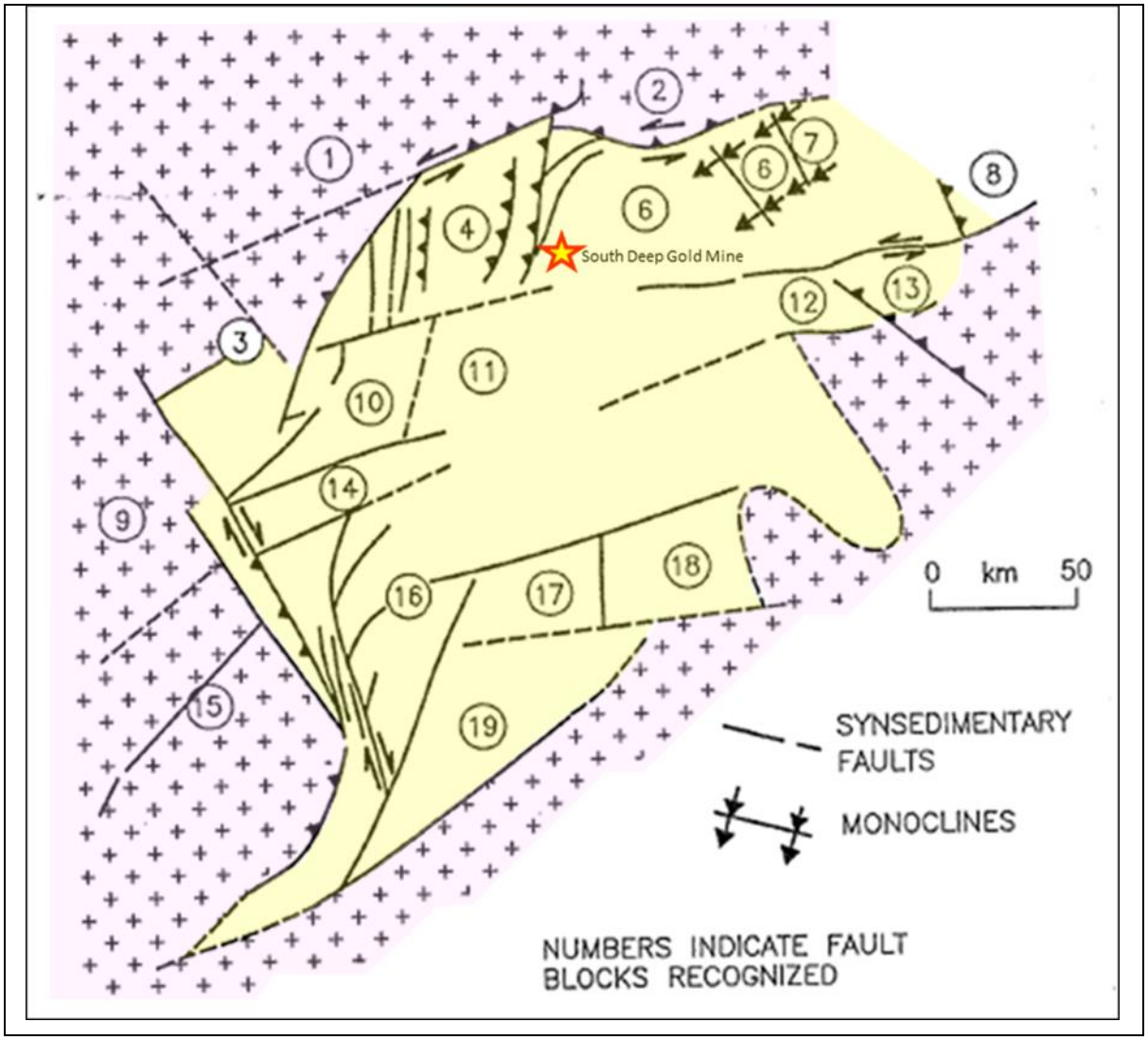


Figure 23: The structural fault zones or lineaments affecting Witwatersrand sedimentation, defined by edges of basement fault blocks. The SDGM lies in the western part of Block 6 (modified after Stanistreet and McCarthy, 1991; McCarthy 1994).

Robb et al. (1991) utilised the Stanistreet and McCarthy Wilson Cycle model as a basis to build a time-constrained depositional framework relating to the deposition of the Witwatersrand Basin as well as its environs and likened the accretion required for the formation of the Kaapvaal Craton to that of the North American Cordilleran Arc. Factors considered in this determination included: 1) plutonic events, 2) volcanic events, 3) sediment deposition, and 4) metamorphic-hydrothermal events:

1) Plutonic Events

Robb et al. (1991) recognised that at least three stages of granite plutonism occurred around the edge of the Witwatersrand Basin, based upon age populations of detrital zircon and monazite grains calculated from $^{207}Pb/^{206}Pb$ ages, namely: 1) Pre-Dominion (more than 3100 Ma); 2) Dominion (3100-3010 Ma); and 3) Randian (2980-2720 Ma) stages.

2) Volcanic Events

The time of Witwatersrand deposition was constrained by the underlying Dominion Group (3074 ± 6 Ma) and the age of the overlying early Ventersdorp volcanism (2709-2643 Ma) at ca. 2709 Ma (Beach and Smith, 2007), also based on single zircon $^{207}Pb/^{206}Pb$. The Crown Lava near the top of the West Rand Group was dated at 2914 ± 8 Ma based on data from Armstrong et al. (1991).

3) Detritus and Sediment Deposition

Robb et al. (1991) utilised $^{207}Pb/^{206}Pb$ ages from detrital zircon and monazite grains obtained by Barton et al. (1989) and Robb et al. (1990) from a number of conglomerates through the Witwatersrand succession, and including the VCR. Ages of the individual detrital zircon grains were noted to become progressively younger upwards through the Witwatersrand stratigraphy, thus implying that detritus was generated from unroofing and erosion of younger granites during development of the basin. The youngest dated zircon per stratigraphic group was used as the maximum age of that unit, thus approximately constraining the age of the Dominion Group at 3096-3074 Ma, the West Rand Group at 2980-2914 Ma and the Central Rand Group at 2840-2714 Ma (Robb et al. 1990). It was concluded that deposition of the Witwatersrand Supergroup was episodic and reflected depositional responses to tectonic and magmatic events occurring in the hinterland.

4) Metamorphic-hydrothermal Events

Robb et al. (1991) identified at least nine separate later metamorphic events which occurred in the environs of the Witwatersrand Basin: 1) 2 940 Ma metamorphic overgrowths on zircons obtained from 3 250 Ma old tonalitic gneisses located in the Kimberley region. 2) 2 883 Ma rutile from a cross-cutting hydrothermal vein in banded tonalitic gneisses southwest of Schweizer-Reneke, possibly related to the emplacement of the Schweizer-Reneke dome at 2 879 Ma. 3) The Schweizer-Reneke dome was also re-set between approximately 2 780 Ma (Pb-Pb) and 2 767 Ma (Rb-Sr). 4) The Dominion lavas were altered, after extrusion by later events dated at c. 2 950 Ma (Pb-Pb pyrite) and c. 2 800 Ma (Pb-Pb). 5) The Outer Granite Gneiss underlying the > 3 074 Ma Dominion sediments within the Vredefort Dome appears to have been affected by an event at c. 3 000 Ma (Rb-Sr), while the Inlandsee Leucogranofels underwent prograde granulite facies metamorphism and dehydration at 2 830 Ma (Hart et al., 1981). 6) The latter event potentially also affected the 3 096 Ma Westerdam dome with a Pb-Pb whole rock age of 2 810 Ma. The same rocks also yield a Rb-Sr whole rock age of 2759 Ma. 7) 3 170 Ma old tonalites in the Johannesburg dome appear to have been isotopically reset during two discrete at 3 030 Ma (Pb-Pb) and the other at 2 268 Ma (Rb-Sr). 8) Several periods of metamorphism and/or hydrothermal activity may have been recorded within the Witwatersrand Basin itself in the form of the authigenic growth of rutile in the Promise Reefs at c. 2 580 Ma, while various generations of authigenic pyrite might have formed at c. 2 500 Ma and c. 2 260 Ma. Kerogen appeared to have been isotopically homogenized at c. 2 320 Ma. Uraninites yielded a Pb-Pb model age of c. 2 040 Ma, coincident with the emplacement of the Bushveld Complex, while Witwatersrand shales passed through their K-Ar blocking temperature at approximately 1 945 Ma ago. 9. The 2 700 Ma Ventersdorp volcanics appeared to have been reset at c. 2 300 Ma (Pb-Pb) and 2 154 Ma (Rb-Sr).

2.4.4 The Witwatersrand Basin – A Successor Basin

The Witwatersrand Basin and its Witwatersrand Supergroup stratigraphic package has long been recognised as only representing a relatively small window in time relating to the complex evolution of the Kaapvaal Craton (Frimmel, 2019).

Burke et al. (1986) solely focussed (as did most other earlier authors such as Brock and Pretorius (1964) and Bickle et al. (1982)) on the Witwatersrand Basin in exclusion to all else.

Stanistreet and McCarthy (1991) attributed the formation of the Witwatersrand Basin and the cessation of sedimentation followed by magmatic outpouring of the Klipriviersberg Lavas and the collision of the Zimbabwe and Kaapvaal Cratons to a full Wilson Cycle.

Later authors (Catuneanu, 2001; Dankert and Hein, 2010) attempted to relate the evolution of the Witwatersrand Basin to events leading to its formation and later tectonic events which affected its evolution. Current views present the Witwatersrand Basin to be a successor basin where fills of different types of basins became stacked on top of each other (Catuneanu, 2001; Dankert and Hein, 2010 and Frimmel, 2019).

The following section relates the evolution of various models supporting the Witwatersrand Basin as being only a single "successor basin" during the Kaapvaal cratonic evolution. Additional complexity has been added to the standard foreland basin theory pertaining specifically to the formation of the Witwatersrand Basin itself by means of adding additional sub-environments in the form of a wedge-top depozone.

2.4.5 Witwatersrand Foreland Basin Partitioning

Catuneanu (2001) was the first to propose partitions in the Witwatersrand foreland system into foredeep, forebulge and backbulge flexural provinces. He likened the formation of the Witwatersrand foreland and its supracrustal loading to that of the Western Interior foreland basin of North America, with the exception that the Witwatersrand foreland basin constituted a continent-continent collision, whereas the Western Interior foreland basin did not. He explained the unique shape of the Witwatersrand Basin (for a foreland) as a factor of Archaean crust being hot and, thus, more capable of intense flexure. He also placed the Witwatersrand foreland system into context in relation to earlier, as well as later, significant events or tectono-stratigraphic settings over time (Figure 24).

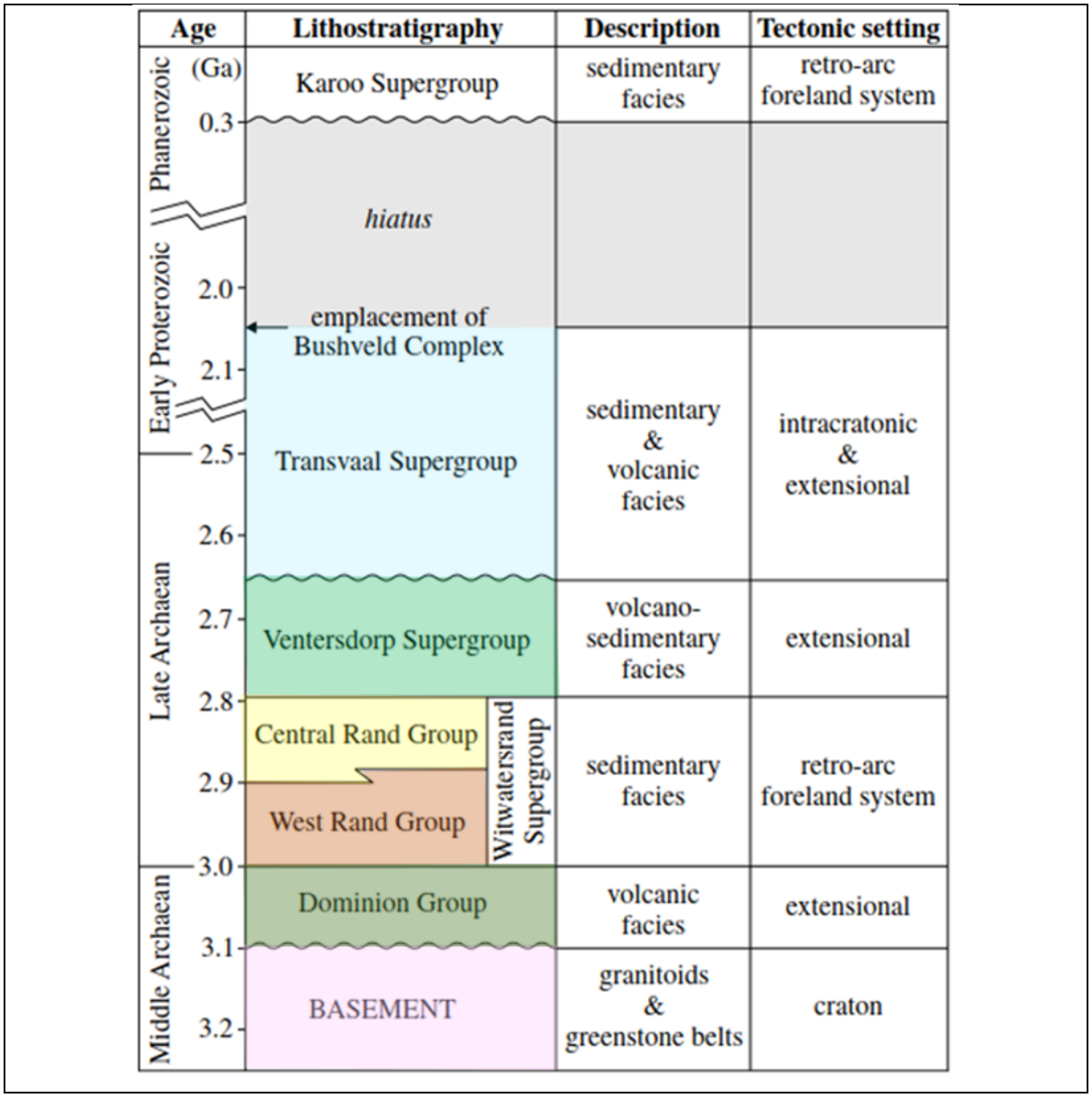


Figure 24: Interpretation of tectonic setting of the Witwatersrand Basin and related basins of the Kaapvaal Craton adapted from Catuneanu (2001).

Catuneanu (2001) indicated that the Witwatersrand Basin, as depicted by earlier foreland models, presented all the diagnostic features of a flexural foredeep environment (Figure 25):

1) a distally thinning wedge of sedimentary fill
2) incorporation of older proximal facies into the thrust fault systems as the orogenic front progrades
3) the proximal truncation and cannibalisation of older sedimentary units into younger units
4) a general transition from older deep marine facies upwards to younger fluvial and non-marine facies; and
5) a progressive shift of the coarser non-marine facies owing to the advance, uplift, and erosion of the orogenic belt.

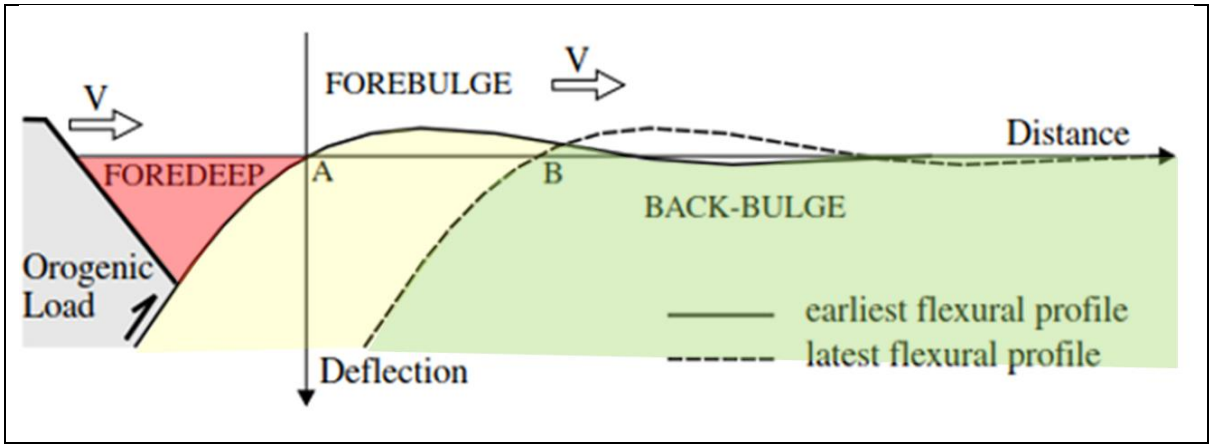


Figure 25: Flexural profile of a foreland system (modified after Catuneanu, 2001; modified from Beaumont et al., 1993; Crampton and Allen, 1995; DeCelles and Giles, 1996). 'V' is the progradation rate of the orogenic load and the associated foreland system.

According to Catuneanu (2001), the position of the flexural forebulge served as a constraint to the extent of the Witwatersrand sedimentation, thus validating or negating the hypothesis of the Witwatersrand Basin being an erosional remnant of a much larger depository as inferred by Tucker (1980), Beukes and Cairncross (1991) and Els (1991). Their inference that the Pongola sequence or Mozaan Group represented an extension of the Witwatersrand Supergroup was negated by Catuneanu (2001) who proposed that the sediments of the Pongola sequence represented the basin-fill of a backbulge depository (Figure 26). These chronological equivalents were thus deposited in far more distal environments within a back-bulge environment than the Witwatersrand Basin sediments.

Subsequent study by Viehmann et al. (2015) utilised rare earths and yttrium ("REY") as well as high-precision Sm–Nd isotope data to compare the ~2.90 Ga Superior-type BIFs from the Witwatersrand Supergroup to the near-contemporaneous BIFs from the correlative Pongola Supergroup and from the Pietersburg Greenstone Belt, respectively. Viehmann et al. (2015) proved that the εNd range of the Witwatersrand BIFs of between -3.95 and -2.25 overlaps that of the Pongola Basin BIFs indicating that both areas were dominated by similar terrigenous REY sources from the Kaapvaal Craton, thereby possibly supporting Catuneanu's (2001) inference that these two basins are related, with the Pongola basin forming a backbulge depository.

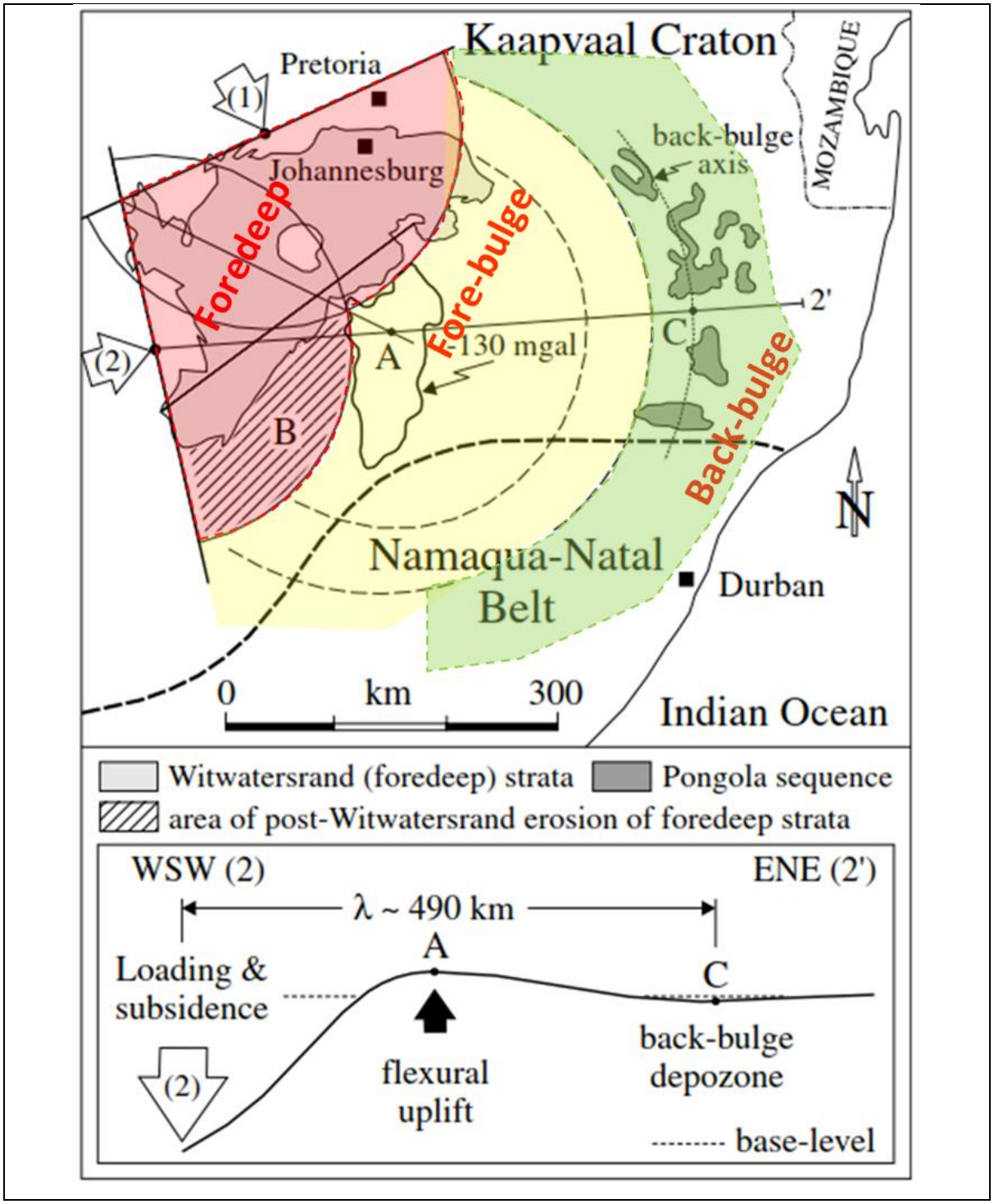


Figure 26: Partitioning of the Witwatersrand and Pongola basins into foredeep, forebulge and backbulge flexural provinces (modified after Catuneanu 2001).

Catuneanu (2001) analysed the stratigraphic features of the Witwatersrand sediments, the pattern of surrounding gravity anomalies and the basal unconformity of the basin's fill. He noted that the fluvial and other non-marine environments progressively migrated towards the southeast (at the expense of the marine environments) within the Witwatersrand Basin, in the same direction as migration of the orogenic front and the associated foreland system. He also noted the general vertical change through the Witwatersrand stratigraphy from being predominantly marine (underfilled) within the West Rand Group to being terrestrial, or overfilled, in the Central Rand Group. He also noted the multiple or stacked basin-wide unconformities throughout the system and how

they become distally conformable. In addition, he noted that typical non-marine foredeep sequences all display upward-fining profiles, similar to all the non-marine sedimentological sequences of the Witwatersrand Supergroup.

Catuneanu (2001) indicated that lateral continuity of depositional sequences across the basin and presence of an interior seaway throughout Witwatersrand times suggested the stratigraphy formed within a single subsiding basin related to a single flexural province or foredeep. The evident lack of distal and proximal correlatives, as well as the configuration of the regional Bouguer anomalies relative to the lack of basement heterogeneities below the basin and to the southeast indicated the flexural forebulge was located further to the southeast of the current preserved Witwatersrand Basin (Catuneanu, 2001). He also suggested that the Bouguer anomaly could be related to a higher elevation of the Moho discontinuity owing to the isostatic uplift associated with the flexural forebulge (Figure 26).

Forebulge unconformity relationships within the Witwatersrand stratigraphy are seen to widen towards the southeast (Catuneanu, 2001), as would be expected with a basin-ward forebulge migration owing to progressive onlap of the foredeep, and an associated increase in the amount of erosion caused by uplift of the forebulge concomitant with the advance of the thrust front (Figure 27). Accordingly, the basal unconformity with the basement becomes less significant away from the orogen towards the most proximal parts of the foredeep, where the contact becomes conformable.

A schematic cross-sectional diagram of the preserved Witwatersrand clastic wedge interpreted in terms of Catuneanu's (2001) foredeep model during its formation, prior to Ventersdorp deformation, is presented in Figure 27.

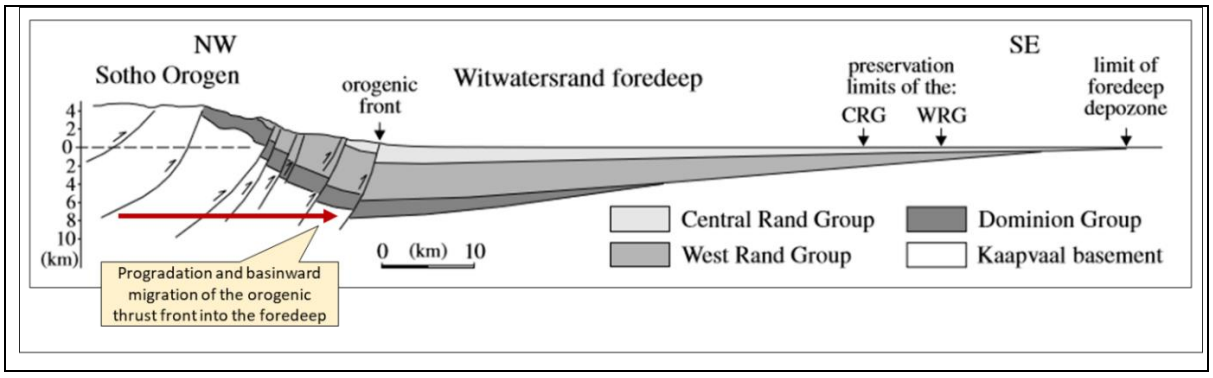


Figure 27: The Witwatersrand foredeep prior to Ventersdorp deformation; CRG = Central Rand Group, WRG = West Rand Group (modified after Catuneanu, 2001).

2.4.6 Wedge-top Depozone

Ori and Friend (1984) were the first to identify smaller sedimentary basins located and carried on active thrust sheets within the Alpine Orogenic Belt. Two areas were highlighted where complexes of basins (Po, Italy and Ebro, Spain) had one compressional margin in which thrust sheets initially formed and then transported actively filling sub-basins by means of piggyback thrust propagation where the high-angle frontal ramp becomes inactive and a new active ramp forms ahead of the old one (Dahlstrom, 1970; Butler, 1982). Ori and Friend (1984) termed all sedimentary basins formed on active thrust sheets "piggyback basins".

DeCelles and Giles (1996) provided a thorough definition of the foreland basin system with four discrete depozones, with the notable addition of the wedge-top depozone (inclusive of piggyback basins) (Figure 28). The foredeep, forebulge and backbulge depozones remained little changed from other tectonostratigraphic models. DeCelles and Giles (1996) indicated that foreland basin systems require that stratigraphic models should be parameterised as doubly tapered prisms in section, rather than the generally accepted "doorstop" wedge shape. Examples were cited for sediment accumulations in the form of wedge-top deposits as being the Cordilleran, Amazonian, and Indonesian orogenic belts, where these deposits extend hundreds of kilometres beyond the respective limits of major flexural subsidence (DeCelles and Giles, 1996).

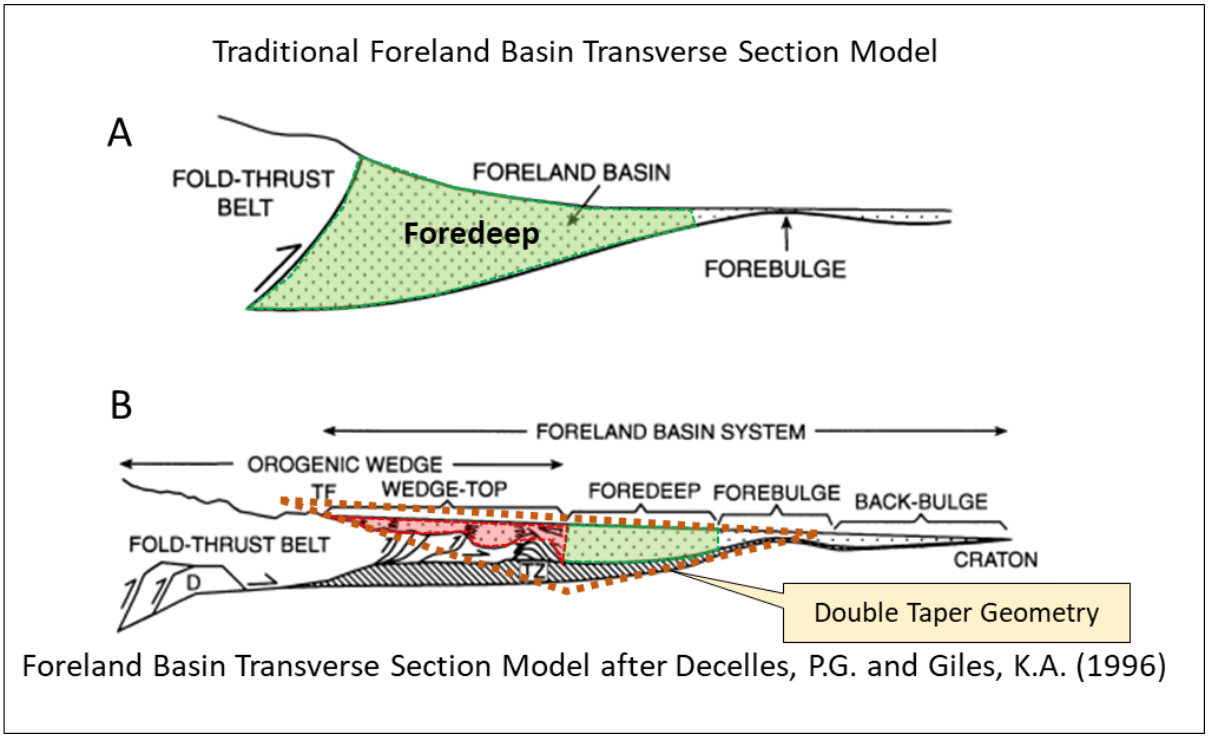


Figure 28: a) Schematic geometry of a traditional foreland basin model in section. b) The wedge-top depozone foreland basin model geometry as proposed by DeCelles and Giles (1996) (modified after DeCelles and Giles, 1996).

Within the Witwatersrand Basin foreland basin context, very little energy has been applied in identifying the wedge-top depozone, excepting Coward et al. (1995) who inferred a piggyback basin morphology on sections of the Government Subgroup within the West Rand Group and on sections of the Johannesburg Subgroup of the Central Rand Group.

DeCelles and Giles (1996) noted with regard to the wedge-top depozone that in many continental thrust belts the limit of significant topography is located far behind the frontal thrust, with large amounts of synorogenic sediment covering the frontal part of the fold-thrust belt because:

1) Frontal thrusts are commonly “blind” and tipping out in the subsurface.
2) Rocks involved in deformation along the fronts of thrust belts are usually very young and soft sediments, while more durable older lithologies occur inland.
3) The sediment that accumulates on top of the frontal part of the orogenic wedge constitutes the wedge-top depozone (Figure 28). This includes piggyback basins (Ori and Friend, 1984), satellite basins and large feeder canyon fills within thrust belt interiors, among others.
4) In subaerial settings, these deposits consist of the coarsest material in the basin-fill (with extreme textural and compositional immaturity), with alluvial and fluvial sediments accumulating proximal to high topographic relief.
5) The wedge-top depozone tapers onto the orogenic wedge, may be many tens of kilometres in length, and lies parallel to the orogen.
6) Wedge-top deposits are characterised by numerous local and regional unconformities and growth structures (Ori and Friend, 1984), including folds and faults.

Suriano et al. (2015) described the Quaternary piggyback basins along the Jáchal River, located along the Western Precordillera in the Argentinian Andes, and indicated that piggyback basins were short-lived and much smaller than the main foredeep basin. Possible transference of sediment was also indicated to take place between piggyback basins and the foredeep via erosion channels or river systems that cut through the interstitial piedmonts (Figure 29).

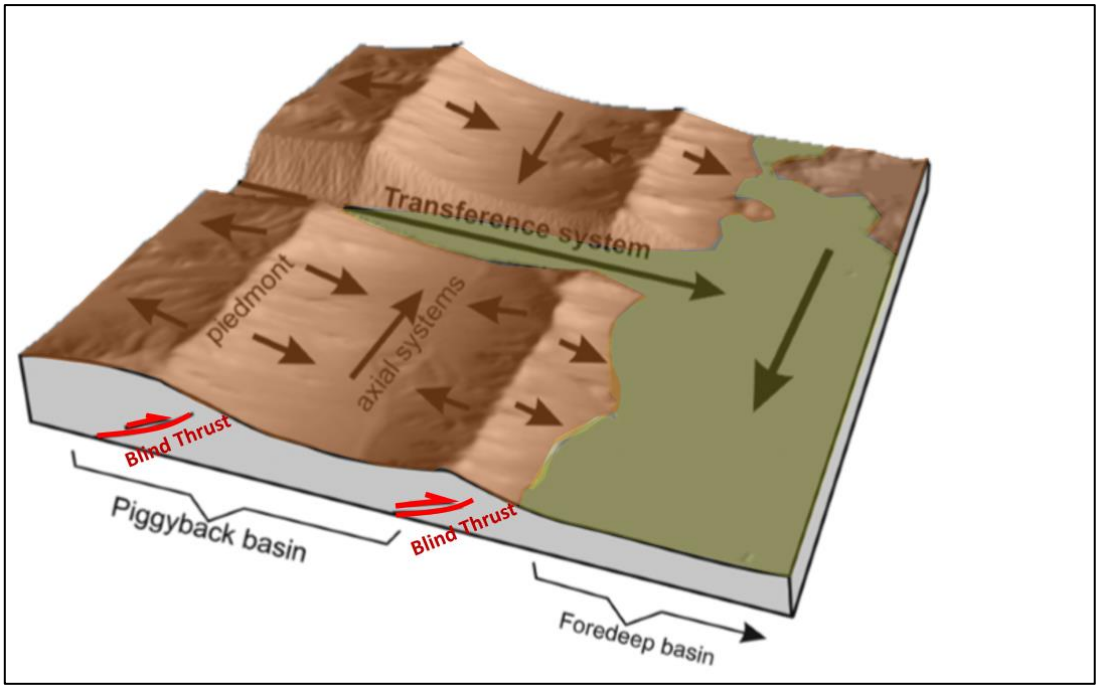


Figure 29: Schematic distribution of the sedimentary circulation in piggyback basins towards the foredeep (Suriano et al., 2015).

2.4.7 Syn-sedimentary Tectonics, Post-tectonic Features and Timing

Dankert and Hein, 2010 related the tectonic evolution of the Witwatersrand Basin to events leading to its formation as well as to several post-depositional events and contributed to the view that the Witwatersrand Basin is only one successor basin in a greater series of basins on the Kaapvaal Craton (Frimmel, 2019).

Dankert and Hein (2010) proposed that five basin-wide tectonic events can be recognised (Figure 30):

1) The first event constituted block-tilting and local fault formation resulting in the deposition of the West Rand Group synchronous to regional-scale unconformity development.
2) The second event related the deposition and some deformation of the Central Rand Group and Venterspost Conglomerate Formation to the formation of a fold-thrust belt at ca. 2.90-2.72 Ga during the Umzawami Event (Dankert and Hein, 2010). This resulted in the formation of syn-sedimentary folds (with mostly NW-trending axes) forming coeval with a series of east-verging thrust faults.
3) The third event was related to extension at ca. 2.71 Ga during which the Klipriviersberg Group erupted into the basin, culminating in the deposition of the Platberg Group at ca. 2.70 Ga owing to graben formation with normal faults with a NW-SE orientation in the Free State Goldfield and NNE-SSW orientation elsewhere.
4) The fourth event is indicated by the ca. 100 Ma hiatus between the Ventersdorp Supergroup and deposition of the sequences of the Transvaal Basin.
5) According to Dankert and Hein (2010), the fifth event (Ukubambana Event) occurred subsequent to and/or during the deposition of the upper Pretoria Group of the Transvaal Supergroup when deformation resulted in the development of a cross-cutting fold-thrust belt at ca. 2.2-2.0 Ga, resulting in local remobilisation of gold. Strike-slip faults trending NE-SW and NW-SE were formed across all the goldfields during this event. It was during this time that the Bushveld Igneous Complex was emplaced (ca. 2.06 Ga) and the Vredefort impact structure was formed (ca. 2.02 Ga).

Interestingly, Dankert and Hein (2010) presented two episodes of extension (compared to the one of Burke et al., 1986; Robb et al., 1991; Stanistreet and McCarthy, 1991) prior to fold-thrust belt development during the formation of the Central Rand Group. The first related to the formation of the Dominion Group, with a short hiatus, followed by the onset of West Rand Group sedimentation also associated with extension and basin formation.

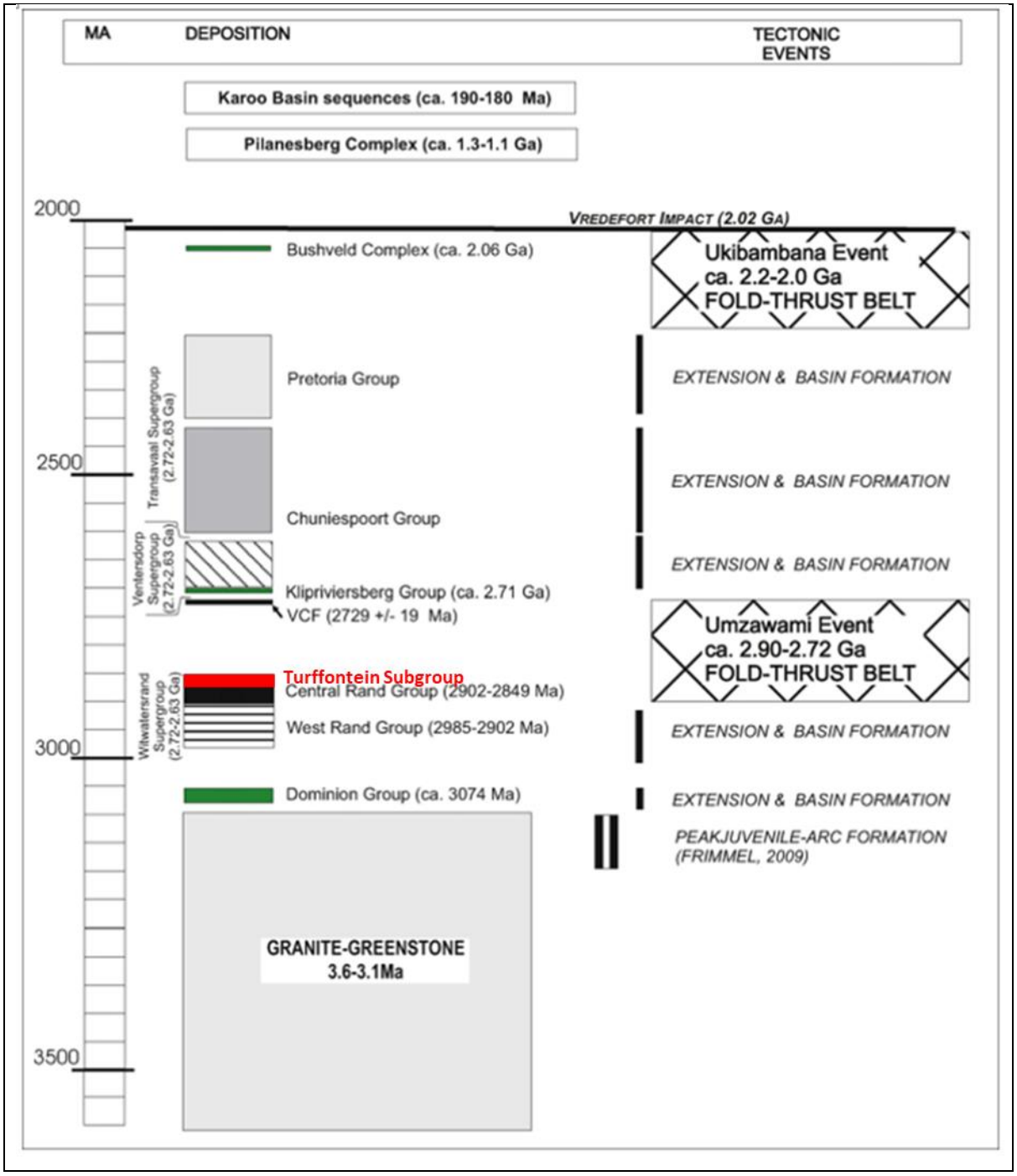


Figure 30: Schematic events chart for depositional and tectonic events for the Witwatersrand Basin region (modified after Dankert and Hein, 2010) with the relative position of the Turffontein Subgroup highlighted in red.

Gibson et al. (2000) presented initial 3D seismic data sections across Western Deep Levels Gold Mine indicating the existence of a thrust (Bank Fault Thrust Pre-cursor) pre-dating and located below the Bank Fault, suggesting the Bank Fault was a re-activated thrust system (Figure 31).

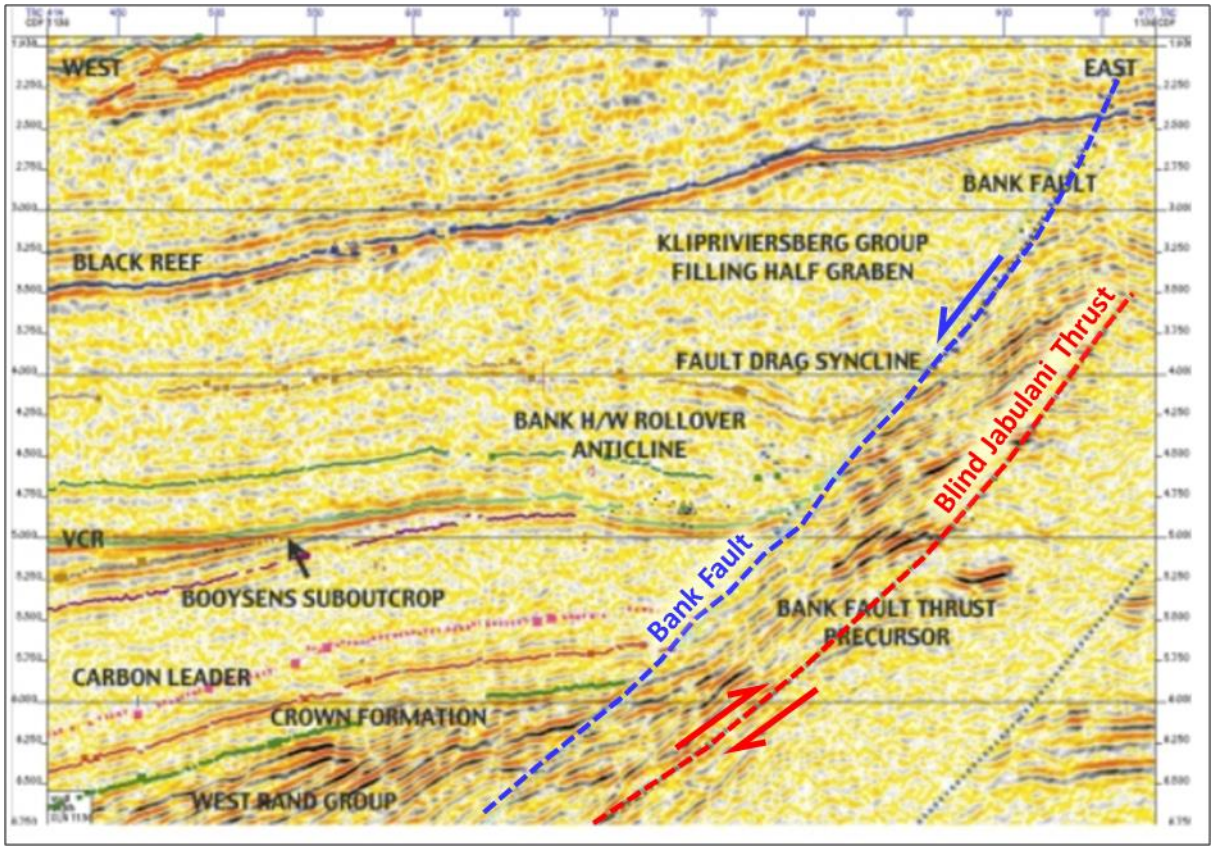


Figure 31: Interpreted seismic section through the Bank Fault on Western Ultra Deep Levels (modified after Gibson et al., 2000).

Manzi (2013) and Manzi et al. (2013) utilised consolidated 3D seismic reflection data over the West Wits Line and West Rand Goldfields spanning the period 1998 to 2003 from various mining companies. The existence of the blind footwall thrust to the Bank fault as identified by Gibson et al. (2000) was confirmed. Similarly, a blind thrust in the footwall to the West Rand Fault was also found. The NNE-SSW striking Bank and West Rand faults, which offset the auriferous reefs, were concluded to represent reactivated blind thrust fault zones, named the Jabulani Thrust (Gibson et al.'s (2000) Bank Fault Thrust Pre-cursor) and the Tandeka Thrust, respectively (Figure 32). Manzi (2013) and Manzi et al. (2013) related the precursor thrust faults to the Umzawami Event (ca. 2.73 Ga) of Dankert and Hein (2010), thus suggesting that these structures were similar in nature to previous inferences by Stanistreet and McCarthy (1991) who indicated that the thrust faults were crosscut by extensional faulting at a later stage.

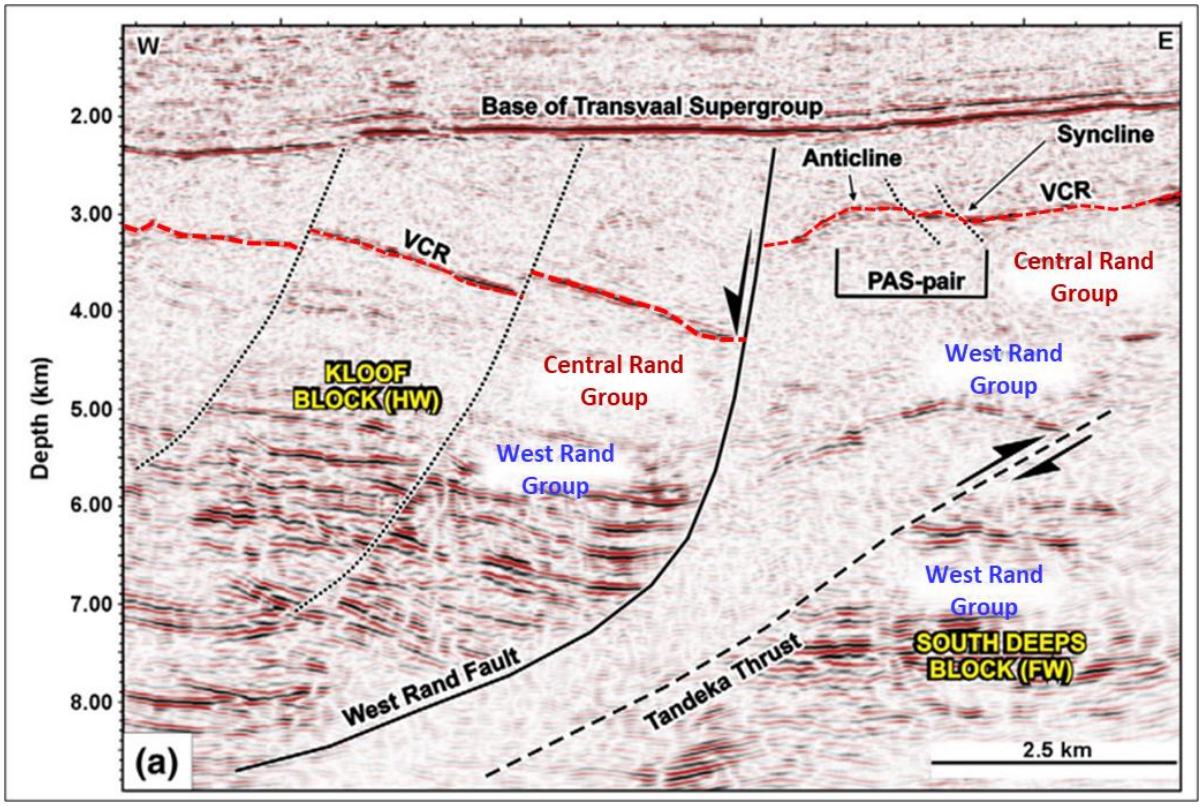


Figure 32: Interpreted seismic section across the listric West Rand Fault, showing the steeply dipping hanging wall (Kloof Block) and the blind Tandeka Thrust (modified after Manzi, 2013).

The seismic data analysed by Manzi (2013) and Manzi et al. (2013) confirmed a depositional hiatus prior to the onset of the Transvaal Supergroup deposition, as well as the unconformable relationships between the West Rand and Central Rand groups and the VCR.

2.4.8 Further Enhancements

Gumsley et al. (2019) obtained 2789 ± 4 Ma and 2787 ± 2 Ma U-Pb isotope dilution-thermal ionization mass spectrometry (ID-TIMS) baddeleyite ages for mafic sills intruding the Witwatersrand Supergroup.

Gumsley et al. (2019) also obtained ages of 2729 ± 5 Ma and 2724 ± 7 Ma from a mafic sill intruding the Pongola Supergroup and indicated that the ages reflect two significant Ventersdorp Supergroup magmatic events: the Klipriviersberg and Platberg. They proposed that the Ventersdorp Supergroup was initiated and terminated with two large igneous provinces (LIPs), the Klipriviersberg and Allanridge, separated by Platberg volcanism and sedimentation and that all three magmatic events may be genetically related to mantle plume(s).

Smith and Beukes (2018) proposed that the lower Witwatersrand and upper Pongola Supergroups of southern Africa show strong litho- and sequence stratigraphic correlation (specifically the Fe-rich units) and that, consequently, they were deposited in different parts of the same basin. The correlation of these units across the entire basin suggests major transgressions, while other iron formations were more limited in their depositional

extent. This correlation further enhances the hypothesis that the Witwatersrand Basin and the Pongola Basin were linked (Catuneanu, 2001).

Contrasting models have been proposed to explain the origin of the mineralisation occurring within the Witwatersrand Basin, including hydrothermal (e.g.: Barnicoat, 1997; Phillips 2011), sedimentary placer, e.g., Minter, 1978) and modified placer (e.g.: Robb et al. ,1991; Robb et al., 1992; Robb et al., 1995; Kirk et al., 2006). This aspect does not form part of the scope of this dissertation and so will not be considered in any further detail.

2.4.9 Growth Structures related to Blind Thrusting in Foreland Basins

Stratigraphic unconformities have long been associated with the occurrence of gold and uranium deposits in the Witwatersrand Basin. Pretorius (1974) indicated that all the exploitable reefs occurred on or immediately adjacent to, or above unconformities.

Germs and Reynolds (1991) inferred a typical rotating onlap for the Upper Elsburg Reef with numerous local unconformities and each subsequent reef cannibalising the underlying units. This geometry may be related to progressive compression and uplift associated with the blind Tandeka thrust during the Umzawami Thrust-fold event of Dankert and Hein (2010).

Riba (1976) suggested that a rotating onlap represented a single progressive unconformity or syn-tectonic cumulative wedge system attached to a tilted depositional surface linked to an uplifting structure (Cabrera et al., 1986) and resulted in stratigraphic growth adjacent to the fold-thrust belt.

Shi et al. (2019) reviewed the Qianjiadian Basin in the western Yanhshan fold and thrust belt in North China. They stated that the geometric characteristics of a progressive unconformity are controlled by the interaction between tectonic activity and deposition. When the vertical uplift rate (T) of the growth structure is greater than the rate of sedimentation the progressive unconformity would present itself as an offlap type in the limb of the thrust fold. When the rate of uplift is less than the rate of sedimentation an onlap geometry results. The spatial range of the angular unconformity is limited, and the contact gradually becomes conformable toward the center of the basin (Figure 33) (Riba, 1976; Ortner et al., 2016; Shi et al., 2019).

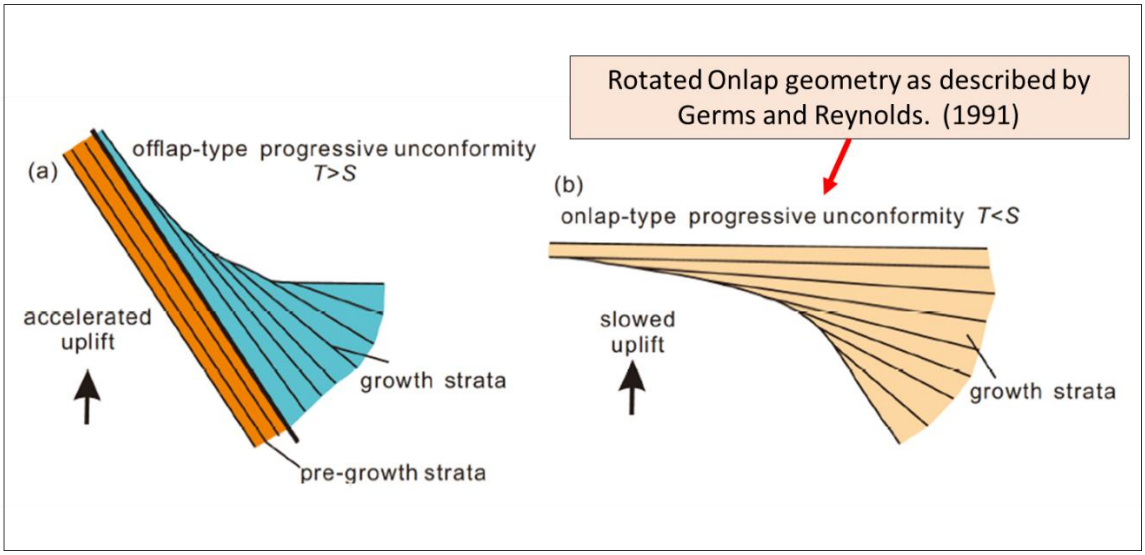


Figure 33: Simplified geometry of progressive unconformities. (a) Offlap-type progressive unconformity and (b) onlap-type progressive unconformity. "T" is the tectonic vertical uplift rate, and "S" is the deposition rate (modified from Riba, 1976; Ortner et al., 2016, Shi et al., 2019).

Alania et al. (2016) studied growth structures within piggy-back basins and growth strata of the Kura foreland fold–thrust belt in Georgia. Interpreted sections from seismic sections present the typical scale of onlaps within Didi Shiraki piggy-back basin. The resultant growth strata become less unconformable and more conformable to disconformable as distance from the thrust-fold increases. (Riba, 1976; Ortner et al., 2016; Shi et al., 2019). The distance over which an individual angular unconformity changes over to being conformable to disconformable tends to vary between 1.5 km and 2.5 km away from the stratigraphic truncation against the overlying strata Figure 34). These measured distances appear similar to those observed on SDGM.

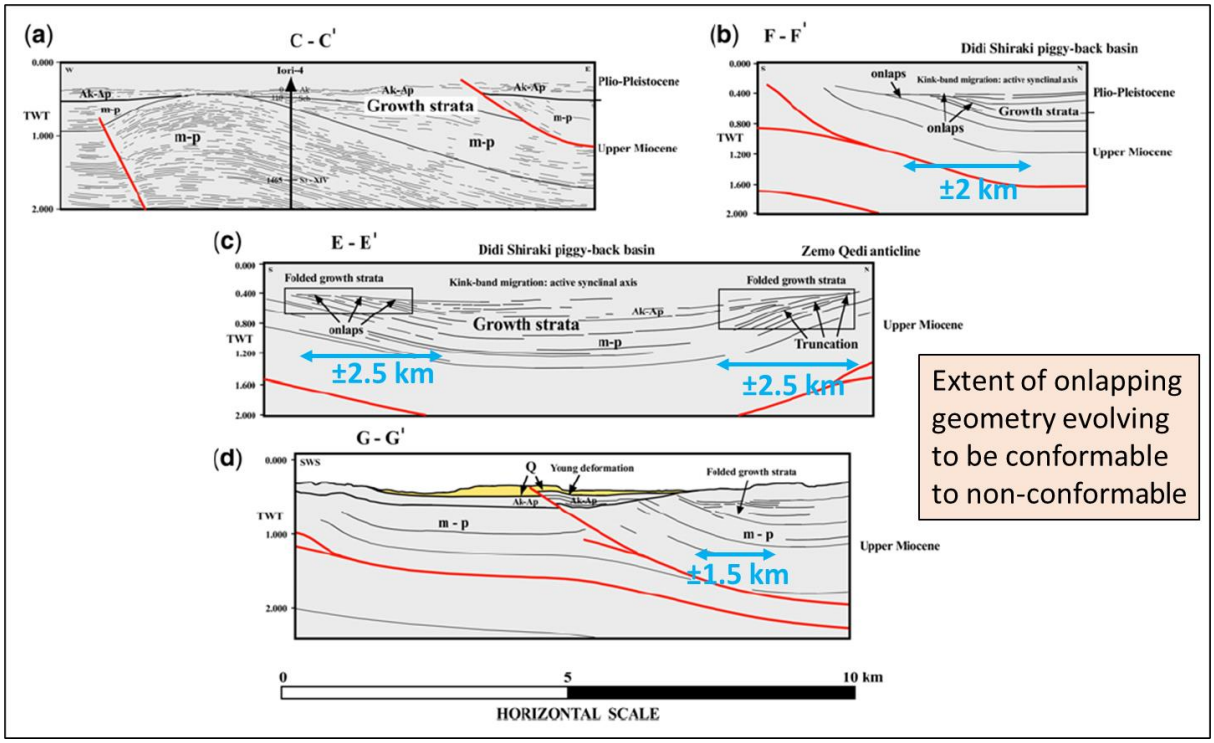


Figure 34: Interpreted line drawing sections of seismic sections from the Didi Shiraki piggy-back Basin, Georgia depicting typical extents of unconformities away from the zone of uplift and stratigraphic truncation of the onlapping strata (Alania et al., 2016)

2.4.10 Synopsis of Development of Strato-tectonic Models

A tectonic link to sedimentation in the Witwatersrand Basin has been proposed since the 'Basin-edge Concept' model was introduced by Brock and Pretorius (1964), which proposed an extensional rift-type environment. Over time, understanding related to basin formation concepts along convergent tectonic plate margins presented alternative interpretations for basin development. Burke et al. (1986) proposed that a foreland basin origin was supported by the tapered (asymmetrical) wedge morphology of the Witwatersrand Basin sedimentary wedge towards the southeast, as well as the change from deep water sediments to a predominantly alluvial environment as encountered in the Central Rand Group, and the faults bounding the north-western margin of the Witwatersrand Basin.

Stanistreet and McCarthy (1991) presented a multiple basin-style model during which the Limpopo Orogeny (Winter, 1987) developed and attributed it to a full Wilson Cycle associated with the collision of the Kaapvaal and Zimbabwe cratons. Local compartmentalisation of the basin into discrete structural blocks bounded by right-lateral wrench faults was also proposed.

Catuneanu (2001) was first to propose a flexural partitioning of the Witwatersrand Basin, with the preserved sedimentary wedge presenting all the diagnostic features of a flexural foredeep environment. Coward et al. (1995) proposed wedge-top "piggyback" basin morphology for parts of the West Rand Group and sections of the Johannesburg Subgroup of the Central Rand Group.

Heller et al. (1988), Jordan and Flemings (1991) and Clevis (2003) proposed an interplay between episodic thrusting and erosional unloading during the molasse stage of a foreland basin that was referred to as a two-phase foreland basin. However, this concept has not been applied to the Witwatersrand Basin.

Dankert and Hein (2010) considered the complete Mesoarchaean to Palaeoproterozoic tectonic evolution of Kaapvaal Craton in the area of the Witwatersrand and proposed that five basin-wide tectonic events could be inferred, of which two were compressional fold-thrust events, the earlier of which (Umzawami Event) represented the deposition of the Central Rand Group. Development of seismic surveying technology subsequent to 2004 assisted in proving the existence of reactivated thrust faults in the footwall of significant regional structures (Manzi et al., 2013) related to the Umzawami Event of Dankert and Hein (2010).

CHAPTER 3: METHODOLOGY

3.1 Introduction, Background and Personal Involvement

In order to relate the methods employed in the data sourcing and analysis adopted, an understanding of the changes to, and the development of, geological stratigraphic and structural modelling methods that have been used at SDGM over the years is essential. Most of the data presented relate to earlier (pre-2010) manually sourced data entered into MS Excel™ spreadsheets or modelled on hardcopy sepia plans, prior to being incorporated into digital space.

From 2001 through to 2005 I was responsible for the generation of the 2D sepia structure plans for SDGM, drawing and projecting geological structures and generating isopach data for incorporation in the digital model.

Sedimentological data was originally sourced from drillhole logs for the sedimentological study conducted by Muntingh et al. (2005), where I was required to identify and define the various stratigraphic units under the scrutiny of Mr D.J. Muntingh, who acted as a reviewer. Additional data was sourced by the geology team under my supervision, and manually captured over the course of four years up to 2010 and interpreted by myself, in my capacity as a Chief Geologist on SDGM. This section specifically describes the manual processes used for the structural modelling and sedimentological data capture with little overlap with the digital methods.

It is important to note that little palaeo-current data has ever been actively collected on SDGM – if at all – and alternative methods have had to be found to infer palaeo-current directions from readily available data such as bed height, percentage conglomerate and clast size trends – with various levels of success. Palaeo-current data collection at SDGM has always been a challenge due for the following reasons:

1) The general massive nature of the conglomerates (with little internal reef quartzite) in the selected mining horizons provides little exposure to sediment types conducive to palaeo-current data collection.
2) The massive mining methodology employed at SDGM results in mining width varying from approximately 2 m to >20 m in some areas, making detailed sedimentological work impractical. Normal trackless excavation size at SDGM is typically 5 m by 5 m in mining face dimension.
3) The large size of the excavations in the mining areas prevents direct access to the mining faces owing to safety concerns.
4) SDGM has always been a production environment with a large team of production geologists. A significant focus has been placed on underground exploration drilling to obtain orebody data away from the access excavations, which is not conducive to traditional palaeo-current studies. This approach is evident in the drillhole dataset presented in this study.

Although I was intimately involved in the digital modelling at SDGM from 2005 to 2010, this study does not describe these processes which are effectively derived from the original manual processes employed by myself and the SDGM geology team of the time. Currently, digital modelling at SDGM is highly progressive owing to continuous upgrades made by the Gold Fields Mineral Resource Management Team in response to technological advancements.

It should be noted that significant and commendable strides have been taken at SDGM to further develop the modelling ability, interpretation, and capacity of the Geology Department at the mine. Challenges as regards collection of palaeo-current data at SDGM will continue into the future owing to the inherent to the nature of the orebody and the required large-scale massive mining methods required to extract the ore.

3.1.1 Sedimentological Data Collection, Processing and Analysis

Between 2009 and 2010, correlation of the Waterpan/Modderfontein stratigraphic nomenclature across the property was completed by reviewing stratigraphic logs of 4502 drillholes drilled to the east of the Waterpan/Modderfontein sub-outcrop. This exercise identified 16 laterally continuous beds across the SDGM property (Obermeyer, 2005). The 16 stratigraphic beds were identified by means of logging laterally continuous conglomeratic zones, underlain by local, but continuous, unconformities and overlain by laterally continuous quartzites across the mine property.

The following sedimentological parameters for each of the 16 stratigraphic beds were collected from the drillhole dataset:

1) Bed height: Bed height represents corrected true bed height calculated perpendicular to the bedding planes. It is colloquially and incorrectly referred to as true channel "width" as used on South African gold mines. Bed height was captured in metres owing to the wide range of bed heights encountered (0 m to 22.5 m).
2) Percentage conglomerate: Percentage conglomerate quantifies the percentage of conglomerate within a valid bed intersection (the balance consisting of quartzite) and for ease of presentation is expressed as a percentage. The percentage conglomerate relates to the intersection width logged in conglomerate intervals and would produce the same value if calculated using the corrected bed height.
3) Average clast size: Average clast size represents the visually dominant clast size diameter captured in mm by mine geologists at the time of core logging and is qualitative in nature.
4) Maximum clast size: The maximum clast size represents the largest empirically measured clast size diameter, captured in mm during core logging.

Data was obtained from three sources, namely historical hardcopy drillhole logs (Figure 91**Error! Reference source not found.**), the mine's digital CAE Datamine Fusion™ database, as well as directly from study of historical surface drillhole core by Muntingh and Obermeyer (Muntingh et al., 2005) (Figure 35) and captured into an MS Excel™ spreadsheet.

Other sedimentological data such as clast make-up (polymictic vs oligomictic), clast sorting or clast roundness were not used in the study as the data was found to be too inconsistent and not standardised. Soft-sediment deformation structures have also not been recorded on SDGM, nor interpretations pertaining to debris flows.



a) Archived historical chisel-split surface drillhole core for drillhole MD38



b) Close-up of historical chisel-split surface drillhole core for drillhole MD38

Figure 35: Historical archived split surface drillhole core from drillhole MD38 (modified after Muntingh et al., 2005) (permission granted by Goldfields to reproduce).

All data was captured into an MS Excel™ database for the study. Empirical measurements were obtained from archived historical surface drillcore, written empirical log data and from recorded empirical measurements from the SDGM CAE Datamine Fusion™ database.

Spatial coordinate data in the form of drillhole collars and bed intercept points were collected and recorded in the MS Excel™ database and cross validated between the hardcopy logs, the drillhole layouts as well as the digital CAE Datamine Fusion™ database by the geology team members. Drillhole collar positions for vertical drillholes were captured from hardcopy drillhole cover sheets, or the mine's drillhole layout file, or measured and scaled directly from mine geological plans where drillhole collars were not readily available from drillhole layouts or drillhole coversheets (Obermeyer, 2004) (Figure 81**Error! Reference source not found.** and Figure 82**Error! Reference source not found.**).

Inclined borehole true reef intercept points were generated/calculated utilising two possible methods:

1) In the absence of a digital Datamine™ drillhole file, the section method along the drillhole azimuth was used and projected to plan view (as per structure plan methodology described in Section **Error! Reference source not found.** and Figure 82)**Error! Reference source not found.**. Intercept points were plotted onto an intercept plan, scaled off and captured into the MS Excel™ database in order to accurately position all captured data on plan.
2) Where digital Datamine™ borehole coordinates were available, points were generated at the bed intercept points. These point data were then exported in an MS Excel™ .csv format and incorporated into the MS Excel™ database (Obermeyer, 2004).

All data were imported into Datamine Studio 3™ for reviewing and validation (in order to ensure all drillhole collars plotted in their relevant areas), palinspastic reconstruction and analysis. Contouring and final presentation of the four parameters were conducted in Datamine Studio RM™.

3.1.1.1 Bed Height

Bed height data represents corrected true bed height calculated perpendicular to the bedding planes. Bedding dip varies locally between 23° and 11° depending on the proximity to local geological structures. A mean bed dip of 17° and a mean bed strike of 090° were applied across the project area to the individual beds to calculate an approximate true bed height per reef in order to simplify calculations. A mean bedding strike of 090° was applied owing to the complex dipping stratigraphic wedge morphology (Figure 36a), which resulted in a radiating bedding strike in proximity to the Upper Elsburg sub-outcrop against the VCR (Figure 36a and b). The base of the EC of the UE7 Member attains a strike of 079° at sub-outcrop, whereas the Elsburg Massives attain a strike of 109° at sub-outcrop (Figure 36c).

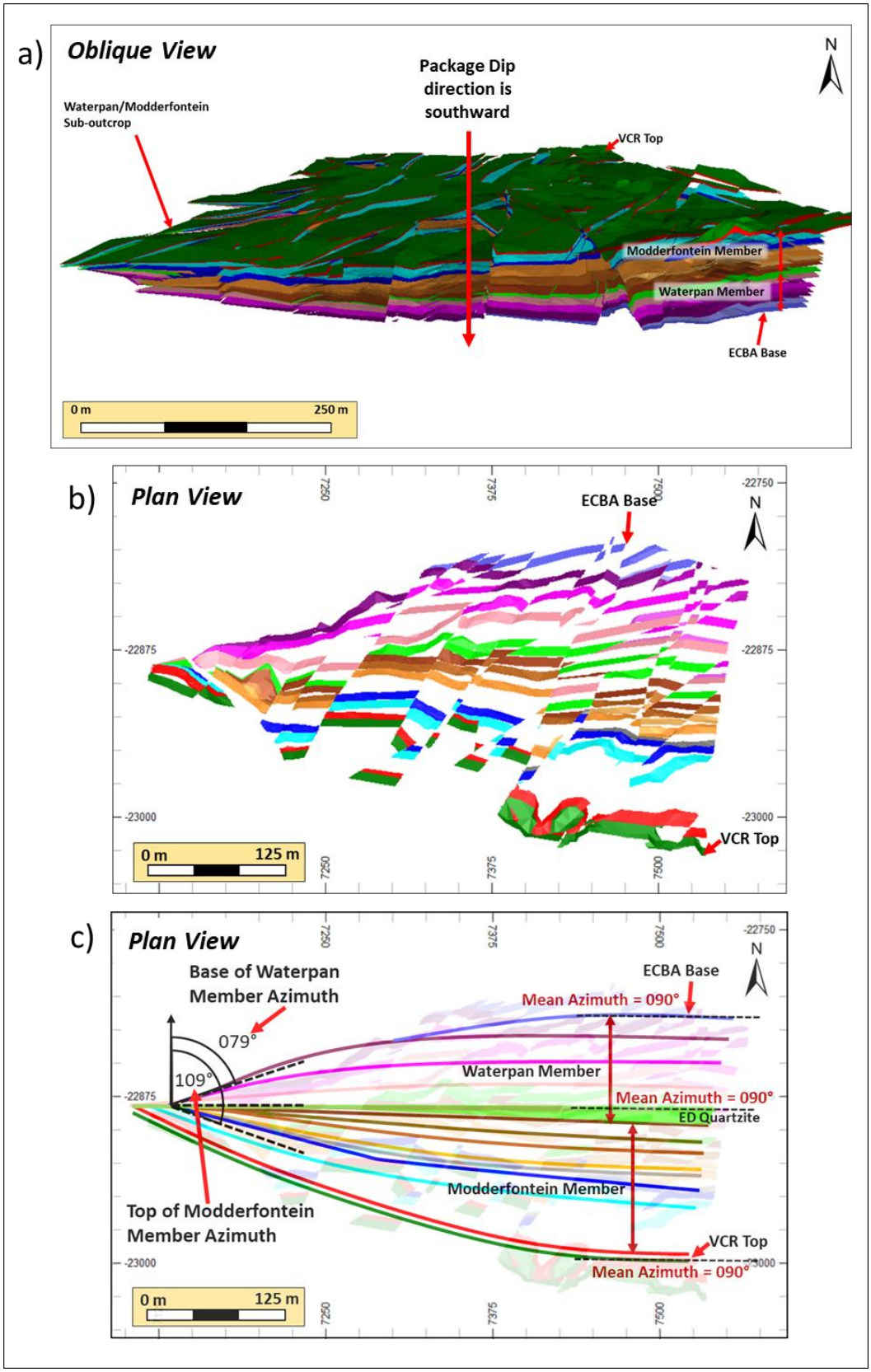


Figure 36: a) Oblique view of a section of the 3D model of the Waterpan (UE7) and Modderfontein (Elsburg Massives) sedimentary wedge and the overlying VCR, dipping towards the south. B) A horizontal section view through the Waterpan/Modderfontein 3D model presenting the complicated strike relationships. C) An interpreted bedding strike from the horizontal wedge slice depicted in b), showing the variation in strike at sub-outcrop and the near E-W strike attained towards the east.

Average general bed strike rotates progressively towards a strike of 090° approximately 250 m to 300 m east from the Upper Elsburg sub-outcrop within the current mining areas (Figure 37). This strike orientations may however vary towards the north. Average strike south of the current mine workings is difficult to determine owing to the wide spacing of the surface drilling.

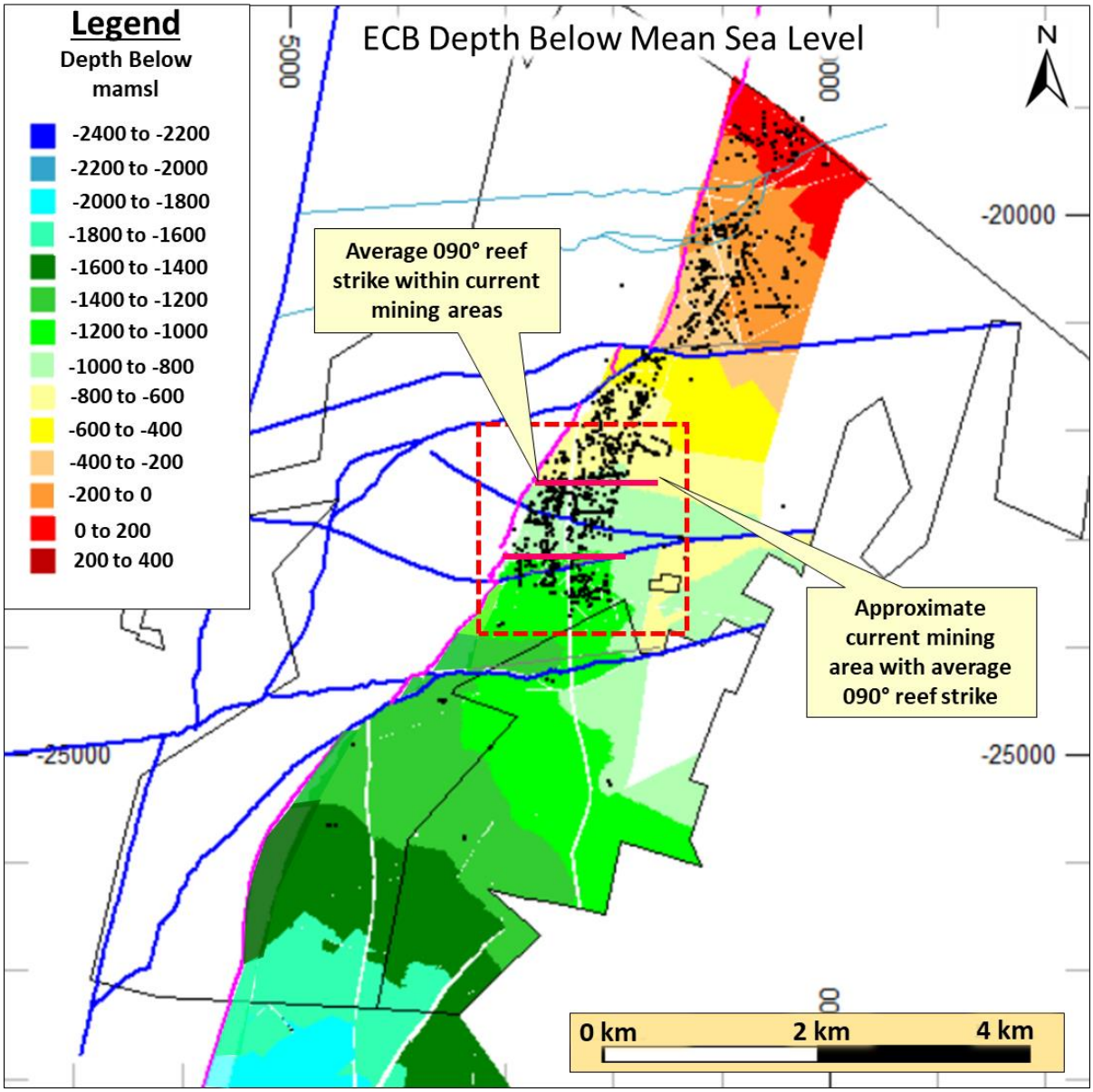


Figure 37: Variation in depth and reef strike for the ECB at SDGM.

The full Upper Elsburg package attains a maximum package thickness of approximately 125 m approximately 1.2 km east of sub-outcrop). This thickness is commonly maintained up to 3 km from sub-outcrop and results in parallel individual bed strikes that strike approximately E-W. Data density beyond 3 km is extremely low owing to the low economic potential encountered this far from the Upper Elsburg sub-outcrop.

A cumulative thickness plot of the Upper Elsburg reef package covering modelled areas is presented in Figure 38 for demonstration purposes. Detailed geological wireframes were not available for the northern areas owing to these areas being mined out and thus not requiring modelling.

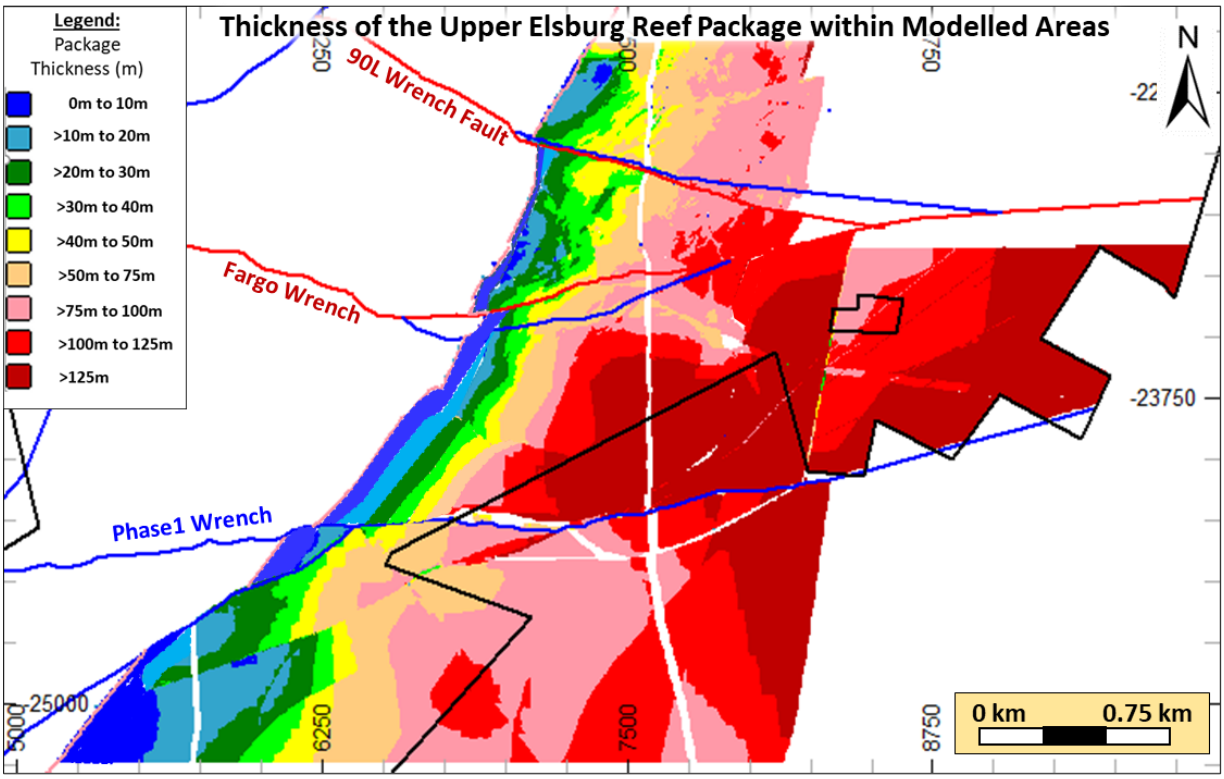


Figure 38: A cumulative thickness plot of the Upper Elsburg reef package for the modelled portion of the SDGM within the study area

Stratigraphic logged reef intervals (as per Figure 10) were captured from the three data sources for each reef. Owing to the limited number of available underground drilling platforms, SDGM holes are generally drilled in multiple orientations. Thus, all captured reef intervals were first projected to represent a vertical intersection length utilising standard trigonometric functions as presented in Step 1 in Figure 39a).

Once all vertical intersection lengths were calculated and captured in the MS Excel™ database all vertical intersection lengths were converted to true bed heights by applying the standard trigonometric function of *Sin* as presented in Figure 39b).

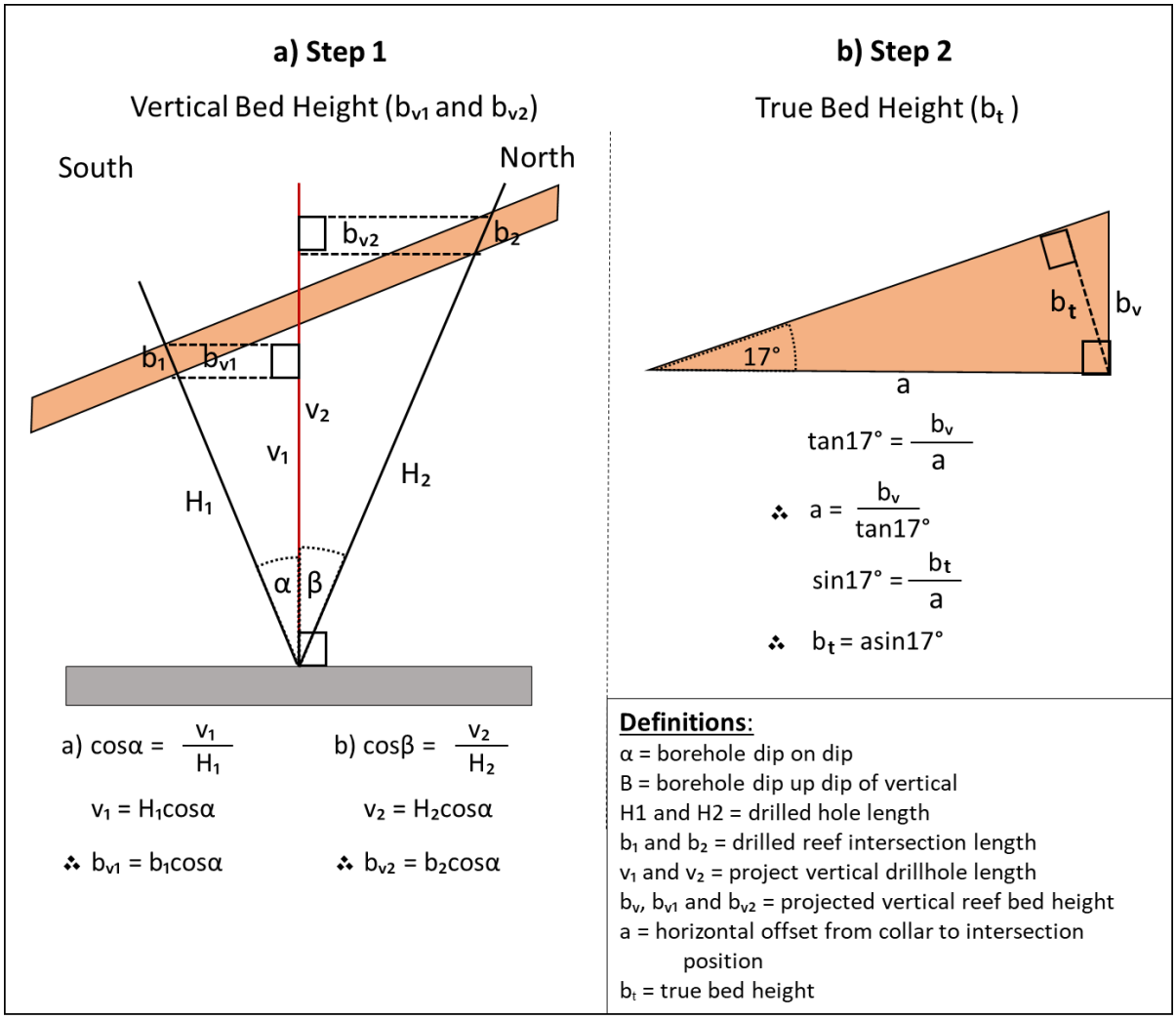


Figure 39: a) Standard trigonometric functions used to calculate vertical bed height (bv_1 or bv_1). B) Trigonometric functions used to convert vertical bed height to true bed height (b_t) at a dip of 17°.

All bed height data are presented in metres. Only valid (not faulted) drillhole data representing full bed intersections were utilised for bed height data interpretation purposes. Drillhole intersections were excluded for a specific bed where a drillhole started or ended within that bed or where a drillhole intersection was faulted. Exclusions to this rule occurred where drillhole collars were found to occur within 0.5 m of underground bed exposures as determined from historical mine cross-cut sections. A combination of digital and manual processes was then used to assess validity of an individual bed intersection. All bed height data was either plotted on mine structure plans to assess the proximity to (or intersection with) possible geological structures, or it was viewed in 3D using Datamine Studio 3™ relative to all surrounding intersections and modelled faults.

Data distribution is adequate for interpretation in existing and historical mining areas located up to 1500 m east of the Waterpan and Elsburg Massives sub-outcrop against the VCR. Data density beyond this distance is directly attributable to the lack of underground mining development and the absence of economically extractable ore. Valid drillhole sections were validated in CAE Datamine Studio™ by checking for outliers where points with excessive and too little reef width was encountered. Outliers were then individually checked and validated for acceptability by means of reverting to the original hardcopy reef logs.

3.1.1.2 Percentage Conglomerate

The cumulative length of conglomerate (matrix- and clast-supported) per measured bed/reef drillhole intersection interval was either measured in centimetres from drillcore or calculated from drillhole logs and then calculated as a percentage of the total reef intercept length. Older drillhole logs with drawn logs, but no "from" and "to" lengths were visually estimated to the nearest visually discernible 10% of conglomerate. Routine validation of percentage calculations was conducted in CAE Datamine Studio™ by checking for outliers in percentage conglomerate where encountered. Outliers were then individually checked and validated for acceptability by means of reverting to the original hardcopy reef logs.

3.1.1.3 Average and Maximum Clast Size

Empirical average and maximum clast size data were captured where available from hardcopy and digital borehole data. Most available mine data is qualitative in nature and relates to an approximate mine-adjusted Udden-Wentworth Scale (Udden, 1914; Wentworth, 1922; Wentworth, 1935; Blair and McPherson, 1999) (Figure 92**Error! Reference source not found.**). Clast sizes logged from drillhole core are difficult to measure accurately when the clast size exceeds the typical drillcore diameters used on the mines, namely AQ and BQ (30.5 mm and 40.7 mm, respectively). The known presence of wide quartz veins and the high frequency of vein quartz clasts in the Upper Elsburg reefs could lead to confusion as larger clasts may be mistaken for wide quartz veins or vice versa, depending on the nature of the contacts. Underground observations may yield clast sizes within the fine boulder grade class as defined by Blair and McPherson (1999). Empirical clast-size data was validated by referring back to hard-copy logs only. Owing to the qualitative nature of the clast size data at a global scale, limited time was allocated to interpretation of clast size, and only broad descriptions of changes in the data are discussed.

The clast size codes were digitally captured into the MS Excel™ database and converted to empirical measurements utilising the mine's adjusted grain sizes (Figure 92**Error! Reference source not found.**b) in order to capture variations.

3.1.1.4 Palinspastic Reconstruction

Palinspastic reconstruction of the drillhole intercept points was conducted across the geological structures identified (as per Figure 90) as representing possible wrench faults for all beds in order to test the sense of movement across the structures. The identified wrench faults were originally assumed to represent preserved post-sedimentary dislocations. Once palinspastic reconstruction based on the bed thickness was conducted, continuity in terms of other sedimentary qualities (for example percentage conglomerate, average and maximum clast size) across these structures was reviewed. In cases where percentage conglomerate was seen to continue across the structure within the reconstructed bad, the structure was inferred to have been active post-sedimentation (in reconstructed space). In instances where palinspastic reconstruction revealed discontinuous sedimentary qualities abruptly terminating against a structure within a reconstructed bed, syn-sedimentary movement was inferred. Most of the structures identified were seen to cross the Upper Elsburg sub-outcrop, and where a lateral dislocation was identified across the structure, it was confirmed that lateral movement had taken place. This was found to be the

case in all historically mapped wrench structures, namely P1 and P1 Wrench Faults as well as the left-lateral faults separating Blocks 3, 4 and 5 (refer to Figure 4).

Geological structures identified during the 2004 seismic survey (Manzi et al., 2013), wrench faults (as identified in Figure 90**Error! Reference source not found.**) and the West Rand Fault, as well as the Modderfontein Waterpan Member Sub-outcrop line were plotted in relation to the drillhole data points using CAE Studio™ (Datamine) software. Fault block numbers were then allocated for palinspastic reconstruction (Figure 4) of the drillhole data.

Block 3 (Figure 40) was selected as the reference polygon relative to which all other drillhole point data in the other blocks would be displaced on average dislocation vectors along the defined wrench faults. Block 3 was selected as it contains the bulk of the data. This resulted in the minimum number of points having to be moved within structural blocks and thus helped to reduce errors. The direction and estimated magnitude of lateral displacement across the wrench faults applied during palinspastic reconstruction equated to the last preserved dislocation of the Upper Elsburg sub-outcrop across the relevant faults prior to the Pilanesburg-aged dykes.

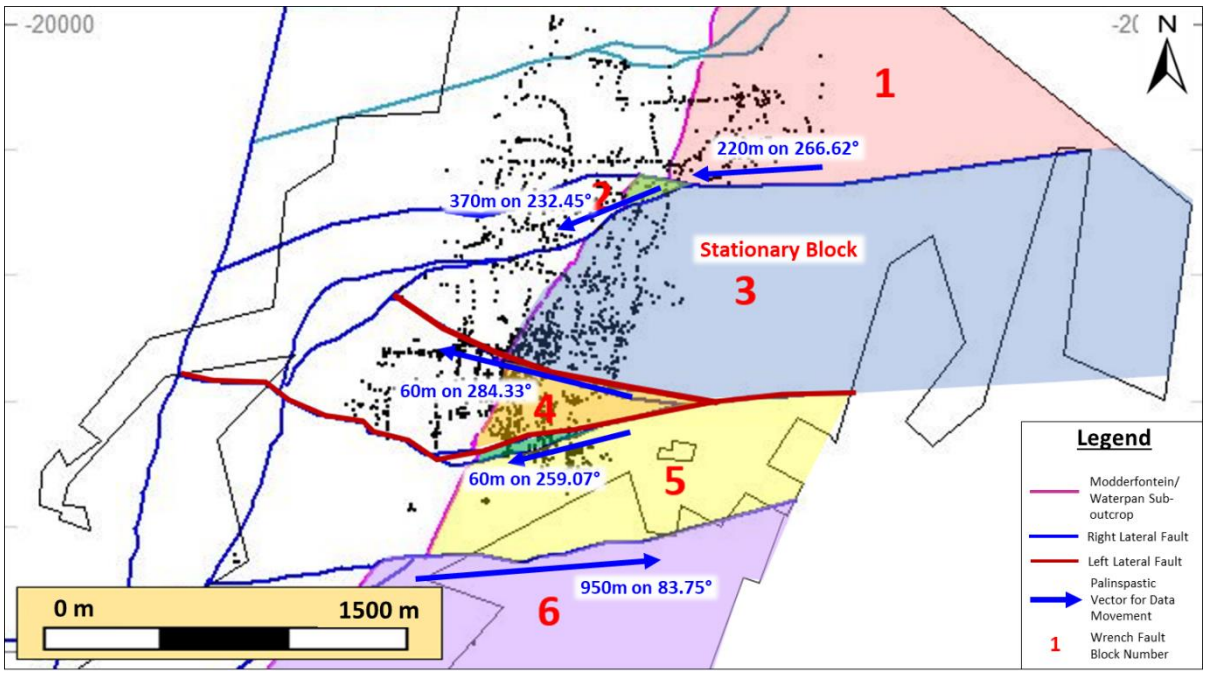


Figure 40: Fault blocks with original dataset before palinspastic reconstruction. Magnitude and direction of the palinspastic reconstruction vectors are represented by blue arrows.

All drillhole points occurring within a structural block were moved as a single entity relative to the preceding block (using Block 3 as the reference block) along the calculated wrench fault movement vector (*i.e.* Block 4, then Block 5 and then Block 6) such that continuity of the Upper Elsburg sub-outcrop was achieved across the interpreted last preserved fault dislocations. Lastly, Block 2 drillhole points and then Block 1 drillhole points were moved relative to Block 3.

Figure 41 demonstrates the palinspastic reconstruction of the Modderfontein/Waterpan sub-outcrop and drillhole data points conducted for Block 4 relative to Block 3.

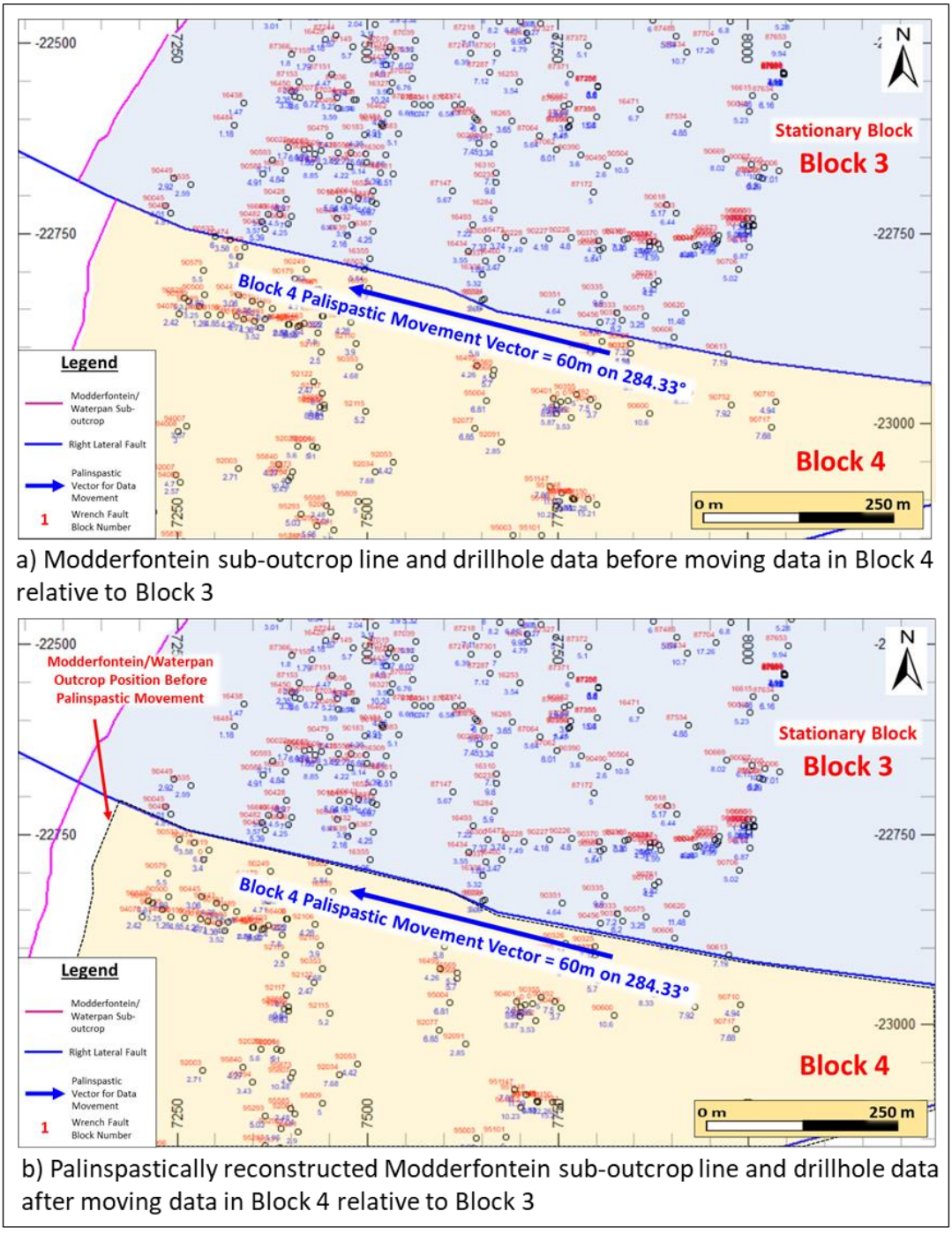


Figure 41: Demonstration of palinspastic movement of the Modderfontein/Waterpan Sub-outcrop and drillhole data points for Block 4 relative to Block 3.

Contouring for the four parameters (bed height, percentage conglomerate, average a maximum clast size) was then conducted to assess possible trends or differences in trends between separate fault blocks.

Datamine Studio RM™ was used to generate contours (Figure 42) for both the original datasets and the palinspastically reconstructed datasets for the parameters of bed height, percentage conglomerate, average clast size and maximum clast size. The contouring tool utilised the minimum curvature algorithm (Datamine Studio

RM™) with no smoothing and cell sizes of 100 m by 100 m. Contour elevation was selected to reflect the value of the attribute.

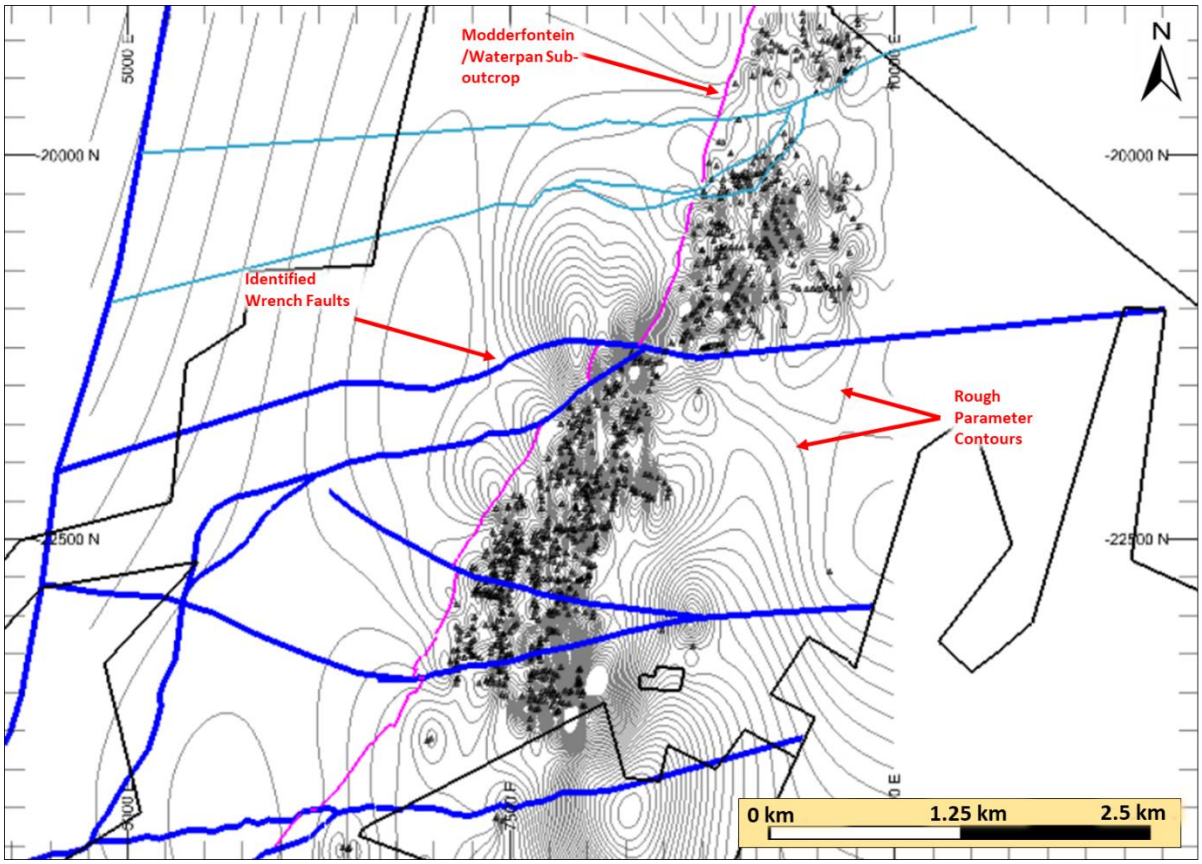


Figure 42: Rough contours for the ECB bed height in SDGM generated in Datamine Studio RM™ prior to palinspastic reconstruction.

The contours for each parameter generated by means of the minimum curvature algorithm were elevated in 3D space from a flat "0" m elevation plan by using the contoured value for the respective parameter, together with the borehole collars, also elevated by their respective same parameter value. This allowed a 3D wireframe to be constructed which emulated the distribution of each parameter modelled. Datamine Studio RM™ software was utilised to generate the parameter elevated contours and resultant 3D wireframe (Figure 43).

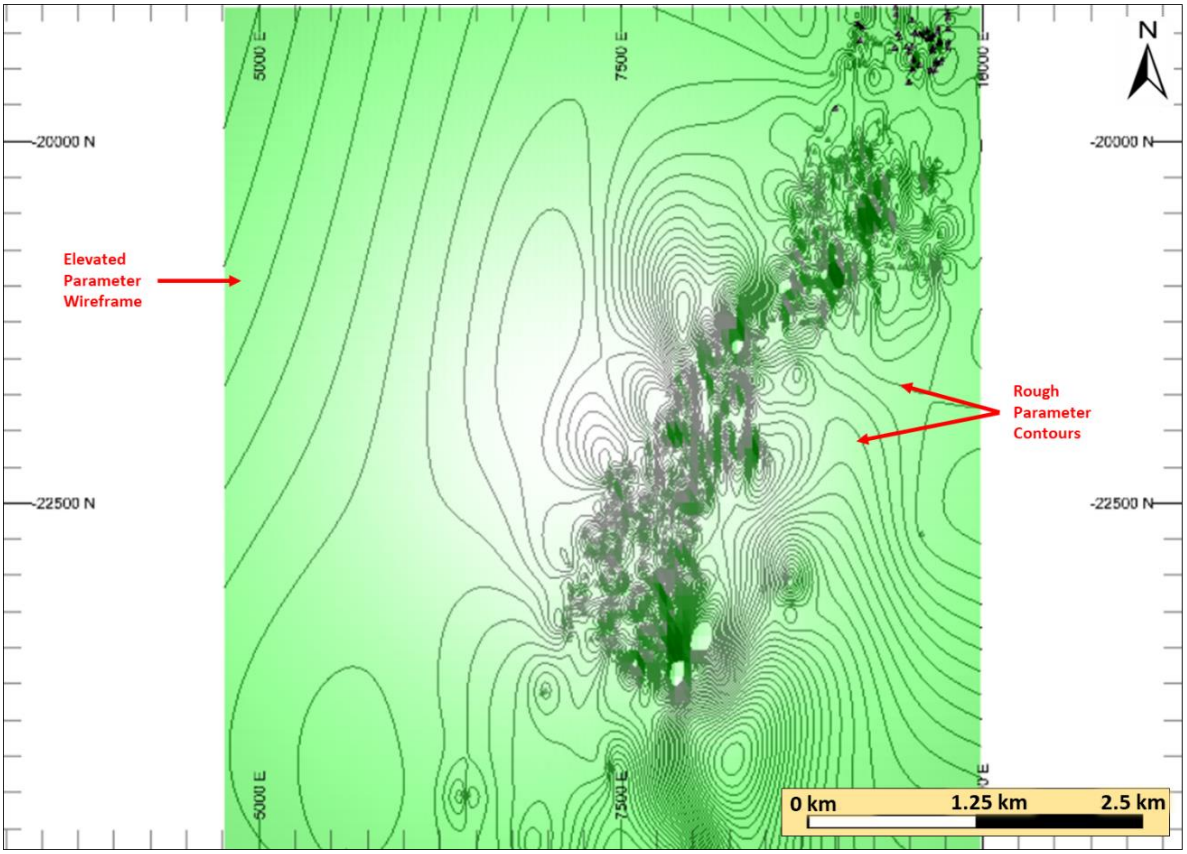


Figure 43: Rough contours for the ECB bed height with the automatically generated wireframe.

The wireframe was then filled with a block model to assist with the colour coding and legends. The block dimensions used to generate the various parameter block models was 25 m (x) X 25 m (y) X 100 m (z) to ensure all wireframes would be filled in the vertical (z) dimension, where the vertical cell size was constrained by the wireframe surface. The block models were then colour coded for presentation purposes as in Figure 44.

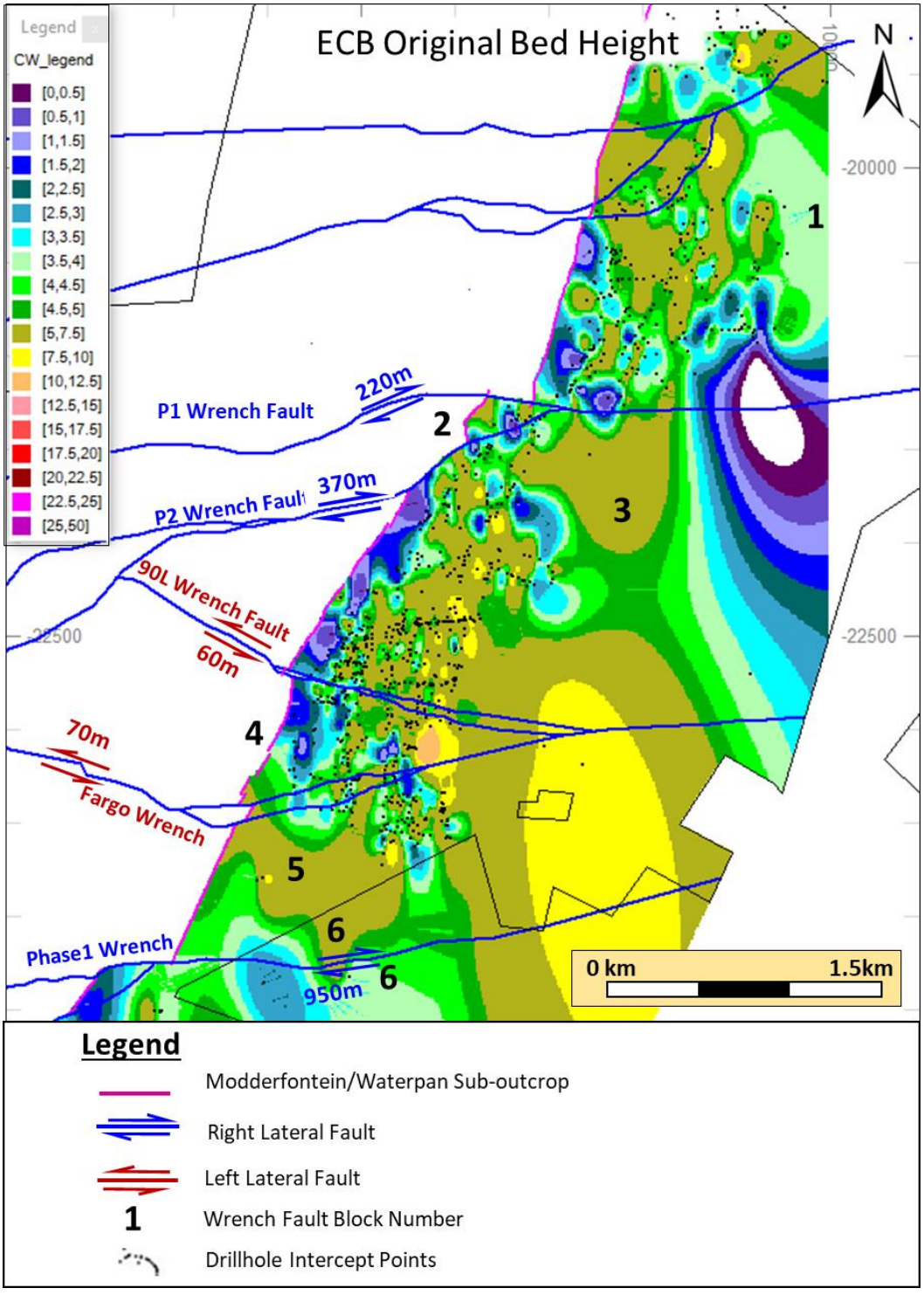


Figure 44: A colour coded block model presenting bed height for the ECB.

Shortcomings associated with contouring non-palinspastically reconstructed data include:

1) Contours cross the interpreted fault limits and preclude pre-faulting interpretation.
2) The contours cross the Modderfontein/Waterpan Sub-outcrop to the west and require trimming and cleaning.

Nonetheless, the method is easily replicated and quick to generate useful results plots. All plots presented in the Results section represent palinspastically reconstructed parameters; however, for comparison the plot for the ECB bed height using original data versus the corresponding plot for palinspastically corrected data is presented in Figure 45.

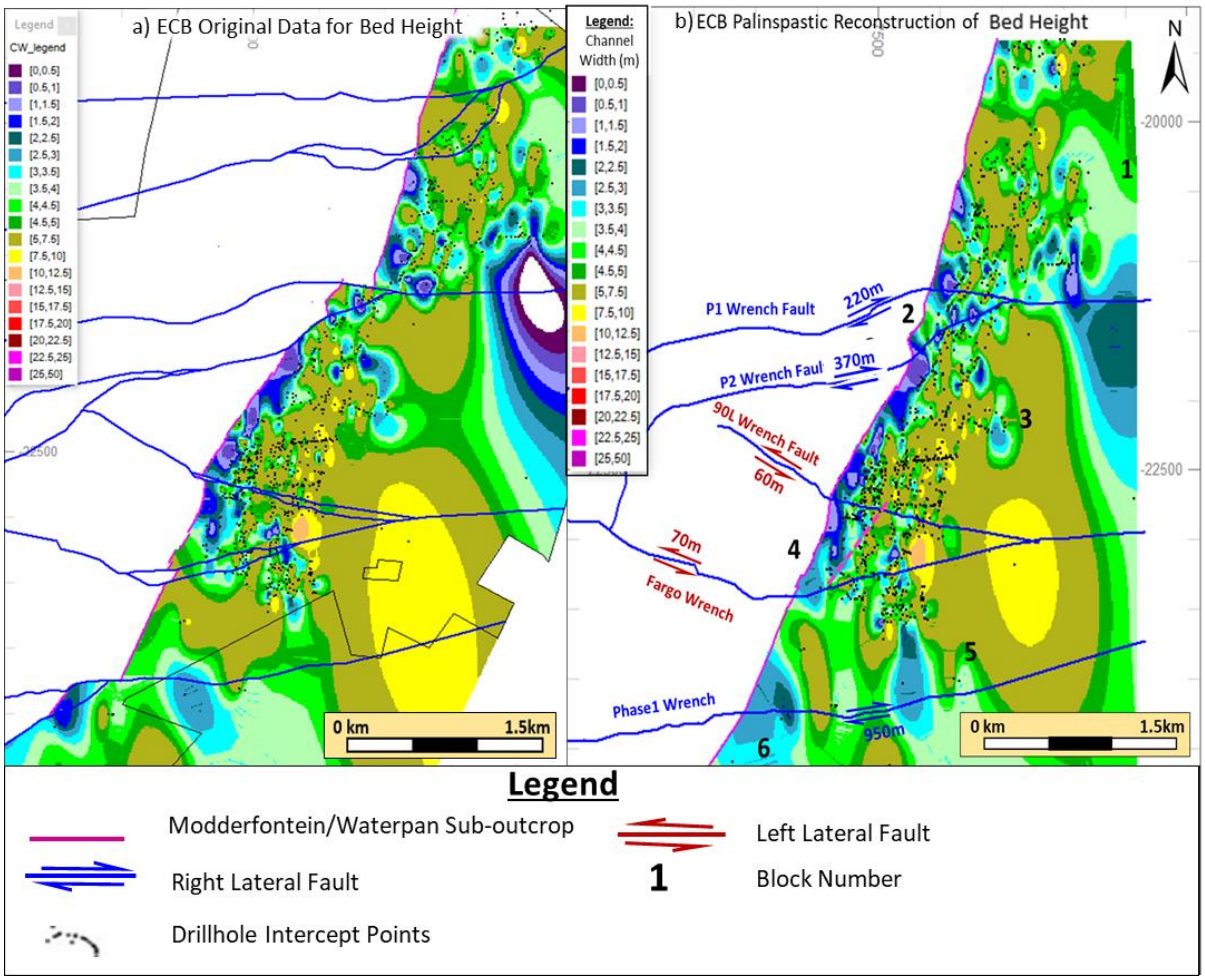
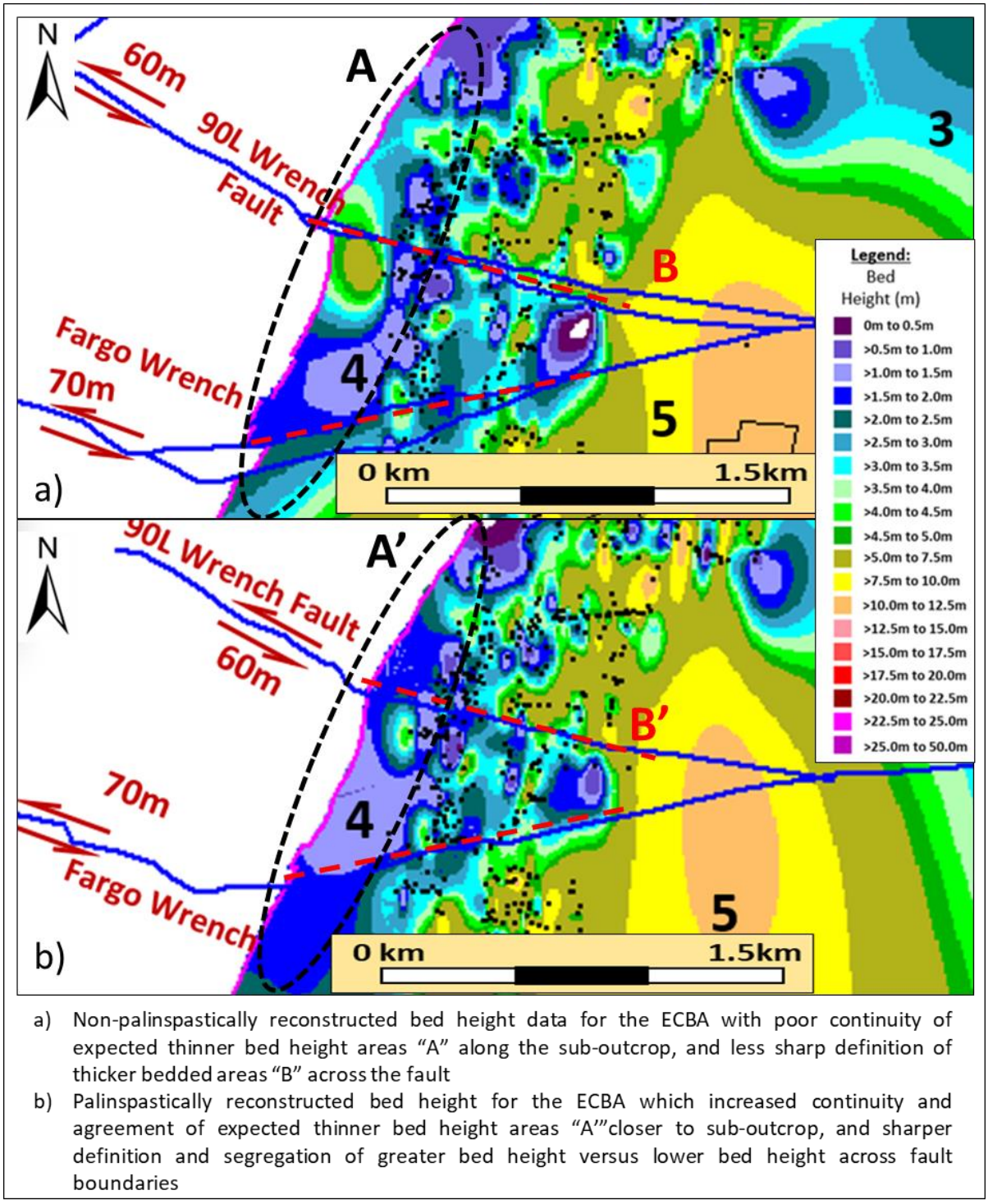


Figure 45: a) A coloured contour plan of the ECB bed height using original uncorrected data. B) A coloured contour plan of the ECB bed height using palinspastically corrected drillhole data points.

Palinspastic reconstruction of the borehole data and Upper Elsburg sub-outcrop resulted in better segregated data zones, which appear to be better constrained within interpreted fault blocks. Areas where data continuity is expected (such as thinner bed height areas close to the sub-outcrop) appear better defined and continuous in the palinspastically reconstructed dataset when compared to the non-palinspastically reconstructed dataset (Figure 46). The higher the borehole data density, the more representative the interpretation; thus, the data density as presented in both renditions of Figure 45 between the southern half of Block 5 and Block 6 would result in a highly speculative interpretation. Therefore, no attempt has been made to interpret Block 6 and thus results or contours in all plots for Block 6 have been deleted in the Results section.



a) Non-palinspastically reconstructed bed height data for the ECBA with poor continuity of expected thinner bed height areas "A" along the sub-outcrop, and less sharp definition of thicker bedded areas "B" across the fault

b) Palinspastically reconstructed bed height for the ECBA which increased continuity and agreement of expected thinner bed height areas "A'"closer to sub-outcrop, and sharper definition and segregation of greater bed height versus lower bed height across fault boundaries

Figure 46: a) Non-palinspastically reconstructed bed height data plot for the ECBA. B) Palinspastically reconstructed bed height dataset for the ECBA.

Trend lines for bed height, percentage conglomerate, average and maximum clast size have been identified based on the dominant visual trends of hot or cold colours in the contour plots. The bed height trend lines specifically identify observable trends not associated with the general westward thinning of the individual beds towards the west against the Upper Elsburg sub-outcrop line.

In the absence of empirical palaeo-current data and the exclusion of geostatistical methods (in terms of the confidentiality agreement, geostatistics does not form part of this study), it is acknowledged that subjectivity could occur in terms of trend identification when reviewing the data plots as opposed to purely objective statistical analysis. Historical published regional maps for the West Rand gold field showing empirical palaeo-current data provide a guide as to what palaeo-current directions should be expected. For instance, Vermaakt and Chunnett (1994; Figure 12) measured NW-to-SE to NNW-to-SSE directions near the present Twin Shaft Complex. Validation of the palaeo-current direction located at the SDGM Twin Shaft Complex was conducted by mapping out the edges of the mined-out workings (Figure 13) which show a similar approximate NW-SE trend. Owing to the stacked and overlapping mine workings within of the Upper Elsburg reef package, similar palaeo-current observations were not possible for these beds.

Osburn et al. (2014) noted geostatistical similarities in orientation (variography) between the VCR and Upper Elsburg Reef Package based on geostatistical modelling at SDGM. This implies that palaeo-current data for the VCR and the Upper Elsburg beds should be similar. Most observed trends should be expected to align with the regional NW-SE to NNW-SSE trends or measurements. Any exceptions to this could imply either incorrect interpretation or an alternative sedimentary fabric not observed elsewhere in the area.

Transition lines, which run normal- or oblique to bed height trends, percentage conglomerate trends and clast size trends are used to indicate sudden changes within fault blocks. Bed height transition lines are thought to represent the transition from eroding or cannibalising action of the unconformity at the base of the overlying bed to preservation of the underlying bed. Trend lines identified in percentage conglomerate plots are thought to represent a transition from primary winnowing directly downstream and adjacent to the scoured pediment facies into the debris-flow floodplain (influx stage) as shown in Figure 47.

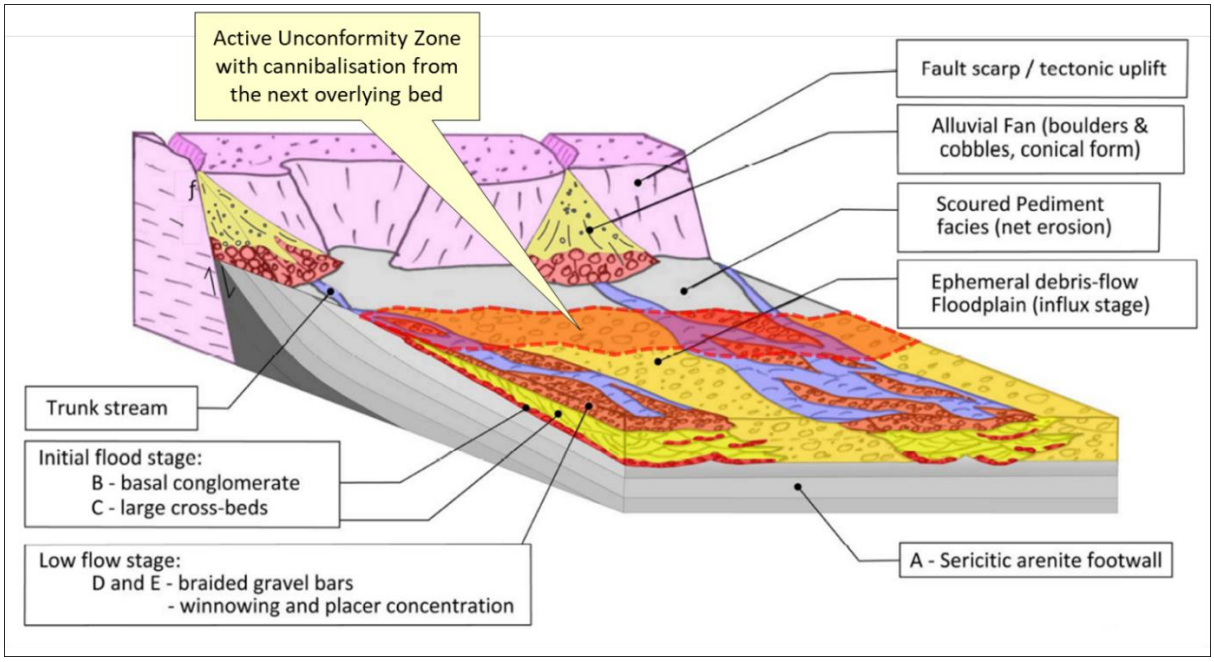


Figure 47: Model showing the main architectural elements of the multistage development of Witwatersrand palaeoplacers (modified after Tucker (1980) and Tucker et al. (2016)).

CHAPTER 4: RESULTS

4.1 Dataset and Presentation

A total of 4502 drillholes including 53 surface drillholes with deflection data were utilised to source the data for the plots and analysis presented in this section. Due to the stacked nature of the reef beds making up the stratigraphy, some holes were utilised for more than one stratigraphic bed. A summary of the data points attributable to each bed or horizon and the analysed parameters is presented below in Table 2.

Table 2: Summary of data points per bed and parameters utilised in the data analysis

Bed	Valid Bed Height Intersections	Percent Conglomerate Data Points	Average Clast Size Data Points	Maximum Clast Size Data Points
VCR	1851	1842	1849	33
MBT	1253	1252	1188	296
MBB	1270	1268	1217	249
MIQ	1136	1134	1025	17
MIT	1295	1293	1229	314
MIB	1092	1092	1003	316
MAD	1061	1061	983	22
MAC	1128	1128	1099	257
ED	1424	1423	1210	9
ECT	1418	1413	1306	435
ECMQ	876	876	839	-
ECMC	1275	1275	1187	403
ECBQ	866	865	814	15
ECB	1208	1206	618	395
ECBAQ	795	793	728	5
ECBA	783	370	262	152
Total Dataset	**18731**	**18291**	**16557**	**2918**

Wrench faulting which has impacted the SDGM property at least post-dates the deposition of the Klipriviersberg Lavas and has necessitated the palinspastic reconstruction of the drillhole data by means of applying an average measured dislocation of the data across each successive wrench fault in order to present a sedimentological model which pre-dates the wrench faulting to assess whether these structures were possibly active during Central Rand Group sedimentation. The magnitude of post-Klipriviersberg wrenching across each fault was calculated by measuring the magnitude of dislocation of the Upper Elsburg sub-outcrop.

Four sets of plots are presented for each bed in the following order:

1) Bed height
2) Percentage conglomerate
3) Average clast size
4) Maximum clast size

Each stratigraphic bed is first presented holistically for each of the four parameters by means of a small-scale plot and includes the full contoured interpretation of Blocks 1 to 5. As previously indicated, Block 6 contoured results have been excluded due to the wide (±1000 m) drillhole spacing. In addition, enlarged sections of the small-scale plot are presented for bed height and percentage conglomerate for each of the structure blocks abutting the faults. Due to the limited empirical clast-size data, the average and maximum clast size plots are only presented as small-scale plots.

Interpretation is only effective to ±1.5 km east of sub-outcrop due to decrease in data density. In areas of higher data density lower conglomerate percentage (<5%) may be interpreted as a true representation of the data. In areas of data paucity, beyond the effective ± 1.5 km, lower percentage conglomerate data should be viewed with caution.

4.2 Stratigraphic Beds

4.2.1 ECBA

4.2.1.1 ECBA Bed Height

Figure 48 presents the palinspastic reconstruction for bed height for the ECBA. In general, the ECBA thins from east to west towards the Upper Elsburg sub-outcrop, with the rate of westward thinning in Block 1 being lower than along the balance of the sub-outcrop to the south. Maximum bed height (>12.5 m to 15 m) is attained in Block 3 approximately 1 km away from the sub-outcrop. A general thickening N-S trend from north to south also occurs. Data density is high within a strip of 1.5 km running parallel to the sub-outcrop. East of this zone, interpretation becomes speculative. Higher bed height trends (excluding the westward thinning) run NNW- SSE while a secondary trend runs sub-parallel (NNE-SSW) in the north to oblique (NNW-SSE) to the sub-outcrop in the south.

4.2.1.2 ECBA Percentage Conglomerate

Figure 49 presents the palinspastic reconstruction for percentage conglomerate for the ECBA. Percentage conglomerate appears to generally decrease to the east. However, interpretation is only effective to ±1.5 km east of sub-outcrop due to decrease in data density. Percentage conglomerate is also seen to increase from north to south. Trends in the percentage conglomerate appear oriented preferentially NNW-SSE.

Comparison of bed height to percentage conglomerate indicates a possible relationship between lower percentage conglomerate and greater bed height as observed in Block 1. Towards the south, in areas of lower bed height, a higher percentage conglomerate occurs.

4.2.1.3 ECBA Average and Maximum Clast Size

Average clast size trend occur for the ECBA is primarily NNW-SSE and crosses over the 90 Level (“90L”) Wrench as well as the Fargo Wrench (Figure 50) in Blocks 3, 4 and 5, while a possible weak NNW-SSE trend may occur in Block 1. A NNW-SSE trend for maximum clast size also crosses the 90L Wrench as well as the Fargo Wrench (Figure 51). Maximum clast size increase in the south, with the maximum occurring notably between the faults bounding Block 4.

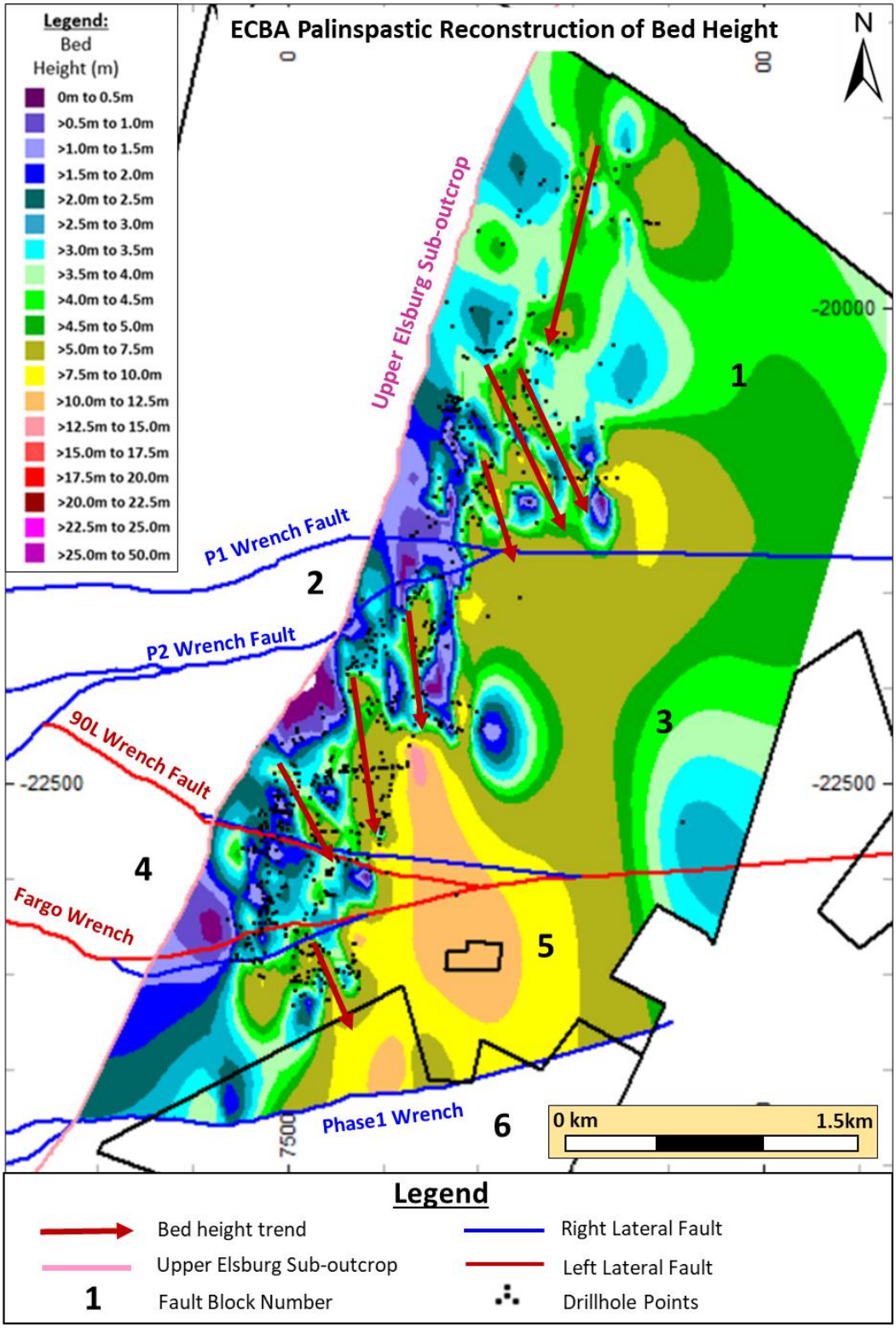


Figure 48: Palinspastic bed height reconstruction for ECBA.

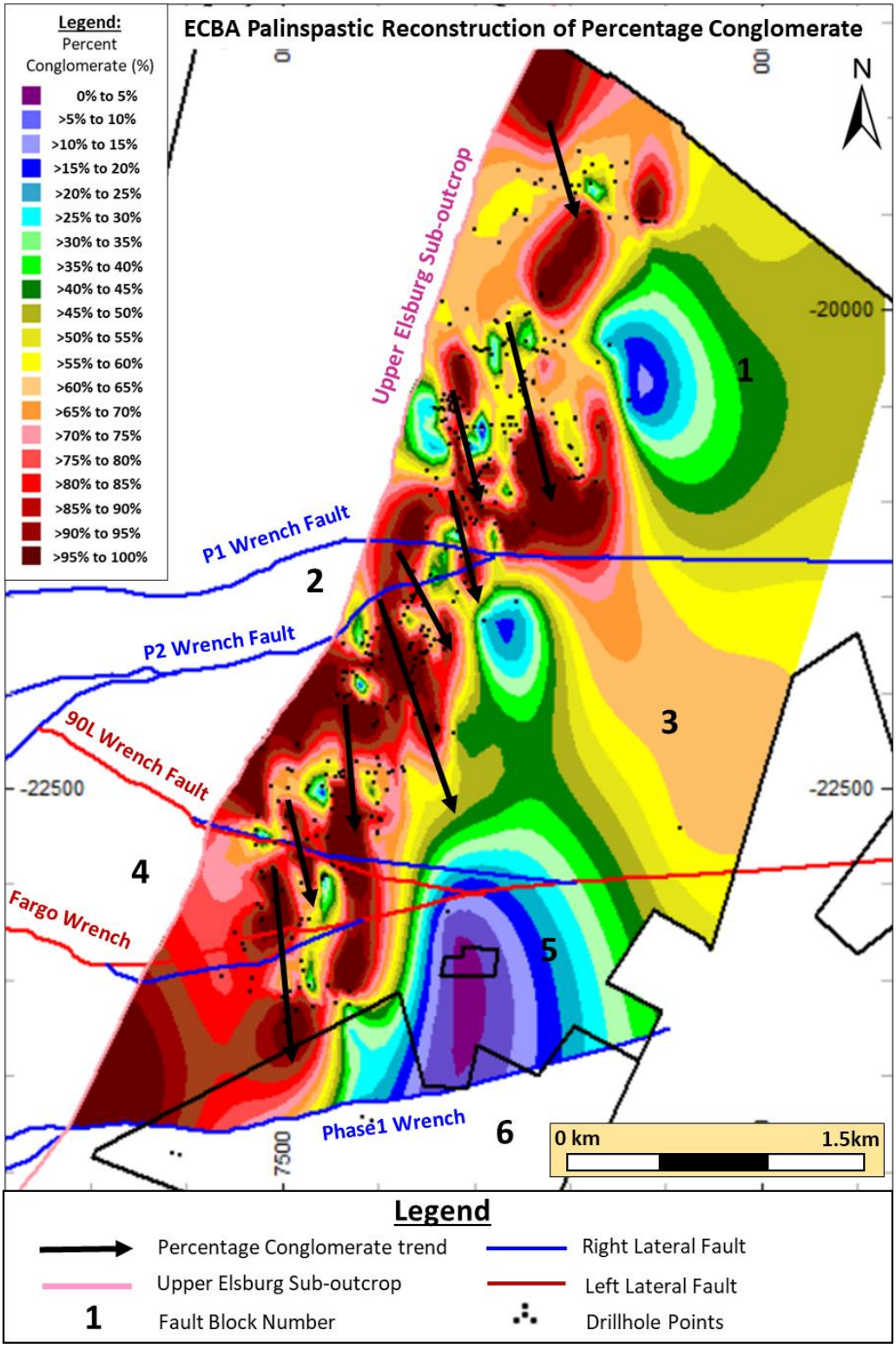


Figure 49: Palinspastic percentage conglomerate reconstruction for ECBA.

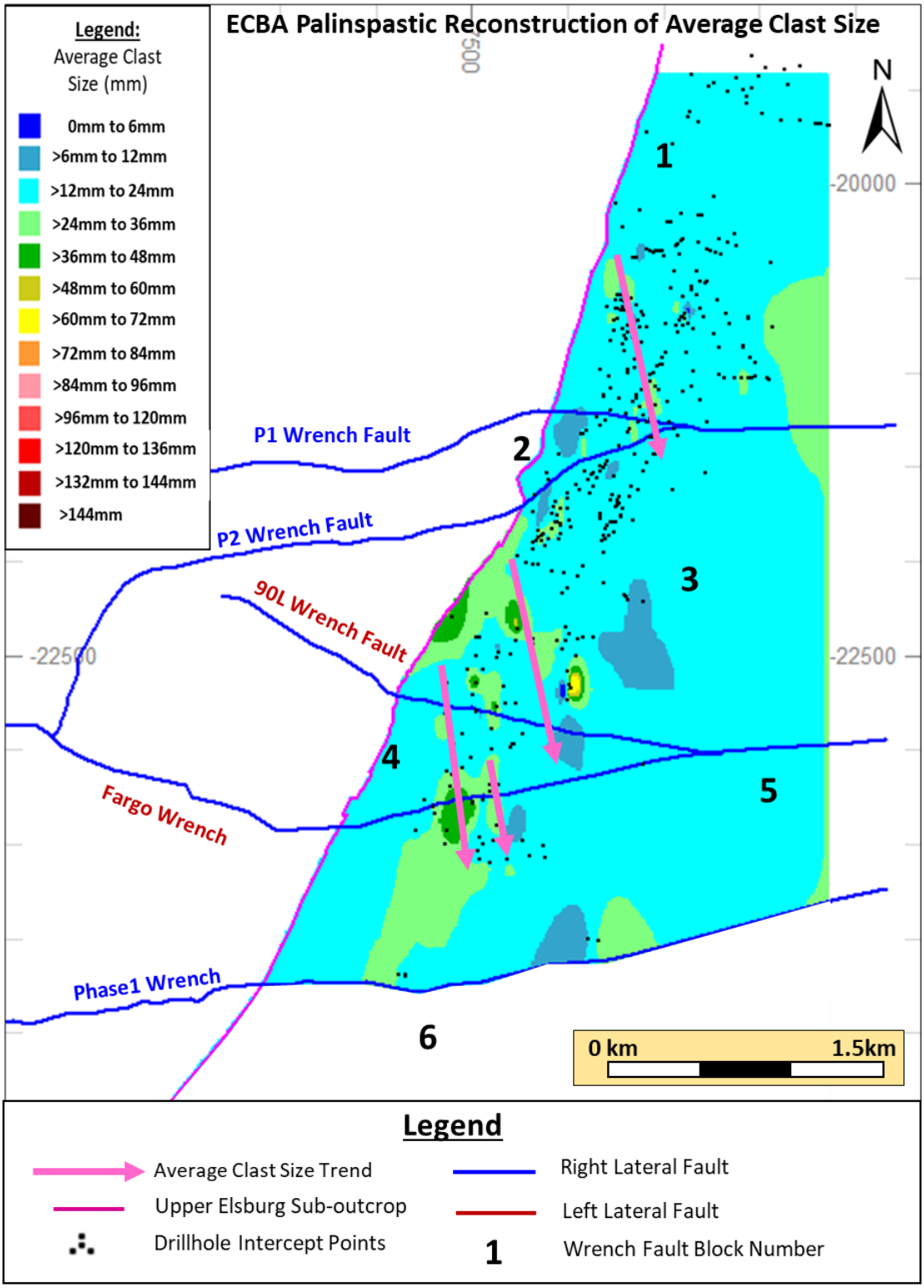


Figure 50: Palinspastic average clast size reconstruction for ECBA.

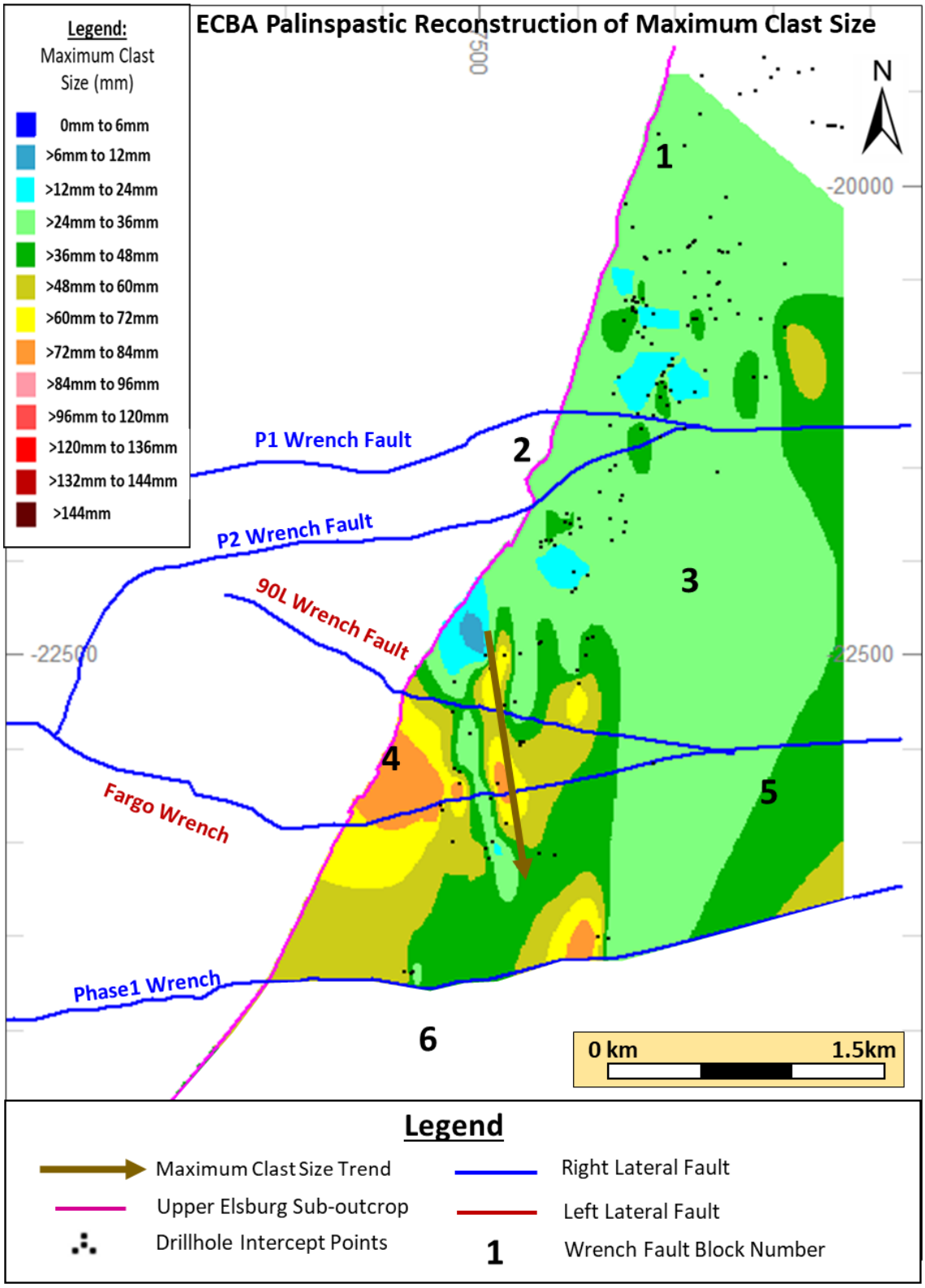


Figure 51: Palinspastic maximum clast size construction for ECBA.

Figure 52 present a combined interpretation of all parameters overlain on top of bed height. Interpreted trends for all the parameters are very similar with a predominant NNW-SSE orientation.

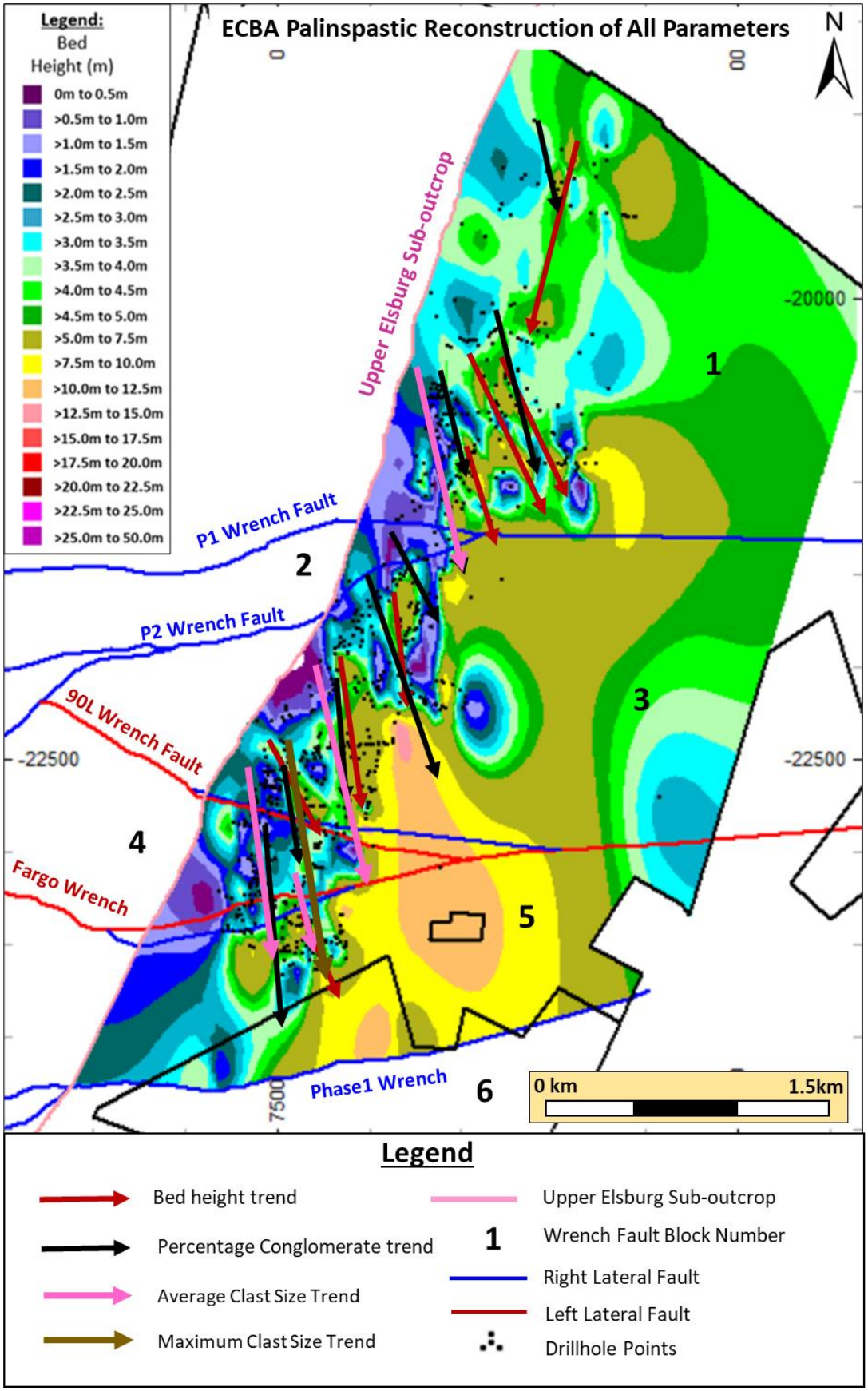


Figure 52: Palinspastic Reconstruction for the ECBA – All Parameters

4.2.1.4 ECBA Detailed Plots

Figure 53 presents an enlarged section of the a) bed height and b) percentage conglomerate plan for the ECBA including Blocks 1, 2 and 3. In Figure 53 a) a zone of lower bed height crosses over P1 Wrench and terminates against P2 Wrench. This zone of thinning appears associated with a high percentage conglomerate. An apparent dislocation of ±300 m appears to offset the thicker zone in Blocks 1 and 2 from that in Block 3 implying inactivity on P1 Wrench, while possible movement on P2 Wrench. Timing of this dislocation is not clear but would post-date ECBA deposition. Nature of movement is also not discernible, though an apparent right-lateral dislocation could have occurred. In addition, movement post-ECBA deposition might have been vertical (up to the north) across P2 Wrench prior to or concurrent with ECBAQ erosion and subsequent deposition.

Figure 54 indicates a zone of thinner ECBA associated with a high percentage conglomerate just south of P2 Wrench (indicated as a dashed pink line). The northern margin of Block 4 up against 90L Wrench is highlighted by a number of alternating nodes of higher and lower bed heights. Correspondingly, nodes of lower percentage conglomerate are located adjacent to 90L Wrench. An apparent, but not distinct dislocation of ±100 m (possibly left-lateral) appears to occur across 90L Wrench for bed height. The alternating nodes of higher and lower bed height serve to indicate the presence, or nearby location of an active structure, thus implying that 90L Wrench might have been active during or after deposition of the ECBA. Nature of movement is not conclusive, but apparent.

Figure 55 presents an offset of a zone of lower bed height of ±100 m right-lateral and ±150 m left-lateral dislocation across the 90L Wrench and Fargo Wrench, respectively. Again, sense and timing of dislocation is speculative due to the unknown amount of erosion of the ECBA by the overlying ECBAQ. Winnowing is not evident within this thinner zone, as percentage conglomerate is highly variable within this zone. This could imply that variable erosion of the blocks might have resulted from uplift of Block 4 during erosion by and deposition of the ECBA.

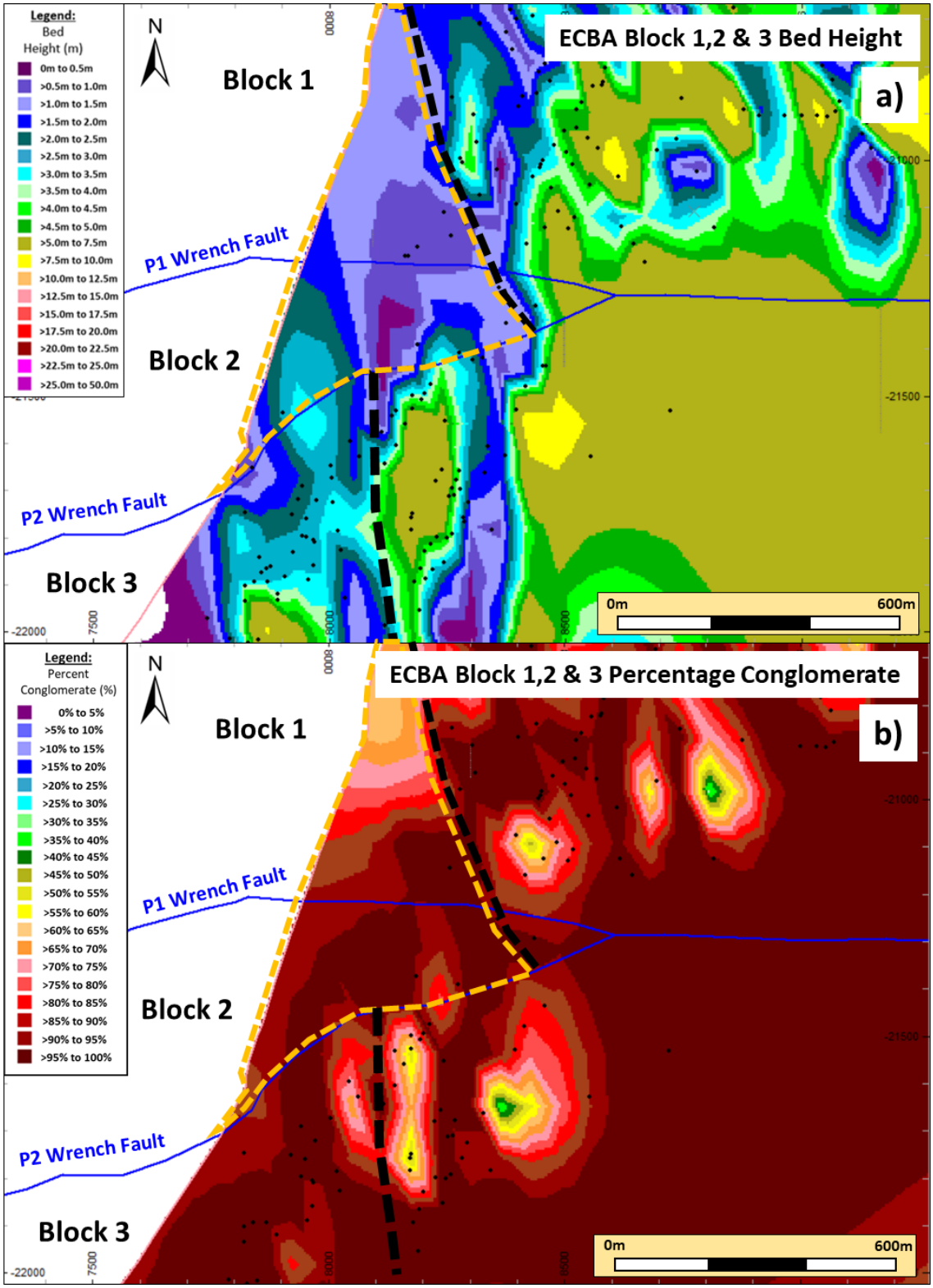


Figure 53: Enlarged Block 2 palinspastic reconstruction for a) bed height for ECBA and b) for percentage conglomerate for ECBA. Yellow polygon in both a) and b) denotes zone of low bed height and high percentage conglomerate terminated on P2 Wrench. Black line indicates significant change in bed height.

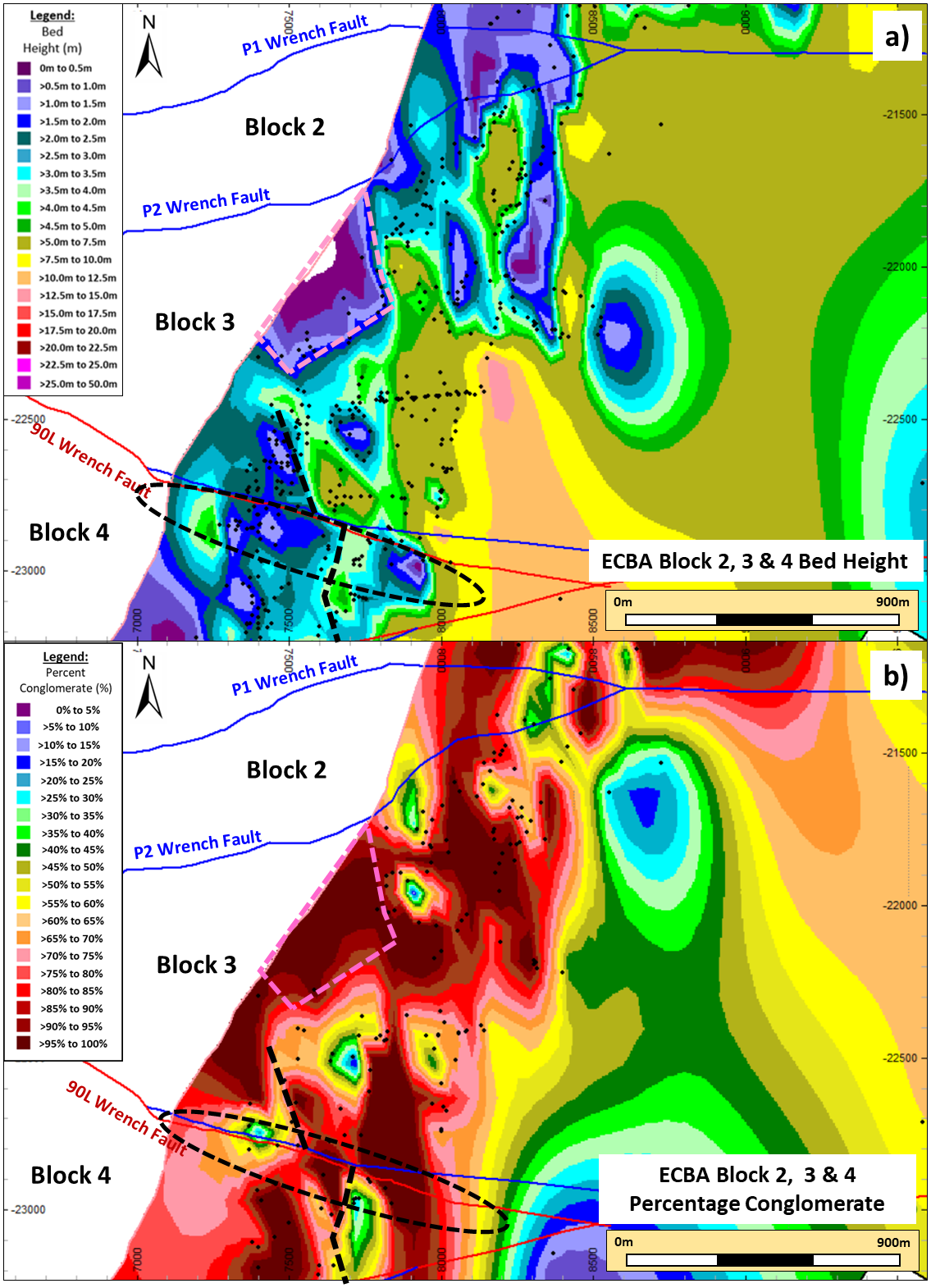


Figure 54: Enlarged Block 3 palinspastic reconstruction for a) bed height for ECBA and b) for percentage conglomerate for ECBA. Pink polygon in a) and b) denotes area of low bed height and high percentage conglomerate. Black ellipses highlight highly variable alternating nodes for both bed height and percentage conglomerate along or adjacent to the 90L Wrench strike.

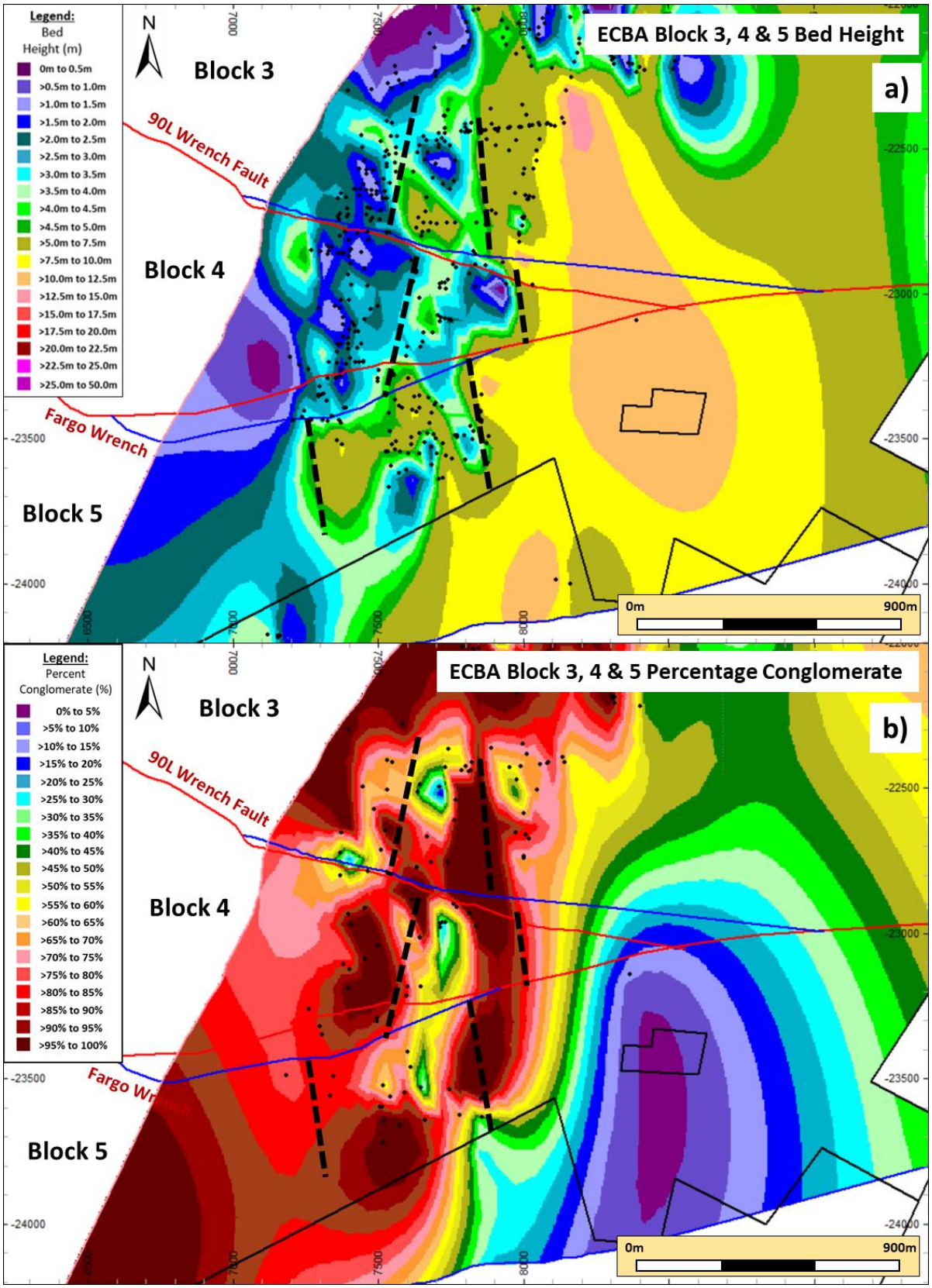


Figure 55: Enlarged Block 4 palinspastic reconstruction for a) bed height for ECBA and b) for percentage conglomerate for ECBA. Black dashed in line in a) and b) denotes possible offsets of a zone of higher bed height.

4.2.2 ECB

4.2.2.1 ECB Bed Height

The palinspastic reconstruction for bed height for the ECB is presented in Figure 101**Error! Reference source not found.**. The ECB gradually thins from the east to west towards the Upper Elsburg sub-outcrop but very seldom thinning to <2 m. Maximum bed height (>10 m to 12.5 m) is reached within the eastern half of Block 4 between the 90L Wrench and Fargo Wrench ±1000 m from sub-outcrop.

A general thickening trend from north (Block 1) to south (Blocks 3, 4 and 5) also occurs. High data density within a strip of 1.5 km running parallel to the sub-outcrop allows for reliable interpretation. East of this zone interpretation is speculative. Higher bed height trends (excluding the westward thinning) run sub-parallel (NW-SE) in the north to oblique (NNW-SSE) relative to the sub-outcrop in the south in Blocks 3, 4 and 5.

4.2.2.2 ECB Percentage Conglomerate

The ECB palinspastic reconstruction for percentage conglomerate is presented in Figure 102. Percentage conglomerate appears to remain relatively constant when moving to the east. The northern portion of Block 1 is an exception to this pattern. Trends in the percentage conglomerate appear oriented preferentially NNW-SSE over Blocks 1 and 5, and N-S in Block 3.

Higher bed height appears to result in a lower percentage conglomerate in the south, while in the north, lower percentage conglomerate is associated with the slightly thinner ECB in Block 1.

4.2.2.3 ECB Average and Maximum Clast Size

The ECB is primarily conglomeratic in nature and typically contains little internal quartzite. Average clast size (Figure 103**Error! Reference source not found.**) for the ECB is smaller in the north (±24 mm), with a marked increase in average clast size occurring in Block 3, where areas may attain average clast sizes >60 mm. A weak average clast size NW-SE trend appears to occur within Block 1 but is difficult to confirm due to low data variability. Trends of NNW-SSE for average clast size are discernible across the 90L Wrench and Fargo Wrench combination.

Maximum clast size for the ECB (Figure 104**Error! Reference source not found.**) seldom exceeds 48 mm. A poorly defined NW-SE maximum clast size trend is interpreted in Block 1. Maximum clast size exceeds 84 mm in the south within Blocks 3, 4 and 5. Trends of NNW-SSE for maximum clast size are discernible across the 90L Wrench and Fargo Wrench combination.

The combined plot of all superimposed parameters on the bed height plot as background is present below in Figure 56.

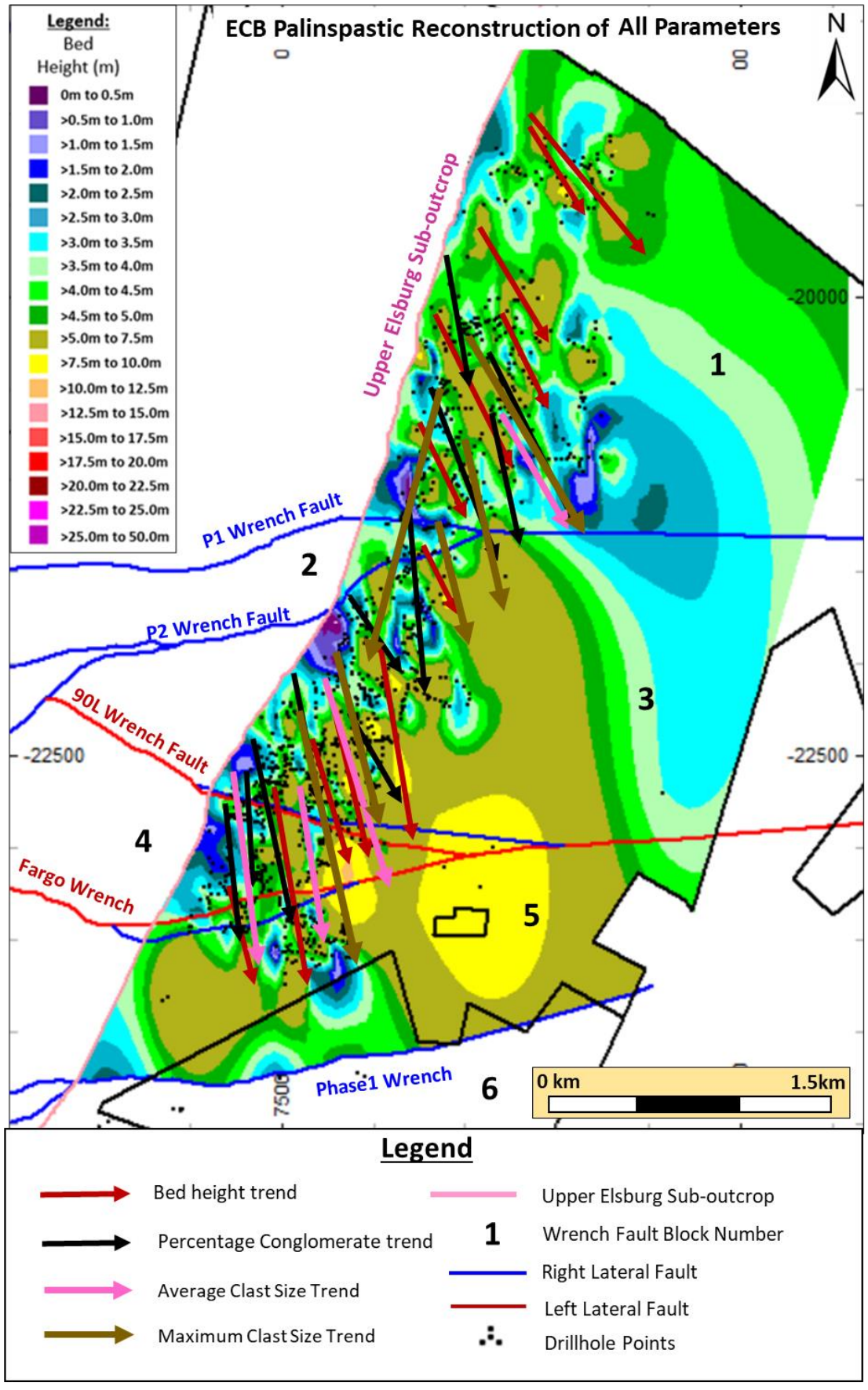


Figure 56: Palinspastic Reconstruction for the ECB – All Parameters

4.2.2.4 ECB Detailed Plots

Figure 57**Error! Reference source not found.** presents an enlarged section of the a) bed height and b) percentage conglomerate plan for the ECB for Blocks 1, 2 and 3 where a zone of lower bed height is interpreted to cross over P1 Wrench. Termination against P2 Wrench is not as clear as in the ECBA and ECBAQ. This thinning appears to be associated with an area of high percentage conglomerate on its southern end. An apparent dislocation of ±400 m appears to offset the thicker zone in Blocks 1 and 2 from that in Block 3. Timing and nature of this dislocation and where it terminates are not clear but could post-date ECB deposition. In addition, movement post-ECB deposition might have been vertical (up to the north) across P2 Wrench prior to or concurrent with ECB erosion and subsequent deposition.

Figure 58**Error! Reference source not found.** indicates a zone of variable bed height ECBAQ associated with associated nodes of variable percentage conglomerate just south of P2 Wrench. The southern margin of Block 3 up against 90L Wrench is highlighted by change from a slightly higher bed height in Block 4 to a lower bed height in Block 3 to the north. A line of variable percentage conglomerate nodes occurs lying sub-parallel to the southern edge of Block 3 near 90L Wrench.

A narrow zone of westward thinning ECB occurs parallel to the Upper Elsburg sub-outcrop in Figure 58**Error! Reference source not found.** a) and is related to the attenuation/erosion of the ECB by the overlying ECBQ due to possible bed cannibalisation.

Figure 59**Error! Reference source not found.** presents a possible ±100 m left-lateral dislocation of a zone of thicker ECB across the 90L Wrench. This thicker zone of ECB is also potentially off-set by a ±100 m right-lateral dislocation across the Fargo Wrench. Timing and magnitude of these relative dislocations is unclear due to the erosion of the ECB by the overlying ECBQ. A zone in the west of Block 4 with a low bed height and an associated higher conglomerate percentage occurs.

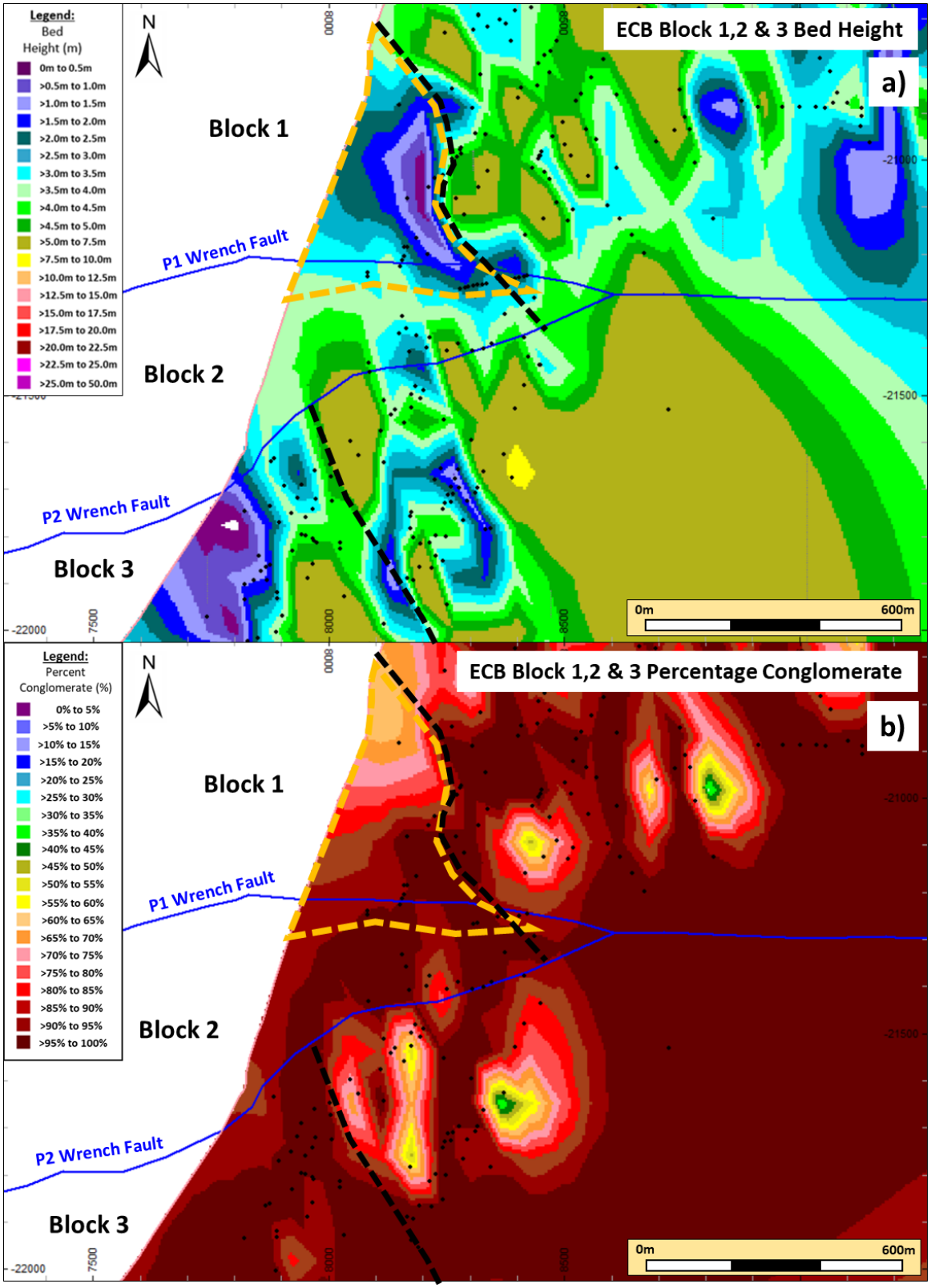


Figure 57: Enlarged Block 2 palinspastic reconstruction for a) bed height for ECB and b) for percentage conglomerate for ECB. Yellow polygon in a) and b) indicates zone of low bed height and variable percentage conglomerate.

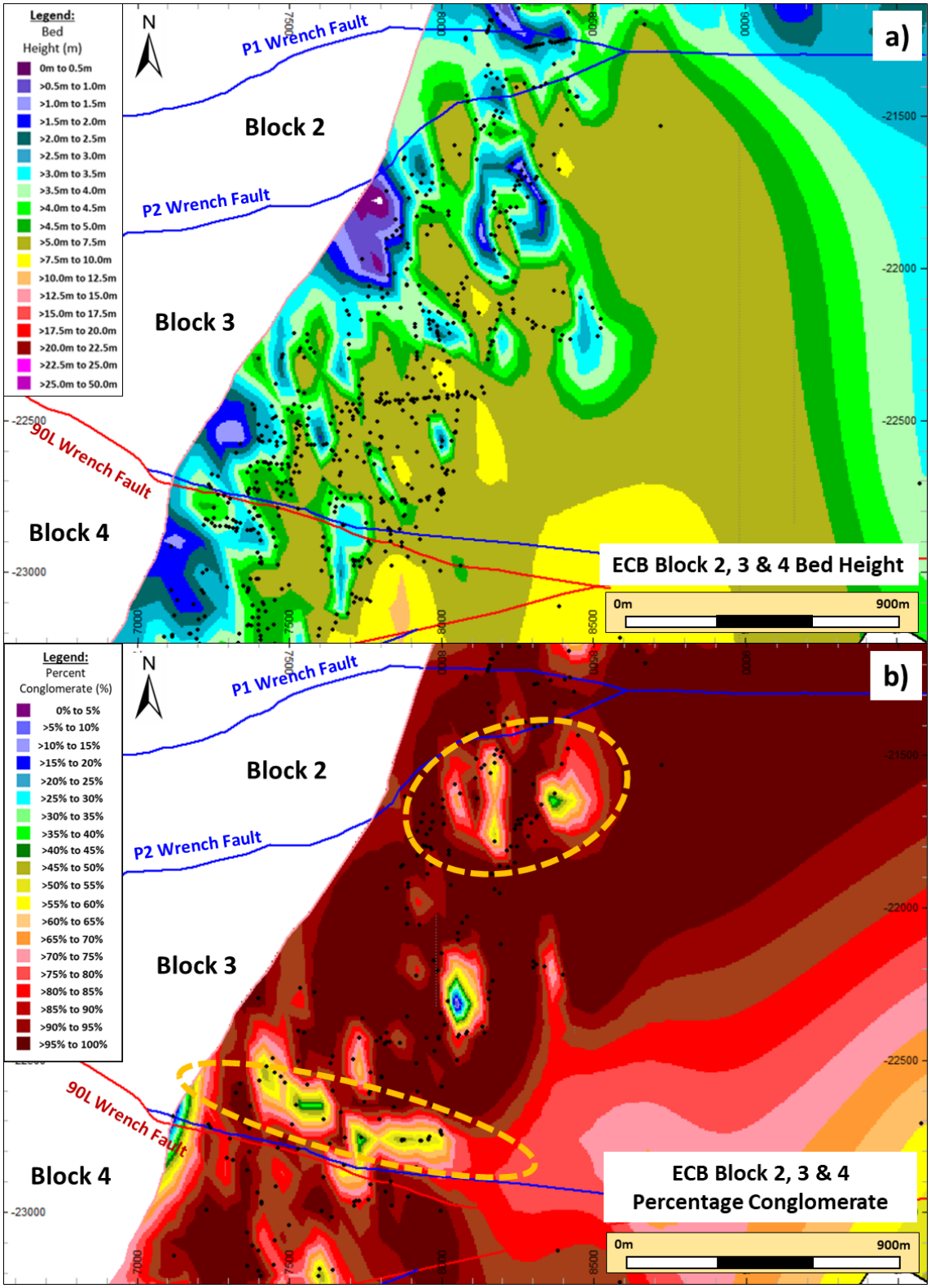


Figure 58: Enlarged Block 3 palinspastic reconstruction for a) bed height for ECB and b) for percentage conglomerate for ECB. Yellow ellipses in b) indicate nodes of variable and alternating percentage conglomerate occurring up against or adjacent to geological structures.

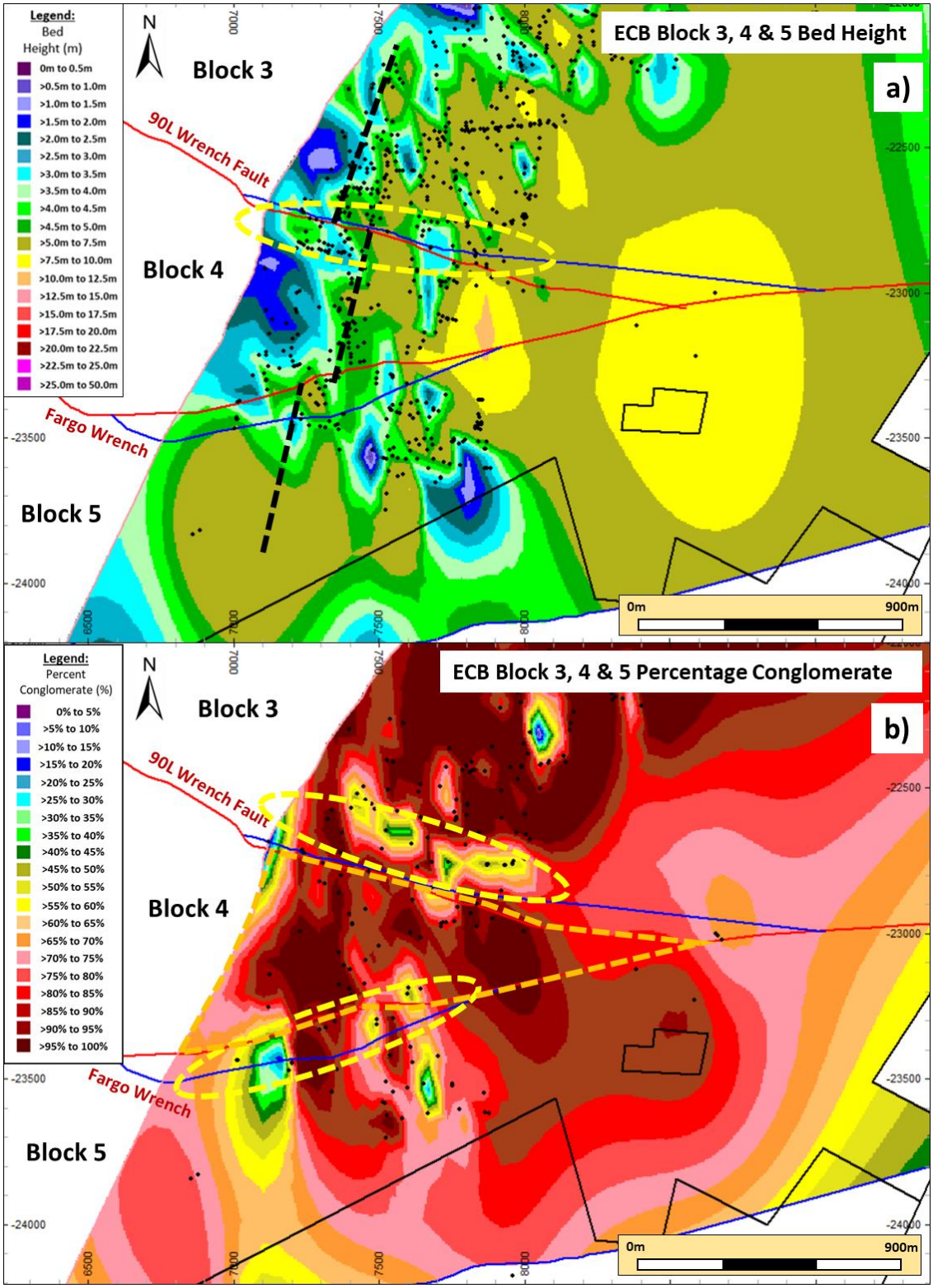


Figure 59: Enlarged Block 4 palinspastic reconstruction for a) bed height for ECB and b) for percentage conglomerate for ECB. Yellow ellipses in a) and b) indicate nodes of variable and alternating percentage conglomerate occurring up against or adjacent to geological structures.

4.2.3 ECT

4.2.3.1 ECT Bed Height

Figure 129**Error! Reference source not found.** presents the palinspastic bed height reconstruction for the ECT. As with other EC beds belonging to the Waterpan Member or Elsburg Individuals, the rate of westward thinning towards the Upper Elsburg sub-outcrop in the northern half of Block 1 appears more gradual than that exhibited elsewhere to the south – especially in proximity to the P1 Wrench and P2 Wrench. General bed height trends in Blocks 1 and 3 are NW-SE, while in Blocks 4 and 5 the trend shifts NNW-SSE, with a component of a N-S trend possibly interpreted in Block 3. The bed height for the ECT seldom exceeds >5 m to 5.5 m. The observed bed height range (>3.0 m to 5.5 m) remains reasonably constant along the entire strike length of the Upper Elsburg sub-outcrop for the ECT.

4.2.3.2 ECT Percentage Conglomerate

Palinspastic reconstruction of the ECT percentage conglomerate (Figure 130**Error! Reference source not found.**) presents a bed highly variable in percentage conglomerate across the project area – especially in the southern half of Block 1 and into Block 2. However, the northern half of Block 1 presents a lower percent conglomerate than elsewhere further to the south. A distinct increase in percentage conglomerate occurs within Blocks 3 and 4, with a possible decrease in percentage conglomerate occurring again within Block 5. The NW-SE percentage conglomerate trend lines in Blocks 1 and 3 mirror those for bed height in Figure 129**Error! Reference source not found.** while in Blocks 4 and 5 percentage conglomerate trends NNW-SSE. However, the secondary N-S bed height trend in Block 3 is not discernible for percentage conglomerate.

4.2.3.3 ECT Average and Maximum Clast Size

Average clast for ECT (Figure 131**Error! Reference source not found.**) presents a distinct increase in average clast size towards the south within Blocks 3, 4 and 5. Average clast size can exceed >72 mm. Average clast size trends (NNW-SSE) appear to cross over the 90L Wrench and Fargo Wrench combination in the south. Blocks 1, 2 and the northern portion of Block 3 show scattered areas of larger average clast size (>24 mm). A possible weak NW-SE trend may be interpreted in Block 1 for average clast size.

Maximum clast size data for ECT (Figure 132**Error! Reference source not found.**) presents NNW-SSE trends similar to with those of average clast size, also with the possible occurrence of a weak NW-SE trend in maximum clast size in Block 1. A zone of smaller maximum clast size (>12 mm to 24 mm) appears to straddle the P1 Wrench and P2 Wrench combination, while a significant increase in maximum clast size (to over >96 mm) is apparent over the 90L Wrench and Fargo Wrench combination in the south. Maximum clast size data was not available for the norther areas of Block 1 and thus was not contoured and interpreted.

The superimposed sedimentary parameters for the ECT are plotted on top of the ECT bed height below in Figure 60.

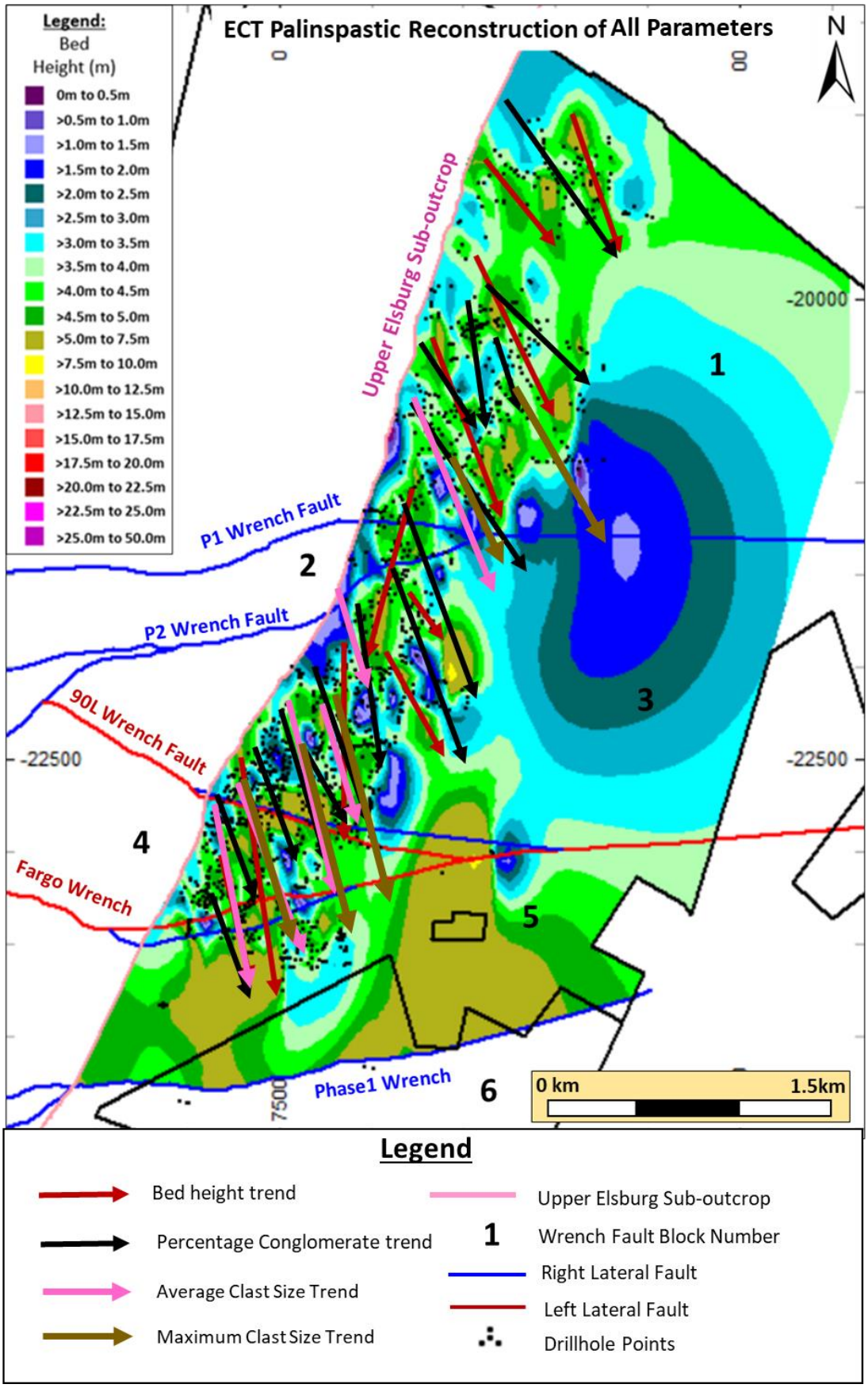


Figure 60: Palinspastic Reconstruction for the ECT – All Parameters

4.2.3.4 ECT Detailed Plots

Figure 61**Error! Reference source not found.** a) depicts the ECT bed height for the southern half of Block 1, Block 2 and the northern portion of Block 3. Bed height trend lines (black dashed lines in Figure 61**Error! Reference source not found.** a) and b)), possibly identifying distinct ECT palaeo-channels, cross over the P1 Wrench, but clearly terminate against the P2 Wrench with an inferred apparent right-lateral dislocation of ±200 m. This dislocation is also apparent in Figure 61**Error! Reference source not found.** b). However, review of the percentage conglomerate plot (Figure 61**Error! Reference source not found.** b)) depicts a definable higher percentage conglomerate zone directly north of the P1 Wrench (purple polygon in Figure 61**Error! Reference source not found.** b)). Termination of the bed height trend on P2 Wrench could infer post-ECT dislocation, or disproportionate erosion due to relative movement of Block 2 prior to ED deposition, while the higher percentage conglomerate highlighted by the purple polygon could possibly relate subtle dislocation on P1 Wrench (possibly throwing down to the north) resulting in conglomerate accumulation north of P1 Wrench.

Figure 62 a) and b) centres on Block 3 for the ECT. The northern margin of Block 3, up against P2 Wrench, is marked by an interpreted continuation of the ECT palaeo-channel identified in Figure 61**Error! Reference source not found.** by a higher bed height and an associated lower percentage conglomerate as identified in Figure 62**Error! Reference source not found.** b) by the yellow circle. The southern margin of Block 2 is characterised by an irregular zone of higher bed height straddling the 90L Wrench (Figure 62**Error! Reference source not found.** a)) highlighted with a yellow ellipse. Similarly, a yellow ellipse along the strike of the 90L Wrench in Figure 62**Error! Reference source not found.** b) highlights alternating nodes of higher and lower percentage conglomerate. Any apparent dislocation across the 90L Wrench is not discernible.

Block 4 (Figure 63**Error! Reference source not found.** a) and b)) highlights (yellow ellipses) zones along the strike of both the 90L Wrench and Fargo Wrench of nodes of alternating higher and lower bed height, and higher and lower percentage conglomerate. Magnitude of possible dislocation across either of the faults is not easily discernible. However, the variable nodes of bed height and percentage conglomerate occurs close to both of the faults. Block 5 shows a distinct increase in bed height, associated with a decrease in percentage conglomerate when compared to Blocks 4 and 3 to the north.

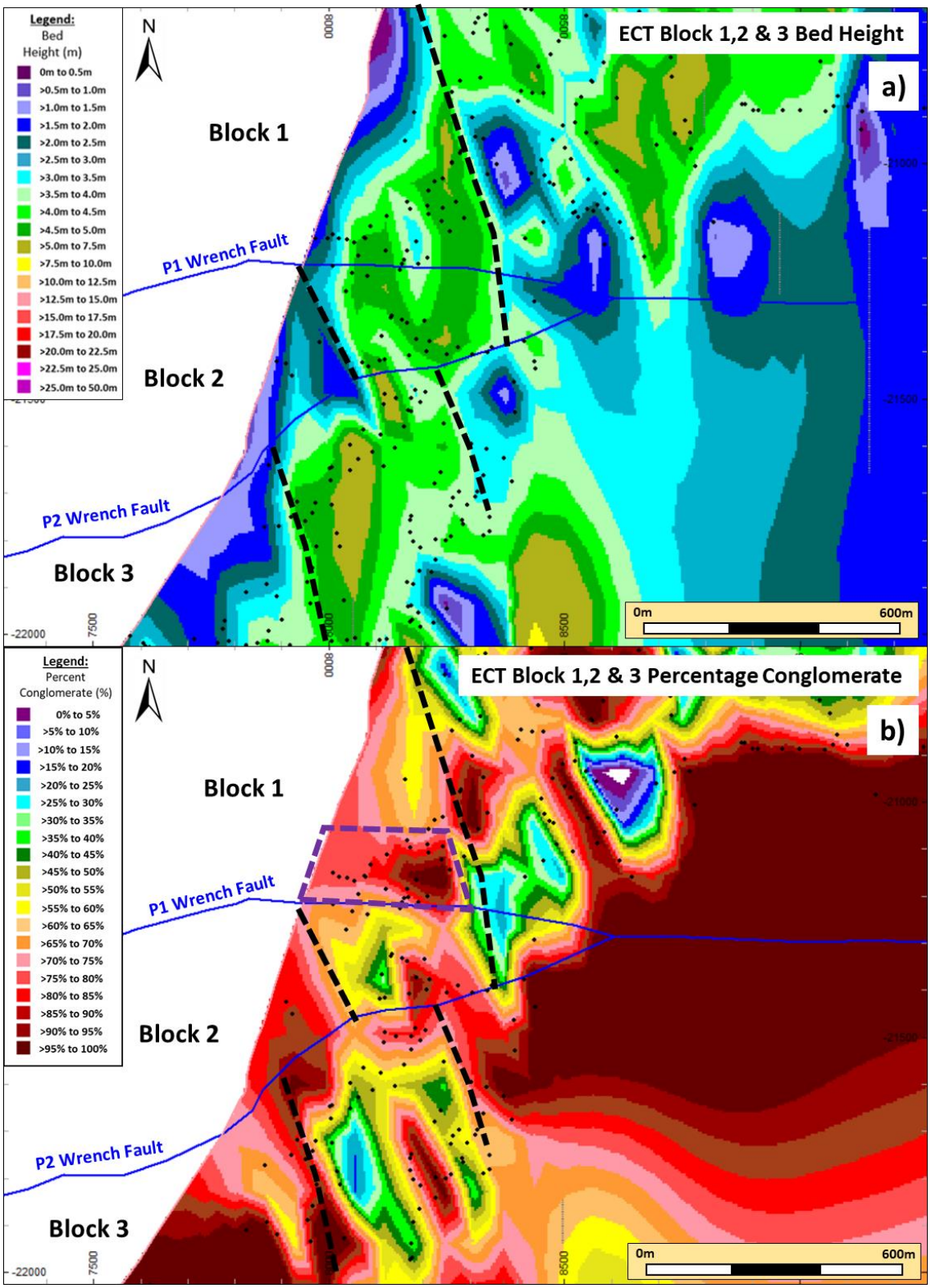


Figure 61: Enlarged Block 2 palinspastic reconstruction for a) bed height for ECT and b) for percentage conglomerate for ECT. Black dashed lines in a) and b) indicated a higher bed height zone offset across P1 Wrench and P2 Wrench. Purple polygon in b) indicates zone of lower bed height with higher percentage conglomerate.

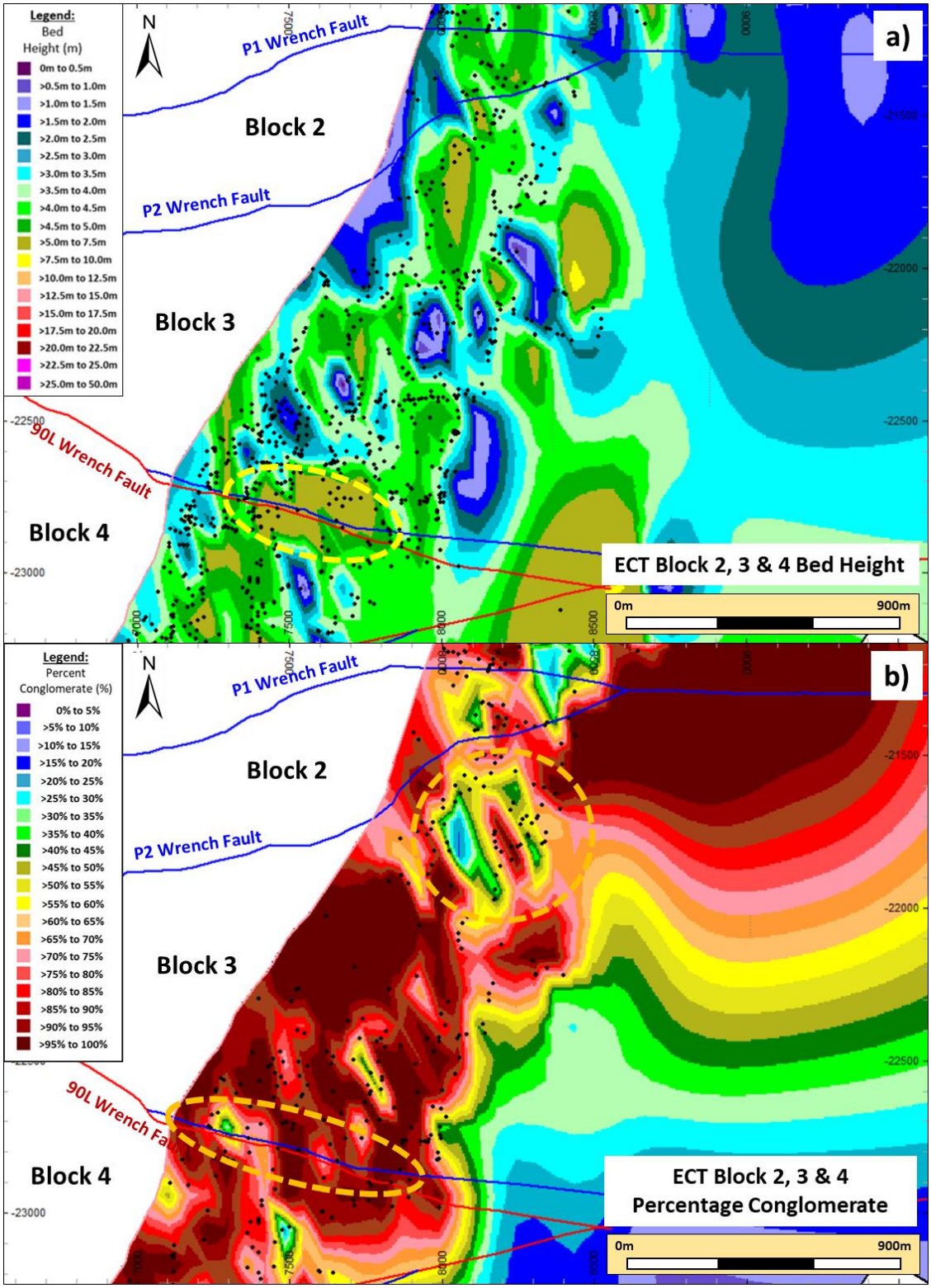


Figure 62: Enlarged Block 3 palinspastic reconstruction for a) bed height for ECT and b) for percentage conglomerate for ECT. Yellow ellipse in a) and b) indicate trends along the strike of P2 Wrench and 90L Wrench of alternating nodes of high and low percentage conglomerate.

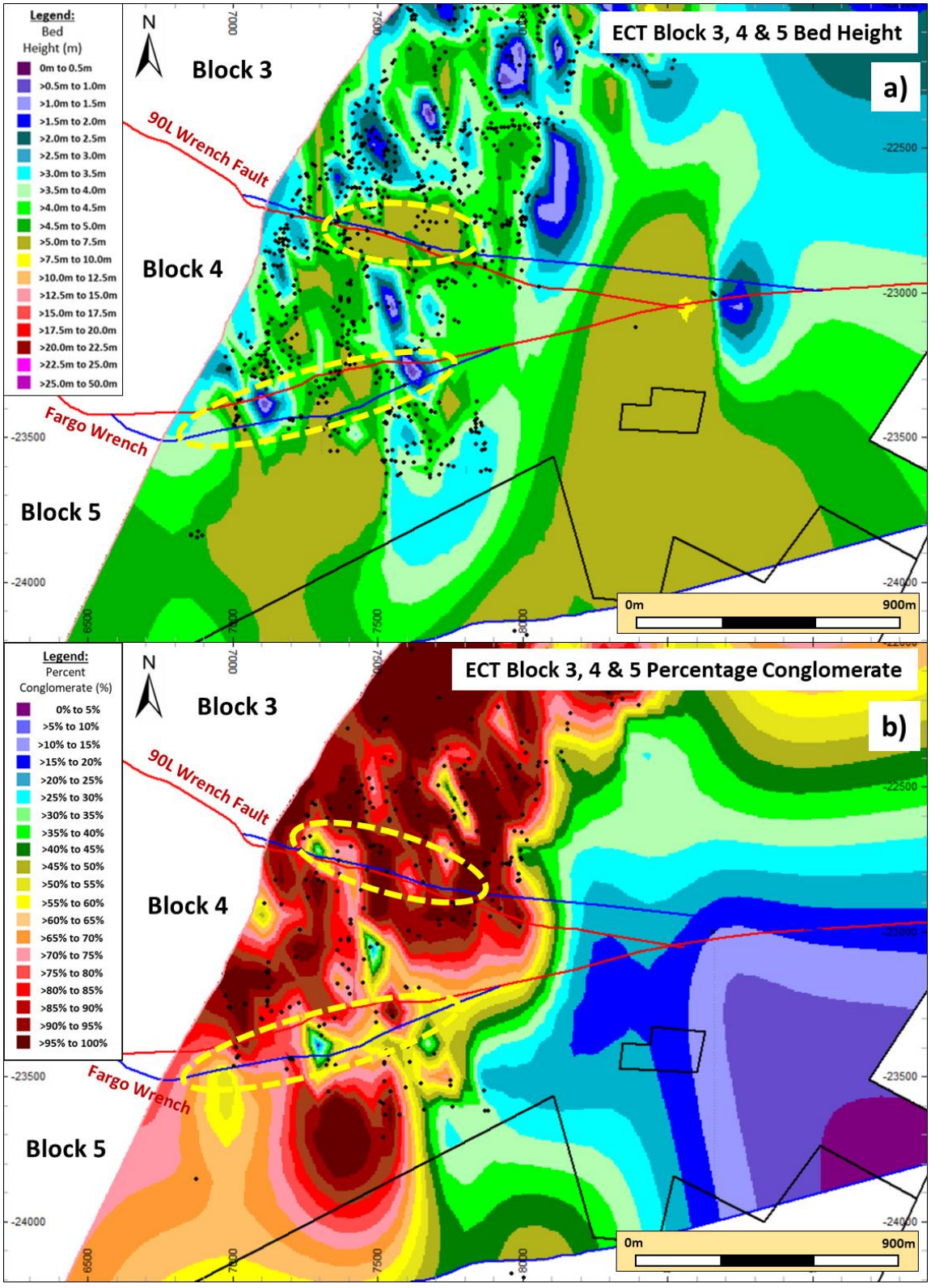


Figure 63: Enlarged Block 4 palinspastic reconstruction for a) bed height for ECT and b) for percentage conglomerate for ECT. Yellow ellipses a) in b) indicate a trend along the strike of 90L Wrench and Fargo Wrench of rapidly alternating nodes of high and low percentage conglomerate and higher and lower bed height.

4.2.4 MAC

4.2.4.1 MAC Bed Height

The palinspastic reconstruction of bed height for the MAC (Figure 141) presents a marked decrease in bed height from north in Block 1 to the Block 5 in the south. The rate of thinning towards the Upper Elsburg sub-outcrop in Block 1 (±4.5 m to 2.5 m) appears less pronounced than that occurring in Blocks 2, 3 and 4 over 1.5 km from sub-outcrop. In Block 3, for example, the rate of thinning towards sub-outcrop over 1 km is from a maximum of ±7.5 m down to 0.5 close into sub-outcrop.

Bed height to the south in Block 5 may exceed 12.5 m in places. Bed height trends are distinctly NNW-SSE across the project area.

4.2.4.2 MAC Percentage Conglomerate

Percentage conglomerate for the MAC generally increases from the north, southwards up to the P1 Wrench and P2 Wrench (Figure 142**Error! Reference source not found.**). Just north of 90L Wrench, a slight decrease in percentage conglomerate is again observed, with another increase in percentage conglomerate occurring in the region of the 90L Wrench and Fargo Wrench.

Lower percentage conglomerate for the MAC generally appears to be associated with greater bed height. Strong NNW-SSE percentage conglomerate trends are nearly aligned with the bed height trends observed in Figure 142.

4.2.4.3 MAC Average and Maximum Clast Size

Average clast size for the MAC (Figure 143**Error! Reference source not found.**) increase markedly from north to south from Block 1 to just north of the 90L Wrench, where average clast size attains a maximum in excess of 84 mm. This larger clast size is seen to dissipate again southward into Block 5 where the relative average clast size is approximately 48 mm to 60 mm. The observable average clast size trends are also oriented NNW-SSE as with the bed height and percentage conglomerate. However, the clast size trends do not appear to cross over the 90L Wrench and Fargo Wrench combination.

The MAC maximum clast size (Figure 144**Error! Reference source not found.**) presents a similar pattern of generally increasing from north to south across the project area. Where the maximum average clast size for the MAC is found directly north of the 90L Wrench, maximum clast size (>96 mm to 120 mm) is found directly in Block 4. The main maximum clast size trend for the MAC is NNW-SSE with a subsidiary NW-SE trend possibly identifiable in Block 3.

A combined plot of the four sedimentary parameters for the MAC superimposed over MAC bed height is presented below in Figure 64.

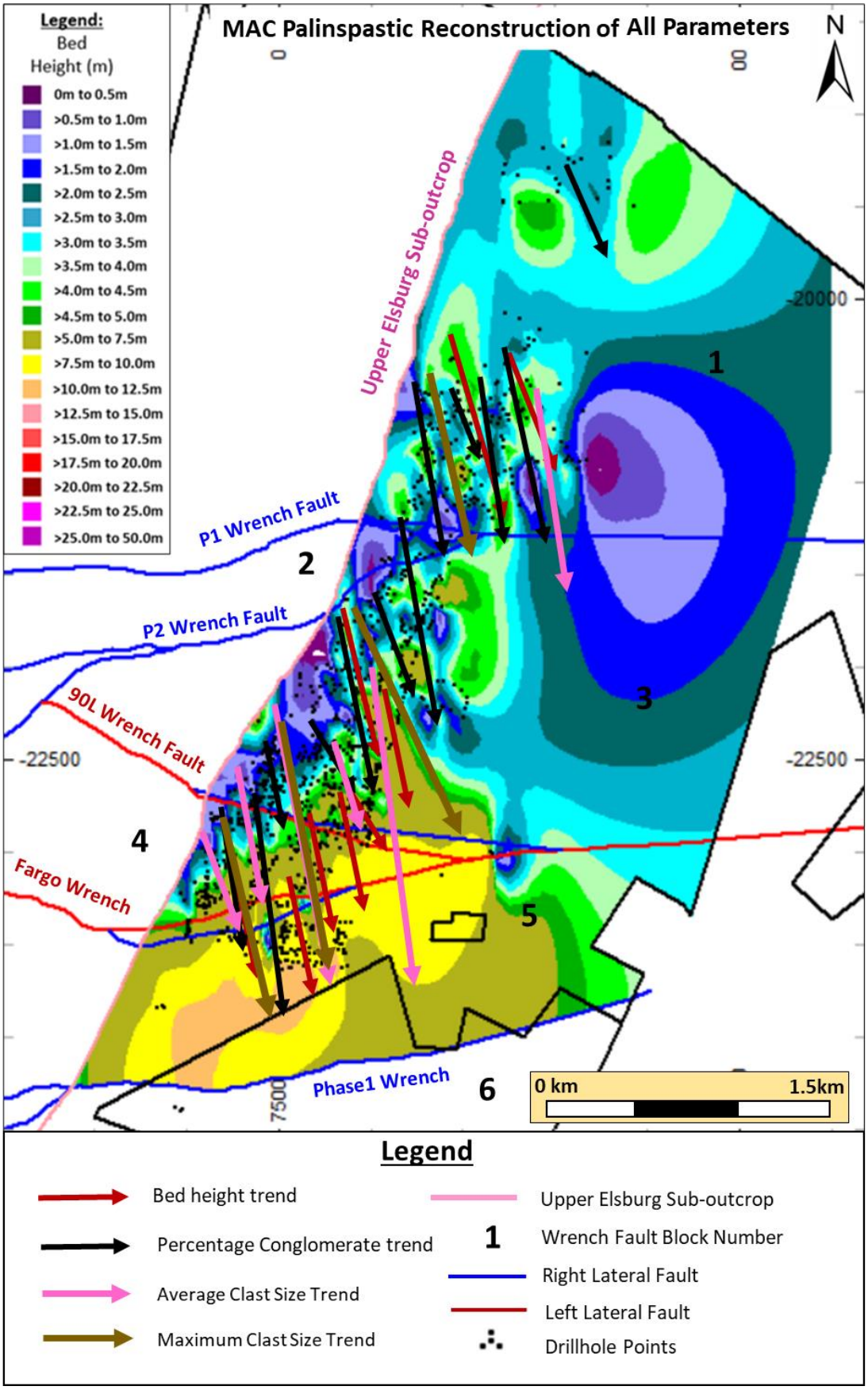


Figure 64: Palinspastic Reconstruction for the MAC – All Parameters

4.2.4.4 MAC Detailed Plots

The enlargement over Block 2 for the MAC (Figure 65**Error! Reference source not found.** a) and b)) presents a distinct lower bed height over Block 2 that over the adjacent Blocks 1 and 3. However, no easily identifiable lateral dislocation across the P1 Wrench and P2 Wrench combination is visible. In addition, the percent conglomerate in Block 2 appears slightly greater than that in the two adjacent blocks. This could potentially imply that Block 2 was moving vertically upward relative to the adjacent blocks during deposition of the MAC resulting in some winnowing over Block 2. The strong NNW-SSE trend is very visible in both Blocks 1 and 3 for both bed height and percentage conglomerate. A set of alternating high and low bed height and percentage conglomerate nodes are located adjacent to, or just south of P2 Wrench, and could possibly support interpretation of some syn-sedimentary structural influence.

The alternating high and low bed height and percentage conglomerate nodes located in the north of Block 3 are clearly visible in Figure 66**Error! Reference source not found.** a) and b) and are highlighted with yellow circles and ellipses. As one progresses southwards in Block 3, the rate of thinning towards sub-outcrop is also seen to increase. The distinctive higher bed height trend (highlighted with a black arrow) appears associated with a correspondingly higher percentage conglomerate trend in Block 3. West of the high percentage conglomerate channel, percentage conglomerate is seen to decrease in Figure 66**Error! Reference source not found.** b) to within close proximity to the 90L Wrench correspondingly with increased bed height. Nodes of variable percentage conglomerate and bed height are seen to trend along or adjacent to the trace of the 90L Wrench in Figure 66**Error! Reference source not found.** a) and b), possibly indicating some syn-sedimentary influence on MAC sedimentation by this structure.

Figure 67**Error! Reference source not found.** a) and b) present the bed height and percentage conglomerate, respectively, for the MAC in Block 4. A distinct increase in percentage conglomerate from Block 3 to Block 4 is observed, with the set of lower percent conglomerate nodes occurring directly north of 90L Wrench (highlighted with yellow ellipse in Figure 67**Error! Reference source not found.** b)). A similar lower percent conglomerate node occurs to the south of Block 4 (highlighted with a red ellipse). These variable zones oriented along- or adjacent to the 90L Wrench and Fargo Wrench could possibly support syn-sedimentary activity on these structures during MAC deposition, with preferential winnowing possibly taking place over Block 4. The magnitude of potential dislocation is not possible to determine, due to the erosion of the MAC by the overlying MAD and MIB. In Block 4 in Figure 67**Error! Reference source not found.** a), a distinct change increase in bed height is seen from Block 4 to Block 5 (lower bed height for Block 4 indicated by red polygon). This could potentially infer a possible relative downward movement of Block 5 relative to Block 4; however, magnitude of dislocation is not possible due to possible erosion by the overlying MAD and MIB beds.

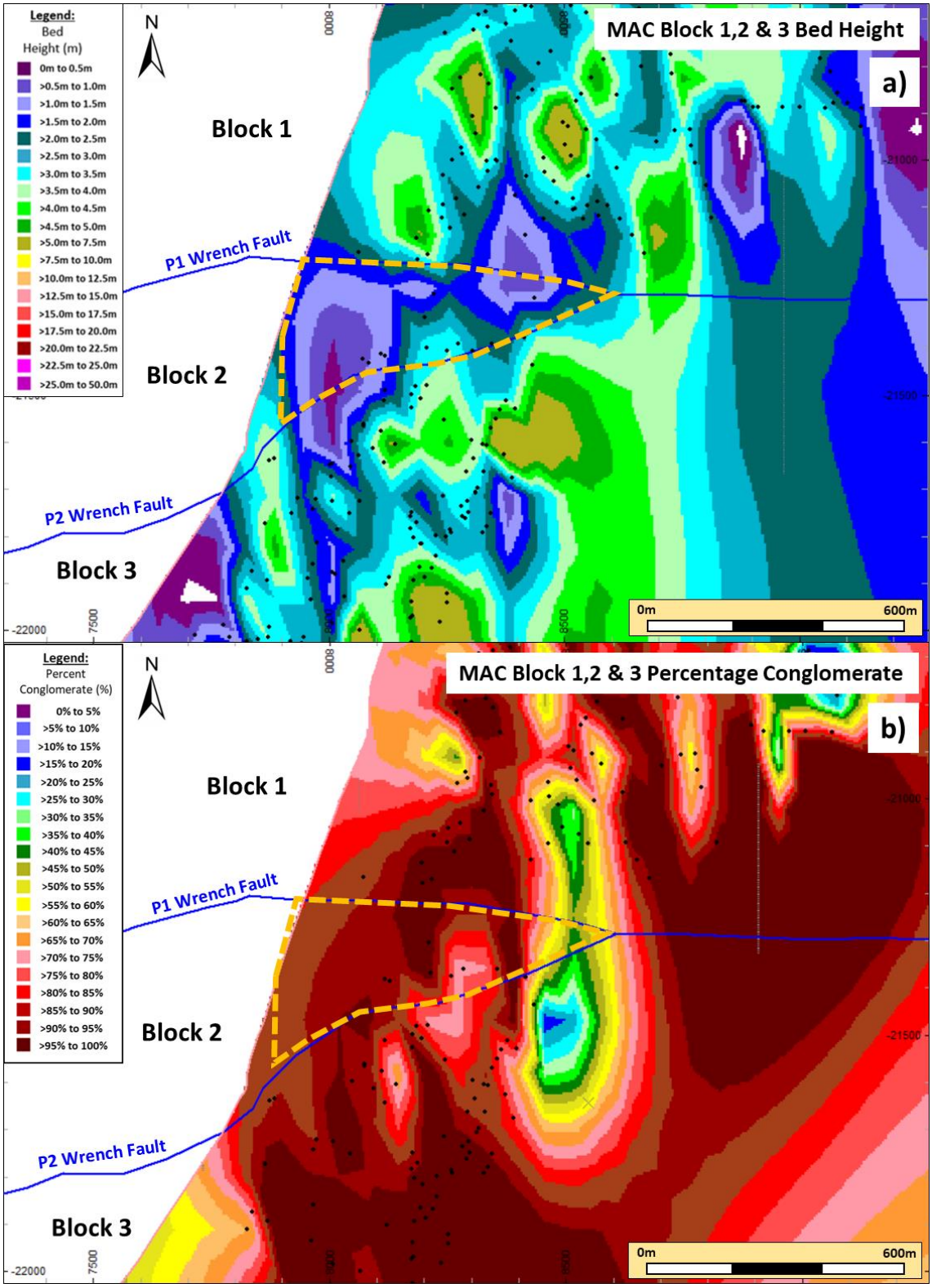


Figure 65: Enlarged Block 2 palinspastic reconstruction for a) bed height for MAC and b) for percentage conglomerate for MAC.

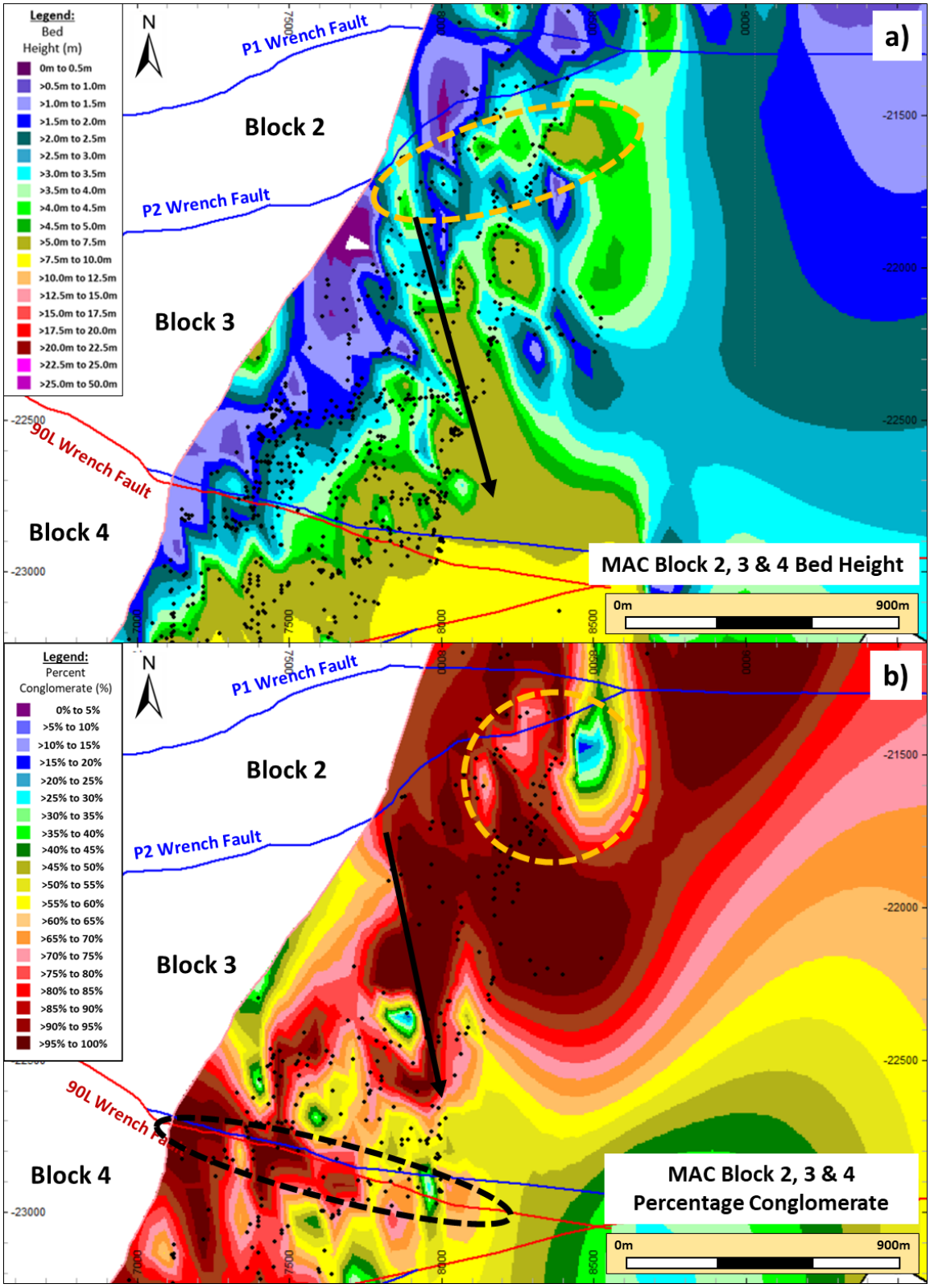


Figure 66: Enlarged Block 3 palinspastic reconstruction for a) bed height for MAC and b) for percentage conglomerate for MAC.

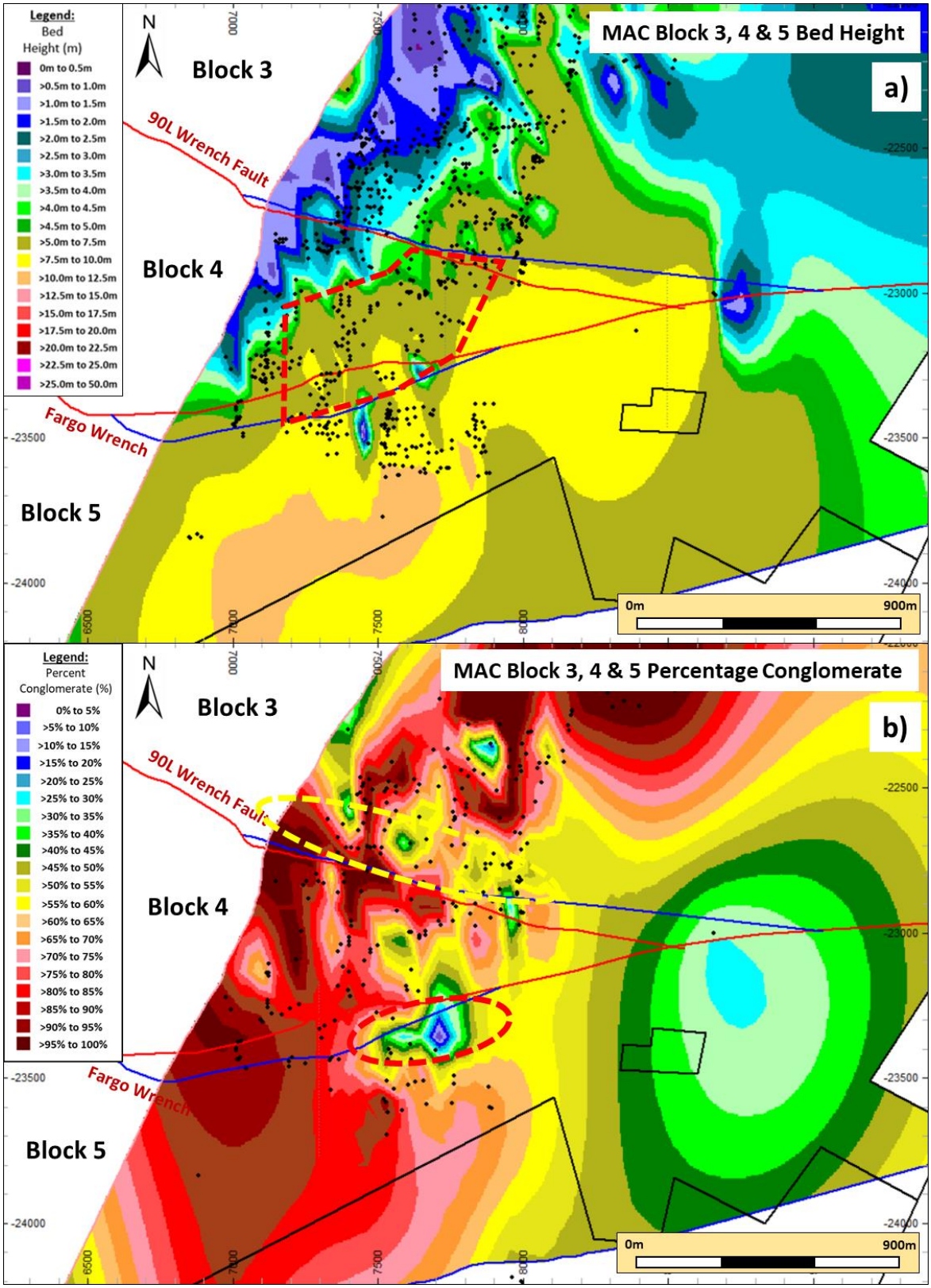


Figure 67: Enlarged Block 4 palinspastic reconstruction for a) bed height for MAC and b) for percentage conglomerate for MAC.

4.2.5 MBB

4.2.5.1 MBB Bed Height

The MBB bed height plot (Figure 177**Error! Reference source not found.**) presents a lower rate of thinning towards the west in the northern half of Block 1. This rate of westward thinning increases southwards towards and over the P1 Wrench and P2 Wrench combination and into Block 3, where a zone of significant thinning in the northern half of Block 3 is evident (<4.5 m). Bed height increaseincreases again in the southern half of Block 3.

Bed height increases significantly across 90L Wrench over Block 4 with little subsequent change towards the south across Fargo Wrench. Block 4 also exhibits a lower rate of attenuation than in Block 3 to the north. Bed height for the MBB is significantly increased in the south whereas the bed height for the MIQ is significantly reduced over the same area (Figure 169**Error! Reference source not found.**). Bed trends within the MBB appear to exhibit a global NNW to -SSE trend.

4.2.5.2 MBB Percentage Conglomerate

Percentage conglomerate generally increases across the project area towards the Upper Elsburg sub-outcrop within the MBB (Figure 178**Error! Reference source not found.**). In the northern part of Block 1, percentage conglomerate is relatively low (±55% to 60%). This increases in the southern half of Block 1 towards P1 Wrench. Across the P1 Wrench and P2 Wrench combination percentage conglomerate decreases significantly as little as 15% to 20%. Further in Block 3 and across Blocks 4 and 5, percentage conglomerate increases significantly to >90%. Percentage conglomerate trends agree with the NNW to -SSE trends observed for MBB Bedbed height (Figure 177**Error! Reference source not found.**).

4.2.5.3 MBB Average and Maximum Clast Size

In general, average clast size for the MBB (Figure 179**Error! Reference source not found.**) increases towards the south. In the north, average clast size is low (>12 mm to 24 mm). Average clast size increases slightly as the P1 Wrench and P2 Wrench combination is approached. A low local average clast size is located close to P2 Wrench. The northern half of Block 3 presents a small average clast size, which increases towards the south as the 90L Wrench is approached. Average clast size is approximately >24 mm to 60 mm in a wide zone straddling the 90L Wrench and Fargo Wrench combination. Average clast size trends are identifiable in the south and cross NNW to -SSE over the 90L Wrench and Fargo WrenchesWrench. Very low data variability within Block 1 precludes average clast size trend interpretation.

Maximum clast size (Figure 180**Error! Reference source not found.**) for the MBB present low data density in the northern half of Block 1 and precludes description and interpretation within this area. Maximum clast increases slightly as the P1 Wrench and P2 Wrench combination are approached from the north. The northern half of Block 3 presents low clast size, which quickly increases towards the south as the 90L Wrench is approached, where

maximum clast size may attain >96 mm to 120mm120 mm over the 90L Wrench and Fargo Wrench combination. Maximum clast size trends are NNW-SSE in all Blocksblocks.

A plot of the combined parameters for the MBB superimposed on bed height is presented below in Figure 68.

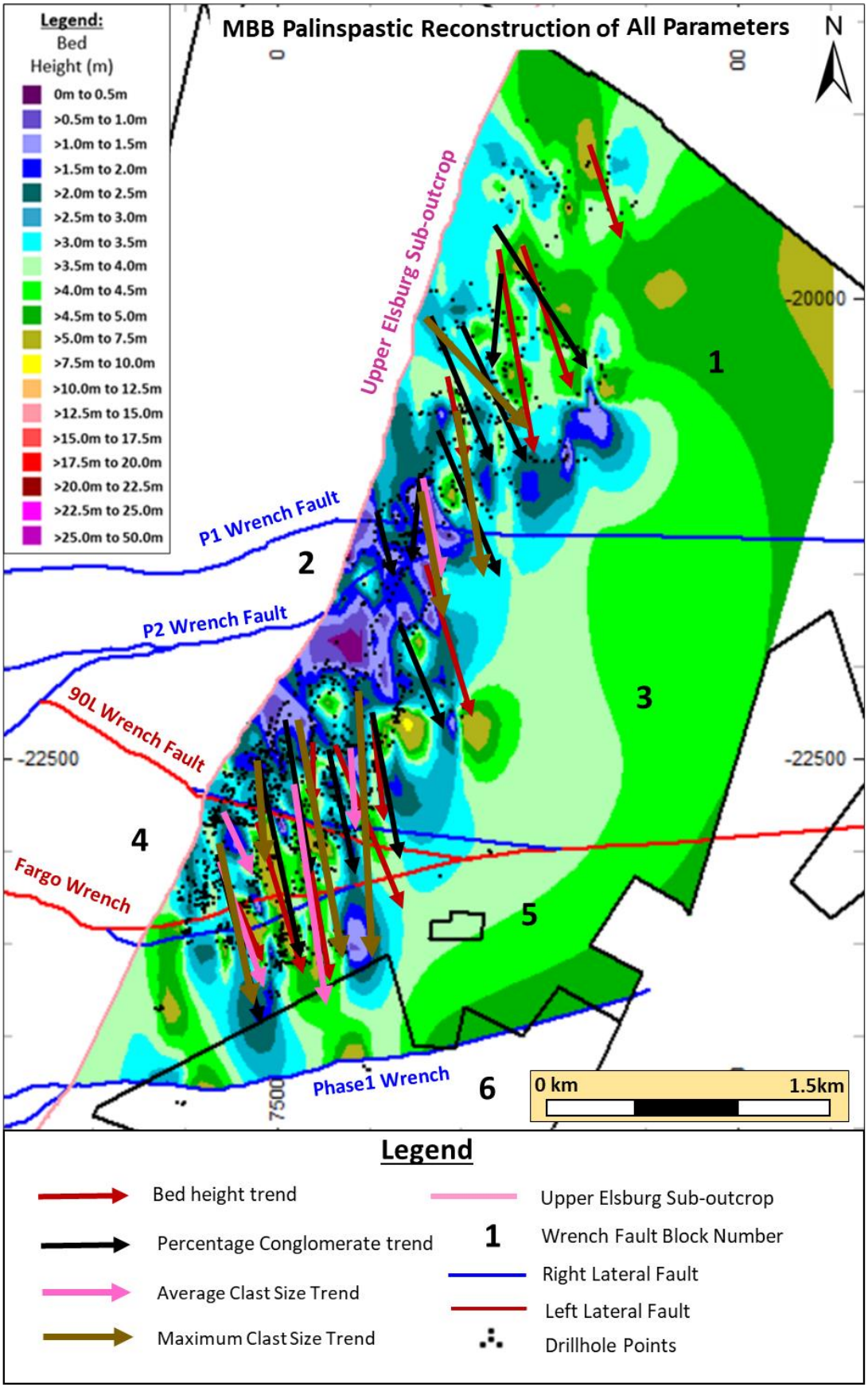


Figure 68: Palinspastic Reconstruction for the MBB – All Parameters

4.2.5.4 MBB Detailed Plots

Figure 69**Error! Reference source not found.** a) and b) presentspresent enlargements of Block 2 for MBB for bed height (Figure 69 **Error! Reference source not found.**a)) and percentage conglomerate Figure 69 **Error! Reference source not found.Error! Reference source not found.**b), respectively. A possible apparent right-lateral dislocation across the P1 Wrench and P2 Wrench combination of ±150 m (based on a transition from lower to higher bed height) may be inferred. Block 2 presents a lower bed height associated with a correspondingly higher percentage conglomerate. This could infer a relative uplift of Block 2 relative to Blocks 1 and 3 which could infer a localised winnow zone (highlighted by yellow polygon). Interpretation of this apparent dislocation is however not supported by the percentage conglomerate data presented in Figure 69**Error! Reference source not found.** b).

Bed height in the northern half of Block 3 (Figure 70**Error! Reference source not found.** a)) is low, but is however associated with a zone of reduced percentage conglomerate abutting P2 Wrench in Figure 70**Error! Reference source not found.** b). Bed height gradually increases southwards in Block 3 as the 90L Wrench is approached. An apparent right-lateral dislocation of ±200 m may be interpreted utilising the western margin of the increased bed height (Blackblack dashed line) in Figure 70**Error! Reference source not found.** a).)). Zones of higher and lower bed height abutting on 90Lwrench (yellow ellipse in Figure 70**Error! Reference source not found.** a)) support interpretation of possible post-sedimentary movement. However, nodes of variable bed height and percentage conglomerate along 90L Wrench may infer some syn-sedimentary influence across the fault.

An enlargement of Block 4 for bed height and percentage conglomerate for the MBB are presented in Figure 71a) and b)), respectively. As described for Figure 70**Error! Reference source not found.** a)), an apparent right-lateral dislocation of ±200 across 90L Wrench may be interpreted. Similarly, a relative right-lateral dislocation of bed height of ±150 m may be inferred across Fargo Wrench in the south. The abrupt change to a zone of lower percentage conglomerate directly to the south of Fargo Wrench would support a dislocation across the fault. These dislocations are apparent and could be equally explained by relative vertical movements of the structures down towards the south post-dating MBB deposition. However, the variable nodes of bed height and percentage conglomerate along the strike and adjacent to the faults could also infer some syn-sedimentary influence by these structures, though this influence is not easily defined.

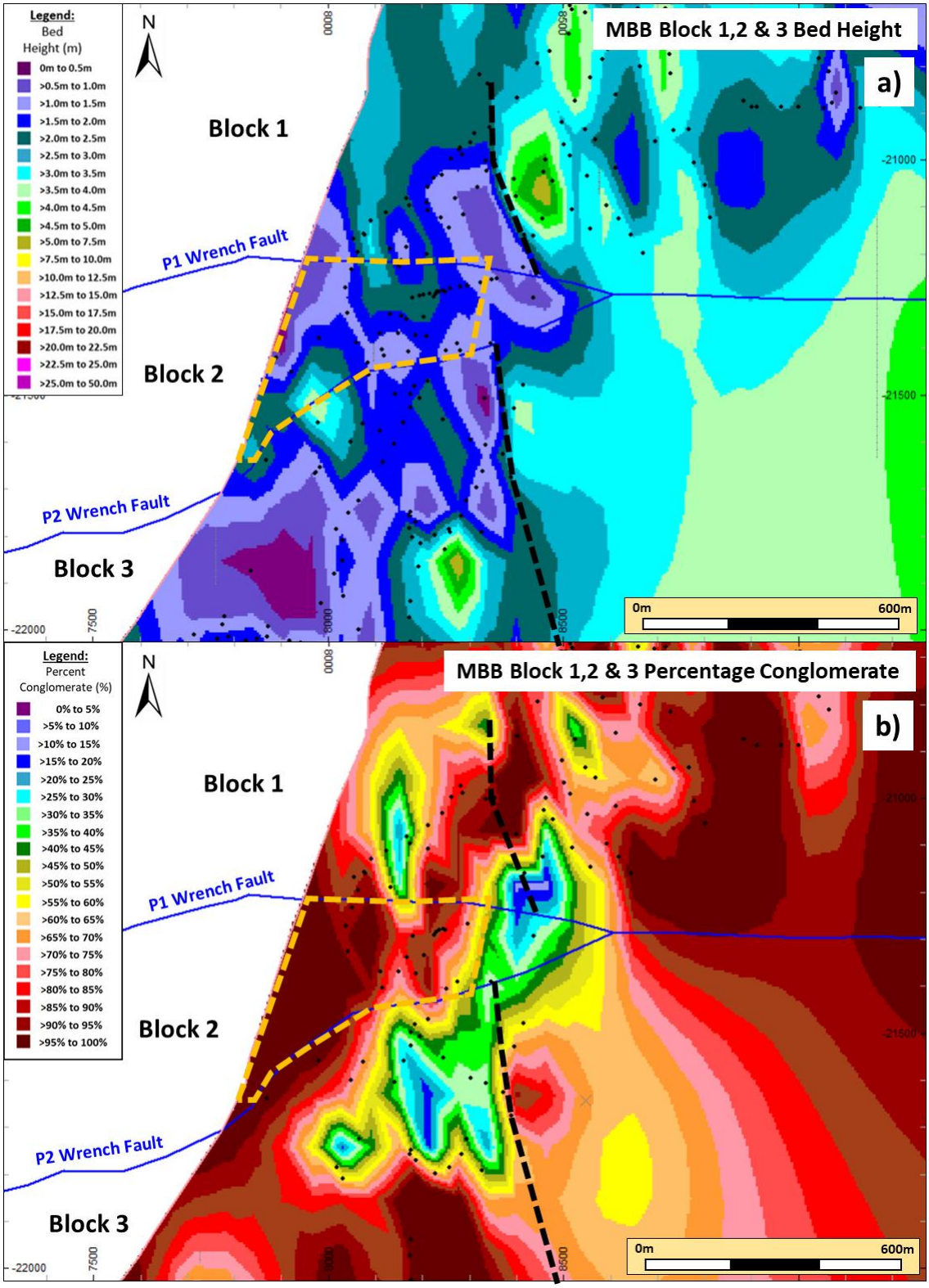


Figure 69: Enlarged Block 2 palinspastic reconstruction for a) bed height for MBB and b) for percentage conglomerate for MBB.

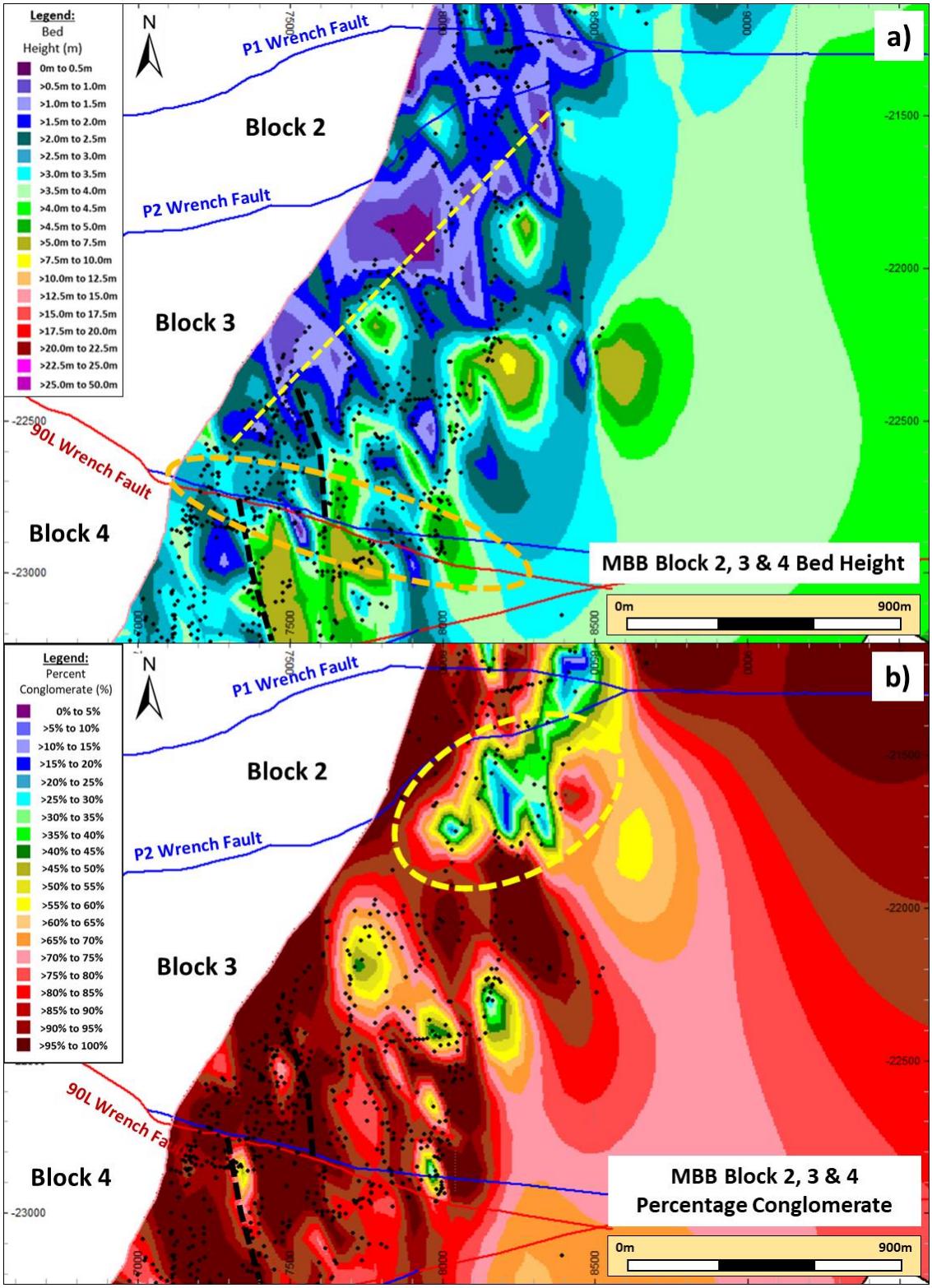


Figure 70: Enlarged Block 3 palinspastic reconstruction for a) bed height for MBB and b) for percentage conglomerate for MBB.

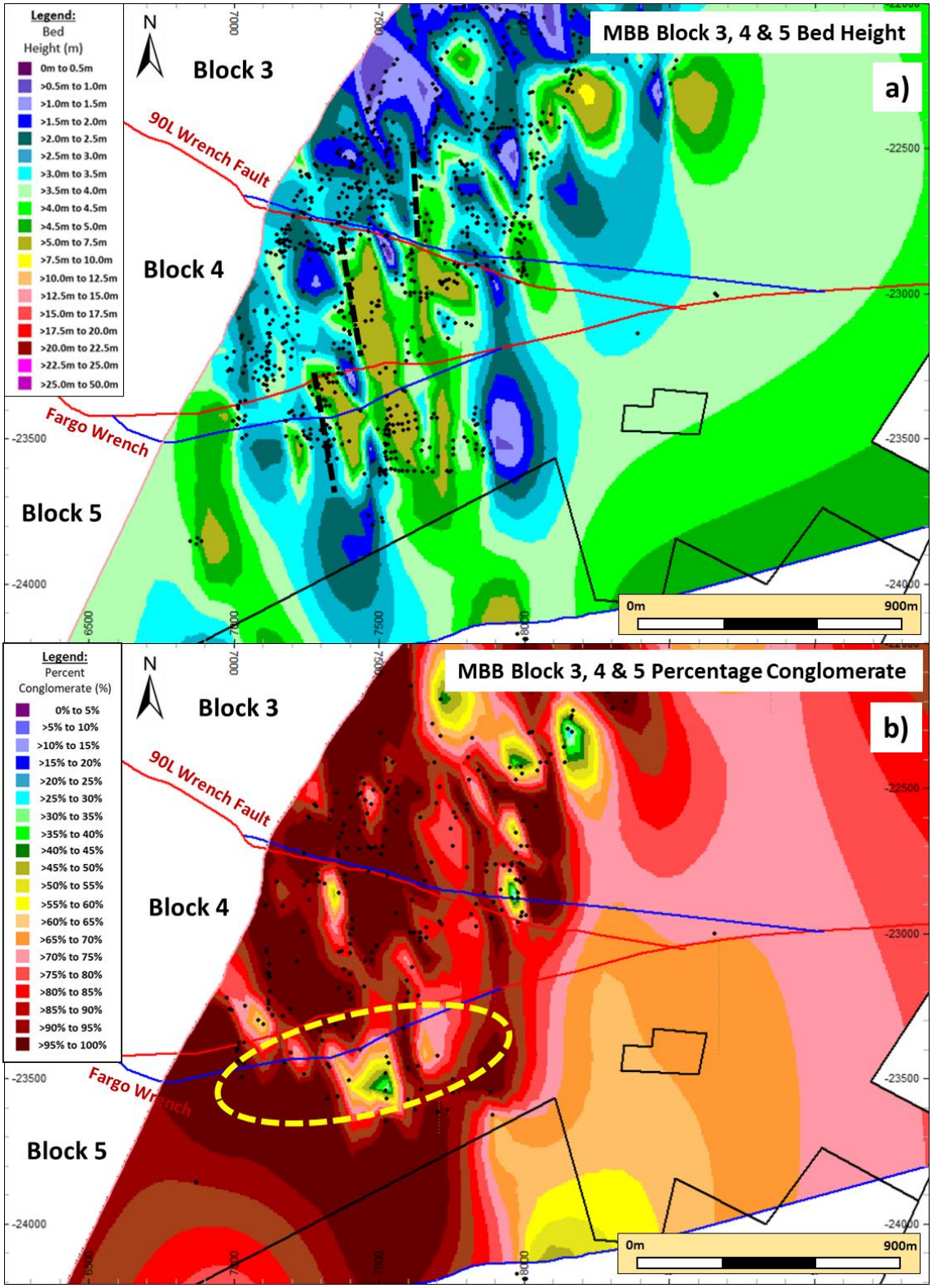


Figure 71: Enlarged Block 4 palinspastic reconstruction for a) bed height for MBB and b) for percentage conglomerate for MBB.

4.2.6 MBT

4.2.6.1 MBT Bed Height

Palinspastic reconstruction of bed height (Figure 181**Error! Reference source not found.**) for the MBT presents a rate of slower attenuation westwards towards the sub-outcrop in the northern half of Block 1, where bed height seldom exceeds 12.5 m. As the P1 Wrench and P2 Wrench combination in the south is approached, the rate of attenuation towards the west increases with extended bed height ranges from a maximum bed height of ± >22 m to 25 m to 0 m near the sub-outcrop. This rate of rapid westward attenuation continues southward along the sub-outcrop right down into Block 4. In general, bed height increases southward towards the 90L Wrench where a reduction in bed height momentarily decreases over 90L Wrench and again increase southwards across Fargo Wrench into Block 5. Bed height trends appear to be oriented NNW-SSE within Blocks 1 to 3, while within Blocks 4 and 5 bed height changes slightly to a possible N-S trend.

4.2.6.2 MBT Percentage Conglomerate

Palinspastic reconstruction of MBT percentage conglomerate (Figure 182) presents a marked decrease in percentage conglomerate towards the south. The northern half of Block 1 is characterised by higher general percentage conglomerate over the zone of lower bed height (Figure 181).

As the MBT bed height increases towards the P1 Wrench and P2 Wrench combination, percentage conglomerate decreases. This decreased percentage conglomerate decrease further still in the southern half of Block 3 as the 90L Wrench is approached from the north. A slight increase in percentage conglomerate occurs (related to the lower bed height) over Blocks 4 and 5 in south. NWW-SSE trends in percentage conglomerate may be identified across the project area within all structural blocks.

4.2.6.3 MBT Average and Maximum Clast Size

Average clast size in the MBT (Figure 183) decreases steadily towards the south in line with the reduced percentage conglomerate (Figure 182). However, zones of higher average clast size (>24 mm to 36 mm) appear to straddle the P1 Wrench towards the juncture of the P1 Wrench and P2 Wrench. Lowest average clast sizes occur over the southern half of Block 3 and over Block 4 in the south. Average clast size trends appear to be aligned NNW-SSE. Maximum MBT clast size (Figure 184) (similar to average clast size) generally decreases southwards into Block 3. Higher bed height and lower percentage conglomerate over this area and into Blocks 4 and 5 result in a lower data density for maximum clast size. However, maximum clast size occurs in Block 5 in the south with a maximum clast size of between >60 mm and 84 mm. Maximum clast size trends for the MBT globally trend NNW-SSE are similar in orientation to average clast size, bed height as well as percentage conglomerate trends. A combined plot of all parameters overlain on bed height for the MBT is presented in Figure 72 and generally shows similar trends for all four parameters.

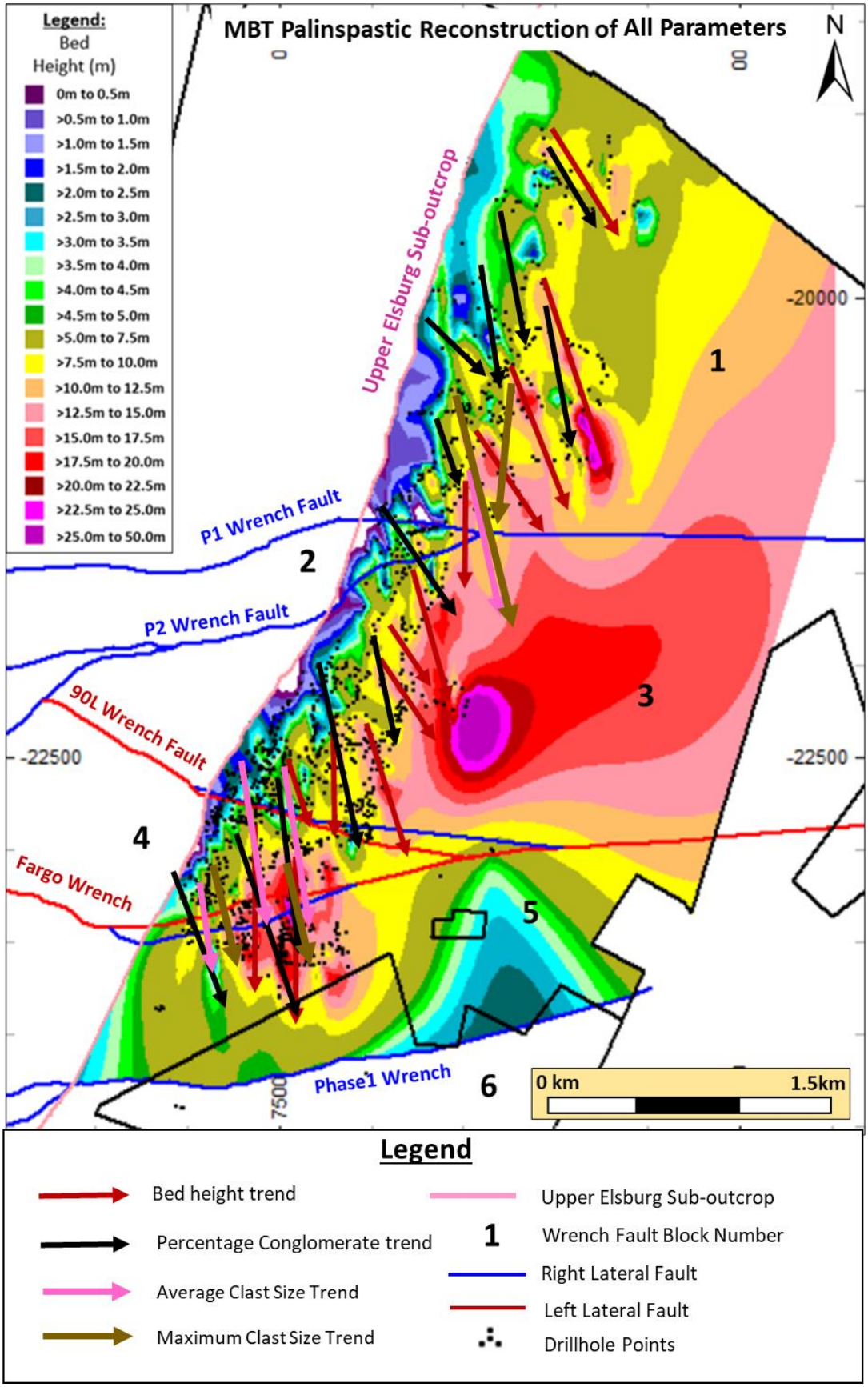


Figure 72: Palinspastic Reconstruction for the MBT – All Parameters

4.2.6.4 MBT Detailed Plots

Bed height data for the MBT over enlarged Block 2 area (Figure 73**Error! Reference source not found.** a)) presents apparent right-lateral dislocations of higher bed height across the P1 Wrench and P2 Wrench of ±300 m and ±200 m, respectively. These dislocations are apparent and could possibly also be related to relative vertical displacements down towards the south. Corresponding percentage conglomerate plot in Figure 73 b) could support dislocation, due to the higher percentage conglomerate zones abutting and terminating against the P2 Wrench.

Figure 74 a) presents the high rate of westward attenuation evident in Block 3. With some elimination of the MBT close into sub-outcrop in the northern half of Block 3. Nodes of both lower bed height and highly variable percentage conglomerate along the strike of 90L Wrench could possibly indicate some syn-sedimentary structural influence during MBT deposition.

The variable nodes of bed height and percentage conglomerate along the strike of 90L Wrench are highlighted by the red ellipse in Figure 75 a) and b). A possible relative right-lateral dislocation of bed height may be interpreted across the 90L Wrench. A possible relative right-lateral dislocation of bed height across Fargo Wrench of ±300 m may also be inferred. The nature and magnitude of these dislocations are not definable, but the variable nodes of bed height and percentage conglomerate along strike and adjacent to these structures could potentially infer some syn-sedimentary influence by these structures on the MBT.

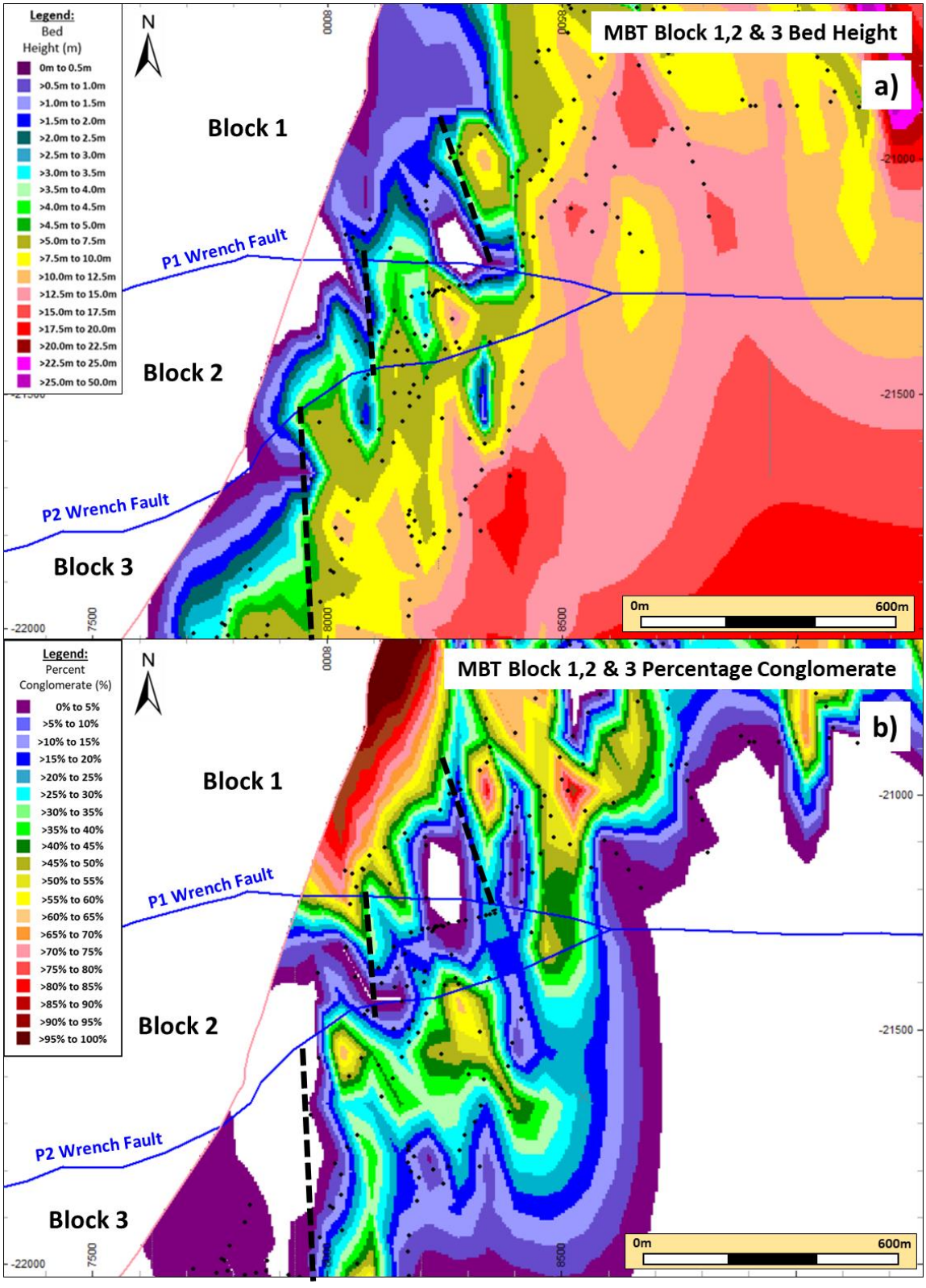


Figure 73: Enlarged Block 2 palinspastic reconstruction for a) bed height for MBT and b) for percentage conglomerate for MBT.

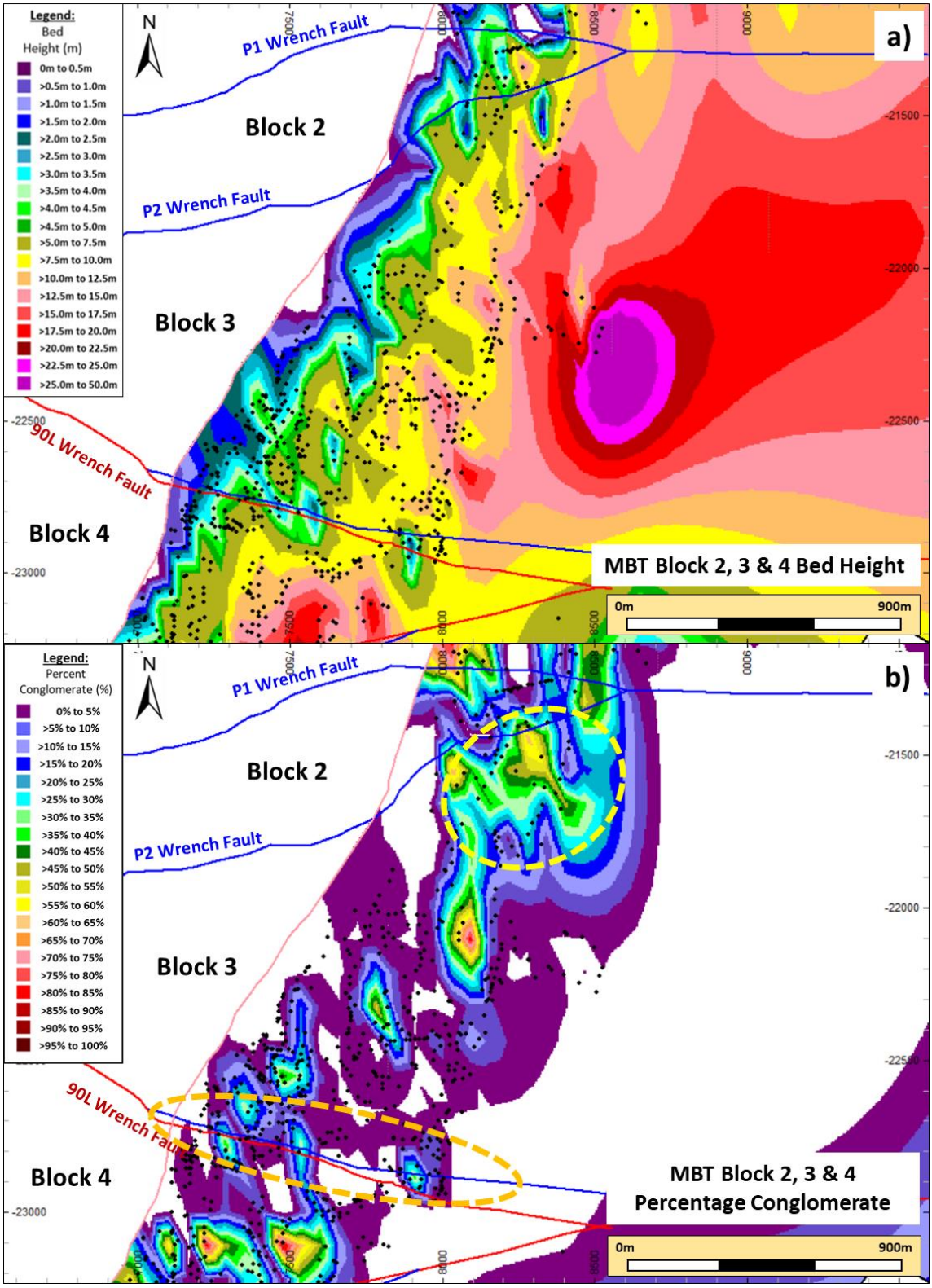


Figure 74: Enlarged Block 3 palinspastic reconstruction for a) bed height for MBT and b) for percentage conglomerate for MBT.

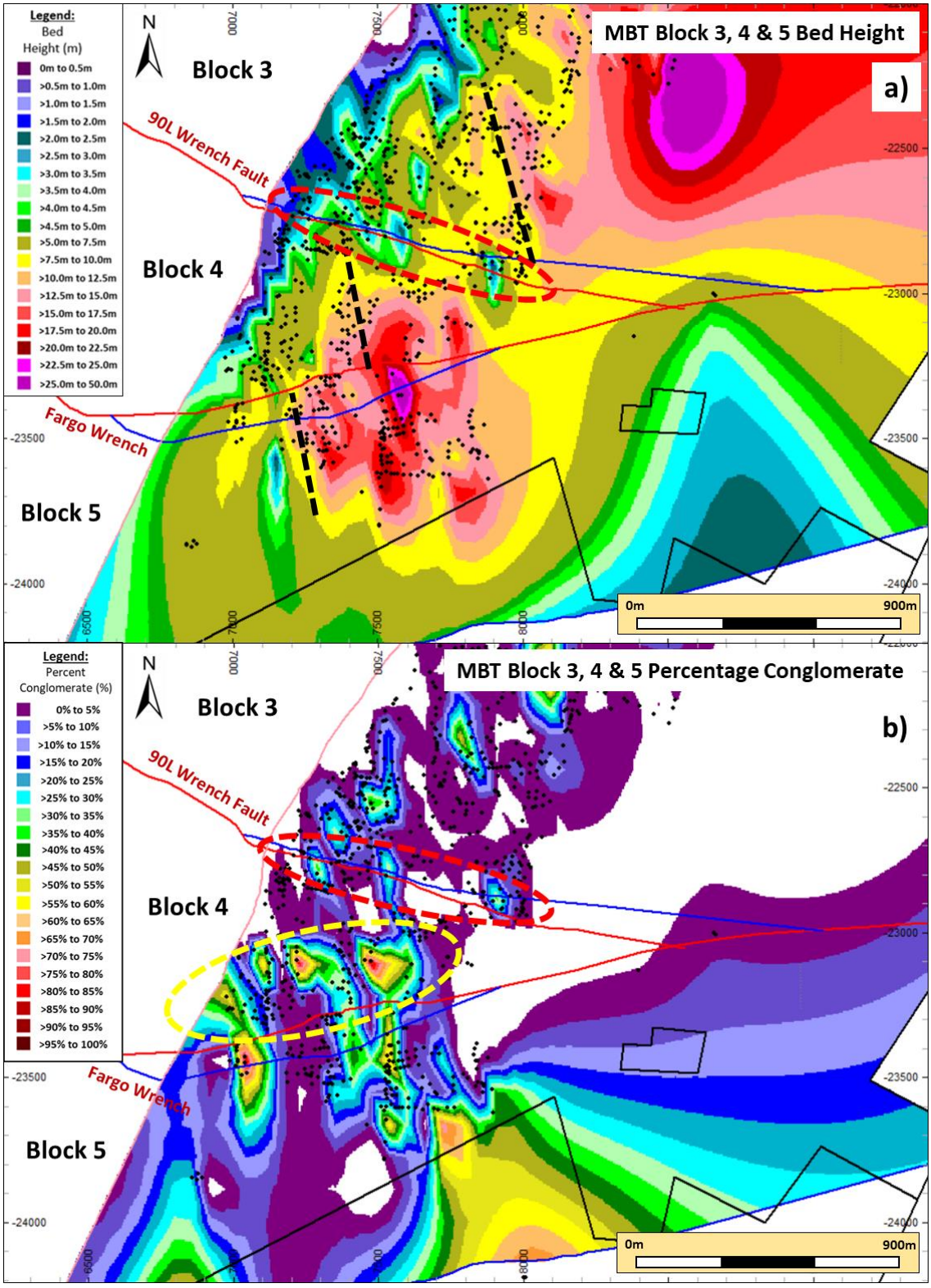


Figure 75: Enlarged Block 4 palinspastic reconstruction for a) bed height for MBT and b) for percentage conglomerate for MBT.

4.3 Consolidated Results Summaries

Due to the volume of data collected and processed as well as the number of beds investigated, the observations for each of the beds are summarised in consolidate results summaries for all the beds in Table 3, Table 4, Table 5 and Table 6 in this section. Where trends were not discernible on a per bed and structure block basis, "ND" was indicated. Table 7 presents a summary of the trends observed per bed and structure

Table 3: Summary table for bed height trends per structure block and bed.

		Bed Height Trends					
Bed	**Primary Lithology**	**Block 1**	**Block 2**	**Block 3**	**Block 4**	**Block 5**	**West of Sub-outcrop**
VCR	**Conglomerate**	NNW-SSE	ND	NNW-SSE	NNW-SSE	NNW-SSE	NW-SE
MBT	**Quartzite/Conglomerate Mix**	NNW-SSE	ND	NNW-SSE	NNW-SSE	N-S	n/a
MBB	**Conglomerate**	NNW-SSE	ND	NNW-SSE	NNW-SSE	NNW-SSE	n/a
MIQ	**Quartzite/Conglomerate Mix**	NW-SE	ND	NNW-SSE	NNW-SSE	NNW-SSE	n/a
MIT	**Conglomerate**	NNW-SSE	ND	NNW-SSE	NNW-SSE	NNW-SSE	n/a
MIB	**Quartzite/Conglomerate Mix**	NW-SE	ND	NNW-SSE	NNW-SSE	NNW-SSE	n/a
MAD	**Quartzite**	NNW-SSE	ND	NNW-SSE	NNW-SSE	NNW-SSE	n/a
MAC	**Conglomerate**	NNW-SSE	ND	NNW-SSE	NNW-SSE	NNW-SSE	n/a
ED	**Quartzite**	NNW-SSE	ND	NNW-SSE	NNW-SSE	NNW-SSE	n/a
ECT	**Conglomerate**	NW-SE	ND	NW-SE	NNW-SSE	NNW-SSE	n/a
ECMQ	**Quartzite**	NNW-SSE	ND	NNW-SSE	NNW-SSE	NNW-SSE	n/a
ECMC	**Conglomerate**	NW-SE	ND	NNW-SSE	NNW-SSE	NNW-SSE	n/a
ECBQ	**Quartzite/Conglomerate Mix**	NNW-SSE	ND	NNW-SSE	NNW-SSE	NNW-SSE	n/a
ECB	**Conglomerate**	NW-SE	ND	NNW-SSE	NNW-SSE	NNW-SSE	n/a
ECBAQ	**Quartzite**	NNW-SSE	ND	NNW-SSE	ND	NNW-SSE	n/a
ECBA	**Conglomerate/Quartzite Mix**	NNW-SSE	ND	N-S	ND	NNW-SSE	n/a

The summary table for percentage conglomerate trends is presented in **Error! Reference source not found.**.

Table 4: Summary table for percentage conglomerate trends per structure block and bed.

		Percentage Conglomerate Trends					
Bed	**Primary Lithology**	**Block 1**	**Block 2**	**Block 3**	**Block 4**	**Block 5**	**West of Sub-outcrop**
VCR	**Conglomerate**	NNW-SSE	ND	NNW-SSE	NNW-SSE	NNW-SSE	n/a
MBT	**Quartzite/Conglomerate Mix**	NNW-SSE	ND	NNW-SSE	NNW-SSE	NNW-SSE	n/a
MBB	**Conglomerate**	NNW-SSE	ND	NNW-SSE	NNW-SSE	NNW-SSE	n/a
MIQ	**Quartzite/Conglomerate Mix**	NNW-SSE	ND	NNW-SSE	NNW-SSE	NNW-SSE	n/a
MIT	**Conglomerate**	NNW-SSE	ND	NNW-SSE	NNW-SSE	NNW-SSE	n/a
MIB	**Quartzite/Conglomerate Mix**	NW-SE	ND	NNW-SSE	NNW-SSE	NNW-SSE	n/a
MAD	**Quartzite**	NW-SE	ND	NNW-SSE	NNW-SSE	NNW-SSE	n/a
MAC	**Conglomerate**	NNW-SSE	ND	NNW-SSE	NNW-SSE	NNW-SSE	n/a
ED	**Quartzite**	NW-SE	NNW-SSE	NNW-SSE	NNW-SSE	NNW-SSE	n/a
ECT	**Conglomerate**	NW-SE	ND	NW-SE	NNW-SSE	NNW-SSE	n/a
ECMQ	**Quartzite**	NNW-SSE	ND	NNW-SSE	NNW-SSE	NNW-SSE	n/a
ECMC	**Conglomerate**	NNW-SSE	NNW-SSE	NNW-SSE	NNW-SSE	NNW-SSE	n/a
ECBQ	**Quartzite/Conglomerate Mix**	NNW-SSE	ND	NNW-SSE	NNW-SSE	NNW-SSE	n/a
ECB	**Conglomerate**	NNW-SSE	ND	N-S	NNW-SSE	NNW-SSE	n/a
ECBAQ	**Quartzite**	NNW-SSE	ND	NNW-SSE	NNW-SSE	NNW-SSE	n/a
ECBA	**Quartzite/Conglomerate Mix**	NNW-SSE	ND	NNW-SSE	NNW-SSE	NNW-SSE	n/a

Error! Reference source not found. and **Error! Reference source not found.** respectively present summaries of the average and maximum clast trends for each bed per structure block.

Table 5: Summary table for average clast size trends per structure block and bed.

		Average Clast Size Trend					
Bed	**Primary Lithology**	**Block 1**	**Block 2**	**Block 3**	**Block 4**	**Block 5**	**West of Sub-outcrop**
VCR	**Conglomerate**	NNW-SSE	ND	NNW-SSE	NNW-SSE	NNW-SSE	n/a
MBT	**Quartzite/Conglomerate Mix**	NNW-SSE	ND	NNW-SSE	NNW-SSE	NNW-SSE	n/a
MBB	**Conglomerate**	ND	ND	NNW-SSE	NNW-SSE	NNW-SSE	n/a
MIQ	**Quartzite/Conglomerate Mix**	NNW-SSE	ND	NNW-SSE	NNW-SSE	NNW-SSE	n/a
MIT	**Conglomerate**	NNW-SSE	ND	NNW-SSE	NNW-SSE	NNW-SSE	n/a
MIB	**Quartzite/Conglomerate Mix**	NW-SE	ND	NNW-SSE	NNW-SSE	NNW-SSE	n/a
MAD	**Quartzite**	NW-SE	ND	NNW-SSE	NNW-SSE	NNW-SSE	n/a
MAC	**Conglomerate**	NNW-SSE	ND	NNW-SSE	NNW-SSE	NNW-SSE	n/a
ED	**Quartzite**	ND	ND	NNW-SSE	NNW-SSE	NNW-SSE	n/a
ECT	**Conglomerate**	NW-SE	ND	NNW-SSE	NNW-SSE	NNW-SSE	n/a
ECMQ	**Quartzite**	ND	ND	NNW-SSE	NNW-SSE	NNW-SSE	n/a
ECMC	**Conglomerate**	NNW-SSE	ND	NNW-SSE	NNW-SSE	NNW-SSE	n/a
ECBQ	**Quartzite/Conglomerate Mix**	ND	ND	NNW-SSE	NNW-SSE	NNW-SSE	n/a
ECB	**Conglomerate**	NW-SE	ND	NNW-SSE	NNW-SSE	NNW-SSE	n/a
ECBAQ	**Quartzite**	ND	ND	NNW-SSE	NNW-SSE	NNW-SSE	n/a
ECBA	**Quartzite/Conglomerate Mix**	NNW-SSE	ND	NNW-SSE	NNW-SSE	NNW-SSE	n/a

Table 6: Summary table for maximum clast size trends per structure block and bed.

		Maximum Clast Size Trend					
Bed	**Primary Lithology**	**Block 1**	**Block 2**	**Block 3**	**Block 4**	**Block 5**	**West of Sub-outcrop**
VCR	**Conglomerate**	ND	ND	NNW-SSE	NNW-SSE	NNW-SSE	n/a
MBT	**Quartzite/Conglomerate Mix**	NNW-SSE	ND	NNW-SSE	NNW-SSE	NNW-SSE	n/a
MBB	**Conglomerate**	NNW-SSE	ND	NNW-SSE	NNW-SSE	NNW-SSE	n/a
MIQ	**Quartzite/Conglomerate Mix**	NNW-SSE	ND	NNW-SSE	NNW-SSE	NNW-SSE	n/a
MIT	**Conglomerate**	NNW-SSE	ND	NNW-SSE	NNW-SSE	NNW-SSE	n/a
MIB	**Quartzite/Conglomerate Mix**	NW-SE	ND	NNW-SSE	NNW-SSE	NNW-SSE	n/a
MAD	**Quartzite**	ND	ND	ND	ND	ND	n/a
MAC	**Conglomerate**	NNW-SSE	ND	NNW-SSE	NNW-SSE	NNW-SSE	n/a
ED	**Quartzite**	ND	ND	NNW-SSE	NNW-SSE	NNW-SSE	n/a
ECT	**Conglomerate**	NW-SE	ND	NNW-SSE	NNW-SSE	NNW-SSE	n/a
ECMQ	**Quartzite**	ND	ND	ND	NNW-SSE	NNW-SSE	n/a
ECMC	**Conglomerate**	ND	ND	NNW-SSE	NNW-SSE	NNW-SSE	n/a
ECBQ	**Quartzite/Conglomerate Mix**	ND	ND	NNW-SSE	NNW-SSE	NNW-SSE	n/a
ECB	**Conglomerate**	NW-SE	ND	NNW-SSE	NNW-SSE	NNW-SSE	n/a
ECBAQ	**Quartzite**	NNW-SSE	ND	NNW-SSE	NNW-SSE	NNW-SSE	n/a
ECBA	**Quartzite/Conglomerate Mix**	ND	ND	NNW-SSE	NNW-SSE	NNW-SSE	n/a

CHAPTER 5: DISCUSSION

5.1 Discussion Outline

The purpose of this study was to assess whether useful stratigraphic and sedimentological evidence existed at SDGM to prove or disprove whether the E-W wrench faults exhibited syn-depositional strike slip tectonics or not.

The absence of palaeo-current data at SDGM due to the massive character of the conglomerates, the size of mining excavations and the related safety concerns still remains a concern. Directly measured palaeo-current data would have assisted in validating the findings in the study and should still be considered as part of SDGM's mapping strategy.

Methods such as regional historical measurements as compiled by Vermaakt and Chunnett (1994) in Figure 12, as well as mapping out the edges of the stoped-out workings in the area of the Twin Shaft Complex in Figure 13, exhibited excellent correlation with each other. The findings from these studies presented an expected NW-to-SE to NNW-SSE palaeo-current direction. Osburn et al. (2014) indicated they had found similarities and a close relationship (in terms of geostatistics and modelling) between the Upper Elsburg reef package and the unconformably overlying VCR.

The aim of the study was to use logged stratigraphic intervals and lithological changes from drillhole data only in the form of bed height, percentage conglomerate and average and maximum clast size data to prove that the wrench faults on SDGM were syn-depositional, in line with those historically indicated by Tucker and Viljoen (1986) further to the north on WAGM

The following research questions were posed in order to assist with proving or disproving the hypothesis:

1) Can sedimentological characteristics of individual beds at SDGM be spatially related to or disrupted by means of palinspastic reconstruction to prove syn-sedimentary lateral movement across E-W striking faults?

2) Are the Upper Elsburg beds at SDGM related or similar sedimentologically to the VCR as indicated by Osburn et al. (2014) thus possibly suggesting continuity of tectonism and sedimentary response between late Central Rand Group and Ventersdorp times?

3) What characteristics (in the absence of geostatistics and gold grade) are most useful in identifying syn-sedimentary movement across the E-W striking wrench structures?

4) Were all E-W striking wrench structures active during the sedimentation of the Upper Elsburg Reefs at all times?

5) Is there evidence for mine-scale wrench fault block compartmentalisation?

General observations have also been recorded and compared to historical findings pertaining to the study area and are discussed towards the end of this section.

5.2 Parameters, Data Reliability and Rules of Application

Sedimentological data which was available for the study included bed height, percentage conglomerate, average clast size and maximum clast size. The availability and resultant usefulness of these parameters is variable and is dependent on the historical detail logged by mine geologists over time. The bed correlation exercise and associated percentage conglomerate calculations (based on logged lithological changes) undertaken by SDGM between 2007 and 2010 presented the most numerous and most accurate data for modelling purposes with 18 731 and 18 291 data points respectively. Average and maximum clast size data per horizon was based on a modified Udden-Wentworth scale due to the different levels of application of logging standards over time and presented 16 557 and 2 918 data points respectively. Findings emanating from the study are based primarily on bed height and percentage conglomerate, while clast size data was viewed as only being indicative.

During palinspastic reconstruction of the data, all data was moved by means of removing the observable dislocation on a wrench fault by lining up the Upper Elsburg sub-outcrop line between adjacent blocks. This effectively removed the post VCR/deposition (Klipriviersberg) dislocation on a structure, leaving the data ready for interpretation to analyse for possible pre-Klipriviersberg movement. No additional structures were inferred or interpreted. Only existent, proven mapped and quantified wrench faults were considered in the study.

The following rules were applied prior to deciding whether a bed was dislocated prior to deposition or erosion by the overlying bed:

1) All palinspastically reconstructed data was first viewed without overlaying the data with the mapped wrench fault network.
2) No data contours were terminated by the structure framework. This was done to prevent bias in interpretation.
3) The mapped wrench fault network was overlain over the data contours and sudden changes coincident with, -or terminated/dislocated against specific identified structures were highlighted.
4) Repetitive changes across a specific structure for each successive bed were sought to eliminate coincidental changes. A structure had to impact more than one bed in order to be identified as being of influence, as well as to eliminate the possibility of physical and chemical weathering processes.

5.2.1 Bed height

Where sudden changes are seen to be coincident with, - or terminated/dislocated against specific identified structures on successive stratigraphic beds, it is possible to imply that movement took place on the structure, if not during, at least directly after a bed was deposited. The chances of sedimentological processes, such as soft sediment deformation, gravel bar occurrence and channel termination occurring in the exact same place within a repetitive sedimentary succession is remote – especially when viewed in conjunction with mapped proven existent geological structures.

These dislocations may be the result of vertical and/or horizontal movement; however, in most cases where apparent extensive lateral movements are interpreted (some in excess of hundreds of meters), due to the relatively low dip angle of the beds, the primary movement vector would have been the lateral component and would indicate at least post-sedimentary movement for a specific bed.

Zones of high frequency alternating high and low bed height that run along (co-incident with) or adjacent to structures where no apparent displacement is clearly visible, when considered in conjunction with percentage conglomerate, indicate the influence of a structure on a bed during sedimentation. This would indicate primarily syn-sedimentary movement on a structure. Sense of movement (up or down) for a certain fault block would be indicated by the relative changes in bed height where a higher bed height (possibly with lower percentage conglomerate) would indicate the down thrown block, while the lower bed height area with a higher percentage conglomerate would indicate the up thrown block. Beds would be thinner and potentially more conglomeratic due to local winnowing before the sediment passes over the fault scarp and onto the down thrown block, where sediment may preferentially accumulate.

Preserved channels (when considering bed height) are identifiable for some of the more conglomeratic beds due to the robust nature of the conglomerate and the associated erosional and unconformable base, especially those conglomeratic beds directly overlying and eroding into underlying quartzitic beds. When considered in conjunction with percentage conglomerate and clast sizes, these channels could potentially (in the absence of palaeo-current data) be indicative of preferred sediment transport direction.

5.2.2 Percentage Conglomerate

Where sudden changes in percentage conglomerate together with changes in bed height, are seen to be coincident with, -or terminated/dislocated against specific identified structures, it presents a strong argument that movement took place on the structure, if not during, at least directly after a bed was deposited.

Zones of higher percentage conglomerate coincident with or adjacent to higher bed heights could be indicative of preserved gravel bars. Often the trends identifiable in the percentage conglomerate plots run parallel to those encountered in the bed height plots and could also possibly inform preferential sediment transportation directions.

Often, areas of low bed height are seen to be coincident with high percentage conglomerate areas. These areas could represent areas where preferential winnowing took place, or entrainment and cannibalisation (by the overlying unconformity) of the quartzite took place, for deposition further downstream. High percentage conglomerate associated with higher bed height could also be indicative of important entry points with significant continuous winnowing onto the fluvial plane and may thus be indicative of the relative intensity of a specific unconformity along the sub-outcrop line, i.e. the higher the percentage conglomerate (with potentially increased clast size), potentially the more erosive the basal unconformity during sedimentation.

5.2.3 Average and Maximum Clast Size

Average clast size forms the third largest dataset. However, the data is in effect interpolative (and not empirical) due to the interpreted adjusted Wentworth Scale applied to written descriptions. Its usefulness is limited to general

trend observations. These trends, when considered in conjunction with bed height and percentage conglomerate, may be used to confirm important entry points of sediment into the area (where average clast sizes are larger), as well as to confirm interpreted transport directions in the absence of palaeo-current direction data.

Maximum clast size data is extremely sparse. However, it is empirical in nature and is thus potentially more informative than the average clast size data. Higher maximum clast size areas would indicate and/or confirm the presence and location of important sediment entry points along the Upper Elsburg sub-outcrop and would also indicate areas where the flow velocity associated with the palaeo-rivers was potentially greatest during sedimentation for any specific bed. Trends in maximum clast size (by virtue of data range), when viewed in conjunction with bed height and percentage conglomerate data, are probably the most reliable when investigating sediment transport directions in the absence of palaeo-current data.

5.3 Possible Sediment Transport Directions

The absence of measured palaeo-current data at SDGM precludes conclusive interpretation of sediment transport directions. However, an opinion in this regard may be inferred when considering trends for the four discussed parameters of bed height, percentage conglomerate, average clast size and maximum clast size.

Where agreement between all trends with respect to these four parameters is achieved, it might be possible to interpret possible preferential sediment transport directions. It is generally accepted that preserved channels present good indicators of local sediment transport direction. When these bed height trends are supported by similar percentage conglomerate, as well as clast size trends, as a unified dataset and would present reasonable evidence of the regional flow patterns and sediment transport directions.

From the above **Error! Reference source not found.**, **Error! Reference source not found.**, **Error! Reference source not found.** and **Error! Reference source not found.**, it is immediately evident that there is very little variation between any of the trend orientations occurring within a specific block, with the exception of Block 1. The predominant trend across all beds and blocks and trend types is NNW-SSE, with the exception of Block 1 rendering some NW-SE trends across all parameter trends, but not specific to any one bed. This would imply some variability in transport direction in the north of the project area, while a strong NNW-SSE trend becomes predominant towards the south.

5.4 SDGM General Interpretations and Observations

The Elsburg Individuals and Upper Elsburg Massives are each made up of stacked unconformities. Each unconformity is overlain by a lower conglomeratic bed and an overlying conformable more quartzitic (possibly more distally deposited) bed (Arthur, 1990; Muntingh et al., 2005; Obermeyer, 2005). Each unconformity erodes into the underlying stratigraphy, thus cannibalising these sediments.

In all, a total of eight such units exist: four in the Elsburg Individuals and three to four in the Upper Elsburg Massives, thus allowing for a total of eight unconformities (excluding the VCR). This naming convention applied to the Upper Elsburg reef package honours this stratigraphic succession with each conglomerate being overlain

by its related quartzitic bed, e.g. ECBA overlain by the ECBAQ. In addition, each successive unit unconformably overlies the previous on an angular unconformity.

In general, the Elsburg Individual conglomerates and overlying quartzites are constituted of less mature sediments, with more non-durables and argillaceous to arkosic quartzite making up the matrix within the conglomerates. The quartzites are also argillaceous to arkosic in nature (Arthur, 1990; Obermeyer, 2005; Muntingh et al., 2005).

In contrast, the conglomerates and quartzites occurring within the Upper Elsburg Massives are more mature. The matrix of these conglomerates and the interstitial quartzites are generally more mature and siliceous in appearance.

In addition, clast size (within the conglomeratic packages) is seen to generally increase upwards in the Elsburg Individuals and Upper Elsburg Massives, respectively. For example, the ECT and ECMC conglomeratic units appear to present a general larger clast size than exhibited by the ECB and ECBA in the Elsburg Individuals, while the MBB and MIT exhibit generally larger clast sizes than the MIB and the MAC (Arthur, 1990; Obermeyer, 2005; Muntingh et al., 2005).

Analysis of the general sedimentological trends for each of the beds as presented within the Results Chapter support the general westward thinning of each bed towards the Upper Elsburg sub-outcrop line where the Upper Elsburg Individuals and Massive Reefs are truncated by the overlying VCR. Each conglomeratic bed capped by its overlying quartzitic bed has been successively eroded or cannibalised by the overlying conglomerate bed within a zone of approximately 200 m to 300 m from the Upper Elsburg sub-outcrop. The effect of erosion and sediment on each beds' accompanying overlying quartzitic unit is evidenced up to 1.0 km to 1.5 km of the sub-outcrop line, where bed height for each bed stabilises with less local variability and approximately where maximum bed height for each bed is attained.

Beyond this point, bed strike for all the beds also trends parallel to sub-parallel relative to each other (Figure 36). This erosion pattern as presented, when combined for all horizons, presents an overall model consistent with the interpreted rotating onlap geometry for each of the Elsburg Individuals and Upper Elsburg Massives, respectively, with the Upper Elsburgs presenting an overall rotating onlap relationship relative to the Elsburg Individuals (Germs and Reynolds, 1991 (after Riba 1976); Obermeyer, 2005; Osburn et al., 2014) (Figure 17**Error! Reference source not found.**).

The rotating onlap unconformity configuration was first described in detail by Riba (1976). He suggested that a rotating onlap represented a single progressive unconformity or syn-tectonic cumulative wedge system attached to a tilted depositional surface linked to an uplifting structure (Cabrera et al., 1986). The resultant cumulative wedge is the direct product of the uplifting process. A rotative onlap as occurring at SDGM would record a decelerating or lessened rate of uplift (Cabrera et al., 1986).

Tucker et al. (2016) indicated that the typical sedimentary environment prevalent during Turffontein sedimentation was that of piedmont erosion surface passing into a debris flow to fluvial braid plain environment. A bed which might be representative of a typical piedmont environment, due to its typically thin bed height towards the west of the Upper Elsburg sub-outcrop and which might present a view of a typical piedmont environment in place during Upper Elsburg times, would potentially be the VCR. In contrast, the wide apron of sedimentation represented along the Upper Elsburg sub-outcrop and along an elongated sedimentary front at any

one time for any specific bed would potentially support the existence of a debris flow to fluvial braid plain environment.

All observed sedimentary trends tend to run predominantly NNW-SSE, with some running NW-SE or N-S in places.

The southward relative increase in bed height for the conglomeratic units tends to increase in conjunction with the percentage conglomerate and average and maximum clast size. This indicates relative activity or erosive strength on the local unconformities to increase southwards as well.

The sedimentary features analysed in this study (bed height, percentage conglomerate, average and maximum clast sizes) generally present NNW-SSE to NW-SE trends similar to a premised sediment transport direction away from the orogen or region of uplift towards the northwest.

Comparison of the observed trends in bed height (Figure 185Figure 185) and percentage conglomerate (Figure 186) and the recorded transport directions (Table 3 and Table 4) for the VCR compare favourably with the historical NNW-SSE to NW-SE palaeo-current directions as indicated by Vermaakt and Chunnett (1994). This lends credence to the interpretation of the palaeo-current trends presented in this study.

In addition, the similarity of palaeo-current interpretations for bed height and percentage conglomerate for the Upper Elsburg beds (based on the same principles) support the observation of Osburn et al. (2014). Interpreted palaeo-current directions observed in all of the Upper Elsburg beds render similar orientations to this of the VCR, thus possibly suggesting continuity of tectonism and sedimentary response between late Central Rand Group and Ventersdorp times.

5.4.1 Bed Height Data Interpretation

Bed height data was easily obtained from all drillholes that provided valid bed intersections and was thus the most complete dataset out of the four collected. General changes from west to east and from north to south were relatively easily identified across the project area for each bed. The significant bed height data density also identified zones of contrasting and alternating bed height.

Generally, bed height for each individual bed increased towards the SE or SSE as distance from the Upper Elsburg sub-outcrop increased.

General changes observed concerning the UE7 included the following:

1) During UE 7 deposition, bed height of the conglomeratic beds generally slightly increased from north to south, with the greatest bed heights per unit generally being recorded in the south, south of the 90L Wrench Fault.
2) During UE7 deposition, bed height for the more quartzitic beds appears to decrease parallel to the Upper Elsburg sub-outcrop towards the south, with the exception of south of the Fargo Wrench Fault.

The slight increase in bed-height of the conglomeratic beds towards the south (concomitant with the decrease in bed-height of the more quartzite units) could indicate progression towards an Elsburg conglomeratic entry point into the depository in the south in the vicinity of the 90 Level Wrench to towards the Phase 1 Wrench. An example of this feature is presented below in Figure 76.

The average rate of westward attenuation for each bed in the northern half of Block 1 is typically lower up against the Upper Elsburg sub-outcrop when compared to other structure blocks. In general, the rate of westward bed attenuation close into sub-outcrop progressively increases as one moves southwards along the sub-outcrop over the two wrench combinations.

Alternating conglomeratic and quartzitic units present differing rates of westward attenuation towards the sub-outcrop, where quarzitic units tend to be eroded more quickly by the overlying unconformity-bound conglomeratic unit.

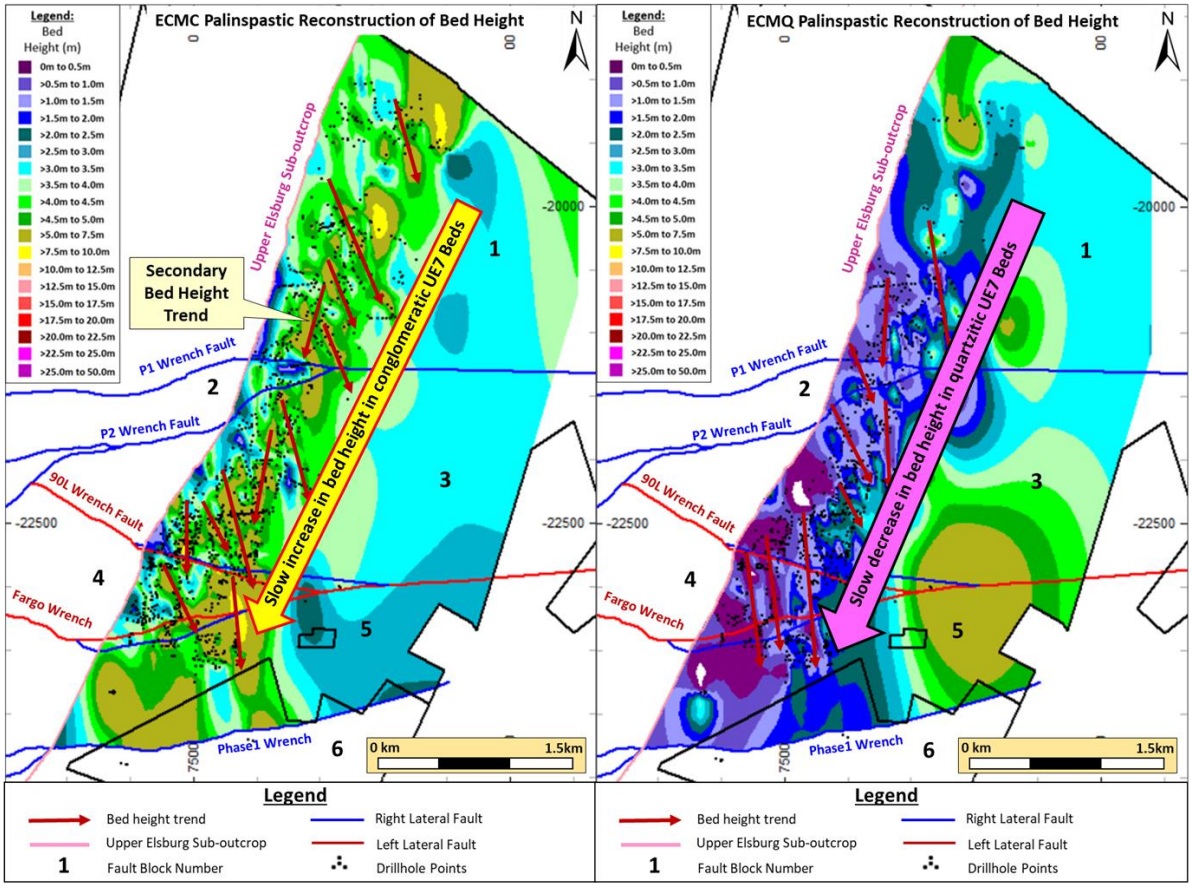


Figure 76: A comparison of bed height between a typical UE7 conglomeratic bed and a quartzitic bed showing the slow southward increase in bed height for the conglomeratic bed versus the slow southward decrease in bed height for a quartzitic bed.

Generally, the preserved ED thickness close to sub-outcrop decreases southwards, possibly indicating change in the erosive activity of the unconformity relating to the overlying Massives.

General changes observed concerning the Elsburg Massives included the following:

1) During deposition of the Massives, bed height for the conglomeratic beds dramatically increases southwards, south of the 90L Wrench Fault.
2) Conversely during deposition of the Massives bed height for the more quartzitic beds appears to decrease significantly south of the 90L Wrench.

These observations possibly indicate and support the existence of a significant Massives conglomeratic entry point in the south in the vicinity of the 90 Level Wrench towards the Phase 1 Wrench as presented below in Figure 77.

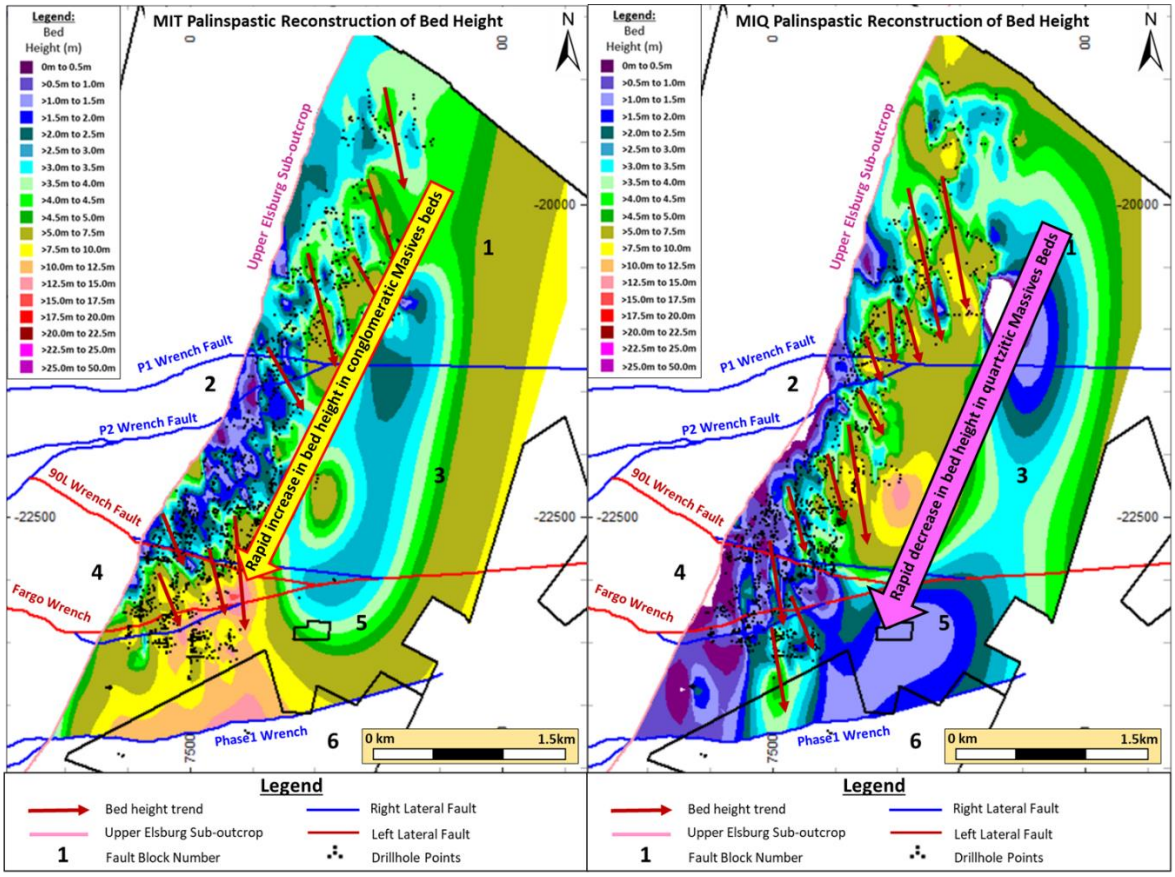


Figure 77: A comparison of bed height between a typical UE7 conglomeratic bed and a quartzitic bed showing the slow southward increase in bed height for the conglomeratic bed versus the slow southward decrease in bed height for a quartzitic bed.

The above general findings agree with findings from both Arthur (1990), as well as Muntingh et al., (2005) and potentially indicate that the deposition of the Massives represented an acceleration in deposition and a heightened rate of uplift in the in hinterland.

5.4.2 Percentage Conglomerate Data Interpretation

Percentage conglomerate data forms the second-most informed dataset. General changes in percentage conglomerate are easily identified across the project area for each bed.

Generally, percentage conglomerate decreases slowly eastwards away from the sub-outcrop, as the active erosion area (of each local unconformity zone) close to the sub-outcrop is exited, local potential for winnowing close to the sub-outcrop is minimised, and the effective slope decreases resulting in the preferential deposition of the heavier, larger clasts with sand content increasing eastwards.

General changes observed concerning the UE7 included the following:

1) During UE 7 deposition, percentage conglomerate generally increased from north to south, with the zones of maximum percentage conglomerate occurring between the P1 Wrench Fault in the north and the Fargo Wrench in the south.
2) During UE7 deposition, the quartzitic beds presented a similar percentage conglomerate increase from north to south occurring between the P1 Wrench Fault in the north and the Fargo Wrench in the south.

An example of the above observations is presented below in Figure 78.

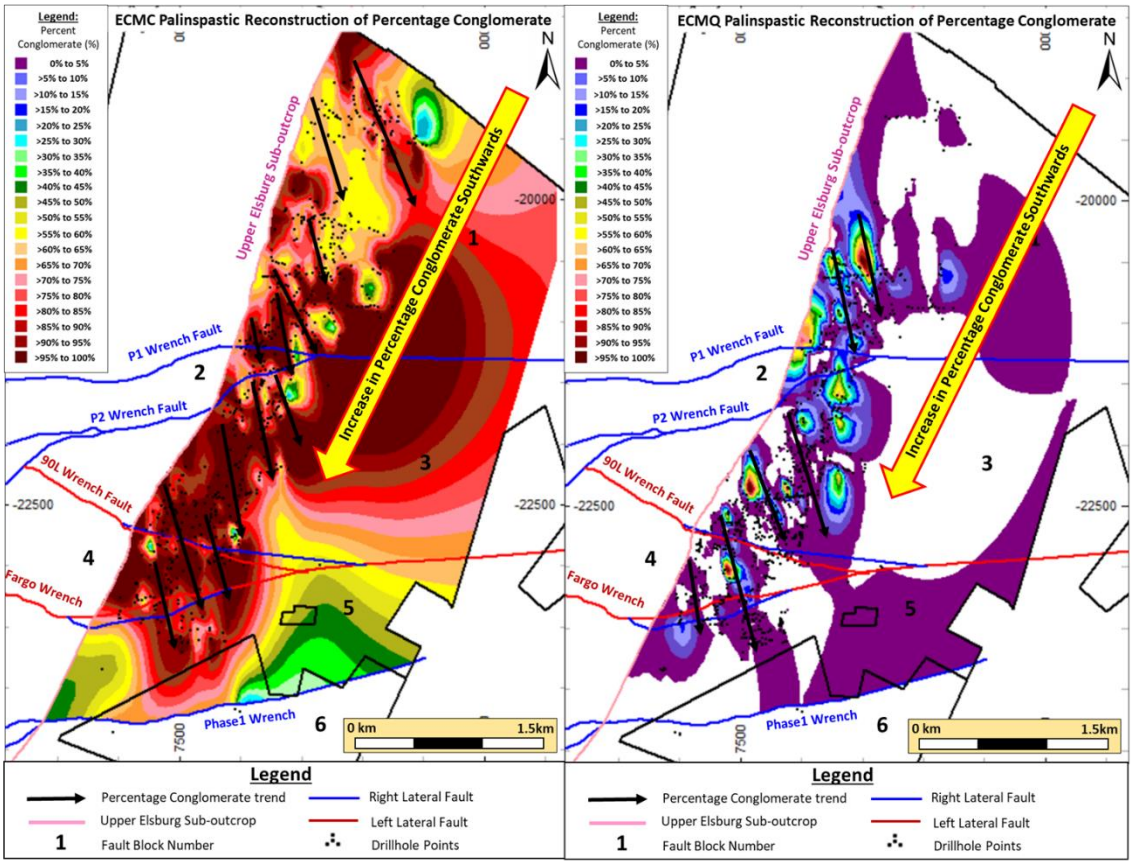


Figure 78: A comparison of percentage conglomerate between a typical UE7 conglomeratic bed and a quartzitic bed showing the slow southward increase in percentage conglomerate for both the conglomeratic bed and quartzitic bed.

General changes observed concerning the Elsburg Massives in relation to percentage conglomerate included the following:

1) During deposition of the Massives, percentage conglomerate increases just north of the P1 Wrench Fault and again in the vicinity of the 90L and Fargo Wrench combination.
2) Similarly, the quartzitic beds also show an increase in percentage conglomerate in similar areas as those of the conglomeratic units.

An example of the above observations is presented below in Figure 79.

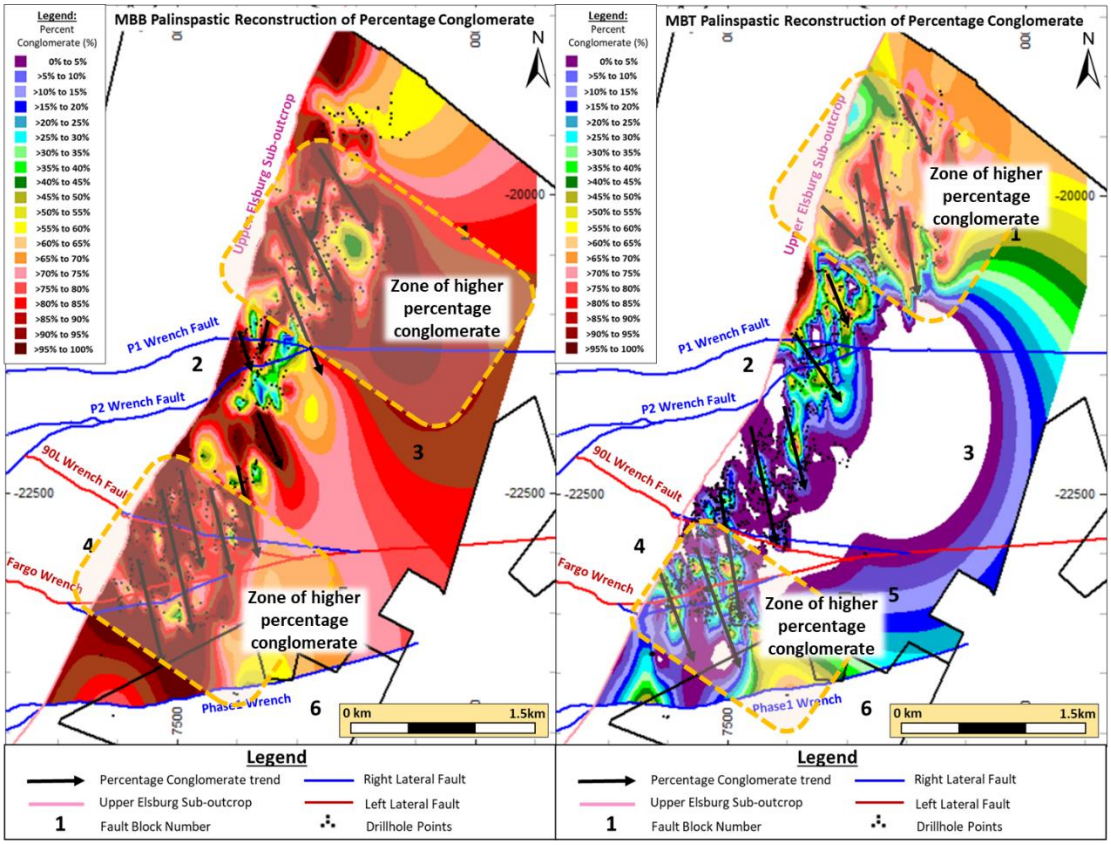


Figure 79: A comparison of percentage conglomerate between a typical Massives conglomeratic bed and a quartzitic bed showing the two areas with increased percentage conglomerate (highlighted in the yellow polygons) just north of the P1 Wrench Fault and in the vicinity of the 90L Wrench and Fargo Wrench Fault combination.

These observations could possibly indicate and support the existence of two significant Massives conglomeratic entry points into the depository.

5.4.3 Average and Maximum Clast Size

Average clast size forms the third largest dataset. However, the data is in effect interpolative (and not empirical) due to the interpreted adjusted Wentworth Scale applied to written descriptions. Its usefulness is limited to general trend observations. These trends, when considered in conjunction with bed height and percentage conglomerate, may be used to confirm important entry points of sediment into the area (where average clast sizes are larger), as well as to confirm interpreted transport directions in the absence of palaeo-current direction data.

Maximum clast size data is sparse. However, it is empirical in nature and is thus potentially more informative than the average clast size data. Higher maximum clast size areas would indicate and/or confirm the presence and

location of important sediment entry points along the Upper Elsburg sub-outcrop and would also indicate areas where the flow velocity associated with the palaeo-rivers was potentially greatest during sedimentation for any specific bed. Trends in maximum clast size (by virtue of data range), when viewed in conjunction with bed height and percentage conglomerate data, are probably the most reliable when investigating sediment transport directions in the absence of palaeo-current data.

Generally, in all cases average and maximum clast size renders a general increase in the south of the project area around the 90L Wrench and Fargo Wrench Fault combination. This agrees with the findings of Muntingh et al. (2005) and could indicate the proximity of the major sediment entry point in this area, as opposed to the possible secondary one in the region of the 90L Wrench as identified in the percentage conglomerate plots in Figure 83.

5.5 SDGM Structures

A summary of the findings relating the observations relative to the individual bed plots and the identified (post-Klipriviersberg) wrenches within the project area is presented in Table 7 below.

The different faults each have their own unique history when considered in conjunction with the plots presented in the above sections. Not all structures present possible syn-sedimentary evidence of activity in the form of localised winnowing or in the form of sedimentary bed height and percentage conglomerate nodes that run parallel to or directly on top of the structure. In many cases, observations might be inconclusive and would require additional work by mine personnel to assess their true nature.

Two legends may be applied to the codes utilised to populate Table 7. The observation legend records whether a visual dislocation of bed height was observed or not. The same codes are utilised to denote whether syn-sedimentary evidence was observed as indicated above.

A dislocation in bed height as used in this study refers to a sharp change in bed height across a structure. It is not possible at this juncture to indicate whether dislocation reflects thinning by the hanging-wall erosive unit or whether it might reflect a syn-depositional irregularity. In all cases, where dislocations have been interpreted, it is inferred that these dislocations are purely post-deposition relative to the affected unit and refer specifically to the horizontal offset of preserved channels across the faults. It should be noted that syn-sedimentary movement might have been possible in such instances, but it is extremely difficult if not impossible to quantify. The dislocations therefore as interpreted suggest syn-Central Rand Group movement which might have taken place during deposition or during a hiatus in deposition, prior to the overlying unit being deposited.

The magnitudes of dislocation or throw across the wrench structures are understood to have a combination of dip-slip and strike slip in accordance with the descriptions of similar structures further to the north on the neighbouring Randfontein Estates No. 4# as described by Tucker et al. (2016), with a preferred dextral sense of movement. However, it is accepted that due to the relatively low bed height and the relatively low bedding dip, that horizontal dislocations as indicated for the relative horizontal offsets of visible channels would be fairly indicative of the real resultant horizontal magnitude of wrench experienced over the deposition of the Upper Elsburgs. It should also be considered that as one progresses upward in the stratigraphy, the observed dislocations within the lower beds would effectively be compounded as each successive bed is wrenched in turn. In order to understand the true

lateral displacement for each bed, the final dislocation for each bed would have to be retrospectively reconstructed by subtracting the lateral displacement of the younger overlying beds from each successive underlying bed. This exercise would be recommended for future study.

If a dislocation of a bed height trend was observed across a fault an element of post-sedimentary activity was immediately accepted, which did not preclude the possible syn-sedimentary component. Where clear observations were not possible due to data density, or due to extremely subtle changes, observations were described as being inconclusive. Where dislocation across structures was encountered, it was characterised as being right-lateral, left-lateral or inconclusive. Dislocations should be considered as relative movements and do not necessarily give a sense of the true throw or wrench component (or combined) across a structure at the time of deposition. For example, a right-lateral expression of dislocation on the maps could present two possible structural scenarios: 1) a true right-lateral, or oblique right-lateral dislocation, or 2) a true down throw fault (down to the south) would render a visual relative right-lateral dislocation. This similarly applies to left-lateral observations.

From Table 7 it may be inferred that the southern 90L Wrench and Fargo Wrench combination was more active structurally with more numerous instances of movement than the P1 Wrench and P2 Wrench combination in the north.

A combination of changes in sedimentary characteristics adjacent to and along the wrench faults identified on SDGM were used to infer syn-sedimentary characteristics on structures as opposed to pure structural character. In cases where distinct changes in percentage conglomerate were observed across structures within a demarcated zone of higher or lower bed height which either was, or was not dislocated across a structure, syn-sedimentary movement was inferred. In cases where deeper bed height trends were not offset across a structure, but a pattern of alternating changes of bed height and percentage conglomerate were found trending adjacent to or coincident with a fault trace, syn-sedimentary influence was inferred, regardless of whether dislocation of bed height trends was observable across a fault or not.

Areas where bed heights were noticeably low but accompanied by high percentage conglomerate, winnowing is considered to have taken place, also resulting in a syn-sedimentary interpretation.

From Table 7, it is evident that not all faults were active or moved at all times or synchronously during the alternating deposition and erosion of the Elsburg Individuals or the Upper Elsburg Massives. For example, the P1 Wrench only commences movement or dislocation during or after ECBQ times, while all other structures present more frequent movement from the outset. Whereas during the deposition of the Massives, lateral movement is observable throughout on the 90L Wrench and Fargo Wrench, during deposition of the MIB through to NIQ no lateral displacement was observed on the P1 Wrench and P2 Wrench.

Most dislocations observed present a relative right-lateral geometry with 90L Wrench only presenting two syn-Central Rand Group left-lateral dislocations. Its preserved configuration (post-Klipriviersberg) is, however, left-lateral.

Due to the repetition of termination of sedimentary bed height and percentage conglomerate in overlying beds, as indicated below in Table 7, it may be concluded that this applied methodology may be use to prove syn-sedimentary lateral movement across E-W striking faults.

Inferring dislocation for the various Upper Elsburg beds with various senses of movement and times of dislocation on different sets of faults as indicated below in Table 7, would support the possibility of fault block compartmentalisation resulting in variant thicknesses and percentage conglomerate occurring in adjacent fault blocks.

Table 7: Summary of findings relating to the structures observed in this study.

	P1 Wrench				P2 Wrench				90L Wrench				Fargo Wrench			
Bed	Dislocated?	Relative Movement Sense?	Syn-sedimentary Evidence?	Post Sedimentary	Dislocated?	Relative Movement Sense?	Syn-sedimentary Evidence?	Post Sedimentary	Dislocated?	Relative Movement Sense?	Syn-sedimentary Evidence?	Post Sedimentary	Dislocated?	Relative Movement Sense?	Syn-sedimentary Evidence?	Post Sedimentary
Preserved: Post-Klipriviersberg	Y	RL	N	Y	Y	RL	N	Y	Y	LL	N	Y	Y	RL	N	Y
VCR	Y	RL	Y	I	Y	RL	Y	I	I	I	Y	I	Y	I	I	Y
MBT	Y	RL	Y	Y	Y	RL	Y	Y	Y	RL	Y	I	I	RL	Y	Y
MBB	Y	I	N	Y	Y	RL	Y	Y	Y	RL	N	Y	Y	RL	Y	Y
MIQ	N	N/A	Y	N	Y	RL	Y	Y	Y	I	Y	Y	Y	RL	Y	Y
MIT	N	N/A	Y	N	N	N/A	Y	N	Y	RL	Y	Y	Y	LL	Y	Y
MIB	Y	RL	Y	Y	N	N/A	Y	N	I	RL	Y	I	I	RL	I	I
MAD	Y	RL	N	Y	Y	RL	I	Y	Y	RL	Y	Y	Y	RL	I	Y
MAC	Y	I	N	Y	Y	I	Y	Y	I	I	Y	I	Y	I	I	Y
ED	N	N/A	I	N	Y	RL	I	Y	Y	RL	Y	Y	Y	RL	Y	Y
ECT	I	I	N	N	Y	RL	N	Y	I	I	Y	I	I	I	Y	I
ECMQ	N	N/A	N	N	Y	RL	Y	Y	Y	RL	Y	Y	Y	RL	Y	Y
ECMC	Y	LL	N	Y	Y	RL	Y	Y	Y	RL	Y	Y	Y	RL	Y	I
ECBQ	Y	I	N	Y	Y	RL	N	Y	N	N/A	Y	I	N	N/A	Y	Y
ECB	N	N/A	N	N	Y	RL	N	Y	Y	LL	Y	I	Y	RL	Y	Y
ECBAQ	N	N/A	N	N	Y	RL	Y	Y	Y	RL	N	Y	Y	RL	I	Y
ECBA	N	N/A	N	N	Y	RL	I	Y	Y	LL	Y	Y	Y	RL	N	Y

Observation Legend

Y	Yes
N	No
I	Inconclusive
N/A	Not Applicable

Interpreted Movement Sense

RL	Right-Lateral
LL	Left-Lateral
I	Inconclusive
N/A	Not Applicable

5.5.1 P1 Wrench

The P1 Wrench would appear to have only commenced movement possibly during ECB times and its movement is marked by intermittent periods of quiescence such as during ED and MIT to MIQ times. Where relative movement for bed height or percentage conglomerate trends could be determined, relative movement sense tends to right-lateral, with left-lateral dislocation only possibly occurring during ECMC times. Possible evidence of syn-sedimentary dislocation in the form of localised winnow zones bounded by the faults and nodes of highly variable bed height and percentage conglomerate along the fault strike or directly adjacent to it, only appear to emerge during ECMQ times and occur intermittently up through the stratigraphy.

5.5.2 P2 Wrench

The P2 Wrench appears to have been active throughout Upper Elsburg times, with the possible exception of during the MIB and MIT times. All interpreted relative senses of movement over the P2 Wrench appear to indicate a highly right-lateral component of movement. Possible syn-sedimentary features in the form of localised winnow zones bounded by the faults and nodes of highly variable bed height and percentage conglomerate along the fault strike or directly adjacent to it, may be traced throughout (with little exception) Upper Elsburg times.

5.5.3 90L Wrench

The 90L Wrench shows evidence for dislocation throughout Upper Elsburg times, with the only period of possible quiescence occurring during ECBQ times. Relative senses of dislocation across the 90L Wrench alternate between left-lateral and right-lateral from ECBA to ECB times. The structure then takes on a distinctive right-lateral sense of dislocation up to MBB times. However, the final sense of preserved dislocation from post-Klipriviersberg times is left-lateral, based upon the mapped positions of the Upper Elsburg sub-outcrop. Syn-sedimentary activity on the structure occur throughout Upper Elsburg times with the exception of the ECBQ and MBB times.

5.5.4 Fargo Wrench

The Fargo Wrench also presents relative dislocations throughout Upper Elsburg times, except during ECBQ times (similar to the 90L Wrench). Most interpreted relative possible dislocations present a right-lateral apparent component, with the exception of the MIT which presents a possible left-lateral dislocation. The Fargo Wrench also exhibits possible syn-sedimentary evidence from ECB times right up to MBT times.

5.6 Applicability of Methodology to Other Areas

SDGM presents an environment of stacked unconformities and stacked conglomerates beds with interstitial quartzitic beds. The noticeable wedge geometry due to the rotating onlap and the associated frequency of the unconformities may be found in other places within the Witwatersrand Basin. On a goldfield-scale, similar deposits (though often not as conglomeratic) may be found on Cooke No. 4 Shaft (Ezulwini) directly to the north of SDGM (Sibanye Stillwater, 2019), which also mines a strike continuation of the SDGM orebody, as well as

the UE1A and E9EC composite reef, colloquially termed the “Middle Elsburgs”. The Upper Elsburgs have also been interpreted and correlated along the West Wits line but are only locally mineable on operations such as Deelkraal and the western side of Kusasalethu Mine (Harmony, 2020).

Elsewhere in the Witwatersrand Basin, similar expressions are located along the western margin of the Free State Goldfield at the old Lorraine Shafts and the newer Target Mine in the form of the stacked Elsburg Reefs and Dreyerskuil Zone at Target Mine located along the western margin of the Free State Goldfield (Tucker et al., 2016).

Methods employed during this study at SDGM would prove useful at most of the operations mentioned to test applicability, though Cooke No. 4 Shaft and Target Gold Mines stand out as a result of their robust reef expressions when compared to the other operations mentioned.

In most other mining areas within the Witwatersrand Basin, the reefs or target beds with basal unconformities are preserved as thin sheets. This presents a challenge to assessing wrench movements when comparing sedimentary parameters such as bed height, as dislocations are less pronounced than those observable in thicker beds.

5.7 SDGM Regional Context and Interpretation

SDGM only forms a small portion of the overall West Rand Goldfield. Recent structural research (Dankert and Hein, 2010; Manzi, 2013; Manzi et al., 2013) has presented a more complex structural history for the West Rand Goldfield. This study attempts to relate the SDGM data and its interpretation to these recent findings and to add context as regards the reef formation at SDGM to this understanding.

The interpretation of Dankert and Hein’s (2010) Umzawami Event presents evidence for syn-Central Rand Group compressional tectonics related to the deposition and some deformation of the Central Rand Group and VCR to the formation of a fold-thrust belt at ca. 2.90-2.72 Ga. This resulted in the formation of syn-sedimentary folds (mostly NW-trending axes) forming coeval with the east-verging thrust faults.

Manzi (2013) and Manzi et al. (2013) confirmed the occurrence of the blind footwall thrust (Jabulani Thrust) to the Bank Fault located in the footwall of the NNE-SSW striking Bank Fault and identified a similar structure below the West Rand Fault (Tandeka Thrust). These blind footwall thrusts were related to the compressional Umzawami Event (ca. 2.73 Ga) of Dankert and Hein (2010) which had a profound effect on the deposition of the Witwatersrand Supergroup.

In addition, based upon the seismic data, Manzi et al. (2013) indicated an apparent nett sinistral movement to the both the Bank Fault/Jabulani Thrust and West Rand Fault/Tandeka Thrust combinations. This is in contrast and opposite in sense to both Stanistreet and McCarthy (1991) and Catuneanu (2001). Both studies by these authors indicated a requisite dextral movement along the boundary faults of the Witwatersrand Basin during basin formation. Eriksson et al. (2005), however, also postulated a left-lateral geometry or sense of movement of basin-wide wrench tectonics associated with the compression from the north generated by collision with the Zimbabwe Craton via the Limpopo Belt and the Kimberley Block from the west during the assembly of the Kaapvaal Craton.

Consideration of the compressive tectonic stresses prevalent during Central Rand Group and VCR times with the projected Tandeka Thrust located in the footwall of the West Rand Fault, is imperative to understanding the syn-sedimentary environment and the deposition of the different lithologies or beds (conglomerates versus quartzites) in the SDGM/West Rand Goldfield. The rotating onlap geometry, as presented by Germs and Reynolds (1991), Obermeyer (2004) and Osburn et al. (2014), requires syn-sedimentary uplift in the hinterland (towards the west) and localised subsidence to the east to accommodate the active sedimentation within a compressive tectonic environment.

SDGM is located on the southern limb of the West Rand Syncline, to the east of the Panvlakte Horst Block (Figure 3) which displaces the stratigraphy down to the east (Tucker and Viljoen, 1986; Tucker et al., 2016). Tucker and Viljoen (1986) and Tucker et al. (2016) related the onlapping geometry of the Middle Elsburg Reefs on the southern limb of the West Rand Syncline to syn-sedimentary movement on the Panvlakte Fault Zone together with the formation of the Panvlakte Anticline. The Panvlakte Fault Zone is interpreted as being extensional in nature and is thus interpreted to have been active during West Rand Group times. However, while this might appear contradictory to the interpretation of Tucker and Viljoen (1986) and Tucker et al. (2016), little is known of the northern extent of the Tandeka Thrust due to the lack of seismic data to the north. It might well be possible that the mechanism of the rotating onlap observed east of the Panvlakte Horst for the Middle Elsburg Reefs could be associated with an undefined northward extension of the Tandeka Thrust. This might speculatively have resulted in sympathetic movement on the Panvlakte Fault Zone during Central Rand Group times.

Importantly, Tucker and Viljoen (1986) and Tucker et al. (2016) noted two primary fault orientations occurring on the southern limb of the West Rand Syncline, and more importantly in the northern areas of WAGM (Figure 3), namely N-S striking normal faults and E-W striking strike-slip faults. The E-W striking strike-slip faults segment the orebody both vertically and horizontally, with a right-lateral displacement of up to 2000 m with a variable lower component of vertical throw. Tucker and Viljoen (1986) interpreted the strike-slip faults to be predominantly pre-Transvaal in age as they did not displace the Black Reef, which unconformably overlies the Witwatersrand and Ventersdorp Supergroups, but importantly some of these structures might have influenced reef morphology during Central Rand Group times. This does not, however, appear to be comprehensively documented. The description of the right-lateral faults by Tucker and Viljoen (1986) and Tucker et al. (2016) would appear to be similar to those described and assessed in this study.

The WSW trending faults south of Westonaria presenting a right-lateral relative displacement of the West Rand and Saxon–Roodepoort–Panvlakte faults as described by Dankert and Hein (2010), also appear to agree with the description of faults assessed in this study.

Little attempt has been made to understand the relative age of the strike-slip faults within the West Rand Goldfield, especially due to the difficulty in relating changes within the typical thin reef geometries encountered in the goldfield across these structures. The thick reef package at SDGM offers a unique opportunity to relate these structures in terms of relative age and potential effect on reef morphology to the regional structural understanding.

The syn-sedimentary evidence presented for the various beds making up the Central Rand Group-aged SDGM reef package implies at least a syn-Central Rand Group age to the current interpreted E-W trending (right-lateral) wrench faults, thus effectively relating their activity to sedimentation just prior to the Klipriviersberg at >2.79 Ga.

This possibly confirms the suspicions of Tucker and Viljoen (1986) and Tucker et al. (2016) and thus postulates that their movements were coeval to the occurrence of, and associated uplift by the Tandeka Thrust.

Consideration of the compressive tectonic stresses prevalent during Central Rand Group and VCR times with the projected Tandeka Thrust located in the footwall of the West Rand Fault, is imperative to understanding the syn-sedimentary environment and the deposition of the different lithologies or beds (conglomerates versus quartzites) in the SDGM/West Rand Goldfield.

Construction of a strain ellipse (Figure 80) to understand the fault configuration at SDGM assists in understanding the structure orientations of potential faults possibly generated during the compressive Umzawami Event and perpetuated during the continued structural history of the area. However, inclusion of the sinistral apparent displacement as indicated by Manzi et al. (2013) is required in order to accommodate the primary expressed right-lateral displacement exhibited on all the wrench faults assessed in this study.

Review of the Central Rand Group relative syn-sedimentary movements presented by the data for all Elsburg Individual and Upper Elsburg Massives, presents an overwhelming interpreted right-lateral fault displacement on all faults concerned (with a few exceptions). This also of course excludes the post-Klipriviersburg deformation events for which the current recorded dislocations across each of the wrench faults are only indicative of movements subsequent to cessation of sedimentation of the VCR.

Alignment of the strain ellipse right-lateral R’ and X shears to that of the modelled wrench structures, could potentially support a parent-daughter relationship between the wrench structures which would potentially be coeval with sigma 1 and the underlying Tandeka Thrust.

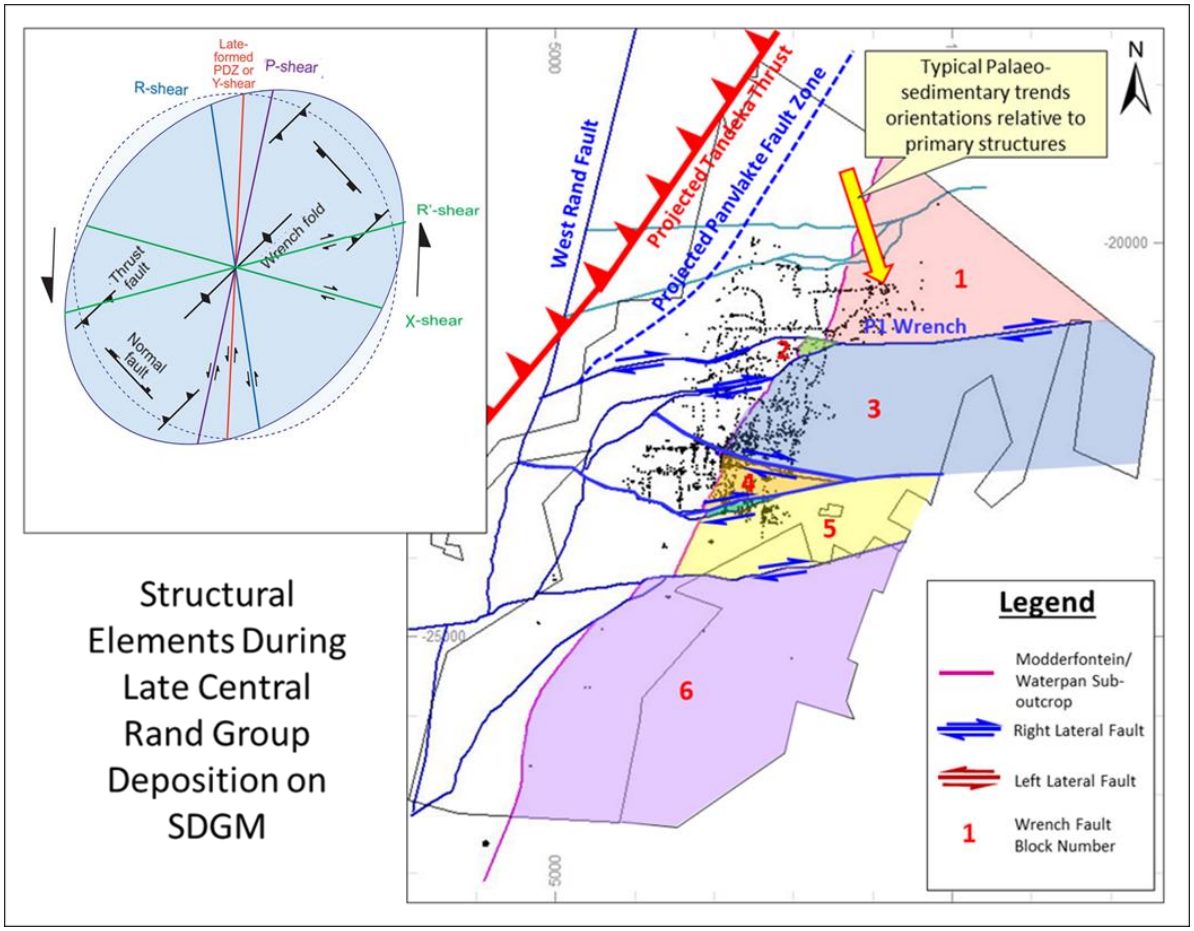


Figure 80: Strain ellipse representing stresses and fracture patterns concurrent with deposition of the Central Rand Group and VCR related to recorded and projected geological structures on SDGM. The yellow arrow indicates the mean sedimentary trends observable in in the results. (Strain ellipse modified after Jackson and Hudec; 2017).

As previously indicated, Riba (1976) suggested that a rotating onlap represented a single progressive unconformity or syn-tectonic cumulative wedge system attached to a tilted depositional surface linked to an uplifting structure (Cabrera et al., 1986). DeCelles and Giles (1996) in contrast related the occurrence of abundant progressive unconformities specifically to wedge-top deposits, where the wedge-top depozone forms part of the orogenic wedge during deformation. According to DeCelles and Giles (1996), areally extensive aprons of alluvial sediment commonly drape the upper surface of the orogenic wedge during periods of non-deformation and highlighted following:

1) The wedge-top depozone includes progressive deformation;
2) Numerous regional and local unconformities;
3) Regional thinning towards the orogenic wedge; and
4) Extreme textural and compositional immaturity of the sediment.

Relating the location of the orogen towards the west of SDGM and the similarities and the evidence of syn-sedimentary deformation both associated with the orogen, as well as that associated with the wrench faults and the extreme variance in the nature of the sediments making up the Upper Elsburg package, it could possibly be argued that within the Witwatersrand Basin context, the sedimentary package on SDGM was formed on the

orogenic wedge in a potential wedge-top environment ahead of the progressive orogenic front (consisting of the Jabulani Thrust and Tandeka Thrust).

It is also possible – though uncertain – that smaller sedimentary basins (such as piggyback basins as described by Ori and Friend, 1984) located within the wedge-top environment could have formed between the progressive thrust sheets to the west of SDGM. The increase in clast size and percentage conglomerate, as well as bed height as evidenced in the region of the 90L Wrench and Fargo Wrench, could be indicative of a significant entry point for sediment from the direction of the orogen or a transference system (as per Suriano et al., 2015) from the interior of the orogenic fold-trust belt to the west to a possible transition to the foredeep in the east possibly commencing on SDGM. Wrench faults as identified could possibly be associated with topographic disturbance due to movement on the underlying thrust fault. However, this point is not conclusive as the original Alps model as presented by Ori and Friend (1984) does not consider the influence of wrench faults in relation to the orogenic fault.

5.8 Conclusions and Recommendations

The absence of empirical palaeo-current data poses a challenge in proving syn-depositional strike-slip tectonics related to E-W striking wrench faults occurring on SDGM. Historical VCR palaeo-current data as well as historical stoping outlines at the SDGM Twin Shaft also on VCR indicate a paleao-current direction of NNW-SSE to NW-SE.

Individual sedimentary qualities including primarily, bed height and percentage conglomerate and to lesser extent, average and maximum clast size per bed derived from drillhole data may be used to confirm the historical palaeo-current data of Vermaakt and Chunnett (1994) specifically for the VCR and assists in confirming Osburne et al.'s (2014) suggestion of continuity of tectonism and sedimentary response between late Central Rand Group and Ventersdorp times.

Palinspastic reconstruction of sedimentological data across the existent W-E striking wrench faults is possible by applying a vector, equivalent in magnitude and direction, to the mapped dislocation of the Upper Elsburg Sub-outcrop.

Palinspastically reconstructed bed height and percentage conglomerate data provide a useful tool to indicate the orientation of individual channels and trends. Where these reconstructed trends or channels for a specific bed are cut off directly by an existing wrench structure, post-depositional (but pre-Klipriviersberg) lateral movement may be implied and provide useful evidence supporting syn-sedimentary strike-slip tectonics.

Recording of dislocations across each wrench fault, as well as their sense of movement for each bed provides a sense of the relative activity associated with each wrench fault. The P1 Wrench was active during deposition of the Massives with a right-lateral sense of dislocation. Post deposition of the ECMC the P1 Wrench presented as a left-lateral structure. In contrast, the P2 Wrench was active throughout deposition of the Upper Elsburg reef package. together with the 90L Wrench. The 90L Wrench presented left-lateral dislocation during early deposition of the ECBA and ECB and changed over to a solely right-lateral sense of movement with ECBQ times. The Fargo Wrench also appears to have been active throughout most of the Upper Elsburg reef package deposition and

primarily presented a right-lateral dislocation, excepting during MIT times with a left-lateral dislocation. Thus, most of the wrench faults appear to have been active throughout the deposition of the Upper Elsburg reef package, with the exception of the P1 Wrench, which only commenced lateral dislocation prior to ECMC times.

The above findings lend credence to the hypothesis that stratigraphic and sedimentological evidence exists at SDGM to support the existence of syn-depositional strike-slip tectonics associated with the E-W wrench faults (right-lateral as well as left-lateral) in line with Tucker and Viljoen (1986) who proposed syn-sedimentary strike-slip movement on similar structures to the north on the Western Areas Gold Mines' North shaft.

Syn-sedimentary tectonics related to the wrench faults had an effect on the characteristic of each individual bed. Possible relative dislocations or movements across the wrench structures presented an overwhelming right-lateral sense of movement. The wrench structures could possibly represent R' and X-type shears within a larger overall transpressional fault system as represented by the Jabulani and Tandeka Faults to the west.

Local compartmentalisation of sediments within single fault blocks may have occurred due to uplift or structural accommodation or flexure along the wrench faults, possibly in the form of growth faults at SDGM, therefore providing evidence of syn-tectonic sedimentary response to wrenching.

It is possible that the rotating onlap geometry at SDGM represents a single progressive unconformity or syn-tectonic cumulative wedge system attached to a tilted depositional surface linked to the Tandeka Thrust in the footwall within a wedge-top environment. It is also possible that SDGM could possibly be located at the preserved transition between the wedge-top and foredeep environment.

The location of the orogen towards the west of SDGM and the evidence of syn-sedimentary deformation and the extreme variance in the type the sediments making up the Upper Elsburg package could possibly indicate that the sedimentary package on SDGM was formed on the orogenic wedge in a potential wedge-top environment ahead of the progressive orogenic front (consisting of the Jabulani Thrust and Tandeka Thrust and their possible inferred piggy-back basins). The increase in clast size and percentage conglomerate as one progresses upwards through the Upper Elsburg reef package, associated with the rotating onlap morphology of stacked unconformites, could possibly be indicative of a significant entry point for sediment from the direction of the orogen or a transference system. The type of orogen inferred could possibly provide evidence for basin partitioning in the UE7 and Upper Elsburg Massives.

It is recommended that an effort should be made to acquire palaeo-current data through support of other sedimentological studies on SDGM.

REFERENCES

Alania, V.M., Chabukiani, A.O., Chagelishvili, R.L., Enukidze, O.V., Gogrichiani, K.O., Razmadze, A.N. and Tsereteli, N.S., 2015. Growth structures, piggy-back basins and growth strata of the Georgian part of the Kura foreland fold–thrust belt: implications for Late Alpine kinematic evolution. In: Sosson, M., Stephenson, R. A. & Adamia, S. A. (Eds,) 2017, Tectonic Evolution of the Eastern Black Sea and Caucasus. Geological Society, London, Special Publications, 428, 171-185.

Armstrong, R.A., Compston, W, Retief, E.A., Williams, I.S., Welke, H.J., 1991. Zircon ion microprobe studies bearing on the age and evolution of the Witwatersrand triad. Precambrian Research 53, 243-266.

Arthur, D.L., 1990. Report on the stratigraphy and sedimentology of the Upper Elsburg strata in the South Deep Project Area. Unpublished Report: JCI Geological Department Gold Unit, 28 p.

Barton, E.S., Compston, W., Williams, I.S., Bristow, J.W., Hallbauer, D.T., Smith, C.B., 1989. Provenance ages for the Witwatersrand Supergroup and the Ventersdorp Contact Reef: constraints from ion microprobe U–Pb ages of detrital zircons. Economic Geology 84, 2012-2019.

Beach, A., Smith, R., 2007. Structural geometry and development of the Witwatersrand Basin, South Africa. In: Ries, A.C., Butler, R.W.H., Graham, R.H. (Eds.), Deformation of the continental crust: The Legacy of Mike Coward: Geological Society, London, Special Publications 272, 533-542.

Beater, C.D., 1982. The Significance of Unconformities in the Development of Witwatersrand Gold and Uranium Placers. Unpublished Thesis. Rhodes University, 130 p.

Beaumont, C., Quinlan, G.M., Stockmal, G.S., 1993. The evolution of the Western Interior Basin: causes, consequences and unsolved problems. Evolution of the Interior Western Basin, Caldwell, W.G.W., Kauffman, E.G. (Eds.), Geological Association of Canada, Special Paper 32, 97-117.

Beukes, N.J., Cairncross, B., 1991. A lithostratigraphic-sedimentological reference profile for the late Archaean Mozaan Goup, Pongola sequence: application to sequence stratigraphy and correlation with the Witwatersrand Supergroup. South African Journal of Geology 94(1), 44-69.

Bickle, M.J., Eriksson, K.A., Roberts, D.G., Hastings, D., Chadwick, B., Clarke, A.M., Ziegler, P.A., Osmaston, M.F., 1982. Evolution and Subsidence of Early Precambrian Sedimentary Basins [and Discussion] Philosophical Transactions of the Royal Society of London. Series A, Mathematical and Physical Sciences 305 (1489), 225-247.

Blair, T.C., McPherson, J., 1999. Grain-size and textural classification of coarse sedimentary particles. Journal of Sedimentary Research 69(1), 6-19.

Brock, B.B., Pretorius, D.A., 1964. Rand basin sedimentation and tectonics. The Geology of Some Ore Deposits of Southern Africa, Haughton, S.H. (Ed.), Vol. 1. Geological Society of South Arica, Johannesburg, 549-600.

Burke, K., Kidd, W.S.F., Kusky, T.M., 1986. Archean foreland basin tectonics in the Witwatersrand, South Africa. Tectonics 5, 439-456.

Burnett, M., 2008. Western Areas Gold Mine (WAGM) North Shaft. Unpublished thesis. University of the Witwatersrand, South Africa.

Butler, R.W.H., 1982. The terminology of structures in thrust belts. Journal of Structural Geology 4, 239-245.

Cabrera, L., Colombo, F., Marzo, M., Riba, O., 1986. Syntectonic intraformational unconformities in alluvial fan deposits, eastern Ebro Basin margins (NE Spain). Special Publications International Association of Sedimentologists 8, 259-271.

Catuneanu, O., 2001. Flexural partitioning of the Late Archaean Witwatersrand foreland system, South Africa. Sedimentary Geology 141-142 (2001), 95-112.Clevis, Q.J.W.A., 2003. Three-dimensional modelling of thrust-controlled foreland basin stratigraphy. Doctoral Thesis. University of Utrecht, 135 p.

Coward, M.P., Spencer, R.M., Spencer, C.E., 1995. Development of the Witwatersrand Basin, South Africa. Early Precambrian Processes, Coward, M.P., Ries, A.C. (Eds.). Geological Society Special Publications. The Geological Society, London, 243-269.

Crampton, S.L., Allen, P.A., 1995. Recognition of forebulge unconformities associated with early-stage foreland basin development: example from north Alpine foreland basin. American Association of Petrology Geological Bulletin 79, 1495-1514.

Dahlstrom, C.D.A., 1970. Structural geology in the eastern margin of the Canadian Rocky Mountains. Bulletin of Canadian Petroleum Geology 18, 332-406.

Dankert, B.T., Hein, K.A.A., 2010. Evaluating the structural character and tectonic history of the Witwatersrand Basin. Precambrian Research 177, 1-22.

DeCelles, P., Giles, K.A., 1996. Foreland Basin Systems. Basin Research 8 (2), 105-123.

Els, B.G., 1991. Placer formation during progradational fluvial degradation: The Late Archaean Middelvlei gold placer, Witwatersrand, South Africa. Economic Geology 86, 29-45.

Eriksson, P.G., Catuneanu, O, Els, B.G., Burnby, A.J., van Rooy, J.L., Popa, M., 2005. Kaapvaal Craton: Changing first- and second order controls on sea level from 3.0 Ga to 2.0 Ga. Sedimentary Geology 176, Issue 1-2, 121-148.

Eriksson, K.A., Turner, B.R., Vos, R.G., 1981. Evidence of tidal processes from the lower part of the Witwatersrand Supergroup, South Africa. Sedimentary Geology 29, 309-325.

Frimmel, H.E., 1994. Metamorphism of Witwatersrand Gold. Exploration and Mining Geology 3, 357-370.

Frimmel, H.E., 2019. The Witwatersrand Basin and Its Gold Deposits. The Archaean Geology of the Kaapvaal Craton, Southern Africa. Regional Geology Reviews, 255-275.

Frimmel, H.E., Groves, D.I., Kirk, J, Rutz, J., Chesley, J., Minter, W.E.L., 2005. The Formation and Preservation of the Witwatersrand Goldfields, the World's Largest Gold Province. Economic Geology One Hundredth Anniversary Volume. Littleton Co.: Society of Economic Geologists, Inc., 769-797.

Frimmel, H.E., Hallbauer, D.K., Gartz, V.H., 1999. Gold mobilizing fluids in the Witwatersrand Basin: composition and possible sources. Mineralogy and Petrology 66, 55-81.

Gartz, V., Frimmel, H., 1999. Complex Metasomatism of an Archaean Placer in the Witwatersrand Basin, South Africa: The Ventersdorp Contact Reef – A Hydrothermal Aquifer? Economic Geology 94, 689-706.

Germs, G.J.B., 1989. The Stratigraphy and Sedimentology of the EC Subzone at W.A.G.M. South Shaft: Geological and Economic Implications. Unpublished Report: JCI Geological Services Sub-Division Research Unit Report 235, 36 p.

Germs, G.J.B., 1990. EC Reef Stratigraphy and sedimentology as an aid to mine planning: A case study. Papers Presented at Geologists Technical Meeting on 17th August 1990. JCI Research Unit 5, 115-134.

Germs, G.J.B., Reynolds, L., 1991. Some Remarks on the "Shoreline" Phenomenon at WAGM North and South Shafts. Unpublished Report: JCI Geological Services Sub-Division Research Unit Report 253, 31 p.

Gibson, M.A.S., Jolley, S.J., Barnicoat, A.C., 2000. Interpretation of ultradeep levels on a 3-D Seismic Survey. The Leading Edge, 3 p.

Gibson, M., 2005. Interpretation of the 2003 South Deep 3D Seismic Survey. Unpublished Geoscience Solution Report for Placer Dome Western Areas Joint Venture, 64 p.

Gold Fields Limited., 2009. South Deep Gold Mine Technical Short Form Report, Resources and Reserves 2009. Report downloaded from the Gold Fields Limited website via URL https://www.goldfields.com/reports/rr_2009/tech_south.php.

Gold Fields Limited., 2011. Overview of the South Deep Project, Gold Fields Company. Presentation downloaded from the Gold Fields Limited website via URL https://www.goldfields.co.za/pdf/presentations_backup/2011/27092011_south_deep_project.pdf. 36 Slides.

Gold Fields Limited., 2013. Shareholders Plan. Public document downloaded from the Gold Fields Limited website via URL https://www.goldfields.com/reports/annual-report-2013/

Gumsley, A., Stamsnijder, J., Larsson, E., Söderlund, U., Naeraa, T., de Kock, M., Salacinska, A., Gaweda, A., Humbert, F. and Ernst, R., 2019. Neoarchean large igneous provinces on the Kaapvaal Craton in southern Africa re-define the formation of the Ventersdorp Supergroup and its temporal equivalents. Geological Society of America Bulletin, 132 (9-10), 1829-1844.

Harmer, R.E., Armstrong, R.A., 2000. New precise dates on the acid phase of the Bushveld and their implications. Abstract. Workshop on the Bushveld Complex, 18th-21st November 2000, Burgersfort. University of Witwatersrand, Johannesburg.

Harmony Gold Mines Limited., 2020. 2020 Mineral Resource and Mineral Reserves Report as at 30 June 2020. Harmony Annual Reports, 142 p.

Hayward, C.L., Reimold, W.U., Gibson, R.L., Robb, LJ., 2005. Gold mineralization within the Witwatersrand basin, South Africa: evidence for a modified placer origin, and the role of the Vredefort impact event. In:

MacDonald I, Boyce AJ, Butler IB, Herrington RJ, Polya DA (eds) Mineral deposits and earth evolution. Geological Society, London, Special Publication 248, 31–58.

Heller, P.L., Angevine, C.L. and Wilson, N.S., 1988. Two phase stratigraphic model of foreland basin sequences. Geology 16, 501-504.

Henkel, H., Reimold, W.U., 1998. Integrated geophysical modelling of a giant, complex impact structure: anatomy of the Vredefort Structure, South Africa. Tectonophysics 287, 1-20.

Jackson, M., and Hudec, M., 2017. Strike-Slip Salt-Tectonic Systems. In Salt Tectonics: Principles and Practice Cambridge: Cambridge University Press, 336-362.

Jordan, T.E. and Flemings, P.B., 1991. Large-Scale Statigraphic Architecture, Eustatic Variation, and Unsteady Tectonism: A Theoretical Evaluation. Journal of Geophysical Research 96, 6681-6699.

Kositcin, N. and Krapez, B., 2004. Relationships between detrital zircon age-spectra and the tectonic evolution of the Late Archaean Witwatersrand Basin, South Africa. Precambrian Research 129, 141-168.

Manzi, M.S.D., 2013. Application of 3D seismic analysis techniques to evaluate ore resources on Kloof, South Deeps and Driefontein gold mines, Witwatersrand Basin, South Africa. PhD Thesis, University of the Witwatersrand, Johannesburg, 208 p.

Manzi, M.S.D., Hein, K.A.A., King, N and Durrheim, J., 2013. Neoarchaean tectonic history of the Witwatersrand Basin and Ventersdorp Supergroup: New constraints from high-resolution 3D seismic reflection data. Tectonophysics 509, 94-105.

Marsh, J.S., 2006. The Dominion Group. The Geology of South Africa, Johnson, M.R., Anhaeusser, C.R. and Thomas, R.J. (Eds.). Geological Society of South Africa, Johannesburg and the Council for Geoscience. 149-154.

McCarthy, T.S., 1994. A Review of the Regional Structural Controls on the Occurrence and Character of the Ventersdorp Contact Reef. Economic Geology Research Unit Information Circular 276, 25 p.

McCarthy, T.S., 2006. The Witwatersrand Supergroup. The Geology of South Africa, Johnson, M.R., Anhaeusser, C.R. and Thomas, R.J. (Eds.). Geological Society of South Africa, Johannesburg and the Council for Geoscience. 155-186.

Minter, W.E.L., 1978. A sedimentological synthesis of placer gold, uranium and pyrite concentrations in Proterozoic Witwatersrand sediments. Fluvial Sedimentology, Miall, A.D., (Ed.). Canadian Society of Petroleum Geologists 5, 801-829.

Muntingh, D.J., Obermeyer, P.G., Swart, Q., 2005. Geology of the Upper Elsburg Reefs at South Deep Gold Mine. Unpublished Technical Audit Report for Placer Dome Western Areas Joint Venture, 66 p.

Myers, R.E., McCarthy, T.S., Stanistreet, I.G., 1989. A Tectono-sedimentary Reconstruction of the Development and Evolution of the Witwatersrand Basin, with Particular Emphasis on the Central Rand Group. Economic Geology Research Unit Information Circular No. 216, 39 pp.

Obermeyer, P.G., 2004. South Deep Structure Plan Construction. Internal Report for Placer Dome Western Areas Joint Venture. 19 p.

Obermeyer, P.G., 2005. Stratigraphy of South Deep – A description. Unpublished Inhouse Report for Placer Dome Western Areas Joint Venture. 12 p.

Ori, G.G, and Friend, P.F., 1984. Sedimentary basins formed and carried piggyback on active thrust sheets. Geology 12, 475-478.

Ortner, H., Kositz, A., Willingshoferm E. and Sokoutis, D., 2016. Geometry of growth strata in a transpressive fold belt in field and analogue model: Gosau Group at Muttekopf, Northern Calcareous Alps, Austria. Basin Res, 28, 731–751.

Osburn, K., Pretorius, H., Kock, D., King, N., Pillaye, R., Hlangwane, M., 2014. Enhanced geological modelling of the Upper Elsburg Reefs and VCR to optimise mechanised mine planning at South Deep Gold Mine. The Journal of the South African Institute of Mining and Metallurgy 114, 275-283.

Page, A.S., 1989. Sedimentological Study of the EC Local Sub-Zone in the 56 – 58 TM³ Area North Shaft Western Areas Gold Mine. Unpublished Report. JCI Geological Services Sub-Division Research Unit Report 238, 40 p.

Phillips, G.N. and Law, J.D.M., 1994. Metamorphism of the Witwatersrand gold fields: A review. Ore Geol. Rev. 9, 1-31.

Pretorius, D.A., 1974. The Nature of the Witwatersrand Gold-Uranium Deposits. University of the Witwatersrand Economic Geology Research Unit, Information Circular No.86, 54 p.

Pretorius, D.A., 1979. The Depositional Environment of the Witwatersrand Goldfields: A Chronological Review of Speculations and Observations. Geocongress 77: Geological Society of South Africa Special Publication 6, 33-55.

Riba, O., 1976. Syntectonic unconformities of the Alto Cardener, Spanish Pyrenees: a genetic interpretation. Sedimentary Geology 15, 213-233.

Robb, L.J., Davis, D.W., Kamo, S.L., 1990. U-Pb ages on single detrital zircon grains from the Witwatersrand Basin, South Africa: constraints on the age of sedimentation and on the evolution of granites adjacent to the basin. Journal of Geology 98, 311-328.

Robb, L.J., Davis, D.W., Kamo, S.L., 1991. Chronological framework of the Witwatersrand and environs: towards a time-constrained depositional model. South African Journal of Geology 93(1), 86-95.

Robb, L.J., Davis, D.W., Kamo, S.L., Meyer, F.M., 1992. Ages of altered granites adjoining the Witwatersrand Basin, with implications for the origin of gold and uranium. Nature 357, 672-680.

Robb, L.J., Meyer, F.M., 1995. The Witwatersrand Basin, South Africa: Geological framework and mineralisation processes. Ore Geology Reviews 10, 67-94.

Robb, L.J. and Robb, V.M., 1998. Gold in the Witwatersrand Basin in The Mineral Resources of South Africa, Wilson, M.G.C. and Anhaeusser, C.R. (Eds.). Handbook 16, 294-349.

SACS (South Africa Committee for Stratigraphy. Task Group for the Witwatersrand Supergroup), 2006. A revised stratigraphic framework for the Witwatersrand Supergroup. Council for Geoscience. 7 p.

Scoates J.S., Friedman R.M., 2008. Precise age of the platiniferous Merensky Reef, Bushveld Complex, South Africa, by the U-Pb zircon chemical abrasion ID-TIMS technique, Econ. Geol., 103, 465–471.

Shi, X., Liu, S. and Lin, C., 2019. Growth structures and growth strata of the Qianjiadian Basin in the western Yanshan fold and thrust belt, North China. Science China Earth Science, 62, 20 p.

Sibanye Stillwater., 2019. Mineral Resources and Mineral Reserves Report 2019. Sibanye Stillwater Annual Reports, 169 p.

Smith, A. and Beukes, N., 2018. Free oxygen and microbial activity in Mesoarchean oceans: a sequence stratigraphic case study of the iron-rich units of the Witwatersrand-Pongola basin of southern Africa. EGU General Assembly Conference Abstracts. 20, 18484.

Stanistreet, I.G., McCarthy, T.S., 1991. Changing tectono-sedimentary scenarios relevant to the development of the late Archaean Witwatersrand Basin. Journal of African Earth Sciences 13, 65-81.

Suriano, J., Limarino, C.O., Tedesco, A.M., Alonso, M.S., 2015. Sedimentation model of piggyback basins: Cenozoic examples of San Juan Precordillera, Argentina from Geodynamic Processes in the Andes of Central Chile and Argentina. Geological Society, London, Special Publications 399, 221-244.

Tankard, A.J., Jackson, M.P.A., Eriksson, K.A., Hobday, D.K., Hunter, D.R., Minter, W.E.L., 1982. Crustal Evolution of Southern Africa: 3.8 Billion Years of Earth History. Springer-Verlag.

Tinker, J., de Wit, M., Grotzinger, J., 2002. Seismic stratigraphic constraints on Neoarchean-Paleoproterozoic evolution of the western margin of the Kaapvaal Craton, South Africa. South African Journal of Geology 105, 107-134.

Tucker, R.F., 1980. The sedimentology and mineralogy of the Composite Reef on Cooke Section, Randfontein Estates Gold Mine, Witwatersrand, South Africa. Unpublished MSc thesis, University of the Witwatersrand, Johannesburg, 335 p.

Tucker, R.F., Viljoen, R.P., 1986. The geology of the West Rand Goldfields, with special reference to the southern limb. Mineral Deposits of Southern Africa 1, Anhaeusser, C.R., Maske, S., (Eds.). The Geological Society of South Africa, 649-688.

Tucker, R.F., Viljoen, R.P. and Viljoen, M.J., 2016. A Review of the Witwatersrand Basin – The World's Greatest Goldfield. Episodes 39(2), 105-133.

Udden, J.A., 1914. Mechanical composition of clastic sediments. Geological Society of America, Bulletin 5, 655-744.

Vermaakt, D.T. and Chunnett, I.E., 1994. Tectono-Sedimentary Processes which Controlled the Deposition of the Ventersdorp Contact Reef within the West Wits Line, in Proceedings of XV CMMI Congress (Johannesburg, 1994). 3, 117–130.

Viehmann, S., Bau, M., Smith, A.J.B., Beukes, N.J., Dantas, E.L., Bühn, B., 2015. The reliability of ~2.9 Ga old Witwatersrand banded iron formations (South Africa) as archives for Mesoarchean seawater: Evidence from REE and Nd isotope systematics. Journal of African Earth Sciences, 111, 322-334.

Wallmach, T., Meyer, F.M., 1990. A petrogenetic grid for metamorphosed aluminous Witwatersrand shales. South African Journal of Geology 93, 93-102.

Wentworth, C.K., 1922. A scale of grade and class terms for clastic sediments. Journal of Geology 30, 377-392.

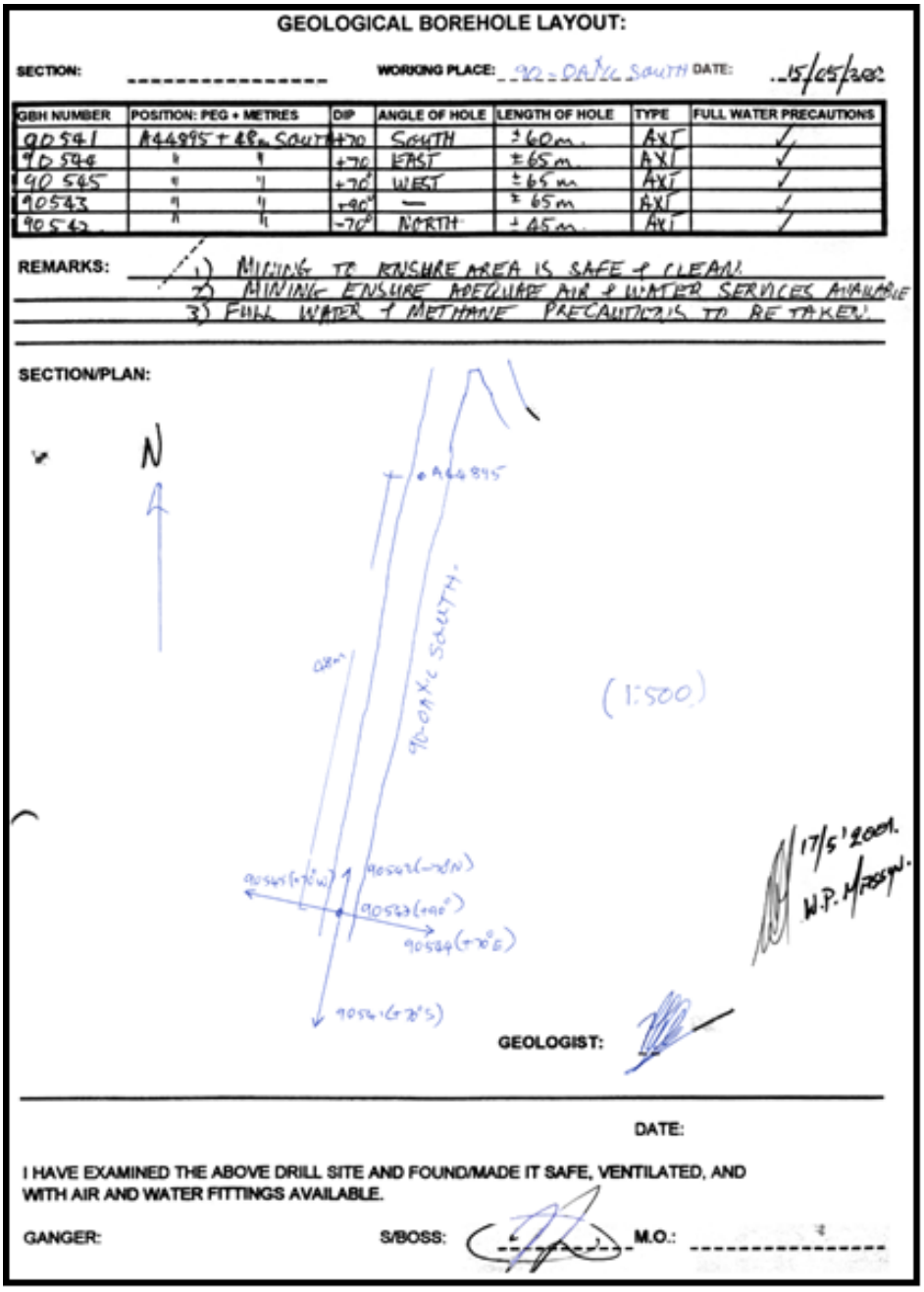
Wentworth, C.K., 1935. The terminology of coarse sediments. National Research Council, Bulletin 98, 225-246.

Winter, H.D., 1987. A cratonic foreland model for the Witwatersrand Basin development in a continental back-arc, plate-tectonic setting. South African Journal of Geology 91(4), 409-427.

Winter, H. de la R., Brink, M.C., 1991. Chronostratigraphic subdivision of the Witwatersrand Basin based on a Western Transvaal composite column. South African Journal of Geology 94, 191-203.

APPENDIX 1

SDGM Structure Plan Construction



GEOLOGICAL BOREHOLE LAYOUT:

SECTION: ---------- WORKING PLACE: 92 = DAVIS SOUTH DATE: 15/05/2001

GBH NUMBER	POSITION: PEG + METRES	DIP	ANGLE OF HOLE	LENGTH OF HOLE	TYPE	FULL WATER PRECAUTIONS
90541	A44895 + 48m SOUTH	-70	SOUTH	± 60m.	AXT	✓
90546	" "	+70	EAST	± 65m.	AXT	✓
90545	" "	+70	WEST	± 65 m	AXT	✓
90543	" "	+90	—	± 65m	AXT	✓
90542	" "	-70	NORTH	± 45m.	AXT	✓

REMARKS:
1) MINING TO ENSURE AREA IS SAFE & CLEAN.
2) MINING ENSURE ADEQUATE AIR & WATER SERVICES AVAILABLE
3) FULL WATER & METHANE PRECAUTIONS TO BE TAKEN.

SECTION/PLAN:

N

A44895

90 DAVIS SOUTH.

(1:500)

90543(090°)

GEOLOGIST:

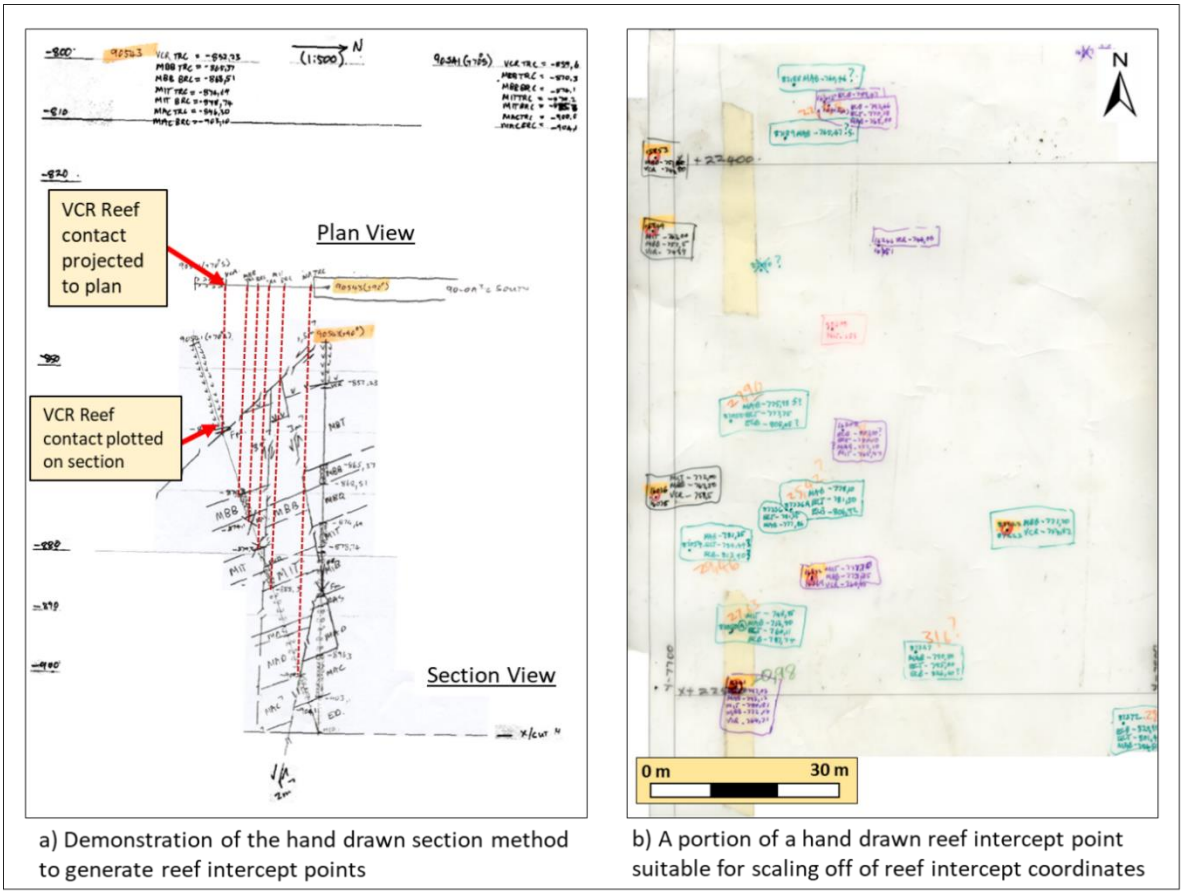
17/5/2001.
W.P. MASON.

DATE:

I HAVE EXAMINED THE ABOVE DRILL SITE AND FOUND/MADE IT SAFE, VENTILATED, AND WITH AIR AND WATER FITTINGS AVAILABLE.

GANGER: S/BOSS: M.O.: ----------

Figure 81: Typical borehole layout as sourced from a borehole layout file (Obermeyer, 2004). Blue arrows indicate planned borehole azimuths from a planned borehole collar position. Each label represents a borehole number and a planned dip (permission granted by Goldfields to reproduce).



a) Demonstration of the hand drawn section method to generate reef intercept points

b) A portion of a hand drawn reef intercept point suitable for scaling off of reef intercept coordinates

Figure 82: Borehole collars for each borehole are checked relative to survey elevations on plan (Obermeyer, 2004) (permission granted by Goldfields to reproduce).

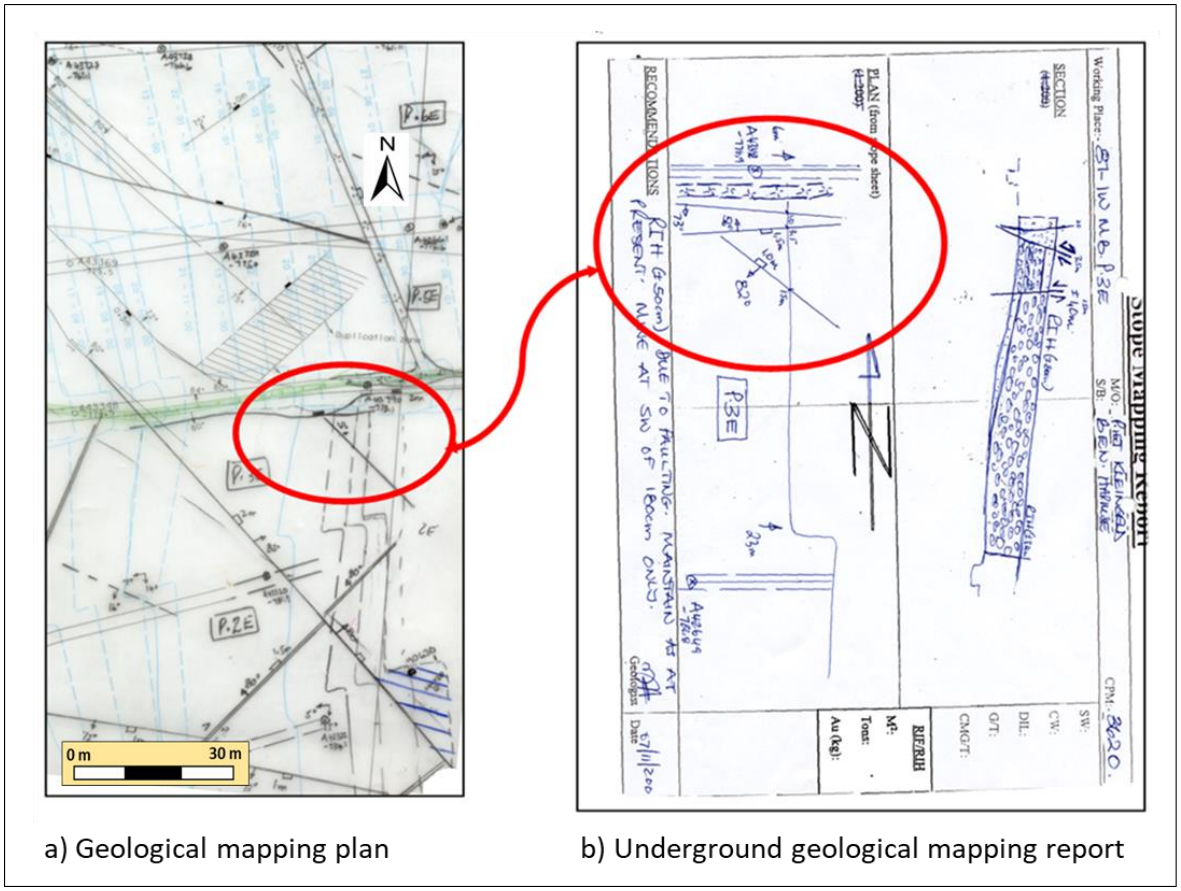
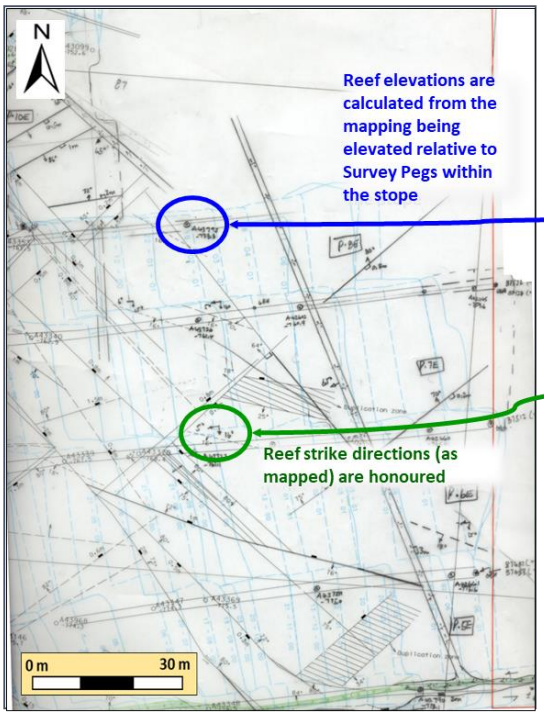
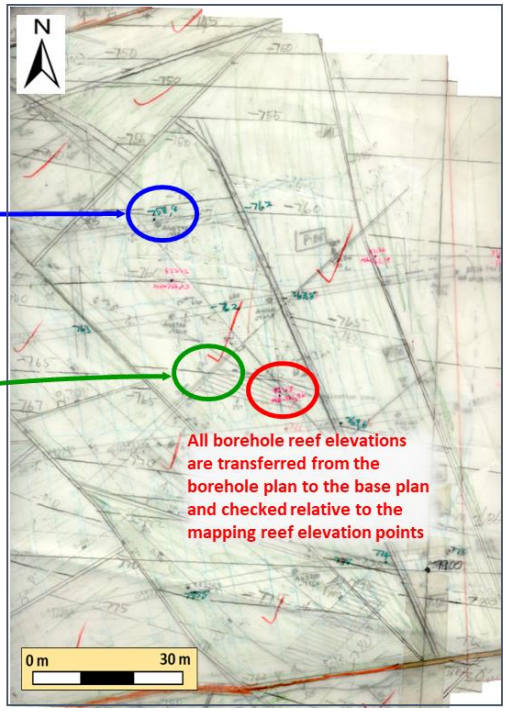


Figure 83: An example of a) a geological mapping plan and a corresponding b) underground mapping report showing some inconsistency in transfer of data (Obermeyer, 2004) (permission granted by Goldfields to reproduce).



a) Plotted reef strikes and survey peg elevations on a stoping plan are transferred to the base plan



b) Structure base plan with transferred reef strikes and survey peg elevations. Note the red ticks in each structure polygon denoting validation

Figure 84: a) Measured and plotted reef strikes with peg elevations. b) Structure base plan with transferred reef strike and survey peg elevation data (Obermeyer, 2004b).

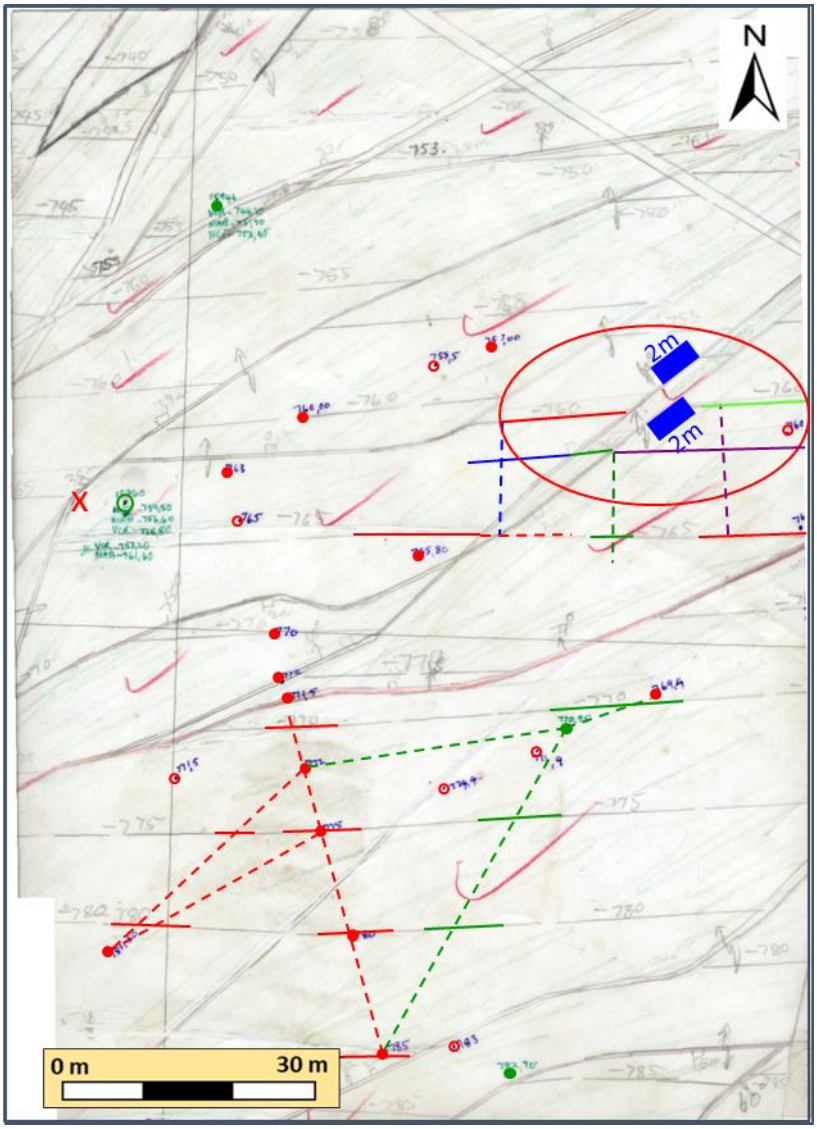


Figure 85: The strike of the reef contours was calculated as a set of simple 3-point problems, while neighbouring fault block contours were correlated by applying mapped throws to the bounding faults (Obermeyer, 2004) (permission granted by Goldfields to reproduce).

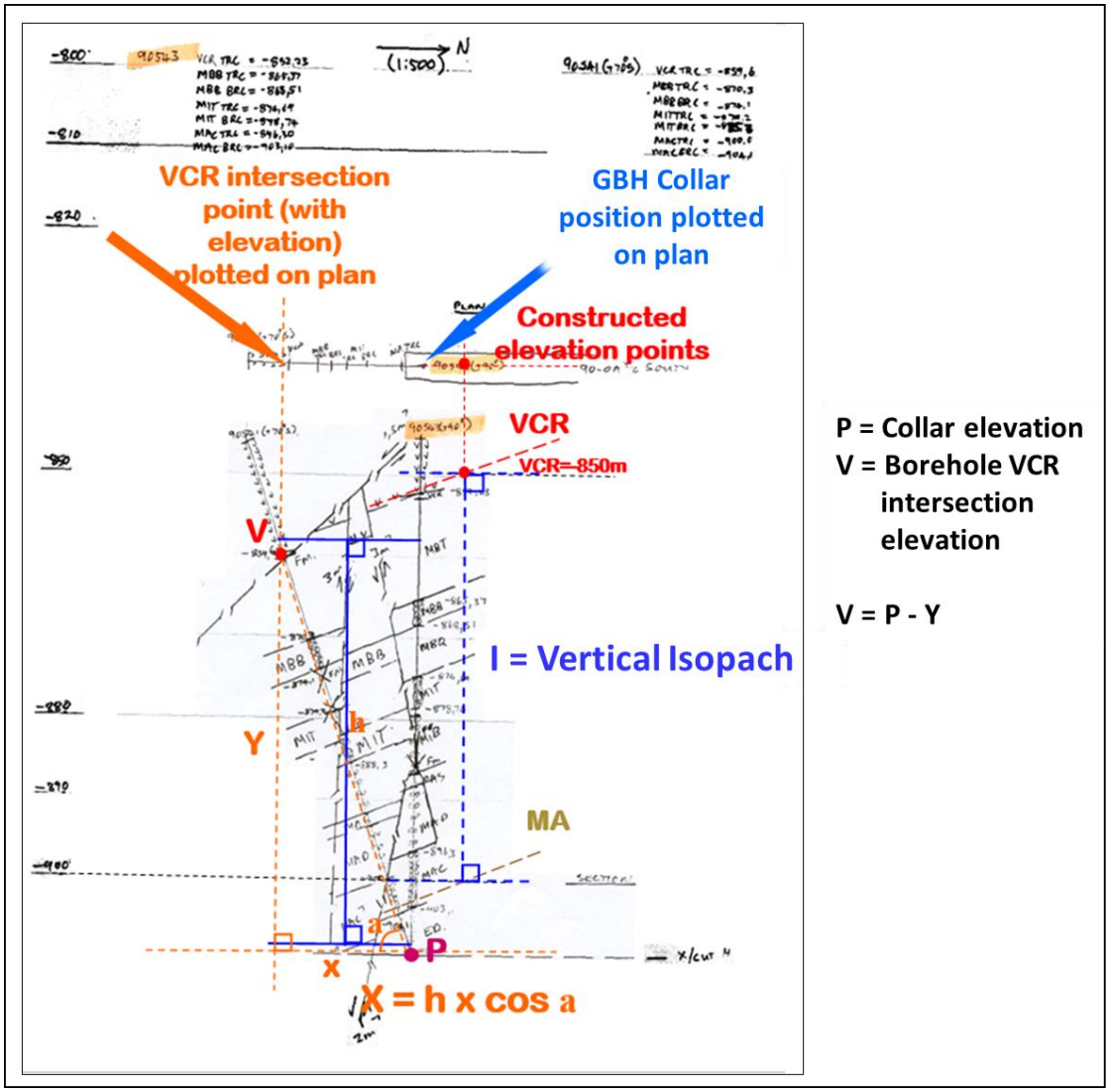


Figure 86: Vertical projection distances for structures and contours were calculated using the difference in elevations between the borehole intersections on the new plan and the base plan (modified from Obermeyer, 2004) (permission granted by Goldfields to reproduce).

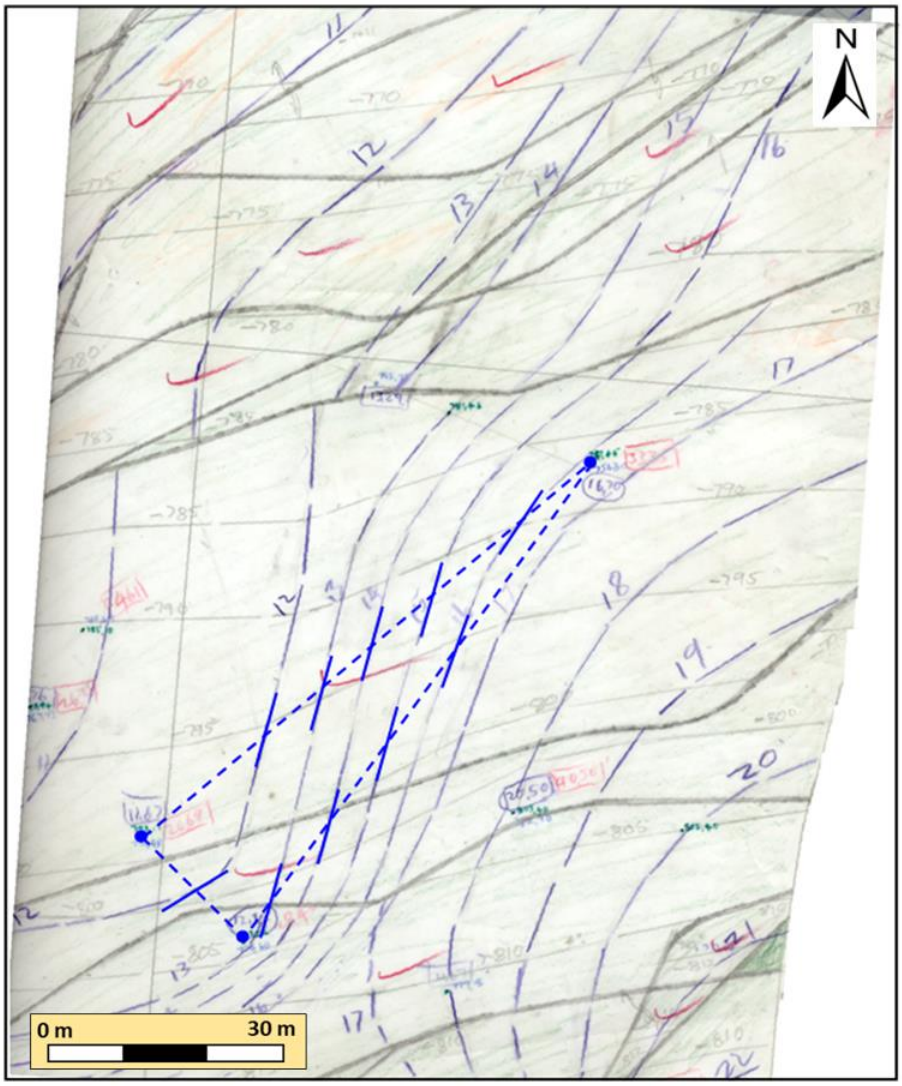


Figure 87: The vertical projection distances, calculated from the boreholes were transferred to the new plan, from the borehole plan as points. These points were triangulated and isolines, or vertical isopachs, were constructed (Obermeyer, 2004) (permission granted by Goldfields to reproduce).

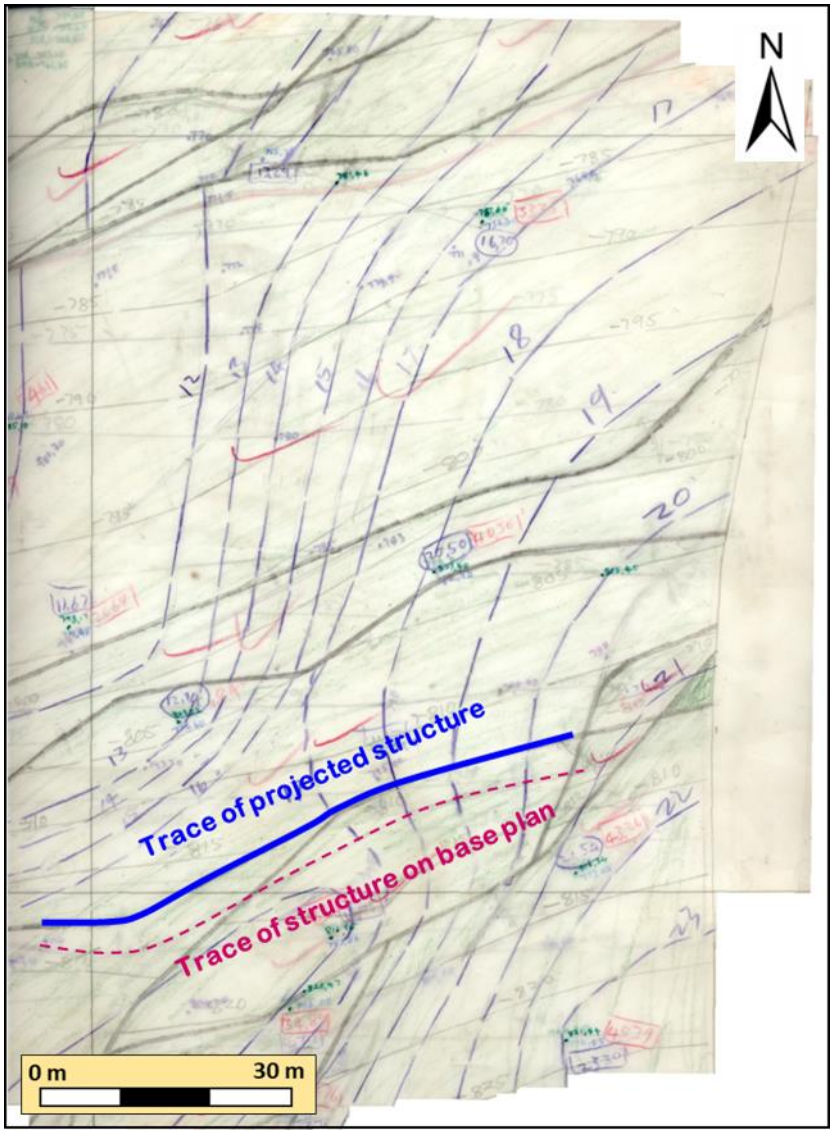


Figure 88: The vertical isopachs gave vertical projection distances between the base plan and the next projected plan. The horizontal off-sets of the faults were calculated by means of trigonometry and the resultant trace line plotted (modified after Obermeyer, 2004) (permission granted by Goldfields to reproduce).

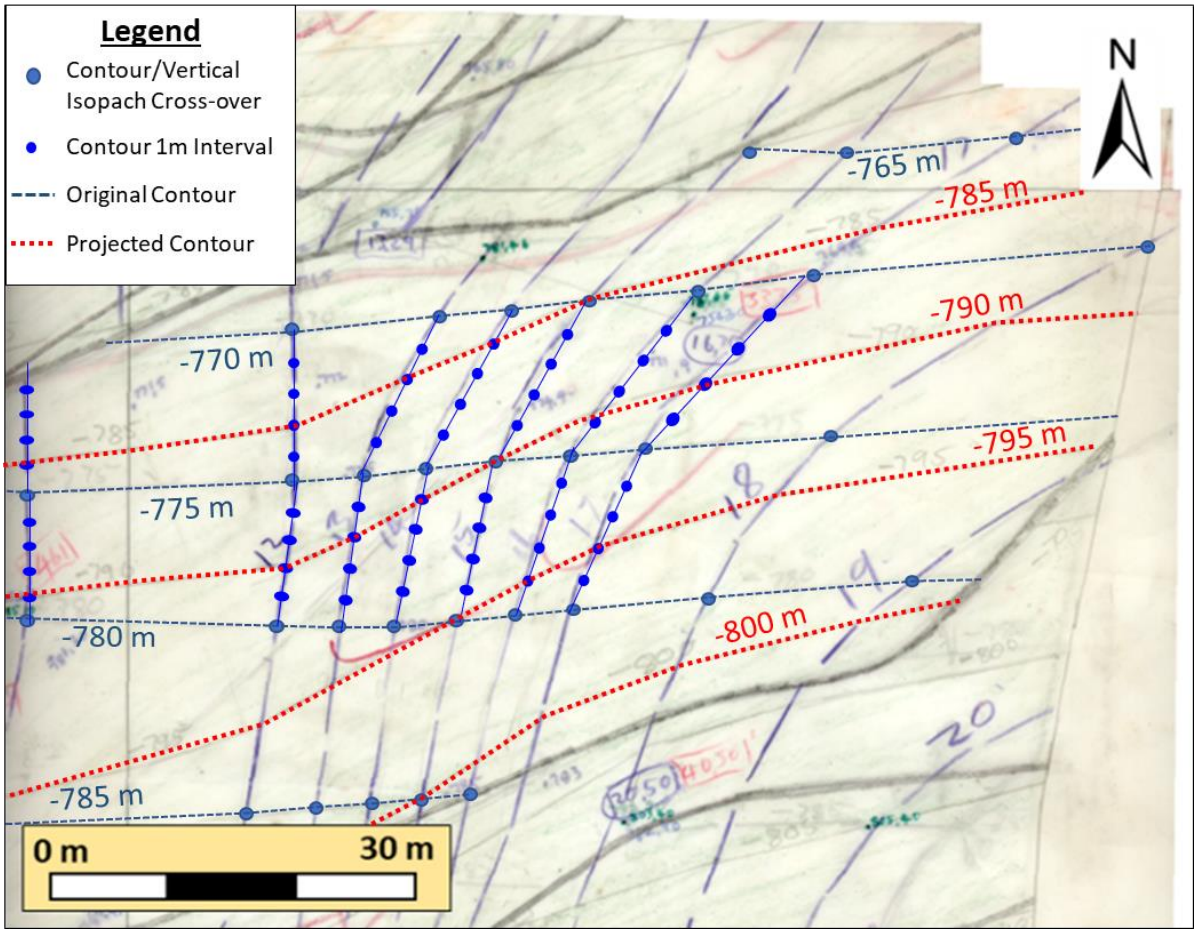


Figure 89: Projection and construction methodology of overlying or underlying beds to ensure accurate volumetrics (adapted from Obermeyer, 2004) (permission granted by Goldfields to reproduce).

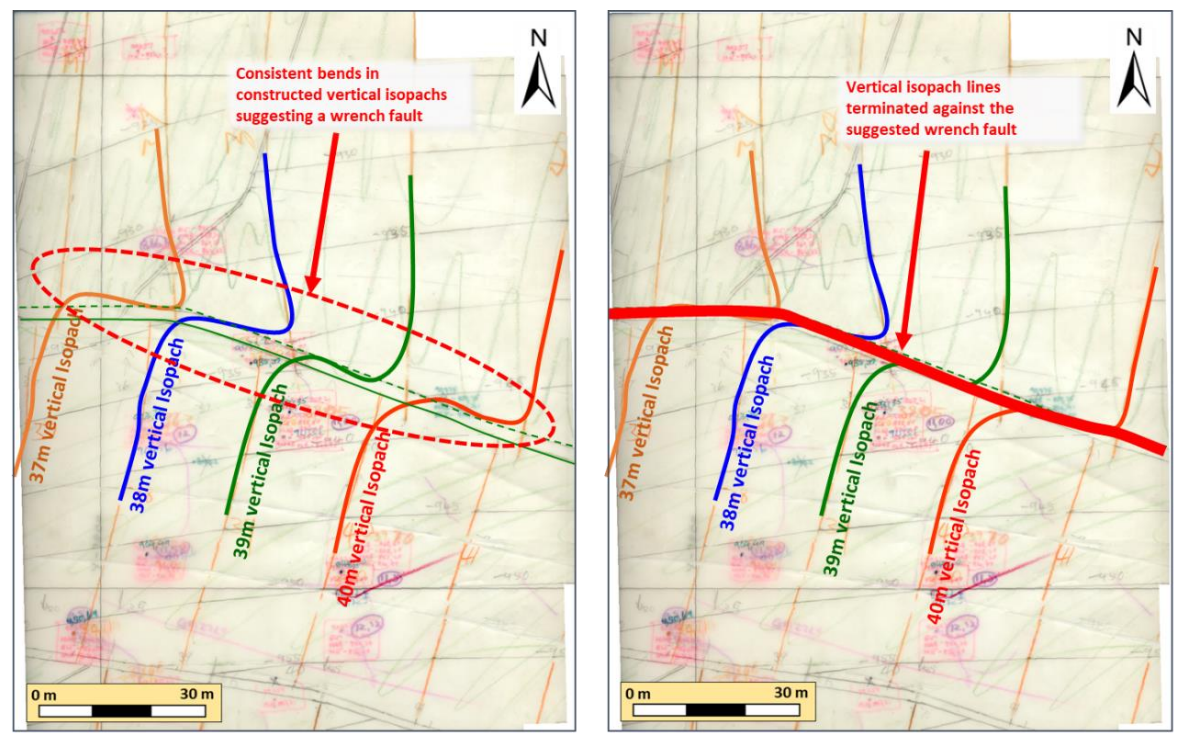
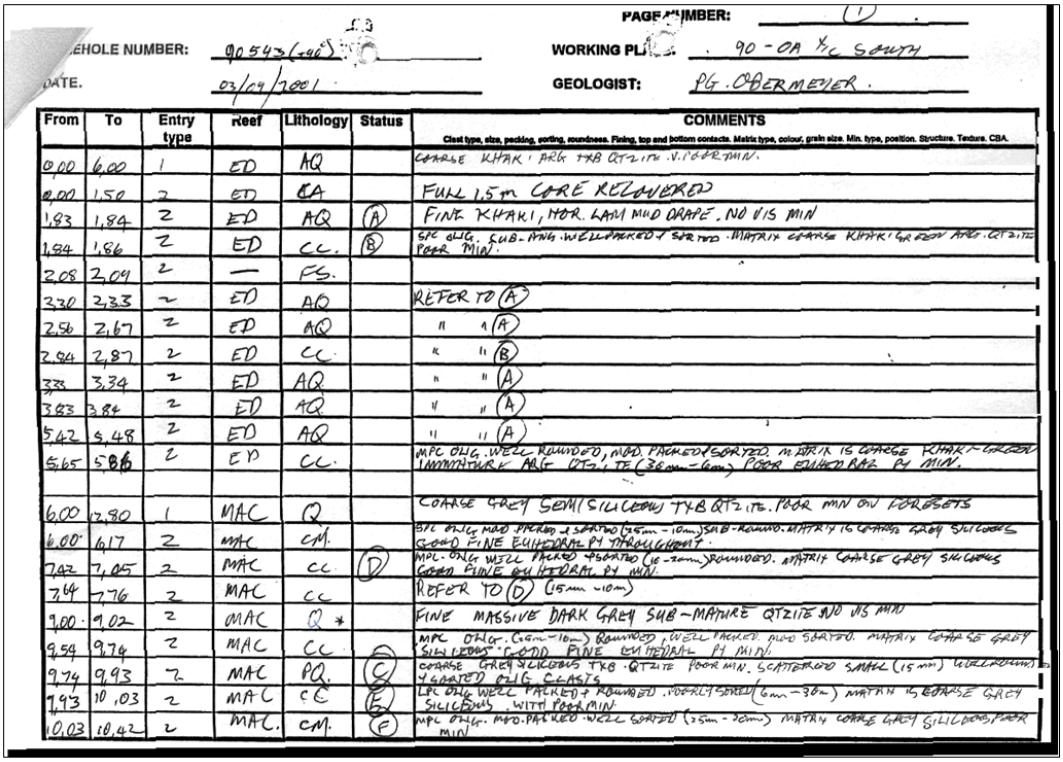


Figure 90: Identification and interpretation of wrench faults at SDGM (modified after Obermeyer, 2004) (permission granted by Goldfields to reproduce).



PAGE NUMBER: 1

DRILLHOLE NUMBER: 90543 (-90°) 13

WORKING PL: 90 - OA ½ C SOUTH

DATE: 03/09/2001

GEOLOGIST: PG. OBERMEYER.

From	To	Entry type	Reef	Lithology	Status	COMMENTS (Clast type, size, packing, sorting, roundness. Fining, top and bottom contacts. Matrix type, colour, grain size. Min. type, position. Structure. Texture. CBA.)
0,00	6,00	1	ED	AQ		COARSE KHAKI ARG TXB QTZITE. V. POOR MIN.
0,00	1,50	2	ED	CA		FULL 1,5m CORE RECOVERED
1,83	1,84	2	ED	AQ	(A)	FINE KHAKI, MOR. LAM MUD DRAPE. NO VIS MIN
1,84	1,86	2	ED	CC.	(B)	SPC CLG. SUB-ANG. WELL PACKED & SORTED. MATRIX COARSE KHAKI/GREEN ARG. QTZITE POOR MIN.
2,08	2,09	2	—	FS.		
2,30	2,33	2	ED	AQ		REFER TO (A)
2,56	2,67	2	ED	AQ		" " (A)
2,84	2,87	2	ED	CC.		" " (B)
3,33	3,34	2	ED	AQ		" " (A)
3,83	3,84	2	ED	AQ		" " (A)
5,42	5,48	2	ED	AQ		" " (A)
5,65	5,86	2	ED	CC.		MPC CLG. WELL ROUNDED, MOD. PACKED & SORTED. MATRIX IS COARSE KHAKI-GREEN IMMATURE ARG QTZ. ITE (3mm-6mm) POOR BANDED BAR BY MIN.
6,00	12,80	1	MAC	Q		COARSE GREY SEMI SILICEOUS TXB QTZITE. POOR MIN ON FORESETS
6,00	6,17	2	MAC	CM.		BPC CLG MOD PACKED & SORTED (25mm-10m) SUB-ROUND. MATRIX IS COARSE GREY SILICEOUS GOOD FINE EUHEDRAL PY MIN ALONG FRACT.
7,02	7,05	2	MAC	CC	(D)	MPC-CLG WELL PACKED SORTED (10-20mm) ROUNDED. MATRIX COARSE GREY SILICEOUS GOOD FINE EUHEDRAL PY MIN.
7,64	7,76	2	MAC	CC		REFER TO (D) (15mm-10m)
9,00	9,02	2	MAC	Q *		FINE MASSIVE DARK GREY SUB-MATURE QTZITE NO VIS MIN
9,54	9,74	2	MAC	CC	(C)	MPC CLG. (25m-10m) ROUNDED, WELL PACKED MOD SORTED. MATRIX COARSE GREY SILICEOUS. GOOD FINE EUHEDRAL PY MIN.
9,74	9,93	2	MAC	PQ.	(G)	COARSE GREY SILICEOUS TXB. QTZITE POOR MIN. SCATTERED SMALL (15mm) WELL ROUNDED & SORTED CLG. CLASTS
9,93	10,03	2	MAC	CC	(F)	LPC CLG WELL PACKED & ROUNDED. POORLY SORTED (6mm-30m) MATRIX IS COARSE GREY SILICEOUS. WITH POOR MIN
10,03	10,42	2	MAC.	CM.	(E)	MPC CLG. MOD. PACKED. WELL SORTED (25mm-30mm) MATRIX COARSE GREY SILICEOUS, POOR MIN

Figure 91: Typical historical SDGM handwritten drillhole lithology log (Obermeyer, 2004) (permission granted by Goldfields to reproduce).

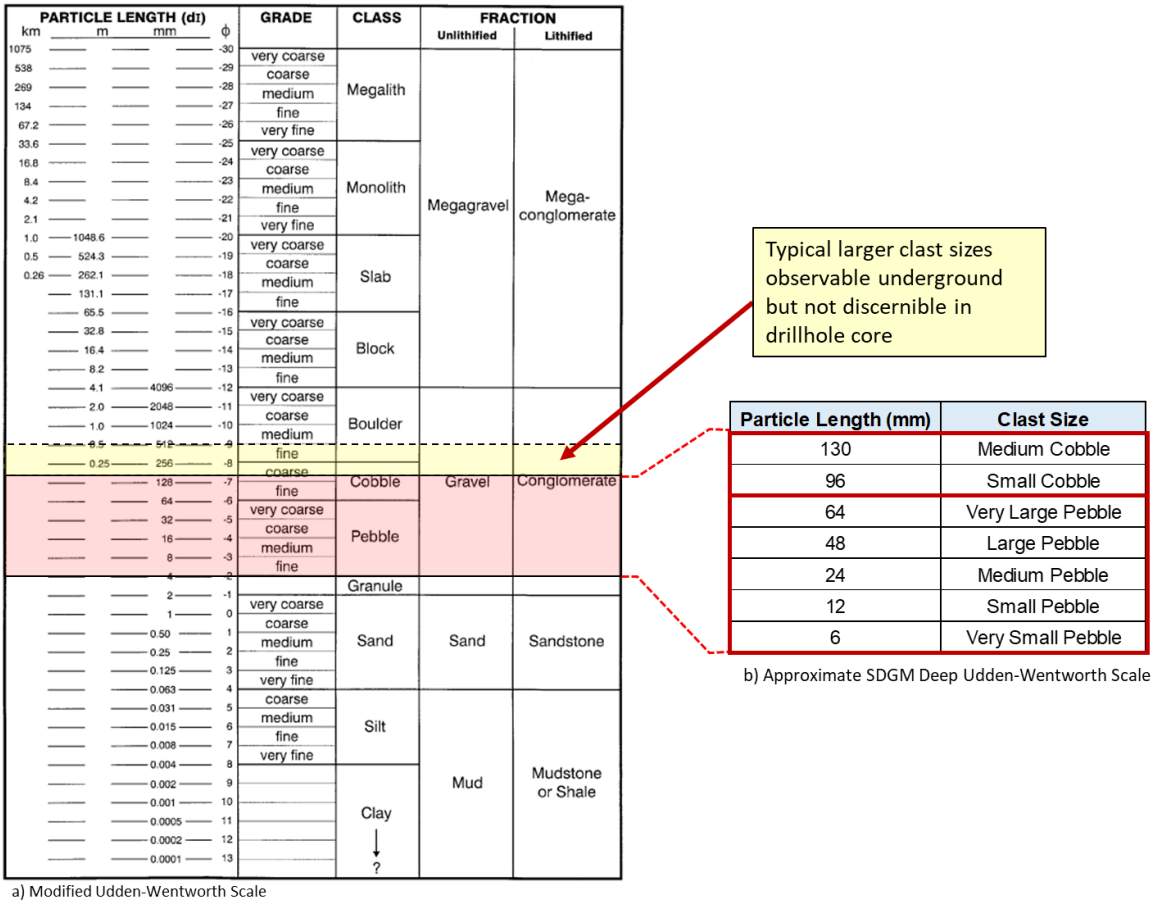


Figure 92: a) Modified Udden-Wentworth scale to better differentiate coarse sediment (modified from Blair and McPherson (1999). b) A reconstructed modified Udden-Wentworth scale as historically interpreted at SDGM for core logging.

APPENDIX 2

Results for the Remainder of the Upper Elsburg Beds

a) **ECBAQ**

i) ECBAQ Bed Height

Figure 93**Error! Reference source not found.** presents the palinspastic reconstruction for bed height for the ECBAQ. The ECBAQ thins from east to west towards the Upper Elsburg Subsub-outcrop, with the rate of westward thinning in Block 1 in the north being lower than along the balance of the sub-outcrop to the south. Maximum bed height (>12.5 m to 15 m) is reached along the northern margin of Fargo Wrench approximately 800 m away from the sub-outcrop. A general thickening trend from north to south also occurs. Data density is high within a strip of 1.5 km running parallel to the sub-outcrop. East of this zone interpretation becomes speculative. Higher bed height trends (excluding the westward thinning) run sub-parallel (NW-SE) in the north to oblique (NNW-SSE) relative to the sub-outcrop in the south.

ii) ECBAQ Percentage Conglomerate

The palinspastic reconstruction for percentage conglomerate for the ECBAQ is presented in Figure 94**Error! Reference source not found.**. Percentage Conglomerateconglomerate appears to generally decrease to the east especially in the north from Block 1 to Block 3. Interpretation is only effective to ±1.5 km east of sub-outcrop due to decrease in data density. Trends in the percentage conglomerate appear oriented preferentially NNW to -SSE over BlocksBlock 1 in the north through to Block 5 in the Southsouth.

Lower bed height appears to result in a higher percentage conglomerate. Towards the south in Block 5, the higher bed height appears to result in lower percentage conglomerate.

iii) ECBAQ Average and Maximum Clast Size

The ECBAQ is primarily quartzitic in nature containing very little conglomerate. Interpretation of average (Figure 95**Error! Reference source not found.**) and maximum clast (Figure 96**Error! Reference source not found.**) is limited. However, a NNW to -SSE trend in average clast size across 90L Wrench and Fargo Wrench is observable and seldom exceeds 24 mm in average clast size.

NNW to -SSE trends for maximum clast size are discernible in Block 1 as well as across the 90L Wrench and Fargo Wrench combination. Maximum clast size (>36mm36 mm to 48mm48 mm) occurs in Block 5.

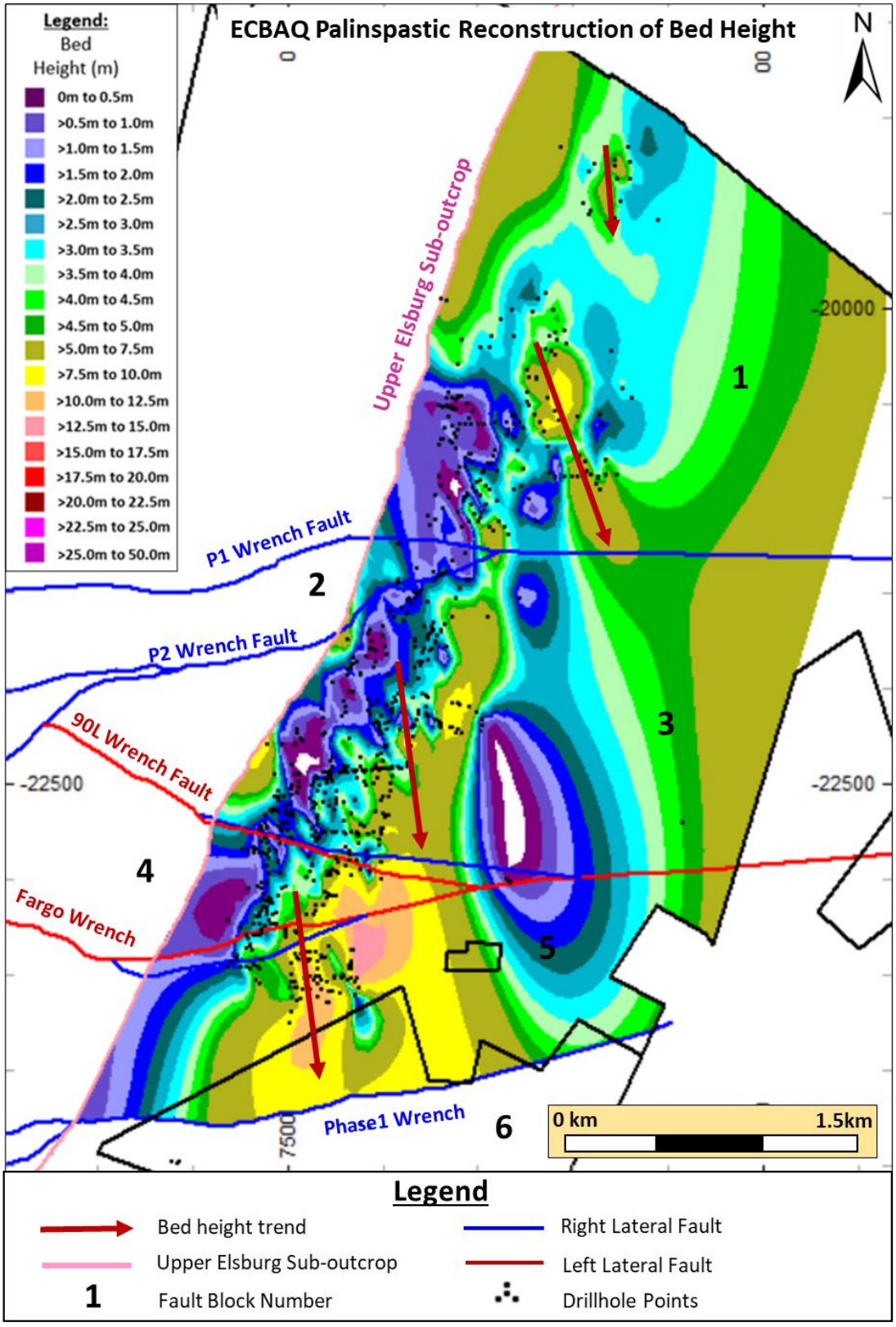


Figure 93: Palinspastic bed height reconstruction for ECBAQ.

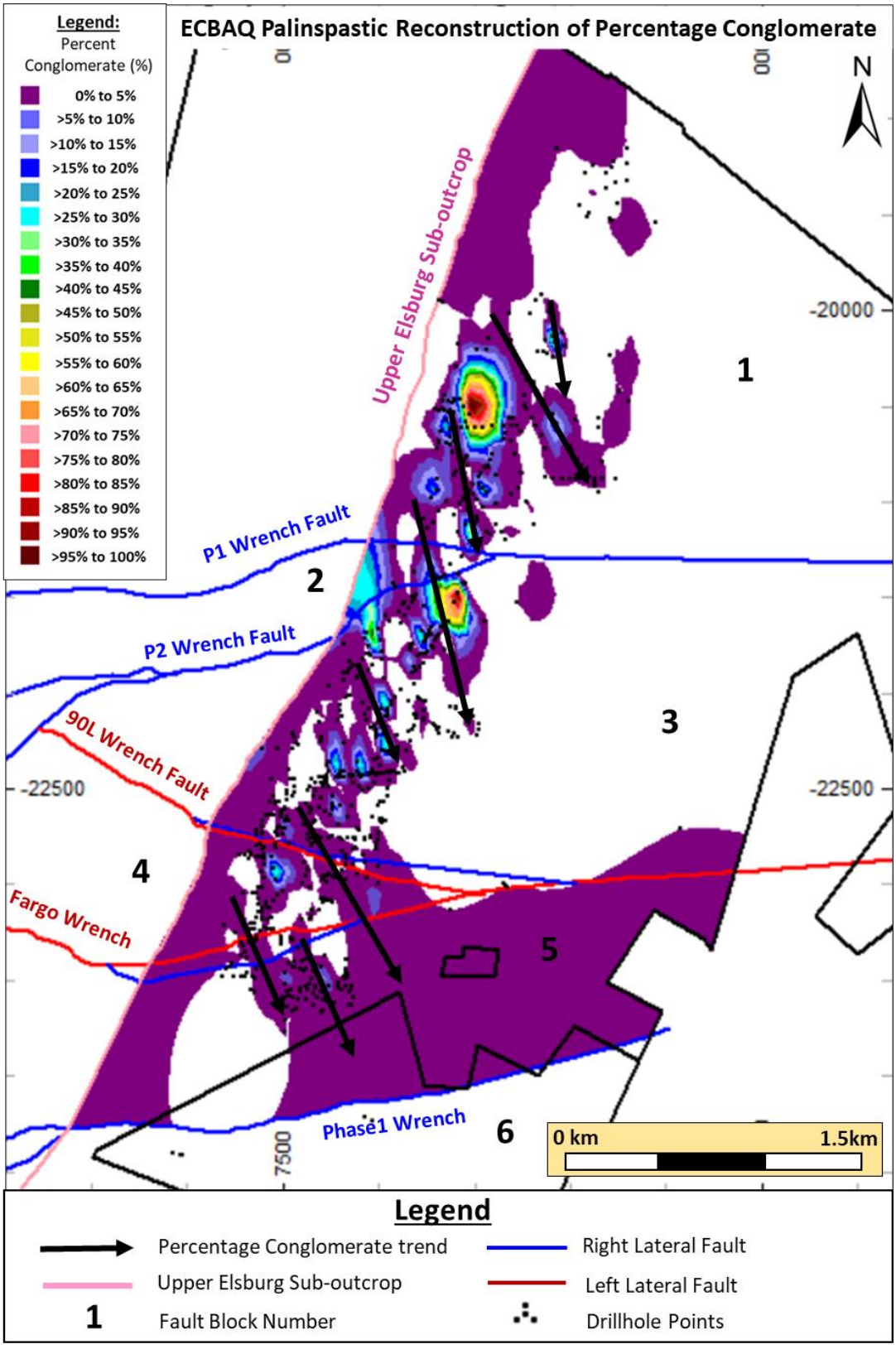


Figure 94: Palinspastic percentage conglomerate reconstruction for ECBAQ.

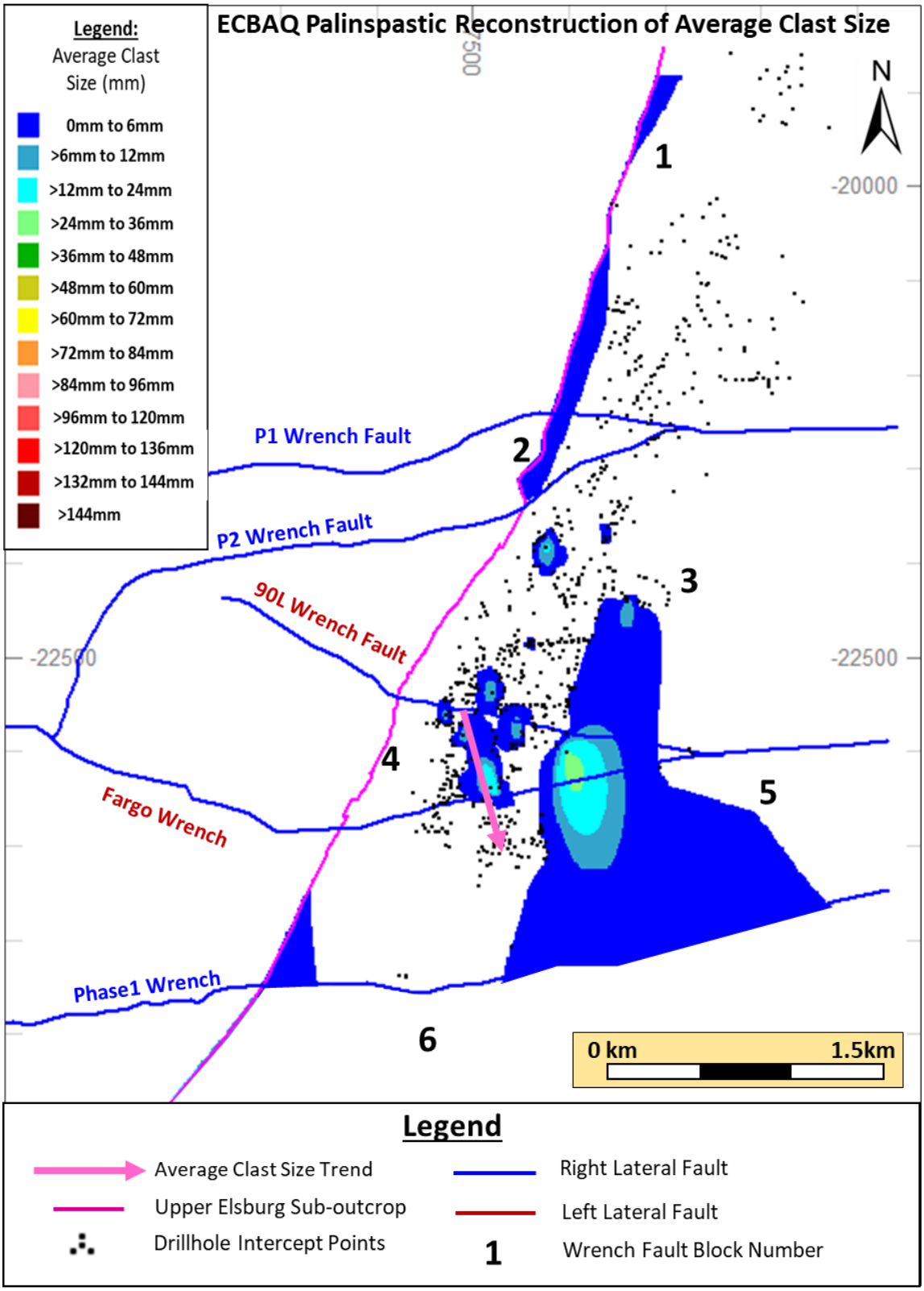


Figure 95: Palinspastic average clast size reconstruction for ECBAQ.

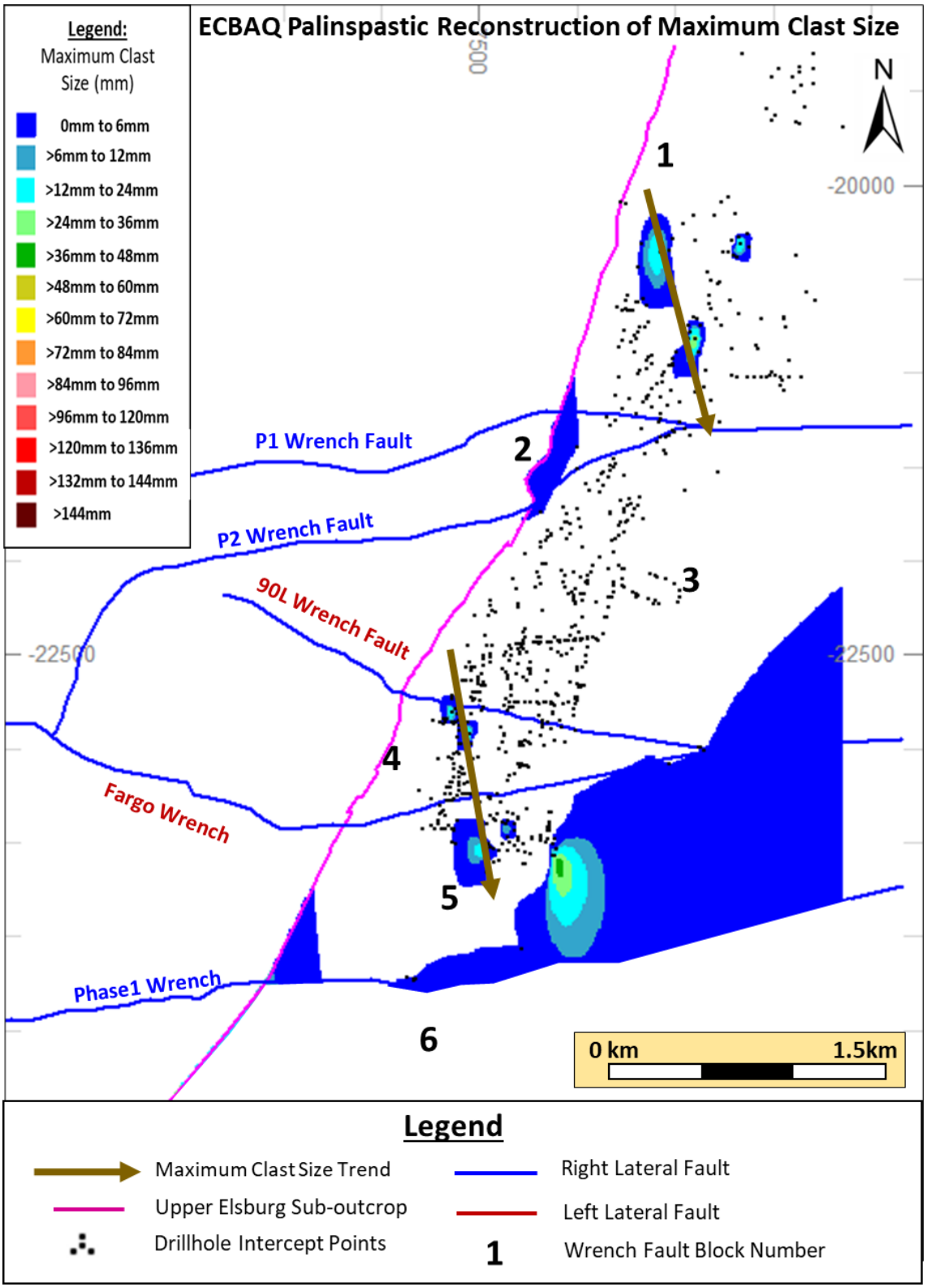


Figure 96: Palinspastic maximum clast size reconstruction for ECBAQ.

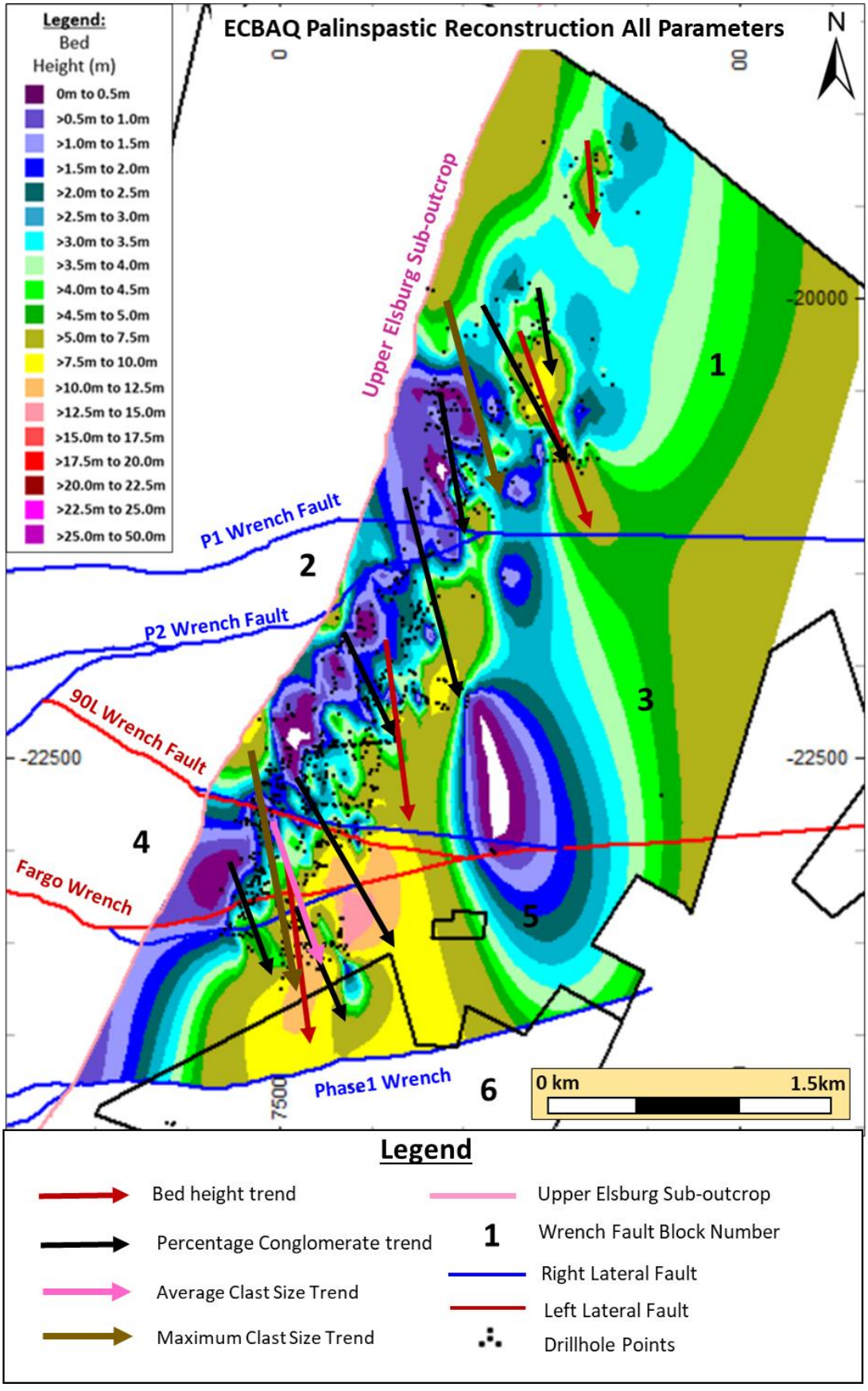


Figure 97: Palinspastic Reconstruction for the ECBAQ - All Parameters

iv) ECBAQ Detailed Plots

Figure 98**Error! Reference source not found.** presents an enlarged section of the a) Bedbed height and b) percentage conglomerate plan for the ECBAQ including Blocks 1, 2, and 3. In Figure 98 a) a zone of lower bed height crosses over P1 Wrench and terminates against P2 Wrench. This zone of thinning appears associated with a lower percentage conglomerate. An apparent dislocation of ± 300m300 m appears to offset the thicker zone in BlockBlocks 1 and 2 from that in Block 3 implying inactivity on P1 Wrench, while possible movement on P2 Wrench as encountered in the ECBA. Timing of this dislocation is not clear, however syn-sedimentary activity should not be excluded. Nature of movement is also not discernible, though an apparent right-lateral dislocation (±300 m) might have occurred. In addition, movement post -ECBA deposition might have been vertical (up to the north) across P2 Wrench prior to or concurrent with ECB erosion and subsequent deposition.

Figure 99 indicatesillustrates a zone of thicker ECBAQ associated with a higher percentage conglomerate just south of P2 Wrench indicate, indicating a localised deepened channel. The northern margin of Block 4 up against 90L Wrench is highlighted by change from a higher bed height in Block 4 to a lower bed height in Block 3 to the north. No apparent dislocations across faults isare discernible.

A trend line of thinner ECBAQ running parallel to the Upper Elsburg Subcropsub-outcrop in Figure 99 a) appears associated with a zone of no conglomerate development in Figure 99 b). This conglomerate -poor strip parallel to the Upper Elsburg Subsub-outcrop is bordered to the west (up against the Subsub-outcrop) and to the east (high-lightedhighlighted by a red polygon) by zones characterised by higher bed height and increased conglomeratic development. Timing of its formation could be related to post-deposition and subsequent erosion and deposition of the ECB.

Figure 100 presents successive apparent right-lateral offsets of zones of lower and higher bed height of ±200 m and ±100 m dislocation across the 90L Wrench and Fargo Wrench, respectively. Timing of this dislocation is unclear due to the erosion of the ECBAQ by the overlying ECB. Winnowing is not evident within this thinner zone, as percentage conglomerate is generally very low in this zone. This couldmay imply that variable erosion of the blocks might have resulted from successive uplift of Block 4 relative to Block 3 and Block 5 relative to Block 4 during erosion by and deposition of the EC.

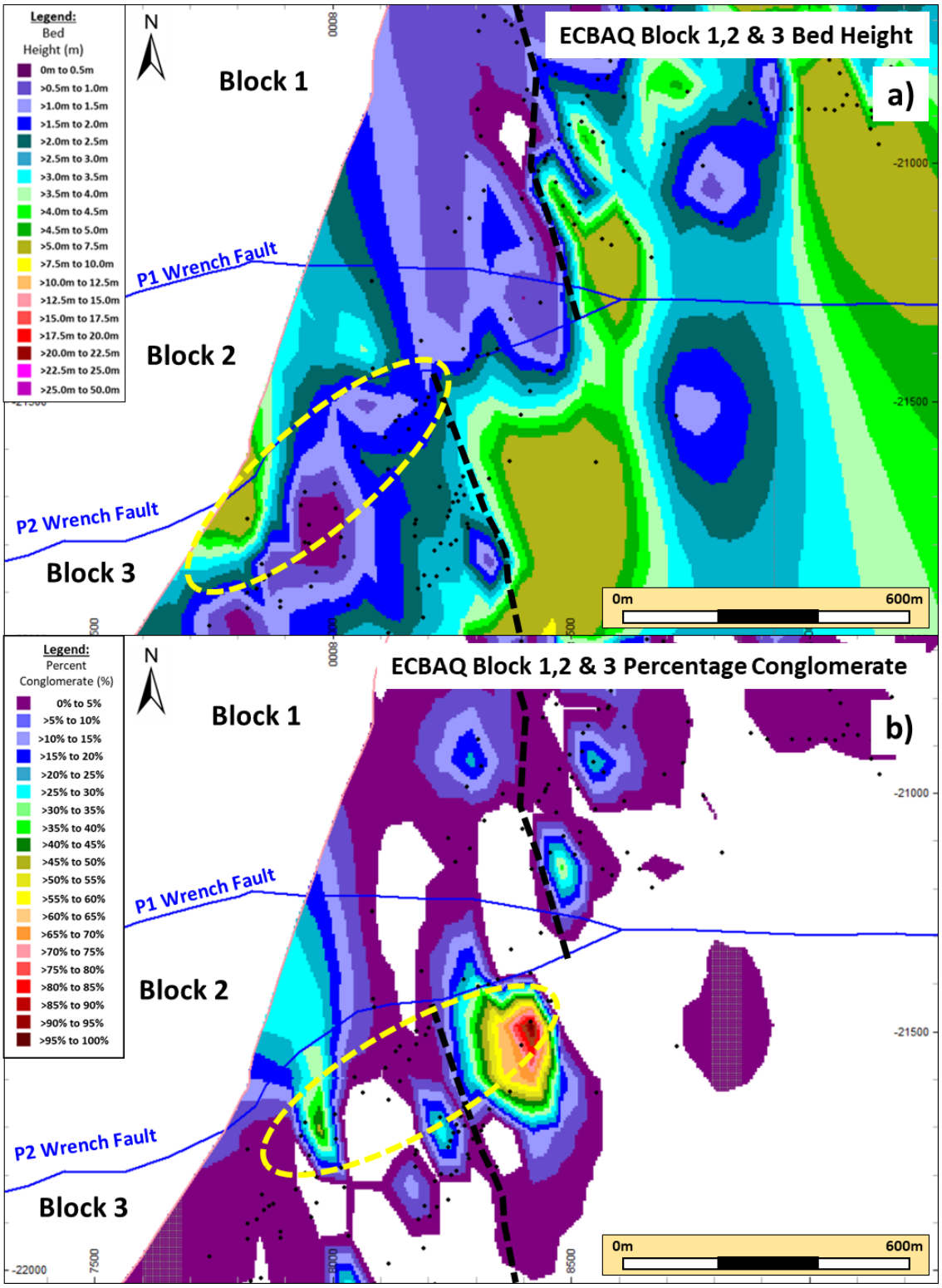


Figure 98: Enlarged Block 2 palinspastic reconstruction for a) bed height for ECBAQ and b) for percentage conglomerate for ECBAQ. Black dashed line in as and b) indicates change in bed height. Yellow ellipse in a) and b) indicates a trend along the strike of 90L Wrench of rapidly alternating nodes of high and low percentage conglomerate.

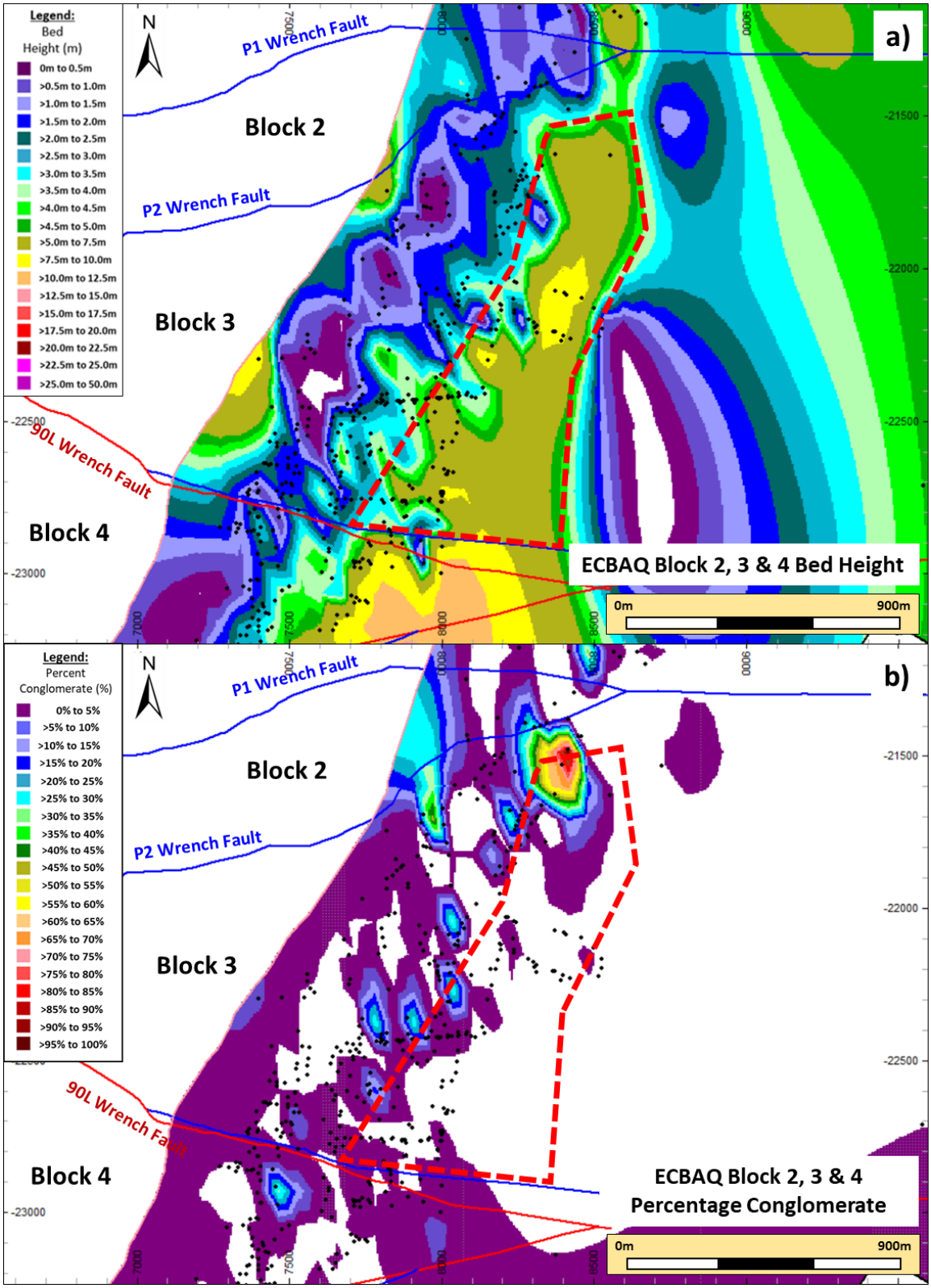


Figure 99: Enlarged Block 3 palinspastic reconstruction for a) bed height for ECBAQ and b) for percentage conglomerate for ECBAQ. Red polygons in a) and b) indicate a zone of high bed height with low percentage conglomerate.

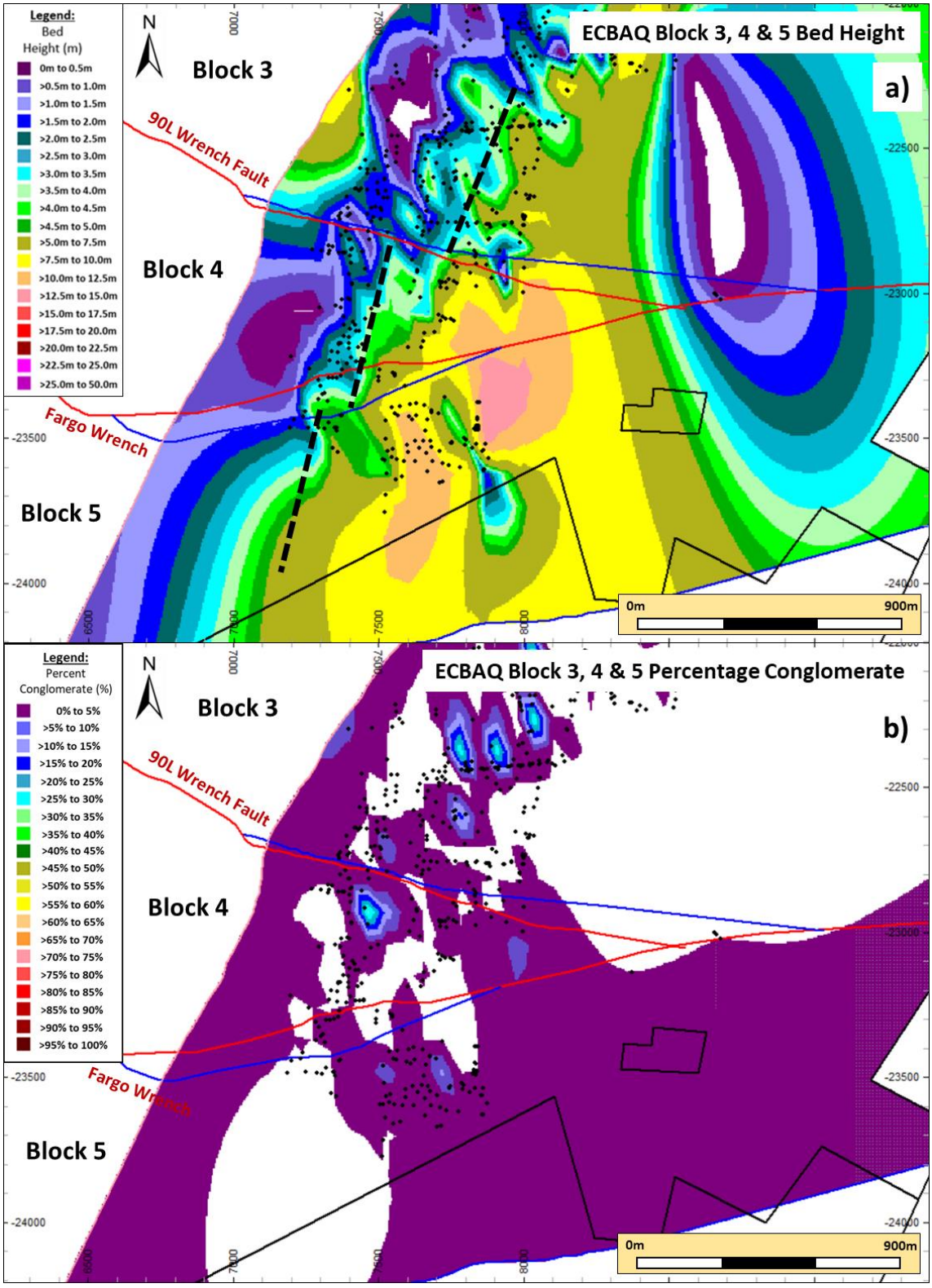


Figure 100: Enlarged Block 4 palinspastic reconstruction for a) bed height for ECBAQ and b) for percentage conglomerate for ECBAQ. Black dashed line in a) indicates possible offset of zone of higher bed height.

b) **ECB**

i) ECB Bed Height

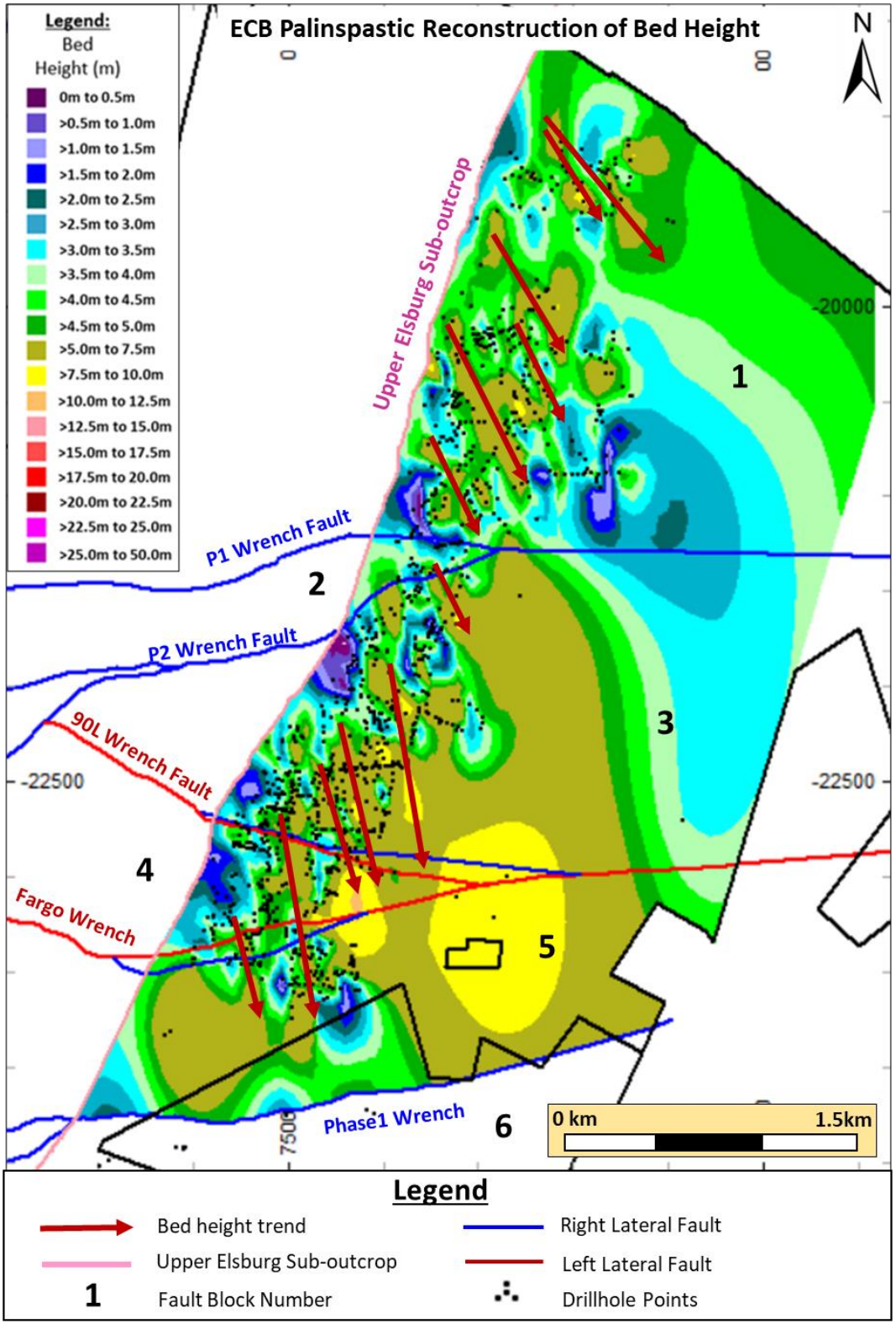


Figure 101: Palinspastic bed height reconstruction for ECB.

ii) ECB Percentage Conglomerate

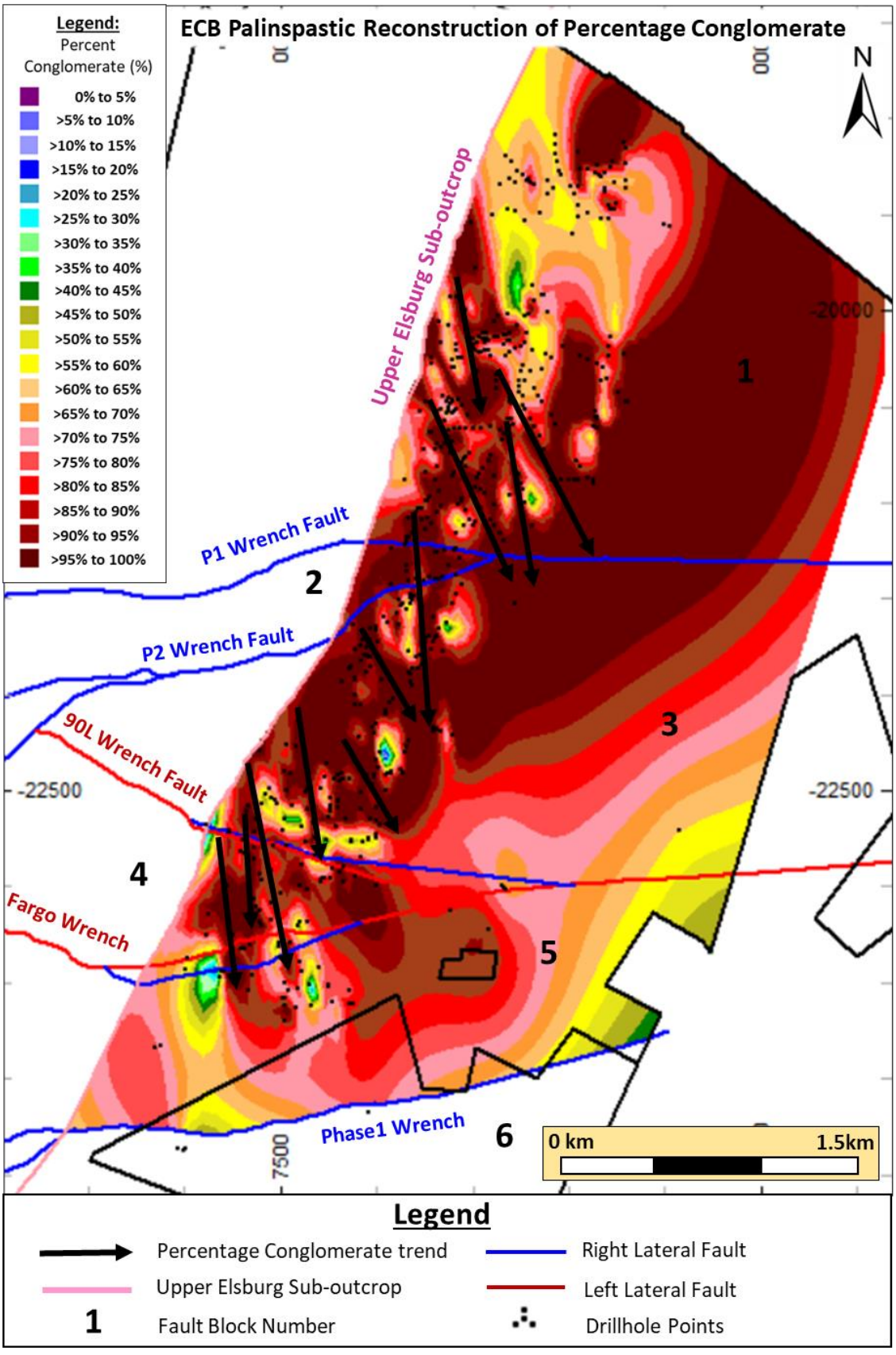


Figure 102: Palinspastic percentage conglomerate reconstruction for ECB.

iii) ECB Average and Maximum Clast Size

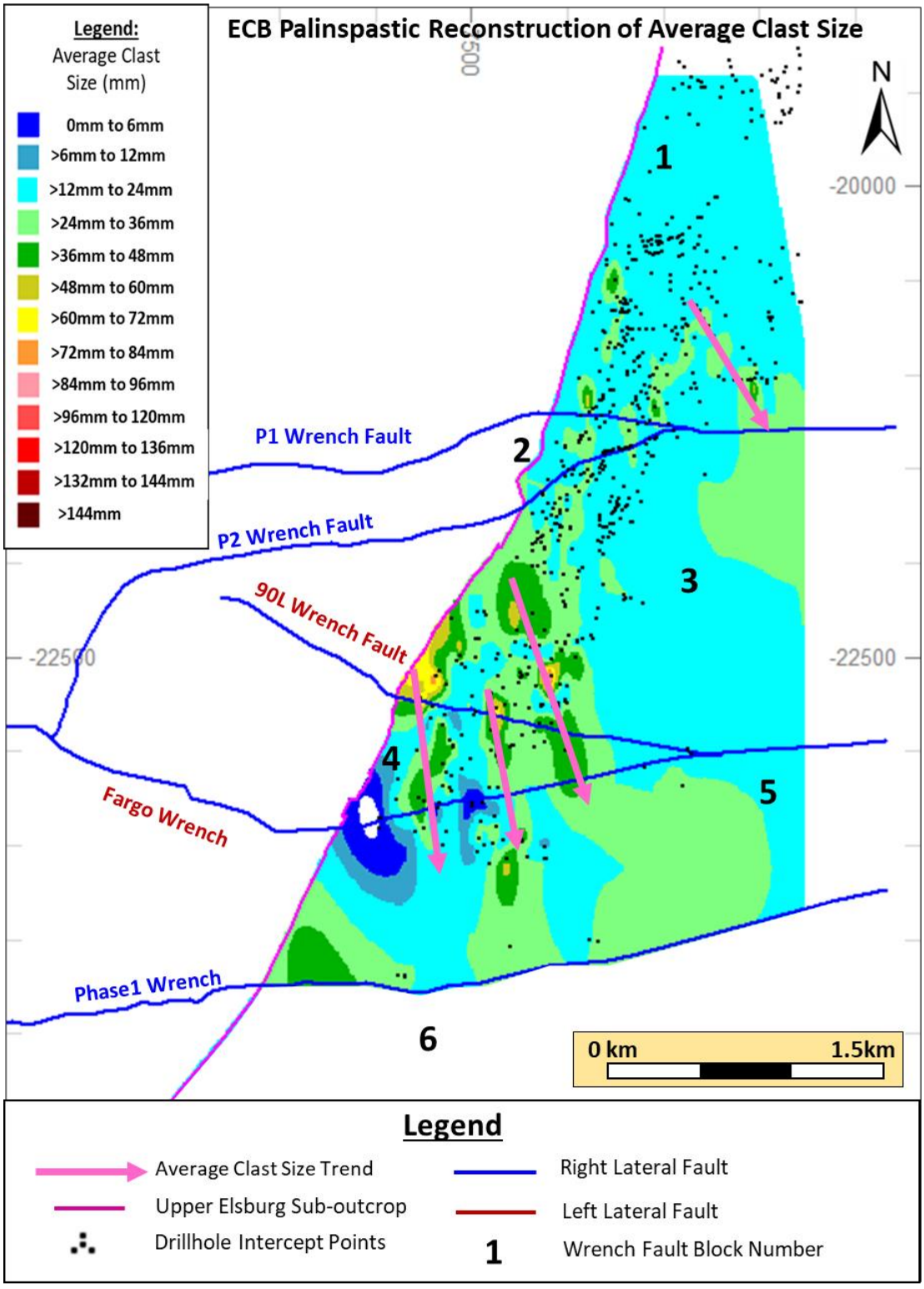


Figure 103: Palinspastic average clast size reconstruction for ECB.

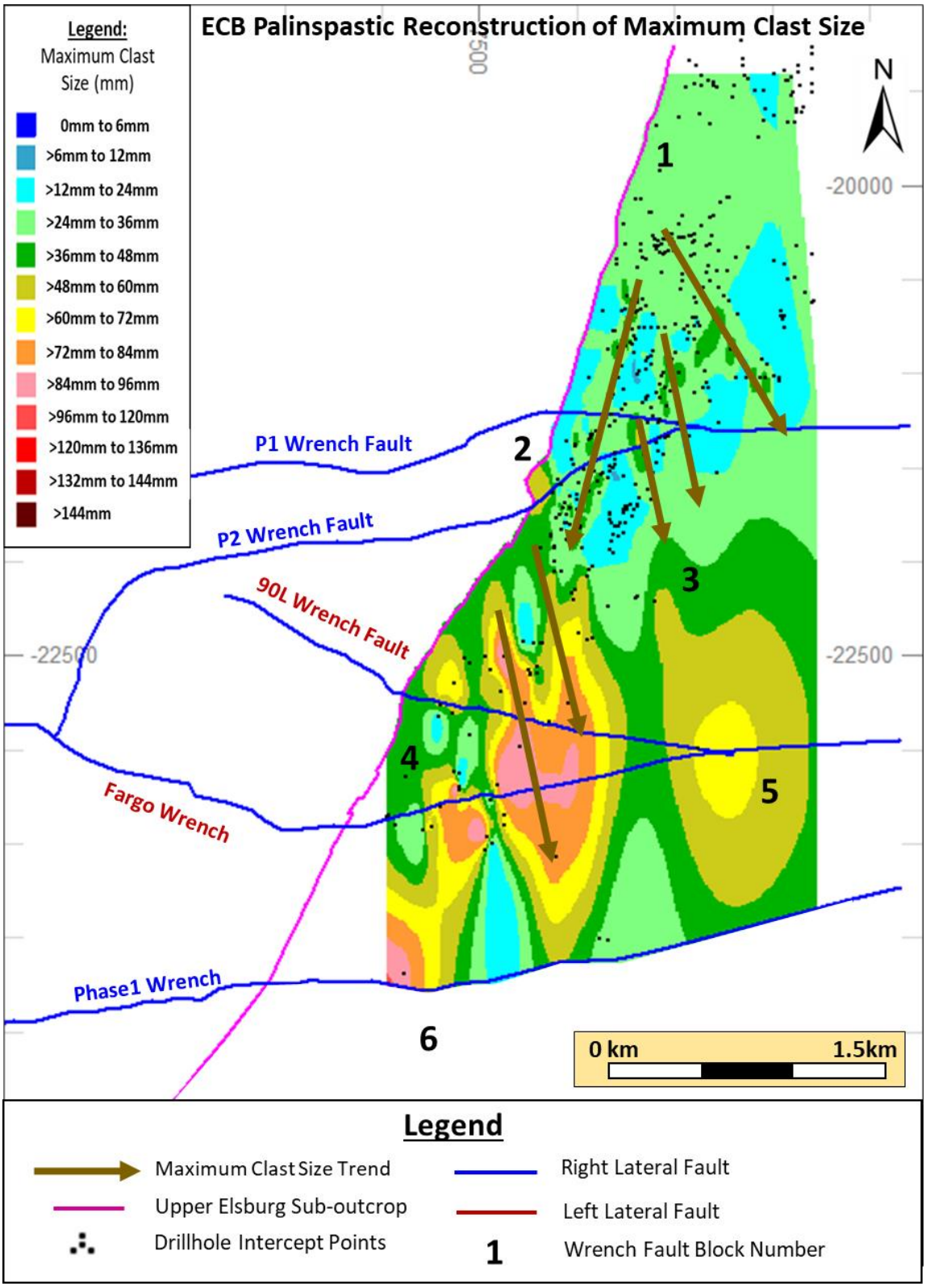


Figure 104: Palinspastic maximum clast size reconstruction for ECB.

c) **ECBQ**

i) ECBQ Bed Height

The palinspastic reconstruction for bed height for the ECBQ is presented in Figure 105. The ECBQ gradually thins from the east to west towards the Upper Elsburg Subsub-outcrop. Attenuation of the ECBQ along the Upper Elsburg Subsub-outcrop varies from north to south. Within Blocks 1 and 2, the ECBQ attains a minimum bed height of approximately 1.5 m, while within the southern blocks, the ECBQ is reducereduced in thickness to a bed height of < 0.5 m along the sub-outcrop.

Maximum bed height (>15 m to 20 m) is attained along the northern margin of Block 5 up against Fargo Wrench.

A general thickening trend from north (BlockBlocks 1 and 2) to south (BlockBlocks 3, 4 and 5) also occurs. The high data density strip parallel to the sub-parallel to the sub-outcrop is approximately 2 km wide. Higher bed height trends (excluding the westward thinning) appear to run NNW-SSE relative to the sub-outcrop in all blocks.

ii) ECBQ Percentage Conglomerate

The ECBQ palinspastic reconstruction for percentage conglomerate is presented in Figure 106. Percentage conglomerate appears to remain relatively patchy when moving to the east. The northern portion of Block 1 presents an exception to this pattern. Trends in the percentage conglomerate appear oriented preferentially NNW to -SSE over Blocks 1, 3 and 5.

Higher bed height in Block 5 does not appear to relate to a change in percentage conglomerate in the south in Block 5, while in the north, a slightly higher percentage conglomerate is associated with the slightly thicker ECBQ in the northern half of Block 1.

iii) ECBQ Average and Maximum Clast Size

The ECBQ is highly variable in conglomeratic content as one moves from north to south. Average clast size (Figure 107) for the ECBQ increases from >12 mm to 24mm24 mm in the north to >48 mm to 60 mm over Blocks 3, 4 and 5. Average clast size trends elude interpretation in the north due to the low variability, as well as low data density. Patchy NNW to -SSE trends for average clast size are discernible across the 90L Wrench and Fargo Wrench combination.

Maximum clast size for the ECBQ (Figure 108) readily exceeds 48 mm over Blocks 3, 4 and 5, with some areas of >60 mm to 72 mm. Maximum clast size trends also appear discernible across the 90L Wrench and Fargo Wrench combination.

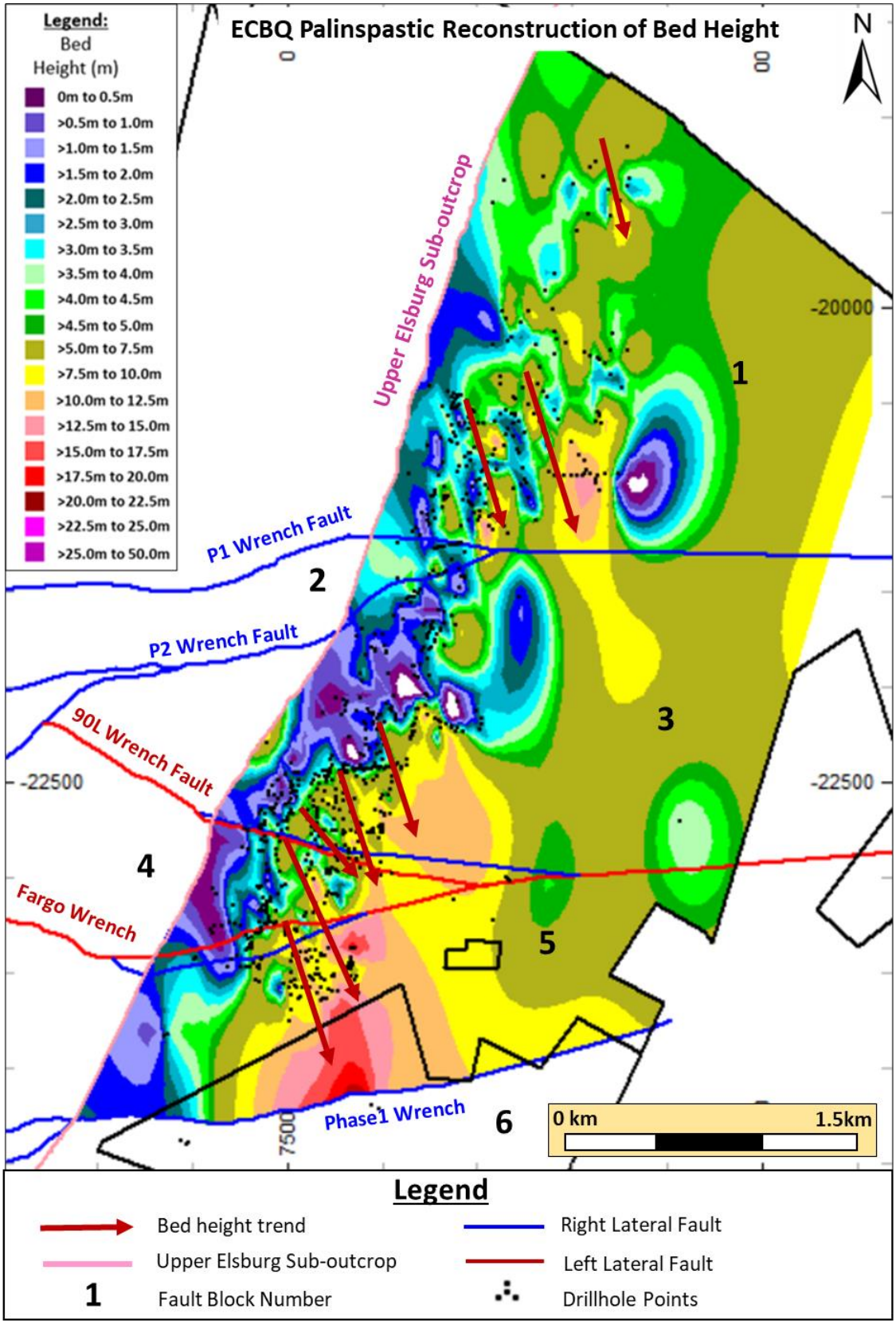


Figure 105: Palinspastic bed height reconstruction for ECBQ.

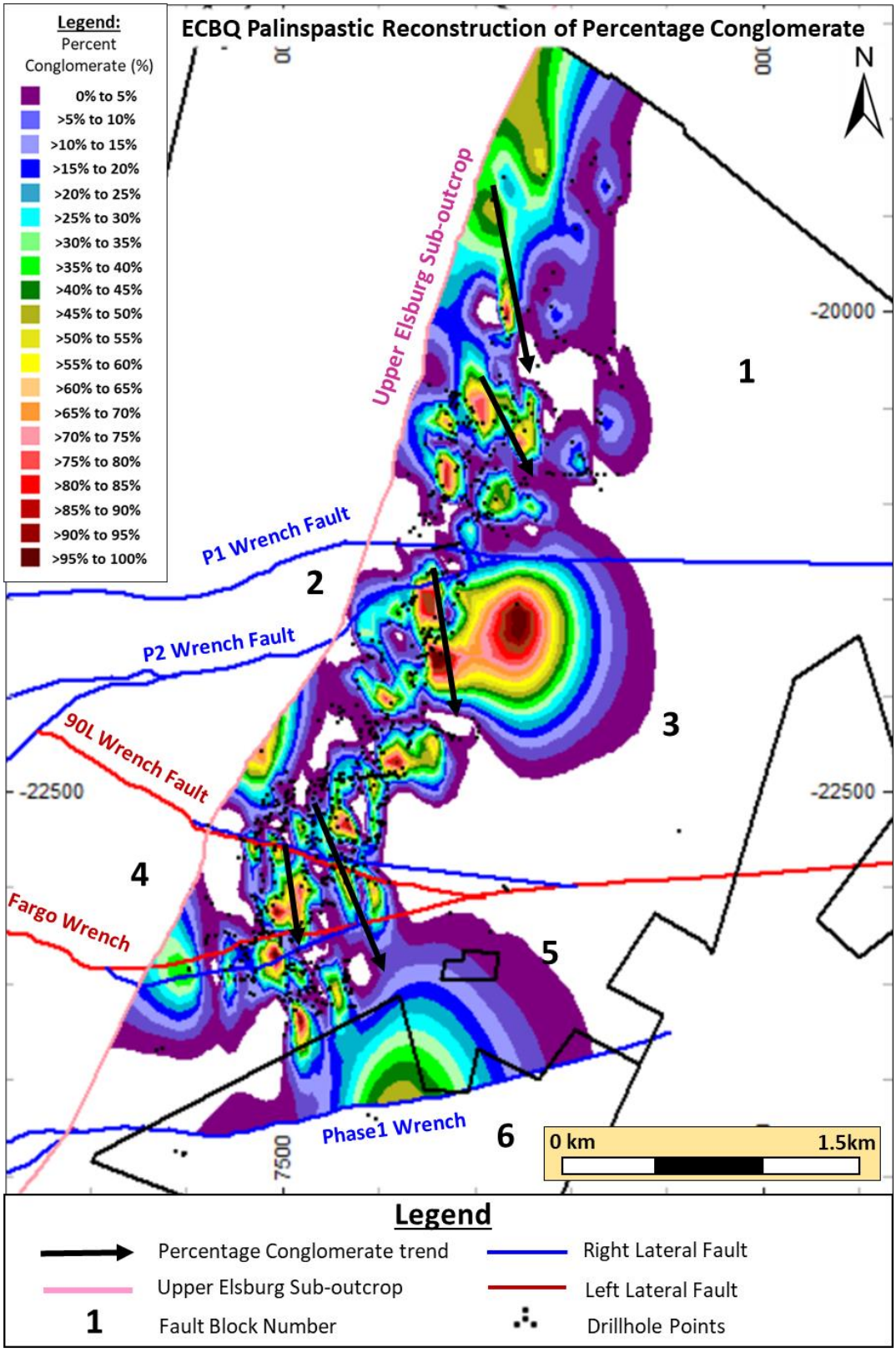


Figure 106: Palinspastic percentage conglomerate reconstruction for ECBQ.

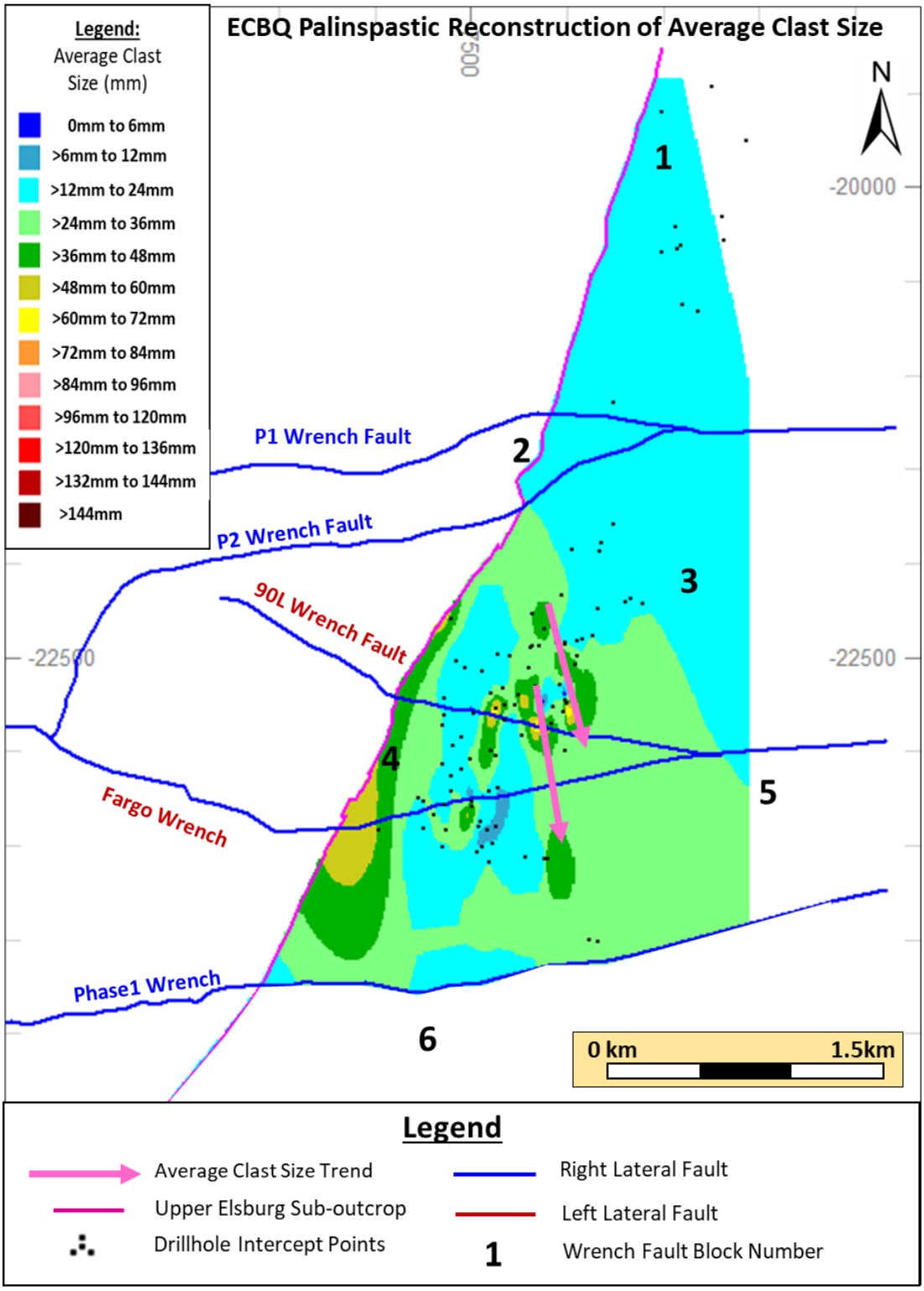


Figure 107: Palinspastic average clast size reconstruction for ECBQ.

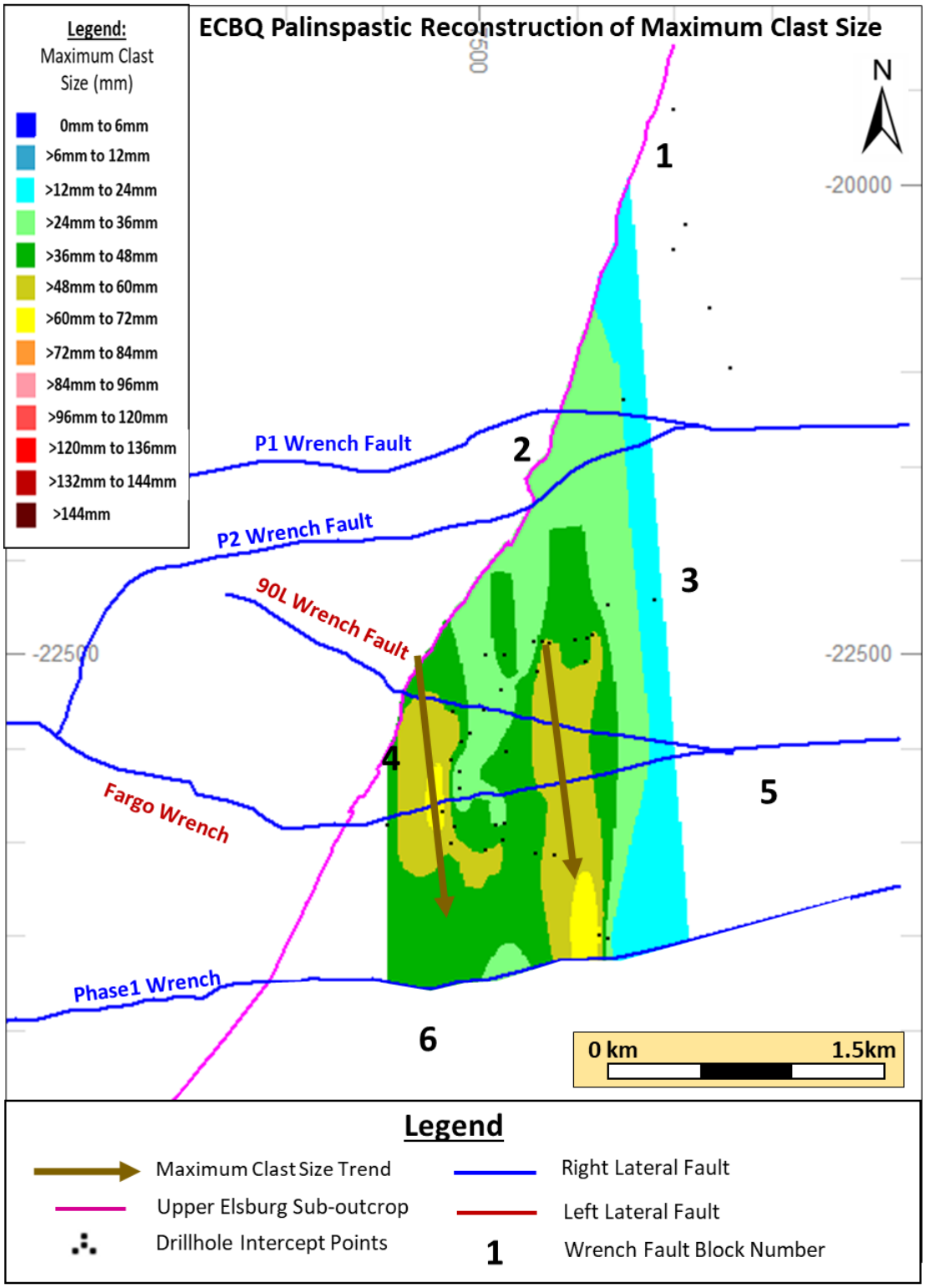


Figure 108: Palinspastic maximum clast size reconstruction for ECBQ.

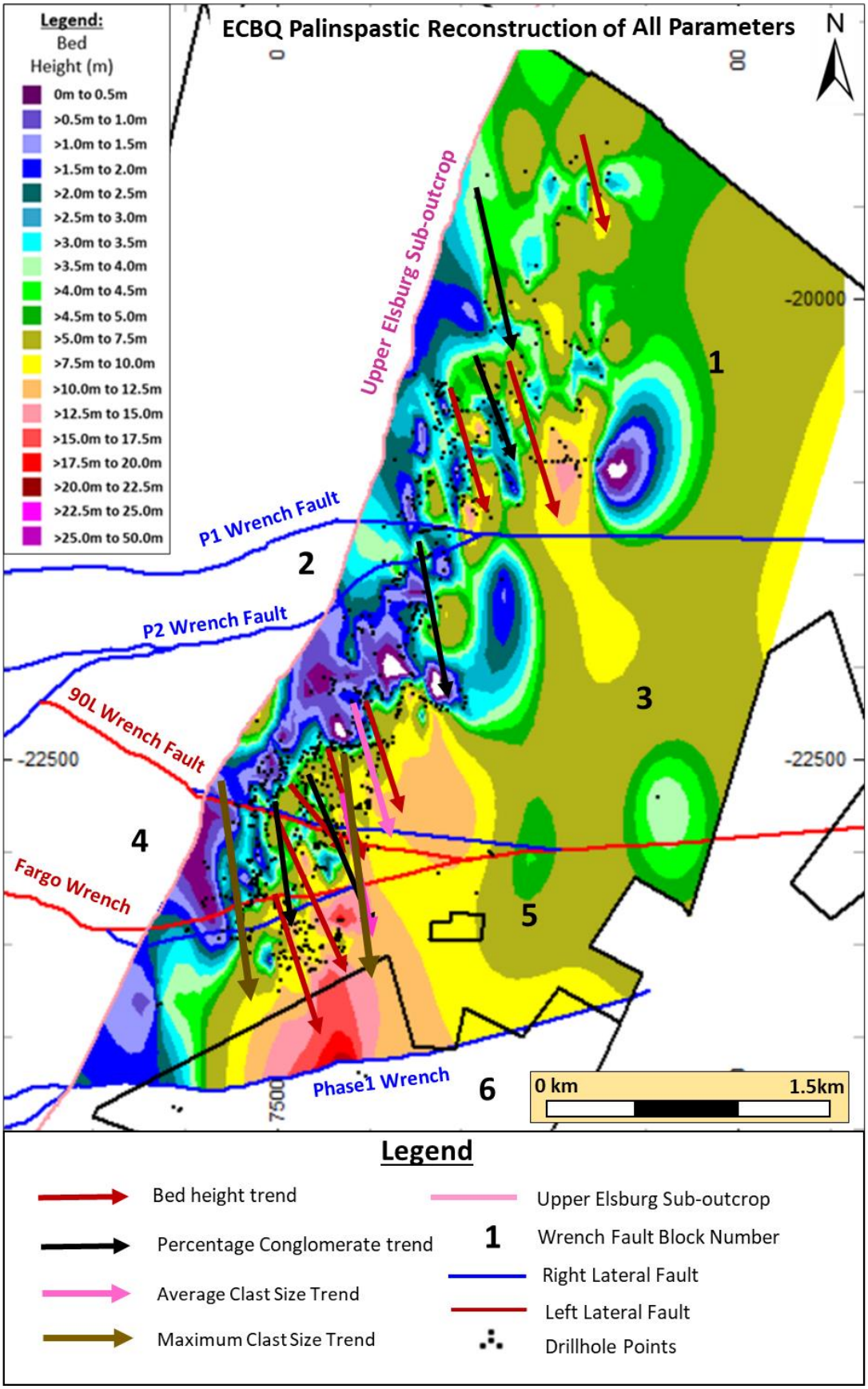


Figure 109: Palinspastic Reconstruction for the ECBQ - All Parameters

iv) ECBQ Detailed Plots

Figure 110**Error! Reference source not found.** presents an enlarged section of the a) Bedbed height and b) percentage conglomerate plan for the ECBQ including Blocks 1, 2, and 3. In Figure 110 a) a zone of higher bed height crosses over P1 Wrench and terminates against P2 Wrench as indicated by the yellow polygon. This thicker zone appears associated with a lower to absent percentage conglomerate. This observation is however not conclusive due to the low data density in Block 2. An apparent nett dislocation of ± 200m200 m appears to offset the thicker zone in Block 1 from that in Block 3. No implications as to which fault is responsible are possible at this point due to the poor continuity due to the low data density in Block 2.

Timing of this dislocation is also not clear but, would post-date ECBQ deposition, however, syn-sedimentary activity is not be excluded. Nature of movement is also not discernible, though an apparent right-lateral dislocation (±200 m) might have occurred. In addition, movement post -ECBQ deposition might have been vertical (down to the north) across P2 Wrench prior to or concurrent with ECB erosion and subsequent deposition resulting in possible growth fault formation.

Figure 111 indicates a zone of thinner ECBQ in Block 3 (yellow ellipse in Figure 111 b)) up against the P2 Wrench, associated with a higher percentage conglomerate also adjacent to the P2 Wrench.

A trend line (yellow dashed line) of thinner ECBQ running sub-parallel to the Upper Elsburg Subcropsub-outcrop in Figure 111 a) appears associated with a zone of little to no conglomerate development in Figure 111 b). This conglomerate poor strip is bordered to the west (up against the Subsub-outcrop) and to the east (high-lightedhighlighted by a red polygon) by zones characterised by localised higher bed height and increased associated conglomeratic development. Timing of its formation could be related to post-deposition and subsequent erosion and deposition of the ECMC.

Figure 112 presents no apparent dislocation across the 90L Wrench and Fargo WrenchesWrench. However, nodes of variable bed height and percentage conglomerate appear to closely follow the southern margin of both structures. This could imply the syn-sedimentary existence but with very limited possible syn-sedimentary activity of the 90L Wrench and Fargo WrenchesWrench during ECBQ deposition or subsequent erosion by the overlying ECMC.

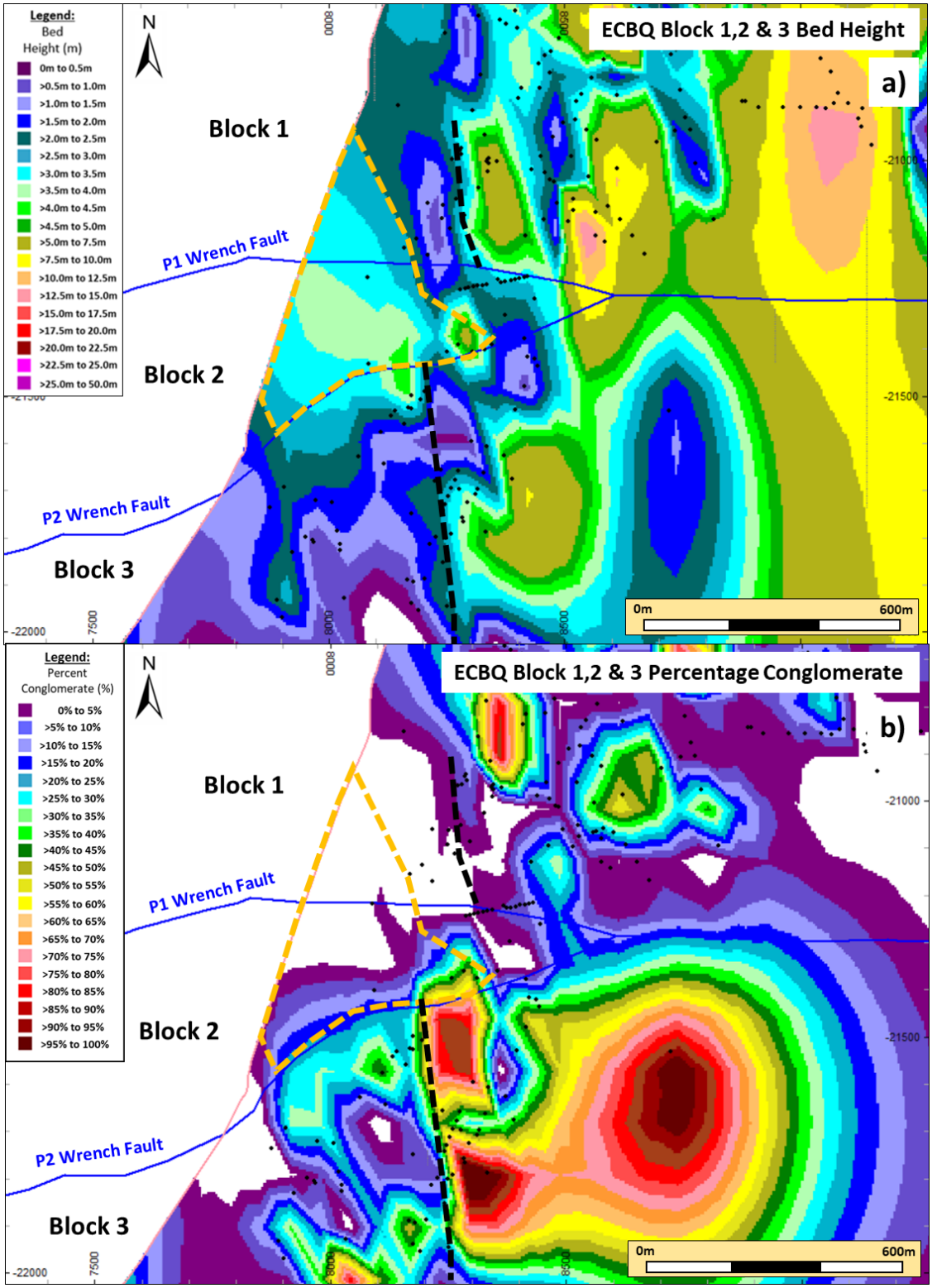


Figure 110: Enlarged Block 2 palinspastic reconstruction for a) bed height for ECBQ and b) for percentage conglomerate for ECBQ. Yellow polygon in a) and b) indicate a zone of lower bed height terminating on P2 Wrench Fault.

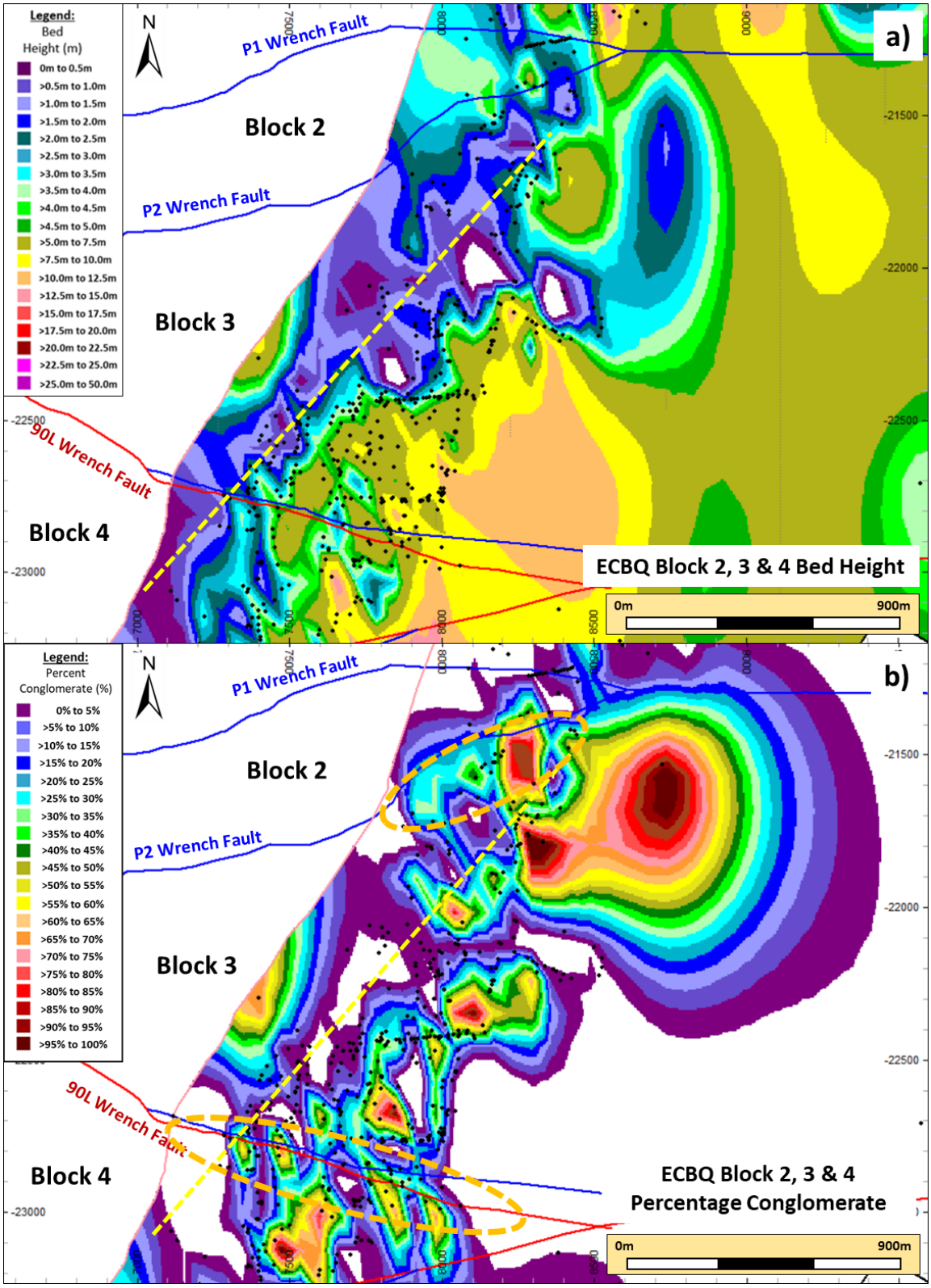


Figure 111: Enlarged Block 3 palinspastic reconstruction for a) bed height for ECBQ and b) for percentage conglomerate for ECBQ. Yellow line in a) and b) indicates a trend of lower bed height east of sub-outcrop with low percentage conglomerate. The yellow ellipse in b) indicates a trend along the strike of 90L Wrench of rapidly alternating nodes of high and low percentage conglomerate.

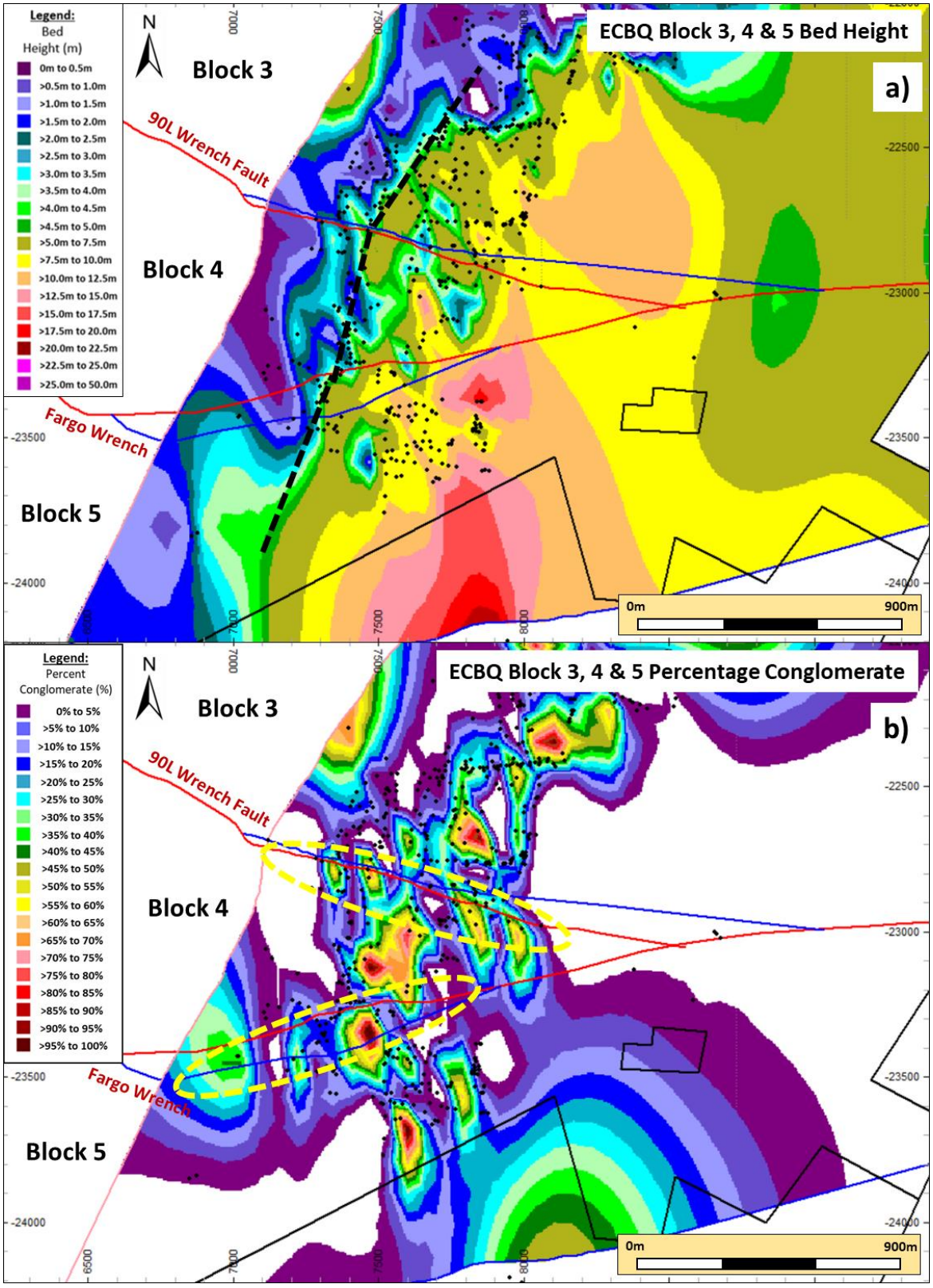


Figure 112: Enlarged Block 4 palinspastic reconstruction for a) bed height for ECBQ and b) for percentage conglomerate for ECBQ. Black line in a) indicates western limit to zone of higher bed height with no dislocation. Yellow ellipses in b) indicate a trend along the strike of 90L Wrench and Fargo Wrench of rapidly alternating nodes of high and low percentage conglomerate.

d) **ECMC**

i) ECMC Bed Height

The palinspastic reconstruction for bed height for the ECMC is presented in **Error! Reference source not found.**. The ECB gradually thins from the east to west towards the Upper Elsburg Subsub-outcrop but very seldom thinning to <2 m. Maximum bed height (>7.5 m to 10 m) is attained sporadically ±1000 m to the east of the sub-outcrop.

No noticeable bed height trends between north (Block 1) and south (BlockBlocks 3, 4 and 5) are seen to occur, however, higher bed heights (>7.5 m) occur in Block 1 and Blocks 4 and 5, with very little bed height data in Block 3 exceeding 7.5 m. Dominant higher bed height trends (excluding the westward thinning) run NW-SE in the north to NNW-SSE in Blocks 1, 3 and 5. A secondary bed height trend, sub-parallel to the sub-outcrop (NNE-SSW)), may also occur in Blocks 1 and 3 (Redred dashed arrows in Figure 113**Error! Reference source not found.**).

ii) ECMC Percentage Conglomerate

The ECMC palinspastic reconstruction for percentage conglomerate is presented in Figure 114. Percentage Conglomerateconglomerate appears to remain relatively constant when moving to the east excepting the northern portion of Block 1 and the western half of Block 2. Visual trend patterns or trend lines in the percentage conglomerate are preferentially oriented NNW to -SSE over Blocks 1, 3, 4 and 5, parallel to the higher bed height trends observed in Figure 113. Higher bed height appears to result in a lower percentage conglomerate in the northern portion of Block 1.

Percentage conglomerate does not appear related to distance from sub-outcrop, as percentage conglomerate can attain >90% conglomerate in the south directly against the sub-outcrop, while in the north percentage conglomerate may be as little as 50% to 60%.

iii) ECMC Average and Maximum Clast Size

The ECMC is primarily conglomeratic in nature, with percentage conglomerate decreasing in Block 1. A comparison between percentage conglomerate (Figure 114) and average clast size (Figure 115) would infer a decrease in average clast size with decreased percentage conglomerate.

Higher average clast size trends (NNW to -SSE) appear to cross over the 90L Wrench and Fargo WrenchesWrench in the south, with an average clast size of >72 mm to 84 mm occurring just north of 90L Wrench in Block 3. A possible weak NNW-SSE average clast size trend may be identified in Block 1.

Maximum clast size for the ECMC (Figure 116) attains a maximum of >84 mm to 96 mm in diameter. The majority of Block 1 in Figure 116 is blank due to the lack of empirical maximum clast size in the area. Maximum

clast size for the ECMC exhibits similar clast size trends (NNW to -SSE), which cross the 90L Wrench and Fargo Wrench combination, to identified bed height, percentage conglomerate and average clast size trends.

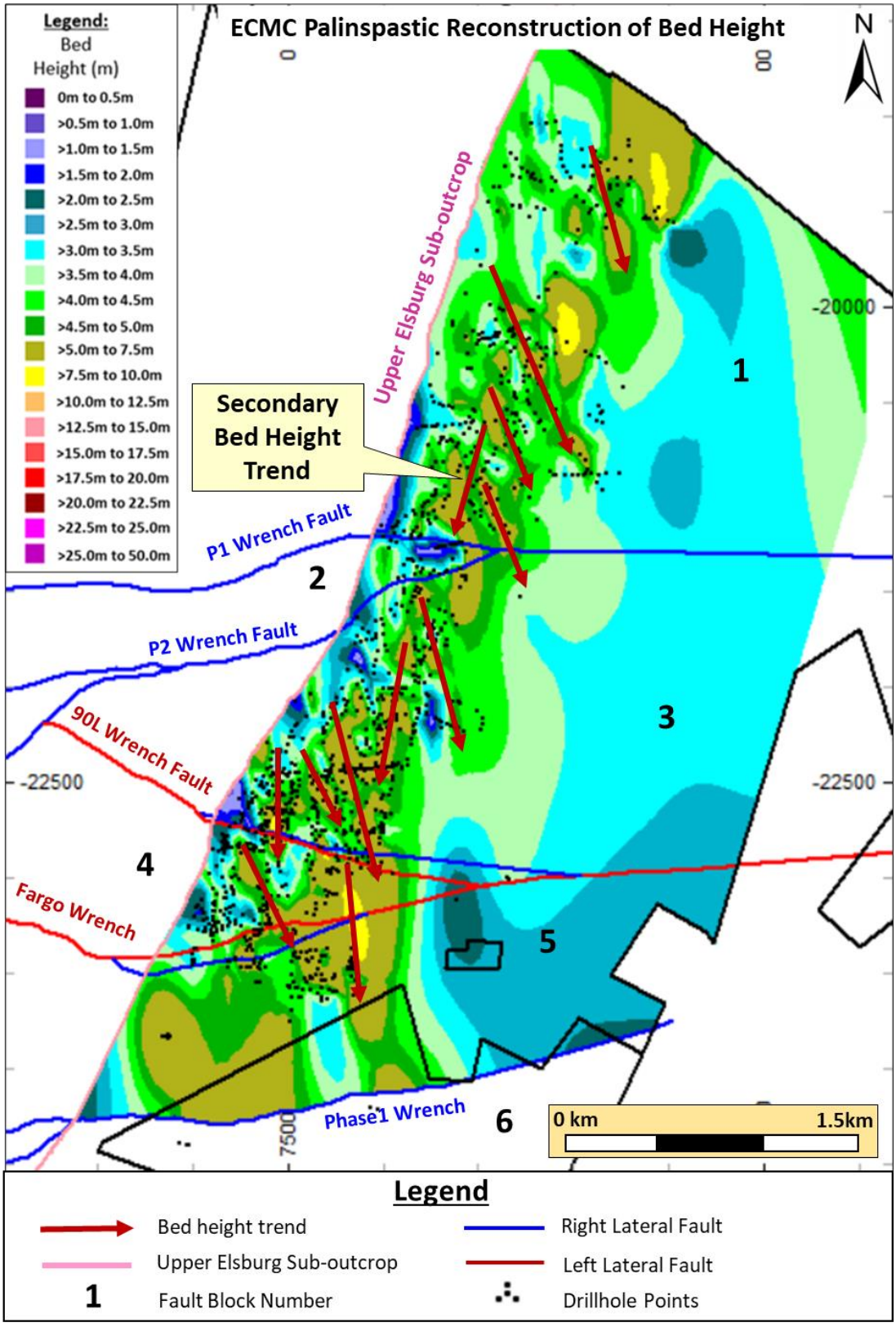


Figure 113: Palinspastic bed height reconstruction for ECMC.

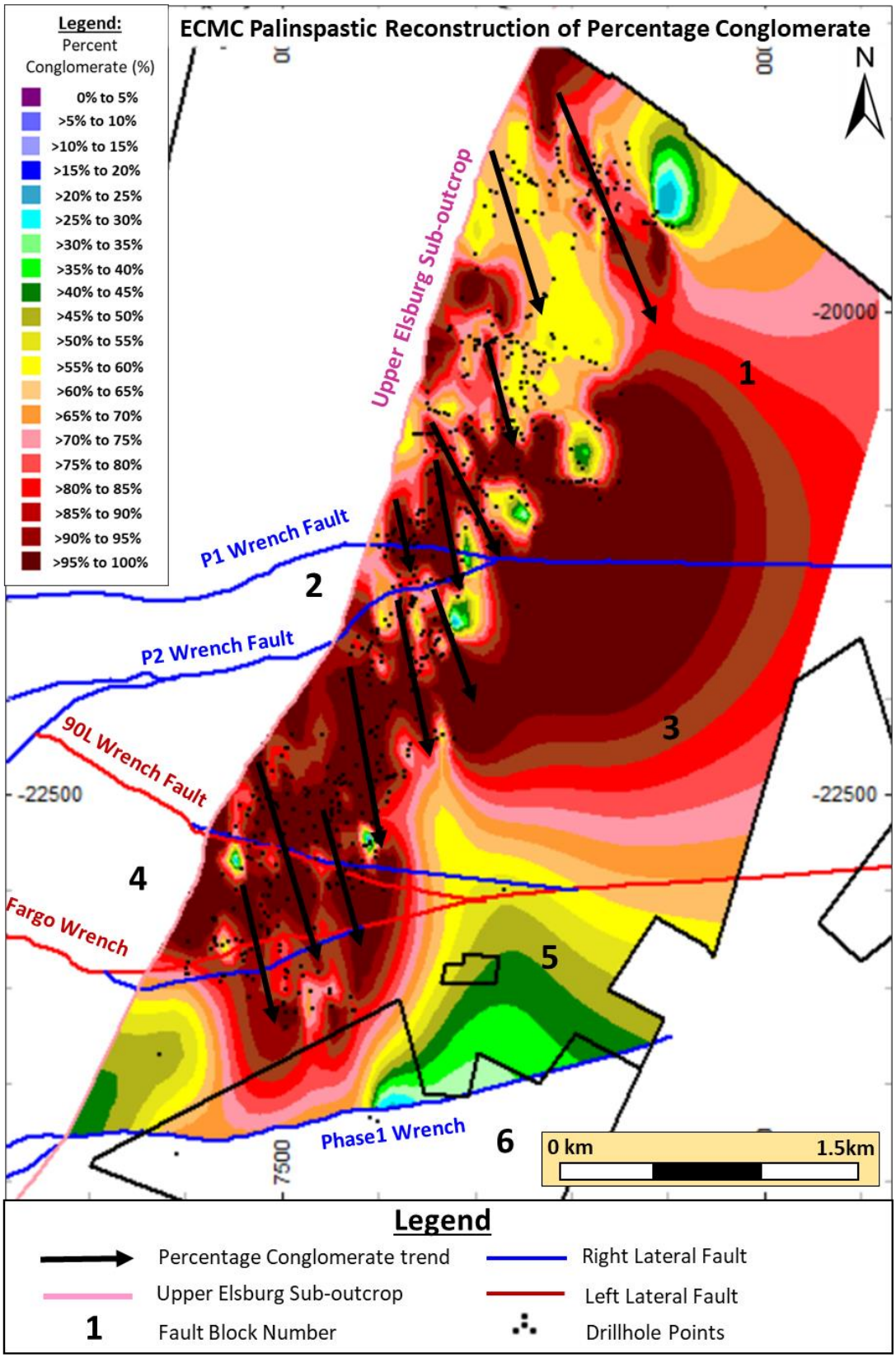


Figure 114: Palinspastic percentage conglomerate reconstruction for ECMC.

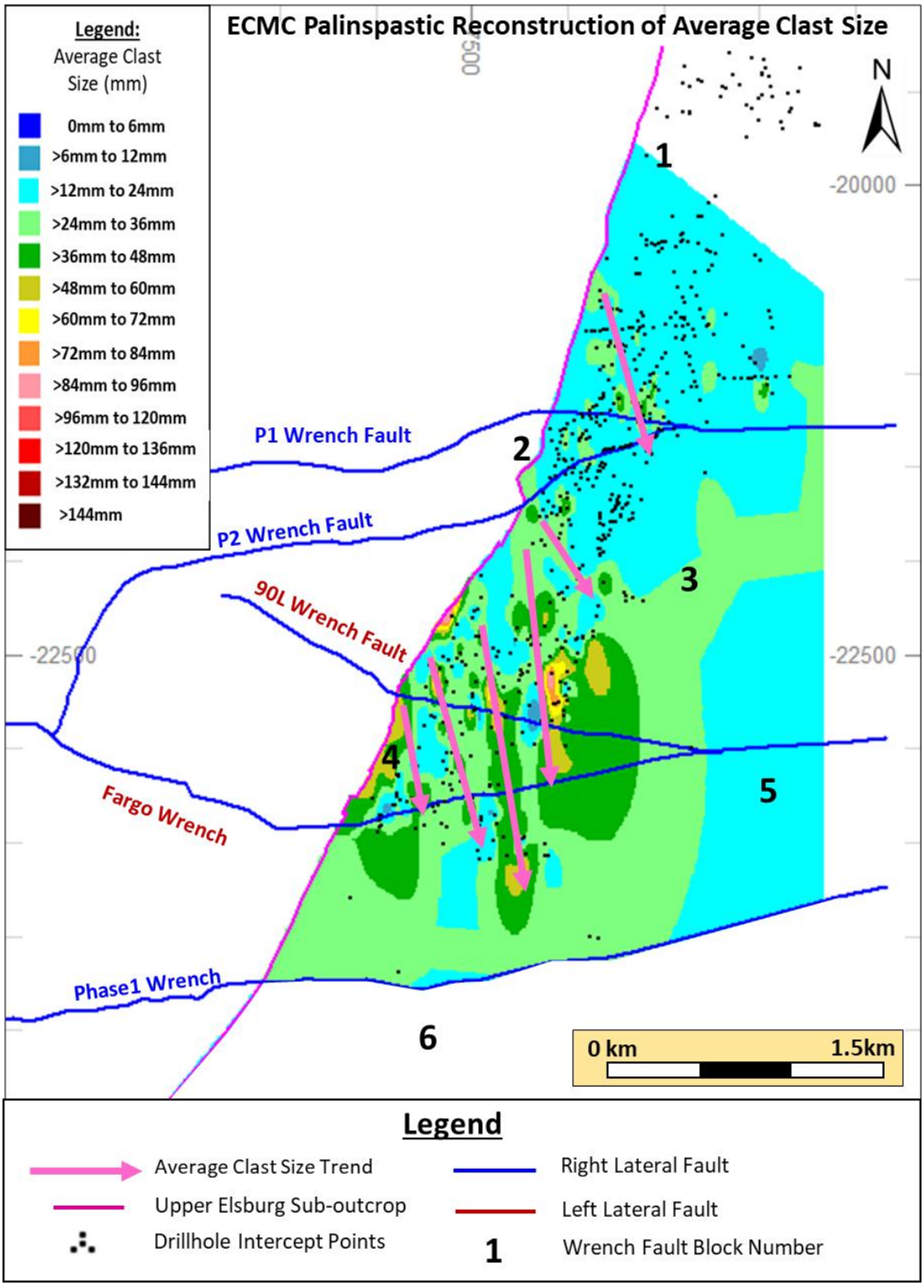


Figure 115: Palinspastic average clast size reconstruction for ECMC.

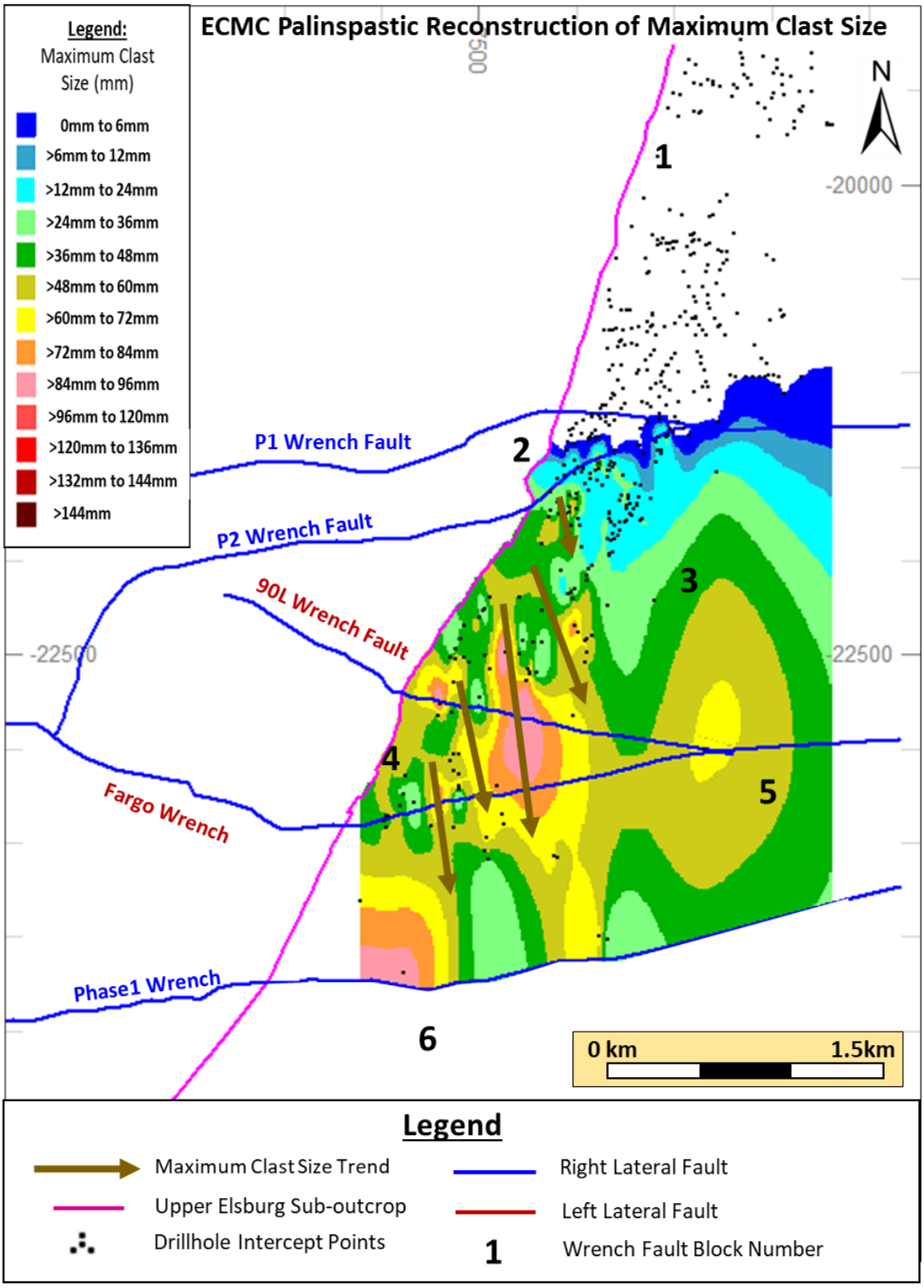


Figure 116: Palinspastic maximum clast size reconstruction for ECMC.

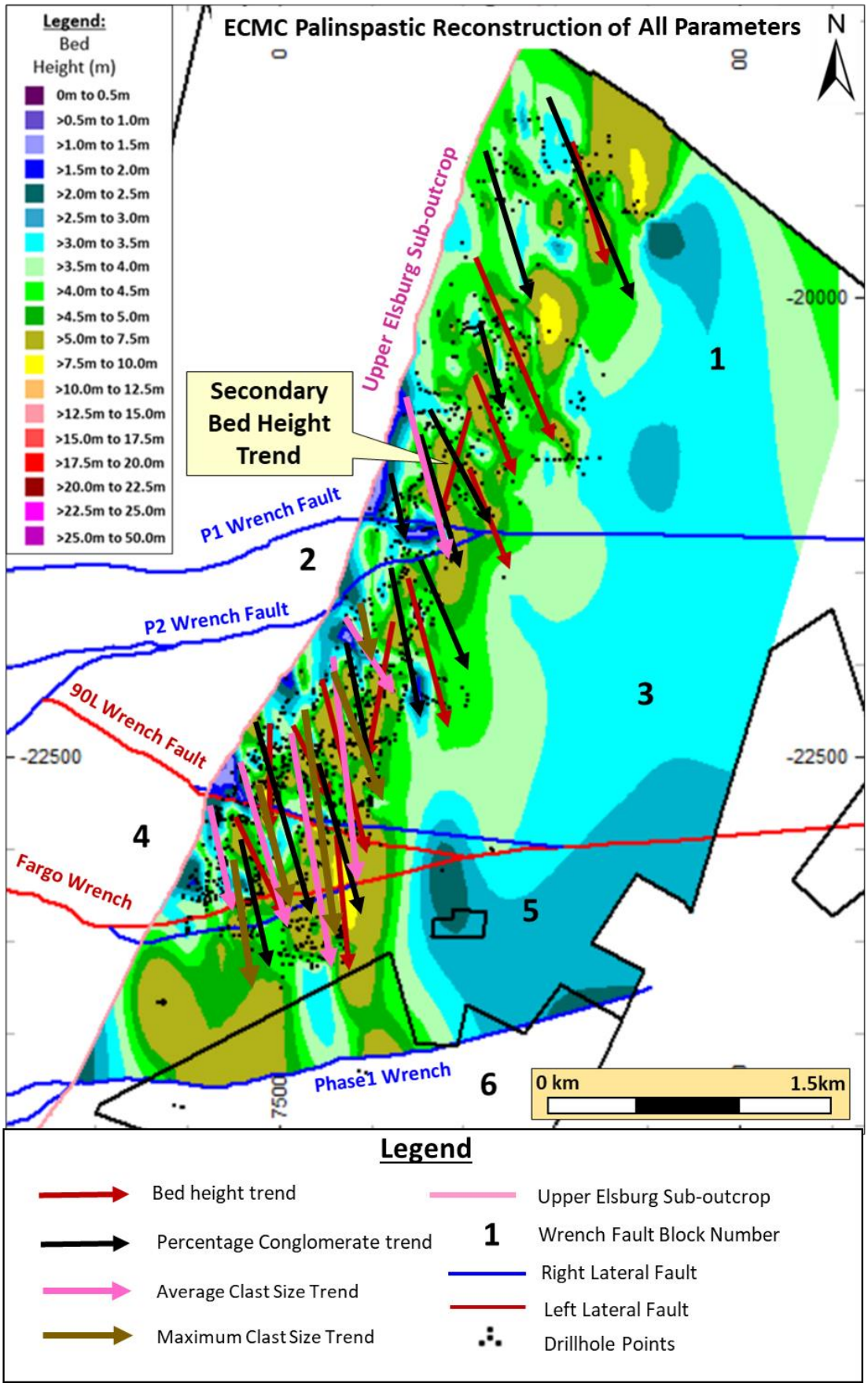


Figure 117: Palinspastic Reconstruction for the ECMC - All Parameters

iv) ECMC Detailed Plots

Figure 118 presents an enlarged section of the a) Bedbed height and b) percentage conglomerate plan for the ECMC centred on Block 2. In Figure 118 a) a zone of lower bed height (highlighted by a yellow polygon) is bound to both north and south by P1 Wrench and P2 WrenchesWrench with areas of higher bed height, respectively. An interpretation of a bed height trend between lower and higher bed height across the P1 Wrench and P2 Wrench combination, is depicted by the black dashed line in Figure 118 a). This interpreted line indicates a possible left-lateral dislocation of ±300 m across P1 Wrench and a possible ±400 m right-lateral dislocation across the P2 Wrench. Interpretation of possible dislocations across these structures is not definitive as disproportionate erosion of the ECMC by the overlying ECMQ and ECT on the 3three structure blocks cannot be excluded. However, the interpretation would require at least a post-ECMC or even a syn-ECMC vertical upward displacement of Block 2 relative to Blocks 1 and 3. Interpretation of the interpreted dislocation for percentage conglomerate in Figure 118 b) is not as apparent or definitive as that presented for bed height.

Figure 119, centred on Block 3, does not present easily identifiable dislocation interpretations across 90L wrenchWrench in the Southsouth. However, the northern margin of Block 3 adjacent to P2 Wrench and Block 2 presents a clear set of alternating high and low percentage conglomerate nodes (highlighted in yellow ellipse in Figure 119 b))) trending sub-parallel to the strike of P2 Wrench. Similarly, alternating higher and lower bed height nodes (Figure 119 a)))) and higher and lower percentage conglomerate nodes (Figure 119 b)) in close proximity to, and along the 90L Wrench strike (both highlighted by yellow ellipses) also occursoccur.

Review of bed height across the 90L Wrench and Fargo Wrench combination could indicatesindicate possible successive apparent right-lateral dislocations forfrom south to north, each of ± 150 m, based on the western margin (identified by a black dashed line in Figure 120 a) of)) bed height of approximately 4.5 m to 5 m. In Figure 120 a) the lower bed height to the west of this trend line in Block 3 is <1.5 m in height, while the dominant bed height for the similar area to the west of the trend line in Block 4, directly south of lower bed height zone Block 3, is ± >2.0 m.

Block 4 in Figure 120 b) presents a distinctly higher percentage conglomerate (Yellowyellow polygon) than the area directly adjacent to Fargo Wrench along the northern margin of Block 5. The yellow ellipse along strike of 90L Wrench highlights the alternating higher – and lower percentage conglomerate nodes as discussed for Figure 119. The apparent differences in bed height and percentage conglomerate presented in Figure 120 are not definitive, but could possibly infer structural influence on sedimentation, possibly in the form of growth faulting or due to possible syn- or post -ECMC structural dislocation.

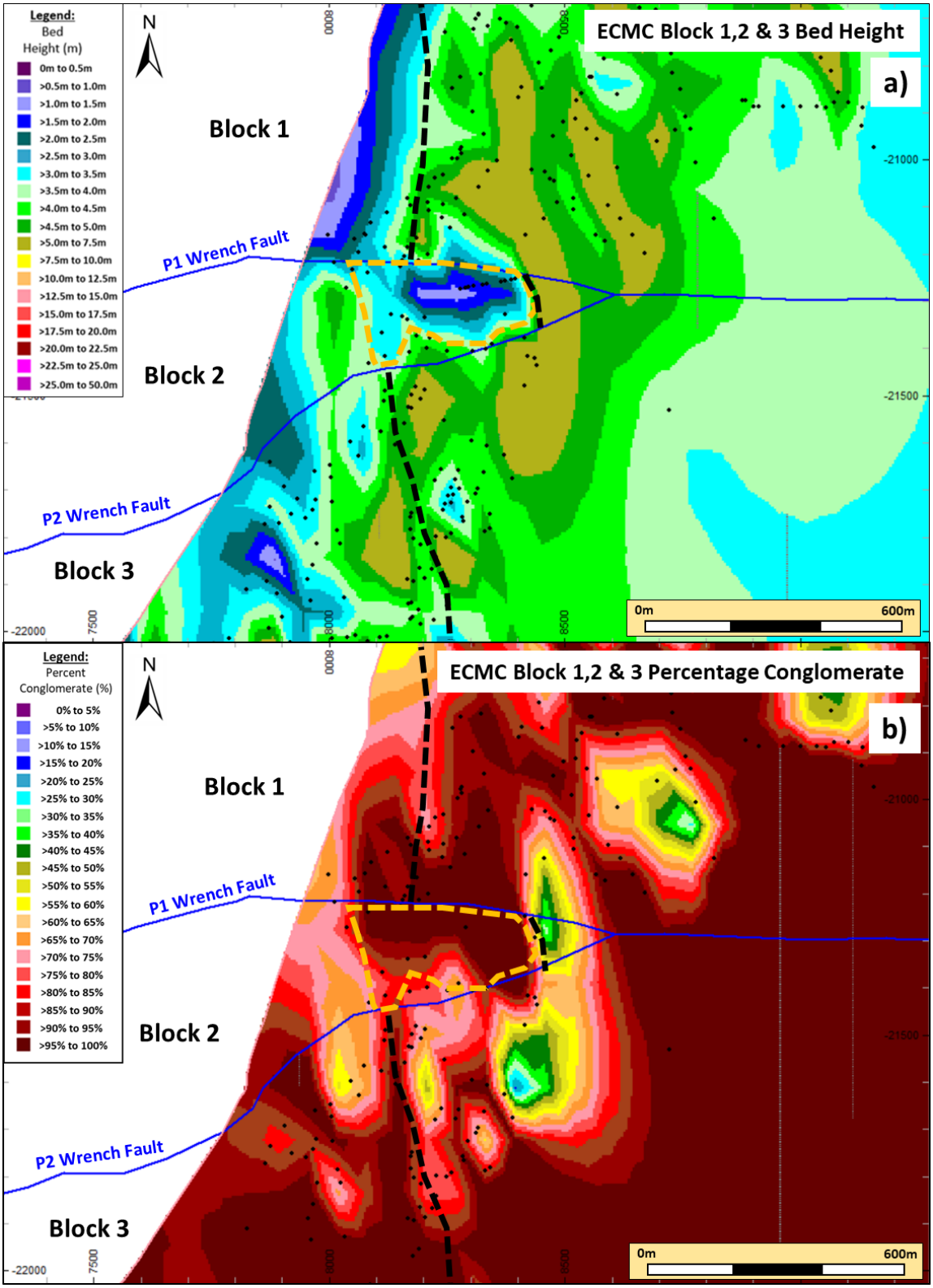


Figure 118: Enlarged Block 2 palinspastic reconstruction for a) bed height for ECMC and b) for percentage conglomerate for ECMC. Black dashed line in a) and b) indicates a change in bed height offset by P1 Wrench and P2 WrenchesWrench. The yellow polygon in a) and b) presents a zone of low bed height and high percentage conglomerate.

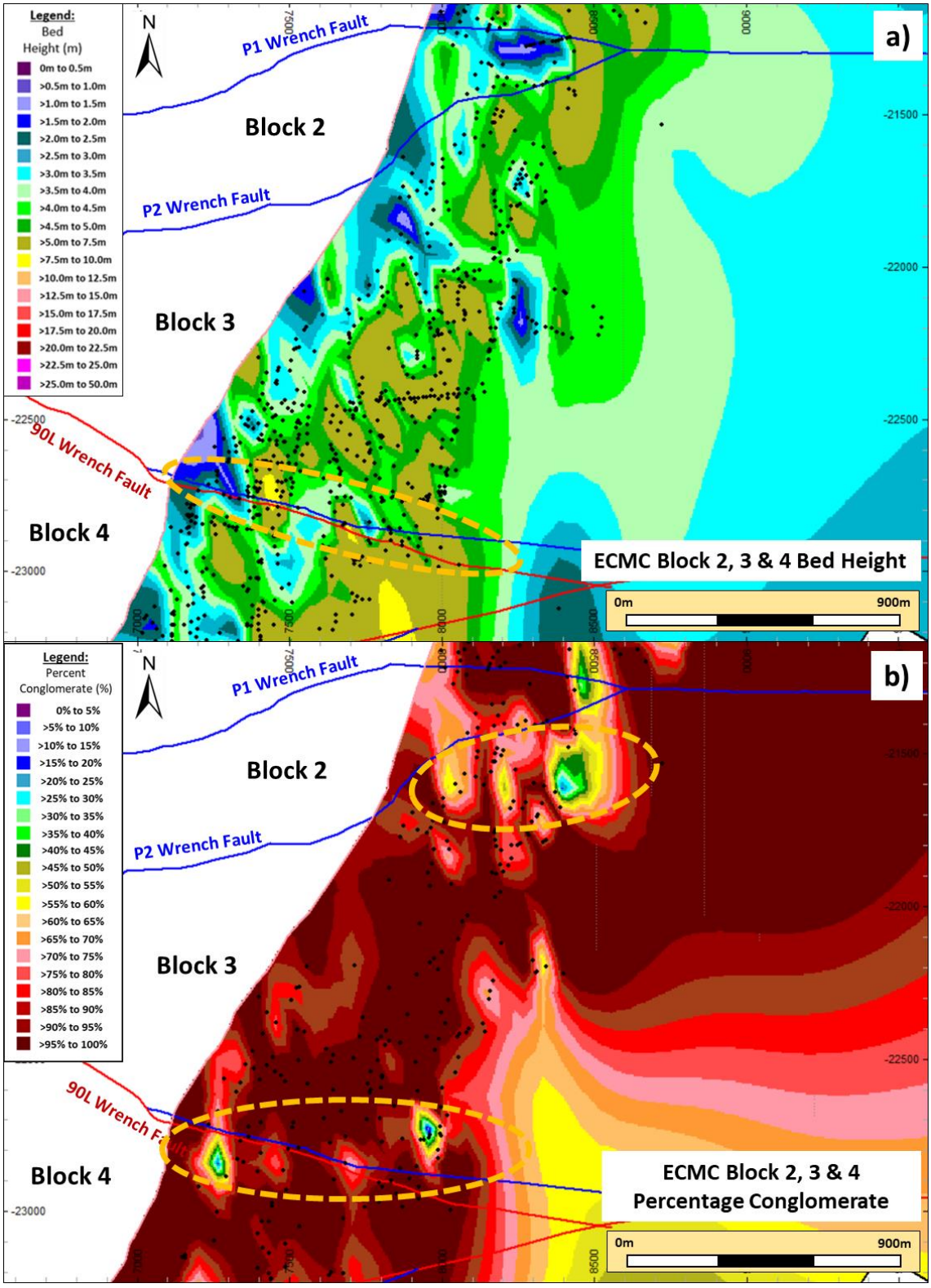


Figure 119: Enlarged Block 3 palinspastic reconstruction for a) bed height for ECMC and b) for percentage conglomerate for ECMC. Yellow ellipses in a) and b) indicate a trend along the strike of P2 Wrench and 90L WrenchesWrench of rapidly alternating nodes of high and low percentage conglomerate.

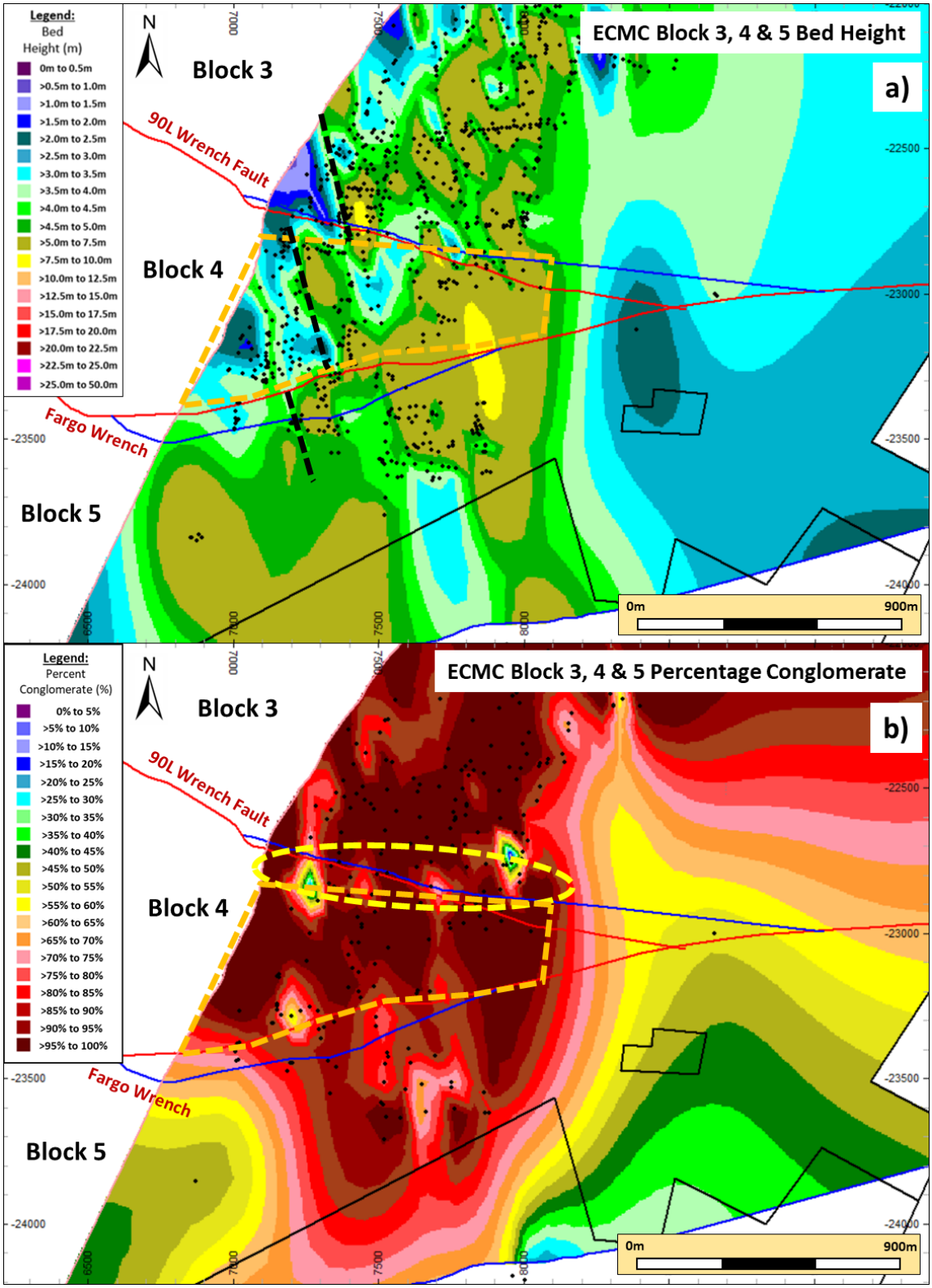


Figure 120: Enlarged Block 4 palinspastic reconstruction for a) bed height for ECMC and b) for percentage conglomerate for ECMC. Yellow polygon in a) and b) indicates zone of variable bed height and high percentage conglomerate. Yellow ellipse in b) indicates a trend along the strike of 90L Wrench of rapidly alternating nodes of high and low percentage conglomerate.

e) **ECMQ**

i) ECMQ Bed Height

Bed height for the ECMQ (Figure 121**Error! Reference source not found.**) decreases westwards very gradually towards the Upper Elsburg sub-outcrop. Bed height for the ECMQ seldom exceeds 2 m within 1000 m of the sub-outcrop. Maximum bed height (>5.0 m) is sporadic and occurs exclusively >1000 m east of the UEUpper Elsburg sub-outcrop within the southern half of Block 1 and the rest of the other blocks. The only area with bed height (>5.0 m) occurring within the 1000 m margin of the UEUpper Elsburg sub-outcrop occurs in the northern part of Block1Block 1.

The westward rate of thinning for the ECMQ is seen to increase southwards. The northern half of Block 1 presents a general higher bed height of >2 m close to the UEUpper Elsburg sub-outcrop, while in the southern half the average bed height attained adjacent to the UEUpper Elsburg sub-outcrop is ± 0.5 m to 1 m, while in. In the south in Blocks 3 and 4, average bed height for the ECMC adjacent to the UEUpper Elsburg sub-outcrop varies between >0 m and 0.5 m. Bed height trend (excluding general westward thinning) generally appears to be NNW to -SSE (Figure 121) across all structure bocksblocks.

ii) ECMQ Percentage Conglomerate

The palinspastic reconstruction for percentage conglomerate for the ECMQ is presented in Figure 122. Percentage Conglomerateconglomerate within all structural blocks is highly variable. Data density allows reasonable interpretation within 1 km and 1.2 km east of the Upper Elsburg sub-outcrop. Percentage conglomerate in the northern half of Block 1 is conspicuously low and agree with the higher bed height for the area presented in **Error! Reference source not found.**. Percentage conglomerate trend lines (Figure 122) in all blocks appear to mirror the bed height trends (NNW to -SSE) observed in Figure 121.

Generally, very few areas of 0% percentage conglomerate within the 1 km data window occur within the southern half of Block 1, Block 2 and the northern half of Block 3 Figure 122). Areas of no conglomerate development become more frequent over the southern portion of Block 3 and Block 4 (Figure 122).

iii) ECMQ Average and Maximum Clast Size

Average (Figure 123) and maximum (Figure 124) clast size data are absent for Block 1, due to the age of the drillhole data. Average and maximum clast size data was obtained for Blocks 3, 4, and 5.

Average clast size (Figure 123) for ECMC seldom exceeds 36 mm, and both average and maximum clast size trends appear to agree with both bed height and percentage conglomerate trends, namely NNW to -SSE. Average clast size trends appear to cross over the 90L Wrench and Fargo Wrench combination; however, this is not apparent for maximum clast size (Figure 124) due to low maximum clast size data density.

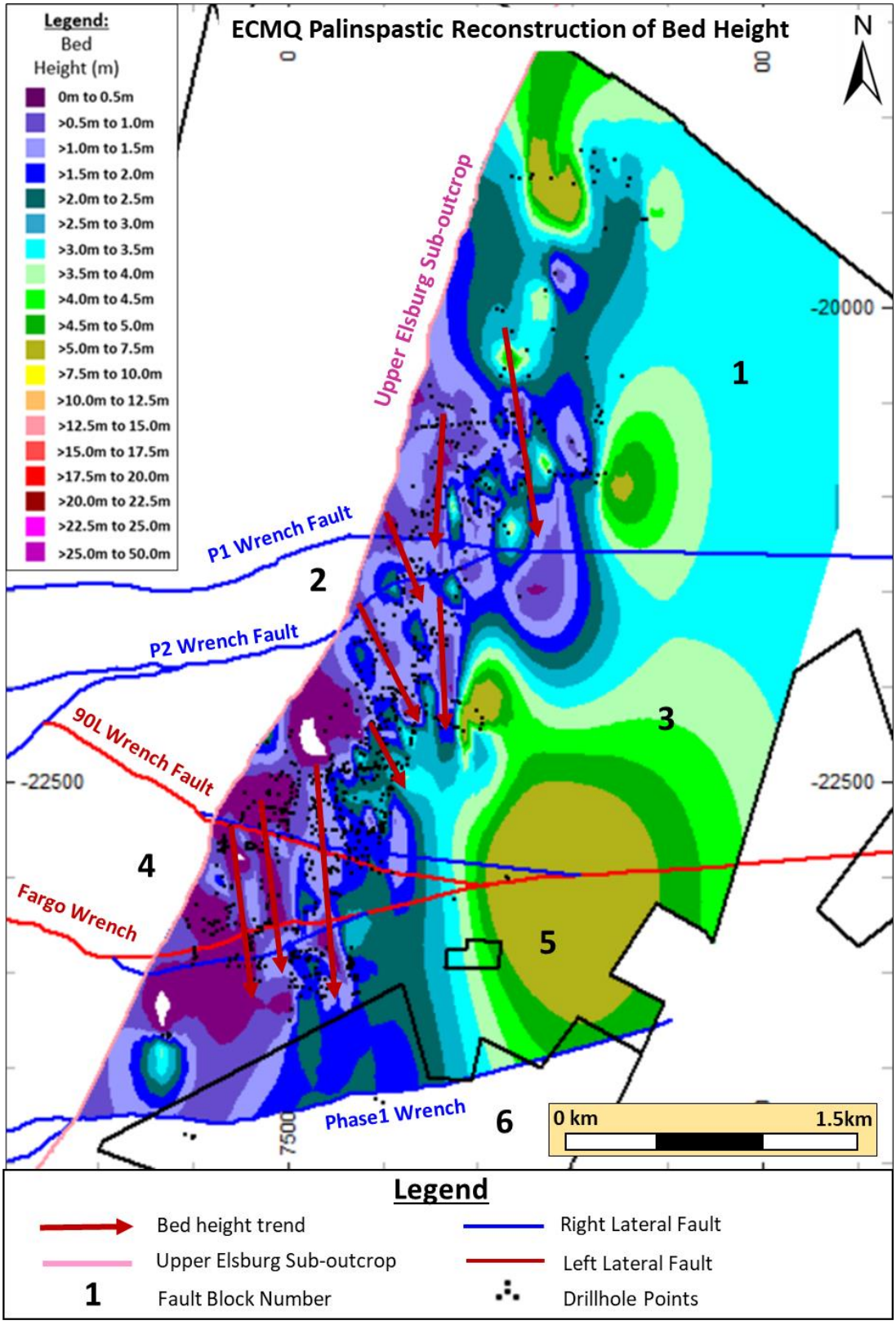


Figure 121: Palinspastic bed height reconstruction for ECMQ.

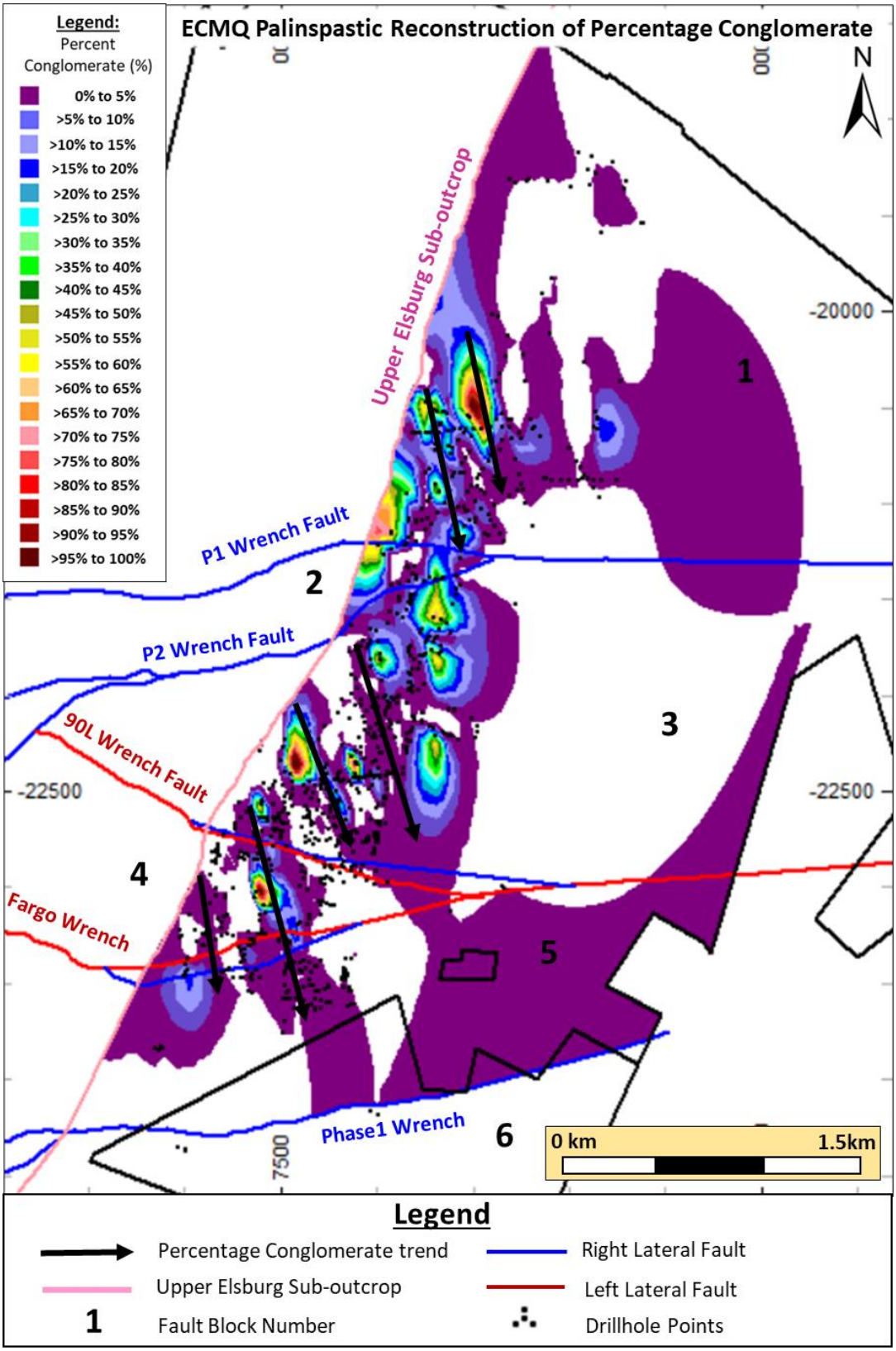


Figure 122: Palinspastic percentage conglomerate reconstruction for ECMQ.

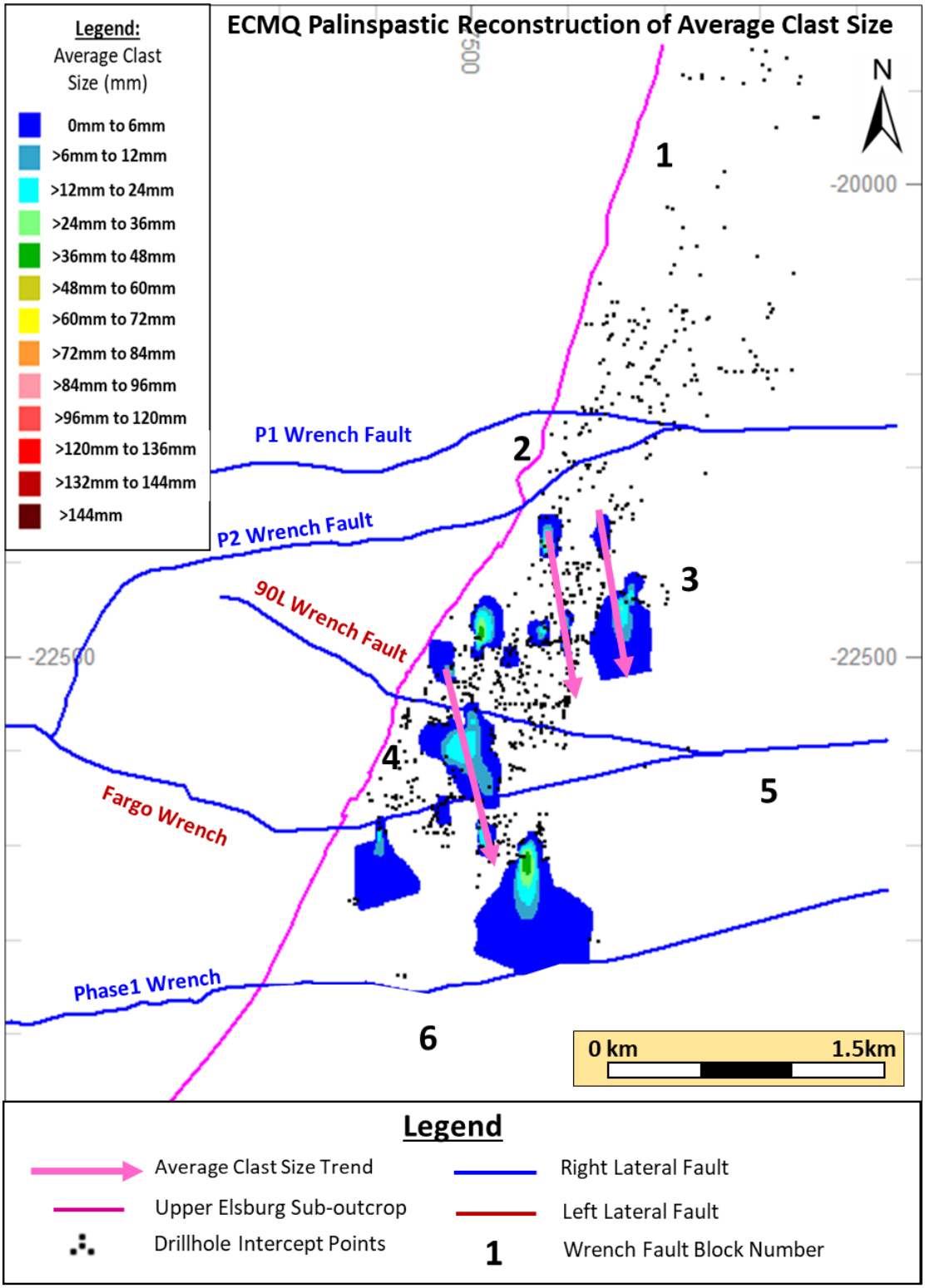


Figure 123: Palinspastic average clast size reconstruction for ECMQ.

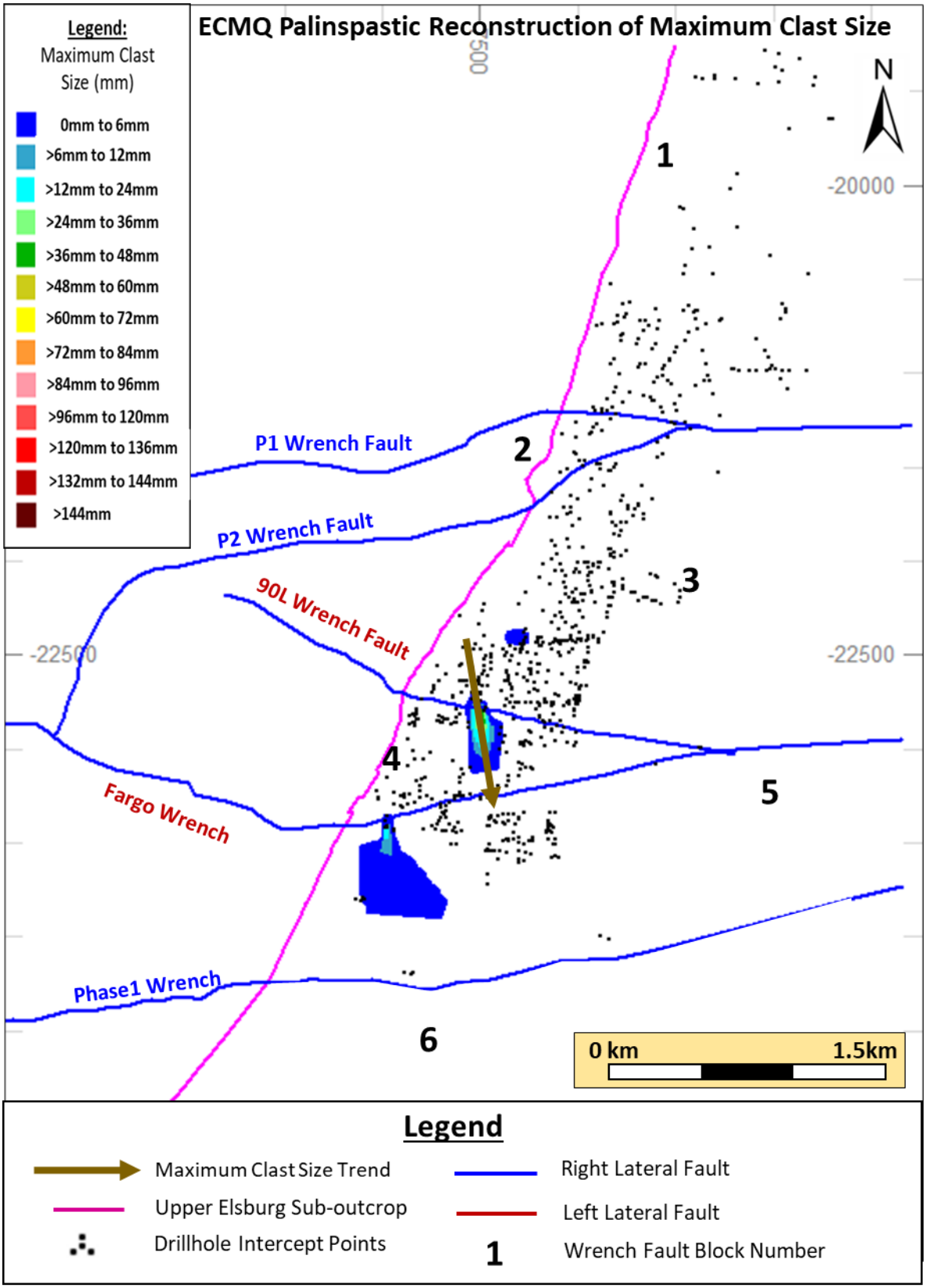


Figure 124: Palinspastic maximum clast size reconstruction for ECMQ.

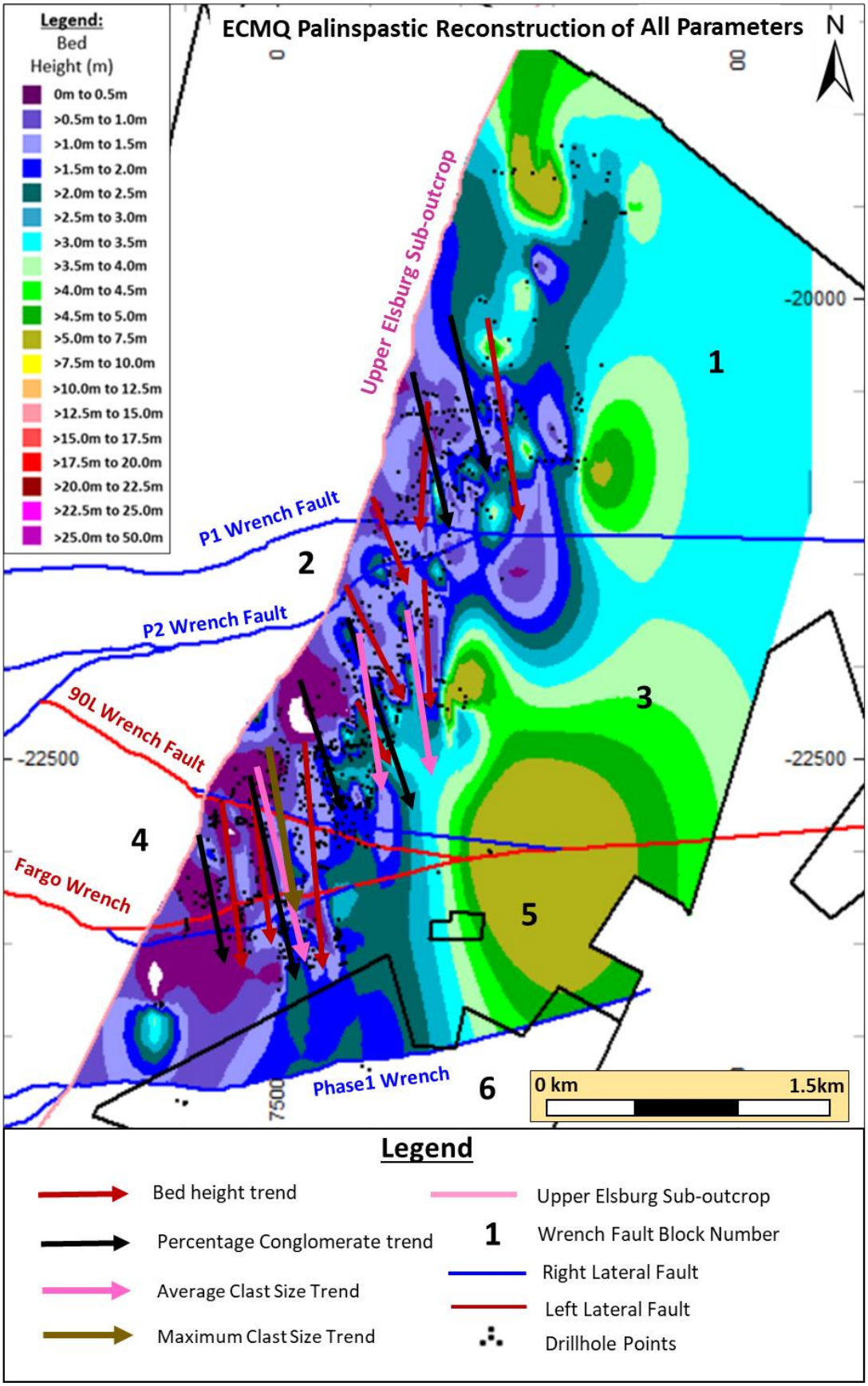


Figure 125: Palinspastic Reconstruction for the ECMQ - All Parameters

iv) ECMQ Detailed Plots

Figure 126 for Block 2 ECMQ presents the area of lower bed height (yellow polygon in Figure 126 a) and b)) with higher percentage conglomerate just north of and straddling the P1 Wrench. An interpretation of the bed height trend (black dashed line in Figure 126 a) and b)) appears to terminate on the P2 Wrench, with an associated apparent right-lateral dislocation across the P2 Wrench of ± 100 m.

This could infer post-ECMQ dislocation. The only possible evidence indicating possible syn-sedimentary structural influence could be the alternating higher and lower bed- height nodes along the strike of P2 Wrench, as indicated in Figure 127 a) by the yellow ellipse, as well as western margin to a thicker (>1.5 m) NNW to -SSE trending bed height trend (black dashed line). Interpretation of the Blackblack dashed trend line in Figure 127 a) could possibly indicate an apparent 200 m right-lateral dislocation across 90L Wrench. Whether this apparent dislocation represents a vertical or horizontal movement across 90L Wrench, is not clear, but could possibly infer either syn-sedimentary structural influence of the 90L Wrench or post-ECMC movement related to subsequent erosion by and deposition of the overlying ECT.

Figure 128a) and b) for the ECMQ are centred on Block 4. The yellow ellipse in Figure 128 a) high-lighthighlights the variable bed height nodes located along the strike of 90L Wrench. The black dashed bed height trend line discussed for Figure 127 is also presented in Block 5, where an apparent right-lateral ±100 m dislocation of the higher bed height and percentage conglomerate trend line is interpreted. The relative timing of these apparent interpreted dislocations is also unclear however they might have occurred due to syn-sedimentary structural influence (as evidenced by the alternating fault strike parallel bed height nodes along the 90L Wrench) or subsequent to ECMQ deposition, but possibly prior to erosion by the overlying ECT.

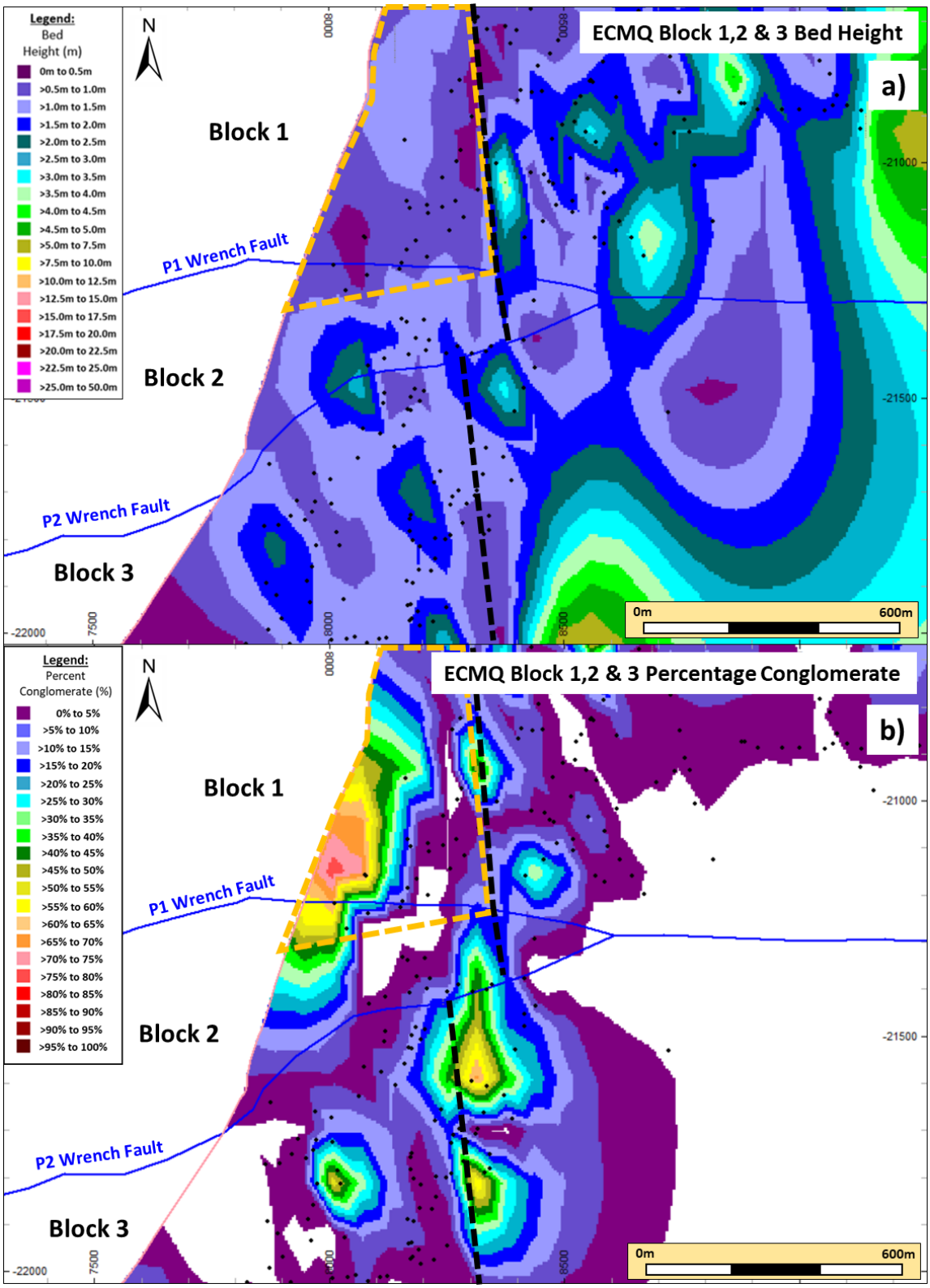


Figure 126: Enlarged Block 2 palinspastic reconstruction for a) bed height for ECMQ and b) for percentage conglomerate for ECMQ. Black dashed line in a) and b) indicate a zone of slightly increased bed height corresponding to higher percentage conglomerate, offset by P2 Wrench. Yellow polygon indicates lower bed height zone with higher percentage conglomerate terminated against P1 Wrench.

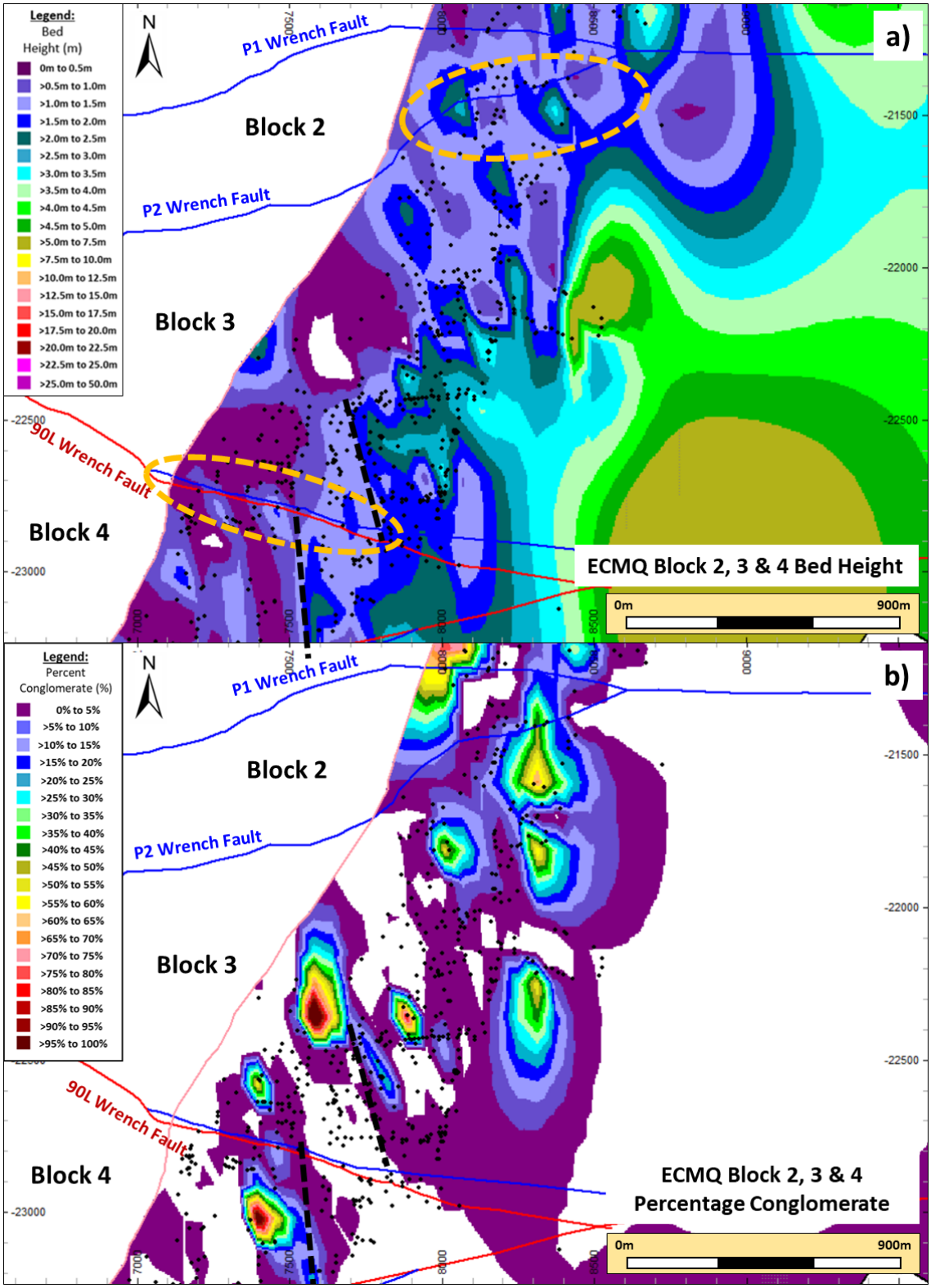


Figure 127: Enlarged Block 3 palinspastic reconstruction for a) bed height for ECMQ and b) for percentage conglomerate for ECMQ. Yellow ellipses in a) indicate a trend along the strike of P2 Wrench and 90L Wrench of rapidly alternating nodes of high and low bed height.

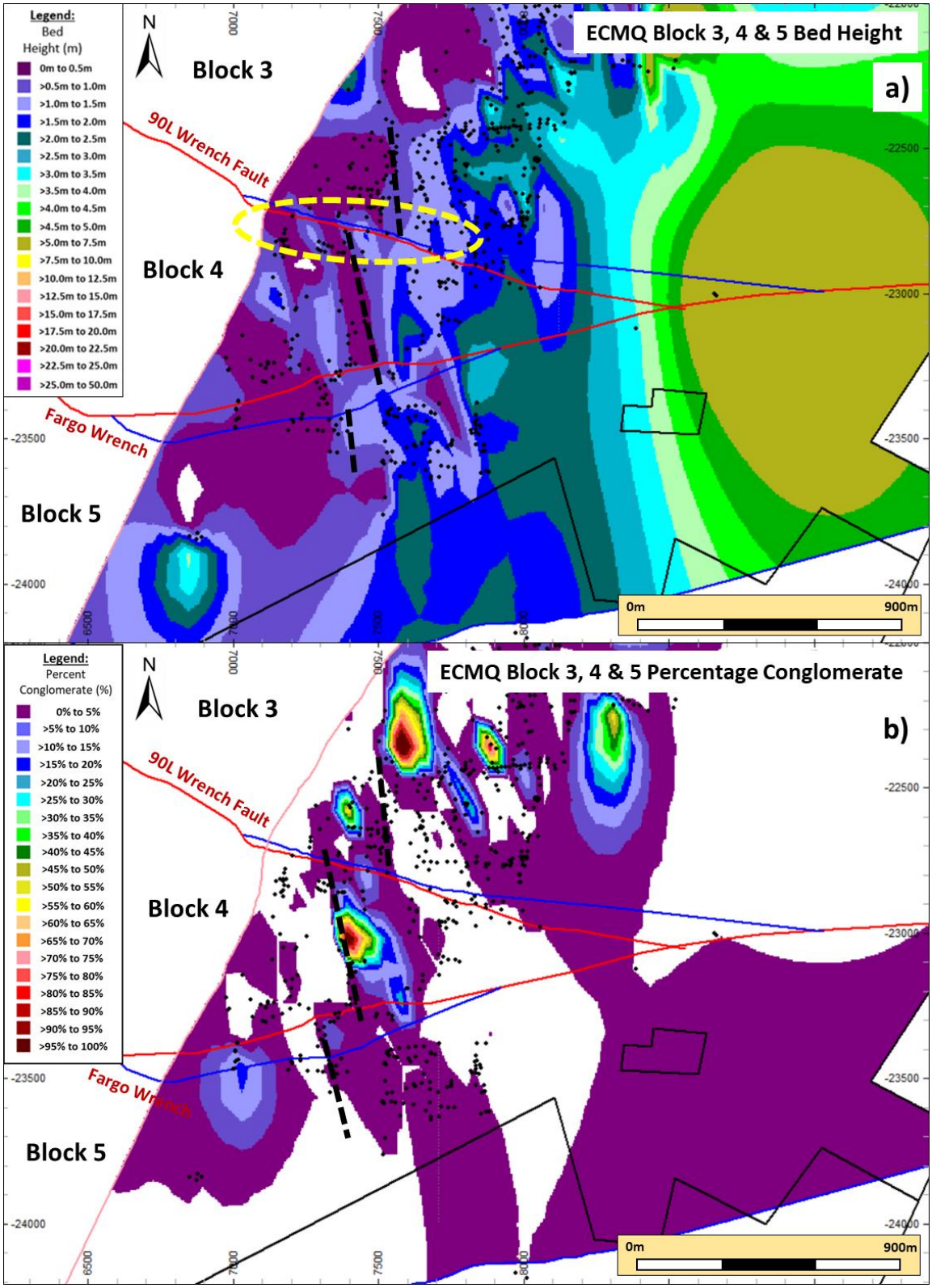


Figure 128: Enlarged Block 4 palinspastic reconstruction for a) bed height for ECMQ and b) for percentage conglomerate for ECMQ. Black dashed line in a) and b) indicate a change in bed height offset by the 90L Wrench and Fargo WrenchesWrench. Yellow ellipse in a) indicates a trend along the strike of 90L Wrench of rapidly alternating nodes of higher and lower percentage conglomerate.

f) **ECT**

i) ECT Bed Height

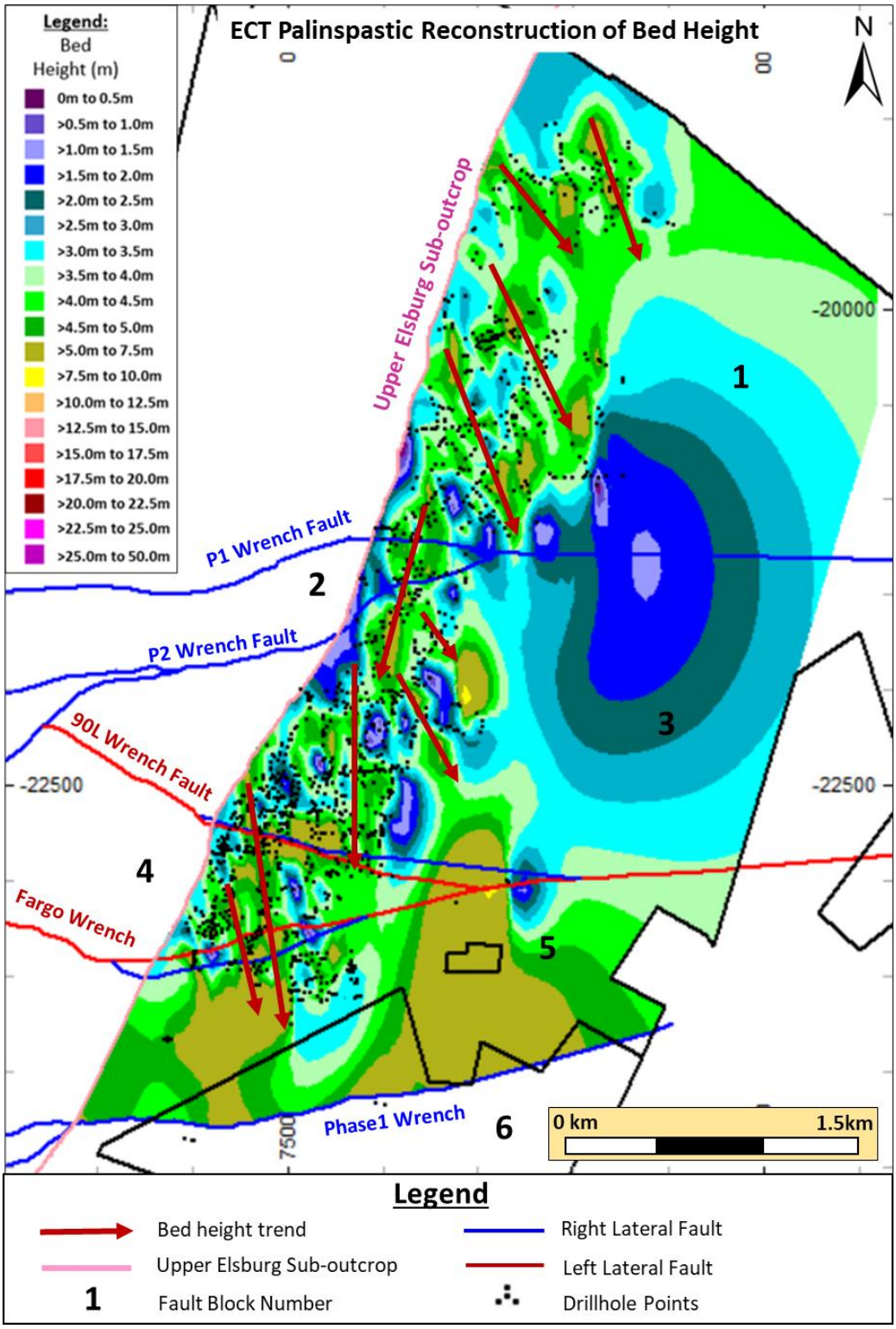


Figure 129: Palinspastic bed height reconstruction for ECT.

ii) ECT Percentage Conglomerate

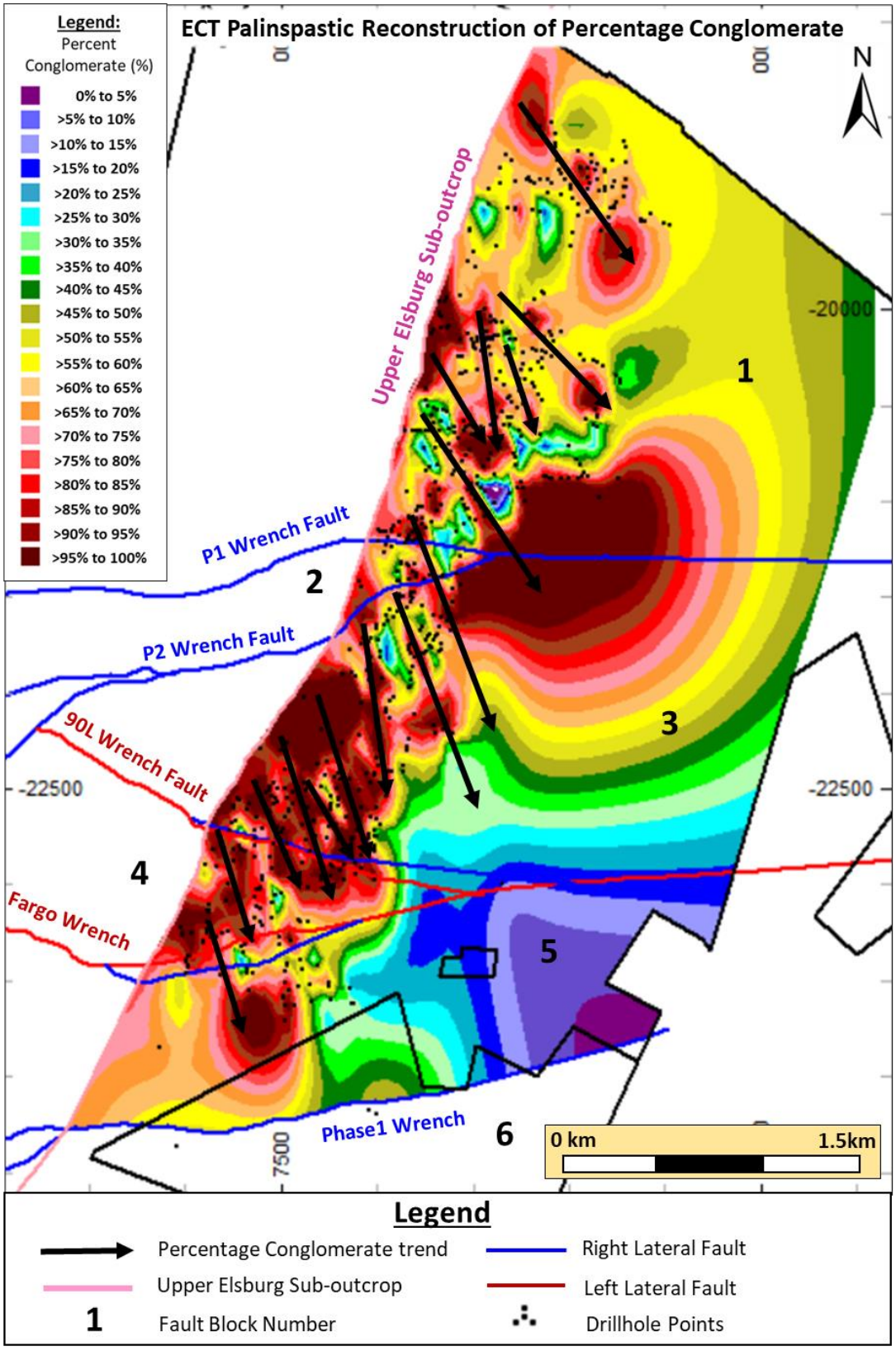


Figure 130: Palinspastic percentage conglomerate reconstruction for ECT.

iii) ECT Average and Maximum Clast Size

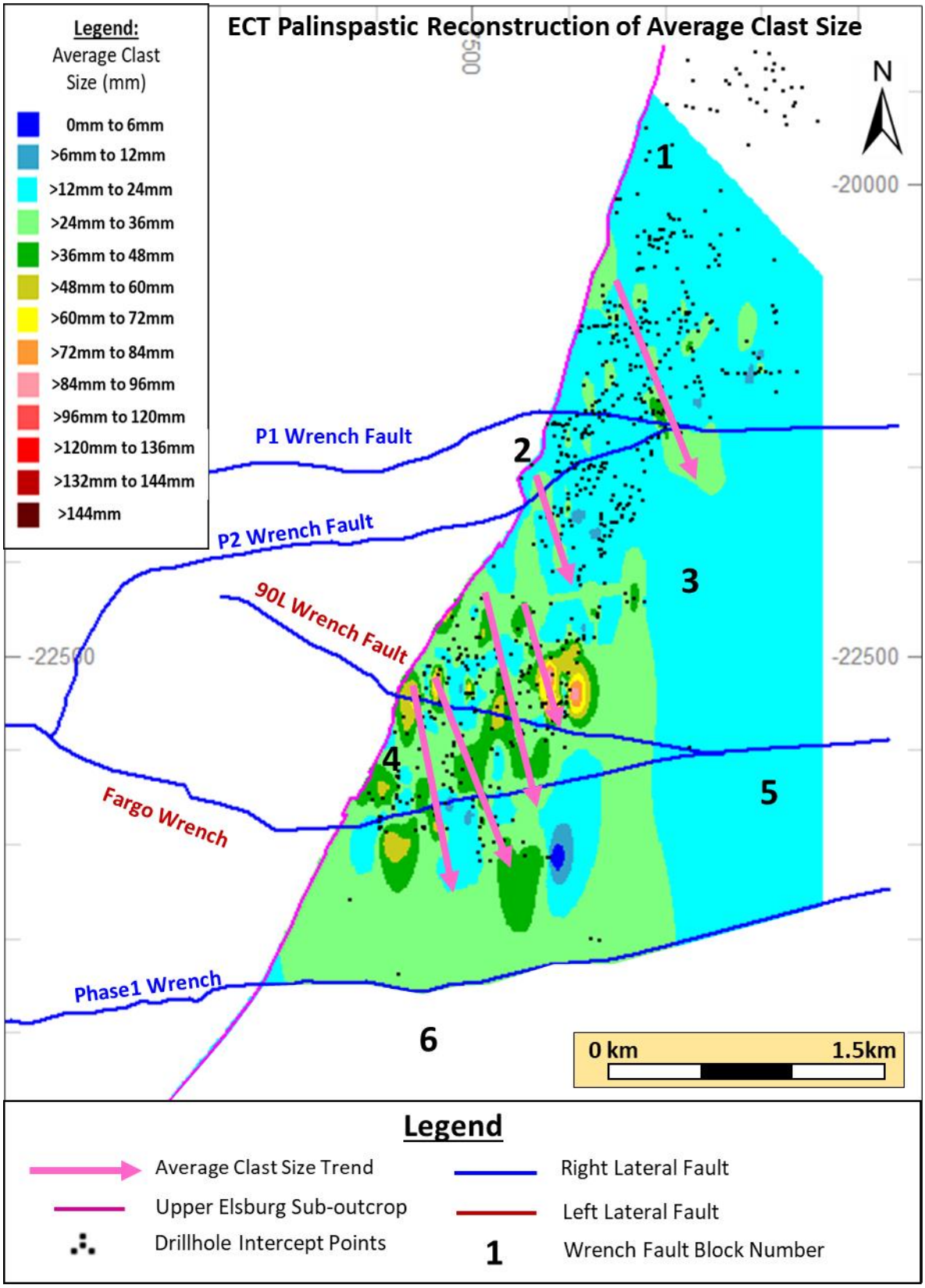


Figure 131: Palinspastic average clast size reconstruction for ECT.

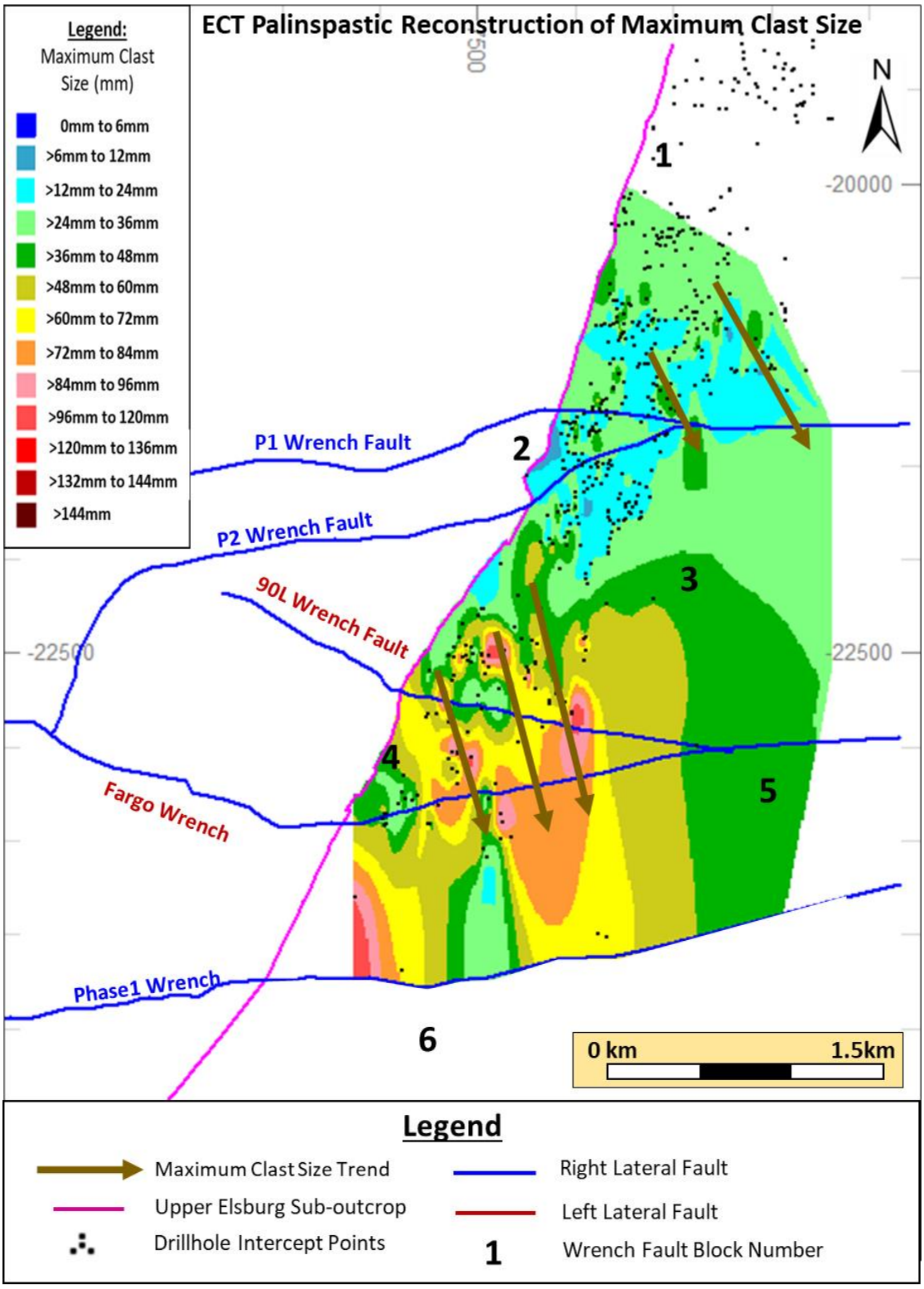


Figure 132: Palinspastic maximum clast size reconstruction for ECT.

g) **ED**

i) ED Bed Height

The palinspastic reconstruction for bed height for the ED is presented in Figure 133. In the north of Block 1, the westward thinning of the ED is seen to be more gradual (>15 m ±1500 m from sub-outcrop to >3 m up against sub-outcrop) when compared to that encountered in the southern half of Block 1 through to Block 5 in the south, where ED may be completely eradicated up against the UEUpper Elsburg sub-outcrop by the overlying erosive unconformable MAC. In the south, in Block 5, bed height exceeds 17 m as close as 1000 m from sub-outcrop.

ECB gradually thins from the east to west towards the Upper Elsburg Subsub-outcrop but very seldom thinning to <2 m. This is suspected to be the result of the limited erosion by the more quartzitic overlying ECBQ. Maximum bed height (>10 m to 12.5 m) is reached within the eastern half of Block 4 between the 90L Wrench and Fargo WrenchesWrench ±1000 m from sub-outcrop. Higher bed height trends (excluding the westward thinning) run oblique (NNW-SSE) relative to the sub-outcrop within Blocks 1, 3, 4 and possibly also Block 5.

iv) ED Percentage Conglomerate

The ED is primarily a quartzite with scattered conglomerate lags sometimes located on bedding planes. Figure 134 indicates a general decrease in percentage conglomerate for the ED towards the east. In addition, the northern half of Block 1 presents a lower conglomerate (seldom exceeding >15% conglomerate) occurrence than elsewhere to the south.

A distinct increase in percentage conglomerate in the ED occurs in the area of the P1 Wrench and P2 WrenchesWrench. Between P2 Wrench and 90L Wrench, percentage conglomerate in the ED decreases to between 0% and 5%. Directly north of the 90L Wrench, percentage conglomerate increases again, with localised zones of higher percentage conglomerate zones in Block 4.

In Block 1 two percentage conglomerate trends are interpreted. The first percentage conglomerate trend line appears to trend NW to -SE with a secondary trend running N to S. In Blocks 2, 3, 4 and 5 a possible NNW to -SSE trend may be identified which is sub-parallel to the bed height trends observed in Figure 133.

v) ED Average and Maximum Clast Size

Very little ED average and maximum clast size data is available in Block 1 in the north of the project area Figure 135 and Figure 136). Average clast data just north of P1 Wrench attains a maximum average clast size of between >12 mm and 24 mm.

Average clast size in the south to the north of 90L Wrench may locally attain an average of clast size of ±36 mm. The average clast size trends appear to cross the 90L Wrench and Fargo Wrench combination in the south and

trend NNW to -SSE. Interpretation is effectively only possible up to 1.5 km to the east of the UEUpper Elsburg sub-outcrop due to the significant decrease in data density to the east.

Maximum clast size renders similar trends to the average clast size (NNW to -SSE) in proximity to 90L Wrench and Fargo WrenchesWrench and maximum clast size appears similar to the average clast size with a maximum of ±36 mm being discernible.

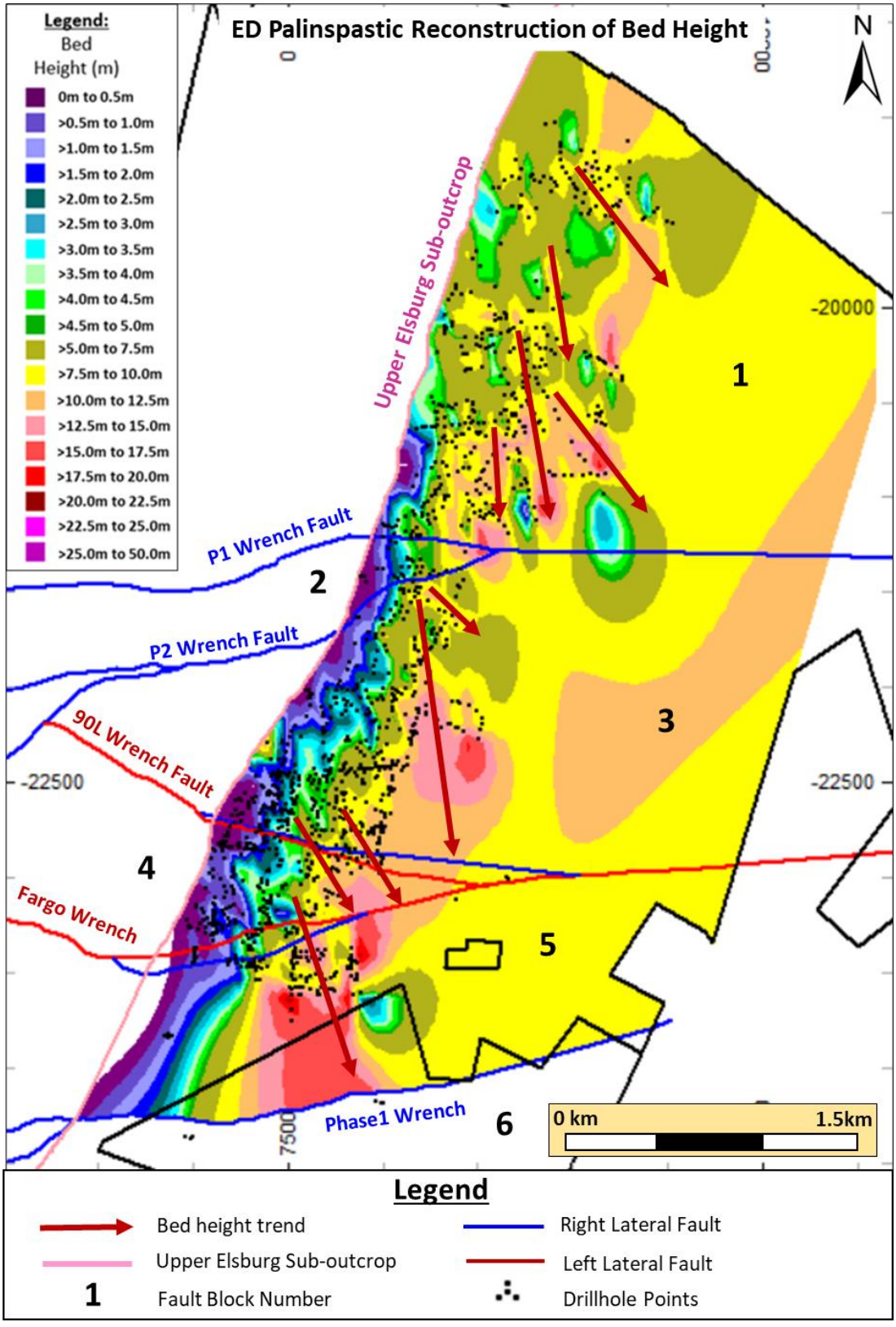


Figure 133: Palinspastic bed height reconstruction for ED.

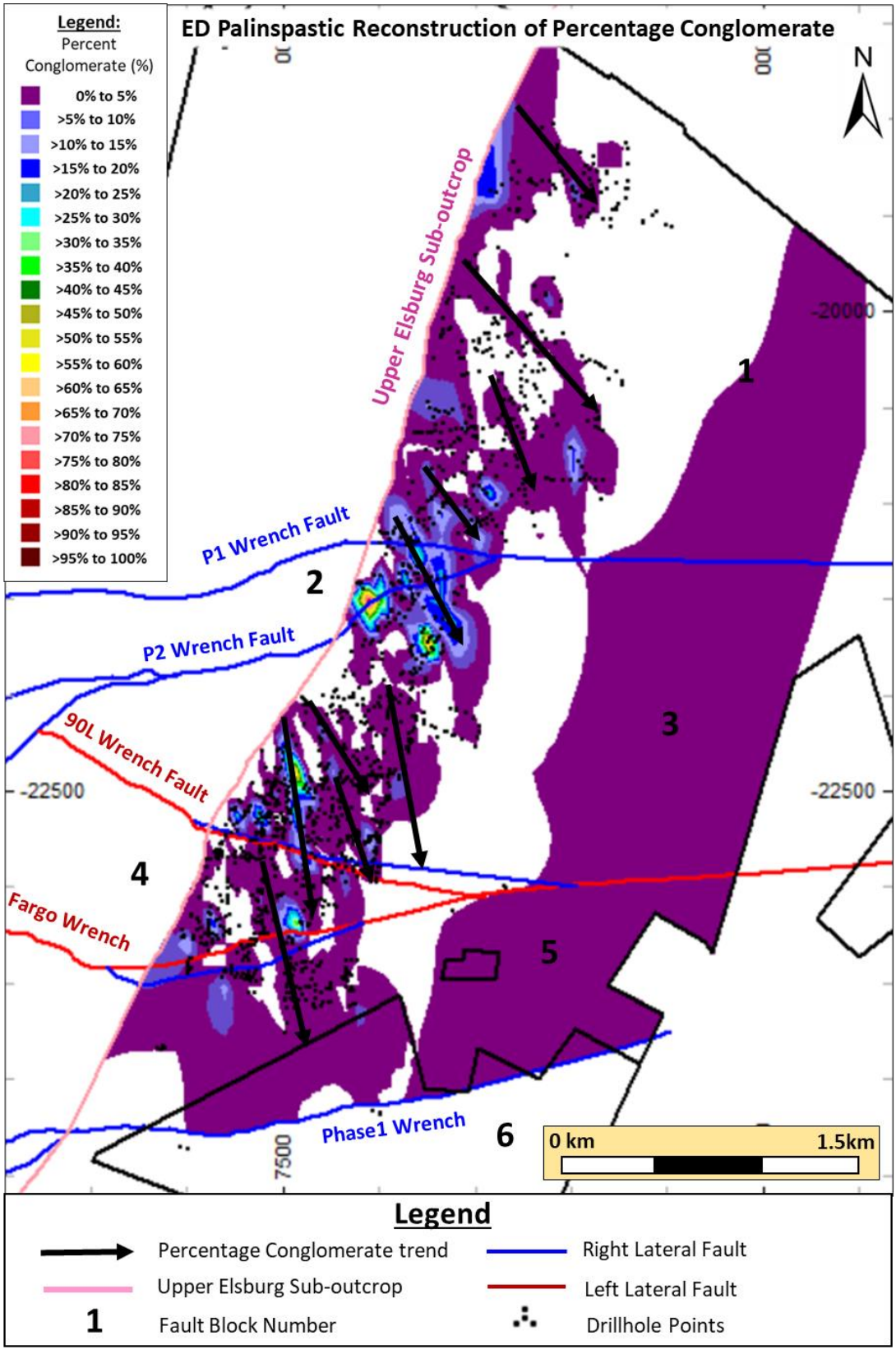


Figure 134: Palinspastic percentage conglomerate reconstruction for ED.

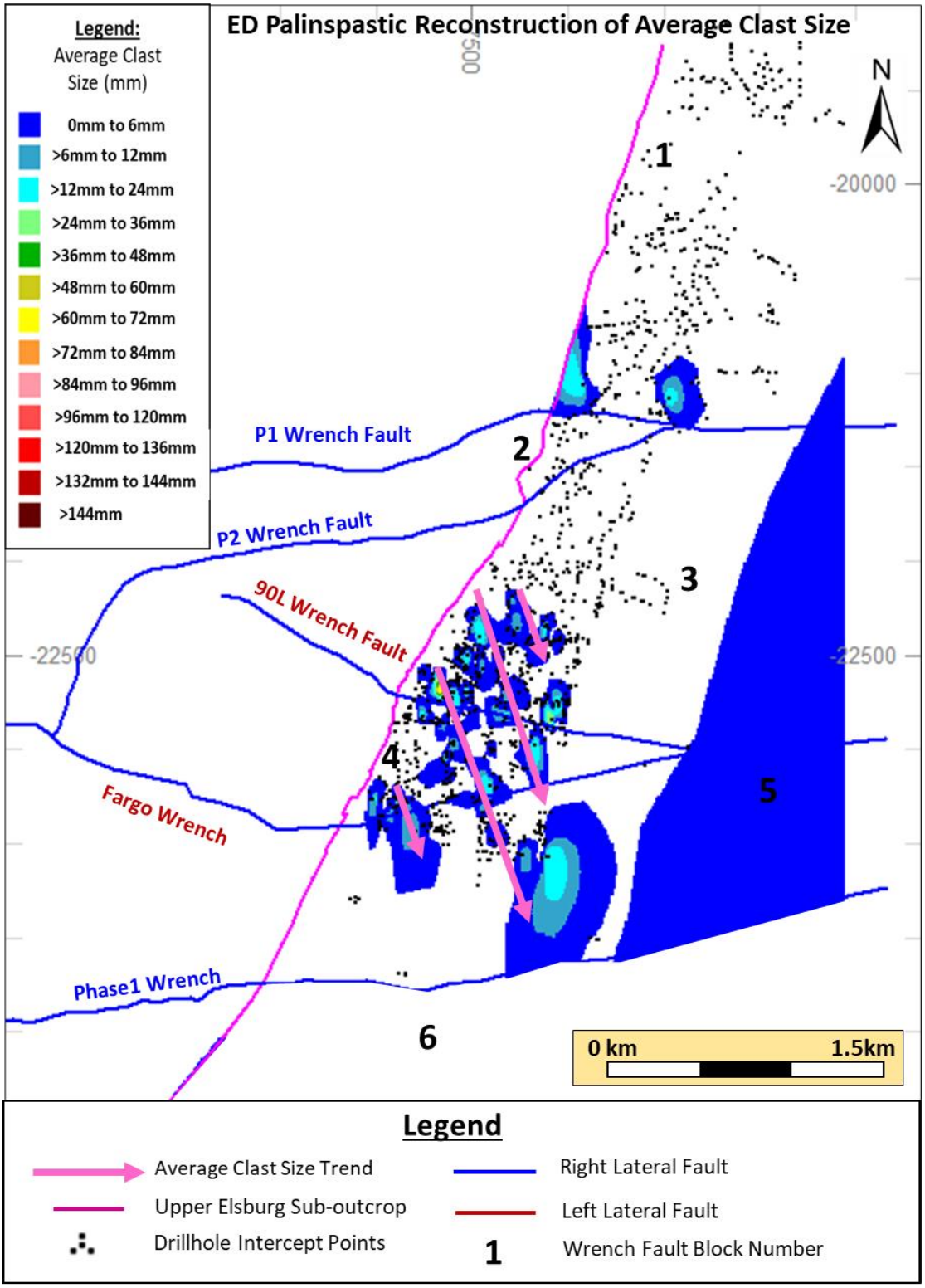


Figure 135: Palinspastic average clast size reconstruction for ED.

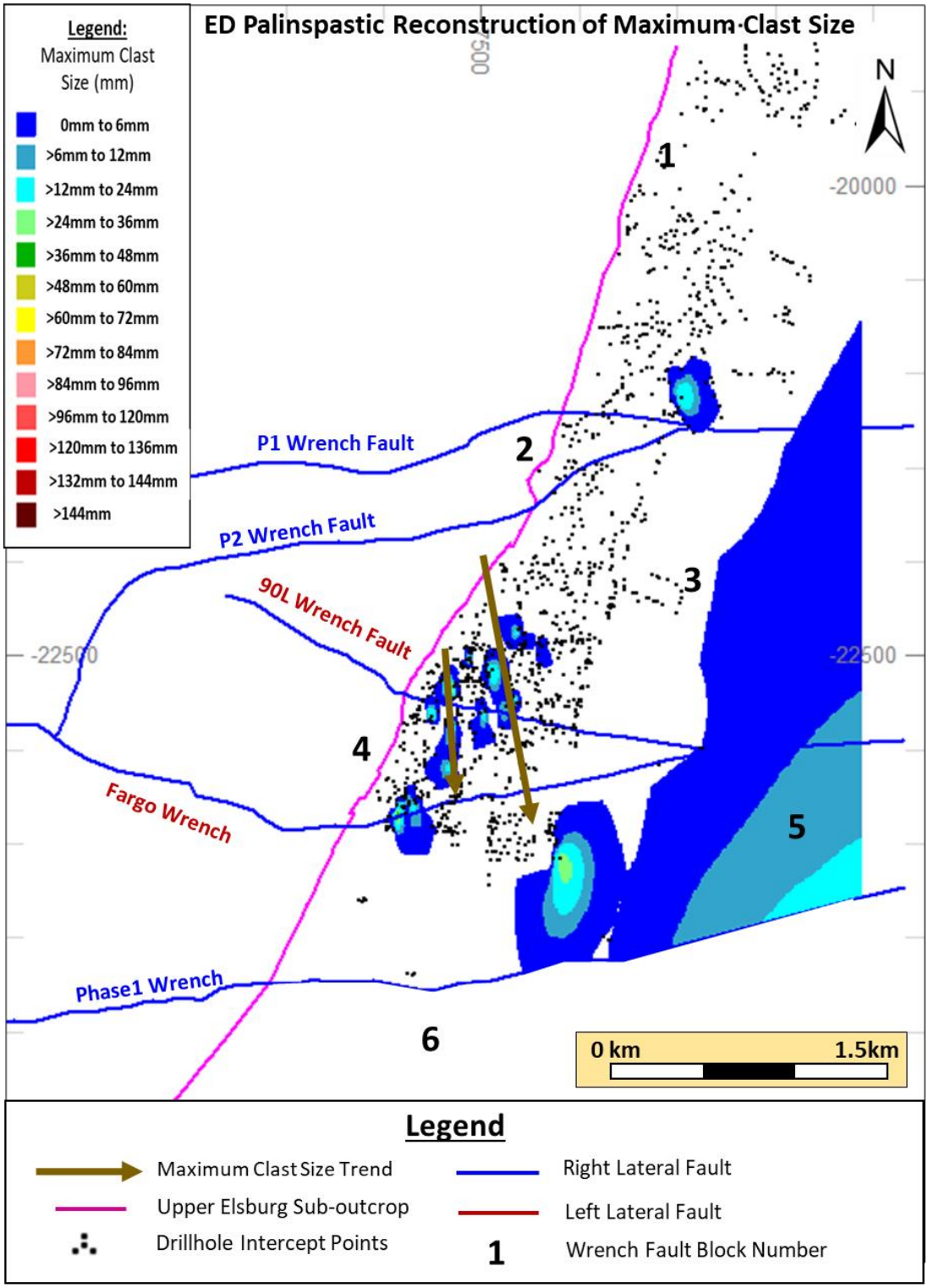


Figure 136: Palinspastic maximum clast size reconstruction for ED.

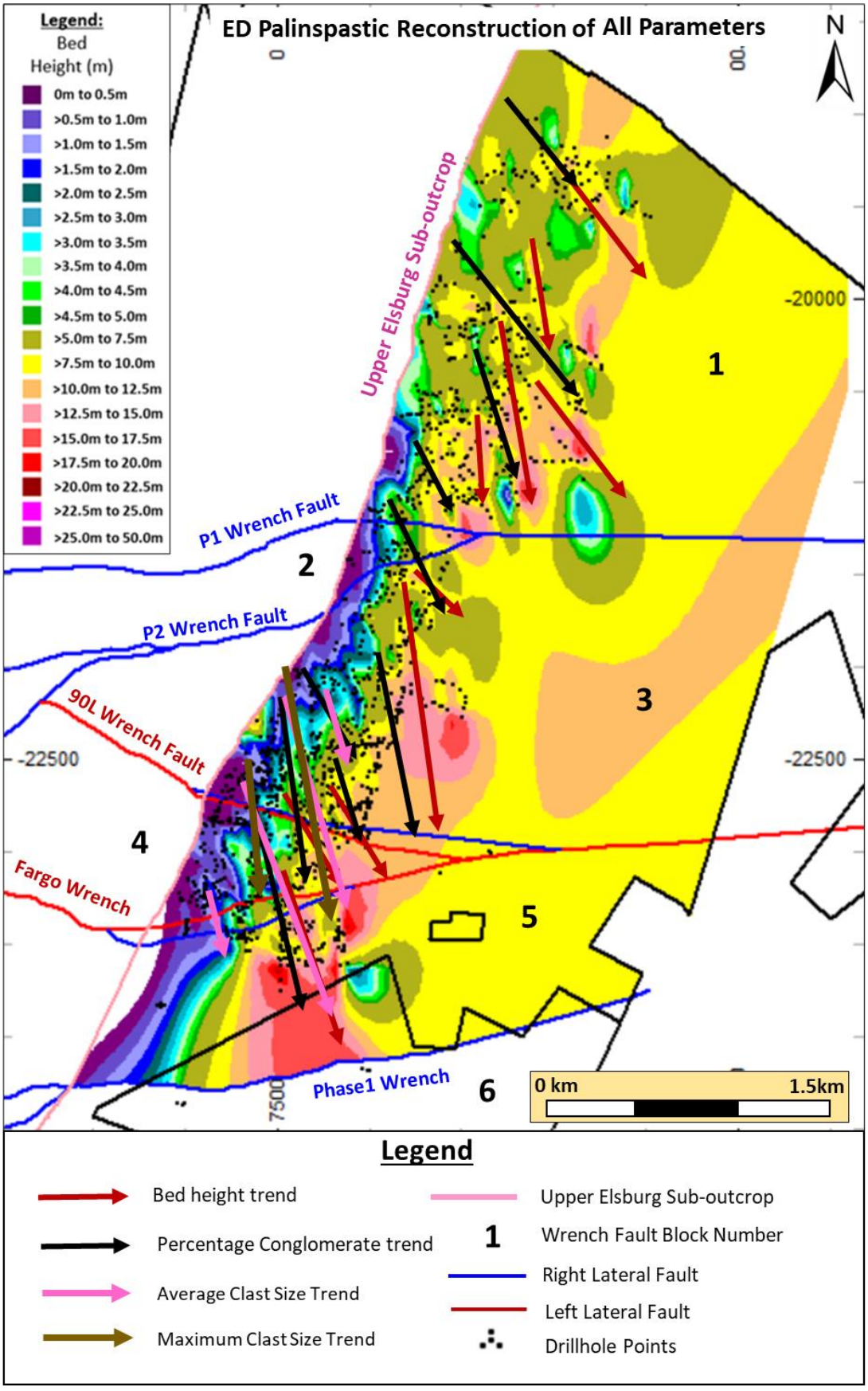


Figure 137: Palinspastic Reconstruction for the ED - All Parameters

vi) ED Detailed Plots

Figure 138 a) presents an interpretation of the ED bed height (black dashed line) running NNW to -SSE, where a zone of thicker bed height is terminated against P2 Wrench but passes through P1 Wrench. This zone however exhibits a lower percentage conglomerate directly south of P1 Wrench in Figure 138 b). The western areas of both blocks show thinning up to the UEUpper Elsburg sub-outcrop, which may be the result of erosion of the ED by the overlying unconformity -bound MAC at the base of the Upper Elsburg Massives. This would imply that possible (but limited) syn-sedimentary structural disturbance across P1 mightmay have taken place, while an apparent right-lateral dislocation is clearly visible across P2 Wrench. This apparent dislocation could be attributable to either vertical displacement up to the north on Block 2 prior to erosion by the MAC, or as a result of actual right-lateral dislocation after ED deposition and related to subsequent erosion by the MAC.

Figure 139 a) relates to Block 3 and depicts a greater bed height directly south of the P2 Wrench. This zone similarly depicts a higher percentage conglomerate up against P2 Wrench as well. Apparent dislocation is not immediately visible (for bed height) across the 90L wrench in the south in this plot, however nodes of variable percentage conglomerate adjacent and north of 90L Wrench could possibly indicate an element of syn-sedimentary influence of the 90L Wrench on the ED.

An enlargement, over Block 4 (Figure 140 a) and b)) for bed height does, however, present a possible apparent right-lateral (±100 m) dislocation of greater bed height across 90L Wrench and another apparent right-lateral dislocation across Fargo Wrench of ±200 m in the south. Potential syn-sedimentary influence is supported by the location of nodes of variable percentage conglomerate directly north of both faults, however definitive senses of movement are not possible across the structures due to the later MAC erosion.

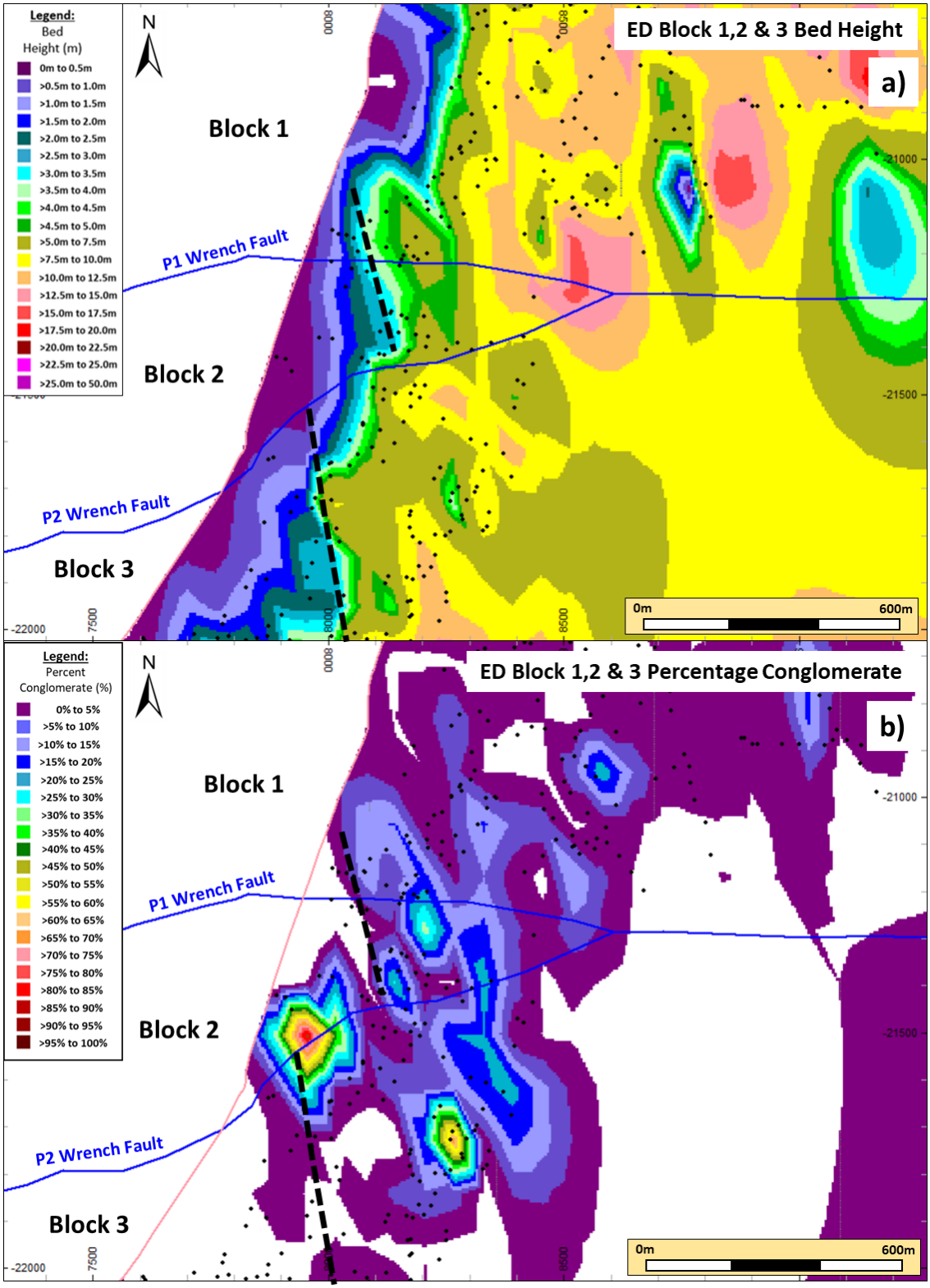


Figure 138: Enlarged Block 2 palinspastic reconstruction for a) bed height for ED and b) for percentage conglomerate for ED.

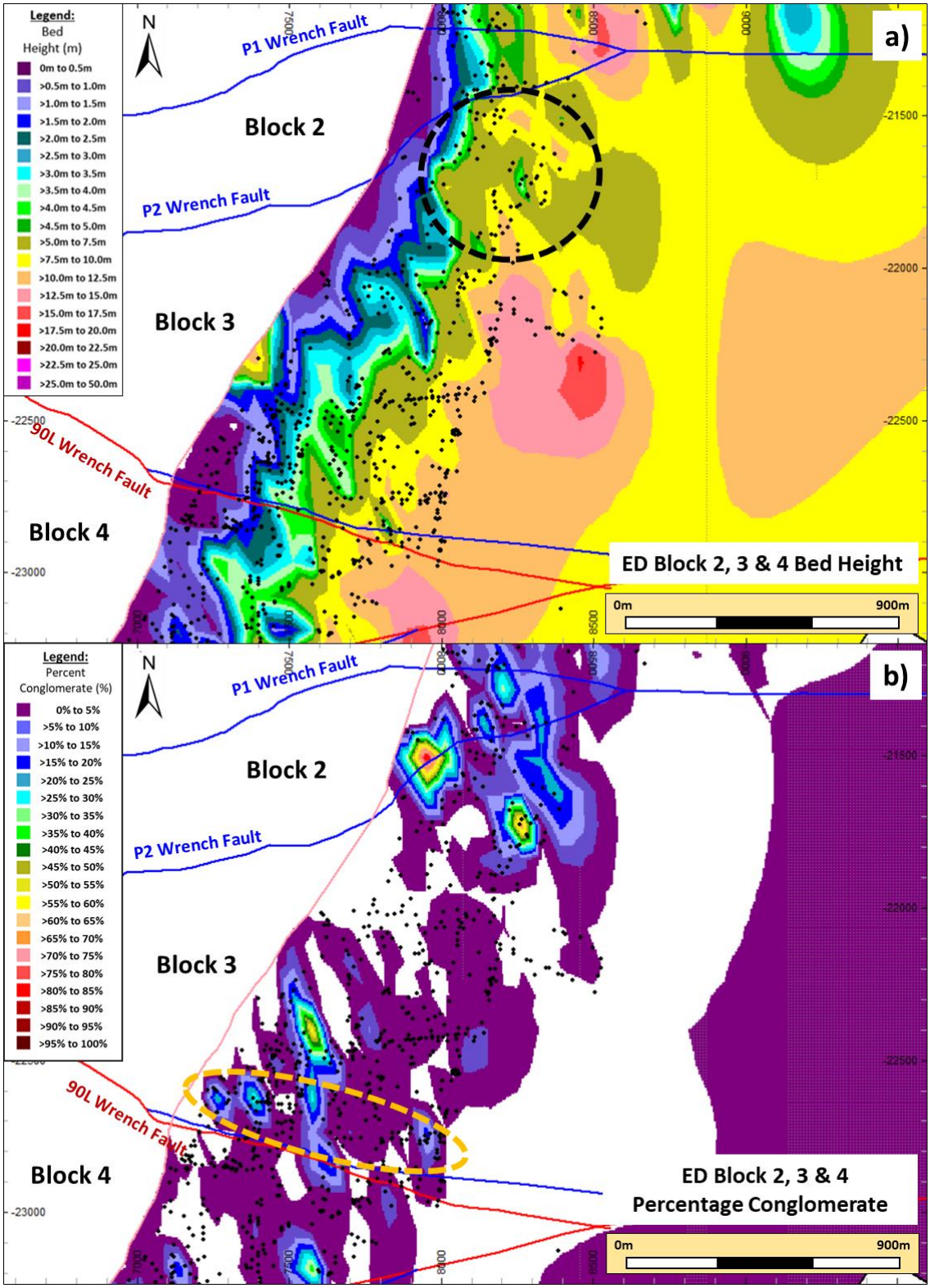


Figure 139: Enlarged Block 3 palinspastic reconstruction for a) bed height for ED and b) for percentage conglomerate for ED.

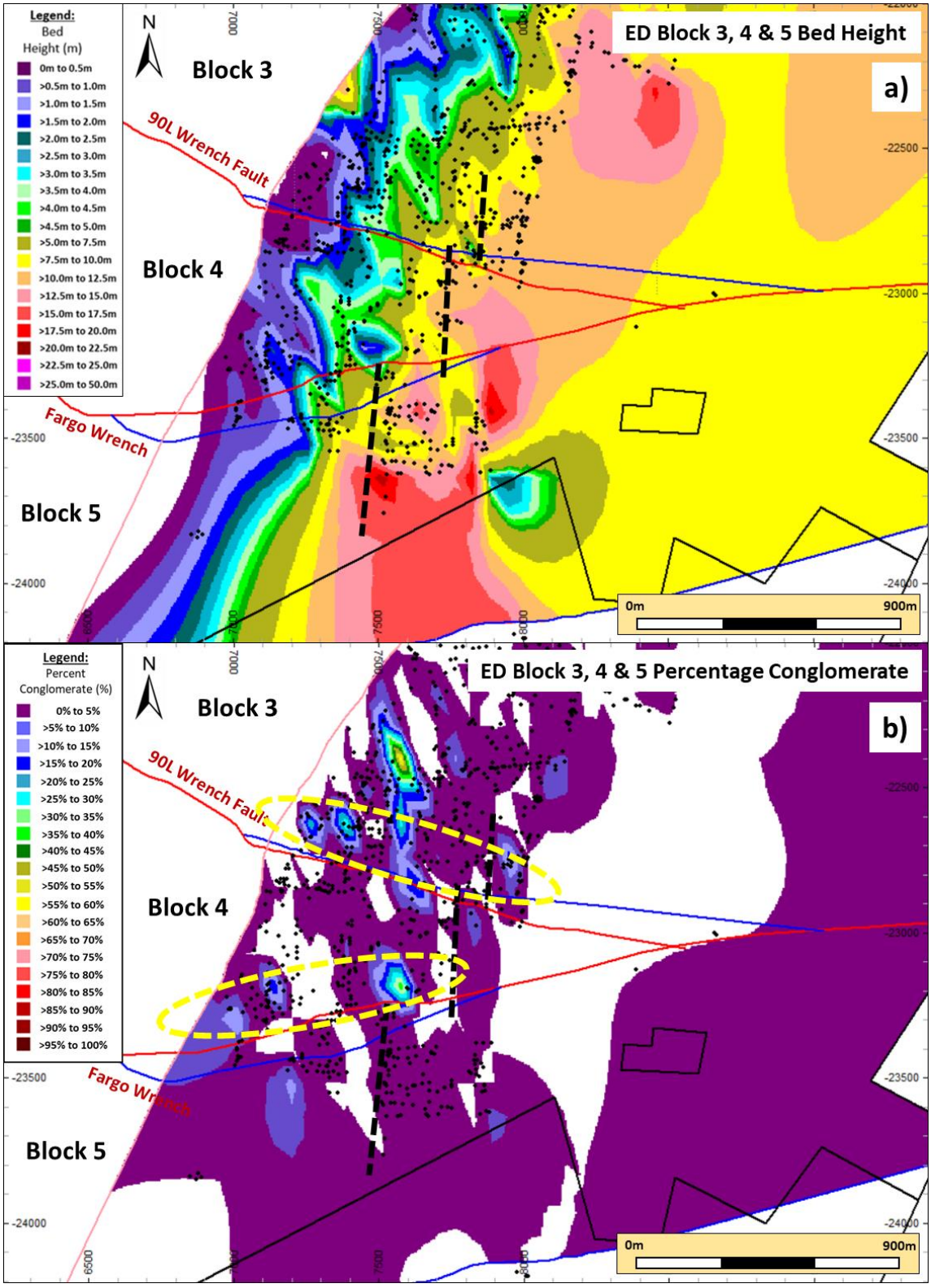


Figure 140: Enlarged Block 4 palinspastic reconstruction for a) bed height for ED and b) for percentage conglomerate for ED.

h) **MAC**

i) MAC Bed Height

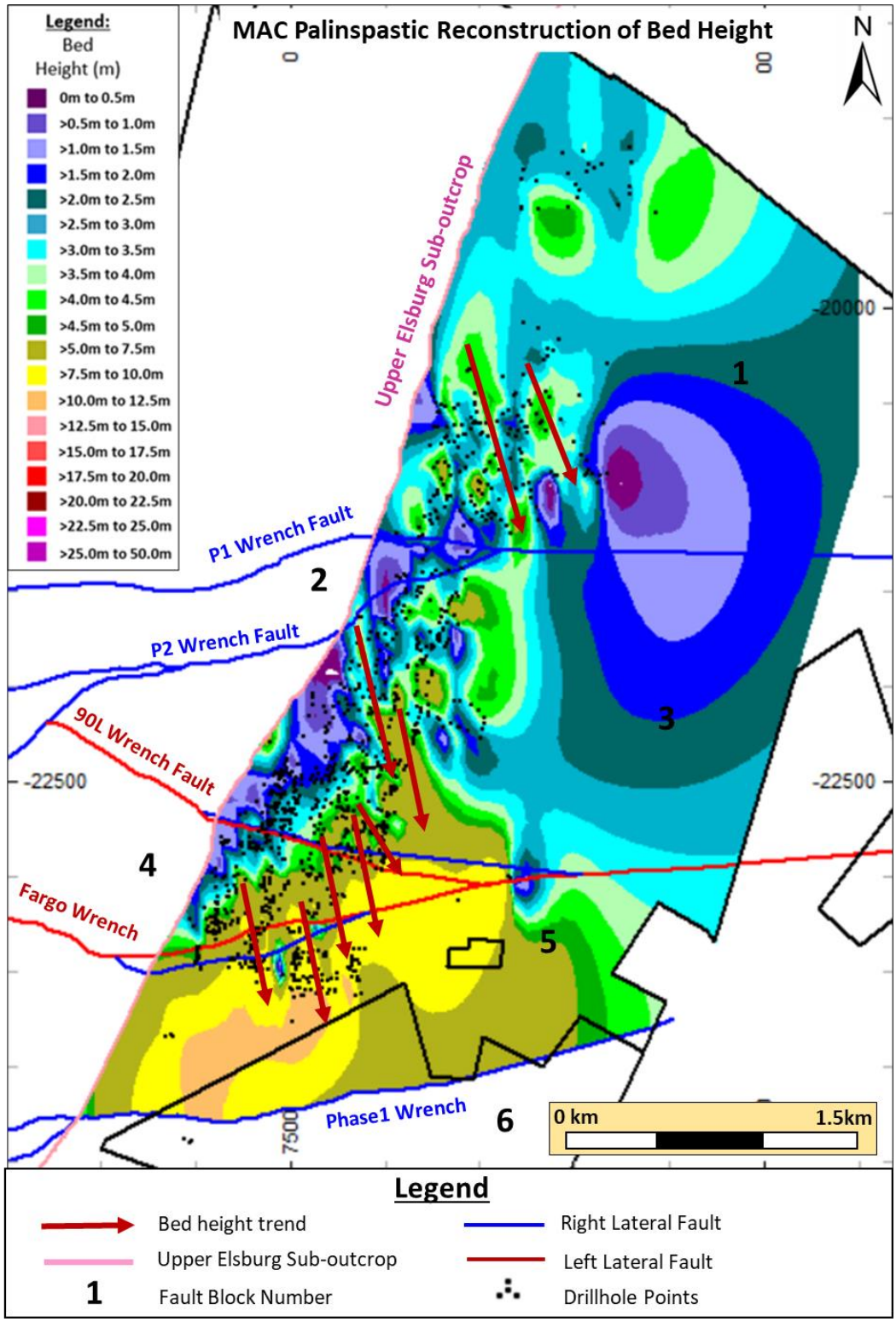


Figure 141: Palinspastic bed height reconstruction for MAC.

ii) MAC Percentage Conglomerate

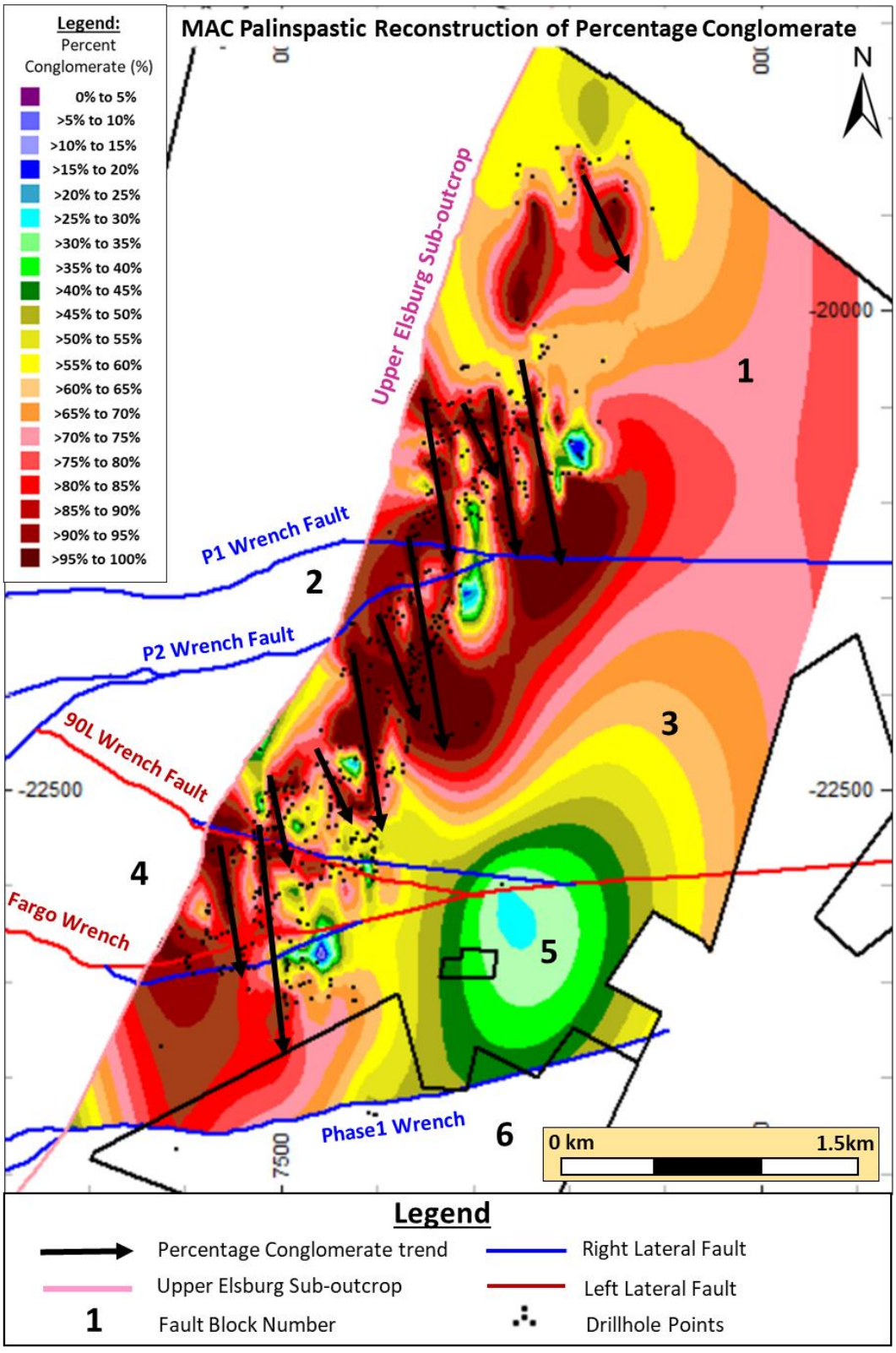


Figure 142: Palinspastic percentage conglomerate reconstruction for MAC.

iii) MAC Average and Maximum Clast Size

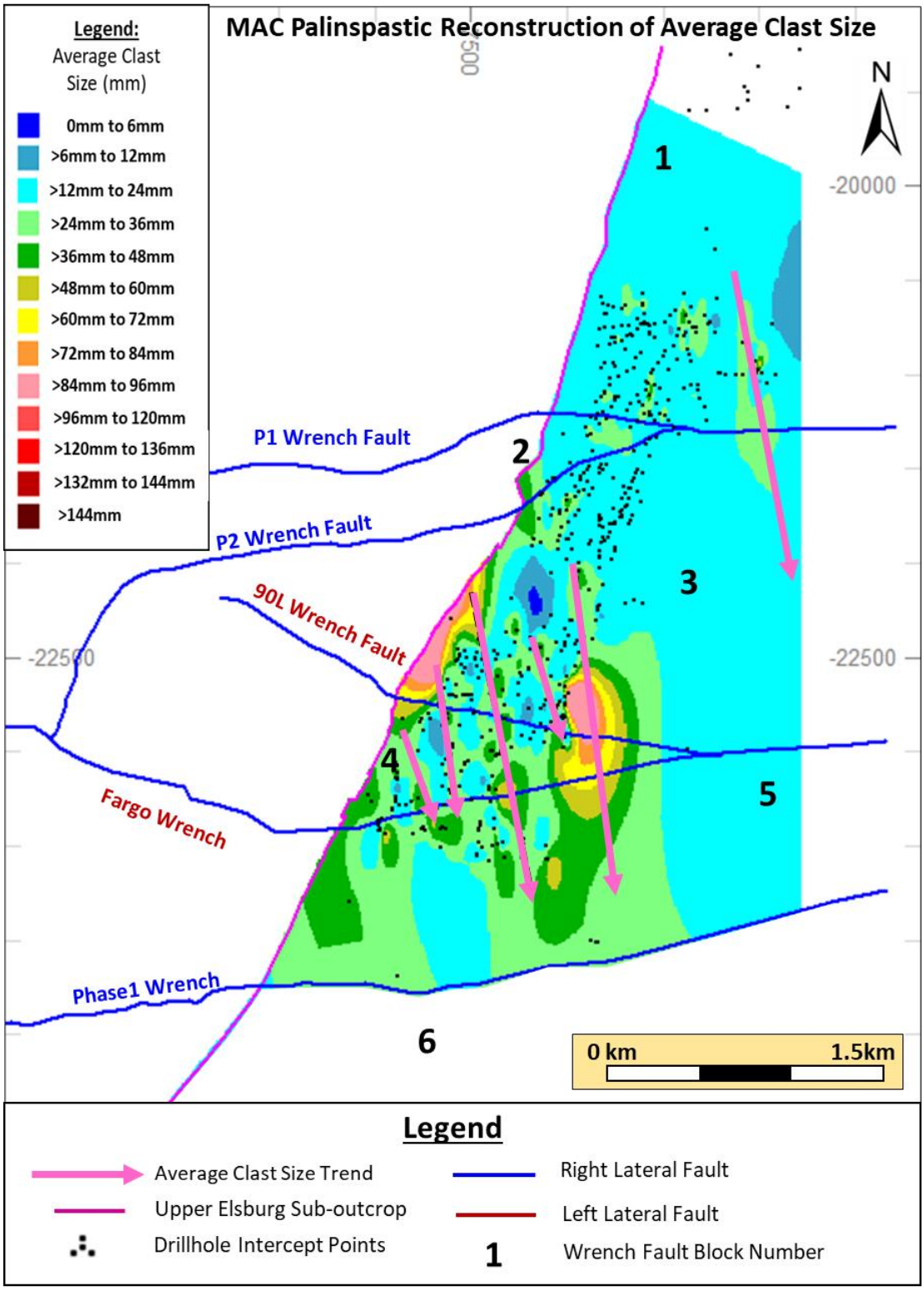


Figure 143: Palinspastic average clast size reconstruction for MAC.

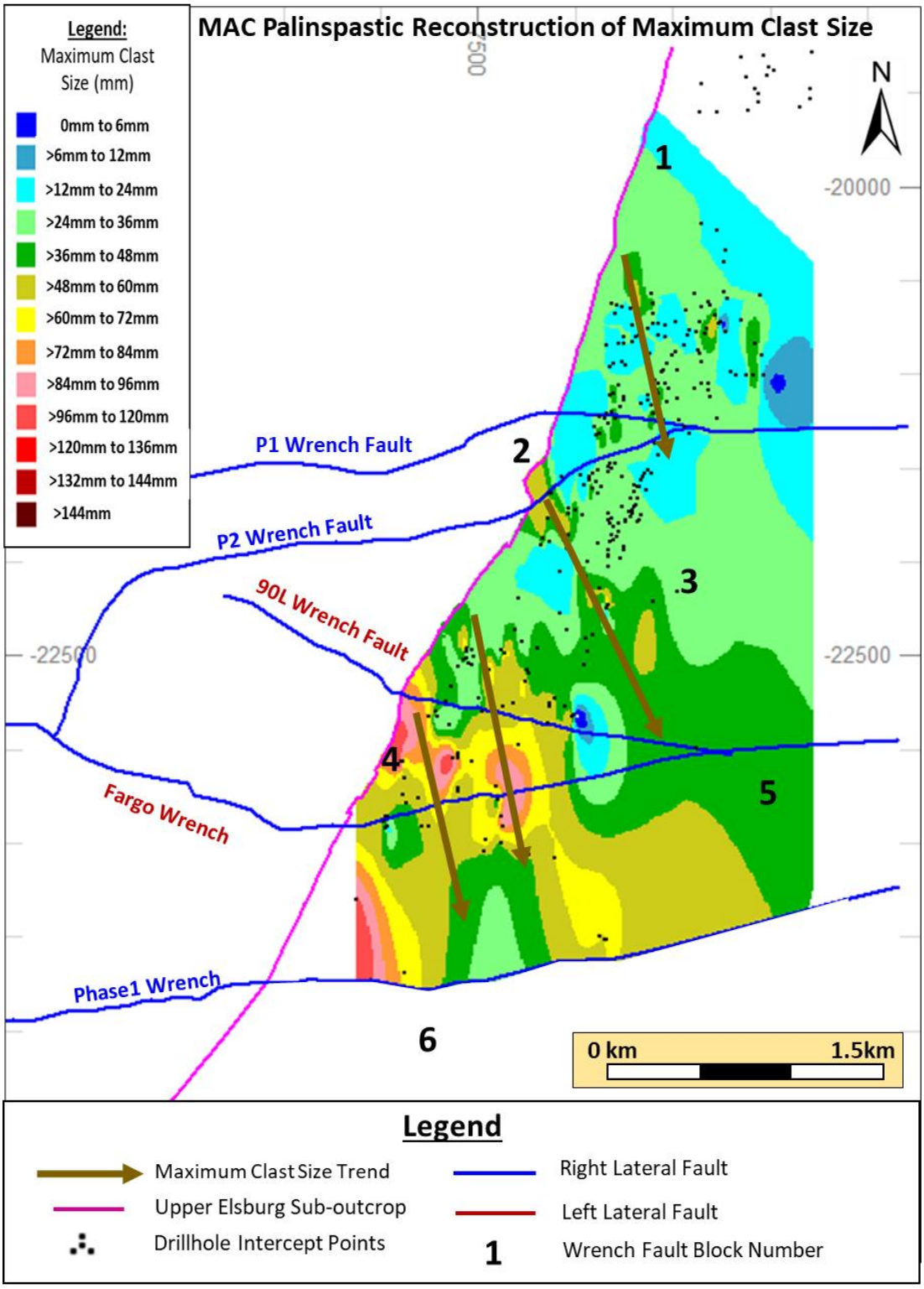


Figure 144: Palinspastic maximum clast size reconstruction for MAC.

i) **MAD**

i) MAD Bed Height

The palinspastic reconstruction for bed height for the MAD is presented in Figure 145. As with the MAC and Elsburg Individualindividual beds, the northern part of Block 1 attenuates towards the sub-outcrop at a somewhat lower rate than further to the south as seen in Block4Block 4. The MAD is totally eliminated against the sub-outcrop towards the middle of Block 1 by the overlying MIB.

General bed height for the MAD increases generally towards the south, attaining a maximum bed height of ±12.5 m approximately 1.2 km east of the UE SubUpper Elsburg sub-outcrop. Identified bed-height trends are approximately NNW to -SSE. Attenuation of the MAD appears to be generally greater eastwards over Block 4 than observed elsewhere.

ii) MAD Percentage Conglomerate

The MAD consists primarily of quartzite with minor interbedded conglomerate. The palinspastic reconstructed percentage conglomerate plot for the MAD Figure 146) depicts a low percentage conglomerate in the northern half of Block 1. Conglomerate content increaseincreases southwards as the P1 Wrench is approached, in conjunction with the increase in bed height. Further southwards, except directly south of the P2 Wrench, the percentage conglomerate for the MAD noticeably decreases. Percentage con glomerateconglomerate trends for the MAD are oriented NW to -SE in the southern half of Block 1 and swing slightly southward to NNW to -SSE towards the south.

iii) MAD Average and Maximum Clast Size

Average clast size (Figure 147) for the MAD remains between >12 mm and 24 mm in Block 1, in line with the increase in percentage conglomerate in the southern half of Block 1. A maximum average clast size of ± 24 mm to 36 mm is attained in the northern portion of Block 3 up against the P2 Wrench. Average clast size trends run NNW to -SSE parallel to the bed height and percentage conglomerate for the southern blocks, while in Block 1 a weak NW-SE trend is inferred. Maximum clast size data for the MAD is relatively sparse and thus interpretation of maximum clast size trends are precluded (Figure 148). A maximum clast size of between >36 mm and 48 mm is achieved in Block 3.

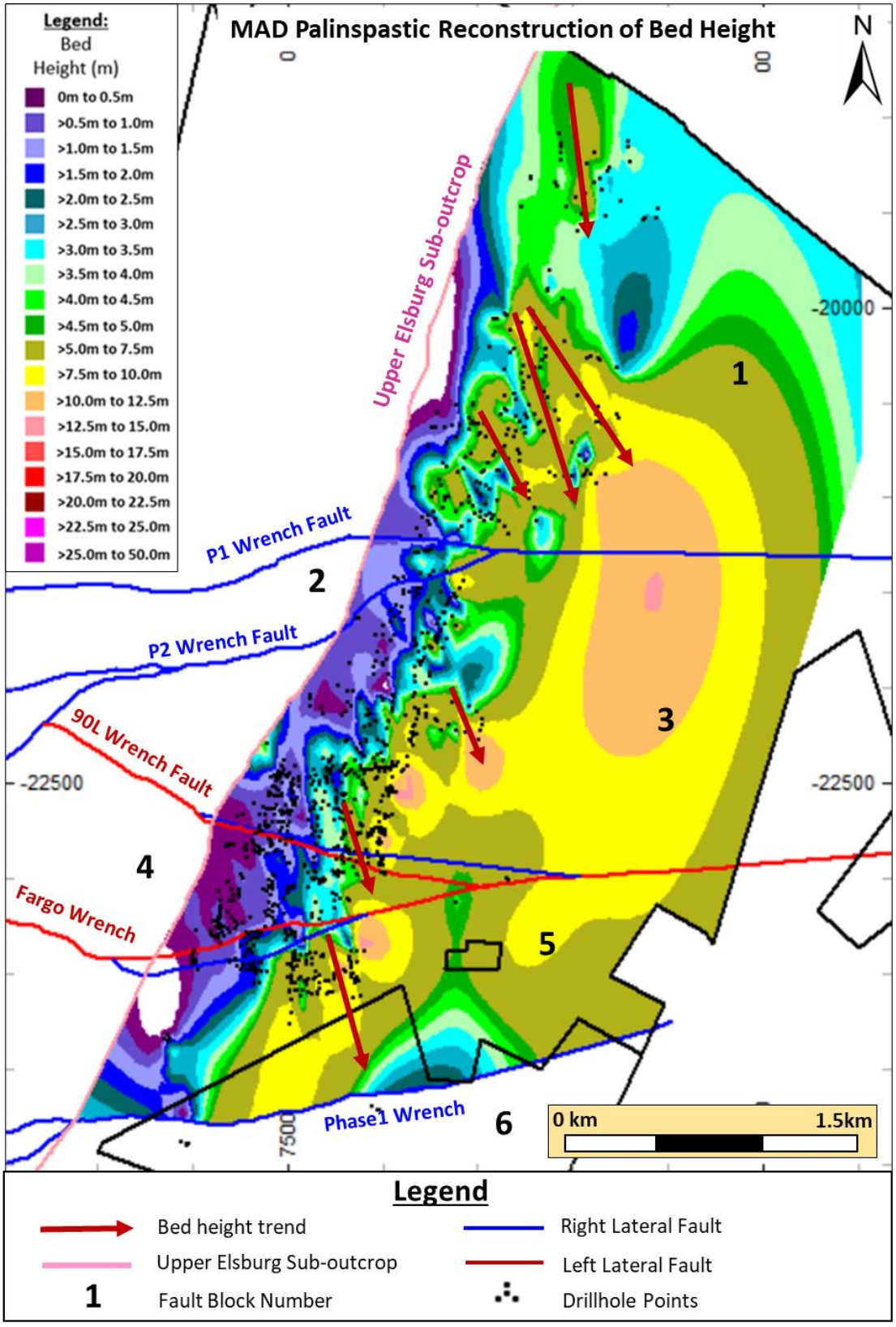


Figure 145: Palinspastic bed height reconstruction for MAD.

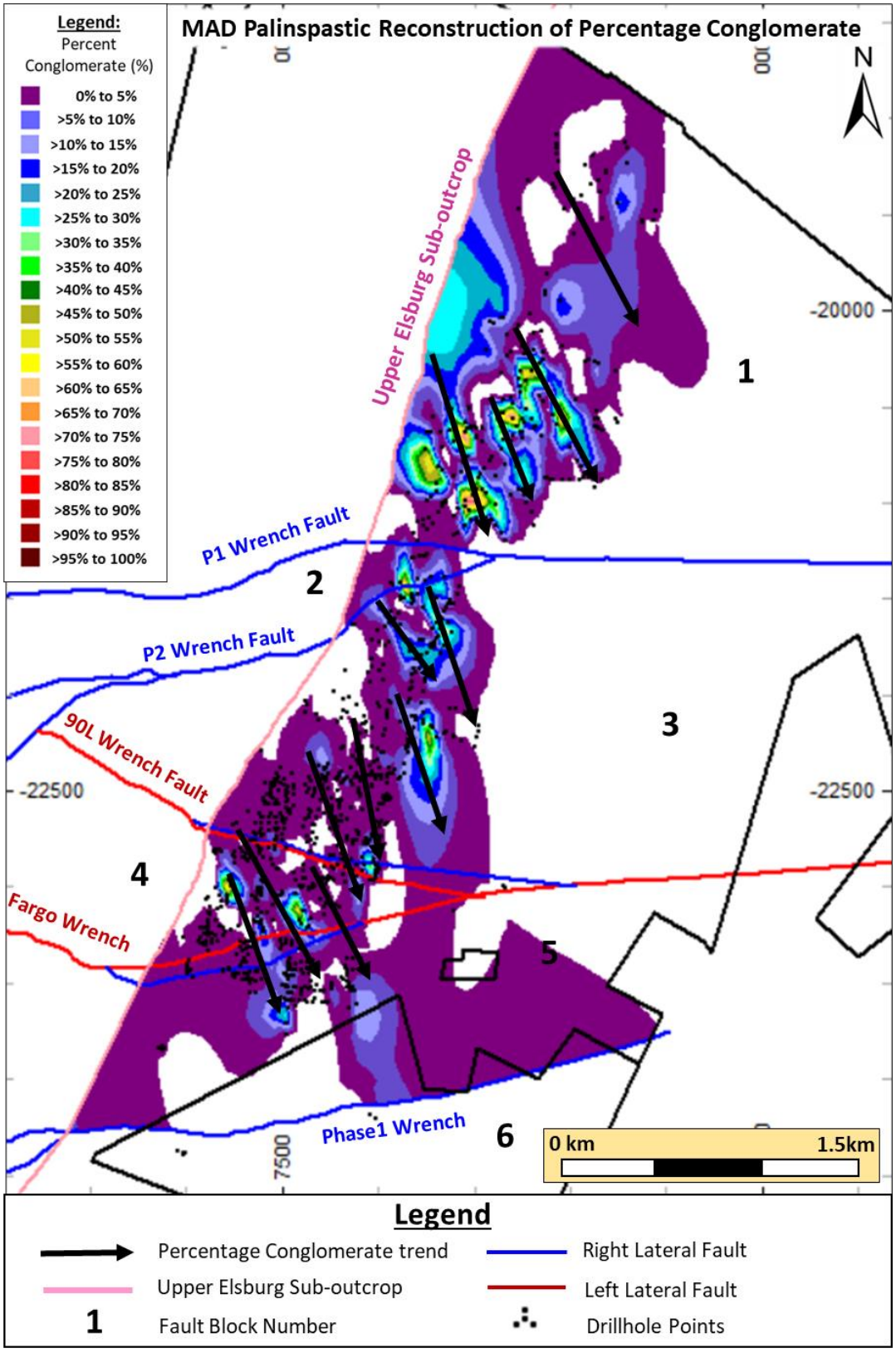


Figure 146: Palinspastic percentage conglomerate reconstruction for MAD.

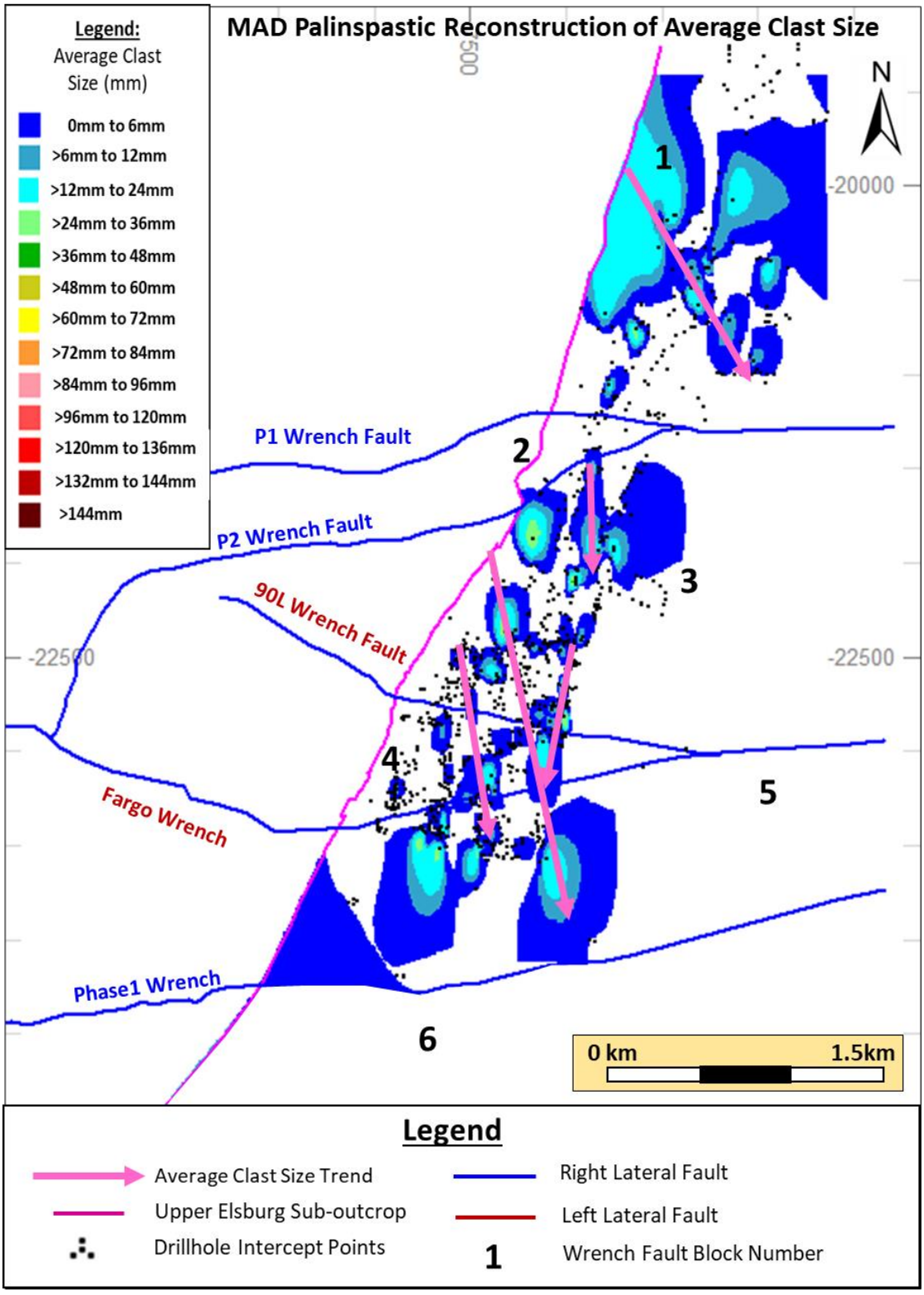


Figure 147: Palinspastic average clast size reconstruction for MAD.

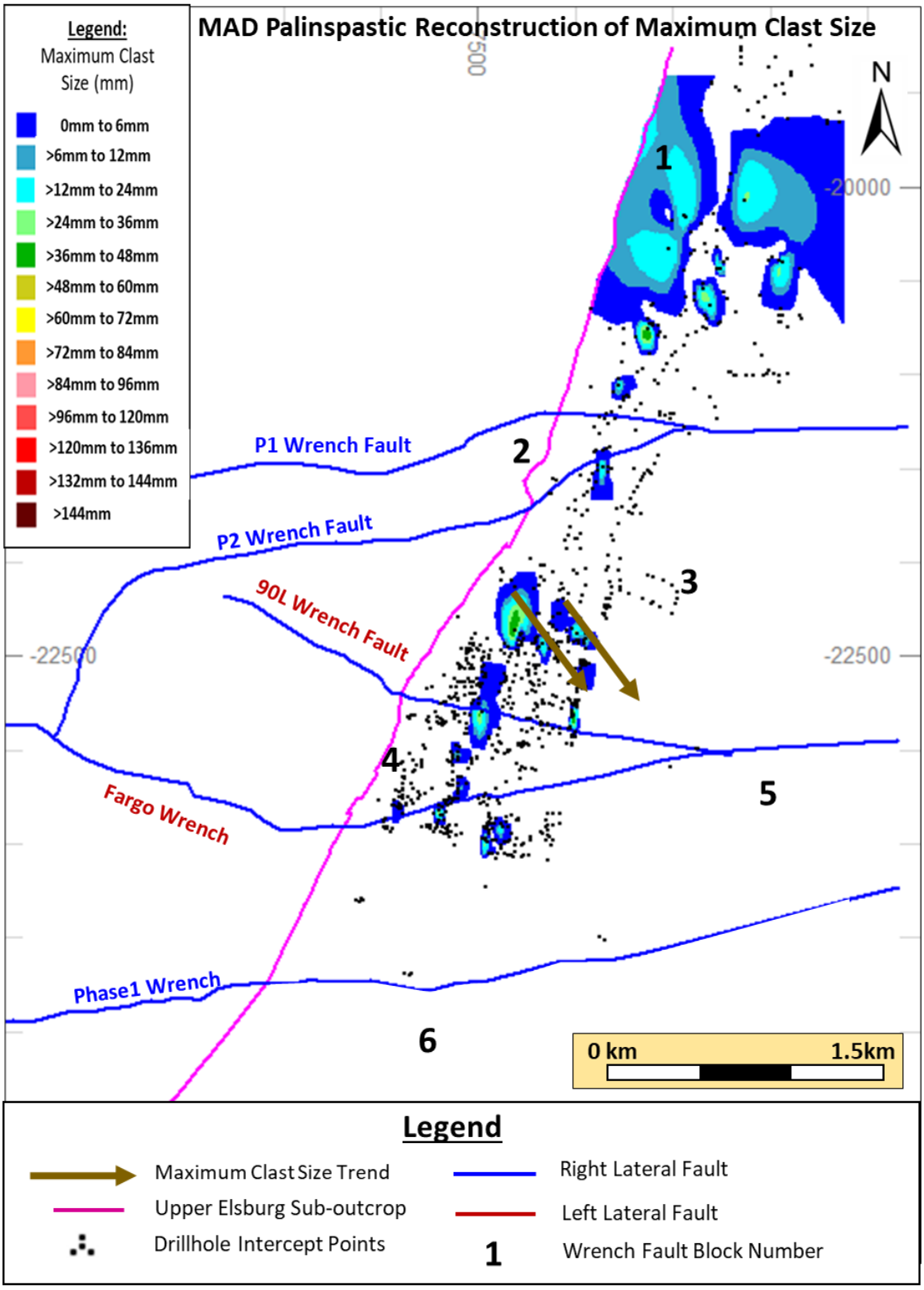


Figure 148: Palinspastic maximum clast size reconstruction for MAD.

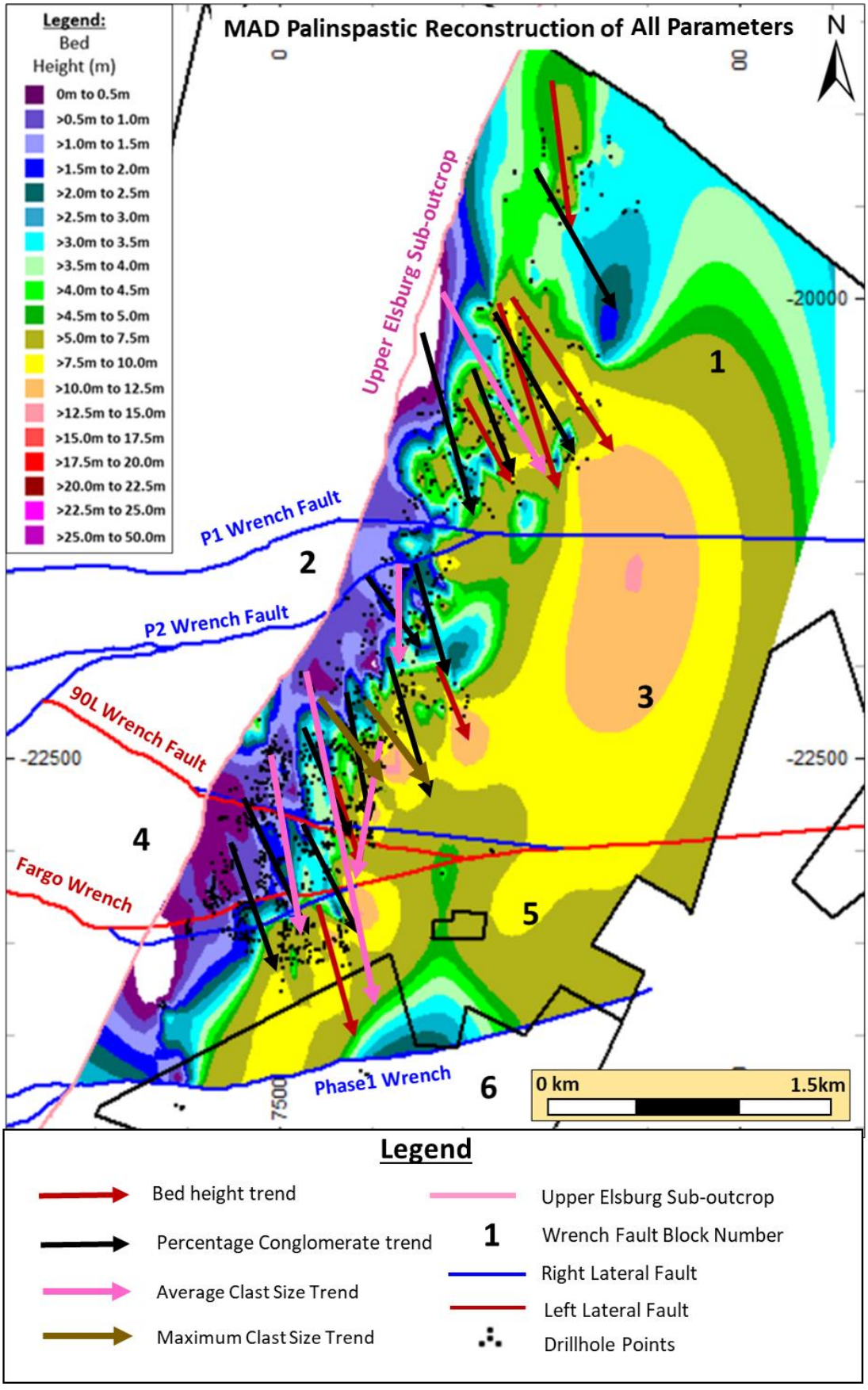


Figure 149: Palinspastic Reconstruction for the MAD - All Parameters

iv) MAD Detailed Plots

A detailed plot (Figure 150a) and b)) for the MAD centred on Block 2 indicates possible 300 m and 150 m right-lateral dislocations of a higher bed height trend across the P1 Wrench and P2 WrenchesWrench, respectively (black dashed lines). These possible dislocations are not as clearly evident in Figure 150 b) for percentage conglomerate. The timing of the dislocations is not definitive; however, it is possible that the variable bed height south of P2 Wrench and lying parallel to it might indicate some syn-sedimentary structural influence. The true nature/magnitude and timing of the dislocations could be both syn- to post -MAD sedimentation depending on how much erosion took place by the overlying MIB. The right-lateral dislocation across the faults could possibly indicate a relative successive downward displacement to the north of each successive fault block.

As previously indicated, the variable nodes of bed height and percentage conglomerate along and in close proximity to Wrenchwrench structures could potentially indicate a component of syn-sedimentary structural activity, as indicated by the yellow ellipse in Figure 151 a)), up against P2 Wrench. Similar variable nodes of variable percentage conglomerate along the 90L Wrench strike could also imply possible syn-sedimentary influence by the structure. In Figure 151 a) a higher bed height trend is interpreted to be right-laterally dislocated by the 90L Wrench by approximately 100 m. This potential dislocation is not easily definable in Figure 151 b).

An enlargement of Block 4 for MAD (Figure 152 a))) for bed height indicates possible right-lateral dislocation of ±100 m across the 90L Wrench and a possible ±400 m dislocation across Fargo Wrench in the south. It is not clear whether this dislocation was syn-sedimentary, however, the more probable dislocation possibly took place post -MAD deposition with erosion by the overlying MIB. Some possible syn-sedimentary structural influence evidence exists in the location of variable percentage conglomerate nodes aligned with the 90L Wrench in Figure 152 b) (highlighted with a yellow ellipse).

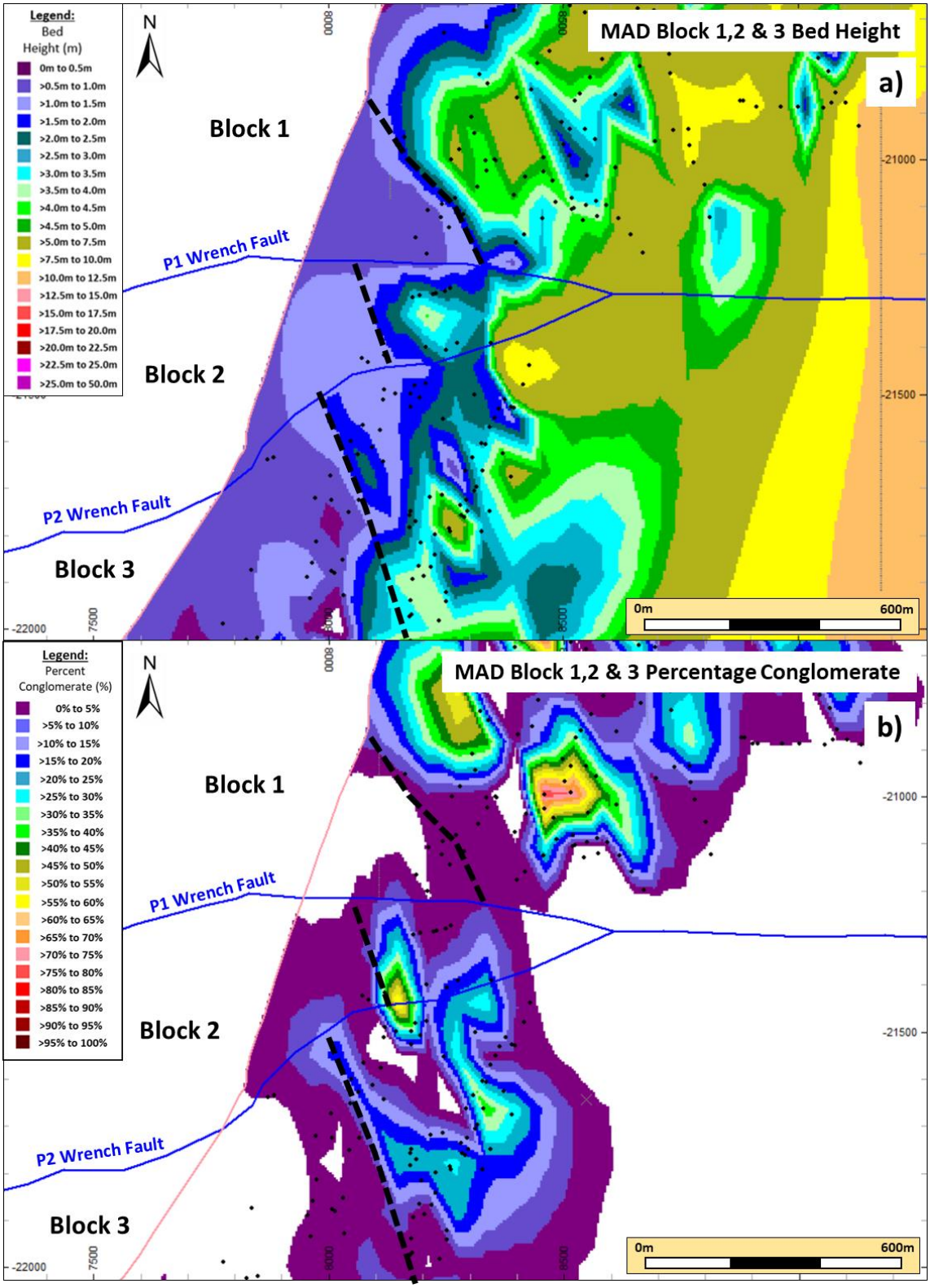


Figure 150: Enlarged Block 2 palinspastic reconstruction for a) bed height for MAD and b) for percentage conglomerate for MAD.

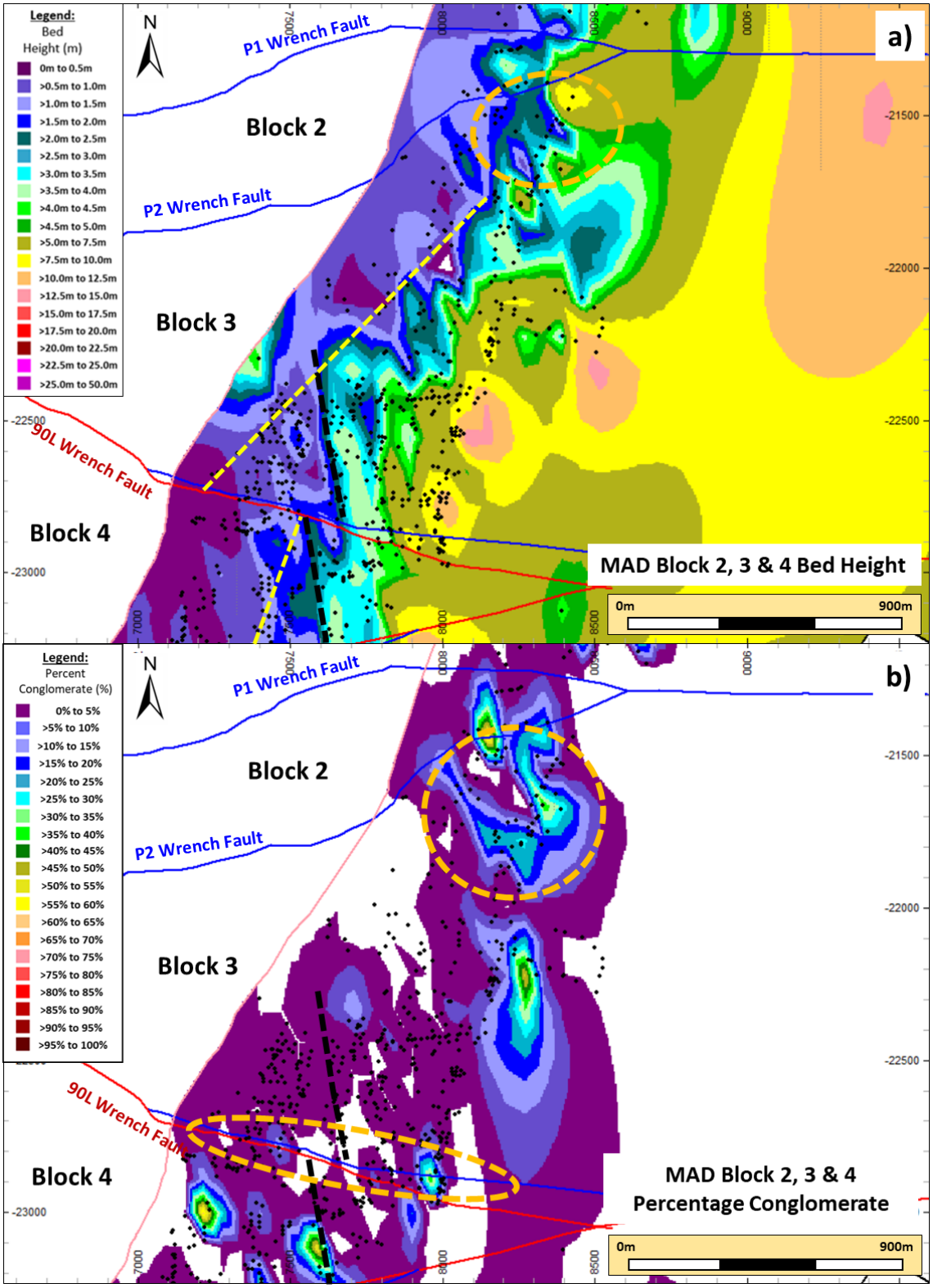


Figure 151: Enlarged Block 3 palinspastic reconstruction for a) bed height for MAD and b) for percentage conglomerate for MAD.

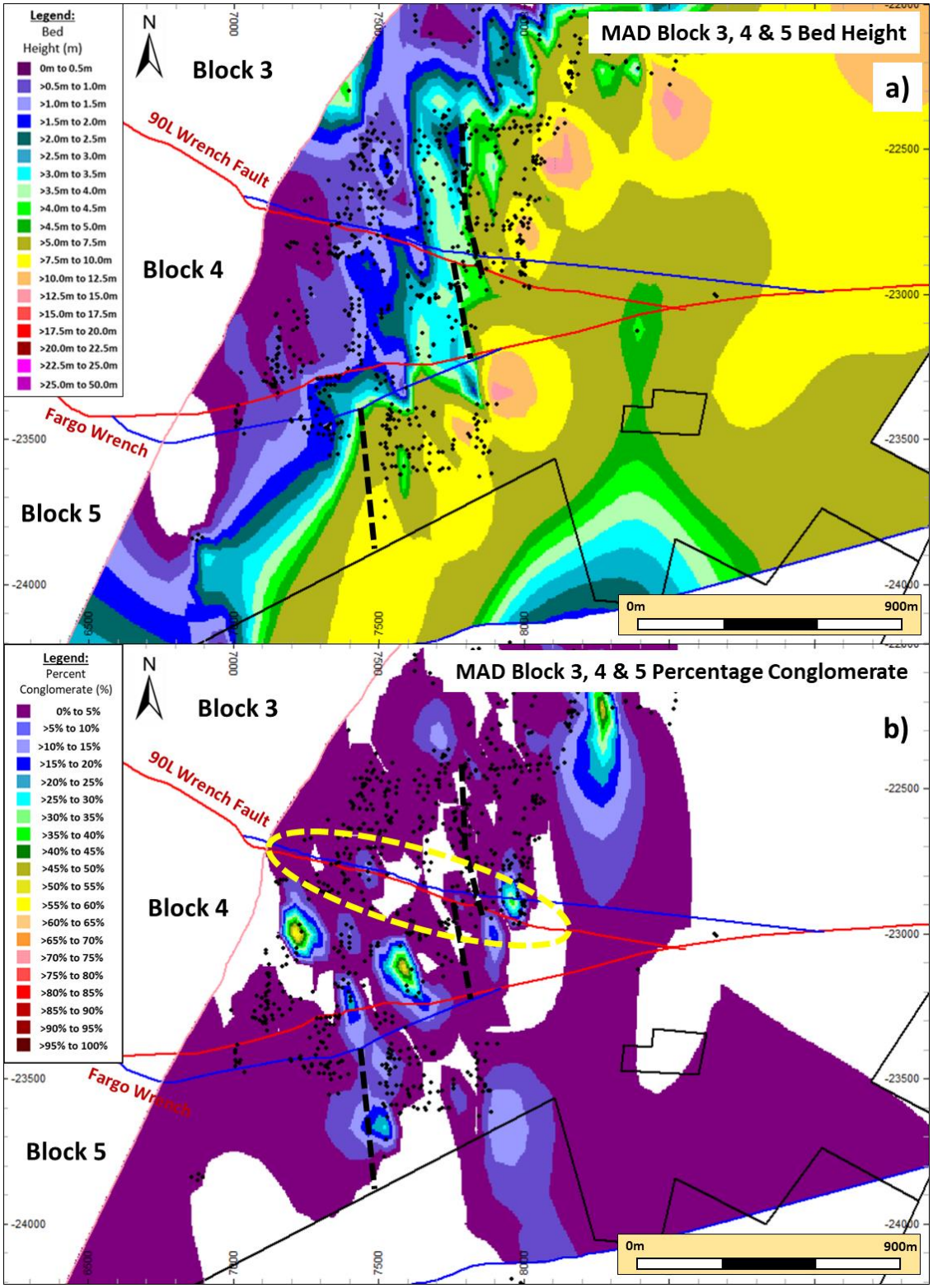


Figure 152: Enlarged Block 4 palinspastic reconstruction for a) bed height for MAD and b) for percentage conglomerate for MAD.

j) **MIB**

i) MIB Bed Height

Palinspastic reconstruction for bed height for the MIB (Figure 153 also indicates a gradual attenuation in the northern half Block 1 towards the sub-outcrop at a somewhat lower rate than further to the south, as seen from the southern half of Block 1 and down into Block4Block 4.

General bed height for the MIB increases generally towards the south, attaining a maximum bed height of >5 m to 7.5 m to a distance of approximately 1.5 km east of the UE SubUpper Elsburg sub-outcrop. Bed-height trends are approximately NNW to -SSE with trends in Block 1 being closer to NW-SE.

ii) MIB Percentage Conglomerate

The MIB consists of variable amounts of quartzite and interbedded conglomerates. The palinspastic reconstructed percentage conglomerate plot for the MAD (Figure 154) depicts an extensive higher percentage conglomerate zone in Block 1. Percentage conglomerate generally decreases southwards as the P1 Wrench is approached in conjunction with the increase in bed height. Further southwards, except directly south of the P2 Wrench, the percentage conglomerate for the MAD noticeably decreases. High percentpercentage conglomerate areas adjacent to the UEUpper Elsburg sub-outcrop in areas of reduced bed height just north of P1 Wrench and in Block 4, could possibly be the result of winnowing in these areas.

Percentage conglomerate trends for the MIB are oriented primarily NNW to -SSE in the south, but nearer to NW-SE in Block 1.

iii) MIB Average and Maximum Clast Size

Average clast size (Figure 155) for the MIB is relatively constant (between >12 mm and 24 mm) in Block 1, Block 2 and the northern half of Block 3. Average clast size becomes more variable southward from approximately the P2 Wrench position. Average clast size trends are NNW to -SSE in all areas with a maximum average clast size >48 mm occurring sporadically in areas just north of and adjacent to the 90L Wrench.

Maximum clast size for the MIB (Figure 156) also exhibits little variability in the northern areas of the Projectproject area. Maximum clast size trends are approximately NW to -SE in orientation. Maximum clast size is attained just north of- and adjacent to the 90L Wrench in Block 3.

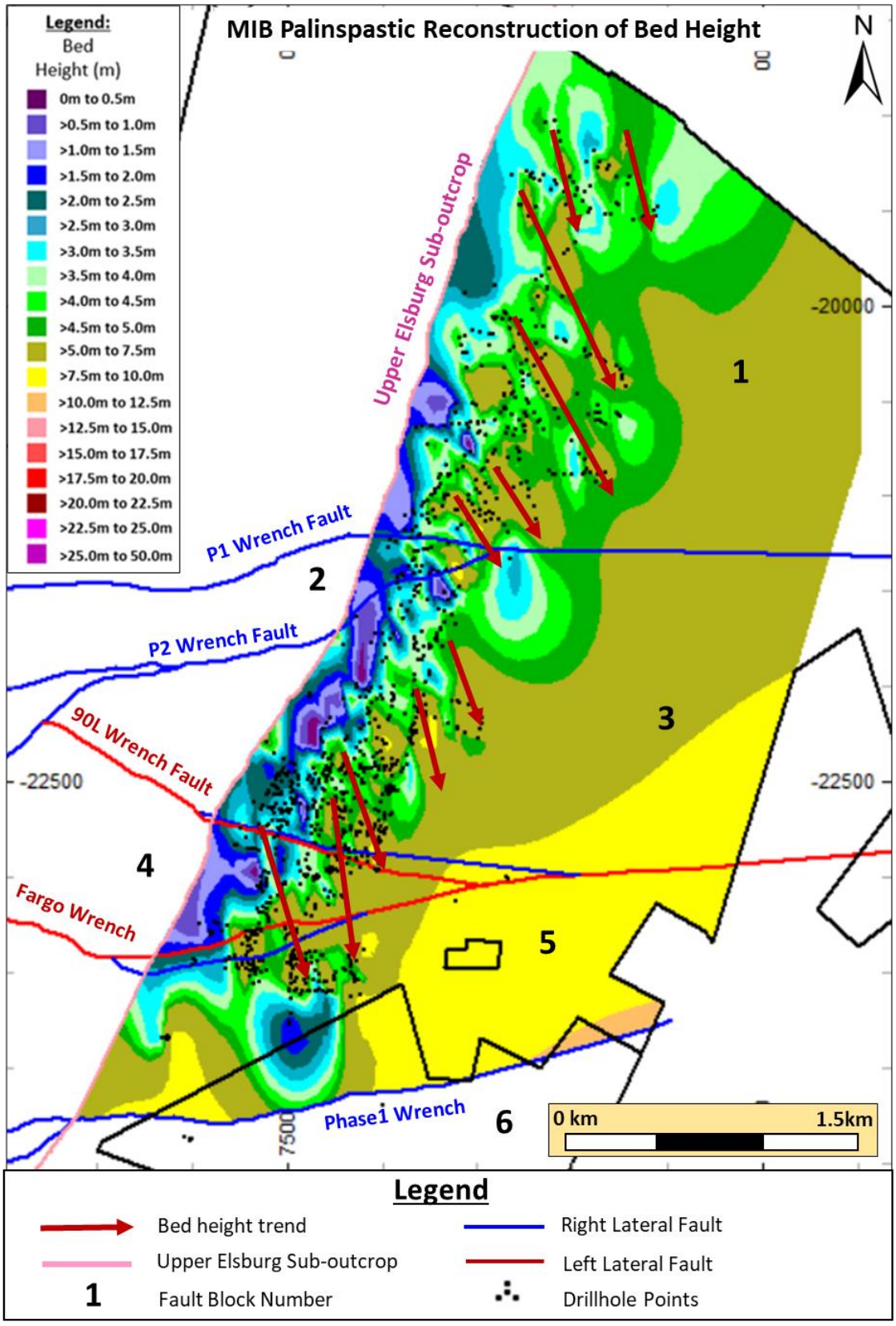


Figure 153: Palinspastic bed height reconstruction for MIB.

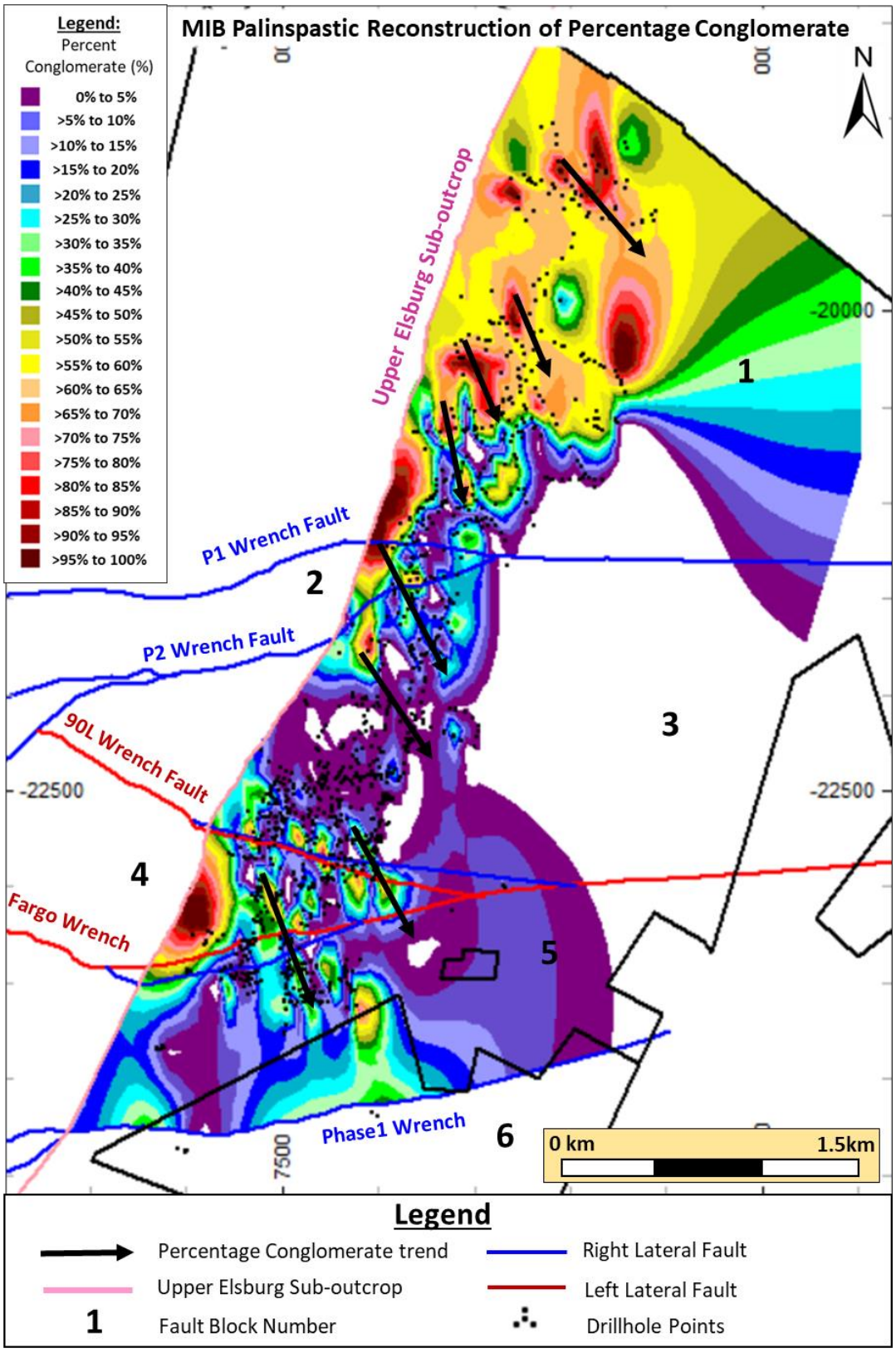


Figure 154: Palinspastic percentage conglomerate reconstruction for MIB.

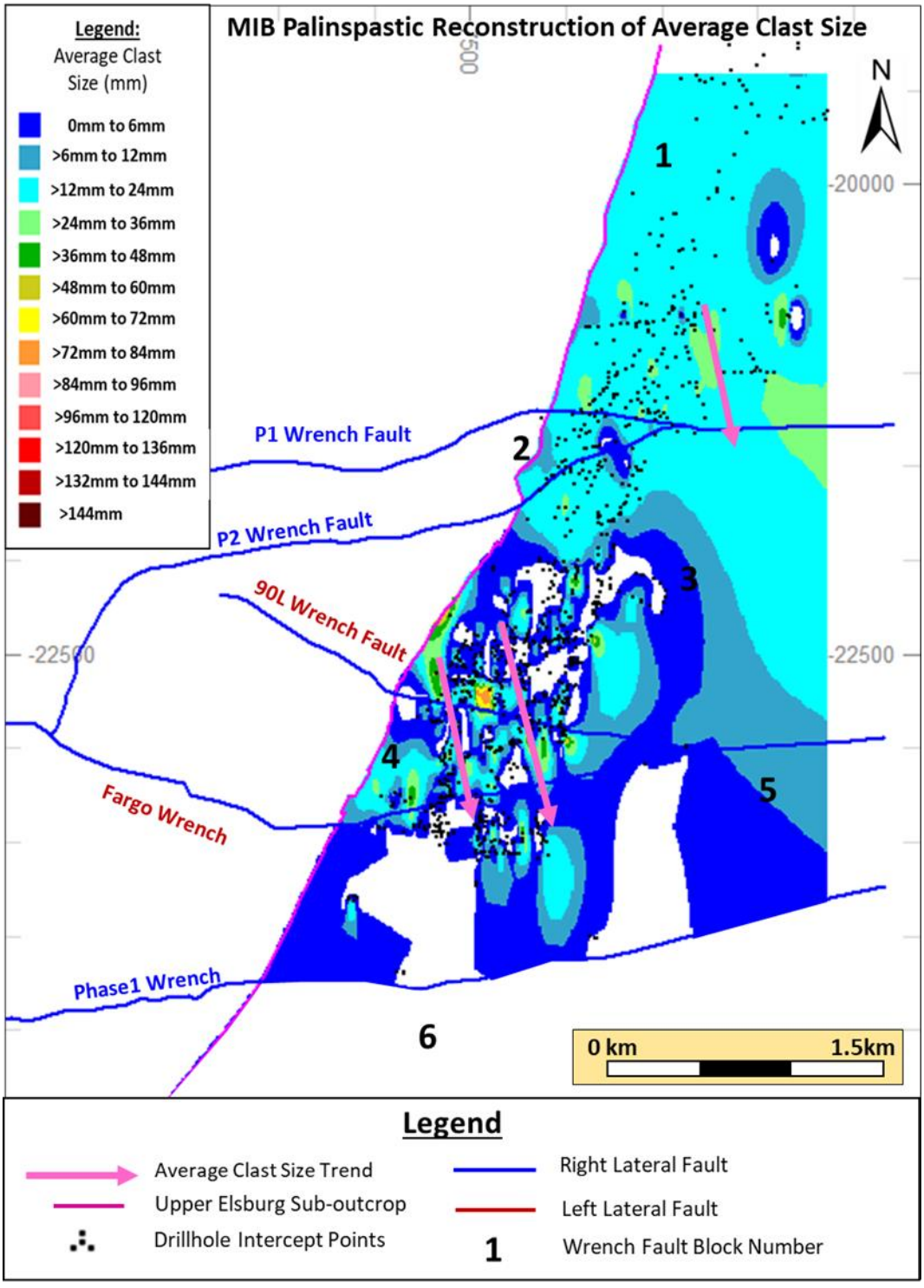


Figure 155: Palinspastic average clast size reconstruction for MIB.

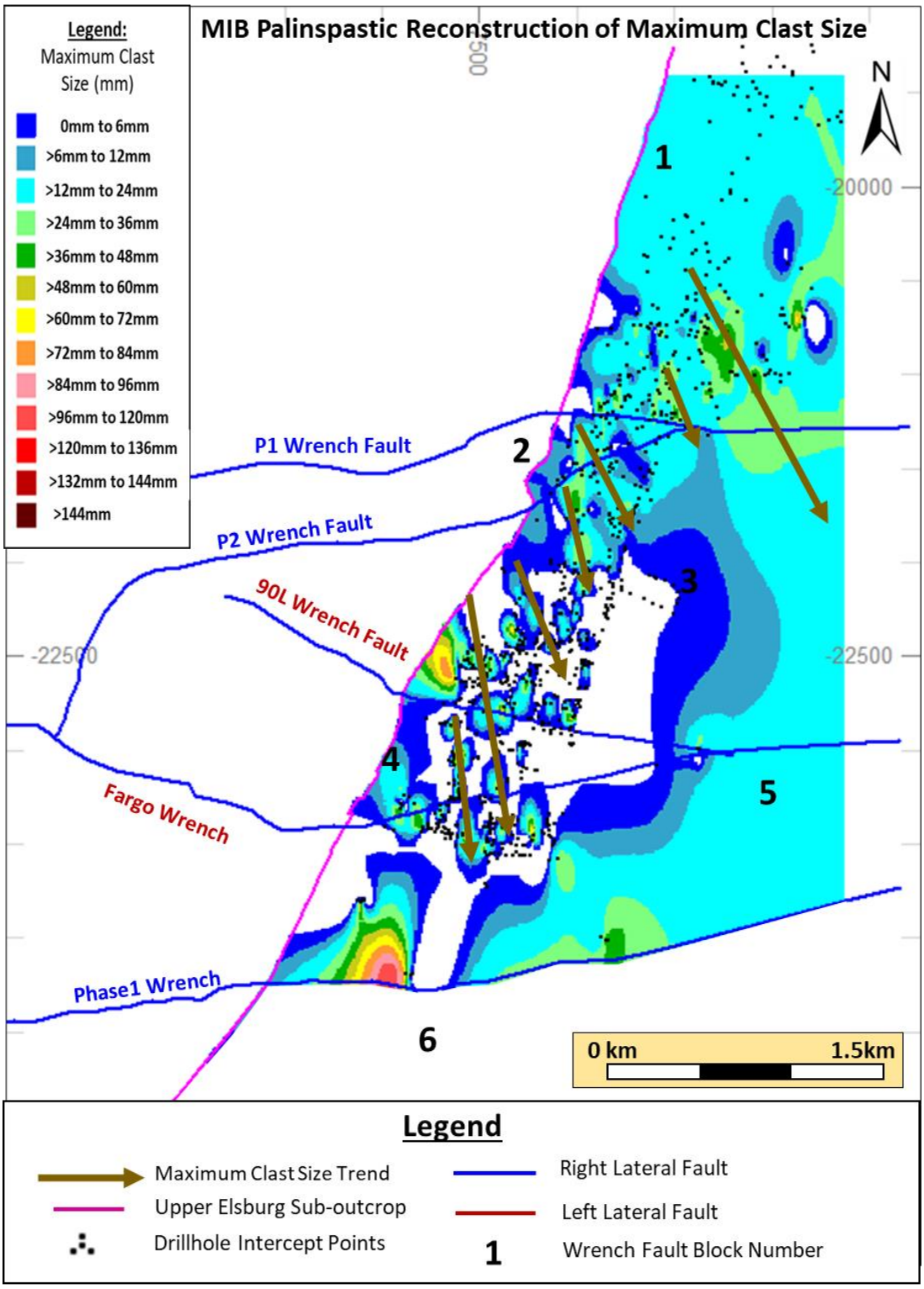


Figure 156: Palinspastic maximum clast size reconstruction for MIB.

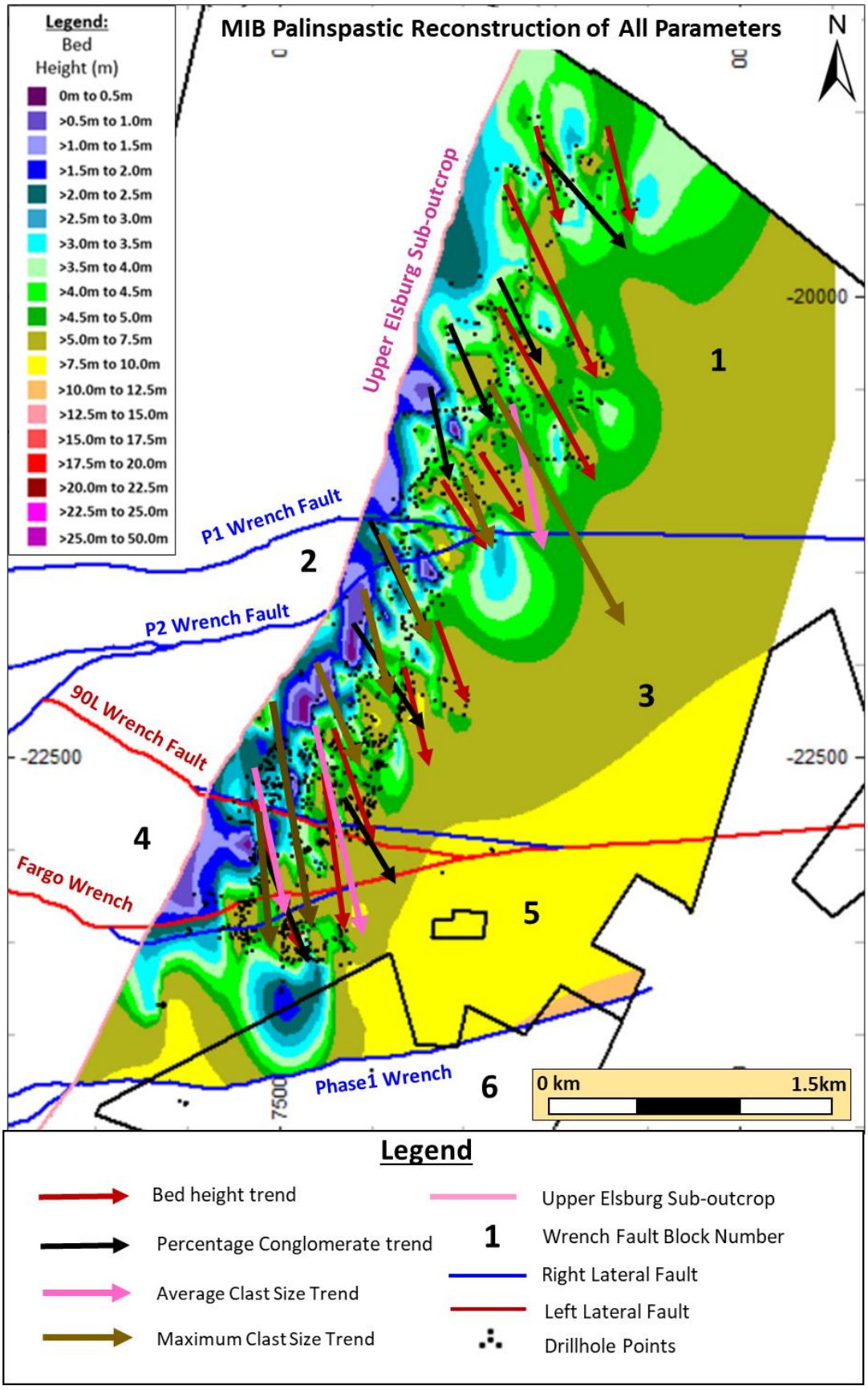


Figure 157: Palinspastic Reconstruction for the MIB - All Parameters

iv) MIB Detailed Plots

A detailed plot (Figure 158 a) and b)) for the MIB centred on Block 2 indicates a possible ±100 m right-lateral dislocation of a higher bed height trend across the P1 Wrench (black dashed line). This possible dislocation is not equally evident in Figure 158 b) for percentage conglomerate. Timing of this interpreted dislocation could possibly have been syn-sedimentary in nature resulting in thinner bed height directly to the north in Block 1 associated with preferential winnowing over the thinner area resulting in higher percentage conglomerate. This would infer a possible relative downward displacement of BlockBlocks 2 and 3 relative to Block 1. Possible syn-sedimentary activity could potentially be inferred on P2 Wrench due to the location of variable bed height and percentage conglomerate nodes occurring along and adjacent to the structure.

Figure 159 a) and b) exhibit variable nodes of bed height and percentage conglomerate directly to the south of P2 Wrench (yellow ellipse) and also straddling and adjacent to the 90L Wrench in the south (highlighted by the black ellipse). These variable nodes could potentially indicate syn-sedimentary influence of these structures during deposition of the MIB. However, the magnitude of influence or possible dislocation of these structures is difficult to determine.

Figure 160 a) and b) show the highly variable bed heights (and preferentially attenuated Block 4) and percentage conglomerate in and around Block 4. An apparent downward to right-lateral dislocation across 90L Wrench for the MIB is indicted by the higher bed height directly north of 90L Wrench, close intoto the sub-outcrop. Magnitude and nature of possible dislocation across Fargo Wrench in the south is precluded due to sparse data density close into sub-outcrop. High percentage conglomerate for the MIB against the sub-outcrop in Block 4 is similar to the thinner bed height in this area and may imply localised winnowing or relative uplift of Block 4 (relative to Block 3 and Block 5) during or subsequent to MIB deposition or subsequent MIT erosion.

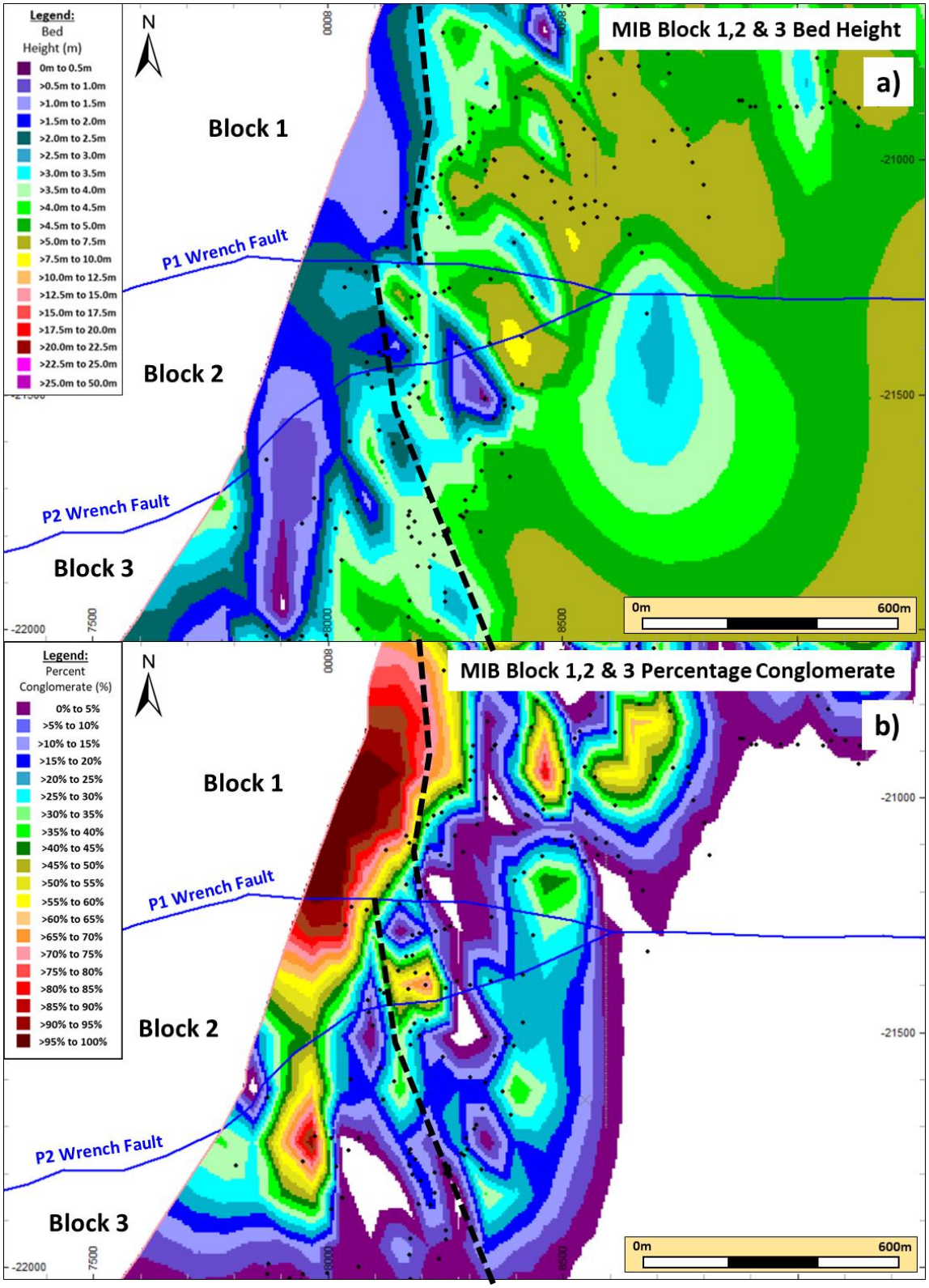


Figure 158: Enlarged Block 2 palinspastic reconstruction for a) bed height for MIB and b) for percentage conglomerate for MIB.

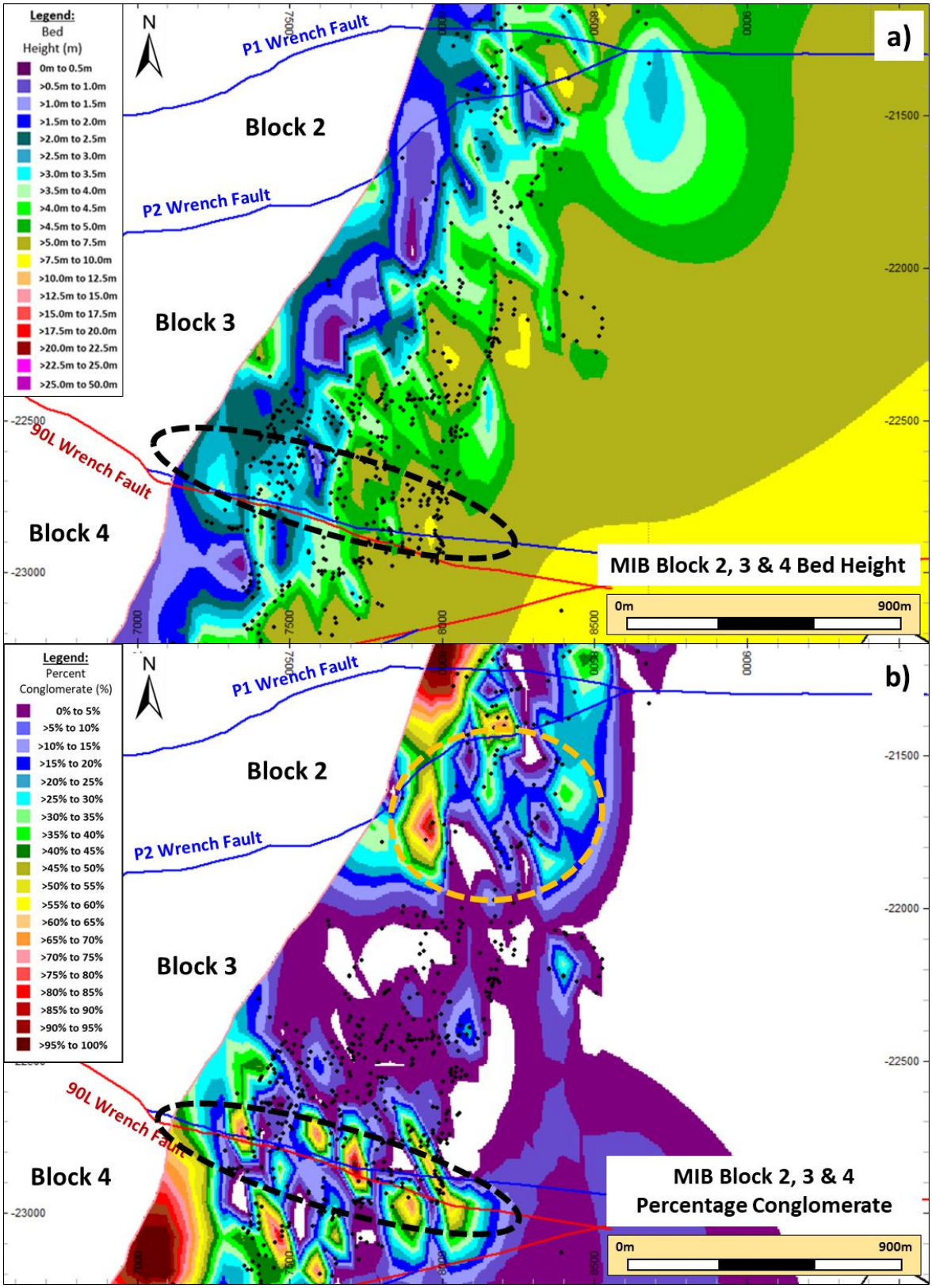


Figure 159: Enlarged Block 3 palinspastic reconstruction for a) bed height for MIB and b) for percentage conglomerate for MIB.

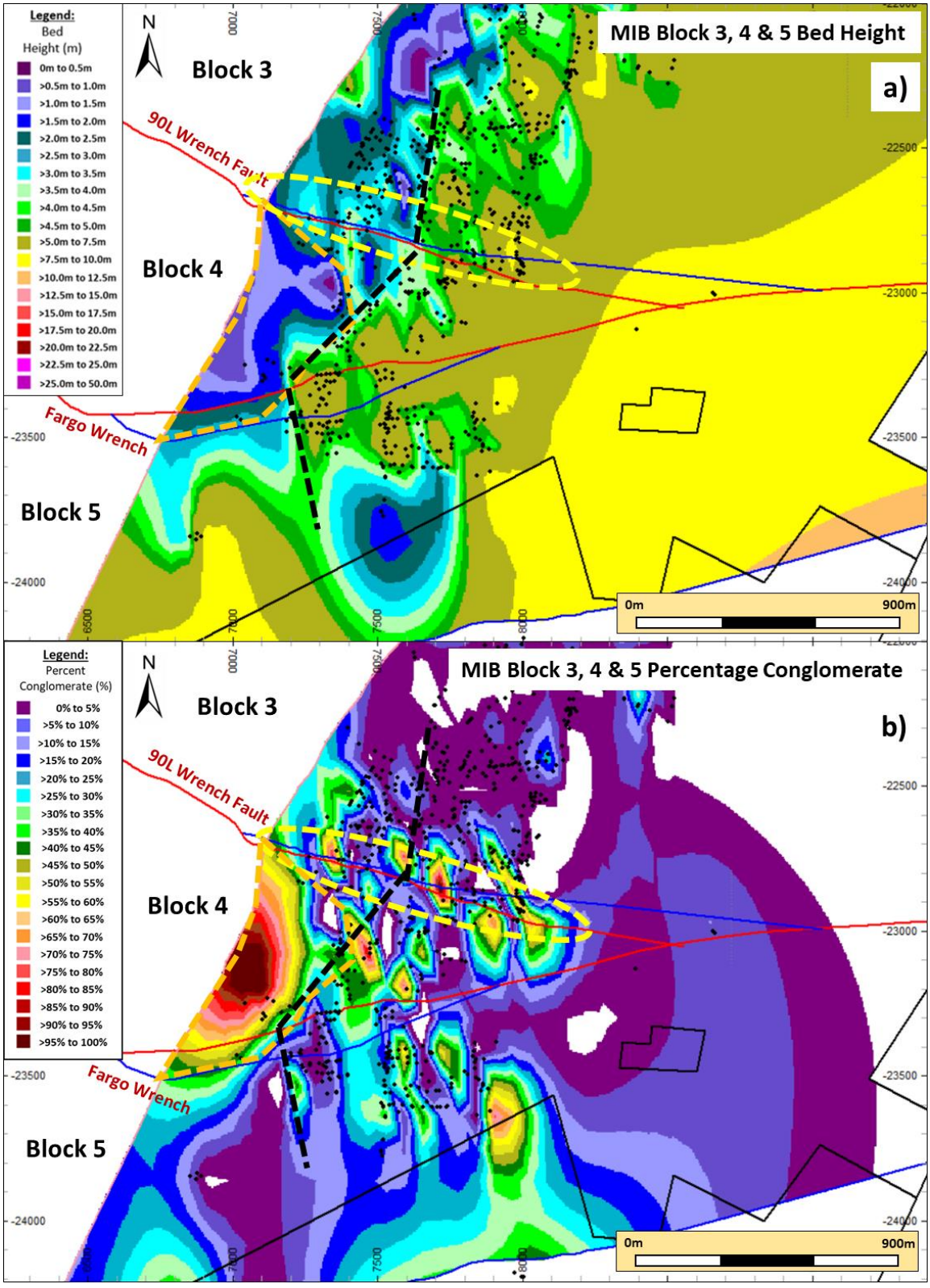


Figure 160: Enlarged Block 4 palinspastic reconstruction for a) bed height for MIB and b) for percentage conglomerate for MIB.

k) **MIT**

l) MIT Bed Height

Palinspastic reconstruction for bed height for the MIT (Figure 161) also indicates a gradual attenuation in the northern half Block 1 towards the sub-outcrop at a somewhat lower rate than further to the south, as seen from the southern half of Block 1 and southward to the 90 Level Wrench in Block 3. This appears to be a general occurrence throughout the Upper Elsburg stratigraphy at SDGM.

General bed height for the MIT decreases significantly across Blocks 2 and 3 and then increases slightly to the south towards the 90L Wrench. Bed heights in Block 1 vary between >2 m and ±7.5 m towards the east approximately 1.5 km east of the sub-outcrop.

Over Block 3, bed height is far more variable (>0.5 m up to 7.5 m). A significant increase in bed height south of the 90L Wrench is evident, but with a lower rate of attenuation towards the west up against the sub-outcrop. Bed height/channel trends are preferentially NNW-SSE in orientation.

ii) MIT Percentage Conglomerate

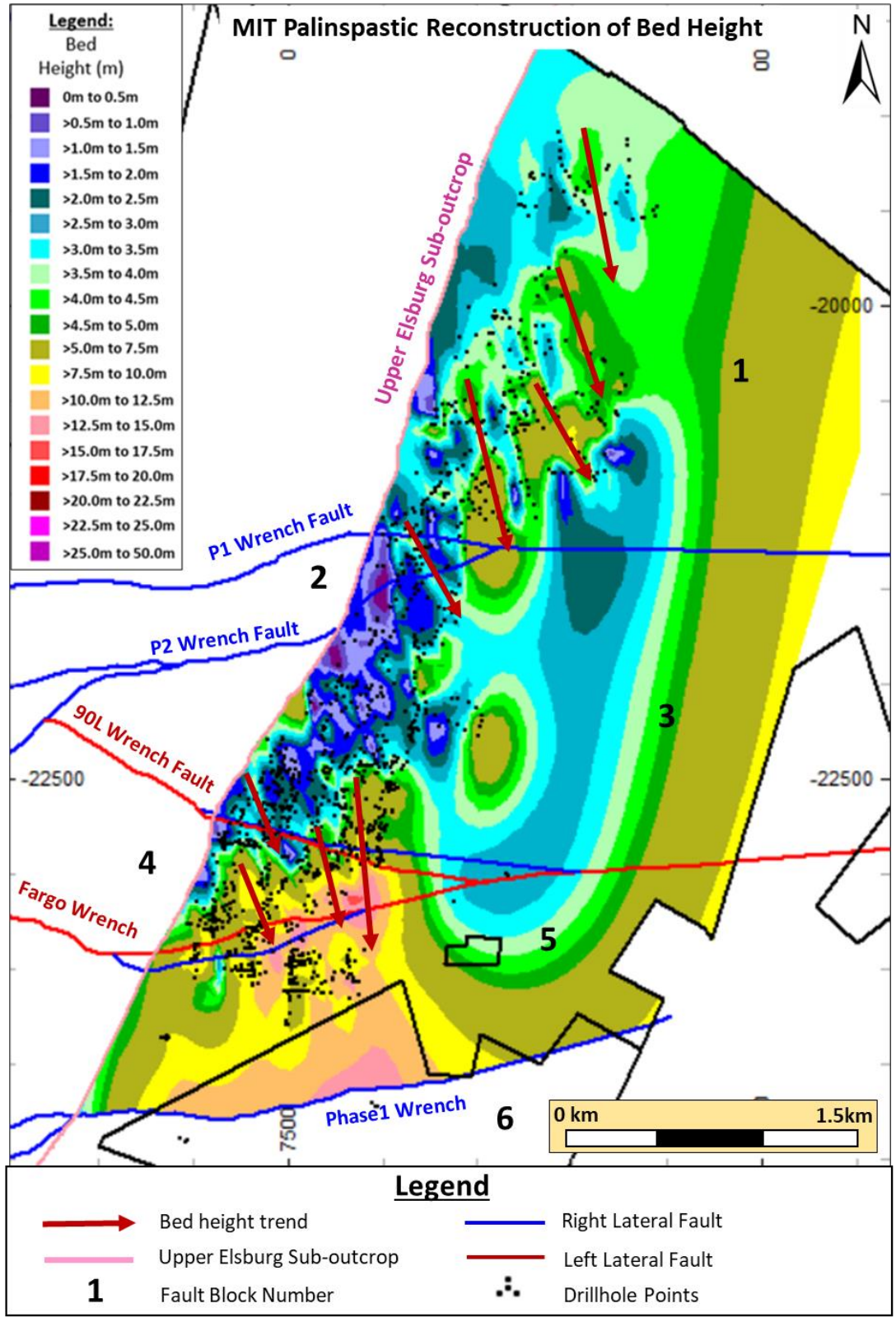
The MIT percentage conglomerate is lowest in the northern half of Block 1 (Figure 162). Percentage conglomerate increases significantly southwards towards the P1 Wrench. This higher percentage conglomerate occurs all along the sub-outcrop to a distance in excess 1.5 km to the east of sub-outcrop with only small local variations occurring. Percentage conglomerate trends are aligned (NNW-SSE) with the bed height trends in Figure 161.

Higher percentage conglomerate and associated lower bed height in Block 3 may be the result of preferential winnowing over this block.

iii) MIT Average and Maximum Clast Size

Average clast size (Figure 163) for the MIT is relatively constant (between >12 mm and 24 mm) in Blocks 1 and 2 and the northern half of Block 3. Average clast size becomes more variable and increases southwards as 90L Wrench is approached. Average clast size trends are NNW-SSE in all areas with a maximum average clast size >72 mm occurring sporadically in areas just north of and adjacent to the 90L Wrench.

Maximum clast size for the MIB (Figure 164) also exhibits little variability in the northern areas of the project area. Maximum clast size trends are approximately NNW-SSE in orientation. Maximum clast size is attained across the 90L Wrench and Fargo Wrench combination in the south with maximum clast sizes exceeding 120 mm in diameter.



.

Figure 161: Palinspastic bed height reconstruction for MIT.

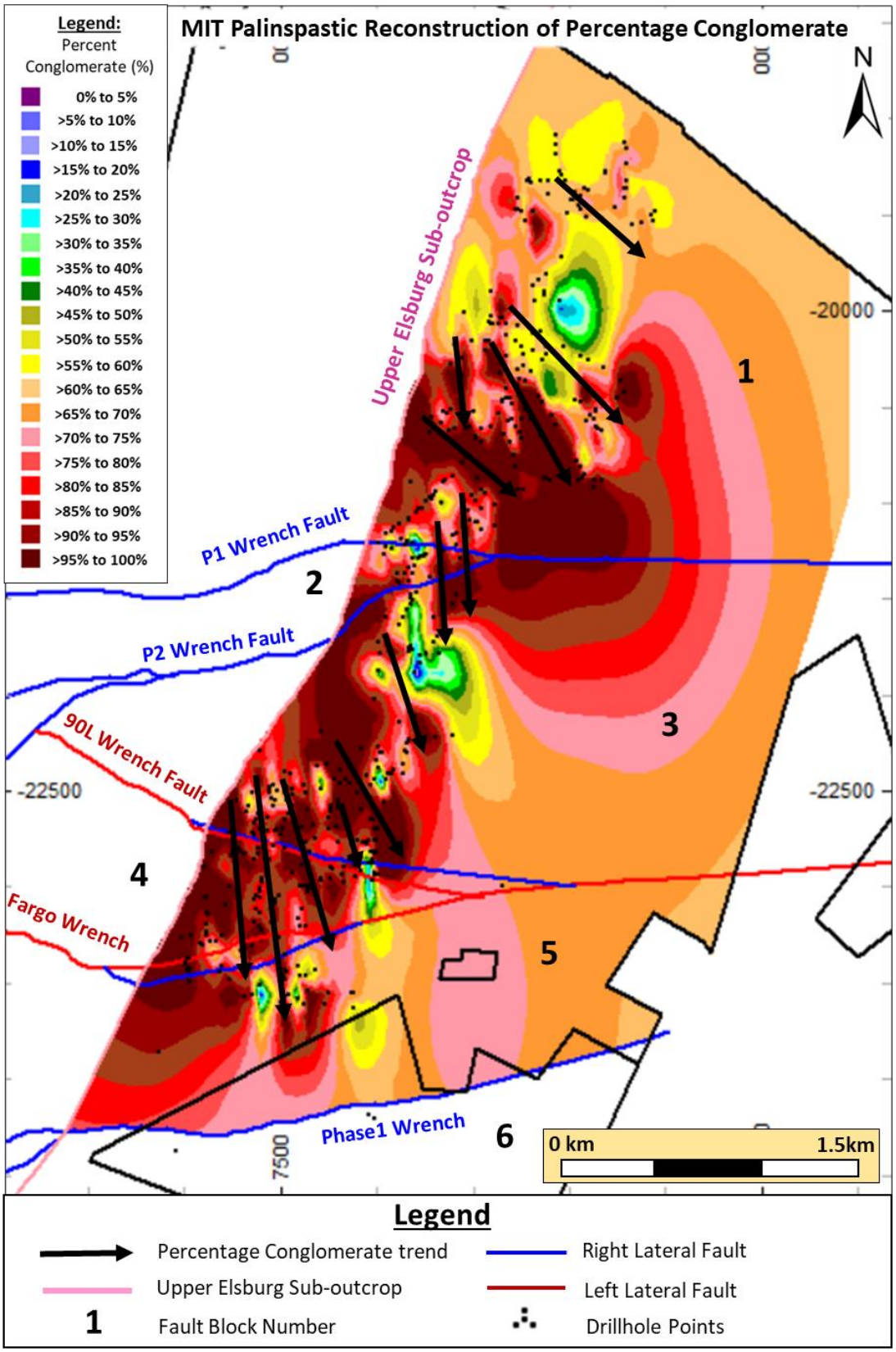


Figure 162: Palinspastic percentage conglomerate reconstruction for MIT.

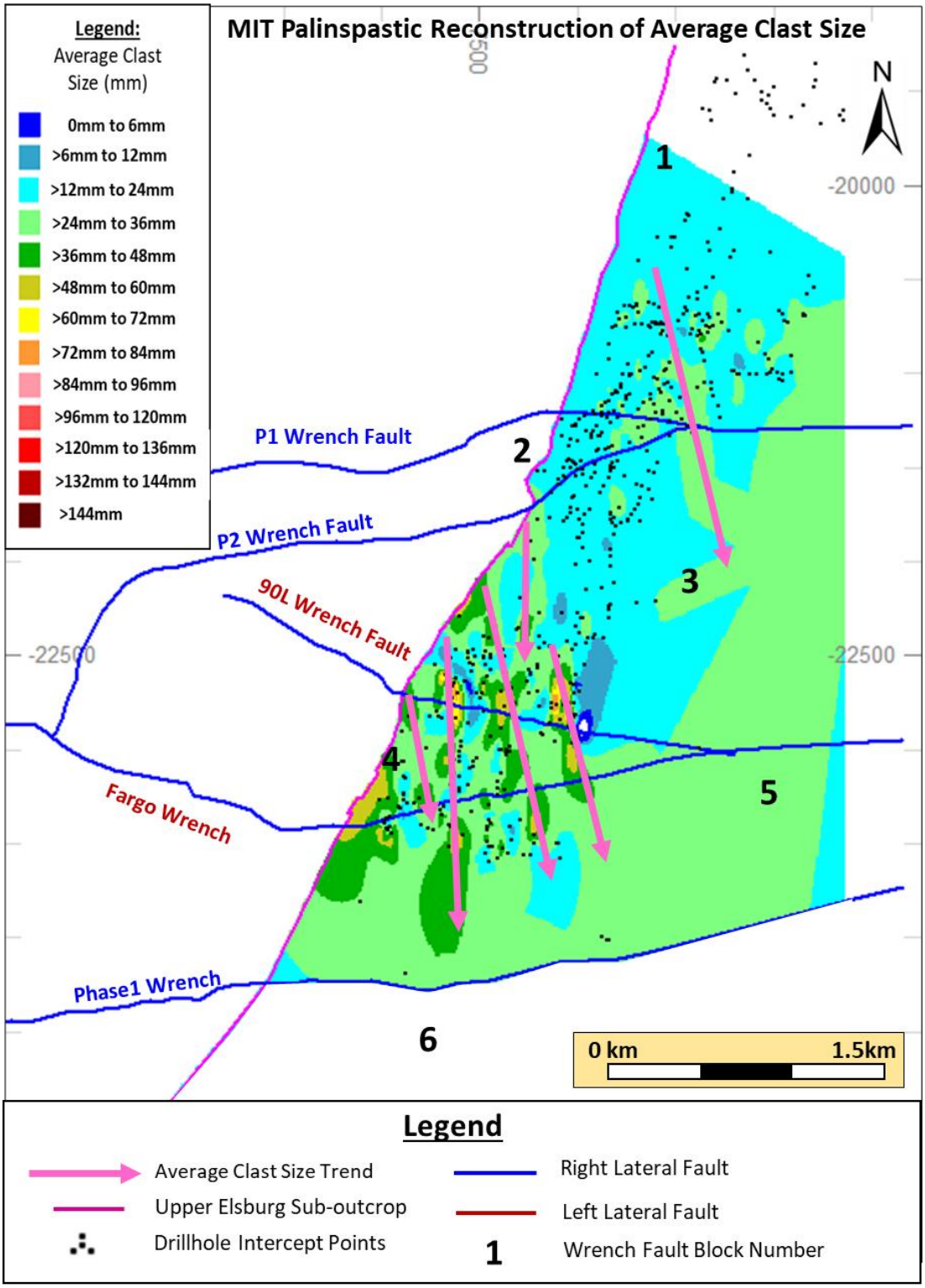


Figure 163: Palinspastic average clast size reconstruction for MIT.

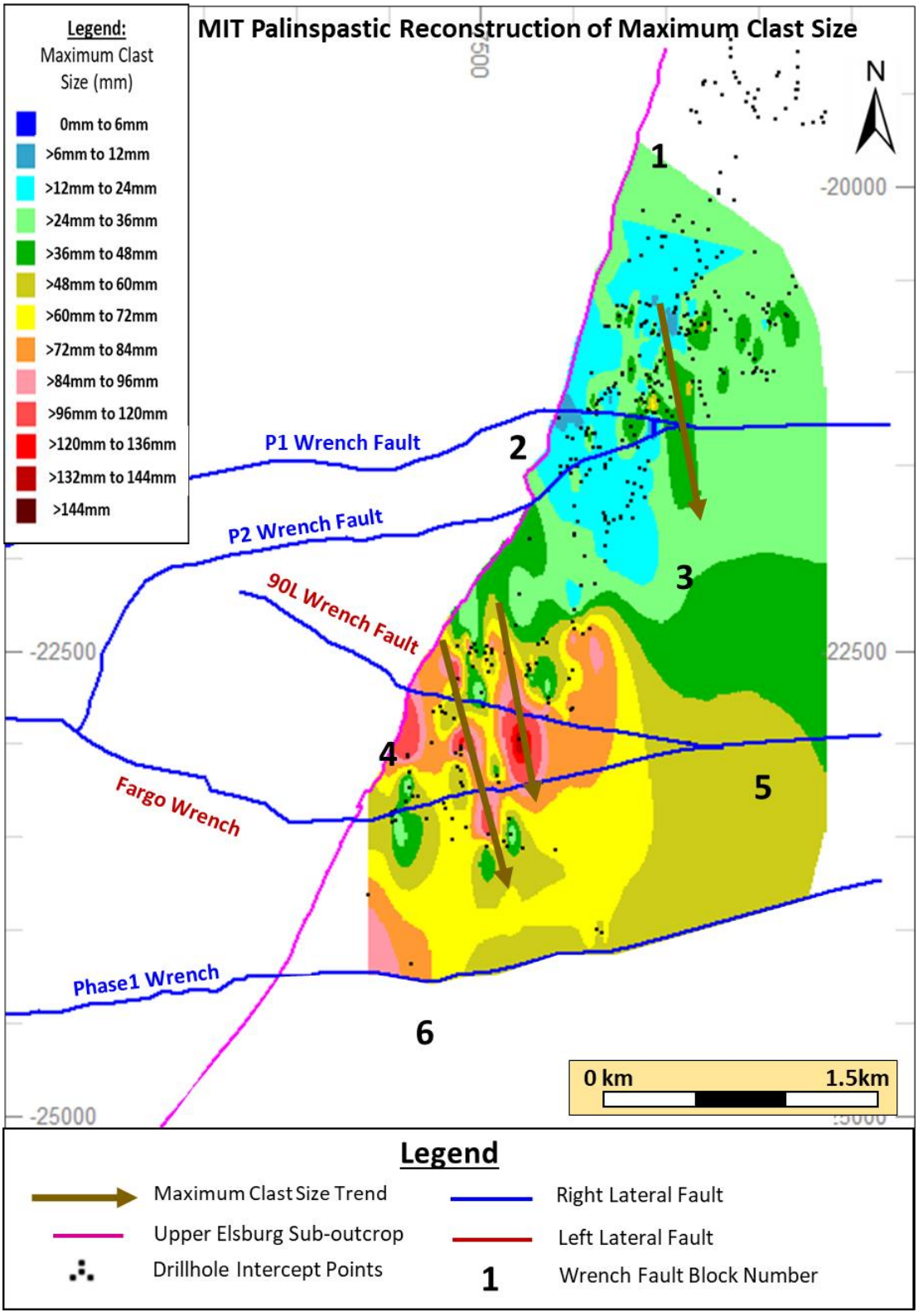


Figure 164: Palinspastic maximum clast size reconstruction for MIT.

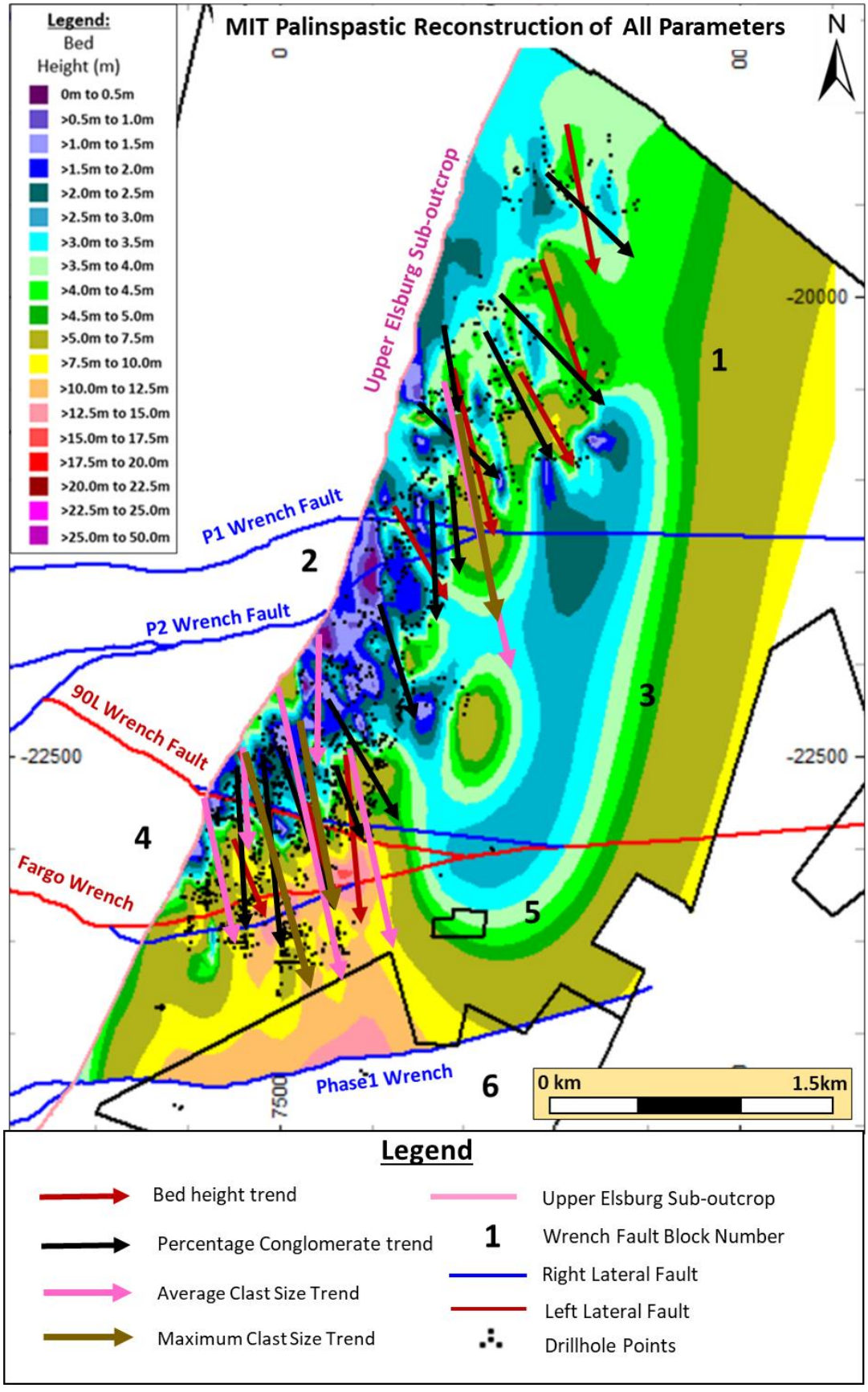


Figure 165: Palinspastic Reconstruction for the MIT - All Parameters

iv) MIT Detailed Plots

Figure 166 presents an enlarged section of the a) bed height and b) percentage conglomerate plan for the MIT including Blocks 1, 2 and 3. Dislocations of neither bed height nor percentage conglomerate are discernible. However, a zone of lower bed height straddles P2 Wrench and covers the western half of Block 2 and the north-western corner of Block 3 (yellow polygon). This attenuated zone exhibits a possible higher percentage conglomerate in the northwest corner of Block 3, which could possibly indicate a localised zone of winnowing. The occurrence of lower percentage conglomerate directly south of the P2 Wrench, as well as the occurrence of nodes of variable bed height and percentage conglomerate straddling the P1 Wrench in Figure 166 b), could potentially imply some syn-sedimentary structural influence on the MIT due to the fault.

Block 3 in Figure 167 b) presents a zone of lower percentage conglomerate just south of P2 Wrench (yellow ellipse). A line of variable bed height and percentage conglomerate nodes straddling and adjacent to 90L Wrench (yellow ellipse in Figure 167 b)) could possibly indicate some syn-sedimentary structural influence by 90L Wrench during MIT deposition.

An apparent right-lateral dislocation of a trend line of higher bed height in Figure 167 a) across 90L Wrench (±400 m) is presented. This trend is however not duplicated in Figure 167 b) for percentage conglomerate. This apparent dislocation may be due to a relative downward displacement of Block 5 relative to Block 4, either during MIT deposition or during subsequent erosion by overlying beds.

Figure 168 a) and b) present the bed height variation and percentage conglomerate centred on Block 4. The apparent right-lateral dislocation of the bed height trend indicated across 90L Wrench in Figure 167 a) and b) is also presented in this plot. Another apparent dislocation of this bed height trend line may be interpreted as a ±200 m left-lateral dislocation across Fargo Wrench. Possible syn-sedimentary structural relationships might be inferred from the location of alternating nodes of variable bed height and percentage conglomerate occurring along and in proximity to both structures. Observed dislocations are only apparent and do not definitively define the sense or magnitude of dislocation across the structures. However, it appears that Block 4 might have been uplifted relative to Blocks 3 and 5, due to the west movement of the bed height trend line.

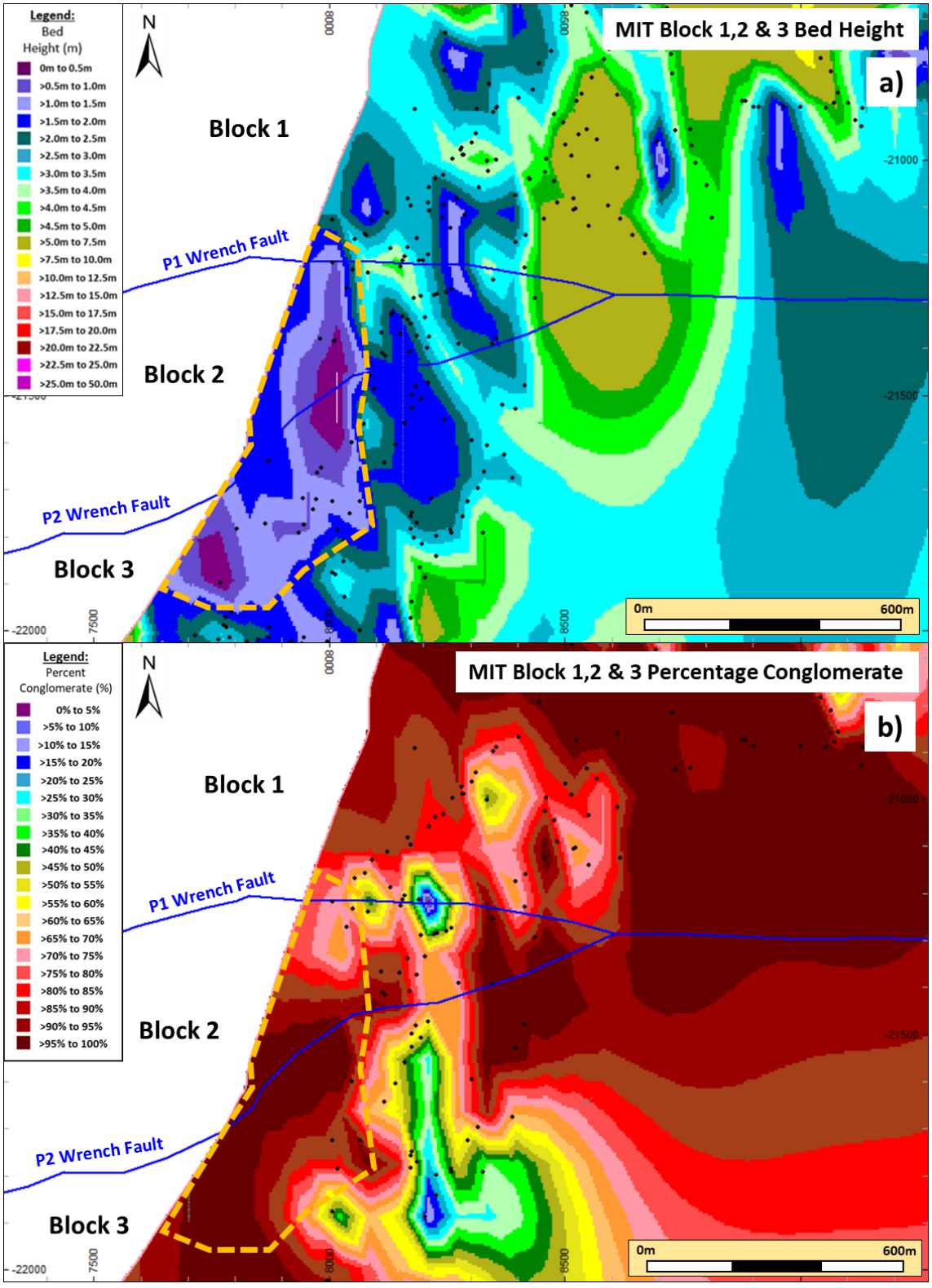


Figure 166: Enlarged Block 2 palinspastic reconstruction for a) bed height for MIT and b) for percentage conglomerate for MIT.

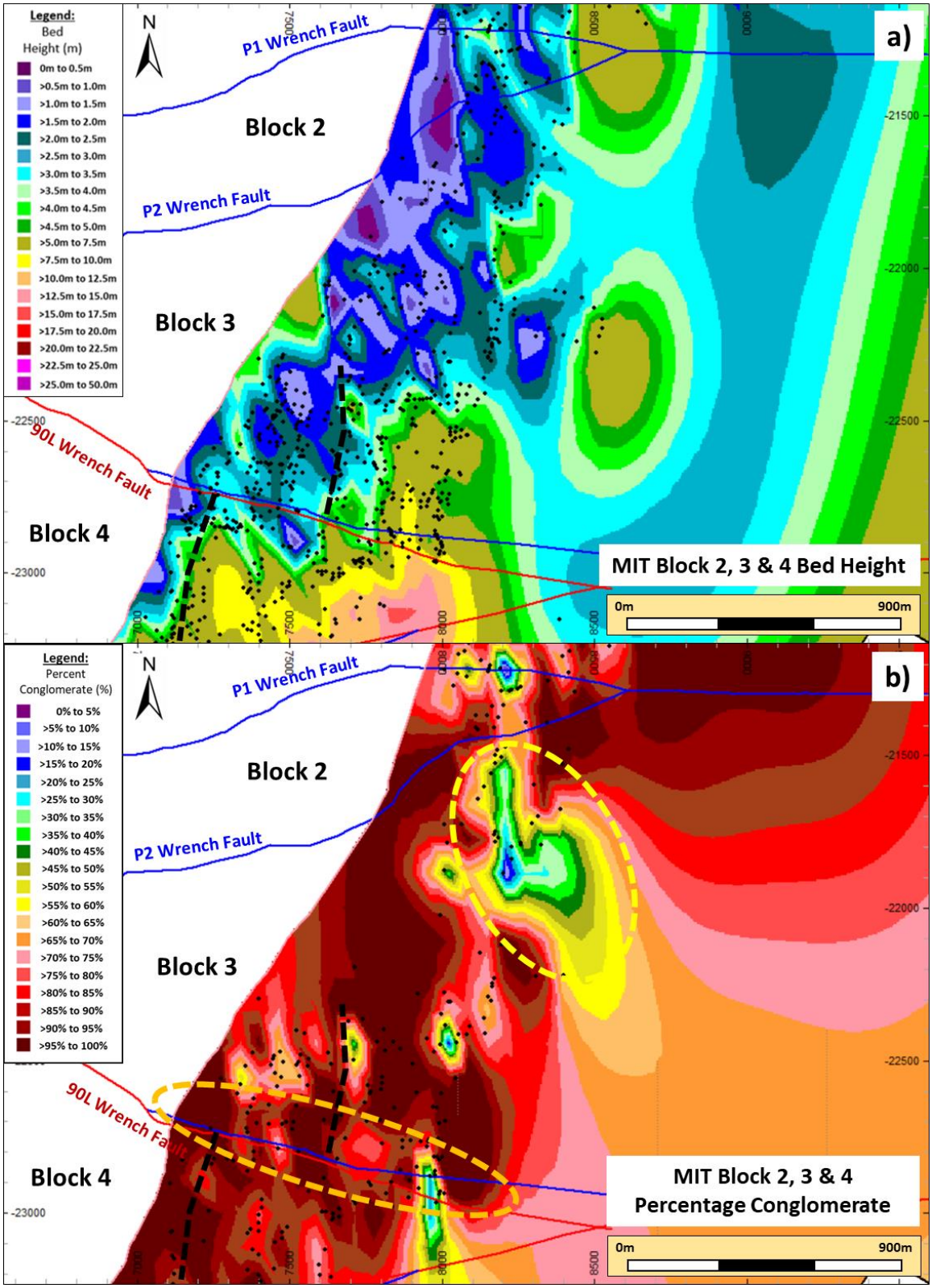


Figure 167: Enlarged Block 3 palinspastic reconstruction for a) bed height for MIT and b) for percentage conglomerate for MIT.

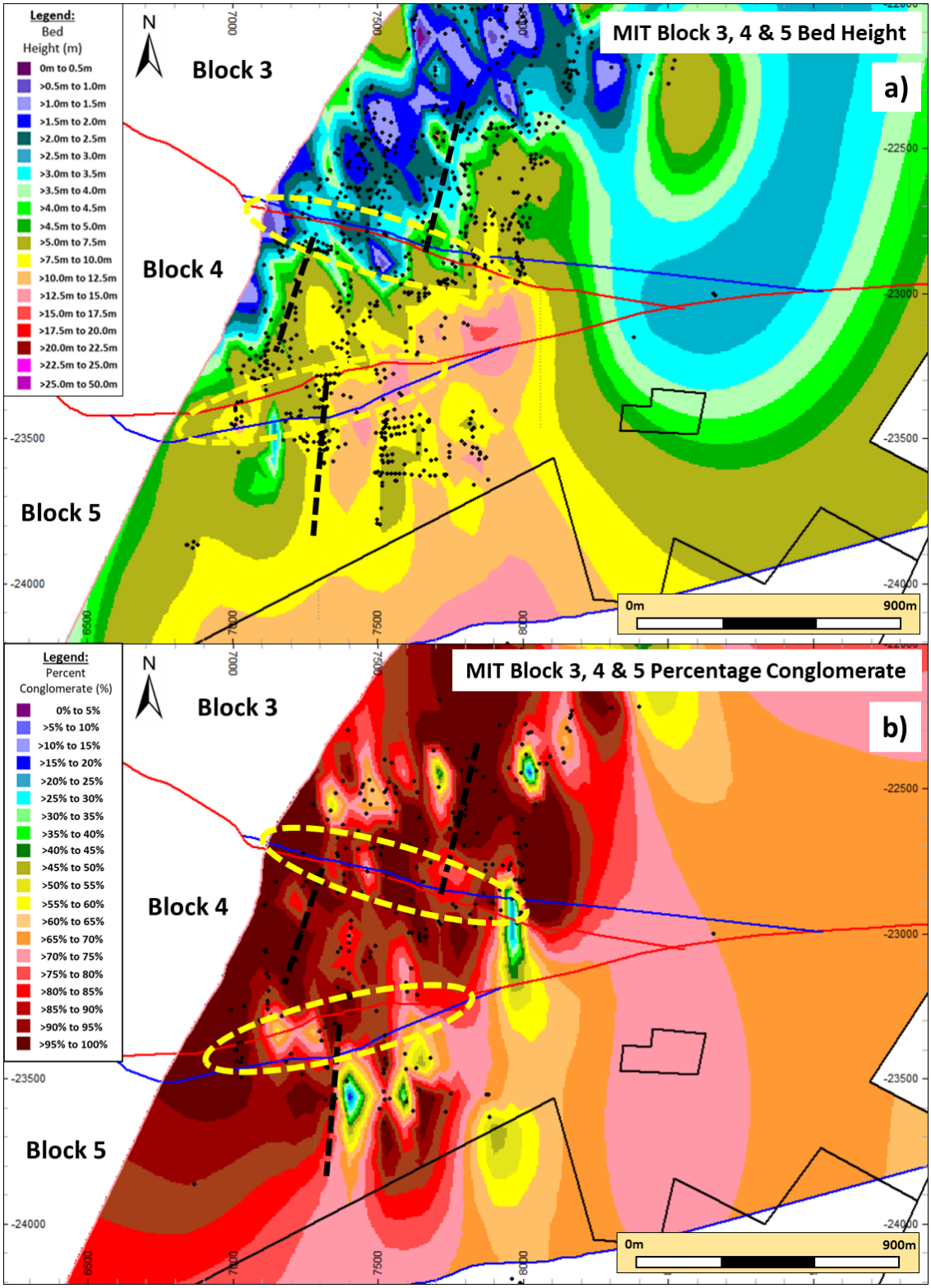


Figure 168: Enlarged Block 4 palinspastic reconstruction for a) bed height for MIT and b) for percentage conglomerate for MIT.

i) MIQ

i) MIQ Bed Height

The MIQ bed height (Figure 169) palinspastic reconstruction presents the westward thinning of all the UEUpper Elsburg beds towards the UEUpper Elsburg sub-outcrop. The rate of this attenuation is low in the northnorthern half of Block 1. The rate of thinning towards the sub-outcrop increases towards the south, with a zone of total elimination of the MIWMIQ over the P2 Wrench in the north of Block 3. Bed height for the MIQ appears to generally increase southwards up until the 90L Wrench is reached. The MIQ is abruptly thinned over BlockBlocks 4 and 5 to the south of 90L Wrench. This could be the result of uplift across the 90L Wrench resulting in higher rates of erosion by the overlying MBB. The maximum bed height attained north of 90L Wrench is ±12.5 m to 15m15 m, while over BlockBlocks 4 and 5, bed height ranges between 0 m close to the UEUpper Elsburg sub-outcrop in the west to a maximum of ± 3.0 m to 3.5 m.

Bed height trends (red arrows) are NW to -SE in Block 1, while to the south in Blocks 3 and 5 these trend NNW to -SSE.

ii) MIQ Percentage Conglomerate

The northern half of Block 1 for the MIQ depicts a low general percentage conglomerate (Figure 170) associated with the higher average bed height (Figure 169). As the MIQ bed height attenuates towards the sub-outcrop in the south of Block 1, percentage conglomerate significantly increases. This could be associated with local winnowing proximal to the sub-outcrop. Percentage conglomerate for the MIQ becomes sporadic towards the south over the P1 Wrench and P2 Wrench combination. Percentage conglomerate (associated with the higher bed height) over Block 3 decreases again, tilluntil Block 4 in the south is reachreached and percentage conglomerate is seen to increase in localised areas to between >60% and 65% across the Fargo Wrench. Primary percentage conglomerate trends appear to primarily trend NNW to -SSE.

iii) MIQ Average and Maximum Clast Size

Little average clast size data is available for the MIQ (Figure 171) in the north due to the age of the data. However, average clast size appears to be up to between 6mm6 mm to 24mm24 mm across the project area. A slight increase is encountered in the south over Blocks 4 and 5 where an average clast size of ±24 mm to 48 mm asis sporadically attained. Average clast trends appear to trend NNW-SSE. However, this inis based upon limited data.

Data density and trend for maximum clast size for the MIQ (Figure 172) is similar to that for average clast size with a NNW-SSE trend in the south. Maximum clast size in the south may attain >48 mm to 72 mm.

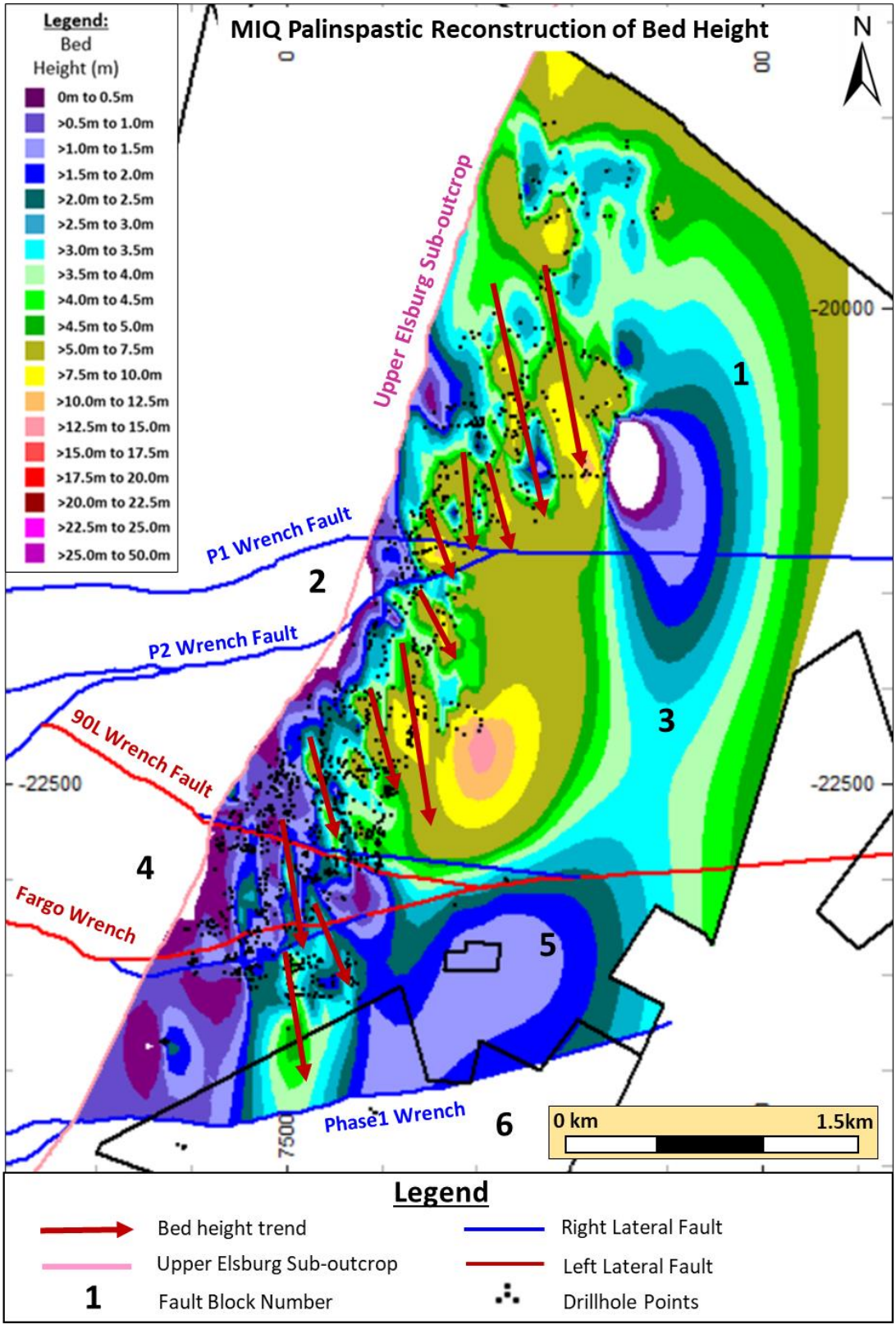


Figure 169: Palinspastic bed height reconstruction for MIQ.

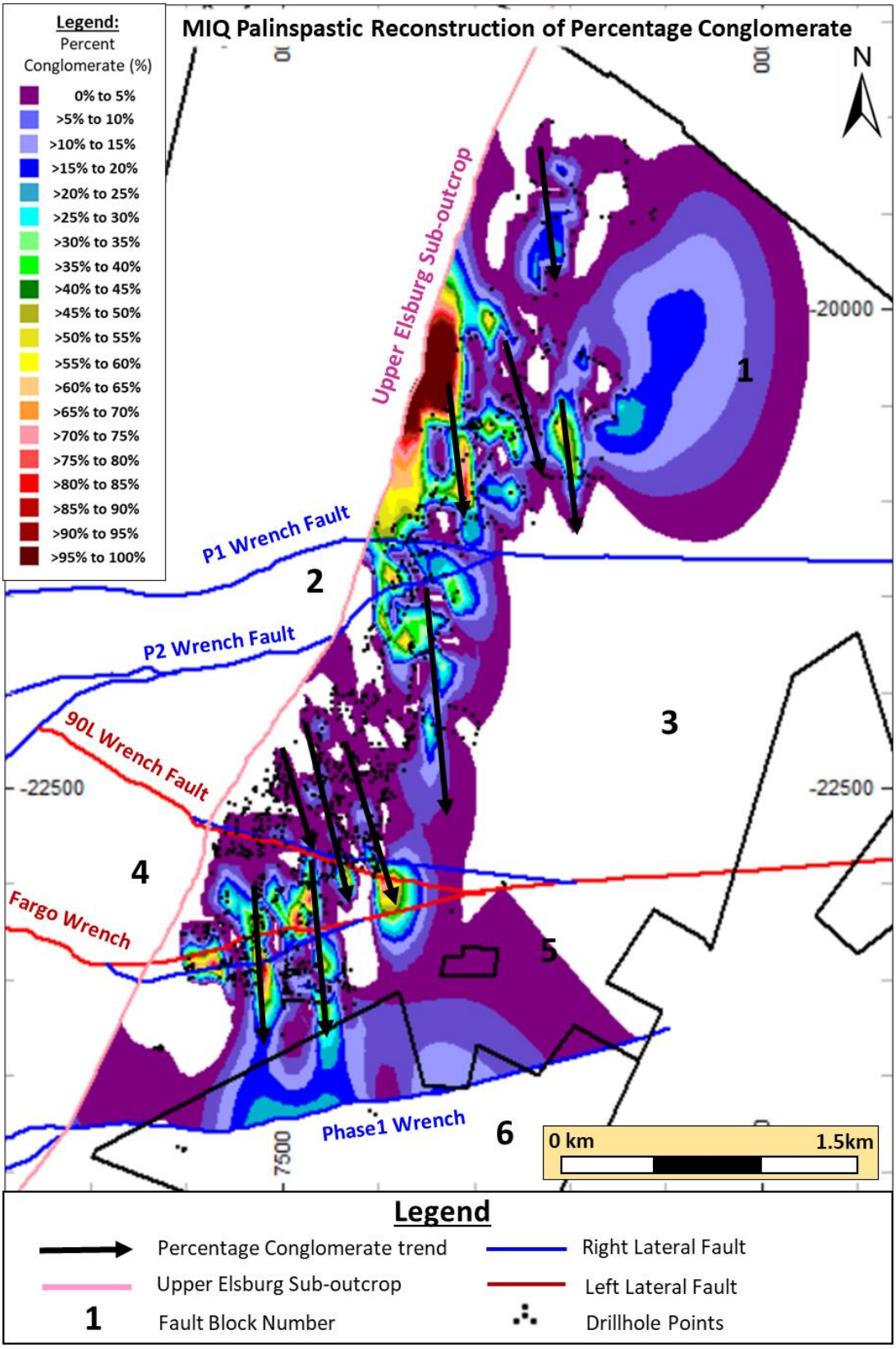


Figure 170: Palinspastic percentage conglomerate reconstruction for MIQ.

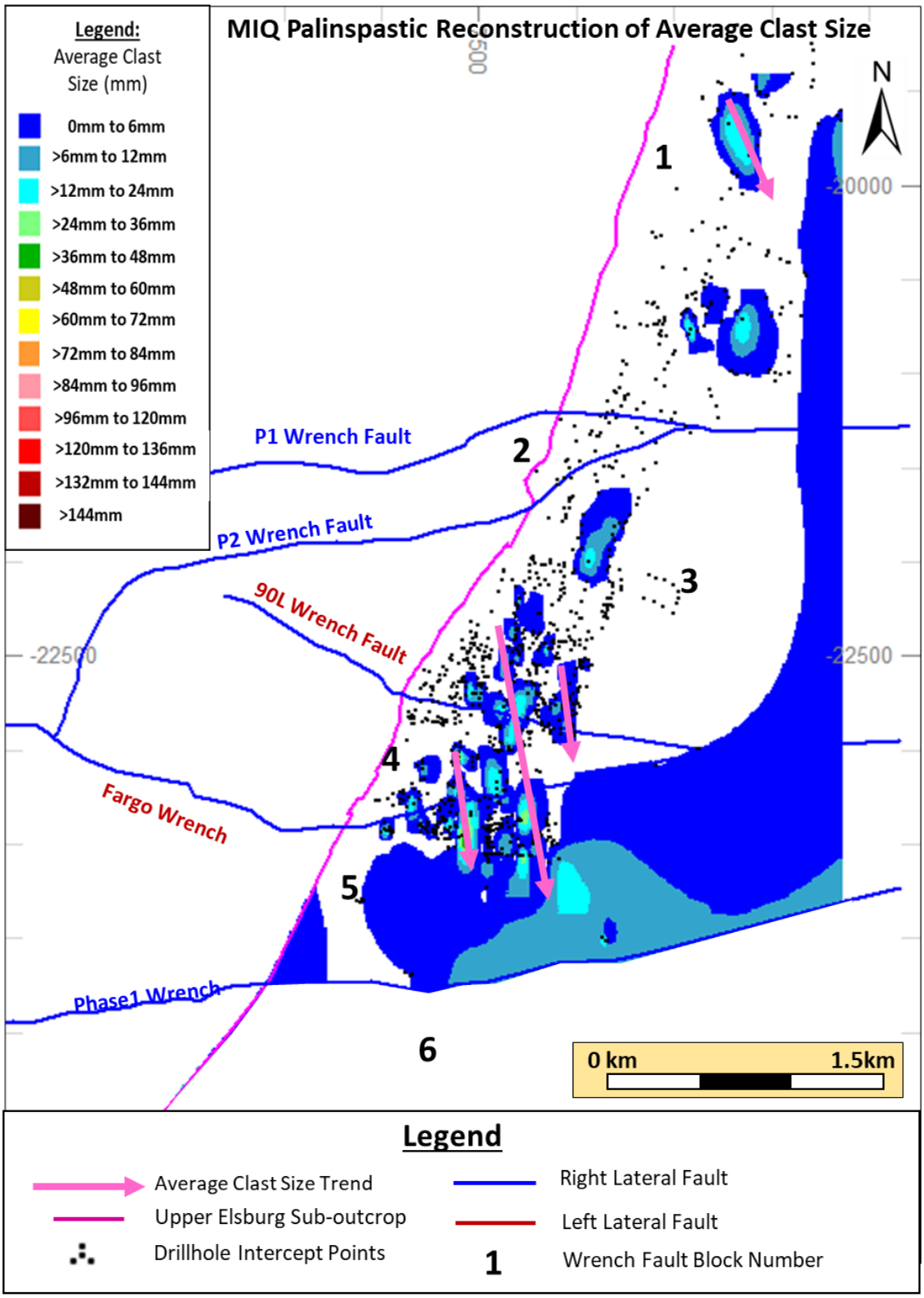


Figure 171: Palinspastic average clast size Reconstruction for MIQ.

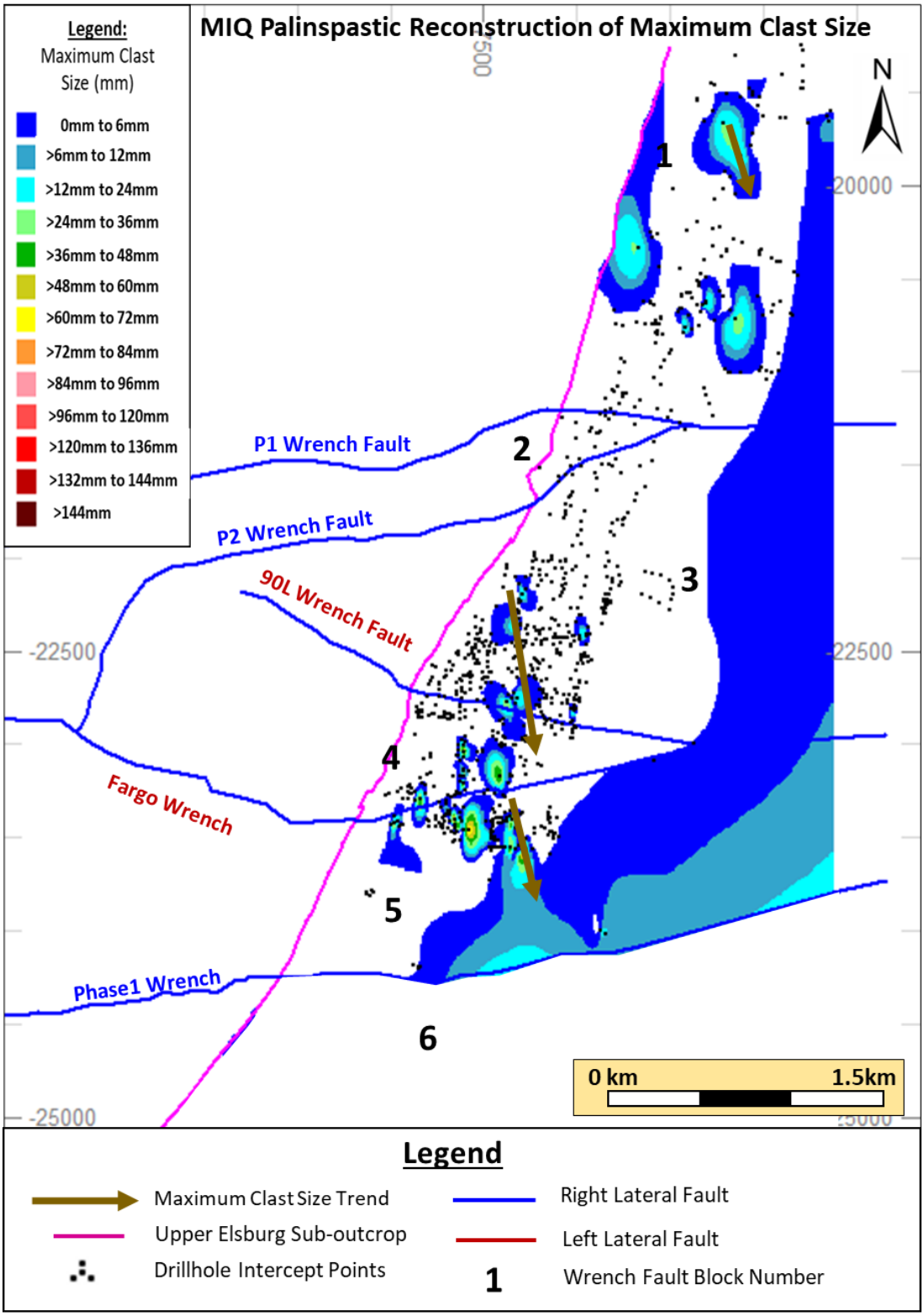


Figure 172: Palinspastic maximum clast size reconstruction for MIQ.

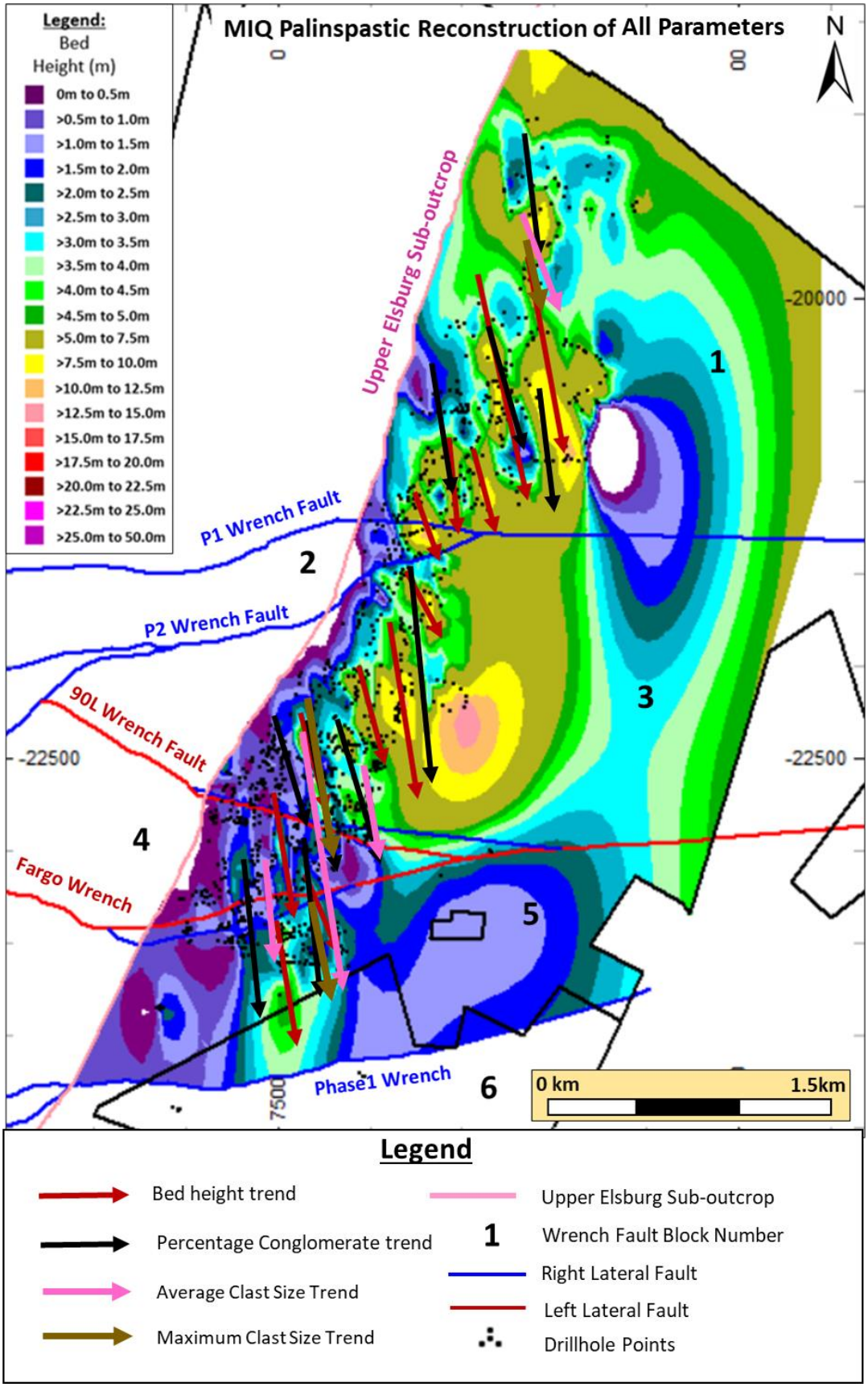


Figure 173: Palinspastic Reconstruction for the MIQ - All Parameters

iv) MIQ Detailed Plots

Figure 174 a) and b) present an enlarged view over Block 2 for bed height and percentage conglomerate, respectively. A zone of higher (>5.0 m) bed height appears dislocated across P2 Wrench by ±200 m (right-lateral) with termination of the associated western zone of low de bed height being terminated on P2 Wrench. Close in towards sub-outcrop the MIQ is totally eliminated by erosion by the overlying MBB. The thinner zone over Block 2 shows an increase in percentage conglomerate which might indicatedindicate a localised area of winnowing. Sense of dislocation across P2 Wrench is only apparent and might be attributable to a vertical movement component across P2 Wrench down towards the south. The timing of this relative dislocation is not necessarily syn-depositional to the MIQ and could be related to local uplift to the north associated with erosion and subsequent erosion by the overlying MBB.

Figure 175 a) and b) presents an enlargement of Block 3 for bed height aand percentage conglomerate, respectively. The MIQ is completely eliminated up against the P2 Wrench in Block 3 to the north. The thinner MIQ in Block 3 abutting on P2 Wrench is also associated with a higher percent conglomerate, as highlighted by the yellow ellipse in Figure 175 b) highlighted by the yellow ellipse.). The higher bed height in Block3Block 3 abutting onto 90L Wrench in the south is characterised by low percentage conglomerate of between 0% to 15% conglomerate. A distinct bed height trend of NNW to -SSE (black dashed line) is identifiable. This higher bed height trend appears to be dislocated (apparent) by some 450 m left -lateral shift. As previously indicated, this dislocation is only apparent and could also be attributable to a vertical movement component on 90L Wrench. A marked increase in percentage conglomerate in Block 4 (Yellowyellow polygon) is also evident and could be attributed to local possible winnowing across the relatively uplifted Block 4.

The enlargement for bed height and percentage conglomerate over Block 4 (Figure 176 a) and b)), respectively) presents the apparent dislocation (possible left-lateral 400 m relative dislocation) across 90L Wrench. Possible apparent right-lateral relative dislocation of >600m600 m across Fargo Wrench could be interpreted by defining the western edge of a zone of higher bed height in Block 5 (black dashed line) in Figure 176 a.). Possible additional evidence of syn-sedimentary influence of Fargo Wrench is defined by the alternating nodes of variable bed height and percentage conglomerate straddling and lying adjacent to Fargo Wrench.

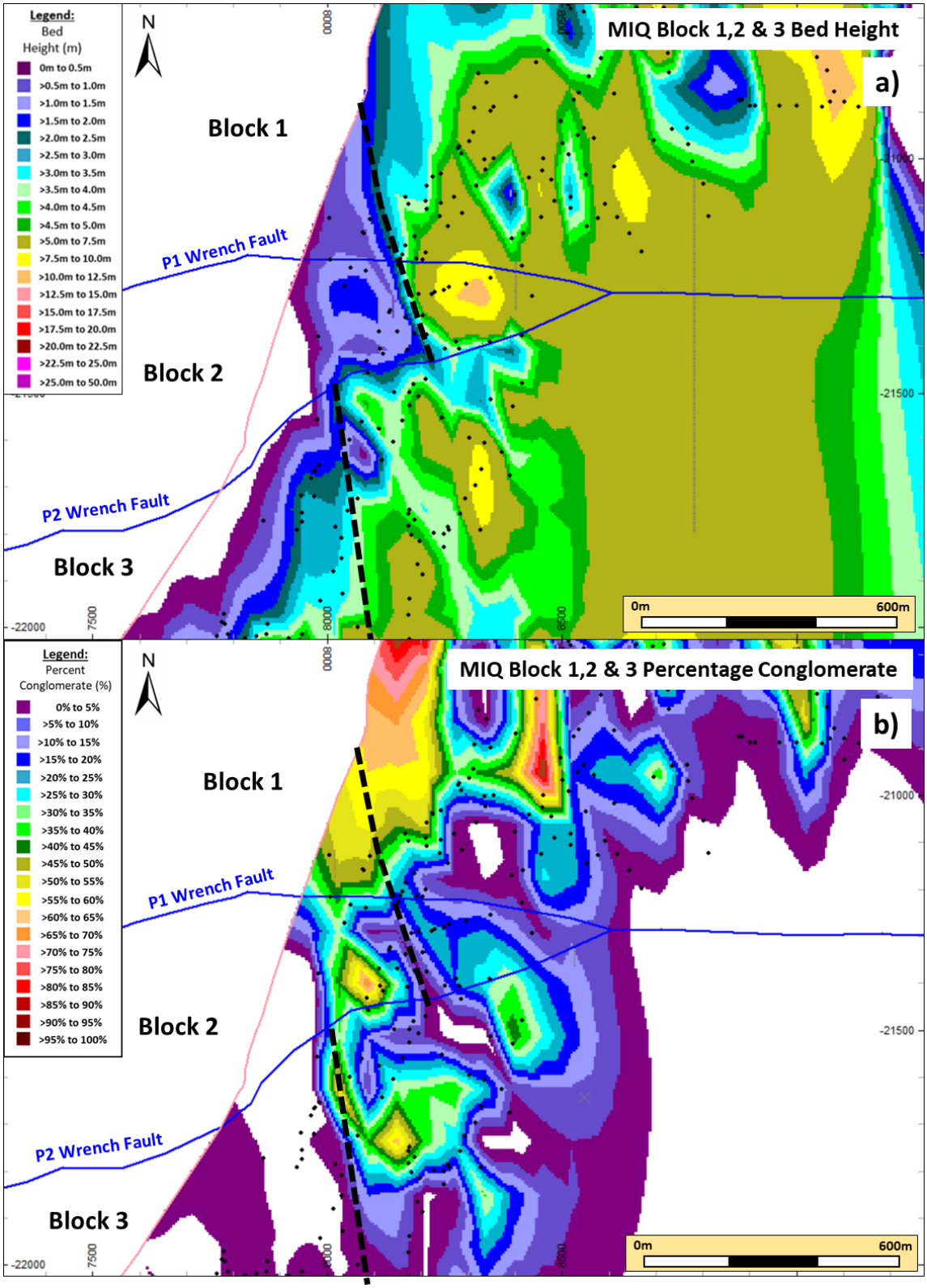


Figure 174: Enlarged Block 2 palinspastic reconstruction for a) bed height for MIQ and b) for percentage conglomerate for MIQ.

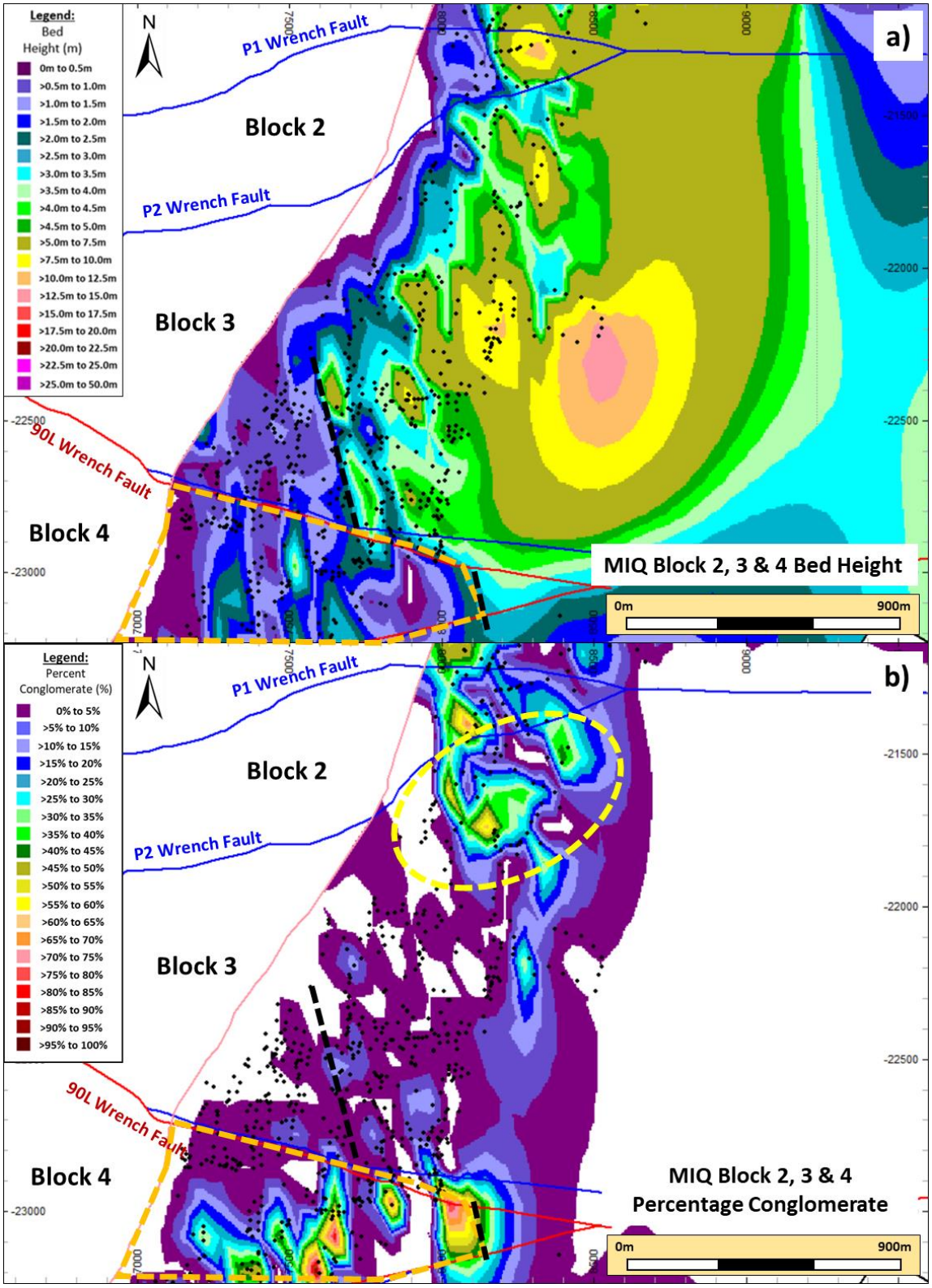


Figure 175: Enlarged Block 3 palinspastic reconstruction for a) bed height for MIQ and b) for percentage conglomerate for MIQ.

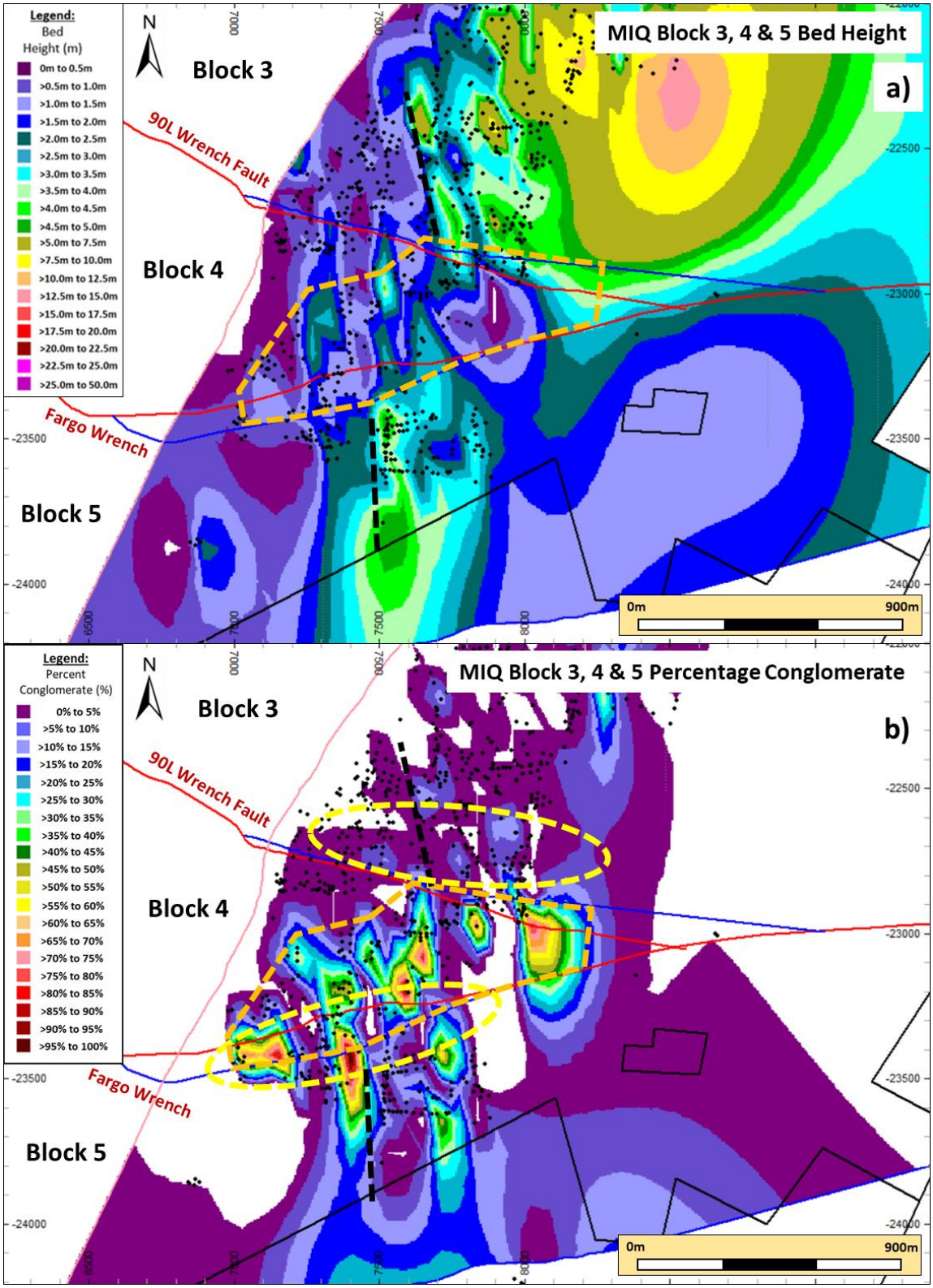


Figure 176: Enlarged Block 4 palinspastic reconstruction for a) bed height for MIQ and b) for percentage conglomerate for MIQ.

j) MBB

i) MBB Bed Height

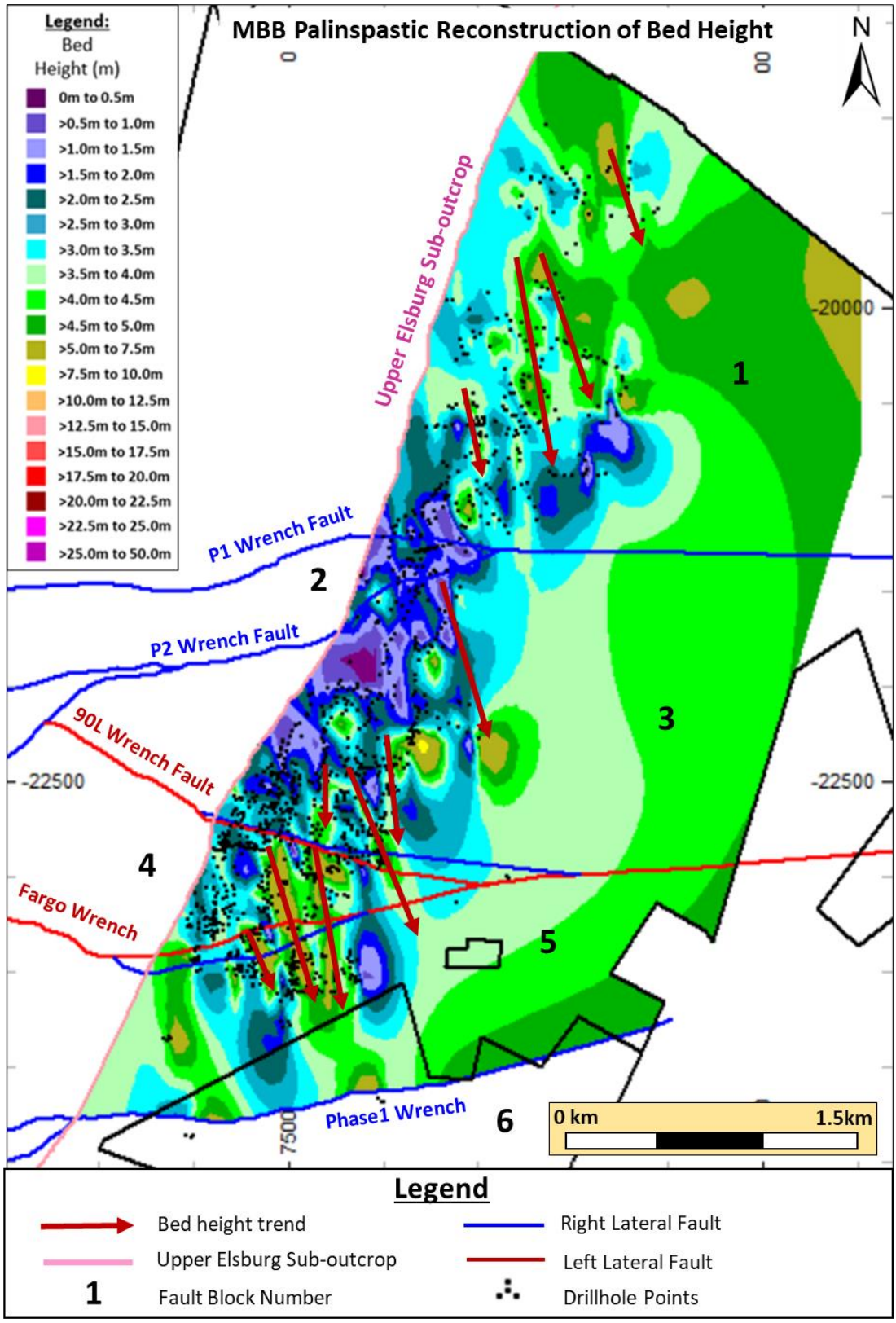


Figure 177: Palinspastic bed height reconstruction for MBB.

ii) MBB Percentage Conglomerate

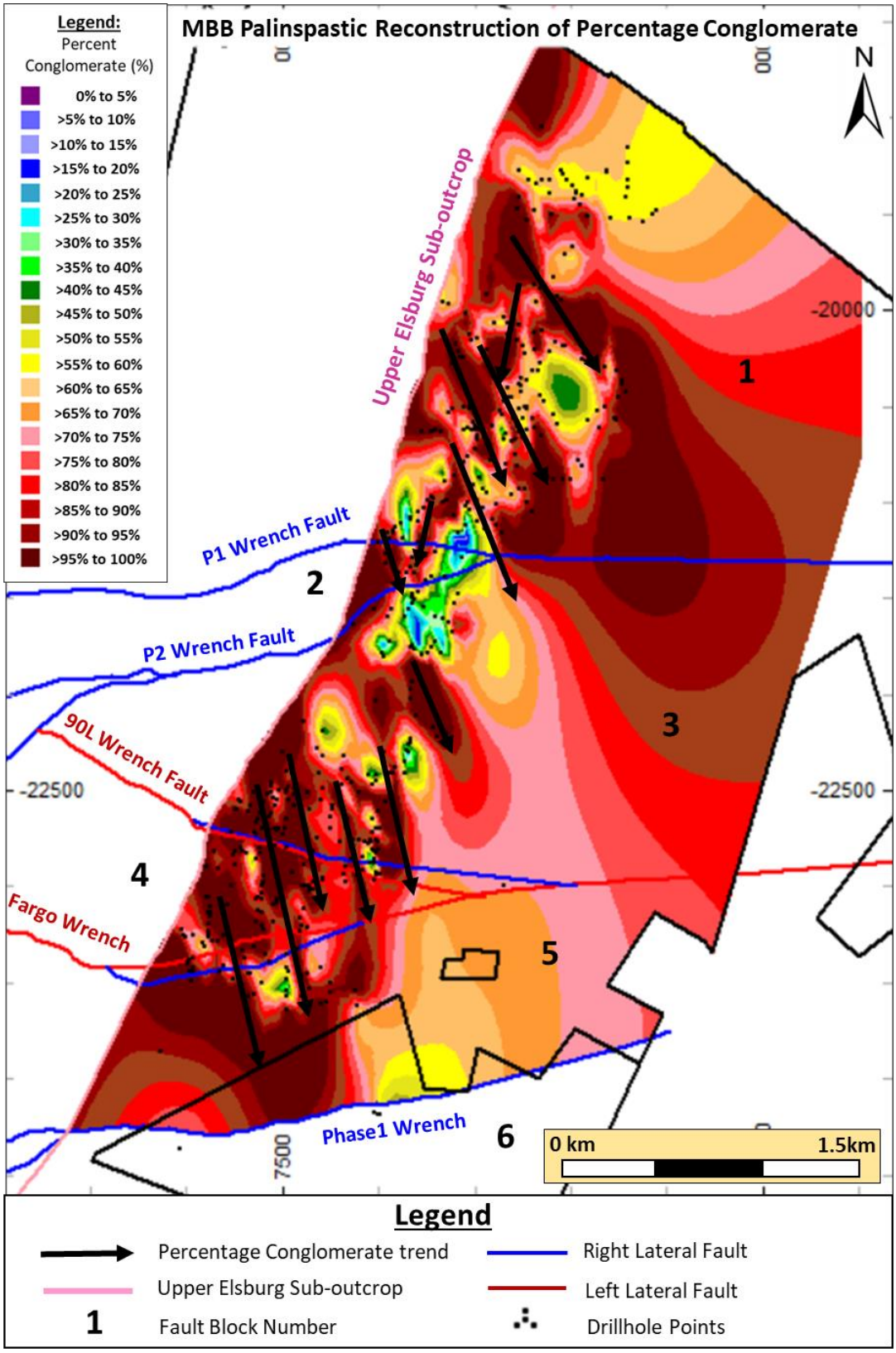


Figure 178: Palinspastic percentage conglomerate reconstruction for MBB.

iii) MBB Average and Maximum Clast Size

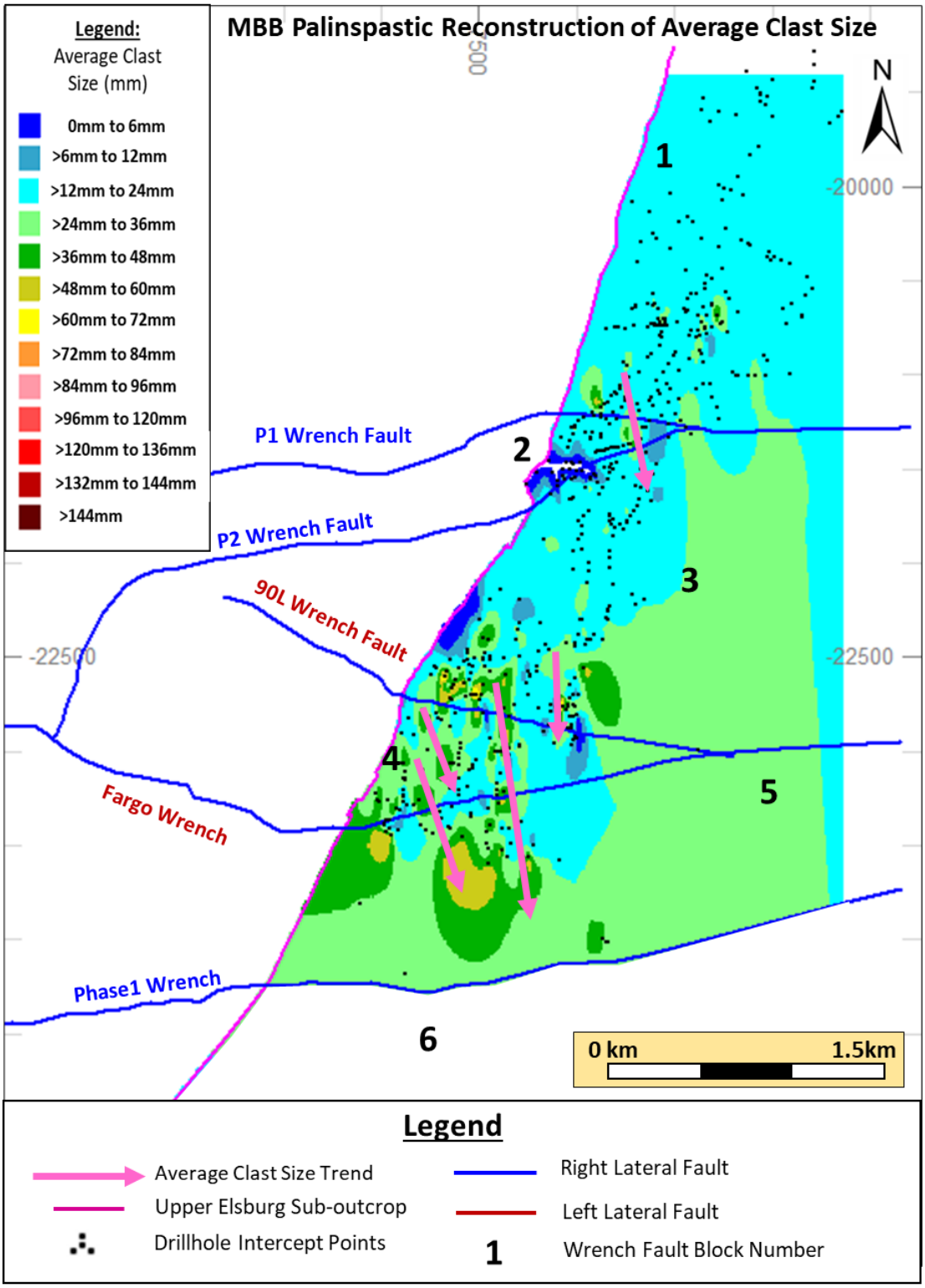


Figure 179: Palinspastic average clast size reconstruction for MBB.

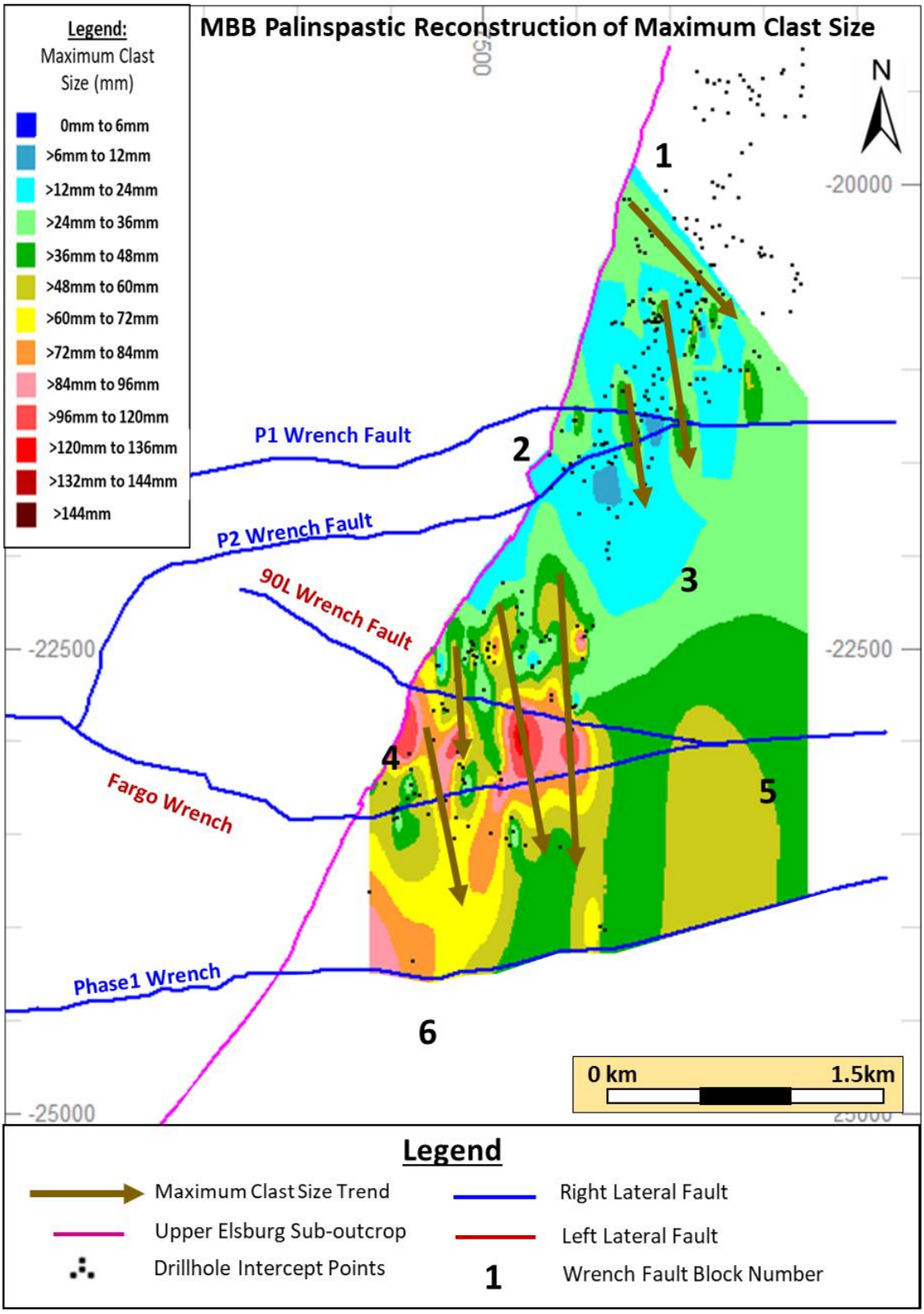


Figure 180: Palinspastic maximum clast size reconstruction for MBB.

k) MBT

i) MBT Bed Height

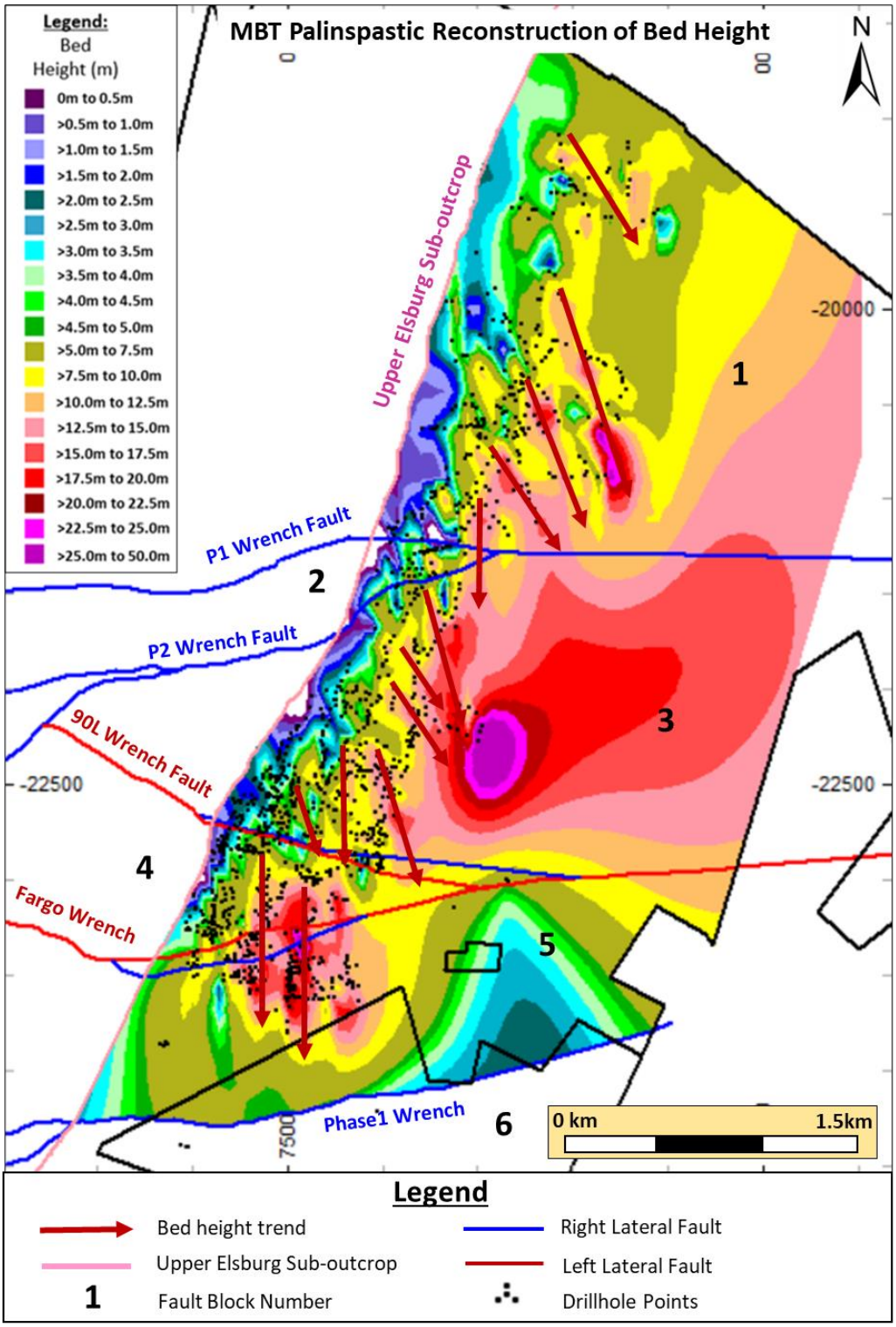


Figure 181: Palinspastic bed height reconstruction for MBT.

ii) MBT Percentage Conglomerate

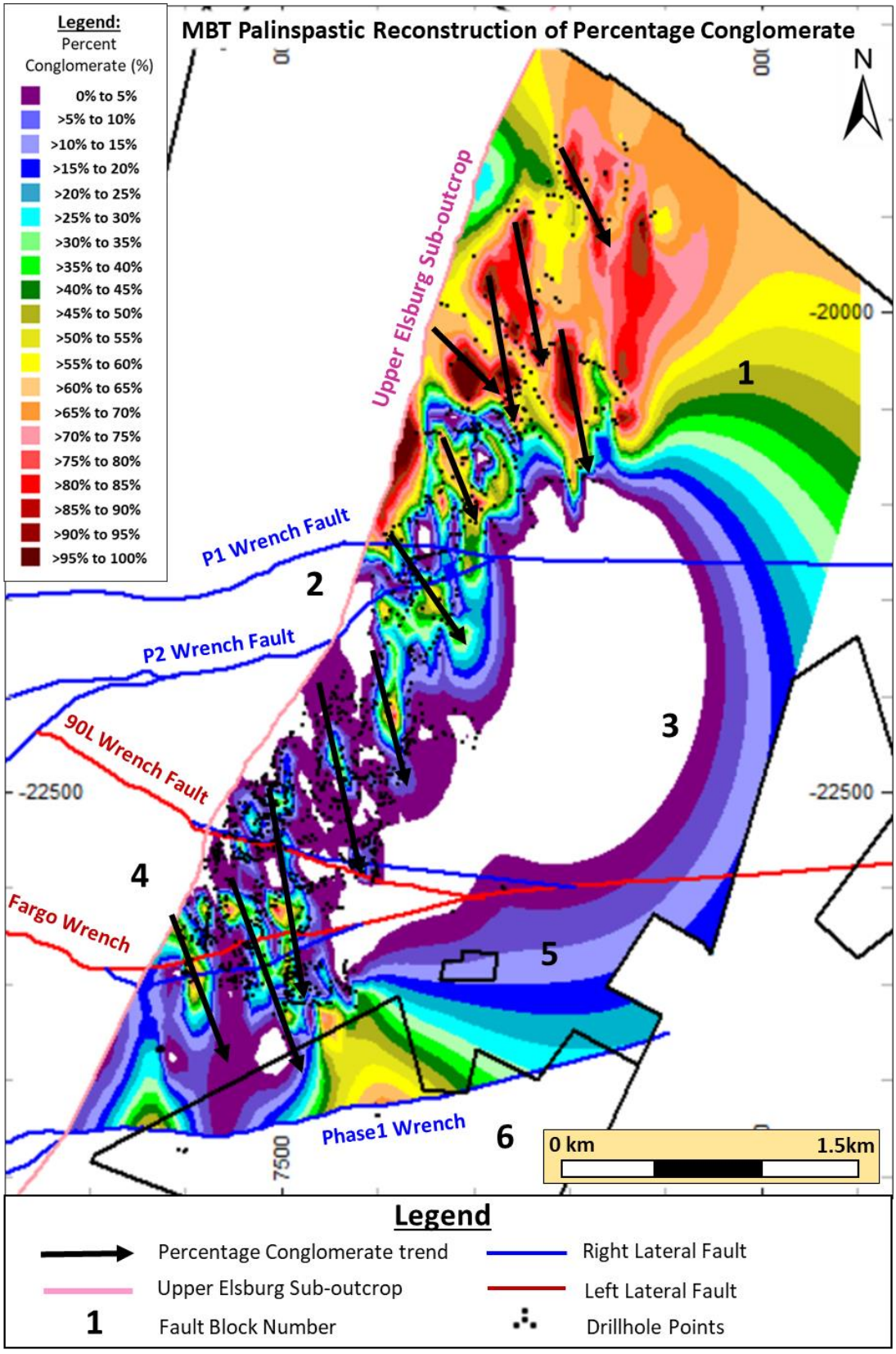


Figure 182: Palinspastic percentage conglomerate reconstruction for MBT.

iii) MBT Average and Maximum Clast Size

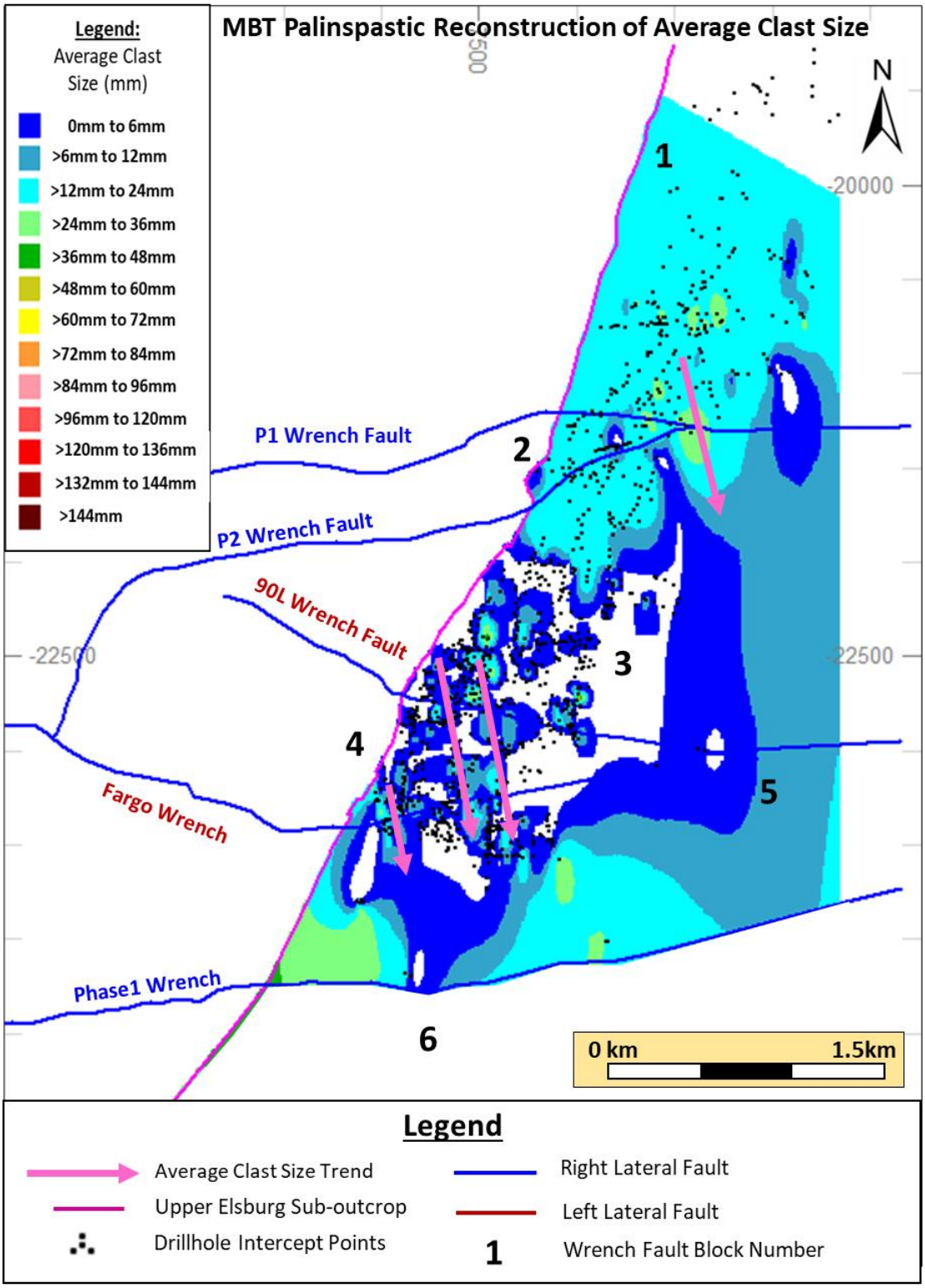


Figure 183: Palinspastic average clast size reconstruction for MBT.

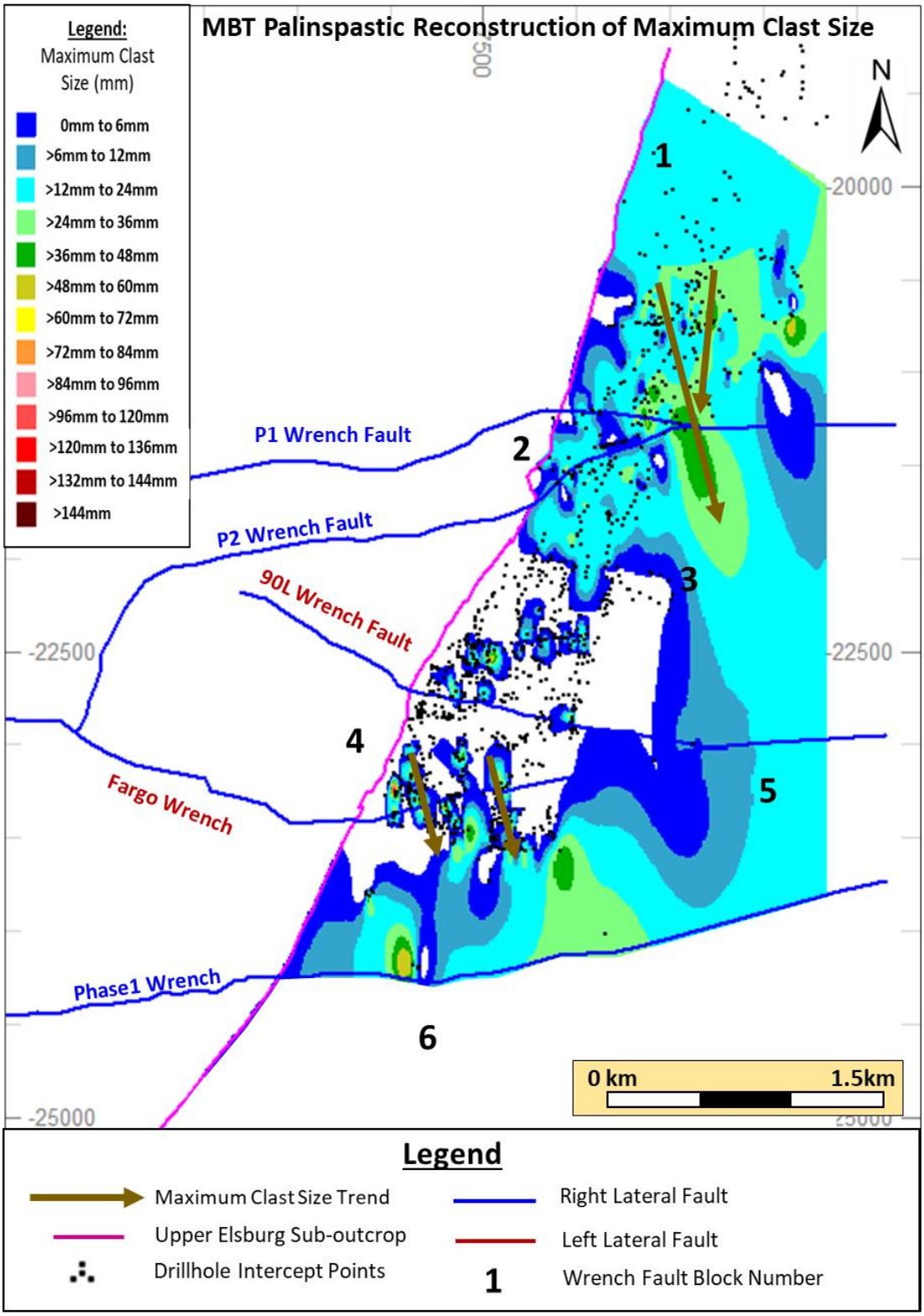


Figure 184: Palinspastic maximum clast size reconstruction for MBT.

l) VCR

i) VCR Bed Height

In general, bed height for the VCR (Figure 185) seldom exceeds 2.0 m to 2.5 m. The palinspastic reconstruction of VCR bed height in Figure 185 presents a slightly higher bed height in the North. Bed height for the VCR appears to decrease over a wide zone from the southern half of Block 1 to right over Block 4 in the south. VCR bed height appears to increase again in the south in Block 5.

VCR bed height trends appear to change from approximately NW-SE to NNW-SSE as the Upper Elsburg sub-outcrop is crossed.

ii) VCR Percentage Conglomerate

Very little percentage conglomerate data for the VCR was available for the drillholes to the west of the Upper Elsburg sub-outcrop and in the northern half of Block 1(Figure 186) and thus precluded interpretation in these areas. Percentage conglomerate is highly variable for the VCR, however general trends are observable. Zones of higher percentage conglomerate are located within the southern half of Block 1 as well as straddling the P1 and P2 Wrench structures. Percentage conglomerate decreases southwards towards the 90L Wrench. An increase in percentage conglomerate occurs in the southern half of Block 4 and into Block 5 in the south. Percentage conglomerate trends for the VCR are interpreted to trend NNW to SSW as with VCR bed height trends observed in Figure 185.

iii) VCR Average and Maximum Clast Size

Average clast size for the VCR to the east of the UE sub-outcrop generally decreases from north to south (Figure 187). Highest average clast size (>24 mm to 36 mm) occurs near the p1 Wrench approximately 1 km from sub-outcrop. Average clast size decreases southwards towards the 90L Wrench where it increases slightly again as the VCR passes over Block 4 and into Block 5. Here average clast size varies between >6 mm and 24 mm.

Limited maximum clast size data is available for the VCR in the north of Block 1 and east of the UE Sub-outcrop (Figure 188). However maximum clast size also decreases towards the south (from a high of>48 mm) in Block 1 to between >6mm to < 48 mm over Blocks 4 and 5 in the south. Average clast size trends, as well as maximum clast size trends exhibit a NNW to SSE orientation.

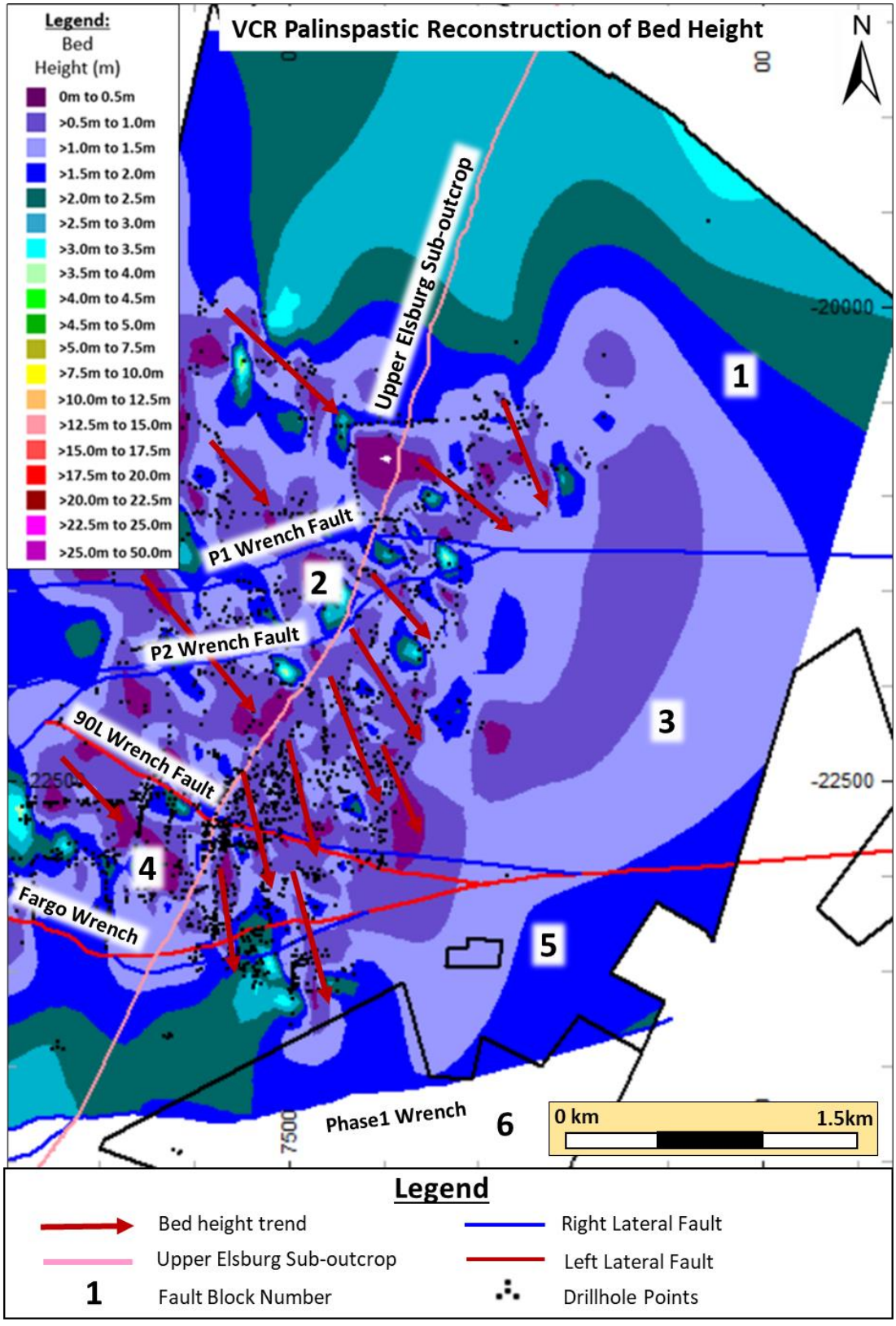


Figure 185: Palinspastic bed height reconstruction for VCR

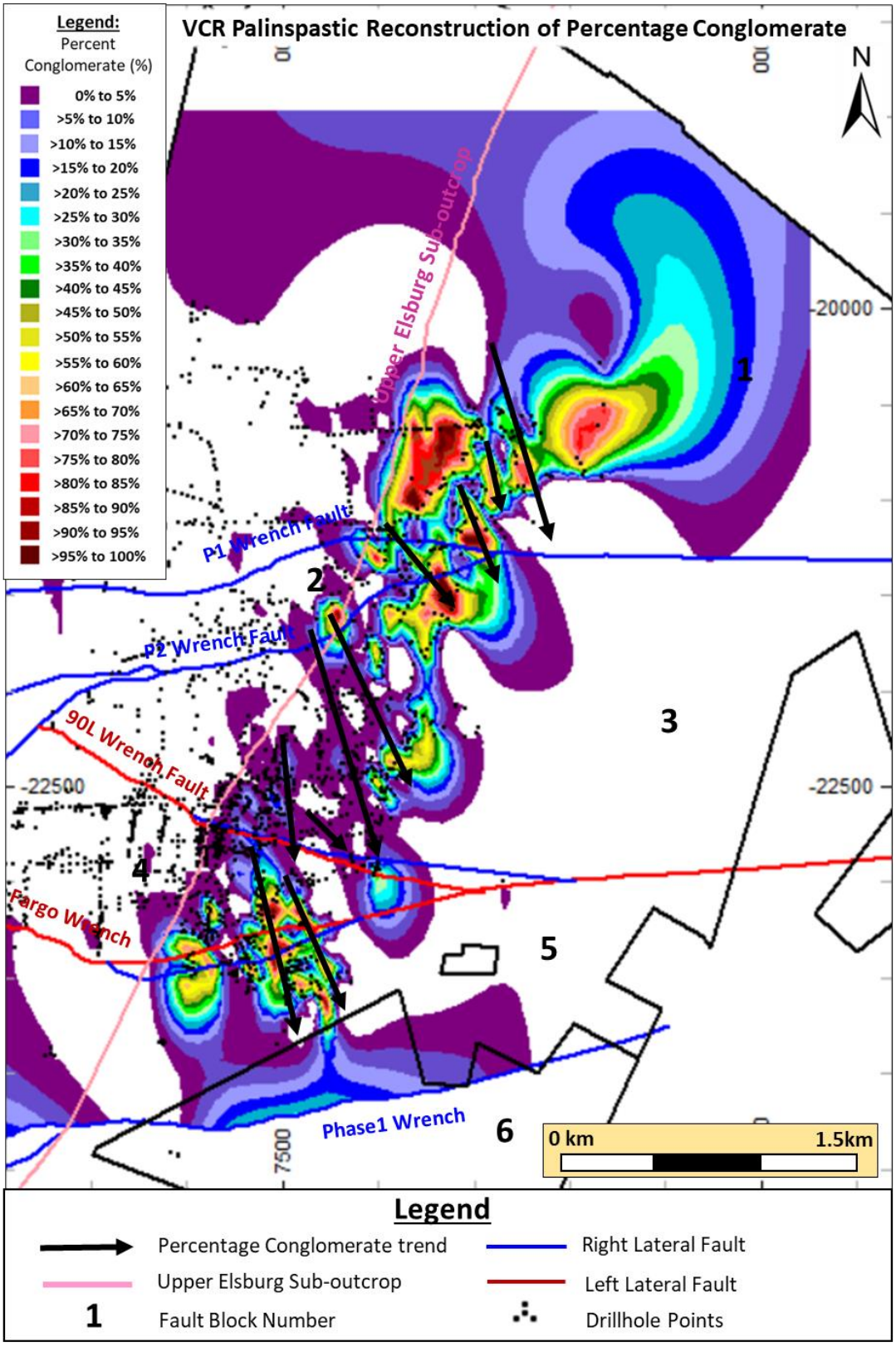


Figure 186: Palinspastic percentage conglomerate reconstruction for VCR

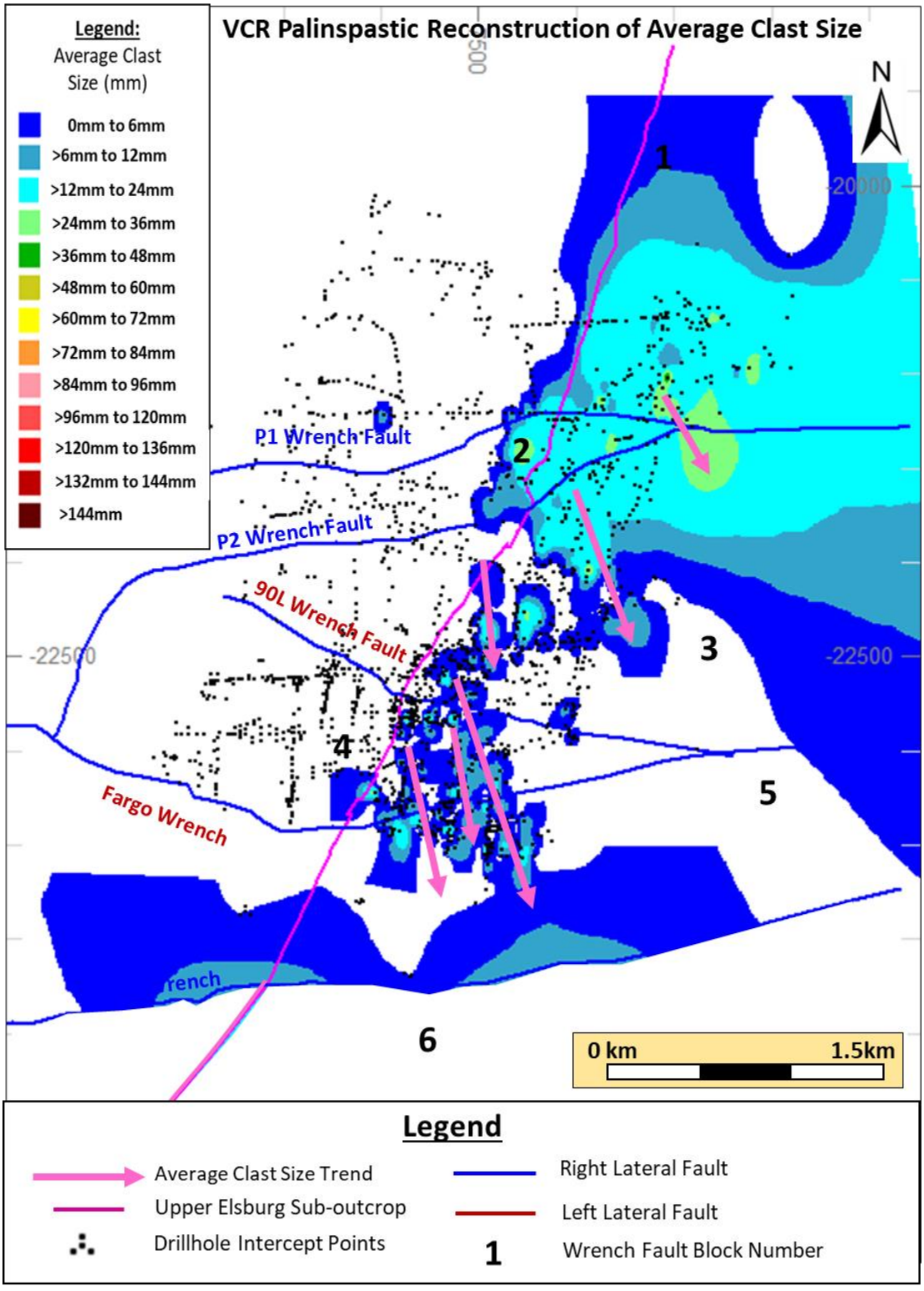


Figure 187: Palinspastic average clast size reconstruction for VCR

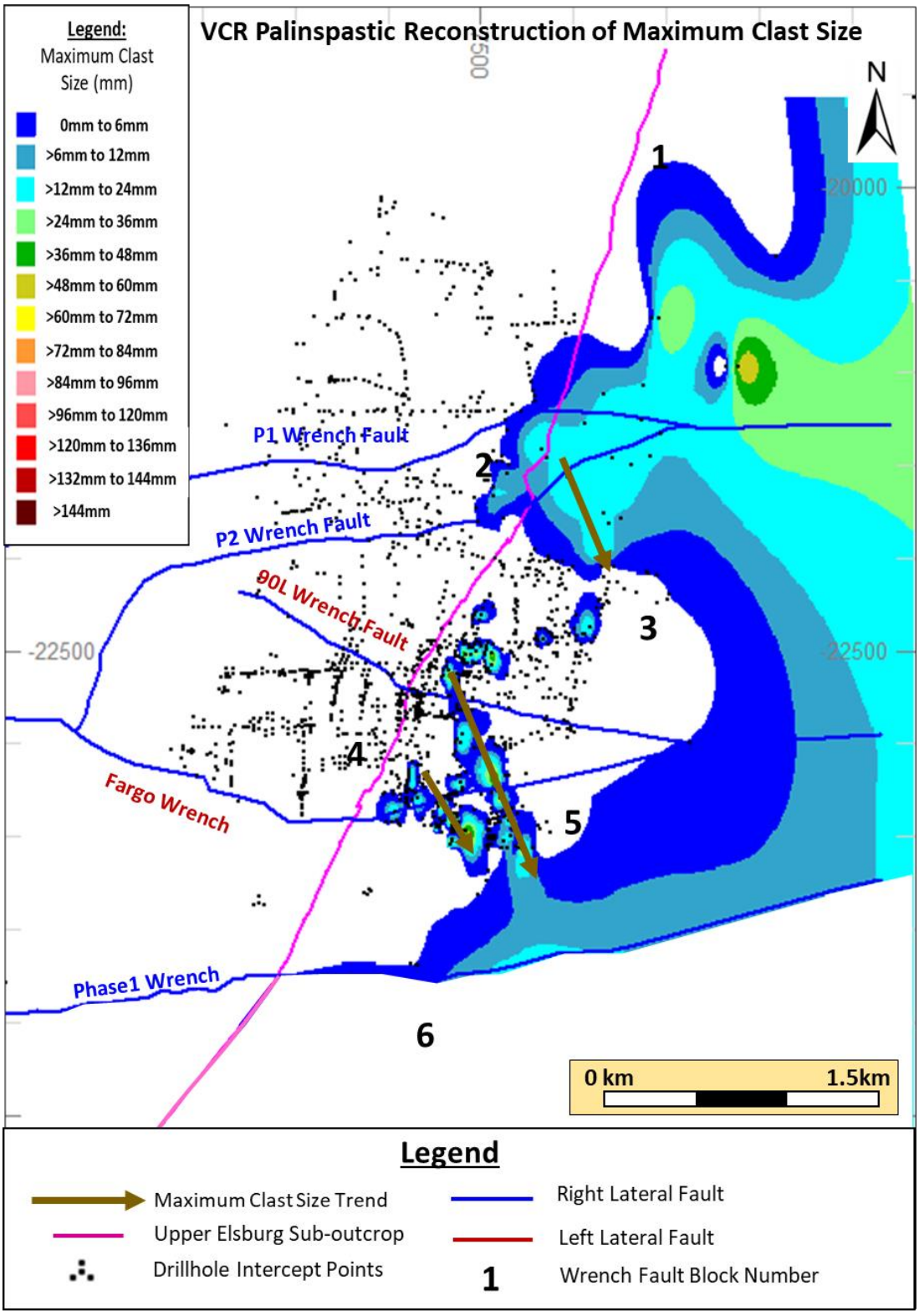


Figure 188: Palinspastic maximum clast size reconstruction for VCR

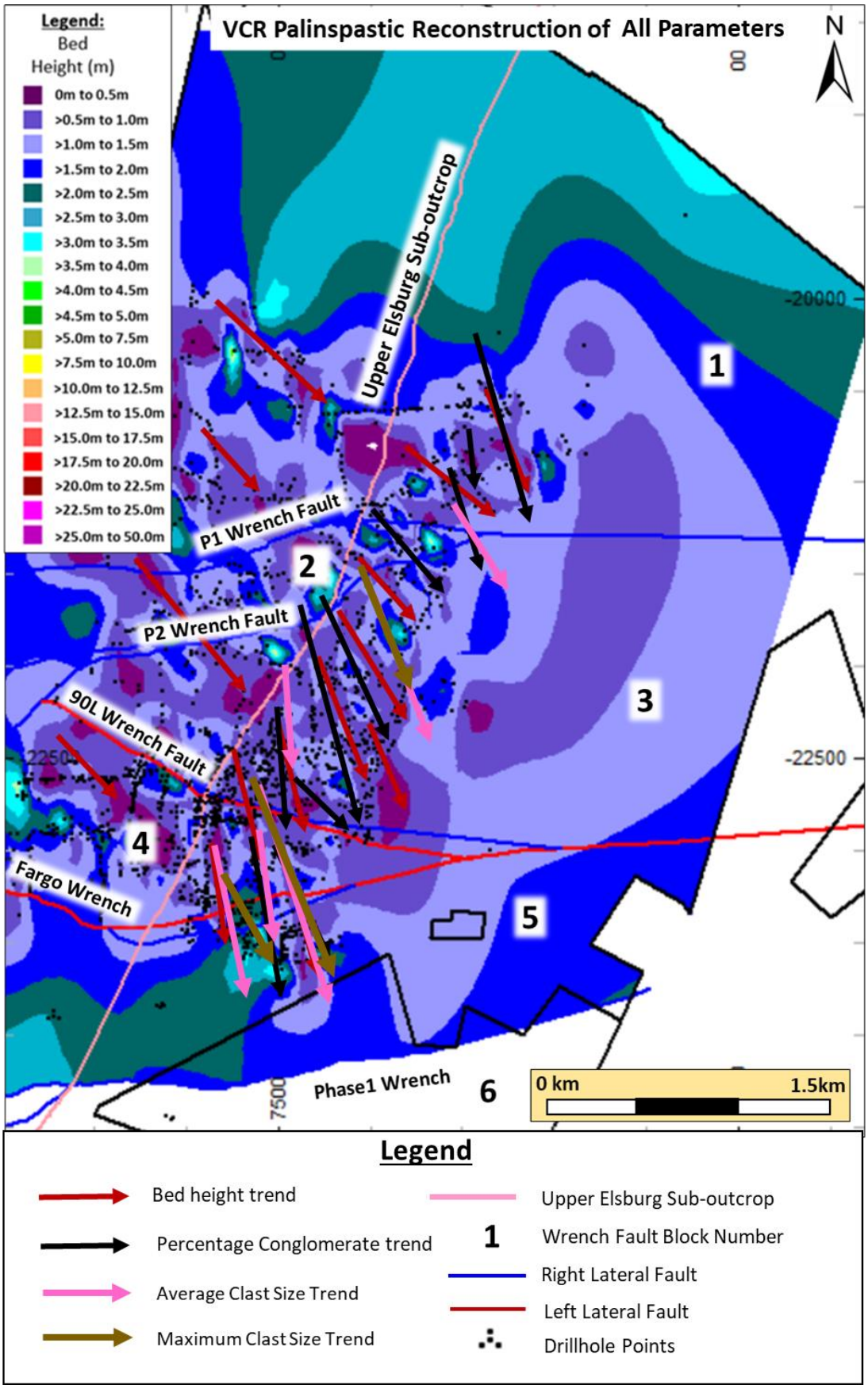


Figure 189: Palinspastic Reconstruction for the VCR - All Parameters

iv) VCR Detailed Plots

Figure 190 a) and b) respectively show the bed height and percentage conglomerate over the P1 and P2 Wrench combination and Block 2. A possible dislocation (based on percentage conglomerate – purple polygon) may be interpreted over P1 Wrench and could possibly be right-lateral in nature. A higher percentage conglomerate zone directly south of P2 (purple dashed polygon) is also visible and indicates a definite right-lateral dislocation on P1 Wrench relative to Block 1 in the north. Possible syn-sedimentary evidence in the form of highly variable nodes of bed height and percentage conglomerate adjacent to the two faults could possibly indicate syn-sedimentary influence on the VCR by the two structures.

In addition, in Figure 190, just to the west of the UE sub-outcrop, two low bed height nodes separated by a small high bed height node (inside yellow ellipse) occur directly west of the Upper Elsburg sub-outcrop. It is thought that these nodes possibly formed as a result of potential footwall topography generated by the underlying Upper Elsburg conglomerate beds.

Figure 191a) and b) respectively present the bed height and the percentage conglomerate for the VCR over Block 3. In general, percentage conglomerate decreases southwards up to the 90L Wrench, while high percentage conglomerate zones (highlighted with yellow ellipse) directly south of the P2 Wrench are present.

In addition, nodes of variable bed height may be seen directly west of the UE sub-outcrop line (circled with a yellow ellipse) in Figure 191a).

Figure 192a) and b) centre on Block 4 in the South. Figure 192a) presents an average lower bed height over Block 4 than encountered directly north and adjacent to the 90L Wrench. Nodes of variable bed height occur directly north of 90L Wrench possibly providing evidence of syn-sedimentary disturbance of the VCR by the 90L Wrench.

The Fargo wrench presents a distinct apparent dislocation between Block4 and Block 5 where VCR in Block 5 is distinctly thicker than in Block. However, movement sense is difficult to establish as percentage conglomerate trends for the VCR are seen to pass relatively undisturbed over Fargo Wrench into Block 5. Variable bed height nodes also occur directly west of the UE sub-outcrop in Block 4, potentially indicating some form of footwall lithological control on VCR sedimentation by the UE conglomerates.

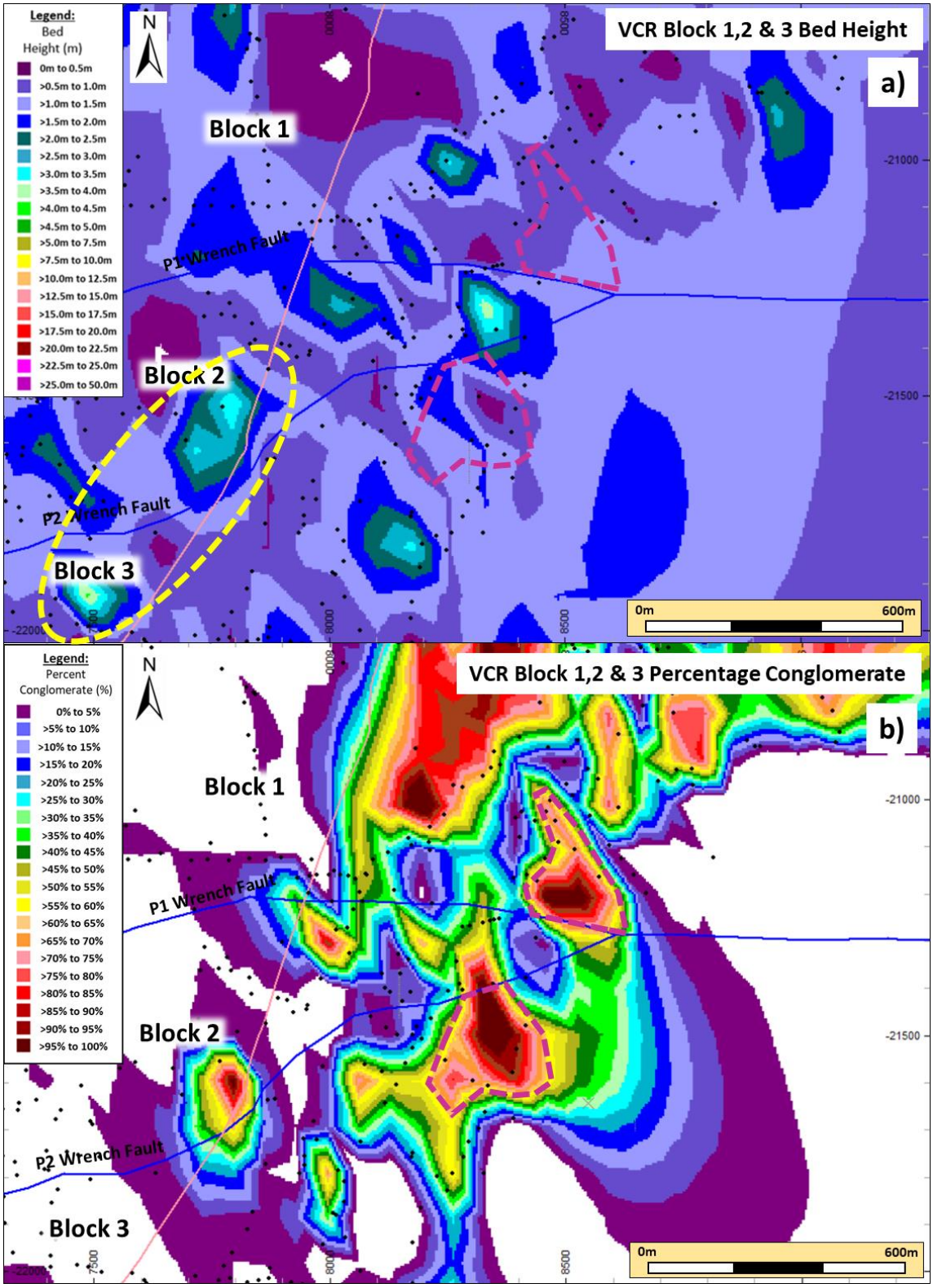


Figure 190: Enlarged Block 2 palinspastic reconstruction for a) bed height for VCR and b) for percentage conglomerate for VCR

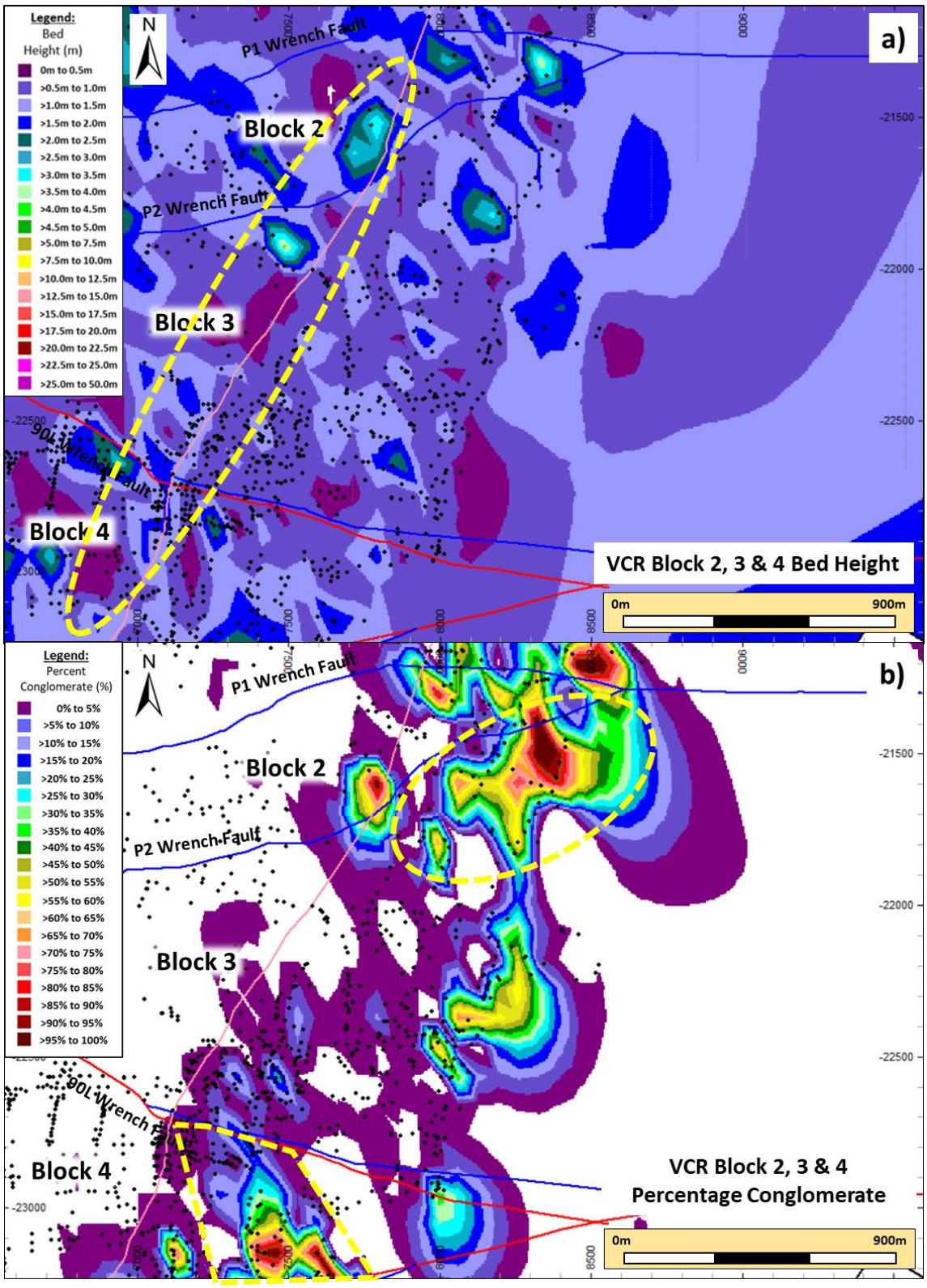


Figure 191: Enlarged Block 3 palinspastic reconstruction for a) bed height for VCR and b) for percentage conglomerate for VCR

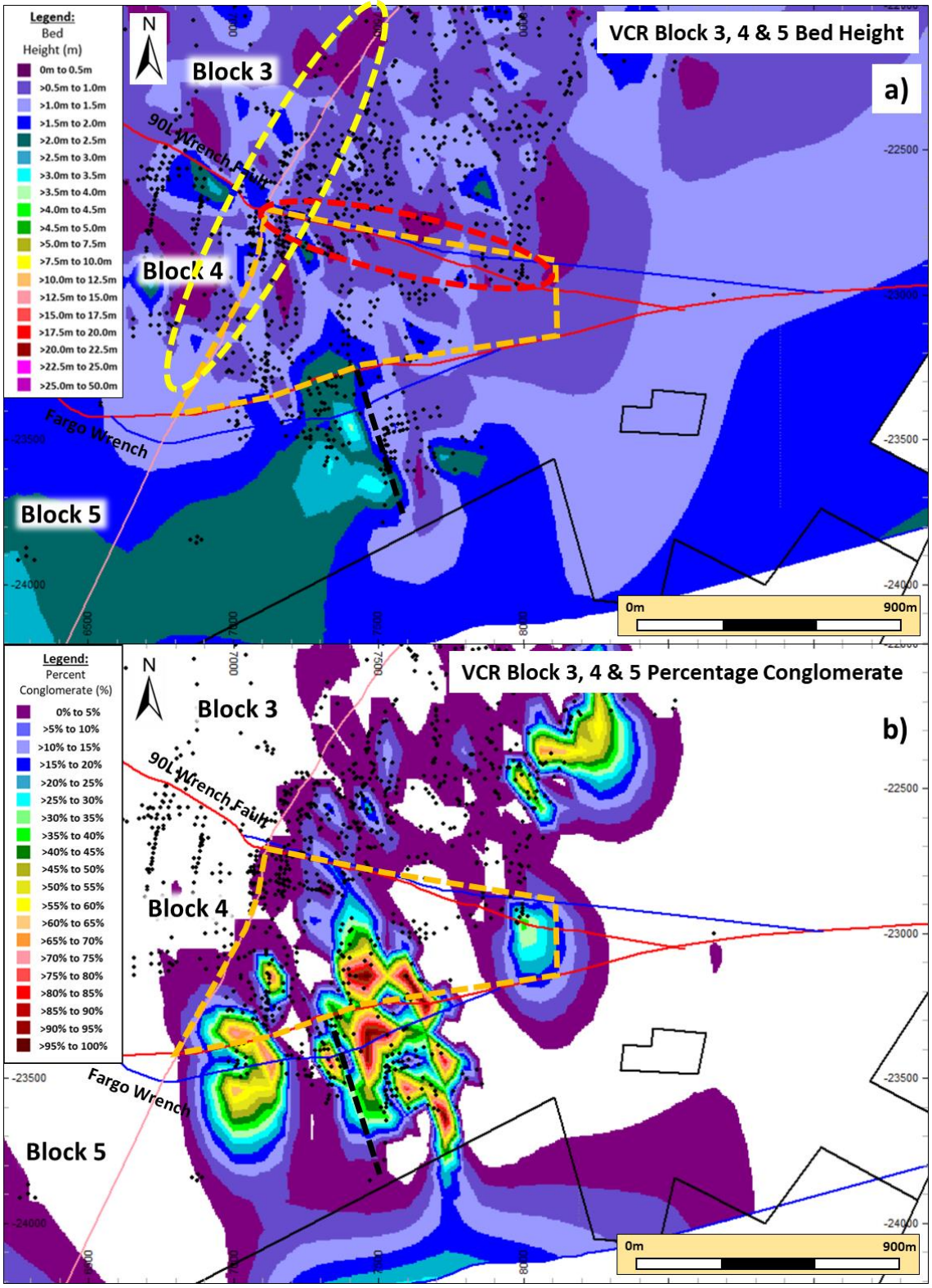


Figure 192: Enlarged Block 4 palinspastic reconstruction for a) bed height for VCR and b) for percentage conglomerate for VCR